Decoupled Voltage Sensitivity Analysis for Cluster-Oriented Smart Grid Operations

Author:
Sasiphong Leksawat

Student ID: 1306097

A thesis submitted in partial fulfillment of the
requirements of the

University of Bolton

for the degree of

Doctor of Philosophy

This research work was carried out

In collaboration with

South Westphalia University of Applied Sciences

Department of Electrical Engineering

Soest, Germany

February 2022

Abstract

The power systems of today use “smart grids” to improve grid operations and energy efficiency. State-of-the-art technologies and advanced control mechanisms have meant the renewable energy sources (RESs) can now be increasingly integrated into power grids. The grid integration of the RESs makes power generation more sustainable but concurrently causes bidirectional energy flow. This can lead to imbalances between phases. Instability during grid operations is consequently concerned, such as overcurrent in power lines and over/under bus voltages. In the power systems, distribution grids are especially affected, since they were not originally designed to handle power generation. The traditional grid operation, which is a centralised architecture, is therefore impractical for smart grids. Accordingly, an active distribution network is required.

In this thesis, an impedance network model and a method for decoupled voltage sensitivity analysis are proposed. Their key contribution to the academic community in the field of smart grids is to enable distributed steady-state analysis based on a clustering power systems approach (CPSA), resulting in decentralised active operations in distributed areas of the smart grids. The voltage sensitivity analysis proposed in this thesis examines the response of voltage magnitude and angle in relation to bus current in sequence systems, active power, and reactive power. The results from the analysis therefore indicate that there are impacts between buses in term of the voltage magnitudes, which can be further used for power management and voltage regulation.

The proposed analysis method is derived from a mathematical description of complex bus voltage, based on the proposed impedance model. It requires only measurement data gathered from the phasor measurement unit, without the information from grid topology. The required measurement data consist of bus voltages, bus currents, and the line currents of the connecting line between the distributed areas. As the foundation of the proposed method, first, the impedance model for each distributed area is determined from the measurement data. Only bus impedances between buses of concern are produced in this step. The impedance model is further used together with the measured voltage of the concerned bus in the sensitivity analysis. The proposed analysis method is devised to deal with both balanced and unbalanced grid conditions.

The accuracy of the proposed analysis method was verified by simulations in three case studies. The results from the first two case studies demonstrated the accurate voltage sensitivity analysis in all selected grid cases under the balanced and unbalanced grid conditions, including the case of the measurement errors up to the maximum of 1% total vector error. Use of the outcome from voltage sensitivity analysis for regulating voltage profile was then examined in the third case study. Once verification was achieved, the

proposed analysis method enabled decoupled voltage sensitivity analysis by using only the measurement data. This makes the proposed method suitable for further use in smart grids.

Further research is recommended, which should give consideration to possible additional measurement errors, dynamic characteristics of the power grid, and the implementation of the proposed method.

Acknowledgement

I would like to express my acknowledgement of the great support from my supervisor, Prof. Dr.-Ing. Egon Ortjohann, for his patience, encouragement, and distinguished supervision throughout my Ph.D. research. His guidance contributed to the successful research and writing of this thesis. I would also like to thank my Director of Studies, Prof. Dr. Danny Morton, for his exceptional advice during the entire research period.

I am very grateful to all my fellow colleagues for their precious feedback, ideas, and friendship. I would like to particularly thank Mr. Andreas Schmelter (Dipl.-Ing), Mr. Tawichai Premgamone (M.Sc.), Mr. Daniel Holtschulte (M.Sc.), and Mr. Jan Kortenbruck (M.Sc.) for their constructive discussions and cooperation. My appreciations also go to all postgraduate and undergraduate students in the laboratory during the period of my research. It was a great time with all of you.

Last but not least, I would like to thank my family for their support and unconditional love throughout this period. None of this could have happened without you.

Declaration

No portion of the work presented in this dissertation has been submitted in support of another award or qualification either at this institution or elsewhere.

Keywords:

Active distribution networks

Clustering power systems approach

Decentralised operations

Grid monitoring and control

Impedance Network Model

Smart grids

Voltage sensitivity analysis

Table of Contents

1. Introduction

Electrical power systems, especially in Europe, are currently in an energy transition phase that enables sustainable energy generation, together with efficient energy utilisation. The outcome of the energy transition is to achieve zero-carbon in energy generation processes, which will change the energy supply structure. Renewable energy source based distributed generating units are replacing bulk fossil-fuels, and nuclear based power plants. The energy supply structure gradually becomes bidirectional rather than conventional unidirectional, as a result. The power systems were, however, not designed for a bidirectional structure, so there is a main challenge for the energy transition: Modernisation of the power systems is required. The smart grid concept is considered in this thesis as a potential solution to the challenges.

This chapter provides the background of this thesis. First, the outlook for present-day power systems is provided. The electrical energy transition and the expected grid modernisation are discussed. Then, the problem statement and motivation for carrying out this research are sequentially delivered to explain why this research was conducted. Next, the research aim and objectives are presented. Other research contributions are also included to highlight the original contributions of this research to the literature. Research limitations are subsequently indicated. Lastly, the structural outline of this thesis is given.

1.1 Power Systems Outlook

With the responsibility to generate and deliver electricity to end users, power systems play an important role in many respects. For example, the power systems of a country are economically driven and quality of life enhancer. Existing power systems have been in operation for decades, after the first power plant was launched in the 19th century [1]. Recently, the power systems have faced various technical and non-technical challenges, for example, grid aging; increased energy demands; and especially, environmental concerns. Climate change and global warming are well-known non-technical challenges facing the industry, which widely affect human society.

Attempts to reduce greenhouse gas emissions is now discussed worldwide. Conventional power systems and base power plants generate significant amounts of greenhouse gases, since fossil fuels are used as the primary source of energy. Nuclear power has also been used also for energy generation as a comparatively cleaner energy source, but many incidents caused by failures of nuclear power plants such as the nuclear disaster in Fukushima, Japan in 2011 [2], caught the public attention, highlighting the fact that this type of energy is not sustainable. The failure of a nuclear power plant can lead to devastating consequences. Therefore, transitioning conventional energy sources to clean, sustainable energy, known as energy transition, is needed for conventional power systems all over the world [3].

This research considers renewable energy sources (RESs) as the key to effective energy transition. However, RESs pose technical challenges to the ability of power systems to work efficiently. Unlike conventional energy sources, locations of RESs are dispersed. Traditionally, the electrical energy flow is unidirectional in a top-down direction. Starting from the generation system, conventional power plants generate electrical energy to power grids. Then, the transmission system transmits the energy to the distribution system, which finally delivers the energy to end users. The RESs, in contrast, are not connected specifically to the generation system. They can also be in the transmission and distribution systems as well. This means that the electrical energy can also flow in a bottom-up direction, resulting in a bi-directional energy flow. The big challenge here is that power systems were not initially designed to support power generation in this way. Consequently, modernisation of the power system is required at the same time as the energy transition [4]. The current situation of the energy transition and the power systems is discussed in the following subsections.

1.1.1 Energy Transition

The energy transition of conventional energy generation towards environmental-friendly and sustainable energy is now an international issue in power engineering circles, with discussions focusing on the need for energy to be produced in a sustainable and efficient way. As reported in World Energy Outlook 2021 by the International Energy Agency (IEA) [5], the Paris Agreement on climate change led to the decision by member countries to ensure that average global temperature increases should not exceed 2 ˚C, and efforts to limit the temperature increase to 1.5 ˚C are pursued with consideration of Net Zero Emissions by 2050 scenario.

Two core components of the energy transition are expanding the use of RESs and improving energy efficiency. The RESs are a promising means of reducing greenhouse gas emissions, and using energy efficiently results in a reduction of electricity generation. Hence, renewable sources of energy are going to be the main sources of energy in power systems, and the energy must be used more efficiently in the meantime. In Europe, targets to increase the share of renewable energy consumption to replace the consumption of the energy from conventional power plants have been announced in the 2030 and 2050 energy strategies [6, 7].

Next, this thesis discusses the energy transition in Germany, since Germany is one of the leading countries in using RESs [8]. Currently available RESs are biomass, hydro energy, geothermal, wind energy, and solar radiation energy [9]. Figure 1.1 depicts the development of the installed power generation capacity of RESs in Germany from 1990 to 2018 [10]. The installed capacity of the RESs in Germany has significantly increased in recent decades. Meanwhile, the installed capacity of bulk power plants, i.e. thermal and nuclear power plants, has continuously reduced [11]. In 2018, the share of renewable energy of gross energy consumption achieved 37.8%, while the share of renewable energy in total electricity generation reached 35% [10, 11].

The installed generation capacity of RESs in Germany will continue to increase in the next few years at least. With goals to guarantee an ongoing expansion of RESs, the German government released the Renewable Energy Sources Act in 2014 [12]. By 2025, 2035, and 2050, the share of renewable energy in gross electricity consumption is targeted to reach 40% to 45%, 55% to 60%, and 80%, respectively. Meanwhile, the share of renewable energy in final energy consumption is expected to reach 18%, 30%, 45%, and 60% by 2020, 2030, 2040, and 2050, respectively.

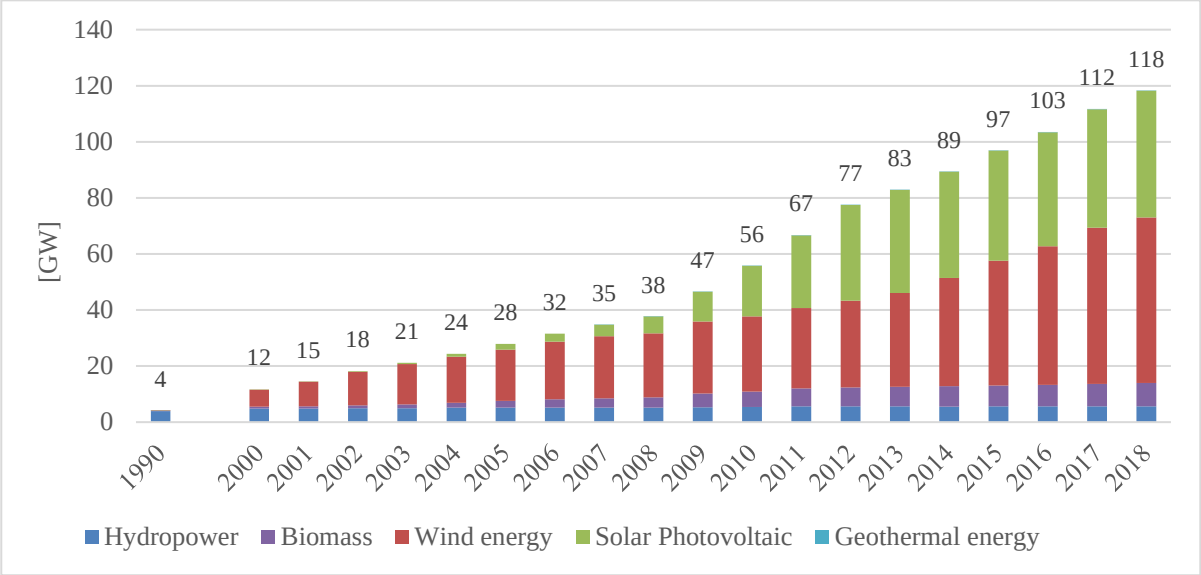

Figure 1.1: Installed power generation capacity of RESs in Germany from 1990 to 2018 [10]

Alongside the expanding use of RESs, the energy transition is also concerned with an improvement of energy efficiency – meaning that the energy must be used more efficiently. A key measure to improve energy efficiency is reducing energy consumption. In Germany, according to the Green Paper on Energy Efficiency [13], primary energy consumption is targeted to reduce by 20% by 2020 and by 50% by 2050 compared with 2008. Also, gross electricity consumption is targeted to reduce by 10% by 2020 and by 25% by 2050 compared with 2008.

Integrating RESs as distributed generation (DG) units to the power system also poses new challenges, since RESs-based DG units can be connected to the power grid at any level. The connection of DG is not restricted only to the upstream generation system, but the DG can also be connected to the distribution level. In 2017, the highest percentage of the total installation capacity of photovoltaic and wind energy systems has been installed in the distribution networks [12]. According to the Bundesnetzagentur [14], medium and low voltage distribution networks carry approximately 64% of the total RESs, and the low-voltage level alone accommodates 22% of the total RESs.

Technical issues such as the reliability and stability of the power grid must be taken into account in the energy transition, which leads to high penetration of RESs and new paradigms

of grid operations. Today power industries around the world also have to work within tight environmental and economic constraints, while ensuring reliability of their energy supply at the same time. Therefore, power systems must be modernised to accommodate state-of-the-art technologies and to facilitate the energy transition.

1.1.2 Grid Modernisation towards Sustainable Power Systems

As sustainable power systems providing net zero emission are widely expected, new advanced technologies are continuously being integrated into the present-day power systems. Thus, power systems are nowadays being modernised to cope with global situations and technological trends. In this section, an overview of the modern, sustainable power systems is provided, as illustrated in Figure 1.2.

In modern power systems, the utilisation of DG units based on RESs is currently prevalent throughout power grids and is likely to continue increasing [15]. As a result of environmental concerns, electric vehicles (EVs) have gradually attracted attention in private and public sectors as well. They are becoming a more popular means of transport, and are also used as controllable loads and distributed sources when they are connected to the power grid [16]. In addition, power electronic devices are important elements of modern power systems [17, 18]. For example, smart inverters can enhance grid operations through reactive power compensation and power quality enhancement [19–21]. Also, the inverters are used as a grid-interface for DG units and EVs.

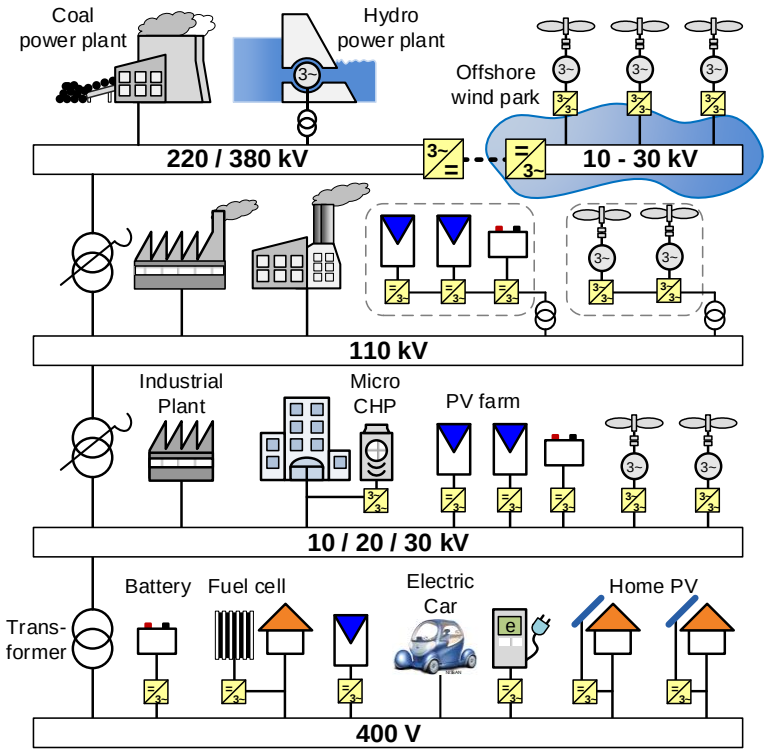

Figure 1.2: Modern, sustainable power systems [22]

Besides grid integration of RESs-based DG units, changes of customer requirements and grid aging affect existing power systems. Currently, customers require highly reliable, secure, and efficient power systems with expected high quality supply [23], including resilience against climate change, extreme weather, and cyber-attack. The requirements of users of the power systems, therefore, constantly change. Each interruption of electricity supply could lead to malfunction of electronic devices and high costs through losses for industrial customers. Whereas the demand of electrical energy increases, existing grid infrastructure and components are getting older and outdated. The increase of energy flow and aging components in the grid have been concerned on grid infrastructure. The existing infrastructure may not be able to handle changed-pattern energy flow in the long run.

Modernisation of the power systems has led to the introduction of smart grids, which are considered as key research for the modern power systems [24–28]. There are several impacts of the smart grid on the power systems. Some examples of the impacts are as follows.

- First, smart grids can integrate and manipulate diverse grid components, e.g., sensors, smart meters, and intelligent electronic devices. Information and communication technologies (ICTs) are incorporated into the power grids to make the grid smart and intelligent [29–31]. With the ICTs, the power grids are also perceived as a digital platform equipped with communication protocols [32].
- Second, with advanced technologies, smart grids will considerably improve grid operation and control, particularly in distribution systems. Applying the smart grid concept will enhance grid visibility and active control at the distribution level [33].
- Third, smart grids are especially going to play an important role in handling the growth of intermittent RESs-based DG units in a sustainable, efficient, and secure way. The smart grids widen the flexibility in operation and control strategies for the power grids and increases the opportunities for utilities in coping with the intermittent nature of RESs. To make a power grid smart, the entire power system will be able to handle bidirectional power and information flows. In addition to the traditional top-down direction, the power and information flows can take place in bottom-up direction from the distribution to the transmission systems.

Owing to the smart grids concept, the RESs, which mostly reside in the distribution level, have more opportunity to participate in grid operation and control. Both users and grid utilities can have benefits from this concept.

1.2 Problem Statement

The energy transition stimulated an increase of RESs-based DG units, including energy storage devices in the modern power systems. Some consumers owning DG units will change to be active customers – so-called prosumers – who can feed power back to the grid and

perhaps bid their resources to the electricity market. This means that electrical power generation is decentralised from the generation systems to the downstream distribution networks. This generation scenario raises concerns over grid stability [34–37]. Since distribution networks were not originally designed to offer power generation, connecting DG units to the power systems has impacted the control and operational management, safety, and reliability. One of the impacts is that the power can be transferred in reverse from the distribution networks to upstream systems when the power in-feed is higher than local demand. Also, high share in power generation of RESs-based DG units can affect voltage and frequency in the power grids [38]. As a consequence, centralised control and stabilisations of the power grid by the transmission systems is no longer practical for future power systems [39, 40]. Figure 1.3 depicts the main differences between conventional and modern power grids. The power systems were originally designed to transfer electrical power in a unidirectional top-down direction, whereas the modern power systems must be able to handle electrical power flow in bidirectional way.

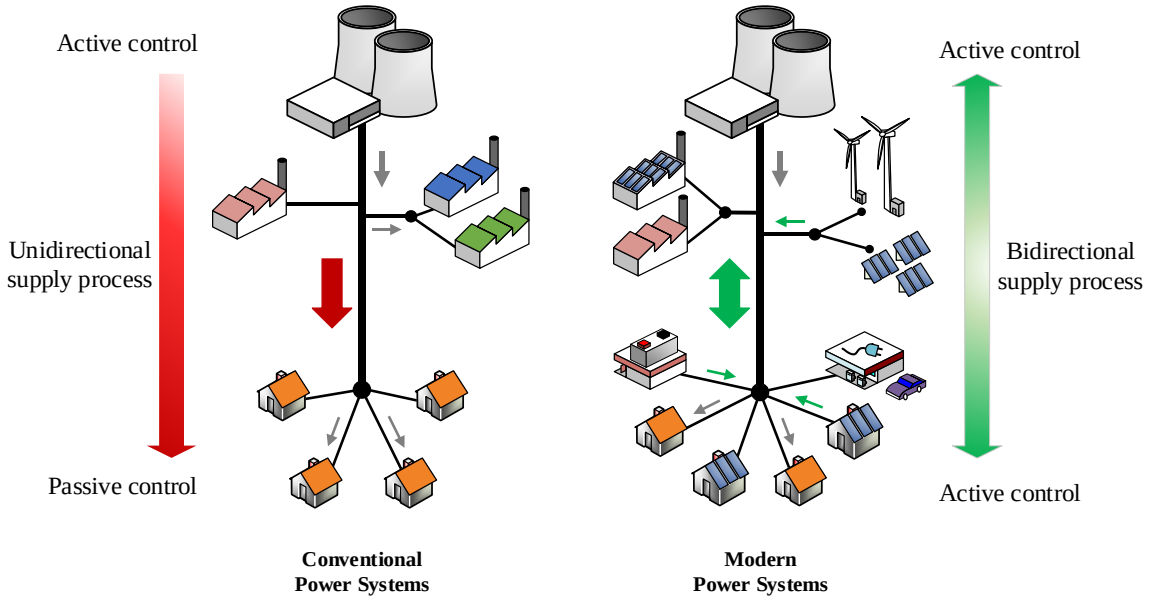

Figure 1.3: Differences between conventional and modern power grids [41]

Traditionally, the active control approach is conducted at the transmission level, and the passive control approach is used at the distribution level. Nonetheless, in the modern power grids, the active control should be decentralised or expanded from the transmission system to the distribution systems so that DG units residing in this grid level can participate in grid control and stabilization [42–45]. The transmission systems operators (TSOs) are generally responsible for monitoring and controlling state variables of the power grids, e.g. frequency and voltage. In contrast, distribution systems are passively operated by a *fit and forget* approach [46]. That is, distribution system operators (DSOs) design grid operations of distribution systems to fit with anticipated operational scenarios at the planning stage [47]. The *fit and forget* approach is therefore inappropriate for accommodating intermittent RESs-

based DG units; the status quo of the available generation from RESs cannot be efficiently included to the grid control.

Advanced functionalities of the modern power grids rely on grid visibility and observability, which is low in present-day distribution networks. The increasing availability of measurement data permits unprecedented visibility and observability to the grid. The measurement data are a key to advanced grid operations. Nowadays, data can be gathered from heterogeneous sources, e.g., a sensor, a smart meter, and a phasor measurement unit (PMU). Although the deployment of the PMU is more common in transmission systems at the moment, an attempt to deploy the PMU in the distribution systems is in progress [48–50].

Additionally, the conventional methods for engineering analysis are complex, and they normally deal with a large amount of data from the complete grid of concern. As a consequence, a high-performance processor for the control unit is required. Since low-voltage grids will increasingly participate in grid control, novel engineering analysis methods must allow decoupling analysis and simple usage. This will facilitate the decentralisation of grid operations from upstream levels down to the grid user in a low-voltage grid to allow active operations in lower grid levels. Besides, decoupling, simple analysis methods also enhance the realisation of online analysis, which can actively reflect actual grid conditions. Together with the novel analysis methods, the use of limited measurement data from the PMU must also be taken into account to show that it can enhance the possibility of developing the new methods in this thesis, as they provide specific information of magnitude and angle of the grid state variables, voltage and current.

1.3 Motivation

The development of active distribution networks based on smart grids is critical for power systems. To accommodate a large amount of RESs and to provide a high quality of services create new challenges to power systems providers. The concept of smart grids is developed to deal with integrating the RESs to power systems, and this concept is now considered to be a promising means for modern power systems [51–53]. By using advanced technologies, the smart grid is aimed to modernise the power grid to cope with requirements of the power grid of the future. Among generation, transmission, and distribution systems, the major impact of grid modernisation takes place at the distribution level. The change of energy supply structure consequently requires a revision of the traditional grid control architecture towards a decentralised structure. Alongside the transmission systems, active distribution networks are expected to have advanced functionalities, e.g., proactive operations, online grid analysis, and smart distribution automation [54–57].

To allow seamless integration of RESs, clustering power systems approach (CPSA) has been developed by the research group from the Laboratory of Power Systems and Power

Economics at South Westphalia University of Applied Sciences, Soest, Germany [58–61]. The CPSA is used as the foundation for developing new contributions to knowledge, and it is one of proposed solutions to the smart grid. The ability for transmission and distribution levels to cooperate is considered, including consistency and interoperability of the whole power systems. Thus, the CPSA is aimed to create consistent interconnected active-controlled areas in the entire power systems in the bottom-up direction, starting from the distribution level. Further detail of the CPSA is provided in Section 2.2.

To realise the smart grid concept, the existing conventional central grid operations must be adapted within the decentralisation paradigm. As the conventional operations and technologies in the transmission systems are still the core of the power systems, the CPSA allows the coexistence between the newly developed operational methods and the conventional ones, regardless of grid level. By taking the features from the CPSA, the characteristics of grid operations similar to interconnected grids from the transmission level should be brought to the distribution grids. Especially, together with measurement data, the CPSA can be adopted to develop advanced operational strategies for leveraging the dispersed RESs.

The property required from a PMU measurement is that the data measured at different buses are synchronised to the same point in time at each sampling, giving opportunities for observing and analysing grid conditions [62–65]. Exploiting the online measurement data will smarten grid operations and analyses of the smart grids. Hence, the advance in measurement and control techniques facilitates the development of smart, advanced functions, e.g. power dispatch management the RESs, operational optimisation, situation awareness support, and self-healing operations. Potential service disruptions and disturbances can be alleviated accordingly. This therefore paves the way for efficient exploitation of RESs and achievement of the energy transition.

1.4 Research Aim and Objectives

The aim of this thesis is to develop a novel method of decoupled voltage sensitivity analysis by using only measurement data. It is developed for steady-state analysis in conjunction with the CPSA, to allow decoupled analysis individually in each distributed area at the distribution level. The developed voltage sensitivity analysis examines the response of voltage magnitude and angle in relation to bus current in sequence systems, active power, and reactive power. To do so, bus impedance parameters, representing an impedance network model, are utilised as the foundation of the analysis method, because the impedance model provides the relationship between buses of a power grid.

This method is expected to enhance online automation in future smart grids. The results will demonstrate a promising way to support power dispatch management and control of the

widespread DG units in voltage profile adjustment. To achieve the aim, the following objectives were fulfilled:

- *To develop a method to construct a network model from measurement data for describing distributed areas based on the CPSA*. Since power grids are likely to operate on a decentralised structure in the future, distributed controlled areas can be expected. In this thesis, the underlying power grid is defined as several cluster areas in accordance with the principle of the CPSA. Traditionally, the network model can be built from topological data to describe the whole grid. Instead, a method to construct a distributed network model from measurement data is developed in this thesis, and the measurement data are assumed to be gathered from phasor measurement by PMU. The resulting distributed network model is able to allow steady-state grid analysis in the decentralised structure to achieve the stated aim.

- *To derive a method for the decoupled voltage sensitivity analysis*. Based on the developed network model, the decoupled voltage sensitivity analysis can be realised. However, a primary requirement of the sensitivity analysis is that it still requires only measurement data. A method for the decoupled voltage sensitivity analysis, which can fulfil this requirement, is thus proposed and derived. As a result, the proposed method allows each cluster area to perform individual voltage sensitivity analysis in a steady-state condition.

1.5 Research Contributions

This research work contributes original knowledge to the academic community in the field of smart grids. A novel method of decoupled steady-state voltage sensitivity analysis is developed for decentralised grid operations based on the principle of the CPSA. By applying the CPSA, consistent decentralised grid structure and operations can be acquired in an entire power system. The contributions of the research are listed as follows:

- *Proposal of a method to determine the network model by using only local measurements for describing distributed areas under the CPSA*. Without using information of grid topology, the network model is built from up-to-date information about the status of a power grid, obtained from the phasor measurement by PMU. Only buses of concern are taken into account. The model can be used to describe both the entire power grid and distributed areas, which operate under either a balanced or unbalanced condition. For the case of the distributed areas, the CPSA is applied to form a network of distributed areas known as cluster areas.

- *Proposal of a flexible, modular, and scalable voltage sensitivity analysis method*. Such a method for decoupled voltage sensitivity analysis requires only the predetermined network model, together with phasor measurement of relevant bus voltage. The analysis

is thus conducted on up-to-date information about the status of a power grid. Regardless of voltage levels, the proposed method is applicable for both the entire power grid and individual distributed area, which operates under either balanced or unbalanced conditions. As a result, the sensitivity of voltage magnitude or angle in relation to active and reactive powers is acquired under a balanced grid condition, and the sensitivity of voltage magnitude or angle in relation to currents in sequence systems is obtained under an unbalanced grid condition.

- *Enhancement of decentralised grid operations and interaction strategy between distributed areas under the CPSA*. Since the methods for determining a network model and performing voltage sensitivity analysis require only measurement data, the sensitivity analysis is executed on a light-weight algorithm. Especially with the application of the CPSA, the data used during the analysis is even smaller, as the cluster areas are distributed from the whole grid area. In addition, together with the CPSA, the proposed methods are developed in such a way that cooperation is achieved between interconnected distributed areas. Cooperation will play a more important role in the future since grid operations currently tend towards a decentralisation structure.

- *Providing the analysis results that can be used together with power dispatch management for voltage profile regulation*. The results from the analysis can be further used as the setpoints or reference values for active controllable elements. Owing to the proposed analysis method, the results are divided into two categories for balanced and unbalanced grid conditions. For feeding to controllable units, the setpoints or reference values of active and reactive powers are computed under a balanced grid condition, while that of symmetrical-component bus currents for controllable units under an unbalanced grid condition.

Figure 1.4 depicts the overview of the stated contributions. For a power grid or cluster area, measurement data from each bus of concern are sent to the analysing or control unit of that grid or area for determination of the network model and the voltage sensitivity analysis. After the sensitivity analysis is complete, the results, depending on the grid condition, can be used as the setpoint or reference value in order to achieve the expected voltage profile regulation.

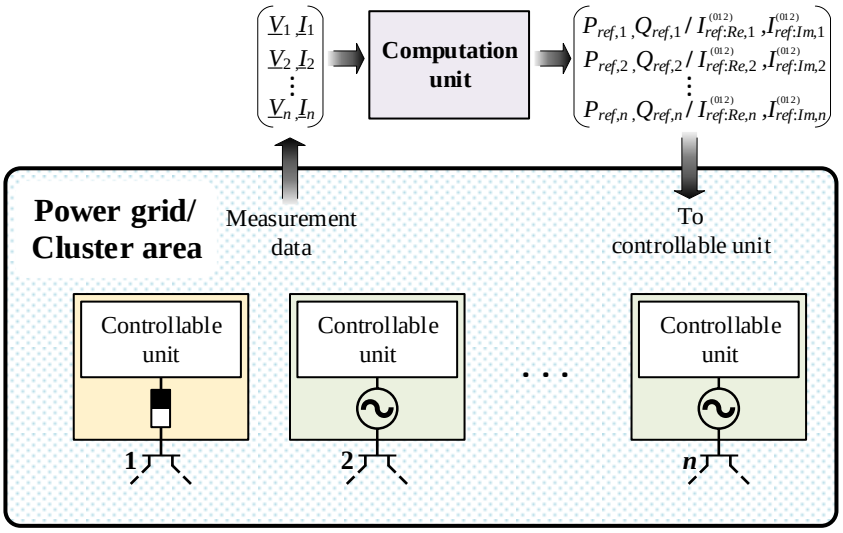

Figure 1.4: Overview of the research contributions

In summary, the contributions facilitate the transformation of the conventional power grids to smart, efficient, sustainable power grids of the future.

1.6 Research Limitations

The intended voltage sensitivity analysis methods require time-synchronized measurement data of voltage and current phasors. This means that at a particular point in time, both data of bus voltage and bus current magnitudes, together with their corresponding phase angle must be available for any required node with consistent data. Currently, only PMU is the measurement device that can provide these time-synchronized data. Therefore, deployment of PMU in the power grid is a prerequisite. Since the proposed analysis methods are aimed to be used at any grid levels from transmission to distribution levels, the availability of PMU in the power grid must be considered.

In the transmission level, the data are likely to be sufficient for the analysis, as PMUs have been deployed in this grid level [66–68]. However, PMUs are presently not yet widely available at the distribution level. Development of these devices are still in progress [69–71]. That is, the fruits of this research are more likely to be seen in the future.

This limitation does not imply that the proposed methods are not feasible in reality. There are other options to fulfil the input requirements to perform the proposed analysis methods; the key concern is to generate time synchronized phasor data. Apart from PMUs, smart meters are a viable option [72, 73]. Although smart meters do not provide phase angle data, their measurements can be processed in state estimation and load flow calculation in order to result in the complete phasor datasets, which are suitable for the proposed methods.

Another assumption made in this research is that the coupling between sequence systems is neglected in the derivation of the analysis methods, as the cable layout is assumed to be

symmetrical. Although unsymmetrical layout of power lines and power cables exists in practice, the conductors of power cables are shielded, and power lines are transposed in many practical cases [74].

1.7 Thesis structure

This thesis contains the content of the proposed voltage sensitivity method. The related components are arranged in six main chapters. The structure of this thesis including the overview of each chapter is provided as follows:

- *Chapter 1*: *Introduction.* The outlook of current situations of the power systems is first elucidated. Then, the problem statement and the motivation of this PhD project are provided. The aim and objectives of the research are subsequently defined. The primary contributions of the conducted research are stated. The outline of the thesis is finally provided in the end of the chapter.

- *Chapter 2*: *State-of-the-Art*. The theories and technologies relevant to the research in this thesis are stated in this chapter. First, the introduction to smart grids is provided. Then, related technologies such as phasor measurement units and ICTs are discussed. Afterwards, an overview of the clustering power systems approach is provided as the foundation of this thesis.

- *Chapter 3*: *Impedance Network Model for Cluster-Based Decentralised Power Grids*. In this chapter, the impedance model used to describe a power grid either as the entire grid or as distributed areas is elaborated. It is called bus impedance parameters developed on the basis of the theory of the bus impedance matrix. This chapter therefore starts with an introduction to the impedance model. The Thévenin's theorem, which is an important component of this thesis, is also included. After that, a discussion of how the bus impedance parameters of a single area were determined is presented. Finally, the integration process of the impact between distributed areas to the predetermined bus impedance parameters is shown.

- *Chapter 4*: *Voltage Sensitivity Analysis for Cluster-Based Decentralised Power Grids*. This chapter begins by discussing various related research articles on voltage sensitivity analysis. Then, the utilisation of the impedance parameters is explained in the formulation of the model for the analysis method; the bus impedance parameters determined in the previous chapter are further discussed in this chapter. Next, the derivation of the proposed method for analysing voltage magnitude and angle sensitivity is delineated. The options for deciding the method are given for balanced and unbalanced grid conditions. Lastly, the application of the results from the analysis is elucidated.

- *Chapter 5*: *Verification of the Proposed Network Model and Voltage Sensitivity Analysis Method*. The impedance network model and the proposed voltage sensitivity analysis method are verified by simulations in this chapter. The accuracy of the proposed method is examined in two case studies. The first case is a medium-voltage grid based on IEEE 37-bus test feeder and an exemplified mesh grid. The second case is performed on a low-voltage grid whose topology is taken from a part of a real distribution grid. The impact of the clustering power systems approach is also stated in the second case study. Finally, in the last case study, an application of the sensitivity analysis for voltage profile regulation is exemplified.
- *Chapter 6*: *Conclusion and future work*. The conclusion of this thesis is drawn in this chapter, where the whole thesis is summarised. Also, anticipated future work that can be further developed from this thesis are given.

2. State of the Art

This chapter presents state-of-the-art technologies relevant to this thesis. Two main features of smart grids are examined here. First, an overview of smart grids and related technologies is provided. Information and communication technologies and a phasor measurement unit are discussed as technologies related to the smart grids. Roles of the related technologies in the smart grids are reviewed. Second, the clustering power systems approach and its applications are explained. This approach aims to be a means to the realisation of the smart grids. The main features of this approach are decentralising grid operations and a control structure. It also has coexisting newly developed grid operations with the conventional ones.

2.1 Smart Grids

Today's power grids face many challenges in different respects. Mainly, they must accommodate the growth of intermittent RESs deployment and handle increased expectations and needs of society [75–78]. Thus, present-day power grids are gradually becoming smarter, and the concept of smart grids is being used to deal with the technical and environmental challenges in a sustainable, efficient, and secure way [79]. The concept of smart grids is currently the focus of research and development to operate future power systems [80]. The developed research which has been carried out for this thesis will add to the body of literature on smart grids. It is hoped this will benefit the progress towards smart grids. Next, this section provides an overview of smart grids.

2.1.1 Overview

Basically, the concept of smart grids is variously described in the literature [81]. Any definition is generally dependent on the outcomes required from, or the purposes of developing smart grids. Among the various definitions, the unifying feature is that the smart grids will benefit the whole existing power grid from generation and transmission, down to distribution systems – including customers. With respect to the expected functionalities of smart grids, a definition released by the European Commission is provided as follows:

"*A Smart Grid is an electricity network that can cost efficiently integrate the behaviour and actions of all users connected to it – generators, consumers and those that do both – in order to ensure economically efficient, sustainable power system with low losses and high levels of quality and security of supply and safety*" [57].

To realise the stated goals from the definition, the smart grid, therefore, requires the coordination between different sectors and technologies. Bidirectional power flow and information flow are inevitable. Along with the direction of the power flow in the power grid, the direction of the information flow also changes in the smart grid [53]. The bidirectional

information flow, from two-way communication, is required to enable the smart grid. For this reason, information and communication technologies (ICTs) are indispensable. The information of power systems – e.g. historical data; grid state; component condition; or commands for smart devices – adds intelligence to the smart grid. With the ICTs, the power grid can effectively accommodate intelligent devices and new advanced operational functions available in the future. New grid components such as smart meters, control, and intelligent devices are integrated to the power grid from utilities at facilities or at the grids – e.g. substations and control centres – to consumers in industrial, commercial, and residential areas [82, 83]. Additionally, reliable and real-time information becomes the key factor in the smart grid for reliable power transfer from the generating units to the end-users. Thus, sensing and measurement technologies are implemented to support fast diagnosis and precise response in advanced grid monitoring and control [61], [79], [84].

In the same manner as the definitions, the functionalities of the smart grid vary in different regions, depending on desired purposes and grid conditions. The common aim of the functionalities is to strengthen the power grid. The smart grid is expected to provide new functionalities and intelligent operations to the power grid. The European Commission mentions the functionalities of a smart grid as follows:

"*A Smart Grid employs innovative products and services together with intelligent monitoring, control, communication, and self-healing technologies in order to:*

- *Better facilitate the connection and operation of generators of all sizes and technologies.*
- *Allow consumers to play a part in optimising the operation of the system.*
- *Provide consumers with greater information and options for how they use their supply.*
- *Significantly reduce the environmental impact of the whole electricity supply system.*
- *Maintain or even improve the existing high levels of system reliability, quality and security of supply.*
- *Maintain and improve the existing services efficiently.*
- *Foster market integration towards European integrated market*." [57]

Accordingly, smart grids introduce new attributes of functionalities to the power grid, such as bi-directional energy flows, two-way communication, and advanced control processes. A comparison between the conventional grid and smart grid is presented in Table 2.1 [85].

Table 2.1: Comparison between existing grid and intelligent grid [85]

Conventional Grid	Smart Grid
Consumers are uninformed and non-participative with power system	Informed, involved, and active consumers - demand response and distributed energy resources
Dominated by central generation- many obstacles exist for distributed energy resources interconnection	Many distributed energy resources with plug-and-play convenience focus on renewables
Limited wholesale markets, not well integrated - limited opportunities for consumers	Mature, well-integrated wholesale markets, growth of new electricity markets for consumers
Focus on outages - slow response to power quality issues	Power quality is a priority with a variety of quality/price options - rapid resolution of issues
Little integration of operational data with asset management - business process silos	Greatly expanded data acquisition of grid parameters - focus on prevention, minimizing impact to consumers
Responds to prevent further damage- focus is on protecting assets following fault	Automatically detects and responds to problems - focus on prevention, minimizing impact to consumer
Vulnerable to malicious acts of terror and natural disasters	Resilient to attack and natural disasters with rapid restoration capabilities

With advanced technologies and automation processes, the smart grid is a modernised version of a conventional power grid. Recently, operational initiatives and related advanced functions for smart grids have been extensively studied [24, 78, 82, 86–89]. Several aspects of the smart grid are expressed, for example, anticipated trends and developments, state-of-the-art implementation of the smart grid concept, and the emerging functionalities. To realise the smart grid, all sectors of the power systems, including utilities and customers, need to play a part. As mentioned, the ICTs are an important factor to connect and coordinate different sectors. In the next section, roles of the ICTs are therefore discussed in more detail.

2.1.2 Information and Communication Technologies

The smart grid is a modern, intelligent power grid, which is incorporated by advanced technologies and functionalities to improve the reliability, efficiency, and sustainability of the power grid. The key to realise the smart grid is the information exchange among various domains [90]. In particular, the smart grid is expected to accommodate a large number of RESs. It therefore requires the information to handle the decentralisation paradigm of grid operations and enable interoperability between different entities [91, 92]. To this end, the information and communication technologies (ICTs) are a crucial component that connects all domains of the smart grid operations. Figure 2.1 illustrates a conceptual model of the roles of ICTs across smart grid domains according to the NIST Framework and Roadmap for Smart Grid Interoperability Standards [93]. With the ICTs, the development of intelligent operations and functionalities to realise the smart grid is facilitated.

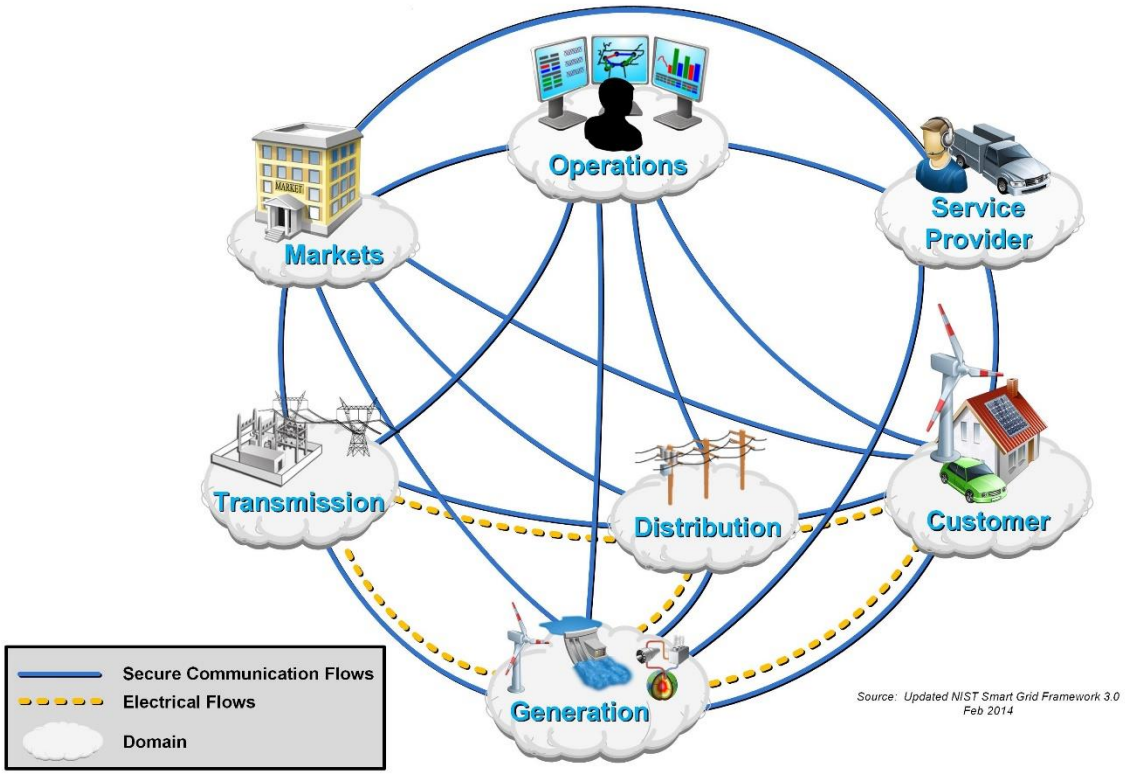

Figure 2.1: Conceptual model of smart grid domains [93]

This conceptual model consists of 7 domains: Markets, Operations, Service Provider, Generation, Transmission, Distribution, and Customer. Bidirectional information exchange among all domains is defined. Additionally, bidirectional power flows between electrical system domains are indicated. The existing actors and elements of each domain can be mapped into the conceptual model as shown in Figure 2.2 [93], in which information flows among the domains are also presented. The interactions, information networks, and possible communication paths are suggested.

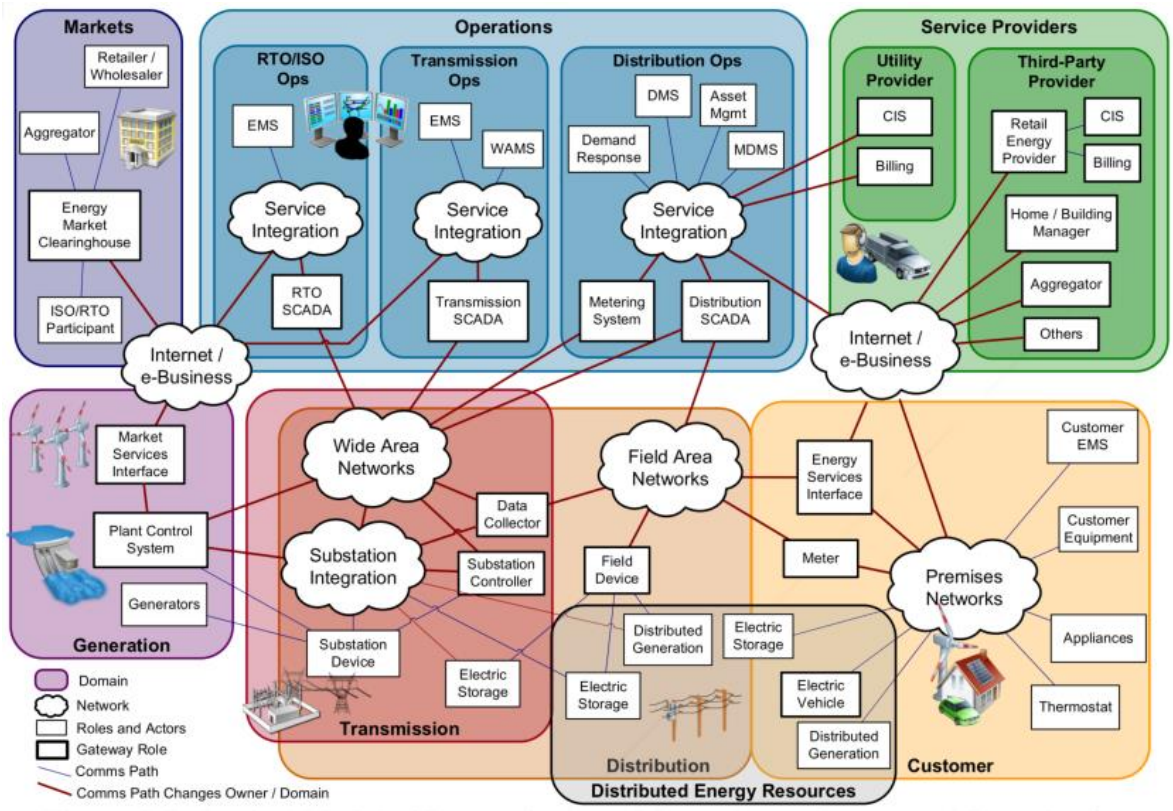

Figure 2.2: Communication paths mapped on the conceptual smart grid domains [93]

In Figure 2.2, there are six primary components, which are domains, information networks, actors, gateway roles, intra-domain and inter-domain communication paths. Each domain represents a group of organisations, systems, devices, or actors involving similar objectives and types of services. Information exchange and sharing are carried out through an information network between computers or devices. The information networks illustrated in this diagram include a wide area network (WAN), field area network (FAN), premises networks, and the Internet. The WAN generally transfers data between remote locations, while the FAN normally transfers data between devices residing in the neighbourhood area [94, 95]. The premises network in this context is a network within the customer domain, which can be a private one or provided by a utility. The Internet, on the other hand, is a public network that is ubiquitously used and is the most pervasive and cost-effective network.

Together with a number of available standards for the internet protocol, the Internet is thus a reasonable choice for communication in the smart grid [26]. Actors in this context represent services, applications, and devices that can make decisions and exchange information with other actors. The communication between actors in different domains is executed through the corresponding interface, represented by the gateway role. The communication within a domain or across domains can be conducted directly between actors or through an information network. Existing communication technologies for these networks are, for example, ZigBee, wireless mesh, cellular network communication, and powerline communication [53, 75].

In conjunction with the ICTs, enhanced sensing and metering technologies are essential to grid monitoring, protection, and control in smart grids [96–98]. They are data sources necessary for intelligent operations, which basically would be unfeasible without having proper data and information. In this thesis, the information of measured voltage and currents phasors are the primary requirements. A phasor measurement unit, which is a contemporary measurement device, is currently an attractive technology [99]. It is expected to be deployed throughout the power systems to measure synchronised phasors and the frequency in real time [100]. The PMU is therefore discussed more in details in the next section.

2.1.3 Phasor Measurement Unit (PMU)

Smart grids consist of multiple technologies. Sensing and metering technologies are a part of the smart grids that enables intelligent grid monitoring, protection, and control. In this thesis, the PMU is taken into account, since it produces phasor measurements of voltages and currents, which are the primary requirement for developing the proposed decoupled voltage sensitivity method. An overview of the PMU aspects relevant to this thesis is thereby provided as follows.

The PMU is a device that offers synchronised phasor measurements of voltage and current signals, frequency, and rate of change of frequency, which are captured in real time at a high rate [101, 102]. Recently, the PMU has been increasingly deployed across transmission and distribution grids [103], [104], [105]. At the distribution level, it can alternatively be called a micro PMU (μPMU), which performs the same tasks [105–107]. According to IEC/IEEE 60255-118-1 [108], at 50 Hz, a required reporting rate of the PMU ranges from 10, 25, 50, and 100 frames per second. Different from the traditional root mean square (RMS) measurement, both the magnitude and phase angle of voltages and currents can be measured by the PMU. Each synchronised phasor measurement, also referred to as a synchrophasor, is obtained together with a timestamp synchronised to the global positioning system (GPS) based on the coordinated universal time (UTC) [108]. Figure 2.3 illustrates voltage, current, and UTC time signals as the inputs for generating synchrophasors by the PMU. The synchronisation process is outside the scope of this thesis, so it is not mentioned here, but can be found in [108].

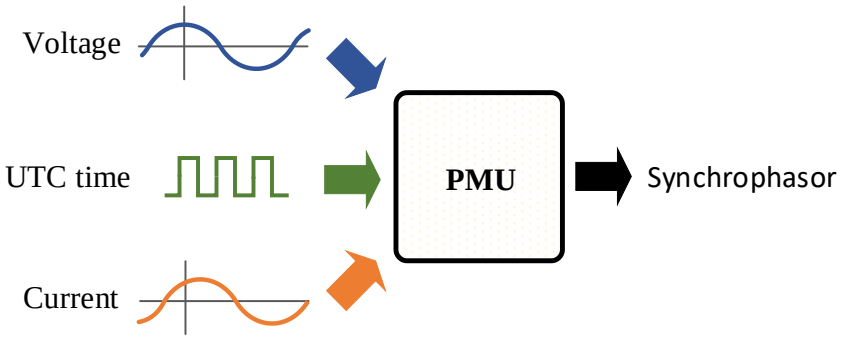

Figure 2.3: Inputs for synchrophasor generation

The timestamp of PMU measurements allows synchronisation of synchrophasors gathered from different utilities. Also, the PMU can generate the information on the up-to-date state of the power systems for either steady-state or dynamic conditions [103]. The data and information from the PMUs can be used, for example, to describe the power grid, to anticipate emerging events, and to conduct corrective actions [109–111]. As a result, power system protection, monitoring, and control are more advanced than before, especially for wide area monitoring systems (WAMS). References [112–116] show that in conjunction with selecting optimal locations for the installation, the PMU enhances accurate observability and visibility of the entire grid to grid operators. Hence, this gives opportunities to grid operators to smarten grid operations and improve the quality of service.

One point of concern, however, is the accuracy of the measurement. The practical synchronisation of PMU measurements is not perfect, and the measurement data can be error prone [117], [118]. According to IEC/IEEE 60255-118-1 [108], a measure to evaluate the accuracy of the PMU is total vector error (TVE). It is the normalised difference between the reference synchrophasor and the measured value at the same point of time from the tested unit. According to IEC/IEEE 60255-118-1 [108], the TVE is defined as

$$TVE(t) = \sqrt{\frac{(\hat{X}_{Re}(t)-X_{Re}(t))^2+(\hat{X}_{Im}(t)-X_{Im}(t))^2}{(X_{Re}(t)-X_{Im}(t))^2}}. \tag{2.1}$$

At the report time t, $\hat{X}_{Re}(t)$ and $\hat{X}_{Im}(t)$ are real and imaginary components of the measured sample, and $X_{Re}(t)$ and $X_{Im}(t)$ are real and imaginary components of the reference sample. From Eq. (2.1), both magnitude and phase angle errors are considered in the TVE.

The TVE of 1% is set as the maximum permissible error. It can be perceived as a circle covering the end of a phasor. This criterion is depicted in Figure 2.4. The measurement conforms to the criterion if the sample, or captured phasor, is inside the circle. Regarding this circle, the maximum error of the phasor magnitude can occur when there is no error in the phase angle. Similarly, the maximum error of the phasor angle is 0.57°, which is 0.01 radian, for synchrophasors in 50 Hz system can occur when there is no error in the phasor magnitude [108]. This phase error is equivalent to a time error of ± 31 µs. The PMU measurements are possible for both steady-state and dynamic applications. In this thesis, the steady-state PMU measurements are assumed to be used for steady-state analysis, where the frequency of the measured signals is constant during the measurement process.

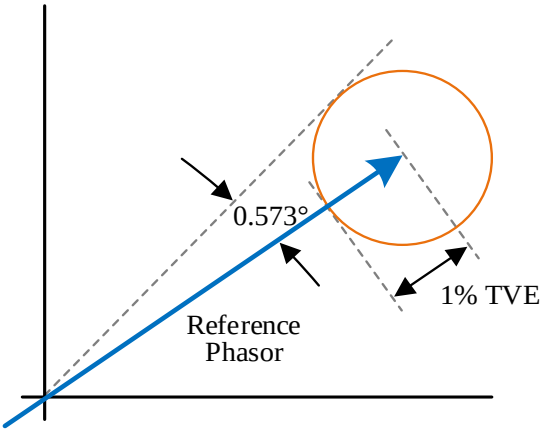

Figure 2.4: 1% TVE Criterion [108]

The basic details of a PMU related to this thesis are delineated in this section. The PMU plays an important role in collecting measurement data of voltage and current phasors for active operations in the smart grids. Nevertheless, alternative measurement sources besides the PMU must be known, since this thesis also focuses on the distribution level. The number of available PMUs may not be enough for the active operations. The µPMU at the distribution level is still under development [119]. In the next section, the concept of the smart meter is introduced, as it is more common to collect measurement data in the distribution grids.

2.1.4 Smart Meter

The increase of intermittent RESs, such as PV, at customer locations can cause imbalances between demand and supply, as well as unbalanced power distribution among phases of power cables, as the power generation of RESs typically fluctuates. This creates the need for information to be unified among grid users to ensure grid stability, especially at the distribution level, in which the observability is low. Utilities have little information about real-time situations within their grids.

Power grids at the distribution level are currently being developed with the smart grid concept in mind. Smart grids employ advanced ICTs and control technologies to form an intelligent power system from generation, transmission, and distribution, to consumer/prosumer levels [120]. In a smart grid, smart meters play a vital role in collecting grid variables information, thus enhancing grid observability [121]. Figure 2.5 shows an example of the location of smart meters in a power grid [122]. A smart meter is connected generally at the building level (Home Area). It allows two-way communication between the meters and their corresponding grid utility to transfer data of energy consumption [123].

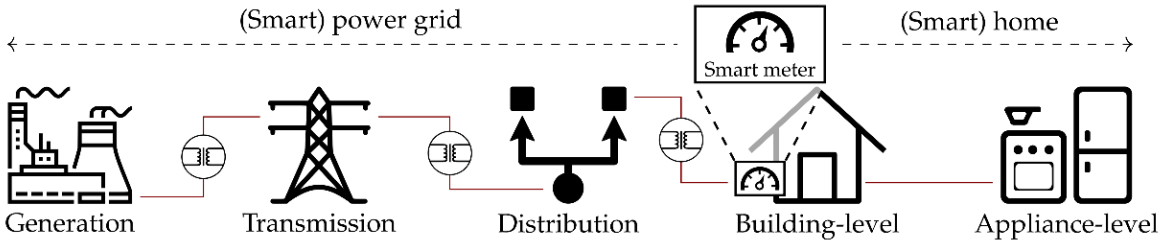

Figure 2.5: An example of the location of smart meters in a power grid [122]

The smart meters provide data of energy usage at periodic interval measurements, which can be configured from daily, hourly, every 15 minutes, or every 5 minutes [90]. Fundamentally, they measure voltage $V(t)$ and current $I(t)$ waveforms at specified sampling rates, which can be used to calculate root mean square (RMS) values over the interval $t_0 < t < t_0+\mathrm{T}$ from the starting time t_0 in the period T. Accordingly, RMS voltage

$$V_{RMS} = \sqrt{\frac{1}{\mathrm{T}}\int_{t_0}^{t_0+\mathrm{T}} V(t)^2 dt} \tag{2.2}$$

and RMS current

$$I_{RMS} = \sqrt{\frac{1}{\mathrm{T}}\int_{t_0}^{t_0+\mathrm{T}} I(t)^2 dt} \tag{2.3}$$

can be determined, as shown in Eqs. (2.2) and (2.3), respectively [122]. Depending on capabilities of a smart meter, one or more of the following measurements can be gathered at every interval [122]:

- RMS voltage (V_{RMS})
- RMS current (I_{RMS})
- Instantaneous power factor
- Instantaneous active power
- Instantaneous reactive power
- Apparent power
- Energy consumption

With the smart meters, provision of data from DG units and flexible demand is possible. The smart meters therefore provide benefits to both customers and utilities [124]. For a customer, a smart meter can remotely transfer information of energy consumption to the utility. By analysing the information, optimal energy consumption can be realized. Also, billing can be presented without human intervention. For a grid utility, data from smart meters can be used in various power system functions such as demand side management, planning for optimal utilization of RES, and energy forecast at for a consumer or even at grid level [125, 126].

In this thesis, the smart meter is not a primary option. It delivers RMS values with low resolution requirements based on the power quality standard [127, 128], since it is mainly developed for a billing function related to the energy consumption [120, 124]. Synchronized measurements are currently not an objective of smart meters. For the developed methods in

this thesis time synchronized measurement of states with high accuracy of phase relation is a must, and only a PMU can provide these data at the moment. These data can be used to determine the impedance model of a considered power grid and sensitivities of voltage magnitudes and phase angles. Next, an approach used in this thesis to define a physical structure of the smart grids is presented. It is known as the "clustering power systems approach".

2.2 Clustering Power Systems Approach (CPSA)

Power systems are now modernised using the smart grid concept, which requires the integration of state-of-the-art technologies, an operational paradigm, and an advanced control mechanism. The conventional operational structure and related technologies are, however, mature and well established. They cannot be changed immediately in a single step. Thus, a newly developed control scheme for the smart grids should comply with the traditional control scheme of the conventional power systems. The CPSA is proposed as a solution to the smart grids by the research group from the Laboratory of Power Systems and Power Economics [129], South Westphalia University of Applied Sciences, Soest, Germany. The idea of this approach is to coexist grid operations between the transmission and distribution systems and define flexible, consistent grid structures in entire power systems.

The structure of this section is as follows. First, research related to the CPSA is discussed to point out the originality of the CPSA and the reason why this approach is used in this thesis. Then, the concept of clustering power systems is detailed. Next, the self-similarity principle used together with the CPSA is examined. How this approach can lead to a well-defined grid structure and anticipate the expansion of active operations from the transmission system to the distribution system is also discussed. Finally, the latest status of the research on the CPSA, which are relevant to this thesis, is given.

2.2.1 Related Research

In parallel to the CPSA, several approaches have been proposed to enable smart grids or active operations in distribution networks. Among the proposed approaches, two of them, microgrid and the cellular power grid, are based on principles similar to the CPSA. To point out the originality of the CPSA, an overview of the microgrid is provided, and the cellular power grid is discussed in this section accordingly.

First, the **microgrid** is a mini version of the power grid, which is designed for small communities in distribution networks [130–133]. Hence, a microgrid can be defined, for example, in a local area, such as a village, a university, industrial site, a building, or a residential unit [134–138]. It consists of groups of loads and Distributed Energy Sources (DERs) composed of DG units and energy storage systems. Fundamentally, the microgrid is expected to be able to operate in either grid-connected mode, when it is connected to the main

power grid, or in islanding mode, when it is disconnected from to the main power grid. An overview of microgrid is portrayed in Figure 2.6 [139].

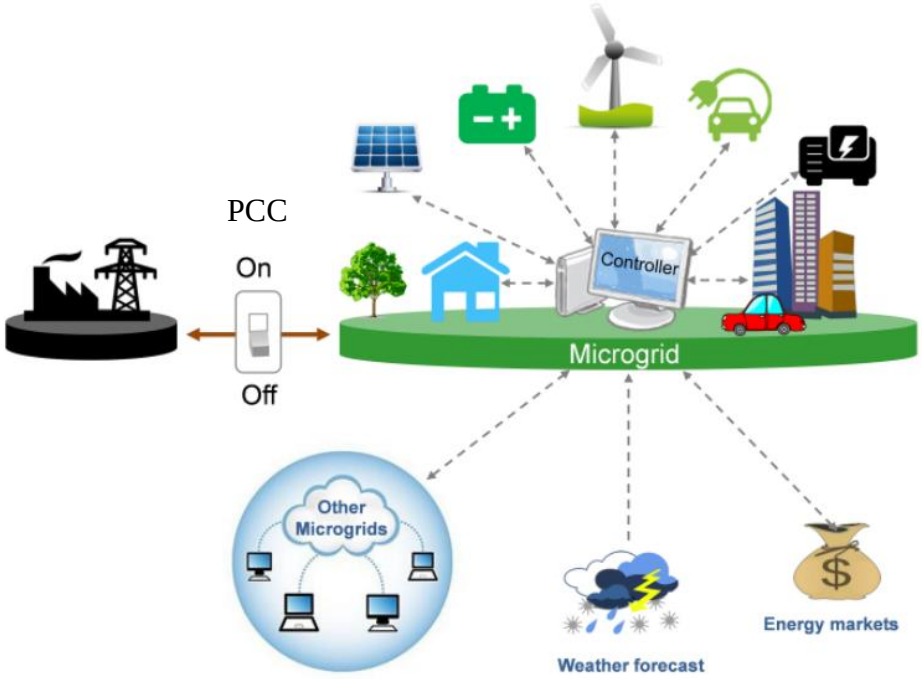

Figure 2.6: An overview of microgrid [139]

The microgrid is connected to the main power grid at the point of common coupling (PCC), which can connect and disconnect the microgrid from the main grid. Since the microgrid is expected to operate in a similar manner to the main power grid, a controller is available in each microgrid for grid control and operation, protection, and to maintain stability [140, 141]. Also, participation by the energy market is another feasible feature of the microgrid. With the availability of local energy sources, the microgrid is able to provide ancillary services and also stimulate energy price reduction by means of the energy market [142]. Moreover, to enable the anticipated functionalities of the microgrid, required information can potentially be gathered from grid elements or other microgrids. Exchanging information between networked microgrids allows possible coordination between microgrids [143–145].

At the moment, many aspects of the microgrid approach are being investigated. Research studies on some functionalities of the microgrid are briefly discussed here to give an overview. In [42], voltage control is decentralised based on the voltage level: high voltage, medium voltage, and low voltage. There, each level is considered as a microgrid. Reference [146] proposes using microgrid, labelled as a group of DERs, for system restoration. In [147–149], the microgrid is used for managing DERs with self-healing capabilities. Each microgrid is solely assumed to be an area with sufficient DERs to maintain power balance, without other specific criteria for the decentralisation.

Next, **the cellular power grid** is discussed, as it has the potential to handle the distributed generation [150, 151]. The principle underlying this approach is to define an energy cell to

balance power generation and consumption from the lowest possible level [152]. According to [150], three main cell types are categorised by size as household cell, business cell, and industry cell, where the household is the smallest cell. By applying this approach, multiple cells are defined on the physical power grids. Figure 2.7 shows a structure of a network of cellular power grids [153]. The cellular network is formed throughout the power systems.

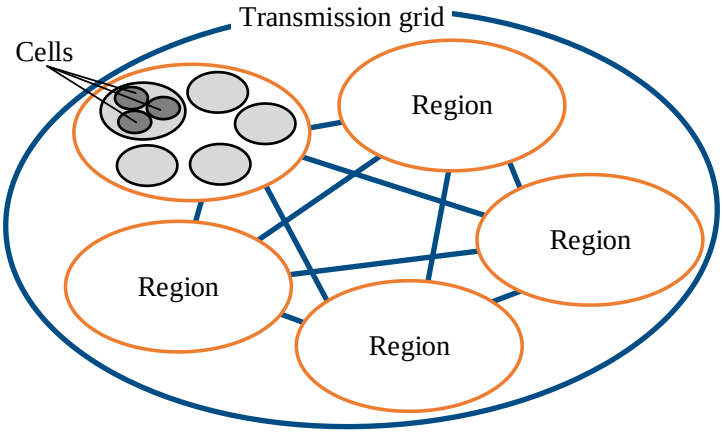

Figure 2.7: Structure of a network of cellular power grids [153]

Similar to the microgrid, the cellular power grid is expected to be able to operate in both isolated and grid-connected scenarios [150]. Accordingly, the balance of power generation and consumption is expected to be possible in each cell. The components of a cell displayed in Figure 2.8 [150] are detailed as follows.

In a cell, there are five energy entities: Generation, Load, Network, Storage, and Converter. As their name implies, Generation represents the generated energy flowing into the cell, while Load indicates the energy drawn from the cell. In case of excessive energy, the energy can be exchanged with the main power grid or other cells as represented by the Network entity [154, 155]. Otherwise, the energy can be stored locally at Storage [156, 157]. Converter in this context is designated for the conversion of electrical energy to another form such as gas or heat [158]. Communication flow and energy flow are assumed to relate to the entities.

The energy transportation is conducted through primary and secondary technologies. In the energy transfer process, primary technologies refer any apparatus directly involving the distribution and transport of the electric energy such as component in the substation i.e. transformer, switchgear, busbar, or feeder [159]. Secondary technologies refer any technology that are indirectly involved in the energy supply process such as grid security, voltage regulation, or measurement [159].

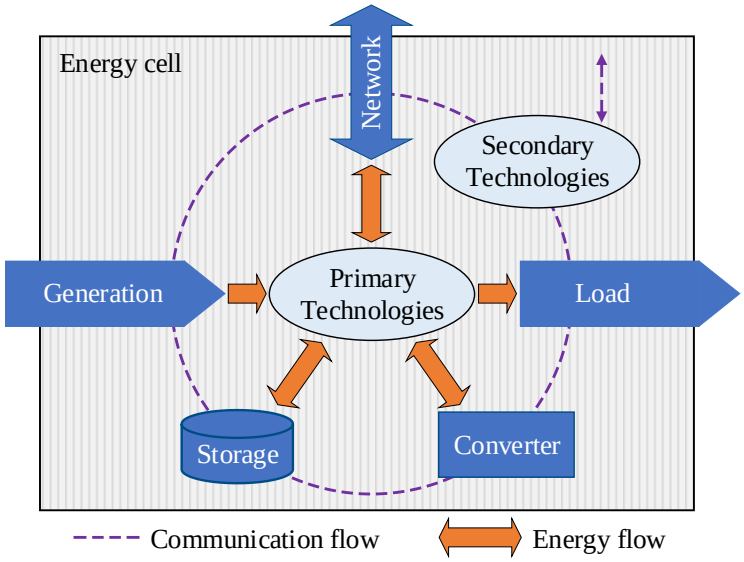

Figure 2.8: Components of an energy cell [150]

To conclude, the forms of microgrid and the cellular power grid are oriented by geographical areas, designed as mini grids. Both microgrid and cellular power grids have the potential to handle the penetration of distributed generations. They allow decentralisation of grid operations and control. Self-sufficient power generation and consumption are expected in the specified microgrid or cell.

The CPSA, in contrast, is not limited to a complete physical area of generation, transmission/distribution, and consumption of energy. Two major differences of the CPSA and the other approaches are stated as follows. First, a cluster area can be created on the underlying power grid ranging from a node (for example, a DG unit) up to a group of grid components (for example, an area with loads, connection lines, and DG units). It is not specific to a bus, substation, or group of components. Also, a clear border and, if necessary, a hierarchical level is defined for each area. This provides high flexibility to the smart grids, depending on the choice of grid operations. Second, with the creation of cluster areas, the CPSA brings interconnected grid characteristics from the transmission systems down to the distribution level. This results in a consistent grid structure and the operation in the entire power system, facilitating seamless grid integration of DG units accordingly.

In the following section, the concept of clustering power systems is discussed. It shows how cluster areas are created on the power systems. Main ideas and key contributions of the CPSA are also provided.

2.2.2 Concept of Clustering Power Systems

As the share of RES in the energy market increases, advanced grid operation and control are crucial, so the RESs need to participate in power system control. A critical aspect of power systems in terms of dealing with the RESs is the distribution network, because it was not originally designed to handle power generation. By adopting the concept of smart grid, the

distribution network is smartened and can evolve to be a brand-new active distribution network [142, 160, 161]. Together with the transmission system, the active distribution network should play an active role in control and monitoring of the power systems, such as for optimising operational schedules and power dispatch. The benefits obtained from the active roles of distribution system operators (DSOs) and their coordination with transmission system operators (TSOs) are discussed in [34] and [162]. The primary idea of the CPSA is therefore to provide an opportunity for distribution networks to use the hierarchical control scheme and actions defined in grid code of ENTSO-E [163], i.e. primary, secondary, and tertiary controls in this context. To this end, the primary principle of this approach is to enable distributed active-controlled areas in the entire power system by expanding the active control scheme and actions from the transmission downwards to the distribution systems.

In order to expand the active control scheme and actions, the grid structure characteristics of the transmission grids is taken into account. The transmission grids are composed of multiple interconnected grids, which should be incorporated to the rest of the power grid. To do so, grid elements on the underlying power grid are defined into several areas, thereafter called “cluster areas” [60]. As the transmission grids are in the form of interconnected grids, the cluster areas are also in the form of interconnected cluster areas to acquire the characteristics of the transmission grids. Figure 2.9 exemplifies the application of the CPSA to create a network of cluster areas for the entire power system [164].

According to the CPSA, a network of cluster areas is created in a bottom-up direction to consider the grid elements from the smallest possible scale [165, 166]. A cluster area can be defined at any place that requires to be actively controlled. Regardless of grid hierarchy, it can be located, for instance, at a residential unit in local area or at utility level in a regional area. In Figure 2.9, this network spans from the consumers or prosumers, who not only consumes but also produces electrical energy, upwards to the DSO level and ultimately to the upstream TSO level. As a result, multilevel interconnected cluster areas are built. With this way of defining areas based on the CPSA, a consistent grid structure throughout the power grid can be acquired. Also, the CPSA does not build up a new grid structure, but rather it makes use of existing power grids. The complexity is thus not added to the power grids.

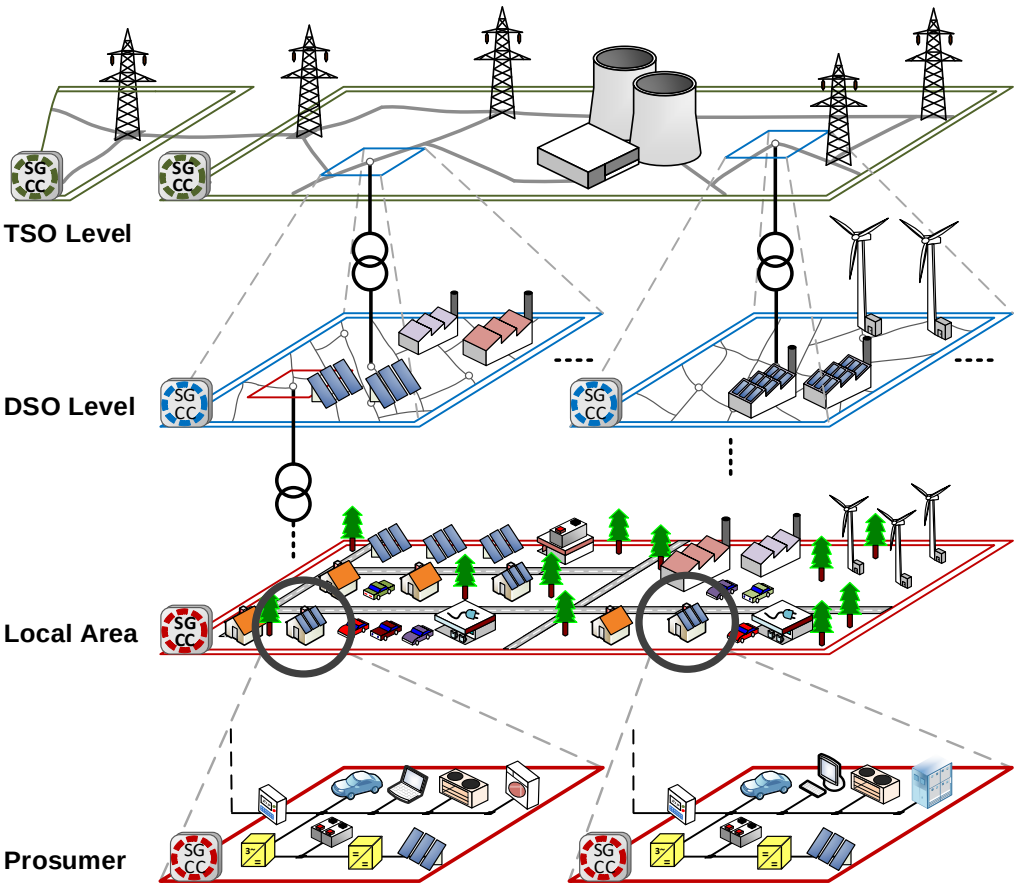

Figure 2.9: The entire power system with the application of the CPSA [164]

Each cluster area, additionally, is monitored by a smart grid cluster controller (SGCC), in which operational functionalities can be implemented and information of grid elements can be manipulated as a platform for decentralised operations [164, 165]. Depending on the operational purposes, the SGCC can manipulate data and perform engineering analyses for each cluster area. Once control functions are implemented in the SGCC, active-controlled functionalities for the corresponding cluster area can be activated [167–169]. The functions of the SGCC are not fixed, since the CPSA is aimed to be flexibly applied at any grid level. The implementation of the functions depends on requirements of the concerned grid level, which can be in the distribution or transmission systems. Accordingly, the functions of the SGCC can be comparable to that of an energy management system (EMS) for cluster areas located in a transmission system. Similarly, they can be compared to that of a distribution management system (DMS) for cluster areas in a distribution network.

This concept, together with the background of the CPSA, have been delineated in this section to provide a basic understanding of this approach. In order to utilise the CPSA, the diversity and complexity of components and infrastructure in the power systems, nevertheless, must be dealt with. To reduce the diversity and complexity, the self-similarity principle is introduced in the following section.

2.2.3 Self-Similarity Principle

Each cluster area, as a result of the CPSA, is composed of various grid components. When considering at an electrical bus or node, similar categories can be seen from the grid components, which thereby can be categorised as a node component and a connecting component. Accordingly, the self-similarity principle is taken into account in the CPSA. To describe a cluster area, a cluster fractal model is developed as depicted in Figure 2.10 [170]. The model indicates the definition and relation of the cluster areas. The node elements are, for example, generating units, loads, and storage systems, while the connecting elements are, for example, transformers and cables [170]. According to this model, each cluster area is managed and controlled by an SGCC. This means, under the CPSA, the management of data flow or command with grid components is also decentralised besides the grid operations [167]. In addition, the hierarchical structure of the power systems is also mimicked in the model. Depending on the underlying power grid, the interconnections among cluster areas are classified into a hierarchical structure – superordinate, ordinate, and subordinate levels. This hierarchy is developed to permit consistency in the structuring of the network of cluster areas throughout the power systems.

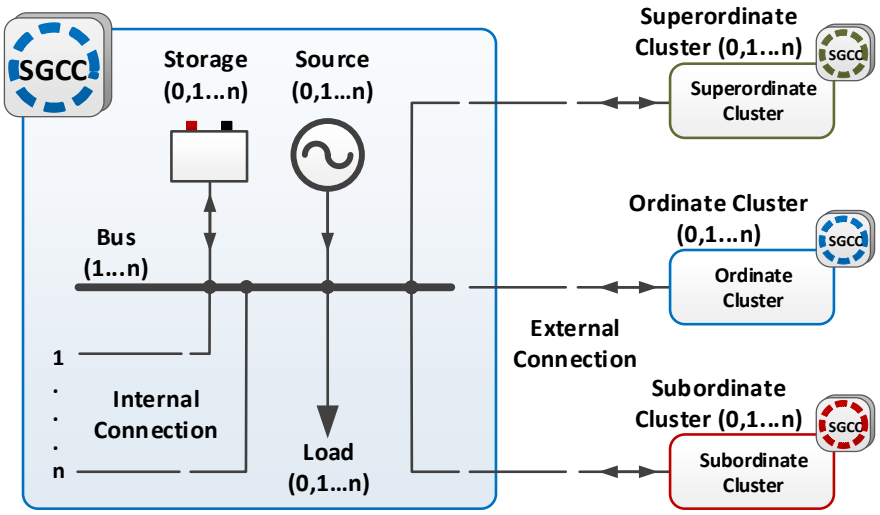

Figure 2.10: Cluster fractal model [170]

Generally, power systems contain multiple electrical levels of the power grids. With the technology advancement, the power grids accommodate a variety of components. To cope with the complexity of the grid structure, a sufficient grid management is required. To this end, the CPSA in combination with the cluster fractal model is a potential solution, as portrayed in Figure 2.11 [171]. Note that the hierarchical level is neglected in this figure since only the management of grid components is focused on. Each cluster area is described by the cluster fractal model. From Figure 2.11, grid components in the network of cluster areas can be repetitively considered as a single grid component by a self-similar description. Only one

model is required to build cluster areas, hence significantly diminishing structural complexity of the power grid.

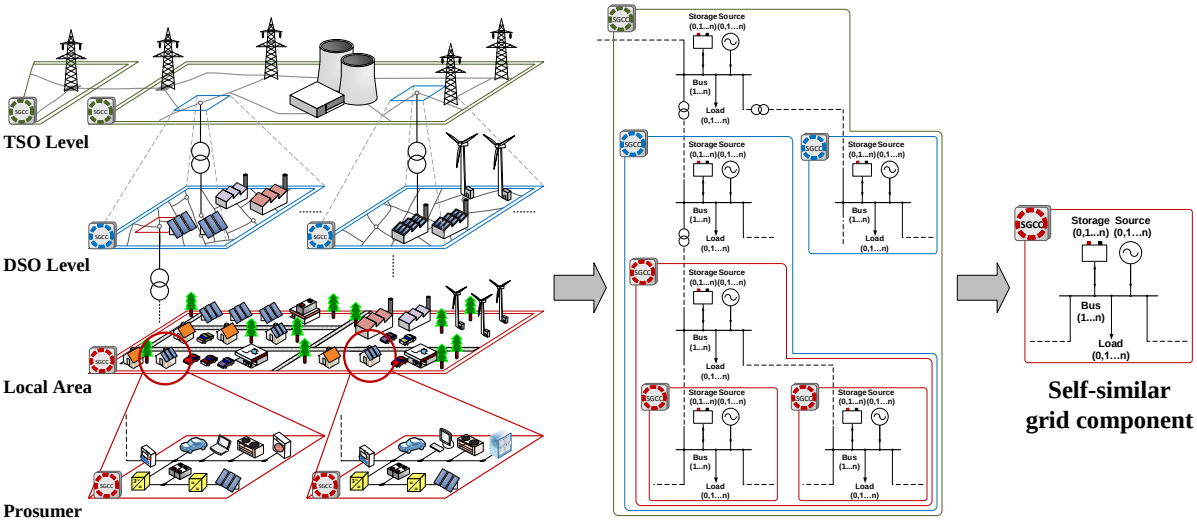

Figure 2.11: Overview of the self-similarity property [171]

In order to enable the operation based on the CPSA concept for future smart grids, coordination and interoperation among interconnected cluster areas are also required. For this reason, each SGCC has a communication capability for interaction with other SGCCs [165, 172]. Similar to the description of each cluster area, the communication strategy between cluster areas are also indicated as displayed in Figure 2.12 [172]. It mimics the physical interconnection between cluster areas.

The cluster communication model describes the interconnections between the SGCCs. The Internet is the communication medium between SGCCs and is secured by virtual private network technology. Each area has its own private network, since it is expected to perform grid operations and manipulate data independently. Moreover, intelligent electronic device (IED) in this context represents communication capability of grid elements.

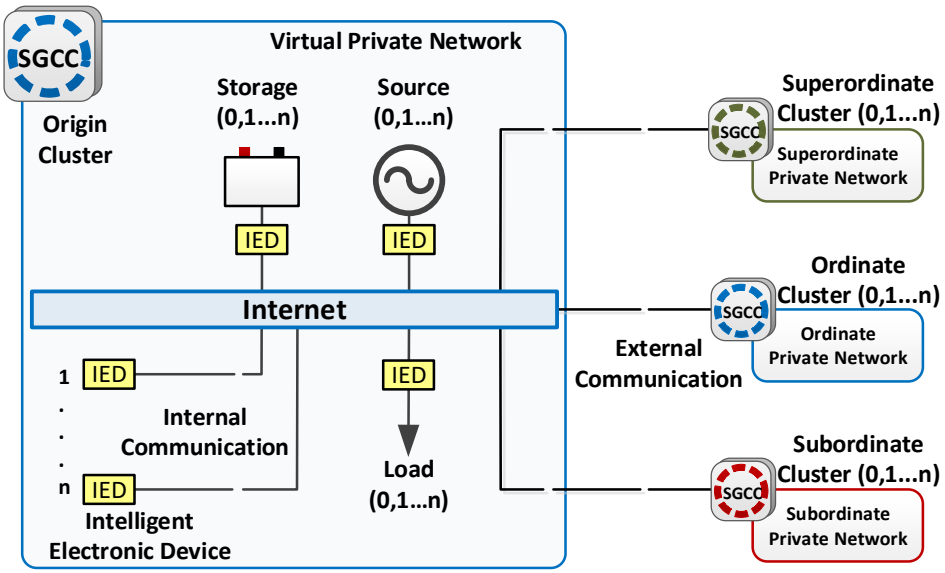

Figure 2.12: Cluster communication model [172]

The self-similarity principle as the cluster fractal model has been elaborated in this section. Together with the CPSA, the cluster fractal model eases the description of the complex modern power systems. Each cluster area resulted from the CPSA can be described in a self-similarity manner and repetitive process for the whole network. Thus, an all-encompassing model can be simply used to manage all the power systems. In the following section, recent research findings based on the CPSA are discussed.

2.2.4 Recent Research on the CPSA

Key advantages of the CPSA are discussed here in terms of two aspects. The first one is the control and functionality aspect. Due to the creation of the network of cluster areas, the CPSA permits a coherent approach for each of structure, operation, and control of the decentralised active power systems. The connections of cluster areas result in a cluster network that establishes the operational characteristics of interconnected grids in the entire power system. The CPSA thus gives an opportunity to the distribution networks to adopt the hierarchical control scheme and functionalities, i.e. primary, secondary, and tertiary controls, from the transmission system. This guarantees compliance of grid operation in the entire power system. Thus, the concept of the CPSA can close the gap of grid operations between transmission and distribution levels, allowing seamless integration and power management of DG units in power systems. This is a sustainable way to decentralise active grid control and operations. To provide some examples, references [58], [60], and [173] present how the conventional control scheme is adopted and utilised in the multilevel cluster areas. As a result, the cluster control applications enable power grids to be stabilized in a bottom-up direction from the unit level up to the transmission level, not only in top-to-down stabilisation. The CPSA is therefore modelled to support the increase of the number of DG units residing in low voltage grids, which has changed the structure of the power generation. According to the hierarchical

control scheme, interconnected cluster areas can exchange power to deal with disturbances which might occur in any cluster area. On the other hand, a cluster area can operate independently in island mode when it is disconnected from the main grid. The principle of the CPSA eases the complexities of future electrical systems and meanwhile retains stability and secure operations.

The second aspect is about data management. Conventionally, the relevant data of a power system are stored at the central control centre of supervisory control and data acquisition (SCADA) system. However, the existence of advanced technologies for smart functions in power systems causes massive data to be transferred within and between the power systems, and the participation of smart appliances will add additional data besides grid components to power systems. Hence, the traditional power systems require a change of data management as well as control systems towards smart, distributed infrastructure [50, 174]. By applying the CPSA, data storage is decentralised, as each cluster area is supposed to manage and manipulate data individually. The decentralisation of data storage offers more efficient data manipulation, together with flexibility, compared to centralised storage to cope with a massive data flow [39, 175–177]. A lot of research based on the CPSA has been published in many publications such as [58–61] and [165, 168, 178].

Thus far, the CPSA has been introduced; and the principles and applications of the CPSA are delineated. In this thesis, an impedance network model and a method for decoupled voltage sensitivity analysis are proposed, in conjunction with the application of the CPSA. This thesis adopts the distributed grid structure of the cluster areas, which can result in a strong step to further develop and realise the smart grids.

2.3 Summary

This chapter reviews the state-of-the-art technologies relevant to this thesis. As the intention of this thesis is to contribute intelligent operations for future smart grids, a general overview of the smart grids is given, and related technologies are first discussed. For this thesis, the PMU is regarded as a core element by which the measurement of synchrophasors can be executed. The measurement data are required in the process of generating the proposed impedance model and performing the proposed decoupled voltage sensitivity analysis. Afterwards, the CPSA, the foundation of this thesis, is elaborated. The originality of this approach is discussed in comparison with two related concepts, which are microgrid and cellular power grids. These concepts are proposed to cope with the penetration of distributed generations and enable decentralisation of grid operation and control. Both microgrid and cellular power grid are formed by defining physical areas on the power grids with the potential energy balance between generators, energy storages, and loads in the areas. The CPSA, nonetheless, is not restricted to these elements, unlike the microgrid and cellular power grid concepts. It allows the creation of distributed areas, named here as cluster areas,

from a node or bus to handle the decentralisation of active control. Key differences between the CPSA and microgrid and cellular power grid are summarised in Table 2.2.

Table 2.2: Differences between CPSA, Microgrid, and Cellular power grid

	CPSA	**Microgrid and Cellular power grid**
Creation of distributed areas	From a node to a group of electrical components or a physical a area	Physical areas with balance in generation and consumption
Expected characteristics	Interconnected grids like in a transmission system.	Individual areas with possibility

The principle of the CPSA is then presented as an approach on which this thesis relies. Each cluster area is described in terms of the cluster fractal model. This model simplifies the description of the cluster areas, and also the whole power system adopted by the CPSA. Lastly, the advantages of the CPSA and an explanation of the published research are provided to exemplify the features of this approach.

In Chapter 3 and Chapter 4, the proposed impedance model and the proposed method for decoupled voltage sensitivity analysis are presented respectively. They will showcase the use of the CPSA, which is outlined in this chapter. As a contribution to the development of the CPSA, the proposed impedance model and analysis method will support the distributed characteristic of the cluster areas for the smart grid operations.

3. Impedance Network Model for Cluster-Based Decentralised Power Grids

To perform grid operations, insight knowledge into the underlying power grid is essential. A grid model is generally used to study the power systems. For steady-state analyses, two prominent models used to describe a power grid are the admittance model and the impedance model [179]. Which model to use depends on the type of analysis that will be carried out. In this thesis, the network model proposed for cluster-based decentralised power grids is based on the impedance model. It is developed to be utilised in conjunction with the clustering power systems approach (CPSA) to enable decoupled voltage sensitivity analysis in which the change of bus voltage at one bus caused by the change of bus current deviation from another bus is analysed. As the operations of a future power grid or smart grid tend towards decentralisation, they entail interoperation among fractions of the power grid. The CPSA defines decentralised areas as "cluster areas" on the power grid. Accordingly, to describe the characteristics of bus voltages in voltage sensitivity analysis, the proposed model must be able to be determined separately, or in a decoupled way, in each cluster area.

In this chapter, the first section introduces the impedance model. Bus impedance matrix and Thévenin's theorem are presented, since they are the basis of the proposed network model. The second section details a bus impedance parameters matrix, which is the proposed impedance model. Step by step determination of the impedance parameters is also discussed. The determination encompasses the analyses of both a single area and multiple areas. Finally, the third section summarises this chapter.

3.1 Introduction to Network Models

Two fundamental network models used in power systems analysis are known as admittance and impedance models. The admittance model describes bus currents of the power grid in the term of bus voltages. In contrast, the impedance model generally describes bus voltages of the power grid in the term of bus currents. They are in the form of a bus admittance matrix and a bus impedance matrix, which are the mathematical inverse of each other [180]. Albeit the impedance model is the foundation for the proposed decoupled voltage sensitivity analysis, both network models are introduced in this section to clarify their characteristics. The relationship between the bus admittance and bus impedance matrices is also pointed out. After that, a basic description of the Thévenin's theorem is provided. The Thévenin's theorem is an important technique that works in conjunction with the impedance model. It provides a key feature that is beneficial to the determination of the proposed network model, i.e. bus impedance parameters.

3.1.1 Bus Admittance and Bus Impedance Matrices

The bus admittance matrix [$\underline{Y}_{bus}$] and bus impedance matrix [$\underline{Z}_{bus}$] are essential tools in the field of electrical engineering for power system analyses. They mathematically describe the voltage-current relationship of a power network. Using either one of the models depends on the type of the analysis, as they have different characteristics. For instance, the matrix [$\underline{Y}_{bus}$] is favourably used in load flow calculations, while the matrix [$\underline{Z}_{bus}$] is widely utilised in fault calculations and contingency analysis [181, 182]. Based on the topological connections between buses, matrices [$\underline{Y}_{bus}$] and [$\underline{Z}_{bus}$] can be determined. Since the aim of this section is to introduce the basic network models, only an overview of [$\underline{Y}_{bus}$] and [$\underline{Z}_{bus}$] is given. The formation of the matrices [$\underline{Y}_{bus}$] and [$\underline{Z}_{bus}$] can be found in literature such as [179, 180].

To envision the overview of [$\underline{Y}_{bus}$] and [$\underline{Z}_{bus}$], Figure 3.1 depicts an exemplified *n*-port network of an *n*-bus power grid. Represented by ports, bus numbers run from 1, 2, to *n*, and number 0 denotes the reference of this network.

Figure 3.1: An exemplified *n*-port network

First of all, the matrix [$\underline{Y}_{bus}$] is taken into account. It can be obtained from nodal equations of the power grid. Since there are *n* buses in this example, *n* nodal equations can be constructed. As a result, the set of the nodal equations of this network is

$$\begin{bmatrix} \underline{I}_1 \\ \underline{I}_2 \\ \vdots \\ \underline{I}_n \end{bmatrix} = \begin{bmatrix} \underline{Y}_{11} & \underline{Y}_{12} & \cdots & \underline{Y}_{1n} \\ \underline{Y}_{21} & \underline{Y}_{22} & \cdots & \underline{Y}_{2n} \\ \vdots & \vdots & \ddots & \vdots \\ \underline{Y}_{n1} & \underline{Y}_{n2} & \cdots & \underline{Y}_{nn} \end{bmatrix} \begin{bmatrix} \underline{V}_1 \\ \underline{V}_2 \\ \vdots \\ \underline{V}_n \end{bmatrix}. \tag{3.1}$$

Evidently, bus currents are described as a linear function of bus voltages in Eq. (3.1). The subscript of bus current $\underline{I}$, bus voltage $\underline{V}$, and admittance $\underline{Y}$ indicates its bus number. For this *n*-node network, the impact of bus voltages $\underline{V}_i$ ($i \in \{1, 2, \ldots, n\}$) on bus currents $\underline{I}_i$ ($i \in \{1, 2, \ldots, n\}$) is represented by the bus admittance matrix

$$[\underline{Y}_{bus}] = \begin{bmatrix} \underline{Y}_{11} & \underline{Y}_{12} & \cdots & \underline{Y}_{1n} \\ \underline{Y}_{21} & \underline{Y}_{22} & \cdots & \underline{Y}_{2n} \\ \vdots & \vdots & \ddots & \vdots \\ \underline{Y}_{n1} & \underline{Y}_{n2} & \cdots & \underline{Y}_{nn} \end{bmatrix}. \tag{3.2}$$

In Eq. (3.2), according to literature such as [179], the diagonal elements, $\underline{Y}_{ij}$ ($i, j \in \{1, 2, \ldots, n\}$; $i = j$), are known as self-admittances or driving-point admittances. These admittances represent the impact of bus voltages on bus currents at the same bus. Similarly, the off-diagonal elements, i.e. $\underline{Y}_{ij}$ ($i, j \in \{1, 2, \ldots, n\}$; $i \neq j$), are called mutual admittances or transfer admittances. Thus, these admittances express the linear impact of bus voltages on bus currents at all other buses.

To observe the impact of bus currents $\underline{I}_i$ ($i \in \{1, 2, \ldots, n\}$) on bus voltages $\underline{V}_i$ ($i \in \{1, 2, \ldots, n\}$), Eq. (3.1) can be rearranged to

$$\begin{bmatrix} \underline{V}_1 \\ \underline{V}_2 \\ \vdots \\ \underline{V}_n \end{bmatrix} = \begin{bmatrix} \underline{Y}_{11} & \underline{Y}_{12} & \cdots & \underline{Y}_{1n} \\ \underline{Y}_{21} & \underline{Y}_{22} & \cdots & \underline{Y}_{2n} \\ \vdots & \vdots & \ddots & \vdots \\ \underline{Y}_{n1} & \underline{Y}_{n2} & \cdots & \underline{Y}_{nn} \end{bmatrix}^{-1} \begin{bmatrix} \underline{I}_1 \\ \underline{I}_2 \\ \vdots \\ \underline{I}_n \end{bmatrix}. \tag{3.3}$$

Inverting the matrix $[\underline{Y}_{bus}]$ results in the matrix $[\underline{Z}_{bus}]$; Eq. (3.3) therefore can be written as

$$\begin{bmatrix} \underline{V}_1 \\ \underline{V}_2 \\ \vdots \\ \underline{V}_n \end{bmatrix} = \begin{bmatrix} \underline{Z}_{11} & \underline{Z}_{12} & \cdots & \underline{Z}_{1n} \\ \underline{Z}_{21} & \underline{Z}_{22} & \cdots & \underline{Z}_{2n} \\ \vdots & \vdots & \ddots & \vdots \\ \underline{Z}_{n1} & \underline{Z}_{n2} & \cdots & \underline{Z}_{nn} \end{bmatrix} \begin{bmatrix} \underline{I}_1 \\ \underline{I}_2 \\ \vdots \\ \underline{I}_n \end{bmatrix}. \tag{3.4}$$

From Eq. (3.4), the bus impedance matrix

$$[\underline{Z}_{bus}] = \begin{bmatrix} \underline{Z}_{11} & \underline{Z}_{12} & \cdots & \underline{Z}_{1n} \\ \underline{Z}_{21} & \underline{Z}_{22} & \cdots & \underline{Z}_{2n} \\ \vdots & \vdots & \ddots & \vdots \\ \underline{Z}_{n1} & \underline{Z}_{n2} & \cdots & \underline{Z}_{nn} \end{bmatrix} \tag{3.5}$$

provides the impact of bus currents on bus voltages of the n-node network in Figure 3.1. Similar to the case of the matrix $[\underline{Y}_{bus}]$, the diagonal elements in Eq. (3.5), i.e. $\underline{Z}_{ii}$ ($i \in \{1, 2, \ldots, n\}$; $i = j$) are known as self-impedances or driving-point impedances, representing the impact of bus currents on bus voltages at the same bus. The off-diagonal elements, i.e. $\underline{Z}_{ij}$ ($i, j \in \{1, 2, \ldots, n\}$; $i \neq j$), are called mutual impedances or transfer impedances. These impedances indicate the impact of bus currents on bus voltages at all other buses.

The matrix $[\underline{Z}_{bus}]$ is adapted in this thesis to be used in the proposed voltage sensitivity analysis, which is delineated in Chapter 4. This property of network voltage representation according to $[\underline{Z}_{bus}]$ is used in order to examine the impact of bus current injected into each bus on network voltages. It allows analysis of voltage change at each bus due to the change of current, which can be inferred to extracted or fed-in active and reactive powers. Another big advantage of $[\underline{Z}_{bus}]$ is that it provides information of Thévenin impedance from the diagonal elements of $[\underline{Z}_{bus}]$, permitting a great contribution to the proposed voltage sensitivity analysis. The basic principle of Thévenin's theorem and its relation to $[\underline{Z}_{bus}]$ is presented in the next section.

3.1.2 Thévenin's Theorem and Its Relation to Bus Impedances

Thévenin's theorem is an essential circuit analysis technique for circuit calculation. It is typically used in linear direct current (dc) and alternating current (ac) circuits [183, 184]. This theorem simplifies and converts the original network containing voltage sources or current sources and linear impedances into an equivalent circuit across a pair of terminals of concern. This equivalent circuit is named as the Thévenin equivalent circuit which is composed of a Thévenin equivalent voltage source $\underline{V}_{Th}$ and a Thévenin impedance $\underline{Z}_{Th}$. Thereby, the Thévenin equivalent circuit gives the characteristic of its original circuit at the concerned terminals. A powerful advantage of this equivalent circuit is that the change between the concerned terminals can be observed without recalculating the whole circuit. This provides an immense benefit to network calculation in term of ease of calculation.

To showcase the application of the Thévenin's theorem, Figure 3.2 illustrates an example of converting a circuit to its Thévenin equivalent circuit. In this example, the Thévenin equivalent circuit looking into terminals *A* and *B* is considered.

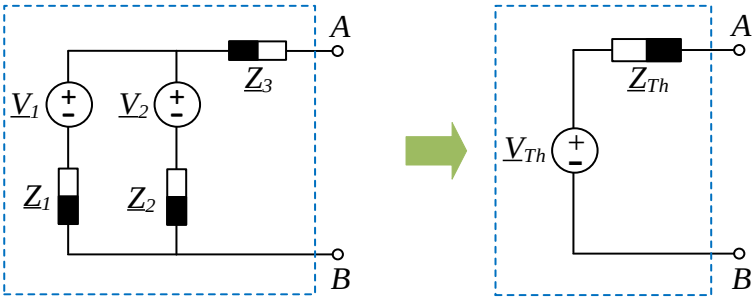

(a) (b)

Figure 3.2: An example of the application of Thévenin's theorem:
(a) Original circuit; (b) Thévenin equivalent circuit

Figure 3.2(a) displays the original circuit consisting of a voltage source $\underline{V}_1$ and three impedances: $\underline{Z}_1$, $\underline{Z}_2$, and $\underline{Z}_3$. As the change between terminals *A* and *B* is considered, the Thévenin equivalent circuit looking into terminals *A* and *B* is determined. In Figure 3.2(b), the components of the original circuit inside the blue dash square are represented as the Thévenin equivalent circuit by a series connection of a Thévenin equivalent voltage source $\underline{V}_{Th}$ and a Thévenin impedance $\underline{Z}_{Th}$. The voltage source $\underline{V}_{Th}$ is the open-circuit voltage measured across terminals *A* and *B*, serving as the original voltage across these terminals in the equivalent circuit, while the impedance $\underline{Z}_{Th}$ is the overall impedance of the original circuit considered at these terminals. The polarity of the source $\underline{V}_{Th}$ depends on the direction of current flow through the impedance between the terminals of concern in the original network [185]. In this case, the current is assumed to flow from terminal *A* to terminal *B*. Similarly, the impedance $\underline{Z}_{Th}$ is the equivalent impedance measured across terminals *A* and *B* in the direction of looking into the circuit of the network. Furthermore, the impedance $\underline{Z}_{Th}$ can be manually calculated as

well. To this end, the internal voltage source is initially short-circuited, as the ideal internal impedance of the voltage source is zero. Then, manual calculation of the impedance $\underline{Z}_{Th}$ can be performed. The use of Thévenin's theorem can be expanded to network analyses of power grids. The same calculation technique executed in the example in Figure 3.2 can be utilised to acquire the Thévenin impedance $\underline{Z}_{Th}$ with respect to the reference point of each bus. The electrical components of a power grid such as generating sources, loads, transformers, power cables or transmission lines can be converted into a single-line diagram to perform as an original circuit. The aforementioned technique to calculate the impedance $\underline{Z}_{Th}$ is not shown in detail here as it is not directly relevant.

In this thesis, the technique to obtain the impedance $\underline{Z}_{Th}$ of each bus from the matrix $[\underline{Z}_{bus}]$ is of interest. The impedance $\underline{Z}_{Th}$ of each bus equals to its corresponding self-impedance in the matrix $[\underline{Z}_{bus}]$ [179]. To demonstrate this technique, the principle of fault analysis using bus impedance matrix is adopted, so bus voltages and currents are separately considered as the present-state and initial quantities. Starting from the present-state quantities, based on the network equation of the *n*-bus network from Eq. (3.4), the present-state bus voltages matrix

$$[\underline{V}] = [\underline{Z}_{bus}][\underline{I}] \tag{3.6}$$

is described in terms of the matrix $[\underline{Z}_{bus}]$ and the present-state bus currents matrix $[\underline{I}]$. For the initial quantities, before reaching the state of bus voltages $[\underline{V}]$ and bus currents $[\underline{I}]$, the initial bus voltage matrix

$$[\underline{V}^0] = [\underline{Z}_{bus}][\underline{I}^0]. \tag{3.7}$$

is described in terms of the matrix $[\underline{Z}_{bus}]$ and the initial bus currents matrix $[\underline{I}^0]$ in the same manner as Eq. (3.6). Subsequently, when a linear characteristic of a power grid is assumed, the change in bus voltages $[\Delta\underline{V}]$ and bus currents $[\Delta\underline{I}]$ can be explained by using the superposition theorem [179, 180]. The bus voltage matrix $[\underline{V}]$ and the bus current matrix $[\underline{I}]$ can be expressed as the algebraic sum of their initial value and the change

$$[\underline{V}] = [\underline{V}^0] + [\Delta\underline{V}] \tag{3.8}$$

and

$$[\underline{I}] = [\underline{I}^0] + [\Delta\underline{I}]. \tag{3.9}$$

Substituting Eq. (3.9) into Eq. (3.6), the voltage matrix $[\underline{V}]$ can be considered as the product of the matrix $[\underline{Z}_{bus}]$ and the algebraic sum of initial bus current matrix $[\underline{I}^0]$ and the matrix of current change $[\Delta\underline{I}]$. Hence, Eq. (3.6) becomes

$$[\underline{V}] = [\underline{Z}_{bus}] \cdot ([\underline{I}^0] + [\Delta\underline{I}]) \tag{3.10}$$

which equals to

$$[\underline{V}] = [\underline{Z}_{bus}][\underline{I}^0] + [\underline{Z}_{bus}][\Delta\underline{I}]. \tag{3.11}$$

In Eq. (3.11), the product of $[\underline{Z}_{bus}][\underline{I}^0]$ equals to $[\underline{V}^0]$, as illustrated in Eq. (3.7). Thus, by mapping $[\underline{V}^0]$ in Eq. (3.7) to Eq. (3.11) , the present-state bus voltages matrix

$$[\underline{V}] = [\underline{V}^0] + [\underline{Z}_{bus}][\Delta\underline{I}] \tag{3.12}$$

is described as the initial voltage plus the change of bus voltage caused by current change. In the following, an example of the impact of current change is given. Assuming only bus current $\underline{I}_i$ at bus i where $i \in \{1, 2, \ldots, n\}$ is changed, whereas the rest of bus current change equals to zero. Based on Eq. (3.12), bus voltage $\underline{V}_i$ at bus i can be understood as

$$\underline{V}_i = \underline{V}_i^0 + \underline{Z}_{ii} \cdot \Delta\underline{I}_i. \tag{3.13}$$

According to [179], Eq. (3.13) can be depicted, as shown in Figure 3.3. The circuit in Figure 3.3 is noticeably comparable with the Thévenin equivalent circuit shown in Figure 3.2(b).

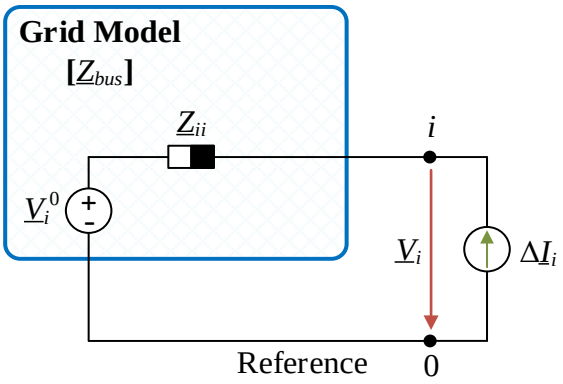

Figure 3.3: Circuit diagram depicting the impact of current change on bus voltage [179]

Since the characteristic of the Thévenin circuit can be inferred from Figure 3.3, for an n-bus power grid, the Thévenin impedance

$$\underline{Z}_{Th,i} = \underline{Z}_{ii} \tag{3.14}$$

at bus i where $i \in \{1, 2, \ldots, n\}$ can be obtained from the diagonal elements $\underline{Z}_{ii}$ of that matrix $[\underline{Z}_{bus}]$.

The Thévenin's theorem is used in this thesis to assist the proposed voltage sensitivity analysis in decentralised areas, i.e. cluster areas. The Thévenin impedance $\underline{Z}_{Th}$ is employed to represent the overall bus impedance at border buses between two interconnected cluster areas. As the bus impedances matrix of each cluster area is calculated, Thévenin impedance $\underline{Z}_{Th}$ at each bus can be selected. Thus, exchanging characteristics between cluster areas can be performed.

3.2 Impedance Model for Cluster-Based Decentralised Power Grids

The impedance model presented in this section is developed and proposed for the analysis of the power grid under the CPSA, where the power grid is defined into various cluster areas.

The proposed impedance model is named here as bus impedance parameters. To clarify, first of all, the definition of the bus impedance parameters is discussed. The relationship between the bus impedance parameters and the bus impedance matrix is indicated. Next, the determination of the bus impedance parameters in each cluster area is described, and it is furthermore related to the process of converting the bus impedance parameters into symmetrical components to cope with the unbalanced grid condition and the process of integrating the influence between interconnected cluster areas when multiple cluster areas are involved. Thus, the determination procedure can be conducted for either a single area or multiple areas, enabling decoupled calculation of the bus impedance parameters.

3.2.1 Bus Impedance Parameters

The impedance model is chosen in this thesis to gain insight into the manner of voltage characteristics for network analysis under the CPSA. Theoretically, a power network is described in the form of a bus impedance matrix [$\underline{Z}_{bus}$], based on the impedance model. The matrix [$\underline{Z}_{bus}$] can be calculated by using information of grid topology, i.e. the arrangement of buses, cable type, and cable length. Depending on the choice of preference, [$\underline{Z}_{bus}$] can be built by either converting from bus admittances or constructing from scratch. Both building procedure of the matrix [$\underline{Z}_{bus}$], however, need the complete information of grid topology, resulting in the full-scale matrix dimension. For this reason, to generate the matrix [$\underline{Z}_{bus}$] requires a considerable amount of the resource in the computing unit. The operations of the power grid in the future, nevertheless, tend towards decentralisation, in which the controlling units are smaller and have less performance compared with that of the central control centres [142, 186, 187]. To build the network model for decentralised operation and analysis with consideration of the limited performance of the computing unit, the amount of required information should be reduced.

In this thesis, to decrease the amount of required information, only buses of concern and their local measurements of bus voltages and bus currents are used to build the impedance network model without knowledge about the grid topology. Since the network model resulted from this process is based on the impedance, but different size from the matrix [$\underline{Z}_{bus}$], calling it the matrix [$\underline{Z}_{bus}$] can be misleading. This resulted impedance model is hence named as bus impedance parameters, thereafter denoted by [$\underline{Z}_{par}$] when they are in the form of a matrix. The matrix [$\underline{Z}_{par}$] is supposed to represent only the voltage-current relationship between buses of concern; the elements relevant to the junction bus(es) are not included. It is introduced here as a reduced version of the matrix [$\underline{Z}_{bus}$], which can be reduced to be the same as the matrix [$\underline{Z}_{par}$] by using node elimination theory such as Kron's reduction technique [179].

Before moving on to the description of the bus impedance parameters, two key differences between the matrices [$\underline{Z}_{par}$] and [$\underline{Z}_{bus}$] must be emphasised. The first one is the building process of the matrices. The matrix [$\underline{Z}_{par}$] is expected to be determined by using only local

measurements of bus voltages and bus currents without knowledge about the grid topology. The second difference is the elements of the matrices. The matrix [$\underline{Z}_{par}$] possesses only bus impedances of the specific buses of concern, whereas the matrix [$\underline{Z}_{bus}$] consists of bus impedances of every single bus of a power grid.

To envision the physical difference between the matrices [$\underline{Z}_{par}$] and [$\underline{Z}_{bus}$], a 5-bus radial grid is displayed as an example in Figure 3.4. Bus 1 is assigned as an unconcerned bus, whereas the rest are concerned. It must be noted that since the aim of this example is only to demonstrate the difference of the matrices of the network model, all quantitative values of this grid are not provided, and the determination of the matrices is not discussed.

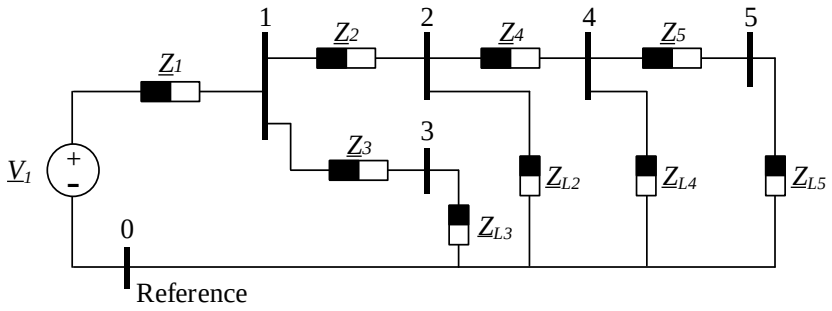

Figure 3.4: Exemplified 5-bus radial grid

The matrices [$\underline{Z}_{bus}$] and [$\underline{Z}_{par}$] of the grid in Figure 3.4 are presented in Figure 3.5(a) and Figure 3.5(b), respectively. The dimension of the matrix [$\underline{Z}_{bus}$] in Figure 3.5(a) is 5×5 because all buses are taken into account. However, bus 1 is omitted out of the matrix [$\underline{Z}_{par}$] because only bus 2 to bus 4 are the buses of concern. The dimension of the matrix [$\underline{Z}_{par}$] Figure 3.5(b) is 4×4 accordingly. In addition, it must be noted that the subscript of each element in Figure 3.5(a) and Figure 3.5(b) indicates the bus number, not the position of the matrix element. More details of the matrix [$\underline{Z}_{par}$] is given later in this section.

$$[\underline{Z}_{bus}] = \begin{bmatrix} \underline{Z}_{11} & \underline{Z}_{12} & \underline{Z}_{13} & \underline{Z}_{14} & \underline{Z}_{15} \\ \underline{Z}_{21} & \underline{Z}_{22} & \underline{Z}_{23} & \underline{Z}_{24} & \underline{Z}_{25} \\ \underline{Z}_{31} & \underline{Z}_{32} & \underline{Z}_{33} & \underline{Z}_{34} & \underline{Z}_{35} \\ \underline{Z}_{41} & \underline{Z}_{42} & \underline{Z}_{43} & \underline{Z}_{44} & \underline{Z}_{45} \\ \underline{Z}_{51} & \underline{Z}_{52} & \underline{Z}_{53} & \underline{Z}_{54} & \underline{Z}_{55} \end{bmatrix} \qquad [\underline{Z}_{par}] = \begin{bmatrix} \underline{Z}_{22} & \underline{Z}_{23} & \underline{Z}_{24} & \underline{Z}_{25} \\ \underline{Z}_{32} & \underline{Z}_{33} & \underline{Z}_{34} & \underline{Z}_{35} \\ \underline{Z}_{42} & \underline{Z}_{43} & \underline{Z}_{44} & \underline{Z}_{45} \\ \underline{Z}_{52} & \underline{Z}_{53} & \underline{Z}_{54} & \underline{Z}_{55} \end{bmatrix}$$

(a) (b)

Figure 3.5: Comparison between the matrices [$\underline{Z}_{par}$] and [$\underline{Z}_{bus}$]

To conclude, an important advantage of the matrix [$\underline{Z}_{par}$] is that the up-to-date network model based on the matrix [$\underline{Z}_{par}$] can be updated in real time from the measurement data. Nevertheless, building an up-to-date matrix [$\underline{Z}_{bus}$] requires the information of up-to-date grid topology, which normally takes longer than the time to collect measurement data. The matrix [$\underline{Z}_{par}$] is, thus, more suitable than the matrix [$\underline{Z}_{bus}$] in an online analysis, which focuses on the

latest state of the grid. Meanwhile, both matrices [$\underline{Z}_{par}$] and [$\underline{Z}_{bus}$] can be used for an offline analysis since they can also be built by using historical data.

The derivation of the matrix [$\underline{Z}_{par}$] is demonstrated in the following. If n buses are concerned, a power grid – or a cluster area when the CPSA is considered – is seen as an n-port network as portrayed in Figure 3.6. This figure is the extended version of the exemplified n-bus network in Figure 3.1. Both bus voltages and currents are assumed to be measured concurrently. The measurement at each point in time is stamped as time t. Number 0 denotes the reference point for bus voltages.

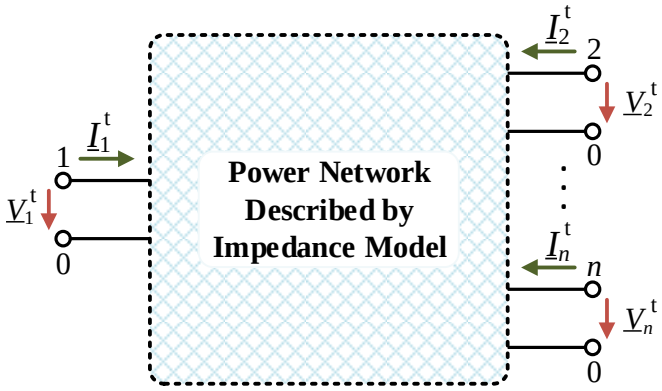

Figure 3.6: An n-port power network representing n buses of concern

To examine the impact of the change of bus currents on bus voltages, for the sake of simplicity, the bus impedance parameters describing only the relationship between bus 1 and bus 2 are taken into account as an example. Based on Figure 3.6, the two-port network between bus 1 and bus 2 is illustrated in Figure 3.7. During time period T, the change of bus currents $\Delta\underline{I}_1^T$ and $\Delta\underline{I}_2^T$ at bus 1 and bus 2 leads to the change of voltages at each bus $\Delta\underline{V}_1^T$ and $\Delta\underline{V}_2^T$, respectively.

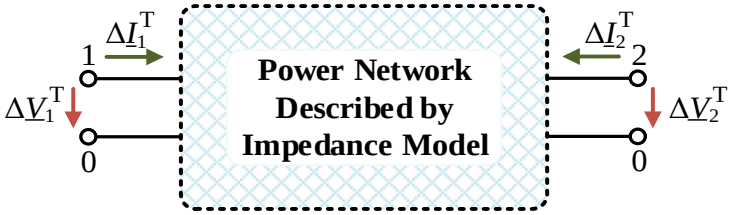

Figure 3.7: Two-port network of bus 1 and bus 2

Since the impedance model is selected to describe the power network, the change of bus voltages $\Delta\underline{V}_1^T$ and $\Delta\underline{V}_2^T$ in Figure 3.7 can be described in terms of bus currents $\Delta\underline{I}_1^T$ and $\Delta\underline{I}_2^T$. By considering time period T_1, the change of bus voltages and bus currents can be described in network equations as

$$\Delta\underline{V}_1^{T_1} = \underline{Z}_{11} \cdot \Delta\underline{I}_1^{T_1} + \underline{Z}_{12} \cdot \Delta\underline{I}_2^{T_1} \tag{3.15}$$

$$\Delta\underline{V}_2^{T_1} = \underline{Z}_{21} \cdot \Delta\underline{I}_1^{T_1} + \underline{Z}_{22} \cdot \Delta\underline{I}_2^{T_1}. \tag{3.16}$$

$\Delta\underline{V}_1^{T_1}$ and $\Delta\underline{V}_2^{T_1}$ in Eqs. (3.15) and (3.16) express the change of bus voltage of bus 1 and bus 2, respectively, during the period T_1. This means that both voltages are influenced by the currents $\Delta\underline{I}_1^{T_1}$ from bus 1 and $\Delta\underline{I}_2^{T_1}$ from bus 2. Accordingly, the impedances $\underline{Z}_{11}$, $\underline{Z}_{12}$, $\underline{Z}_{21}$, and $\underline{Z}_{22}$ are bus impedance parameters between bus 1 and bus 2. The impedances $\underline{Z}_{11}$ and $\underline{Z}_{22}$ represent self-impact of the current change at bus 1 and bus 2, respectively. On the other hand, the impedances $\underline{Z}_{12}$ and $\underline{Z}_{21}$ represent the impact of current change at one bus on the voltage change at the other bus, which is between bus 1 and bus 2.

To determine the impedances $\underline{Z}_{11}$, $\underline{Z}_{12}$, $\underline{Z}_{21}$, and $\underline{Z}_{22}$, only Eq. (3.15) and Eq. (3.16) are not enough. The number of equations is still less than the number of unknown variables at the moment. In this case, one more set of network equations for another time period is required. By considering time period T_2, new network equations are

$$\Delta\underline{V}_1^{T_2} = \underline{Z}_{11} \cdot \Delta\underline{I}_1^{T_2} + \underline{Z}_{12} \cdot \Delta\underline{I}_2^{T_2} \tag{3.17}$$

$$\Delta\underline{V}_2^{T_2} = \underline{Z}_{21} \cdot \Delta\underline{I}_1^{T_2} + \underline{Z}_{22} \cdot \Delta\underline{I}_2^{T_2}. \tag{3.18}$$

Eq. (3.17) and Eq. (3.18) describe the change of bus voltages, $\Delta\underline{V}_1^{T_2}$ and $\Delta\underline{V}_2^{T_2}$, caused by the change of bus currents $\Delta\underline{I}_1^{T_2}$ and $\Delta\underline{I}_2^{T_2}$ during the period T_2 at bus 1 and bus 2. At this point, the number of equations equals to the number of the bus impedance parameters between bus 1 and bus 2. Since the equations of voltage change are linear, Eqs. (3.15) to (3.18) can be arranged as the matrix

$$\begin{bmatrix} \Delta\underline{V}_1^{T_1} & \Delta\underline{V}_1^{T_2} \\ \Delta\underline{V}_2^{T_1} & \Delta\underline{V}_2^{T_2} \end{bmatrix} = \begin{bmatrix} \underline{Z}_{11} & \underline{Z}_{12} \\ \underline{Z}_{21} & \underline{Z}_{22} \end{bmatrix} \begin{bmatrix} \Delta\underline{I}_1^{T_1} & \Delta\underline{I}_1^{T_2} \\ \Delta\underline{I}_2^{T_1} & \Delta\underline{I}_2^{T_2} \end{bmatrix} \tag{3.19}$$

to solve this equation system. The matrix $[\underline{Z}_{par}]$, thus, can be determined by multiplying the inverse of the matrix of current change on both sides in Eq. (3.19), as illustrated in

$$\begin{bmatrix} \underline{Z}_{11} & \underline{Z}_{12} \\ \underline{Z}_{21} & \underline{Z}_{22} \end{bmatrix} = \begin{bmatrix} \Delta\underline{V}_1^{T_1} & \Delta\underline{V}_1^{T_2} \\ \Delta\underline{V}_2^{T_1} & \Delta\underline{V}_2^{T_2} \end{bmatrix} \begin{bmatrix} \Delta\underline{I}_1^{T_1} & \Delta\underline{I}_1^{T_2} \\ \Delta\underline{I}_2^{T_1} & \Delta\underline{I}_2^{T_2} \end{bmatrix}^{-1}. \tag{3.20}$$

Eq. (3.20) shows the determination of the matrix $[\underline{Z}_{par}]$ between bus 1 and bus 2. The matrix is square, and the dimension of the matrix, i.e. the number of rows or column, reflexes the number of buses. By applying the same procedure, Eq. (3.20) can be expanded to any power grid with *n* number of ports, which represent buses of concern. Thus, the matrix

$$\begin{bmatrix} \underline{Z}_{11} & \underline{Z}_{12} & \cdots & \underline{Z}_{1n} \\ \underline{Z}_{21} & \underline{Z}_{22} & \cdots & \underline{Z}_{2n} \\ \vdots & \vdots & \ddots & \vdots \\ \underline{Z}_{n1} & \underline{Z}_{n2} & \cdots & \underline{Z}_{nn} \end{bmatrix} = \begin{bmatrix} \Delta\underline{V}_1^{T_1} & \Delta\underline{V}_1^{T_2} & \cdots & \Delta\underline{V}_1^{T_n} \\ \Delta\underline{V}_2^{T_1} & \Delta\underline{V}_2^{T_2} & \cdots & \Delta\underline{V}_2^{T_n} \\ \vdots & \vdots & \ddots & \vdots \\ \Delta\underline{V}_n^{T_1} & \Delta\underline{V}_n^{T_2} & \cdots & \Delta\underline{V}_n^{T_n} \end{bmatrix} \cdot \begin{bmatrix} \Delta\underline{I}_1^{T_1} & \Delta\underline{I}_1^{T_2} & \cdots & \Delta\underline{I}_1^{T_n} \\ \Delta\underline{I}_2^{T_1} & \Delta\underline{I}_2^{T_2} & \cdots & \Delta\underline{I}_2^{T_n} \\ \vdots & \vdots & \ddots & \vdots \\ \Delta\underline{I}_n^{T_1} & \Delta\underline{I}_n^{T_2} & \cdots & \Delta\underline{I}_n^{T_n} \end{bmatrix}^{-1} \tag{3.21}$$

provides the general equation system for the *n*-port power network or cluster area, depicted in Figure 3.6. In turn, Eq. (3.21) can be understood in a short form as

$$[\underline{Z}_{par}] = [\Delta \underline{V}^{\mathrm{T}}][\Delta \underline{I}^{\mathrm{T}}]^{-1}. \tag{3.22}$$

where $[\Delta \underline{V}^{\mathrm{T}}]$ is the matrix of bus voltage changes, and $[\Delta \underline{I}^{\mathrm{T}}]$ is the matrix of bus current changes. All the matrices are square, and their dimension depends on the number of ports or buses of concern, which is $n \times n$ in this context.

Based on the general equation system in Eq. (3.21), the determination of the bus impedance parameters of *n*-port power network requires the information bus voltage and current changes for *n* time periods at each bus. To solve the system of linear equations and allow the system to have one unique solution, linear independency of rows and columns in both matrices of bus voltage and bus current changes in Eq. (3.21) must be ensured. That is, the matrix rank of both matrices must match, and both matrices must have full rank. A rank tells the number of linearly independent row or column vectors in the matrix [188]. For example, the rank of the matrix $[\Delta \underline{V}^{\mathrm{T}}]$ and matrix $[\Delta \underline{I}^{\mathrm{T}}]$ must be 2 and *n* for Eq. (3.20) and Eq. (3.21), respectively.

3.2.2 Determination of Bus Impedance Parameters

The matrix $[\underline{Z}_{par}]$ is expected to be available for either single-area power grid or cluster areas under the CPSA. The method of determining the matrix $[\underline{Z}_{par}]$ is developed to be the same for any case. The local measurement of bus voltages and currents from concerned buses are employed. In the following, the determination of the matrix $[\underline{Z}_{par}]$ is delineated. First of all, the concept of the CPSA for the cluster areas must be taken into account, as it is applied on the underlying power grid. The overview of this concept is depicted in Figure 3.8, in which the CPSA creates *m* cluster areas to the exemplified *n*-port network. The matrix $[\underline{Z}_{par}]$ of each cluster area is, accordingly, designated as $[\underline{Z}_{par,Cj}]$ where $j \in \{1, 2, \ldots, m\}$. That is, the matrix $[\underline{Z}_{par}]$ of the entire grid is divided into *m* matrices from $[\underline{Z}_{par,C1}]$ to $[\underline{Z}_{par,Cm}]$. Under the CPSA, multiple cluster areas are interconnected as a network. Each cluster area collects measurement data only from the data sources residing in its boundary.

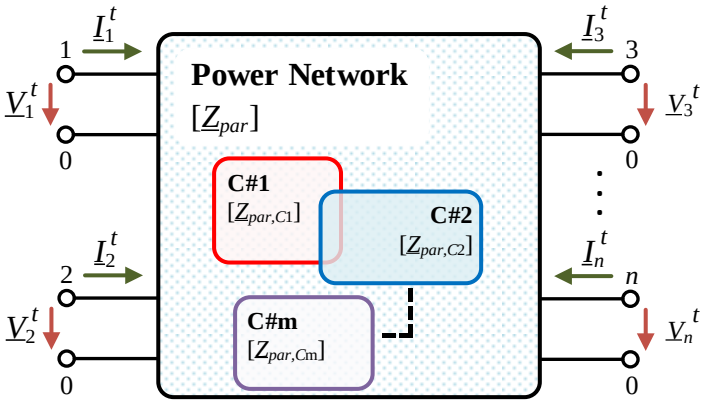

Figure 3.8: An *n*-port power network with *m* cluster areas

The cluster areas are generally interconnected as a network, as a result from the CPSA. At least, there is one border zone overlapping between two adjacent cluster areas looked from the grid view. It must be noted that in order to demonstrate the determination of the matrix $[\underline{Z}_{par}]$, only one border zone is demonstrated in this section as an example.

Figure 3.9 illustrates a border zone between two cluster areas, cluster 1 and cluster 2. Sequentially, Figure 3.10 displays the border zone considered by each cluster area. Observed from Figure 3.9 and Figure 3.10, bus *g* and bus *f* are in the border zone of cluster 1 and cluster 2, respectively. These two buses are also members of both cluster areas, but they are regarded differently in each area. Bus *g* is considered as the external bus – called "border bus" thereafter – of cluster 1, because it is the decoupling point in the area of cluster 2. Bus *f* is considered as the border bus of cluster 2 because it is the decoupling point in the area of cluster 1. In each cluster area, other buses besides the border bus are known as internal buses.

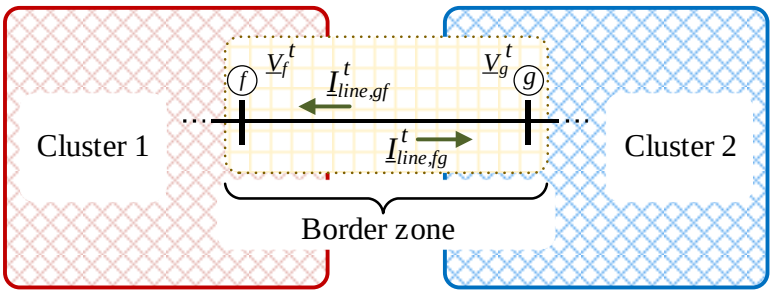

Figure 3.9: An example of the border zone between two cluster areas

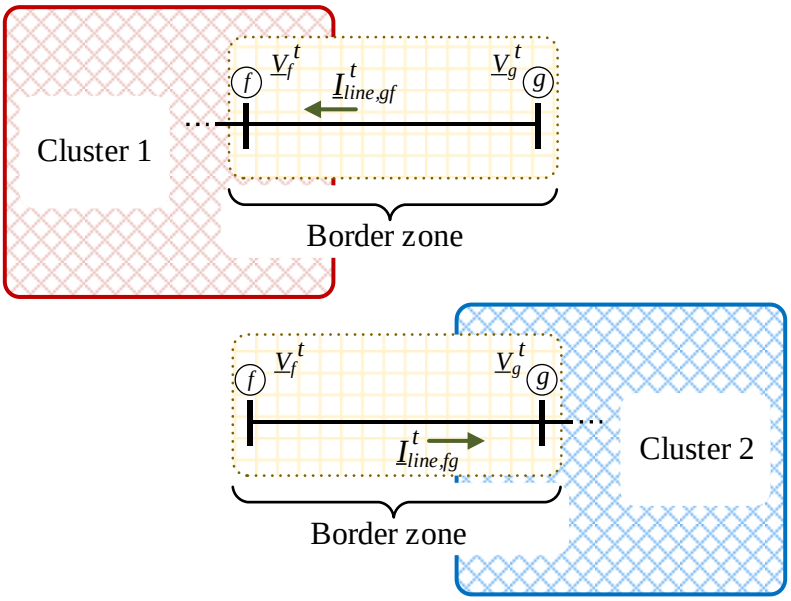

Figure 3.10: An example of the border zone looked from each cluster area

Under the CPSA, grid operations are decentralised from the entire grid to multiple cluster areas. This is also applied to the data management. For this reason, each cluster area collects measurement data only from the data sources residing in its boundary. In this thesis, the constraints of data collection from internal buses and the border bus are different. They are defined as follows.

Collection of voltage data:

- Phasors of bus voltages from all buses of concern (Either internal or border buses)

Collection of current data:

- Phasors of bus currents flowing into or out of the power grid from the internal buses of concern
- Phasors of line current(s) flowing in the cable pertaining to the border bus in the direction of flowing into the cluster area

After the data are collected, the matrix $[\underline{Z}_{par}]$ can be determined. Based on Eq. (3.21), bus voltage and bus current changes are required. Since the matrix $[\underline{Z}_{par}]$ is a square matrix, if a cluster area is regarded as an n-port network, the dimension of the matrix $[\underline{Z}_{par}]$ is $n \times n$. Hence, the information of bus voltage and bus current changes must come from n time periods to perform matrix operations. Aside from ensuring mathematical conditions for matrix operations during the calculation, up-to-date matrix $[\underline{Z}_{par}]$ is also essential. In the calculation of bus voltage and bus current changes, the latest possible measured voltage and current are thus referred as the reference time point. Accordingly, at least n+1 number of data sets of bus voltages and bus currents are required to ensure $n \times n$ matrix dimension.

If T_k is the time period between time $t_{(n+1)}$ and time t_k where $k \in \{1, 2, \ldots, n\}$, the change of bus voltages $\Delta\underline{V}^{T_k}$ at bus i during the time period T_k is

$$\Delta\underline{V}_i^{T_k} = \underline{V}_i^{t_{(n+1)}} - \underline{V}_i^{t_k} \tag{3.23}$$

and the change of bus currents $\Delta\underline{I}^{T_k}$ at bus i or at the border bus g whose adjacent bus is designed as bus f during the time period T_k is

$$\Delta\underline{I}_i^{T_k} = \begin{cases} \underline{I}_i^{t_{(n+1)}} - \underline{I}_i^{t_k} & \text{if } i \in \{1, 2, \ldots, n\} \\ \underline{I}_{line,gf}^{t_{(n+1)}} - \underline{I}_{line,gf}^{t_k} & \text{if } i = g; g \neq f;\ g, f \in \{1, 2, \ldots, n\} \end{cases}. \tag{3.24}$$

Bus voltage $\underline{V}_i^{t_{(n+1)}}$, bus current $\underline{I}_i^{t_{(n+1)}}$, and line current $\underline{I}_{line,gf}^{t_{(n+1)}}$ are measured at the latest possible time $t_{(n+1)}$, whereas bus voltage $\underline{V}_i^{t_k}$, bus current $\underline{I}_i^{t_k}$, and line current $\underline{I}_{line,gf}^{t_k}$ are measured at the time t_k. The subscript i, g, and f denotes the bus number where $i, g, f \in \{1, 2, \ldots, n\}$. Accordingly, when the voltage $\Delta\underline{V}_i^{T_k}$ and current $\Delta\underline{I}_i^{T_k}$ from Eq. (3.23) and Eq. (3.24)

are related to the newest data, i.e. $\underline{V}_i^{t_{(n+1)}}$ and $\underline{I}_i^{t_{(n+1)}}$ or $\underline{I}_{line,gf}^{t_{(n+1)}}$, bus impedance parameters reflecting the most recent situation of the power grid can be acquired.

Thus far, the utilisation of the local measurements, bus voltages and bus currents, to determine the matrix $[\underline{Z}_{par}]$ has been clarified. To this end, substituting the change of bus voltage $\Delta\underline{V}_i^{\mathrm{T}k}$ and the change of bus current $\Delta\underline{I}_i^{\mathrm{T}k}$ in Eq. (3.21) results in the general form of matrix of bus voltage change

$$\begin{aligned}\left[\Delta\underline{V}^{\mathrm{T}}\right] &= \begin{bmatrix} \Delta\underline{V}_1^{\mathrm{T}_1} & \Delta\underline{V}_1^{\mathrm{T}_2} & \cdots & \Delta\underline{V}_1^{\mathrm{T}_n} \\ \Delta\underline{V}_2^{\mathrm{T}_1} & \Delta\underline{V}_2^{\mathrm{T}_2} & \cdots & \Delta\underline{V}_2^{\mathrm{T}_n} \\ \vdots & \vdots & \ddots & \vdots \\ \Delta\underline{V}_n^{\mathrm{T}_1} & \Delta\underline{V}_n^{\mathrm{T}_2} & \cdots & \Delta\underline{V}_n^{\mathrm{T}_n} \end{bmatrix} \\ &= \begin{bmatrix} \underline{V}_1^{t_{(n+1)}} - \underline{V}_1^{t_1} & \underline{V}_1^{t_{(n+1)}} - \underline{V}_1^{t_2} & \cdots & \underline{V}_1^{t_{(n+1)}} - \underline{V}_1^{t_n} \\ \underline{V}_2^{t_{(n+1)}} - \underline{V}_2^{t_1} & \underline{V}_2^{t_{(n+1)}} - \underline{V}_2^{t_2} & \cdots & \underline{V}_2^{t_{(n+1)}} - \underline{V}_2^{t_n} \\ \vdots & \vdots & \ddots & \vdots \\ \underline{V}_n^{t_{(n+1)}} - \underline{V}_n^{t_1} & \underline{V}_n^{t_{(n+1)}} - \underline{V}_n^{t_2} & \cdots & \underline{V}_n^{t_{(n+1)}} - \underline{V}_n^{t_n} \end{bmatrix}\end{aligned} \tag{3.25}$$

and the general form of matrix of bus current change

$$\begin{aligned}\left[\Delta\underline{I}^{\mathrm{T}}\right] &= \begin{bmatrix} \Delta\underline{I}_1^{\mathrm{T}_1} & \Delta\underline{I}_1^{\mathrm{T}_2} & \cdots & \Delta\underline{I}_1^{\mathrm{T}_n} \\ \Delta\underline{I}_2^{\mathrm{T}_1} & \Delta\underline{I}_2^{\mathrm{T}_2} & \cdots & \Delta\underline{I}_2^{\mathrm{T}_n} \\ \vdots & \vdots & \ddots & \vdots \\ \Delta\underline{I}_n^{\mathrm{T}_1} & \Delta\underline{I}_n^{\mathrm{T}_2} & \cdots & \Delta\underline{I}_n^{\mathrm{T}_n} \end{bmatrix} \\ &= \begin{bmatrix} \underline{I}_1^{t_{(n+1)}} - \underline{I}_1^{t_1} & \underline{I}_1^{t_{(n+1)}} - \underline{I}_1^{t_2} & \cdots & \underline{I}_1^{t_{(n+1)}} - \underline{I}_1^{t_n} \\ \underline{I}_2^{t_{(n+1)}} - \underline{I}_2^{t_1} & \underline{I}_2^{t_{(n+1)}} - \underline{I}_2^{t_2} & \cdots & \underline{I}_2^{t_{(n+1)}} - \underline{I}_2^{t_n} \\ \vdots & \vdots & \ddots & \vdots \\ \underline{I}_n^{t_{(n+1)}} - \underline{I}_n^{t_1} & \underline{I}_n^{t_{(n+1)}} - \underline{I}_n^{t_2} & \cdots & \underline{I}_n^{t_{(n+1)}} - \underline{I}_n^{t_n} \end{bmatrix}.\end{aligned} \tag{3.26}$$

Since the bus impedance parameters are based on the impedance model, the bus impedance parameters matrix

$$\begin{aligned}\left[\underline{Z}_{par}\right] &= \begin{bmatrix} \underline{Z}_{11} & \underline{Z}_{12} & \cdots & \underline{Z}_{1n} \\ \underline{Z}_{21} & \underline{Z}_{22} & \cdots & \underline{Z}_{2n} \\ \vdots & \vdots & \ddots & \vdots \\ \underline{Z}_{n1} & \underline{Z}_{n2} & \cdots & \underline{Z}_{nn} \end{bmatrix} \\ &= \begin{bmatrix} R_{11} & R_{12} & \cdots & R_{1n} \\ R_{21} & R_{22} & \cdots & R_{2n} \\ \vdots & \vdots & \ddots & \vdots \\ R_{n1} & R_{n2} & \cdots & R_{nn} \end{bmatrix} + j \begin{bmatrix} X_{11} & X_{12} & \cdots & X_{1n} \\ X_{21} & X_{22} & \cdots & X_{2n} \\ \vdots & \vdots & \ddots & \vdots \\ X_{n1} & X_{n2} & \cdots & X_{nn} \end{bmatrix}\end{aligned} \tag{3.27}$$

can be divided to resistance and reactance parts.

Same as the case of matrix [$\underline{Z}_{bus}$], the diagonal elements $\underline{Z}_{ii}$ ($i \in \{1, 2, \ldots, n\}$) of [$\underline{Z}_{par}$] describe the impact of current change on voltage change at the same bus. This also applies to the resistances R_{ii} and reactances X_{ii}, where $i \in \{1, 2, \ldots, n\}$. Also, off-diagonal elements $\underline{Z}_{ij}$ ($i, j \in \{1, 2, \ldots, n\}$; $i \neq j$) describe the impact of current change at one bus on voltage change at another bus. Again, this also applies to the resistances R_{ij} and reactance X_{ij}, where $i, j \in \{1, 2, \ldots, n\}$ and $i \neq j$.

To summarise, the matrix [$\underline{Z}_{par}$] is determined by using only measured bus voltages and currents. How to prepare the measured bus voltages and bus currents for calculating the matrix [$\underline{Z}_{par}$] is shown in Eq. (3.25) and Eq. (3.26), respectively. The matrix [$\underline{Z}_{par}$] is composed of resistance and reactance parts, as illustrated in Eq. (3.27). Up to this point, the determination of the bus impedance parameters is valid if the condition of the power grid is balanced. However, an unbalanced grid condition can happen during grid operations, especially at the distribution level. The effect of an unbalanced condition therefore must be considered. A powerful method used to cope with this effect is the symmetrical components.

3.2.3 Determination of Bus Impedance Parameters in Sequence Systems

Grid condition in power systems is generally maintained to stay balanced. If the three-phase system is concerned, a set of state variables, such as voltages and currents, consists of three phase components [189]. Under a balanced condition, the magnitude of all components is identical, and meanwhile the angle displacement between adjacent phasors is equal at 120º. Nonetheless, the condition of power systems is not always balanced. Especially, in low-voltage distribution networks, the grid accommodates single-phase loads and DG units, which adversely cause an unbalanced condition. Consequently, the magnitudes of phasors are different, and/or the angle displacements between adjacent phasors are not equal at 120º. To tackle the unbalanced condition in the grid, the symmetrical components technique is used in this thesis for the determination of bus impedance parameters. Based on this technique, a three-phase unbalanced phasor is equal to the summation of its symmetrical components from three sequence systems: positive, negative, and zero sequences [181]. Each sequence is independent from other sequences. This means that the change of current in one sequence does not cause voltage change in another sequence. In this section, the conversion of the original bus impedance parameters into zero-, positive-, and negative-sequence bus impedance parameters is taken into account. In the following context, the three-phase system is denoted here as phase *a*, *b*, and *c*, while zero, positive, and negative sequences are designated by 0, 1, and 2, respectively.

First, the calculation of the symmetrical components of bus voltages and currents is discussed. To convert the phasor of each phase into the symmetrical components is normally referred to phase *a*. The relationship between the change of bus voltage at each phase and their symmetrical components

$$\begin{bmatrix} \Delta\underline{V}_a \\ \Delta\underline{V}_b \\ \Delta\underline{V}_c \end{bmatrix} = \begin{bmatrix} 1 & 1 & 1 \\ 1 & \underline{a}^2 & \underline{a} \\ 1 & \underline{a} & \underline{a}^2 \end{bmatrix} \begin{bmatrix} \Delta\underline{V}^{(0)} \\ \Delta\underline{V}^{(1)} \\ \Delta\underline{V}^{(2)} \end{bmatrix} \tag{3.28}$$

where $\underline{a}$ is a complex operator at the value of e^{j120^o} can be described. The voltages $\Delta\underline{V}_a$, $\Delta\underline{V}_b$, and $\Delta\underline{V}_c$ are the change of bus voltage at phase *a*, *b*, and *c*. The voltages $\Delta\underline{V}^{(0)}$, $\Delta\underline{V}^{(1)}$, and $\Delta\underline{V}^{(2)}$ are the change of bus voltage in zero, positive, and negative sequence, respectively. The coefficient matrix

$$[\underline{A}] = \begin{bmatrix} 1 & 1 & 1 \\ 1 & \underline{a}^2 & \underline{a} \\ 1 & \underline{a} & \underline{a}^2 \end{bmatrix}. \tag{3.29}$$

is defined. On the other hand, the symmetrical components can be converted back to phase components. By multiplying the inverse of [$\underline{A}$] in Eq. (3.29) to both sides of Eq. (3.28), the change of bus voltage in sequence systems

$$\begin{bmatrix} \Delta\underline{V}^{(0)} \\ \Delta\underline{V}^{(1)} \\ \Delta\underline{V}^{(2)} \end{bmatrix} = \frac{1}{3}\begin{bmatrix} 1 & 1 & 1 \\ 1 & \underline{a} & \underline{a}^2 \\ 1 & \underline{a}^2 & \underline{a} \end{bmatrix} \begin{bmatrix} \Delta\underline{V}_a \\ \Delta\underline{V}_b \\ \Delta\underline{V}_c \end{bmatrix} \tag{3.30}$$

can be resolved. The inverse of the coefficient matrix [$\underline{A}$] is denoted by

$$[\underline{A}]^{-1} = \frac{1}{3}\begin{bmatrix} 1 & 1 & 1 \\ 1 & \underline{a} & \underline{a}^2 \\ 1 & \underline{a}^2 & \underline{a} \end{bmatrix}. \tag{3.31}$$

In the same manner as the case of bus voltages, the relationship between the change of bus current at each phase and their symmetrical components

$$\begin{bmatrix} \Delta\underline{I}_a \\ \Delta\underline{I}_b \\ \Delta\underline{I}_c \end{bmatrix} = \begin{bmatrix} 1 & 1 & 1 \\ 1 & \underline{a}^2 & \underline{a} \\ 1 & \underline{a} & \underline{a}^2 \end{bmatrix} \begin{bmatrix} \Delta\underline{I}^{(0)} \\ \Delta\underline{I}^{(1)} \\ \Delta\underline{I}^{(2)} \end{bmatrix} \tag{3.32}$$

can be described. The currents $\Delta\underline{I}_a$, $\Delta\underline{I}_b$, and $\Delta\underline{I}_c$ are the change of bus current at phase *a*, *b*, and *c*, and the currents $\Delta\underline{I}^{(0)}$, $\Delta\underline{I}^{(1)}$, and $\Delta\underline{I}^{(2)}$ are the change of bus current in zero, positive, and negative sequence, respectively. By multiplying the inverse of [$\underline{A}$] in Eq. (3.31) to both sides of Eq. (3.32), the change of bus current in sequence systems

$$\begin{bmatrix} \Delta\underline{I}^{(0)} \\ \Delta\underline{I}^{(1)} \\ \Delta\underline{I}^{(2)} \end{bmatrix} = \frac{1}{3}\begin{bmatrix} 1 & 1 & 1 \\ 1 & \underline{a} & \underline{a}^2 \\ 1 & \underline{a}^2 & \underline{a} \end{bmatrix} \begin{bmatrix} \Delta\underline{I}_a \\ \Delta\underline{I}_b \\ \Delta\underline{I}_c \end{bmatrix} \tag{3.33}$$

can be calculated. Eqs. (3.30) and (3.33) are then employed here to convert three-phase bus voltages and currents into the symmetrical components in sequence systems, since the measured data are in phase components. Accordingly, the bus impedance parameters in the

sequence systems can be determined. By applying Eq. (3.30) to $[\Delta \underline{V}^{T}]$ from Eq. (3.25), the matrices of the change of bus voltages – $[\Delta \underline{V}^{T(0)}]$, $[\Delta \underline{V}^{T(1)}]$, and $[\Delta \underline{V}^{T(2)}]$ – in the sequence systems can be computed. In the same way, by applying Eq. (3.33) to $[\Delta \underline{I}^{T}]$ from Eq. (3.26), and the matrices of the change of bus currents in the sequence systems – $[\Delta \underline{I}^{T(0)}]$, $[\Delta \underline{I}^{T(1)}]$, and $[\Delta \underline{I}^{T(2)}]$ – can be obtained. Since the sequence systems are independent, the determination of the bus impedance parameters separately for each sequence is possible. The matrices of zero-sequence bus impedance parameters

$$\left[\underline{Z}_{par}^{(0)}\right] = \begin{bmatrix} \Delta \underline{V}_1^{T1(0)} & \Delta \underline{V}_1^{T2(0)} & \cdots & \Delta \underline{V}_1^{Tn(0)} \\ \Delta \underline{V}_2^{T1(0)} & \Delta \underline{V}_2^{T2(0)} & \cdots & \Delta \underline{V}_2^{Tn(0)} \\ \vdots & \vdots & \ddots & \vdots \\ \Delta \underline{V}_n^{T1(0)} & \Delta \underline{V}_n^{T2(0)} & \cdots & \Delta \underline{V}_n^{Tn(0)} \end{bmatrix} \cdot \begin{bmatrix} \Delta \underline{I}_1^{T1(0)} & \Delta \underline{I}_1^{T2(0)} & \cdots & \Delta \underline{I}_1^{Tn(0)} \\ \Delta \underline{I}_2^{T1(0)} & \Delta \underline{I}_2^{T2(0)} & \cdots & \Delta \underline{I}_2^{Tn(0)} \\ \vdots & \vdots & \ddots & \vdots \\ \Delta \underline{I}_n^{T1(0)} & \Delta \underline{I}_n^{T2(0)} & \cdots & \Delta \underline{I}_n^{Tn(0)} \end{bmatrix}^{-1} \tag{3.34}$$

positive-sequence bus impedance parameters

$$\left[\underline{Z}_{par}^{(1)}\right] = \begin{bmatrix} \Delta \underline{V}_1^{T1(1)} & \Delta \underline{V}_1^{T2(1)} & \cdots & \Delta \underline{V}_1^{Tn(1)} \\ \Delta \underline{V}_2^{T1(1)} & \Delta \underline{V}_2^{T2(1)} & \cdots & \Delta \underline{V}_2^{Tn(1)} \\ \vdots & \vdots & \ddots & \vdots \\ \Delta \underline{V}_n^{T1(1)} & \Delta \underline{V}_n^{T2(1)} & \cdots & \Delta \underline{V}_n^{Tn(1)} \end{bmatrix} \cdot \begin{bmatrix} \Delta \underline{I}_1^{T1(1)} & \Delta \underline{I}_1^{T2(1)} & \cdots & \Delta \underline{I}_1^{Tn(1)} \\ \Delta \underline{I}_2^{T1(1)} & \Delta \underline{I}_2^{T2(1)} & \cdots & \Delta \underline{I}_2^{Tn(1)} \\ \vdots & \vdots & \ddots & \vdots \\ \Delta \underline{I}_n^{T1(1)} & \Delta \underline{I}_n^{T2(1)} & \cdots & \Delta \underline{I}_n^{Tn(1)} \end{bmatrix}^{-1} \tag{3.35}$$

and negative-sequence bus impedance parameters

$$\left[\underline{Z}_{par}^{(2)}\right] = \begin{bmatrix} \Delta \underline{V}_1^{T1(2)} & \Delta \underline{V}_1^{T2(2)} & \cdots & \Delta \underline{V}_1^{Tn(2)} \\ \Delta \underline{V}_2^{T1(2)} & \Delta \underline{V}_2^{T2(2)} & \cdots & \Delta \underline{V}_2^{Tn(2)} \\ \vdots & \vdots & \ddots & \vdots \\ \Delta \underline{V}_n^{T1(2)} & \Delta \underline{V}_n^{T2(2)} & \cdots & \Delta \underline{V}_n^{Tn(2)} \end{bmatrix} \cdot \begin{bmatrix} \Delta \underline{I}_1^{T1(2)} & \Delta \underline{I}_1^{T2(2)} & \cdots & \Delta \underline{I}_1^{Tn(2)} \\ \Delta \underline{I}_2^{T1(2)} & \Delta \underline{I}_2^{T2(2)} & \cdots & \Delta \underline{I}_2^{Tn(2)} \\ \vdots & \vdots & \ddots & \vdots \\ \Delta \underline{I}_n^{T1(2)} & \Delta \underline{I}_n^{T2(2)} & \cdots & \Delta \underline{I}_n^{Tn(2)} \end{bmatrix}^{-1} \tag{3.36}$$

can be determined. Eqs. (3.34) to (3.36) illustrate general equations to calculate the bus impedance parameters in each sequence separately. It must be noted that if the condition of the grid is balanced, the matrix $[\underline{Z}_{par}]$ from a normal calculation is equal to the matrix $[\underline{Z}_{par}^{(1)}]$, since zero- and negative- sequence components of bus voltages and currents are of zero magnitude. Otherwise, all matrices $[\underline{Z}_{par}^{(0)}]$, $[\underline{Z}_{par}^{(1)}]$, and $[\underline{Z}_{par}^{(2)}]$ must be taken into account.

In this section, the determination of the matrix $[\underline{Z}_{par}]$ in sequence systems is presented. This step is applied to the process of calculating the change of bus voltages and bus currents delivered in the previous section, which is Section 3.2.2. To summarise, Figure 3.11 depicts the determination of the matrix $[\underline{Z}_{par}]$ with consideration of cluster areas, which are called decentralised power grids in the general term. The sequence matrices $[\underline{Z}_{par,Cj}^{(0)}]$, $[\underline{Z}_{par,Cj}^{(1)}]$, and $[\underline{Z}_{par,Cj}^{(2)}]$ are acquired at the end of the process depicted in Figure 3.11. The subscript *Cj* is specified as number of cluster areas where $j \in \{1, 2, \ldots, m\}$.

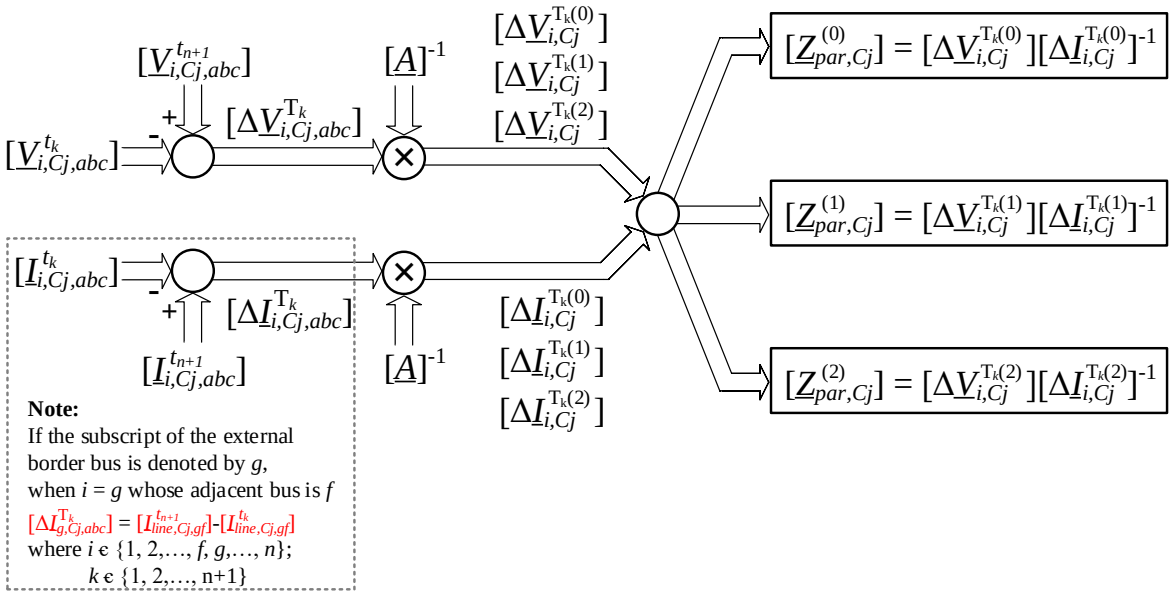

Figure 3.11: Flowchart of determination of bus impedance parameters in cluster area

So far, if the target of the analysis is only for the entire power grid as one single area, the determination of the matrix $[\underline{Z}_{par}]$ is done in this section. Nevertheless, if the target is for decentralised areas, i.e. cluster areas, the influence of interconnected areas must be considered. The determination of the matrix $[\underline{Z}_{par}]$ needs one more step to integrate with the influence from interconnected areas. The integration is stated in the next section.

3.2.4 Integration of the Influence of Interconnected Cluster Areas

Decentralised operations generally mean that the manipulation of grid operation is distributed from the centre. Instead of controlling the entire grid from the control centre, the operations are separately performed in multiple local areas of the grid. Since the power grid in each region is synchronised, the influence of interconnected decentralised areas, i.e. cluster areas in this context, must be considered when they exist. After that, each cluster area can perform the analysis independently. This means that the determination of the matrix $[\underline{Z}_{par}]$ will be incorrect without consideration of the influence of interconnected cluster areas.

This section delineates a successive step from the previous section for the determination of the matrix $[\underline{Z}_{par}]$. As an approach to enable decentralised operations, the CPSA creates interconnected cluster areas in the distribution level to imitate the characteristics of the interconnected grids from the transmission level. The influence of interconnected grids can be obtained at the border in the form of bus impedances [179]. For this reason, the influence of interconnected cluster areas can be integrated at the border of each cluster area as well. In this thesis, the Thévenin's theorem is chosen to produce a model representing the influence of interconnected cluster areas. Based on the Thévenin's theorem, the components of an original circuit can be represented by an equivalent voltage source and an equivalent impedance, known as Thévenin equivalent voltage source $\underline{V}_{Th}$ and Thévenin impedance $\underline{Z}_{Th}$, respectively,

as discussed in Section 3.1.2. However, the voltage source $\underline{V}_{Th}$ is not involved here. To correct the matrix $[\underline{Z}_{par}]$ determined separately in each cluster area, the interconnected cluster areas have to exchange their impedance $\underline{Z}_{Th}$ looking into their cluster area from the border bus and then integrate the impedance $\underline{Z}_{Th}$ to their existing matrix $[\underline{Z}_{par}]$. In the following, first, the selection and exchange method of Thévenin impedance is introduced. Afterwards, the modification method for the integration of the influence of interconnected cluster areas is exemplified. It must be noted that these methods are applicable for each sequence system, if the matrix $[\underline{Z}_{par}]$ are individually available in zero- and negative- sequence components. Nonetheless, the sequence systems are not mentioned thereafter to ease the explanation.

Selection and Exchange of Thévenin Impedance

The Thévenin impedance in this context represents the behaviour of the interconnected cluster areas at the border bus. Typically, there are two methods to obtain the values of Thévenin's impedances. The first one is using Thévenin's theorem to calculate the impedances directly. The other one is acquiring from the diagonal elements of bus impedance matrix $[\underline{Z}_{bus}]$, which in this context can be bus impedance parameters $[\underline{Z}_{par}]$. In this thesis, the method of acquiring the Thévenin impedance from the diagonal elements is employed. Since grid topology is assumed to be unknown, the direct calculation of the impedances by using Thévenin's theorem is not possible.

Two cluster areas from Figure 3.9 are used to give an example and assumed to be located on an n-bus network. Figure 3.12 illustrates the exchange of the impedance $\underline{Z}_{Th}$ from cluster 1 to cluster 2. The bus number in cluster 1 runs from 1, …, f, g, while the bus number in cluster 2 is run from f, g, …, n. The matrices $[\underline{Z}_{par,C1}]$ and $[\underline{Z}_{par,C2}]$ have already been predetermined. According to Figure 3.12, the border zone is composed of bus f and bus g where the exchange of in the impedance $\underline{Z}_{Th}$ happens. The circle around the bus name indicates the border of each cluster area. Thus, bus f is the border bus of cluster 2. This means cluster 2 requires the Thévenin impedance $\underline{Z}_{Th,C1}$, i.e. $\underline{Z}_{ff,C1}$, at bus f from cluster 1 to be integrated.

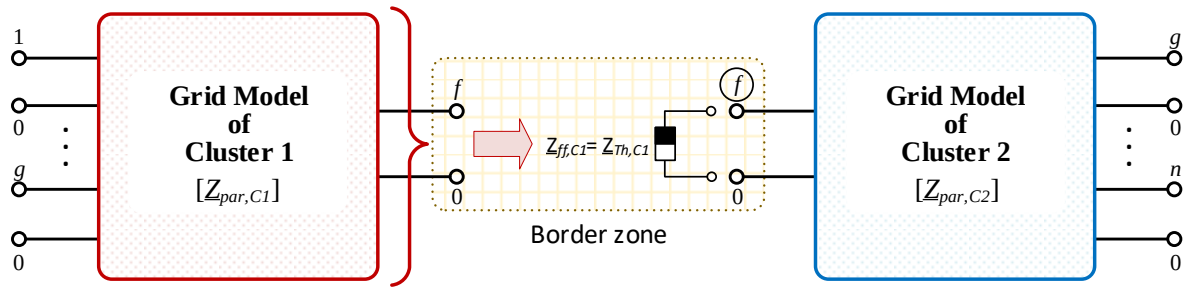

Figure 3.12: Exchange of the Thévenin impedance from cluster 1 to cluster 2

In turn, Figure 3.13 illustrates the exchange of the impedance $\underline{Z}_{Th}$ from cluster 2 to cluster 1. bus g is the border of cluster 1. It can be seen that bus g is the border of cluster 1 in this case.

Therefore, cluster 1 requires the Thévenin impedance $\underline{Z}_{Th,C2}$, i.e. $\underline{Z}_{gg,C2}$, at bus g from cluster 2 to be integrated.

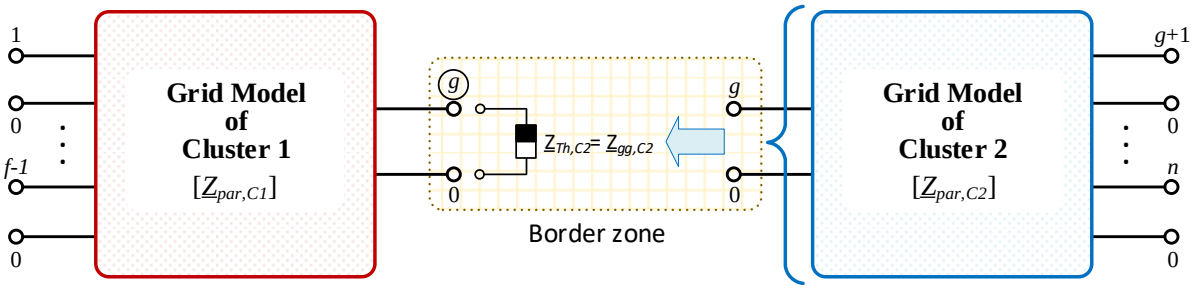

Figure 3.13: Exchange of the Thévenin impedance from cluster 2 to cluster 1

The Thévenin impedance is selected from the diagonal element of the required bus. For the sake of the explanation, bus impedance parameters of cluster 1

$$[\underline{Z}_{par,C1}] = \begin{bmatrix} \underline{Z}_{11,C1} & \cdots & \underline{Z}_{1f,C1} & \underline{Z}_{1g,C1} \\ \vdots & \ddots & \vdots & \vdots \\ \underline{Z}_{f1,C1} & \cdots & \underline{Z}_{ff,C1} & \underline{Z}_{fg,C1} \\ \underline{Z}_{g1,C1} & \cdots & \underline{Z}_{gf,C1} & \underline{Z}_{gg,C1} \end{bmatrix} \tag{3.37}$$

and bus impedance parameters of cluster 2

$$[\underline{Z}_{par,C2}] = \begin{bmatrix} \underline{Z}_{ff,C2} & \underline{Z}_{fg,C2} & \cdots & \underline{Z}_{fn,C2} \\ \underline{Z}_{gf,C2} & \underline{Z}_{gg,C2} & \cdots & \underline{Z}_{gn,C2} \\ \vdots & \vdots & \ddots & \vdots \\ \underline{Z}_{nf,C2} & \underline{Z}_{ng,C2} & \cdots & \underline{Z}_{nn,C2} \end{bmatrix} \tag{3.38}$$

are assigned. For cluster 1, since bus g is the border, the impedance $\underline{Z}_{Th,C2}$ required from cluster 2 is selected from the self-impedance $\underline{Z}_{gg,C2}$ of the matrix $[\underline{Z}_{par,C2}]$ in Eq. (3.38). For cluster 2, bus f is the border, so the impedance $\underline{Z}_{Th,C1}$ required from cluster 1 is selected from the self-impedance $\underline{Z}_{ff,C1}$ of the matrix $[\underline{Z}_{par,C1}]$ in Eq. (3.37). To summarise, the impedances $\underline{Z}_{Th,C1}$ and $\underline{Z}_{Th,C2}$ are

$$\underline{Z}_{Th,C1} = \underline{Z}_{ff,C1} \tag{3.39}$$

$$\underline{Z}_{Th,C2} = \underline{Z}_{gg,C2}. \tag{3.40}$$

Figure 3.14 and Figure 3.15 display how the impedances $\underline{Z}_{Th,C1}$ and $\underline{Z}_{Th,C2}$ represent their cluster area. The impedance $\underline{Z}_{Th,C1}$ in Figure 3.14 is seen from bus f into cluster 1, and the impedance $\underline{Z}_{Th,C2}$ in Figure 3.15 is seen from bus g into cluster 2. To give an example, the grid topology in these two figures is assumed to be connected in a radial formation for simplicity purposes. The sequence notation is not defined at the phase impedances, as only their phase quantities are involved before being converted to the symmetrical components. Moreover, all voltage or current sources are left out, because this description emphasises the calculation of Thévenin impedance.

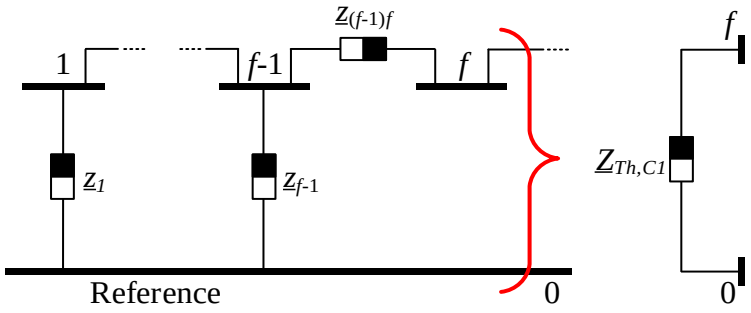

Figure 3.14: The Thévenin impedance looking from bus f into cluster 1

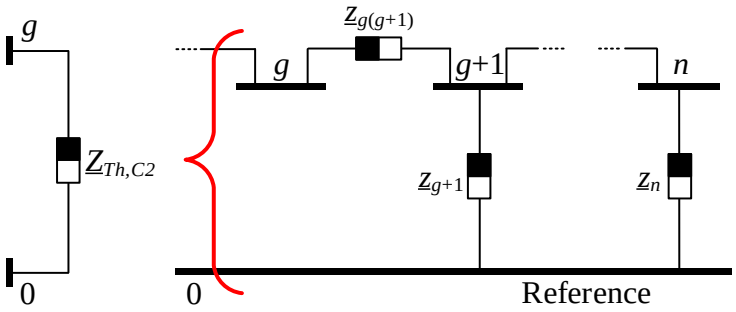

Figure 3.15: The Thévenin impedance looking from bus g into cluster 2

The impedances $\underline{Z}_{Th,C1}$ and $\underline{Z}_{Th,C2}$ can be then exchanged after they have already been selected and prepared. The next step is to integrate the impedances to the predetermined bus impedance parameters. In this case, the impedance $\underline{Z}_{Th,C1}$, which is $\underline{Z}_{ff,C1}$, will be integrated to the impedance $\underline{Z}_{ff,C2}$ of the matrix $[\underline{Z}_{par,C2}]$, and the impedance $\underline{Z}_{Th,C2}$, which is $\underline{Z}_{gg,C2}$, will be integrated to the impedance $\underline{Z}_{gg,C1}$ of the matrix $[\underline{Z}_{par,C1}]$.

Bus Impedance Modification Method

This modification method allows the impedance $\underline{Z}_{Th}$ to be integrated into the existing matrix $[\underline{Z}_{par}]$ of the cluster area. That is, the matrix $[\underline{Z}_{par}]$ will be updated or modified to include the impact of $\underline{Z}_{Th}$. The updated matrix $[\underline{Z}_{par}]$ will function as though the impedance $\underline{Z}_{Th}$ is practically added to the grid. For this reason, the modification method depends on the addition of a new element to the existing grid. Knowing how the impedance $\underline{Z}_{Th}$ is added to the existing grid is indispensable. In this case, the impedance $\underline{Z}_{Th}$ is known that it is connected from the border bus to the reference point, as the impedance $\underline{Z}_{Th}$ is its self-impedance looking into another cluster area. Considering back to the case of Figure 3.12, the integration of the impedance $\underline{Z}_{Th,C2}$ to the border bus of cluster 1 and $\underline{Z}_{Th,C1}$ to the border bus of cluster 2 are depicted in Figure 3.16 and Figure 3.17, respectively.

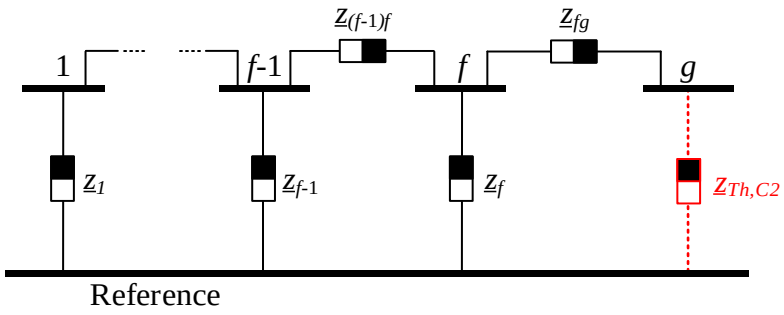

Figure 3.16: Integrating the Thévenin impedance from cluster 2 to the border bus of cluster 1

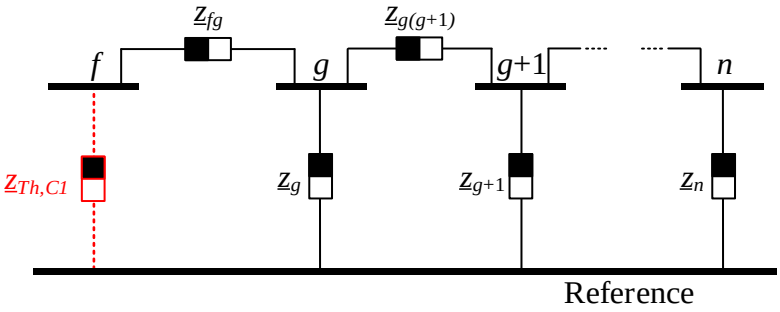

Figure 3.17: Integrating the Thévenin impedance from cluster 1 to the border bus of cluster 2

Accordingly, the modification is executed in the condition that a new impedance is added from an existing bus to the reference. The modification method in the following explanation is adapted from [179, 180]. The modification of the matrix $[\underline{Z}_{par,C1}]$ of cluster 1 is discussed as an example. Figure 3.18 portrays how the impedance $\underline{Z}_{Th,C2}$ is added to bus g. Bus g' is a pretend bus acting as a new bus connected to bus g. As the impedance $\underline{Z}_{Th,C2}$ is connected between bus g and the reference, bus g' is short-circuited to the reference.

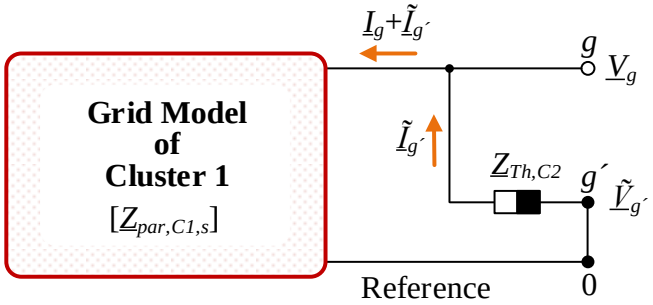

Figure 3.18: Adding the impedance $\underline{Z}_{Th,C2}$ to bus g

The addition of the impedance $\underline{Z}_{Th,C2}$ to bus g introduces an additional current $\tilde{\underline{I}}_{g'}$ flowing from bus g'. Consequently, bus voltage $\underline{V}_g$ at bus g is impacted, and the current flowing from bus g to the grid becomes the initial current $\underline{I}_g$ plus the current $\tilde{\underline{I}}_{g'}$. Bus voltage $\underline{V}_g$ caused by the addition of current $\tilde{\underline{I}}_{g'}$ to the existing grid is

$$\underline{V}_g = \left(\underline{I}_g + \tilde{\underline{I}}_{g'}\right) \cdot \underline{Z}_{gg,C1} = \underline{I}_g \underline{Z}_{gg,C1} + \tilde{\underline{I}}_{g'} \underline{Z}_{gg,C1}. \tag{3.41}$$

As the initial quantities, the term $\underline{I}_g \cdot \underline{Z}_{gg,C1}$ equals the initial voltage $\underline{V}_g^0$, which exists before the impedance $\underline{Z}_{Th,C2}$ is added. Afterwards, replacing the voltage $\underline{V}_g^0$ in Eq. (3.41) yields

$$\underline{V}_g = \underline{V}_g^0 + \tilde{\underline{I}}_{g'} \underline{Z}_{gg,C1}. \tag{3.42}$$

The voltage $\underline{V}_g$ is the combination of the initial voltage $\underline{V}_g^0$ and the change of bus voltage caused by the current $\tilde{\underline{I}}_{g'}$ flowing through the self-impedance $\underline{Z}_{gg,C1}$ of bus g. Next, bus g´ is regarded as it is connected further from bus g. By extending from Eq. (3.42), bus voltage $\tilde{\underline{V}}_{g'}$ therefore is understood as

$$\tilde{\underline{V}}_{g'} = \underline{V}_g + \tilde{\underline{I}}_{g'} \underline{Z}_{Th,C2}. \tag{3.43}$$

In Eq. (3.43), the voltage $\underline{V}_g$ and the term $\tilde{\underline{I}}_{g'} \underline{Z}_{Th,C2}$ constitute bus voltage $\tilde{\underline{V}}_{g'}$. Then, substituting the voltage $\underline{V}_g$ from Eq. (3.42) to Eq. (3.43) yields

$$\tilde{\underline{V}}_{g'} = \underline{V}_g^0 + \tilde{\underline{I}}_{g'} \underline{Z}_{gg,C1} + \tilde{\underline{I}}_{g'} \underline{Z}_{Th,C2}. \tag{3.44}$$

The term of voltage $\underline{V}_g^0$ in Eq. (3.44) can be then expanded to its initial network equation of voltage at bus g to describe voltage $\tilde{\underline{V}}_{g'}$. Meanwhile, the term of the current $\tilde{\underline{I}}_{g'}$ can be combined. This results in

$$\tilde{\underline{V}}_{g'} = \underline{I}_1 \underline{Z}_{g1,C1} + \cdots + \underline{I}_f \underline{Z}_{gf,C1} + \underline{I}_g \underline{Z}_{gg,C1} + \tilde{\underline{I}}_{g'} \left(\underline{Z}_{gg,C1} + \underline{Z}_{Th,C2} \right). \tag{3.45}$$

In Eq. (3.45), the current $\tilde{\underline{I}}_{g'}$ from bus g' is added to the initial network equation in which the bus number runs from 1, 2, …, g. Now, the number of buses becomes g'. Since the matrix of bus impedances is symmetry, additional row and column are added to build a new set of network equations. Based on Eq. (3.45), new set of network equations is

$$\begin{bmatrix} \underline{V}_1 \\ \vdots \\ \underline{V}_f \\ \underline{V}_g \\ \tilde{\underline{V}}_{g'} \end{bmatrix} = \begin{bmatrix} \underline{Z}_{11,C1} & \cdots & \underline{Z}_{1f,C1} & \underline{Z}_{1g,C1} & \underline{Z}_{1g,C1} \\ \vdots & \ddots & \vdots & \vdots & \vdots \\ \underline{Z}_{f1,C1} & \cdots & \underline{Z}_{ff,C1} & \underline{Z}_{fg,C1} & \underline{Z}_{fg,C1} \\ \underline{Z}_{g1,C1} & \cdots & \underline{Z}_{gf,C1} & \underline{Z}_{gg,C1} & \underline{Z}_{gg,C1} \\ \underline{Z}_{g1,C1} & \cdots & \underline{Z}_{gf,C1} & \underline{Z}_{gg,C1} & \underline{Z}_{gg,C1} + \underline{Z}_{Th,C2} \end{bmatrix} \begin{bmatrix} \underline{I}_1 \\ \vdots \\ \underline{I}_f \\ \underline{I}_g \\ \tilde{\underline{I}}_{g'} \end{bmatrix} \tag{3.46}$$

where new elements are covered in the red dashed boundary. Up to this point, the impact of the impedance $\underline{Z}_{Th,C2}$ is still not integrated into the matrix $[\underline{Z}_{par,C1}]$ of cluster 1; only the bus impedances related to bus g' are added to the network questions in Eq. (3.46). In the following, the integration process is delineated.

To integrate the impedance $\underline{Z}_{Th,C2}$ into the matrix $[\underline{Z}_{par,C1}]$ bus g' will be eliminated. The elimination starts from considering the voltage $\tilde{\underline{V}}_{g'}$. Since bus g' is short-circuited to the reference, the voltage $\tilde{\underline{V}}_{g'}$ equals to zero.

$$\tilde{\underline{V}}_{g'} = 0 \tag{3.47}$$

As a consequence, the bus impedances related to bus g' can be eliminated by using Kron's reduction technique [179]. For cluster 1, the matrix $[\underline{Z}_{par,C1}]$ in Eq. (3.37) therefore can be modified element by element to include the influence from cluster 2 by using the following modifying equation.

$$\underline{Z}_{ij,C1}^{final} = \underline{Z}_{ij,C1} - \frac{\underline{Z}_{i(g+1)}\underline{Z}_{(g+1)j}}{\underline{Z}_{gg}+\underline{Z}_{Th}} \tag{3.48}$$

where $i, j \in \{1, 2, \ldots, g\}$ and bus g is the border bus. Hence, the final matrix of bus impedance parameters

$$[\underline{Z}_{par,C1}] = \begin{bmatrix} \underline{Z}_{11,C1}^{final} & \cdots & \underline{Z}_{1f,C1}^{final} & \underline{Z}_{1g,C1}^{final} \\ \vdots & \ddots & \vdots & \vdots \\ \underline{Z}_{f1,C1}^{final} & \cdots & \underline{Z}_{ff,C1}^{final} & \underline{Z}_{fg,C1}^{final} \\ \underline{Z}_{g1,C1}^{final} & \cdots & \underline{Z}_{gf,C1}^{final} & \underline{Z}_{gg,C1}^{final} \end{bmatrix} \tag{3.49}$$

is obtained after the modification. Based on Eq. (3.48), the influence of cluster 2 in the form of $\underline{Z}_{Th,C2}$ is integrated to all bus impedances, as shown in Eq. (3.49). This integration process can be applied to the matrix $[\underline{Z}_{par}]$ of any cluster area, utilising the modifying equation. Eq. (3.48) is, however, specific for this example. In order to clarify how to use this equation, regardless of the presented example, the modifying equation in general case of a cluster with n number of buses is

$$\underline{Z}_{ij}^{final} = \underline{Z}_{ij} - \frac{\underline{Z}_{i(n+1)}\underline{Z}_{(n+1)j}}{\underline{Z}_{gg}+\underline{Z}_{Th}} \tag{3.50}$$

where $i, j \in \{1, 2, \ldots, n\}$ and bus g is the border bus. Afterwards, by using Eq. (3.50), the final matrix

$$[\underline{Z}_{par}] = \begin{bmatrix} \underline{Z}_{11}^{final} & \underline{Z}_{12}^{final} & \cdots & \underline{Z}_{1n}^{final} \\ \underline{Z}_{21}^{final} & \underline{Z}_{22}^{final} & \cdots & \underline{Z}_{2n}^{final} \\ \vdots & \vdots & \ddots & \vdots \\ \underline{Z}_{n1}^{final} & \underline{Z}_{n2}^{final} & \cdots & \underline{Z}_{nn}^{final} \end{bmatrix} \tag{3.51}$$

in the case of n number of buses in which the impedance $\underline{Z}_{Th,}$ is newly integrated to bus g can be computed. This section provides the last step that enables the decoupled determination of the matrix $[\underline{Z}_{par}]$, which will not be completed without considering the influence of its interconnected cluster areas. The Thévenin impedance $\underline{Z}_{Th}$ is employed to represent the influence of each cluster. It can be selected from a self-impedance in the predetermined matrix $[\underline{Z}_{par}]$, depending on which bus is connected to the interconnected cluster areas. Eqs. (3.39) and (3.40) show the selection of the impedance $\underline{Z}_{Th}$. Subsequently, the selected impedance $\underline{Z}_{Th}$ needs to be exchanged between the interconnected cluster areas. In turn, the exchanged impedance $\underline{Z}_{Th}$ will be integrated to the predetermined matrix $[\underline{Z}_{par}]$. Eq. (3.50) is the general equation for updating each element in the matrix $[\underline{Z}_{par}]$ where $i, j \in \{1, 2, \ldots, n\}$. As a result of the integration, Eq. (3.51) illustrates a general final matrix $[\underline{Z}_{par}]$ after the

original predetermined matrix is updated. The matrix [$\underline{Z}_{par}$], then, is ready-to-use for the voltage sensitivity analysis presented in the next chapter. Finally, the method presented in this section can be applied to each sequence individually, if the predetermined matrix [$\underline{Z}_{par}$] is in the sequence systems.

3.3 Summary

The impedance model proposed for network analysis of cluster-based decentralised power grids is proposed in this chapter. The aim of this model is to enable decoupled voltage sensitivity analysis based on the CPSA. It allows analysing the change of bus voltages caused by the change of bus currents. The proposed impedance model is comprised of bus impedance parameters [$\underline{Z}_{par}$]. It is developed on the basis of a bus impedance matrix [$\underline{Z}_{bus}$]. The difference between the matrices [$\underline{Z}_{par}$] and [$\underline{Z}_{bus}$] is that the matrix [$\underline{Z}_{par}$] solely accommodates bus impedances of the buses of concern in the power grid or cluster area, while the matrix [$\underline{Z}_{bus}$] contains bus impedances of all buses. Therefore, if all buses are relevant for the analysis, the matrices [$\underline{Z}_{par}$] and [$\underline{Z}_{bus}$] will be identical.

The determination of the matrix [$\underline{Z}_{par}$] requires only local measurements of bus voltages and bus currents without knowledge about the grid topology. The method of determining the matrix [$\underline{Z}_{par}$] is developed in such a way that the matrix [$\underline{Z}_{par}$] can be calculated individually for each cluster area when the CPSA is taken into account. This provides an advantage that the measured data can be directly exploited and manipulated by each cluster area. Besides, the matrix [$\underline{Z}_{par}$] can be realised in sequence systems so that it can deal with both balanced and unbalanced conditions of the power grid.

When the CPSA or cluster areas are also considered, the determination of the matrix [$\underline{Z}_{par}$] described above needs an additional step. The influence of interconnected cluster areas must be aware. Accordingly, the Thévenin impedance $\underline{Z}_{Th}$ from the Thévenin's theorem is used to transfer the influence or the characteristic from a cluster to integrate to its interconnected bus, and vice versa. It is subsequently integrated into the predetermined [$\underline{Z}_{par}$] by using the bus impedance modification method. The original elements are recalculated to include the impact of the impedance $\underline{Z}_{Th}$, resulting in [$\underline{Z}_{par}$]. Once this integration process is accomplished, the matrix [$\underline{Z}_{par}$] of each cluster area is ready to be further utilised.

Finally, the matrix [$\underline{Z}_{par}$] is built using an uncomplicated method. It provides, in addition, an up-to-date impedance model for either balanced or unbalanced grid conditions and also supports the distributed characteristics of cluster areas from the CPSA. In the next chapter, the bus impedance parameters of the matrix [$\underline{Z}_{par}$] are leveraged in voltage sensitivity analysis, which is expected to be decoupled for each cluster area.

4. Voltage Sensitivity Analysis for Cluster-Based Decentralised Power Grids

The advent of DG technologies has provided great benefits to power systems in operational and environmental aspects. At the same time, nevertheless, the integration of the DG units into the power grids poses technical challenges to power system operations, as stated in Chapter 1. In this chapter, a method for decoupled voltage sensitivity analysis is proposed for steady-state analysis of voltage magnitude and voltage angle sensitivities. This proposed analysis method is the consecutive process after the determination of bus impedance parameters [$\underline{Z}_{par}$], presented in Chapter 3. In this thesis, the proposed method for the sensitivity analysis embraces the flexibility constraint of the CPSA. Essentially, as the primary constraint, only local synchrophasor measurements of bus voltages and currents are required. Different from using the classical method for voltage sensitivity analysis, the topology of a power grid is assumed to be unknown and is not included in the analysis.

For a power grid, the resulting sensitivity values represent the effects and strength of the concerned buses on the specified condition of their power grid in the manner of voltage magnitude and angle [190], which indicates the response of voltage magnitude or angle to the deviation of another electrical parameter of interest. The primary intention of this chapter is to utilise the outcome of voltage sensitivity analysis for specifying power or current setpoints to facilitate the participation of DG units in grid operations. The proposed method is intended to be feasible for any grid level from distribution to transmission systems and are devised specifically for both unbalanced and balanced grid conditions.

Normally, the voltage sensitivity analysis is also concerned with the analysis and study of the response from the generators under fault or short circuit circumstances that can potentially happen in the power grids. Either power electronic interfaced or non-power electronic interfaced DG units can contribute current during a fault. In a balanced fault, only a positive sequence current will contribute. In an unbalanced fault, additionally, negative or zero sequence currents can contribute in response to a fault [191–193]. Hence, to enable maximum usability of the outcome from the proposed analysis method, the sensitivity of voltage magnitude and angle in relation to sequence currents is provided in this thesis. With this analysis, the proposed method enables the analysis for both unbalanced and balanced grid conditions. Depending on analysis purposes, the state of a power grid can be analysed; the allocation of DG can be studied; and the participation of the DG in grid operations, which is the main target here, can be facilitated.

In addition, the complex components of the sequence currents are beneficial to the sensitivity analysis, since they are the fundamental components. They can be further used or related to

other parameters such as phase powers or phase currents when required. In this thesis, based on the sensitivities in relation to the sequence currents, an option for analysing the voltage sensitivity in relation to active and reactive powers is given for a balanced grid condition. The expected outcomes from the proposed analysis method are listed as follows:

For the unbalanced grid condition

- Sensitivity of **voltage magnitude** at **phase *a*, *b*, and *c*** in relation to **real and imaginary components** of **bus current in zero, positive, and negative sequence systems**
- Sensitivity of **voltage angle** at **phase *a*, *b*, and *c*** in relation to **real and imaginary components** of **bus current in zero, positive, and negative sequence systems**

For the balanced grid condition

- Sensitivity of **phase voltage magnitude** in relation to **active and reactive powers**
- Sensitivity of **phase angle** in relation to **active and reactive powers**

As a main contribution that the sensitivity values can be used together with the power dispatch management for voltage profile regulation, Figure 4.1 illustrates the use of current or power setpoints. Based on the sensitivity values, setpoints or reference values for active controllable elements can be determined. For feeding to controllable units C_i where bus number $i \in \{1, 2, \ldots, n\}$, the setpoints or reference values of active and reactive powers $P_{set,i}$ and $Q_{set,i}$ are computed under the balanced grid condition, while that of complex symmetrical-component bus currents $I^{(s)}_{set:Re,i}$ and $I^{(s)}_{set:Im,i}$ are computed under the unbalanced grid condition.

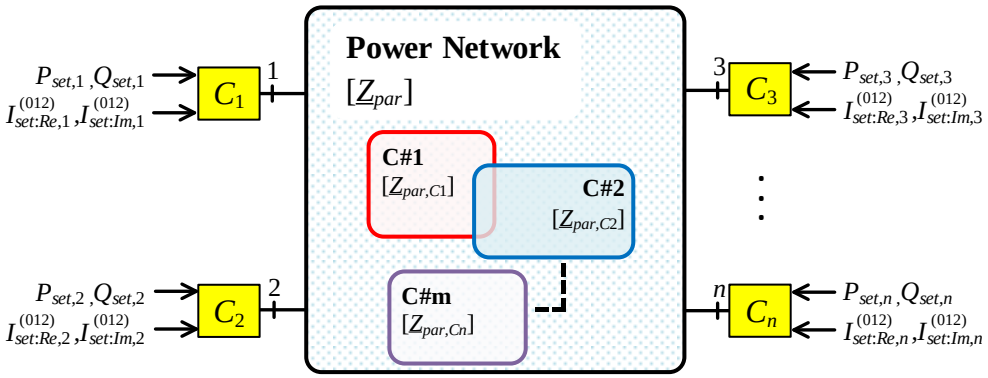

Figure 4.1: Use of setpoints determined from the outcomes of voltage sensitivity analysis

The terms of bus impedance parameter matrix $[\underline{Z}_{par,Ci}]$, where $i \in \{1, 2, \ldots, n\}$, are shown in Figure 4.1 to emphasise that they are used in conjunction with the proposed voltage sensitivity analysis, which allows decoupled analysis as well. Hence, the proposed analysis method is applicable for the analysis in either a whole grid or cluster-based grids.

The structure of this chapter is provided as follows. First, the related research on voltage sensitivity analysis is discussed, where the classical analysis method and new developed methods from another research are explored. Second, the formulation of the voltage models for voltage sensitivity analysis is delineated, as it is the foundation to develop the voltage sensitivity analysis method. Third, after the models have been described, the derivations of the sensitivity of voltage magnitude and angle under the unbalanced grid condition are presented. Fourth, the voltage sensitivity analysis for the unbalanced grid condition is further derived to provide the sensitivity analysis of voltage magnitude and angle under the balanced grid condition. Lastly, the applications of outcomes from the voltage sensitivity analysis for voltage profile regulation are discussed.

4.1 Related Research

This section reviews research related to voltage sensitivity analysis in order to fill the gap in the literature. First, the classical method and other research on voltage sensitivity analysis are described to give an overview on the existing analysis methods. Then, the fundamental of state estimation, which is an alternative to voltage sensitivity analysis, is reviewed, as the proposed methods can also estimate voltage magnitude and angle. Lastly, the selection criteria to develop the proposed analysis methods are presented. The research gap from related work is discussed. As a result, this review will indicate the development of a novel voltage sensitivity analysis in this thesis.

4.1.1 Voltage Sensitivity Analysis

This section discusses research related to this thesis. There are now many available methods of voltage sensitivity analysis, developed for different situations. Classically, the sensitivities of voltage magnitude and angle can be obtained from the inverse of the Jacobian matrix, resulting from the load flow calculation process. Hence, the complete grid topology information, such as cable data and connection between buses, is required to generate the Jacobian matrix. To perform a load flow calculation, node parameters depending on bus types are also needed such as voltage magnitude $|\underline{V}|$ and phase angle δ, active power P and reactive power Q. To envision the load flow calculation process, based on the system of load flow equations [194], voltage sensitivity coefficients can be determined from the inverse of the Jacobian matrix, which is shown in

$$\begin{bmatrix} [\Delta\delta] \\ [\Delta|\underline{V}|] \end{bmatrix} = \begin{bmatrix} [J_{P\delta}] & [J_{PV}] \\ [J_{Q\delta}] & [J_{QV}] \end{bmatrix}^{-1} \begin{bmatrix} [\Delta P] \\ [\Delta Q] \end{bmatrix} \tag{4.1}$$

where the change of voltage magnitude $[\Delta|\underline{V}|]$, phase angle $[\Delta\delta]$, active power $[\Delta P]$ and reactive power $[\Delta Q]$ can be grouped into the matrix form.

Accordingly, the Jacobian matrix

$$\begin{bmatrix} [J_{P\delta}] & [J_{PV}] \\ [J_{Q\delta}] & [J_{QV}] \end{bmatrix} = \left[\begin{array}{ccc|ccc} \frac{\partial P_2}{\partial \delta_2} & \cdots & \frac{\partial P_2}{\partial \delta_n} & \frac{\partial P_2}{\partial |\underline{V}_2|} & \cdots & \frac{\partial P_2}{\partial |\underline{V}_n|} \\ \vdots & J_{P\delta} & \vdots & \vdots & J_{PV} & \vdots \\ \frac{\partial P_n}{\partial \delta_2} & \cdots & \frac{\partial P_n}{\partial \delta_n} & \frac{\partial P_n}{\partial |\underline{V}_2|} & \cdots & \frac{\partial P_n}{\partial |\underline{V}_n|} \\ \hline \frac{\partial Q_2}{\partial \delta_2} & \cdots & \frac{\partial Q_2}{\partial \delta_n} & \frac{\partial Q_2}{\partial |\underline{V}_2|} & \cdots & \frac{\partial Q_2}{\partial |\underline{V}_n|} \\ \vdots & J_{Q\delta} & \vdots & \vdots & J_{QV} & \vdots \\ \frac{\partial Q_n}{\partial \delta_2} & \cdots & \frac{\partial Q_n}{\partial \delta_n} & \frac{\partial Q_n}{\partial |\underline{V}_2|} & \cdots & \frac{\partial Q_n}{\partial |\underline{V}_n|} \end{array}\right] \tag{4.2}$$

is the term of the coefficient matrix whose components can also be grouped as submatrices. For the load flow calculation, there must be at least one reference or slack bus [180]. If bus 1 is assumed to be a slack, the Jacobian matrix can be envisioned as shown in Eq. (4.2). Evidently, the Jacobian matrix provides the relationship between the change of active and reactive powers, ΔP and ΔQ, and the change of voltage magnitude and phase angle, $\Delta|\underline{V}|$ and $\Delta\delta$. Hence, the sensitivities of voltage magnitude and angle in relation to active and reactive powers can be computed. This method is obviously involved with multiple processes and a considerable amount of data, which depends on the power grid size. A larger grid will consequently lead to a computation based on a larger size of the Jacobian matrix.

In addition to the classical method, there are also other proposed methods that reduce the computational complexity in the analysis. Two categories of analysis methods are considered in this context. The first category is the voltage sensitivity analysis methods that are derived from the information of the topological structure and line parameters. Voltage sensitivity analysis methods in [195–202] are proposed only for the radial grid topology, and the unbalanced condition is not considered. On the other hand, the methods in [203, 204] consider the unbalanced grid condition, and the grid topology is not fixed. The second category is the voltage sensitivity analysis methods that utilise only measurement data. Thus, these methods allow online analyses, as they do not require topological information. The methods proposed in [205–208] use the PMU measurement to compute the relationship between voltage change (magnitude and angle) and power change (active and reactive powers). Nonetheless, the possible grid condition for the analysis is not mentioned here. Furthermore, the voltage sensitivity analysis in [209] uses measurement data of smart meters. Thereby, only the sensitivity of voltage magnitude is discussed; the sensitivity of voltage angle is not included.

Although the analysis method proposed in this thesis also belongs to the second category in which only voltage and current measurements from PMU are used, the contribution is that this method is applicable for both balanced and unbalanced conditions and any type of grid topology. The proposed method also works with decoupled analysis when local areas, i.e. cluster areas based on the CPSA, are considered.

4.1.2 State Estimation

To ensure stability of power systems, grid state variables, i.e., magnitudes and phase angles of voltages and currents, as well as active and reactive powers, are concerned. In real-time power system monitoring and control, the control centre of a grid utility receives a large amount of measurement data such as active and reactive, bus voltages, line and bus currents, including switches and breakers status [210, 211]. These data are further used to monitor the status of the power grid and to conduct control actions in accordance with objectives of the operation. However, since these data are gathered from measurements, errors and noises must be taken into account to leverage the data efficiently.

State estimation is an important tool to monitor grid state variables and concurrently to cope with measurement errors. [212, 213]. Typically, the state estimation is aimed to provide an accurate and complete set of voltage magnitudes and phase angles [214, 215]. With statistical and optimization algorithms, it can filter bad data out [212]; it can also deal with random measurement noises and with incomplete information [216–218]; and it can handle false data attacks [219].

For power system state estimation, an estimates matrix [G] for a linearized system can be determined by Eq. (4.3), and subsequently state vectors [x_e] of estimated values at iteration k can be determined by Eq. (4.4) [220]. The state vectors in [x_e] are complex node voltages in the considered power network. The matrix [H] represents the Jacobian matrix, while the matrix $[R]^{-1}$ represents the covariance matrix. The nonlinear equations [$h([x_e])$] can contain the equations of complex node voltage magnitudes and powers, as well as complex line powers between nodes. The matrix [z_m] is defined to accommodate measurement data. In case measurements are obtained from PMU, complex node voltages are considered. The equation used in the matrix [$h([x_e])$] depends on the vectors in [z_m].

$$[G] = [H([x_{e,k}])]^T [R]^{-1} [H([x_{e,k}])] \tag{4.3}$$

$$[x_{e,k+1}] = [G]^{-1} [H([x_{e,k}])]^T [R]^{-1} \left[[z_m] - h([x_{e,k}]) \right] + [\Delta x_{e,k+1}] \tag{4.4}$$

Figure 4.2 shows the workflow diagram of Eq. (4.4), which is the nonlinear state estimation [220]. In this workflow, the matrix $[J]^{-1}$ is the product of the transposed Jacobian matrix $[H[x_e]^k]^T$ and the covariance matrix $[R]^{-1}$. At the beginning, the matrix $[x_e^0]$ of initial voltage vectors is indicated to calculate initial coefficients of the Jacobian matrix [H] and initial results of the nonlinear equations [h]. Then, the difference $[z_m\text{-}h(x_e)^k]$ can be computed. Sequentially, the vector differences $[\Delta x_e^0]$ can be determined. Finally, the process is stopped when the differences $[\Delta x_e^k]$ fulfil, i.e. lower than, the stopping criteria ε_x.

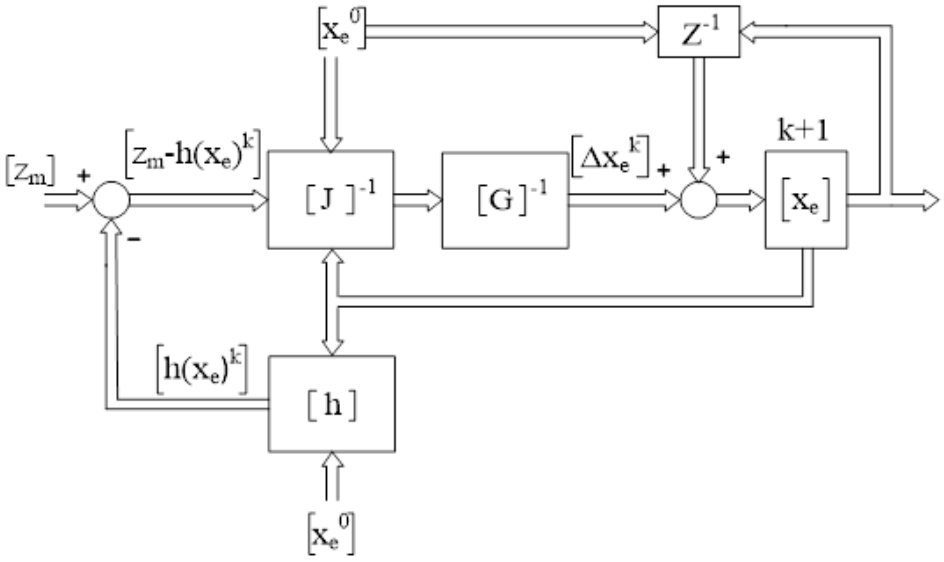

Figure 4.2: Overview of state estimation workflow [220]

To estimate state variables, the state estimation requires existing measurement data together with grid topology data, including status of switching devices and line parameters. The results from state estimation subsequently can be used to determine other quantities (which cannot be measured or are missing from measurements) of power systems such as complex bus currents, power loss in the grid, and power consumption and generation at buses. Load flow calculation is a usual technique to determine these quantities [210].

Similar to the proposed analysis method, clearly, the state estimation can also be used to determine, or estimate, voltage magnitudes and angles caused by the change of bus powers or bus currents. Nonetheless, the change will be initially identified in the form of load profile, based on available measurement data, in which data of the entire concerned grid will be involved. Also, grid topology, line parameters, switching statuses are required to perform the state estimation. With these sets of data, the state estimator can generate estimated complex bus voltages of the entire grid.

In contrast, the proposed analysis methods require only measurement data to calculate the complex bus voltages, without the knowledge of grid topology and a network model. In addition, the proposed methods also allow an analysis of a specific bus, thus simplifying the estimation of complex voltage caused by the change of bus power or bus current.

Since measurement data are critical for the proposed methods, the state estimation can serve as a compensation to the proposed methods in the preparation of the measurement data. This can deal not only measurement noises and errors, but also the problem of lacking enough measurement devices can be mitigated.

Currently, there are many research publications about the improvement of the state estimation, especially in distribution networks, where the observability is still low. In general,

the data sources of the state estimation in distribution level are smart meter, SCADA, PMU, and pseudo measurement. Ref. [221] presents a state estimation algorithm considering the uncertainty of line parameters and minimum number of smart meter measurement for near-real-time monitoring. Ref. [222] proposes the use of advanced metering infrastructure (AMI) set-up and an approach for synthesising pseudo-measurement data to improve accuracy of state estimation. Based on the available real measurements, synthetic load profiles of non-observable, or non-metered users, are created. Ref. [223] proposes a technique to generate synthetic measurements with different sets of measurements among phases in order to improve the estimation of phase angles. Moreover, uncertainty of network data and allocation of meters in the power grid are of concern. State estimation can allow the availability of a limited number of measurement devices. Refs. [214, 224–226] analyse optimal meter placement to enhance the accuracy of state estimation.

With the help of state estimation, the measurement data therefore will be accurate to the state of the grid, as the state estimation solves errors and noises, including missing data, in a measurement. By using state estimation together with load flow calculation, bus voltage magnitudes and angles can be determined, as an alternative to only the PMU measurements. However, with this approach, topology data are needed.

4.1.3 Selection Criteria

Following the review of literature, including publications about related topics of the power systems and voltage sensitivity analysis, current problems and the research gap are identified in the form of selection criteria. By fulfilling these selection criteria, the method is expected to enable a voltage sensitivity analysis, which can support active operations at any grid level. The criteria to select the proposed method are summarized as follows.

1. *The analysis method must be applicable for an analysis at any grid level*. Owing to the existence of RESs-based DG units in the distribution level, active operations will be expanded from the transmission down to the distribution systems, in the modern power systems. Accordingly, newly developed functions should be flexible for use at any grid level. The characteristics of different voltage levels, e.g. R/X ratio, should be overcome.
2. *The analysis method must not require grid topology data.* In the transmission system, the information of grid topology is complete for performing a power system analysis. However, in the distribution system, the information of grid topology is typically incomplete. There is often a lack of up-to-date topology data, such as switching status and local changes [119]. Performing newly developed functions therefore should be feasible without using grid topology information. Due to the advancement of metrology, such as PMU and smart meters, measurement data can increase

observability in the power systems, including at the distribution level [70, 227]. Using measurement data to perform an analysis is therefore favourable in this thesis.

3. *The analysis method must require only measurement data of concerned buses to perform an analysis*. In addition to what data are required, the amount of measurement data for a voltage sensitivity analysis is critical. An analysis should require only the data from the concerned buses, or controllable buses in the context of this thesis. Unlike the classical method, where the data of all buses are required to form the Jacobian matrix, newly developed methods should use less data than the complete data of the whole power grid. Especially when there is only specific measurement data, (e.g. voltages and currents), of concerned buses required, the amount of data in the analysis process significantly reduces. This also leads to faster analysing time.
4. *The analysis method must be possible for both balanced and unbalanced grid conditions*. Under a balanced condition, only one phase is analysed in a voltage sensitivity analysis. The sensitivity of the magnitude and the sensitivity of phase angle caused by a change of bus power or bus current are equal for all phases, since all phases feed-in or extract power equally. Nevertheless, under an unbalanced condition, the voltage sensitivity is different on each phase. Fed-in or extracted power is different in each phase, causing unequal sensitivity of voltage magnitude and angle among phases. At the transmission level, the power grids are generally under a balanced condition. On the other hand, at the distribution level, the power grids are usually under an unbalanced condition. To achieve an analysis method that can be used at any grid level, the newly developed method therefore must be able to cope with both grid conditions.

Selection criteria for the analysis requirements then are used to compare different existing methods which can be used to perform voltage sensitivity analysis. A comparison matrix is illustrated in Table 4.1. It shows the comparison between the classical method, state estimation, and related research. The classical method, which is based on the Jacobian matrix, and the state estimation clearly provide the same characteristics in the selection criteria. Although both can be applicable to any grid level and to all grid conditions, they do not satisfy the other two criteria. They require grid topology and data from all buses to compute the sensitivity values in the classical method and to estimate voltage in the state estimation, respectively. It is noteworthy that none of the related research satisfies all selection criteria. Also, none are declared to be possible for all grid conditions.

Table 4.1: Comparison matrix among different voltage sensitivity analysis methods

Selection criteria	Classical method	State estimation	Related research
Applicable to any grid level	Yes	Yes	Yes/No
Executable without grid topology	No	No	Yes/No
Only data from concerned buses sufficient for the input	No	No	No
Possible for all grid conditions	Yes	Yes	No

In this thesis, therefore, the voltage sensitivity analysis methods are developed to meet all the criteria, indicated in Table 4.1. In the next section, the formulation of the voltage sensitivity analysis model is introduced. Characteristics and description of voltage change are provided.

4.2 Formulation of the Voltage Sensitivity Analysis Model

The voltage sensitivity analysis proposed in this thesis examines the response of voltage magnitude and angle in relation to bus current in sequence systems, active power, and reactive power. To do so, the predetermined bus impedance parameters are utilised as the foundation of the method for executing the proposed analysis in this section, since the impedance model matrix $[\underline{Z}_{par}]$ provides the relationship between buses of a power grid. In the following subsections, adapting the matrix $[\underline{Z}_{par}]$ to the required target of the analysis is shown first. The adapted version of the matrix $[\underline{Z}_{par}]$ is afterwards used to formulate the model of bus voltages. In the later section, the model will play an important role in the derivation of the proposed voltage sensitivity analysis.

4.2.1 Utilisation of the Bus Impedance Parameters

As the foundation of the proposed method of voltage sensitivity analysis, the bus impedance parameters from the matrix $[\underline{Z}_{par}]$ determined in Chapter 3 are further utilised here. Based on the impedance model, the matrix $[\underline{Z}_{par}]$ enables the analysis of the relationship between the change of bus voltages and the change of bus currents. The analysis is aimed to be feasible for any grid level and is applicable for both balanced and unbalanced conditions. For this reason, instead of considering bus currents, the relationship between phase voltages and sequence currents is analysed. Accordingly, the bus impedance parameters will be the intermediate entity, connecting phase voltages and symmetrical components of bus currents in sequence

systems. How the bus impedance parameters are prepared for the voltage sensitivity analysis is presented here:

The definition of the bus voltage used in the analysis is worth discussing first. If an *n*-bus power grid is considered, the bus voltage

$$\underline{V}_i^{t_k} = \underline{V}_i^{t_{k-1}} + \Delta\underline{V}_{ih}^{\mathrm{T}_1} \tag{4.5}$$

of bus *i* at the latest time t_k is regarded as the the combination of its initial voltage $\underline{V}_i^{tk\text{-}1}$ at the time t_{k-1} and its voltage change $\Delta\underline{V}_{ih}^{\mathrm{T1}}$ caused by bus *h* in the period T_1 between times t_k and t_{k-1}, where *k* is a positive integer and $i, h \in \{1, 2, \ldots, n\}$. For the simplicity purpose, the time and period indicators *t* and T will be left out, and the term of time t_{k-1} will be defined as the known value *K*. Hence, Eq. (4.5) is rewritten as

$$\underline{V}_i = \underline{V}_i^K + \Delta\underline{V}_{ih}. \tag{4.6}$$

This means that the voltage $\underline{V}_i$ is the expected voltage that happens after the known voltage $\underline{V}_i^K$ is added by the voltage change $\Delta\underline{V}_{ih}$. Since only measurement data are expected to be exploited during the voltage sensitivity analysis, the known voltage $\underline{V}_i^K$ is defined here as the measured voltage, which already existed at the time when the analysis was performed. Subsequently, to explore in more detail, the relationship between the bus voltage at bus *i* and the current change at bus *h* is examined, as depicted in Figure 4.3. The resistance R_{ih} and reactance X_{ih} are obtained from the bus impedance parameter $\underline{Z}_{ih}$ between bus *i* and bus *h*, and they will be discussed afterwards.

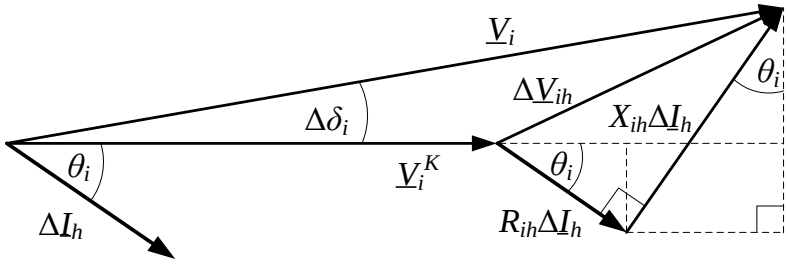

Figure 4.3: Phasor diagram of voltage $\underline{V}_i$ at bus *i* caused by current change at bus *h*

For the next step, as three-phase system is focused, voltages $\underline{V}_{a,i}$, $\underline{V}_{b,i}$, and $\underline{V}_{c,i}$ are assigned to bus *i*. The subscripts *a*, *b*, and *c* indicate the corresponding phase of each voltage. This notation is applied to the known voltage and the change of voltage as well. Thus, Eq. (4.6) can be written in the matrix form of three phase system as

$$\begin{bmatrix} \underline{V}_{a,i} \\ \underline{V}_{b,i} \\ \underline{V}_{c,i} \end{bmatrix} = \begin{bmatrix} \underline{V}_{a,i}^K \\ \underline{V}_{b,i}^K \\ \underline{V}_{c,i}^K \end{bmatrix} + \begin{bmatrix} \Delta\underline{V}_{a,ih} \\ \Delta\underline{V}_{b,ih} \\ \Delta\underline{V}_{c,ih} \end{bmatrix}. \tag{4.7}$$

As mentioned at the beginning of this chapter, the proposed voltage sensitivity analysis proposed in this thesis examines the response of voltage magnitude and angle in relation to bus current in sequence systems. The terms of voltage changes in Eq. (4.7) are discussed in this step. They are converted here into symmetrical components to observe the impact from sequence currents on phase voltages. According to the conversion process in Section 3.2.3, applying Eq. (3.28) to the term of voltage changes in Eq. (4.7) yields

$$\begin{bmatrix} \underline{V}_{a,i} \\ \underline{V}_{b,i} \\ \underline{V}_{c,i} \end{bmatrix} = \begin{bmatrix} \underline{V}_{a,i}^{K} \\ \underline{V}_{b,i}^{K} \\ \underline{V}_{c,i}^{K} \end{bmatrix} + \begin{bmatrix} 1 & 1 & 1 \\ 1 & \underline{a}^2 & \underline{a} \\ 1 & \underline{a} & \underline{a}^2 \end{bmatrix} \begin{bmatrix} \Delta\underline{V}_{ih}^{(0)} \\ \Delta\underline{V}_{ih}^{(1)} \\ \Delta\underline{V}_{ih}^{(2)} \end{bmatrix} \tag{4.8}$$

where $\Delta\underline{V}_{ih}^{(0)}$, $\Delta\underline{V}_{ih}^{(1)}$, and $\Delta\underline{V}_{ih}^{(2)}$ are designated for voltage changes in zero-, positive-, and negative-sequence systems, respectively. The coefficient matrix is obtained from the matrix $[\underline{A}]$ in Eq. (3.29). This matrix converts phase components into their symmetrical components. At this point, the term of sequence voltage changes in Eq. (4.8) can be subsequently converted into sequence currents to relate the impact of currents in symmetrical components on phase voltages. Since the current flow is independent in each of the sequence systems [181], the relationship between sequence voltages and currents can be expressed by

$$\begin{bmatrix} \Delta\underline{V}_{ih}^{(0)} \\ \Delta\underline{V}_{ih}^{(1)} \\ \Delta\underline{V}_{ih}^{(2)} \end{bmatrix} = \begin{bmatrix} \underline{Z}_{ih}^{(0)} & 0 & 0 \\ 0 & \underline{Z}_{ih}^{(1)} & 0 \\ 0 & 0 & \underline{Z}_{ih}^{(2)} \end{bmatrix} \begin{bmatrix} \Delta\underline{I}_{h}^{(0)} \\ \Delta\underline{I}_{h}^{(1)} \\ \Delta\underline{I}_{h}^{(2)} \end{bmatrix}. \tag{4.9}$$

The coupling between sequence systems is neglected because cable layout is assumed to be symmetrical here for the sake of simplicity. Now, the predetermined matrix $[\underline{Z}_{par}]$ plays a role. The impedances $\underline{Z}_{ih}^{(0)}$, $\underline{Z}_{ih}^{(1)}$, and $\underline{Z}_{ih}^{(2)}$ are picked up from the matrix $[\underline{Z}_{par}]$ in sequence systems. These impedances represent the impact of the change of sequence currents $\Delta\underline{I}_h^{(0)}$, $\Delta\underline{I}_h^{(1)}$, and $\Delta\underline{I}_h^{(2)}$ at bus h on bus voltages at bus i. Next, substituting Eq. (4.9) in Eq. (4.8) yields

$$\begin{bmatrix} \underline{V}_{a,i} \\ \underline{V}_{b,i} \\ \underline{V}_{c,i} \end{bmatrix} = \begin{bmatrix} \underline{V}_{a,i}^{K} \\ \underline{V}_{b,i}^{K} \\ \underline{V}_{c,i}^{K} \end{bmatrix} + \begin{bmatrix} 1 & 1 & 1 \\ 1 & \underline{a}^2 & \underline{a} \\ 1 & \underline{a} & \underline{a}^2 \end{bmatrix} \begin{bmatrix} \underline{Z}_{ih}^{(0)} & 0 & 0 \\ 0 & \underline{Z}_{ih}^{(1)} & 0 \\ 0 & 0 & \underline{Z}_{ih}^{(2)} \end{bmatrix} \begin{bmatrix} \Delta\underline{I}_{h}^{(0)} \\ \Delta\underline{I}_{h}^{(1)} \\ \Delta\underline{I}_{h}^{(2)} \end{bmatrix}. \tag{4.10}$$

Accordingly, the relationship between phase voltages and sequence currents is achieved. Multiplying the coefficient matrix $[\underline{A}]$ and matrix of sequence bus impedance parameters in Eq. (4.10) subsequently leads to

$$\begin{bmatrix} \underline{V}_{a,i} \\ \underline{V}_{b,i} \\ \underline{V}_{c,i} \end{bmatrix} = \begin{bmatrix} \underline{V}_{a,i}^{K} \\ \underline{V}_{b,i}^{K} \\ \underline{V}_{c,i}^{K} \end{bmatrix} + \begin{bmatrix} \underline{\tilde{Z}}_{a,ih}^{(0)} & \underline{\tilde{Z}}_{a,ih}^{(1)} & \underline{\tilde{Z}}_{a,ih}^{(2)} \\ \underline{\tilde{Z}}_{b,ih}^{(0)} & \underline{\tilde{Z}}_{b,ih}^{(1)} & \underline{\tilde{Z}}_{b,ih}^{(2)} \\ \underline{\tilde{Z}}_{c,ih}^{(0)} & \underline{\tilde{Z}}_{c,ih}^{(1)} & \underline{\tilde{Z}}_{c,ih}^{(2)} \end{bmatrix} \begin{bmatrix} \Delta\underline{I}_{h}^{(0)} \\ \Delta\underline{I}_{h}^{(1)} \\ \Delta\underline{I}_{h}^{(2)} \end{bmatrix} \tag{4.11}$$

In Eq. (4.11), the multiplication of the two coefficient matrices results in the converting bus impedance parameters, denoted by $[\underline{\tilde{Z}}_{par,ih}]$. These impedances in the matrix $[\underline{\tilde{Z}}_{par,ih}]$ provide the relationship between phase voltages and the change of bus currents in sequence systems. The bus impedances $\underline{\tilde{Z}}_{a,ih}^{(s)}$, $\underline{\tilde{Z}}_{b,ih}^{(s)}$, and $\underline{\tilde{Z}}_{c,ih}^{(s)}$ have the impact on their corresponding phase, where $s \in \{0, 1, 2\}$. The same as the matrix $[\underline{Z}_{par}]$, the matrix $[\underline{\tilde{Z}}_{par,ih}]$ consists of real and imaginary components, described as

$$\begin{bmatrix} \underline{\tilde{Z}}_{a,ih}^{(0)} & \underline{\tilde{Z}}_{a,ih}^{(1)} & \underline{\tilde{Z}}_{a,ih}^{(2)} \\ \underline{\tilde{Z}}_{b,ih}^{(0)} & \underline{\tilde{Z}}_{b,ih}^{(1)} & \underline{\tilde{Z}}_{b,ih}^{(2)} \\ \underline{\tilde{Z}}_{c,ih}^{(0)} & \underline{\tilde{Z}}_{c,ih}^{(1)} & \underline{\tilde{Z}}_{c,ih}^{(2)} \end{bmatrix} = \begin{bmatrix} \tilde{R}_{a,ih}^{(0)} & \tilde{R}_{a,ih}^{(1)} & \tilde{R}_{a,ih}^{(2)} \\ \tilde{R}_{b,ih}^{(0)} & \tilde{R}_{b,ih}^{(1)} & \tilde{R}_{b,ih}^{(2)} \\ \tilde{R}_{c,ih}^{(0)} & \tilde{R}_{c,ih}^{(1)} & \tilde{R}_{c,ih}^{(2)} \end{bmatrix} + j \begin{bmatrix} \tilde{X}_{a,ih}^{(0)} & \tilde{X}_{a,ih}^{(1)} & \tilde{X}_{a,ih}^{(2)} \\ \tilde{X}_{b,ih}^{(0)} & \tilde{X}_{b,ih}^{(1)} & \tilde{X}_{b,ih}^{(2)} \\ \tilde{X}_{c,ih}^{(0)} & \tilde{X}_{c,ih}^{(1)} & \tilde{X}_{c,ih}^{(2)} \end{bmatrix}. \tag{4.12}$$

The real part of $[\underline{\tilde{Z}}_{par,ih}]$ is denoted by $[\tilde{R}_{ih}]$, which is the matrix of resistances $\underline{\tilde{R}}_{a,ih}^{(s)}$, $\underline{\tilde{R}}_{b,ih}^{(s)}$, and $\underline{\tilde{R}}_{c,ih}^{(s)}$ where $s \in \{0, 1, 2\}$. In the meantime, the imaginary part of $[\underline{\tilde{Z}}_{par,ih}]$ is denoted by $[\tilde{X}_{ih}]$, which is composed of reactances $\underline{\tilde{X}}_{a,ih}^{(s)}$, $\underline{\tilde{X}}_{b,ih}^{(s)}$, and $\underline{\tilde{X}}_{c,ih}^{(s)}$ where $s \in \{0, 1, 2\}$.

To prepare for the proposed voltage sensitivity analysis, the development of the converting bus impedance parameters $[\underline{\tilde{Z}}_{par,ih}]$ has been elaborated. As a result, the components of $[\tilde{R}_{ih}]$ and $[\tilde{X}_{ih}]$ are obtained in Eq. (4.12). In the next section, the matrix $[\underline{\tilde{Z}}_{par,ih}]$, including $[\tilde{R}_{ih}]$ and $[\tilde{X}_{ih}]$, is discussed in more detail, as they play an essential role in formulating the model of bus voltages for the sensitivity analysis.

4.2.2 Models of Bus Voltages

In order to analyse the characteristics of bus voltages and their corresponding angles, a model of bus voltage is of importance. This section discusses the voltage model that will be employed in the voltage sensitivity analysis, in which the relationship between phase voltages and the sequence currents is determined. In the following, the discussion continues from Eq. (4.11) in Section 4.2.1.

To simplify the description, the matrices of bus voltages, known voltages, converting impedances, and the change of sequence currents in Eq. (4.11) are rewritten as

$$\left[\underline{V}_i\right] = \left[\underline{V}_i^K\right] + \left[\underline{\tilde{Z}}_{par,ih}\right]\left[\Delta \underline{I}_h^{(012)}\right] \tag{4.13}$$

where subscripts i, $h \in \{1, 2, \ldots, n\}$ are designated for an n-bus power grid. In Eq. (4.13), matrices of phase voltages and their known value are reduced into $[\underline{V}_i]$ and $[\Delta \underline{V}_i^K]$. The matrix $[\Delta \underline{I}_h^{(012)}]$ is designated for the change of sequence currents. Similar to the case of phase voltages, sequence currents $\Delta \underline{I}_h^{(s)}$ at bus h are the combination of their known value $\Delta \underline{I}_h^{K(s)}$ and their current change $\Delta \underline{I}_h^{(s)}$, where $s \in \{0, 1, 2\}$. The sequence currents $\underline{I}_h^{(0)}$, $\underline{I}_h^{(1)}$, and $\underline{I}_h^{(2)}$ at bus h are from zero-, positive-, and negative-sequence, respectively. Since each sequence system is independent, the current $\underline{I}_h^{(s)}$ can be understood in the form of matrix

$$\begin{bmatrix} \underline{I}_h^{(0)} \\ \underline{I}_h^{(1)} \\ \underline{I}_h^{(2)} \end{bmatrix} = \begin{bmatrix} \underline{I}_h^{K(0)} \\ \underline{I}_h^{K(1)} \\ \underline{I}_h^{K(2)} \end{bmatrix} + \begin{bmatrix} \Delta\underline{I}_h^{(0)} \\ \Delta\underline{I}_h^{(1)} \\ \Delta\underline{I}_h^{(2)} \end{bmatrix}. \tag{4.14}$$

Considering that the matrices in Eq. (4.14) are described as $[\underline{I}_h{}^{(012)}]$ and $[\underline{I}_h{}^{K(012)}]$, the matrix of current change $[\Delta\underline{I}_h{}^{(012)}]$ therefore can be understood as

$$\left[\Delta\underline{I}_h^{(012)}\right] = \left[\underline{I}_h^{(012)}\right] - \left[\underline{I}_h^{K(012)}\right]. \tag{4.15}$$

Subsequently, replacing Eq. (4.15) in Eq. (4.13) yields

$$\left[\underline{V}_i\right] = \left[\underline{V}_i^K\right] + \left[\underline{\tilde{Z}}_{par,ih}\right]\left[\left[\underline{I}_h^{(012)}\right] - \left[\underline{I}_h^{K(012)}\right]\right]. \tag{4.16}$$

To analyse the sensitivity of bus voltage magnitude and angle, the complex from of all elements in Eq. (4.16) are further examined. First, phase voltages can be expressed as

$$\left[\underline{V}_i\right] = [V_{i:Re}] + j[V_{i:Im}]. \tag{4.17}$$

The matrices $[\underline{V}_{i:Re}]$ and $[\underline{V}_{i:Im}]$ in Eq. (4.17) contain real and imaginary components of the phase voltages in $[\underline{V}_i]$. Meanwhile, the complex form of the known phase voltages is

$$\left[\underline{V}_i^K\right] = [V_{i:Re}^K] + j[V_{i:Im}^K]. \tag{4.18}$$

The matrices $[V_{i:Re}^K]$ and $[V_{i:Im}^K]$ in Eq. (4.18) accommodate real and imaginary components of the known voltages in $[\underline{V}_i^K]$. By applying the same notation, the matrices of complex sequence currents and their known values are

$$\left[\underline{I}_h^{(012)}\right] = \left[I_{h:Re}^{(012)}\right] + j\left[I_{h:Im}^{(012)}\right] \tag{4.19}$$

and

$$\left[\underline{I}_h^{K(012)}\right] = \left[I_{h:Re}^{K(012)}\right] + j\left[I_{h:Im}^{K(012)}\right]. \tag{4.20}$$

The matrices $[I_{h:Re}^{(012)}]$ and $[I_{h:Im}^{(012)}]$ in Eq. (4.19) and $[I_{h:Re}^{K(012)}]$ and $[I_{h:Im}^{K(012)}]$ in Eq. (4.20), respectively, present the real and imaginary components for sequence currents and their known values. Besides voltages and currents, the matrix $[\underline{\tilde{Z}}_{par,ih}]$ is also available in the complex form as

$$\left[\underline{\tilde{Z}}_{par,ih}\right] = [\tilde{R}_{ih}] + j[\tilde{X}_{ih}] \tag{4.21}$$

where resistance $[\tilde{R}_{ih}]$ and reactance $[\tilde{X}_{ih}]$ are referred to Eq. (4.12). Accordingly, Eq. (4.13) can be expanded in the complex form. Substituting Eq. (4.13) with Eqs. (4.17) to (4.21) yields

$$\begin{aligned}[V_{i:Re}] + j[V_{i:Im}] = {} & [V_{i:Re}^K] + j[V_{i:Im}^K] \\ & + \left[[\tilde{R}_{ih}] + j[\tilde{X}_{ih}]\right]\left[\left[I_{h:Re}^{(012)}\right] + j\left[I_{h:Im}^{(012)}\right]\right] - \left[\left[I_{h:Re}^{k(012)}\right] + j\left[I_{h:Im}^{K(012)}\right]\right]\Bigg]. \end{aligned} \tag{4.22}$$

Eq. (4.22) presents the complete description of complex phase voltages at bus *i* in the form of matrix. However, only current change at bus *h* is taken into account in Eq. (4.22). In practice, the current change can happen at more than one bus, and all the changes can affect phase voltages at bus *i*. In the following, only complex components of the phase voltage are examined. Together with calculating the product of $[\tilde{R}_{ih}]$ and $[\tilde{X}_{ih}]$ and the sequence currents $I_{h:Re}^{(s)}$ and $I_{h:Im}^{(s)}$ of all *n* buses where $i, h \in \{1, 2, \ldots, n\}$, the real component $\underline{V}_{p,i:Re}$ and the imaginary component $\underline{V}_{p,i:Im}$ of phase voltage, where phase $p \in \{a, b, c\}$, can be elaborated as

$$V_{p,i:Re} + jV_{p,i:Im} = V_{p,i:Re}^{K} + jV_{p,i:Im}^{K} + \sum_{h=1}^{n}\sum_{s=0}^{2}\left[\left(\tilde{R}_{p,ih}^{(s)} I_{h:Re}^{(s)} - \tilde{X}_{p,ih}^{(s)} I_{h:Im}^{(s)}\right) + j\left(\tilde{X}_{p,ih}^{(s)} I_{h:Re}^{(s)} + \tilde{R}_{p,ih}^{(s)} I_{h:Im}^{(s)}\right)\right] - \left[\left(\tilde{R}_{p,ih}^{(s)} I_{h:Re}^{K(s)} - \tilde{X}_{p,ih}^{(s)} I_{h:Im}^{K(s)}\right) + j\left(\tilde{X}_{p,ih}^{(s)} I_{h:Re}^{K(s)} + \tilde{R}_{p,ih}^{(s)} I_{h:Im}^{K(s)}\right)\right]. \quad (4.23)$$

Here, Eq. (4.23) demonstrates how the bus voltages $\underline{V}_{p,i:Re}$ and $\underline{V}_{p,i:Im}$ at bus *i* are affected by sequence currents of all *n* buses. At phase *a*, the known real- and imaginary-component voltages $V_{p,i:Re}^{K}$ and $V_{p,i:Im}^{K}$ are combined to the products of the resistive and reactive components $\tilde{R}_{p,ih}^{(s)}$ and $\tilde{X}_{p,ih}^{(s)}$ and the sequence currents $I_{h:Re}^{(s)}$ and $I_{h:Im}^{(s)}$, as well as the known currents $I_{h:Re}^{K(s)}$ and $I_{h:Im}^{K(s)}$, where $s \in \{0, 1, 2\}$. From this point, all elements in Eq. (4.23) are in the real and imaginary parts. The real-component voltage

$$V_{p,i:Re} = V_{p,i:Re}^{K} + \sum_{h=1}^{n}\sum_{s=0}^{2}\left[\left(\tilde{R}_{p,ih}^{(s)} I_{h:Re}^{(s)} - \tilde{X}_{p,ih}^{(s)} I_{h:Im}^{(s)}\right) - \left(\tilde{R}_{p,ih}^{(s)} I_{h:Re}^{K(s)} - \tilde{X}_{p,ih}^{(s)} I_{h:Im}^{K(s)}\right)\right] \quad (4.24)$$

and imaginary-component voltage

$$V_{p,i:Im} = V_{p,i:Im}^{K} + \sum_{h=1}^{n}\sum_{s=0}^{2}\left[\left(\tilde{X}_{p,ih}^{(s)} I_{h:Re}^{(s)} + \tilde{R}_{p,ih}^{(s)} I_{h:Im}^{(s)}\right) - \left(\tilde{X}_{p,ih}^{(s)} I_{h:Re}^{K(s)} + \tilde{R}_{p,ih}^{(s)} I_{h:Im}^{K(s)}\right)\right] \quad (4.25)$$

can be individually deduced, where $p \in \{a, b, c\}$. It can be interpreted from Eqs. (4.24) and (4.25) that both complex-component voltages $\underline{V}_{p,i:Re}$ and $\underline{V}_{p,i:Im}$ are a function of the currents $I_{h:Re}^{(s)}$ and $I_{h:Im}^{(s)}$, as resistance $\tilde{R}_{p,ih}^{(s)}$, reactance $\tilde{X}_{p,ih}^{(s)}$, and other known voltages and currents are constant. In this thesis, Eqs. (4.24) and (4.25) are the models for the derivation of the proposed method for voltage sensitivity analysis.

So far, the model for voltage sensitivity analysis has been formulated. As the target of the sensitivity analysis is to observe the sensitivity of phase voltages to the change of sequence currents, the bus impedance parameters from Chapter 3 are adapted to relate the phase and sequence quantities. The matrix $[\underline{\tilde{Z}}_{par,ih}]$ of converting bus impedance parameters is acquired as a result, if phase voltages at bus *i* and sequence currents at bus *h* are observed. Then, the models of real- and imaginary-component voltages are deduced. By extracting all elements of the phase voltages, converting impedances, and sequence currents into the complex form, the models describing phase voltages are created. The models of complex-component voltages

$\underline{V}_{p,i:Re}$ and $\underline{V}_{p,i:Im}$ are illustrated in Eqs. (4.24) and (4.25), respectively. They will be leveraged in the following section to derive the proposed method of voltage sensitivity analysis.

4.3 Methods for Voltage Sensitivity Analysis under an Unbalanced Grid Condition

This section presents the methods proposed for voltage magnitude and angle sensitivity analyses in relation to bus currents in sequence systems. These methods are meant to be applicable for power grids under an unbalanced condition. Focused on the three-phase system, the sensitivities of voltage magnitude and angle at each phase *a*, *b*, and *c* with regard to the sequence currents are sequentially derived in the following subsections. The derivations illustrate that the impact of the sequence currents on voltage magnitude and angle at different buses can be studied by using only measurement data. Apart from the bus impedance parameters, a mere measured voltage is required to complete a sensitivity analysis.

4.3.1 Voltage Magnitude Sensitivity in Relation to Sequence Currents

Voltage magnitude is one of the state variables that is controlled during the grid operation. In continental Europe, the state of power grids in transmission systems is considered as normal if, for instance, the voltage magnitude of all buses is in the range of 0.90 to 1.118 pu at the defined reference voltages between 110 kV to 300 kV [228]. Also, in low-voltage distribution networks, the permissible range of voltage magnitude is ±10% of the nominal value [46]. In this section, the proposed method for analysing the sensitivity of voltage magnitude to individual real and imaginary components of sequence currents is deduced on the basis of Eqs. (4.24) and (4.25). In the following, the analysis of bus voltage at phase *a* is discussed as per the example, while the analysis of bus voltage at other phases can be performed in the same way. Starting from the fundamental voltage description, for an *n*-bus grid, the bus voltage $\underline{V}_{a,i}$ ($i \in \{1, 2, \ldots, n\}$) at phase *a* of bus *i* is considered in the complex form as

$$\underline{V}_{a,i} = V_{a,i:Re} + jV_{a,i:Im}. \tag{4.26}$$

Based on Eq. (4.26), the magnitude $|\underline{V}_{a,i}|$ of the voltage $\underline{V}_{a,i}$ is

$$\left|\underline{V}_{a,i}\right| = \sqrt{V_{a,i:Re}^2 + V_{a,i:Im}^2}. \tag{4.27}$$

Eq. (4.27) provides a general way to determine the magnitude of a complex number or a vector. Next, the relationship between the magnitude $|\underline{V}_{a,i}|$ and sequence currents at bus *h* can be related by substituting Eqs. (4.24) and (4.25) in Eq. (4.27). This yields

$$\left|\underline{V}_{a,i}\right| = \sqrt{\begin{aligned}&\left(V_{a,i:Re}^{K} + \sum_{h=1}^{n}\sum_{s=0}^{2}\left[\left(\widetilde{R}_{a,ih}^{(s)} I_{h:Re}^{(s)} - \widetilde{X}_{a,ih}^{(s)} I_{h:Im}^{(s)}\right) - \left(\widetilde{R}_{a,ih}^{(s)} I_{h:Re}^{K(s)} - \widetilde{X}_{a,ih}^{(s)} I_{h:Im}^{K(s)}\right)\right]\right)^2 \\ &+ \left(V_{a,i:Im}^{K} + \sum_{h=1}^{n}\sum_{s=0}^{2}\left[\left(\widetilde{X}_{a,ih}^{(s)} I_{h:Re}^{(s)} + \widetilde{R}_{a,ih}^{(s)} I_{h:Im}^{(s)}\right) - \left(\widetilde{X}_{a,ih}^{(s)} I_{h:Re}^{K(s)} + \widetilde{R}_{a,ih}^{(s)} I_{h:Im}^{K(s)}\right)\right]\right)^2\end{aligned}}. \tag{4.28}$$

According to Eq. (4.28), the terms of resistance $\tilde{R}_{a,ih}^{(s)}$ and reactance $\tilde{X}_{a,ih}^{(s)}$, where $s \in \{0, 1, 2\}$ and $i, h \in \{1, 2, \ldots, n\}$, are obtained from the predetermined bus impedance parameters. Concurrently, the known voltages and known sequence currents are obtained from measurement data. For this reason, the resistance, reactance, and known quantities are regarded as constant. Hence, the magnitude $|\underline{V}_{a,i}|$ in Eq. (4.28) can be understood as a function

$$|\underline{V}_{a,i}| = f\left(I_{1:Re}^{(0)}, I_{1:Re}^{(1)}, I_{1:Re}^{(2)}, \ldots, I_{n:Re}^{(0)}, I_{n:Re}^{(1)}; I_{n:Re}^{(2)}, I_{1:Im}^{(0)}, I_{1:Im}^{(1)}, I_{1:Im}^{(2)} \ldots, I_{n:Im}^{(0)}, I_{n:Im}^{(1)}, I_{n:Im}^{(2)}\right) \quad (4.29)$$

which consists of real and imaginary parts of sequence currents. At this point, the sensitivity of voltage magnitude $|\underline{V}_{a,i}|$ to sequence currents can be derived by taking derivative with respect to any sequence current. As an example, taking derivative of Eq. (4.28) with respect to positive-sequence current at bus 1 is conducted. First, the sensitivity of the magnitude $|\underline{V}_{a,i}|$ to real-component sequence current $I_{1:Re}^{(1)}$ is demonstrated. Differentiating $|\underline{V}_{a,i}|$ in Eq. (4.28) with respect to the current $I_{1:Re}^{(1)}$ results in

$$\frac{\partial|\underline{V}_{a,i}|}{\partial I_{1:Re}^{(1)}} = \frac{\tilde{R}_{a,i1}^{(1)}\left(V_{a,i:Re}^{K}+\sum_{h=1}^{n}\sum_{s=0}^{2}\left[\left(\tilde{R}_{a,ih}^{(s)}I_{h:Re}^{(s)}-\tilde{X}_{a,ih}^{(s)}I_{h:Im}^{(s)}\right)-\left(\tilde{R}_{a,ih}^{(s)}I_{h:Re}^{K(s)}-\tilde{X}_{a,ih}^{(s)}I_{h:Im}^{K(s)}\right)\right]\right)}{\sqrt{\left(V_{a,i:Re}^{K}+\sum_{h=1}^{n}\sum_{s=0}^{2}\left[\left(\tilde{R}_{a,ih}^{(s)}I_{h:Re}^{(s)}-\tilde{X}_{a,ih}^{(s)}I_{h:Im}^{(s)}\right)-\left(\tilde{R}_{a,ih}^{(s)}I_{h:Re}^{K(s)}-\tilde{X}_{a,ih}^{(s)}I_{h:Im}^{K(s)}\right)\right]\right)^{2}+\left(V_{a,i:Im}^{K}+\sum_{h=1}^{n}\sum_{s=0}^{2}\left[\left(\tilde{X}_{a,ih}^{(s)}I_{h:Re}^{(s)}+\tilde{R}_{a,ih}^{(s)}I_{h:Im}^{(s)}\right)-\left(\tilde{X}_{a,ih}^{(s)}I_{h:Re}^{K(s)}+\tilde{R}_{a,ih}^{(s)}I_{h:Im}^{K(s)}\right)\right]\right)^{2}}}$$

$$+\frac{\tilde{X}_{a,i1}^{(1)}\left(V_{a,i:Im}^{K}+\sum_{h=1}^{n}\sum_{s=0}^{2}\left[\left(\tilde{X}_{a,ih}^{(s)}I_{h:Re}^{(s)}+\tilde{R}_{a,ih}^{(s)}I_{h:Im}^{(s)}\right)-\left(\tilde{X}_{a,ih}^{(s)}I_{h:Re}^{K(s)}+\tilde{R}_{a,ih}^{(s)}I_{h:Im}^{K(s)}\right)\right]\right)}{\sqrt{\left(V_{a,i:Re}^{K}+\sum_{h=1}^{n}\sum_{s=0}^{2}\left[\left(\tilde{R}_{a,ih}^{(s)}I_{h:Re}^{(s)}-\tilde{X}_{a,ih}^{(s)}I_{h:Im}^{(s)}\right)-\left(\tilde{R}_{a,ih}^{(s)}I_{h:Re}^{K(s)}-\tilde{X}_{a,ih}^{(s)}I_{h:Im}^{K(s)}\right)\right]\right)^{2}+\left(V_{a,i:Im}^{K}+\sum_{h=1}^{n}\sum_{s=0}^{2}\left[\left(\tilde{X}_{a,ih}^{(s)}I_{h:Re}^{(s)}+\tilde{R}_{a,ih}^{(s)}I_{h:Im}^{(s)}\right)-\left(\tilde{X}_{a,ih}^{(s)}I_{h:Re}^{K(s)}+\tilde{R}_{a,ih}^{(s)}I_{h:Im}^{K(s)}\right)\right]\right)^{2}}}. \quad (4.30)$$

From Eq. (4.30), the multiplier term of the positive-sequence resistance $\tilde{R}_{a,i1}^{(1)}$ is actually the real-component voltage $\underline{V}_{a,i:Re}$ from Eq. (4.24), and meanwhile the multiplier term of the positive-sequence reactance $\tilde{X}_{a,i1}^{(1)}$ is the imaginary-component voltage $\underline{V}_{a,i:Im}$ from Eq. (4.25). Moreover, the denominator term of Eq. (4.30) is literally the magnitude $|\underline{V}_{a,i}|$ from Eq. (4.28). When all these conditions are adopted, Eq. (4.30) can be therefore rewritten as

$$\frac{\partial|\underline{V}_{a,i}|}{\partial I_{1:Re}^{(1)}} = \frac{\tilde{R}_{a,i1}^{(1)}V_{a,i:Re}+\tilde{X}_{a,i1}^{(1)}V_{a,i:Im}}{|\underline{V}_{a,i}|}. \quad (4.31)$$

The resistance $\tilde{R}_{a,i1}^{(1)}$ and reactance $\tilde{X}_{a,i1}^{(1)}$ appear, as they provide the connection between bus voltage at phase *a* of bus *i* and the positive-sequence currents at bus 1. The sensitivity of the magnitude $|\underline{V}_{a,i}|$ to the real-component sequence current $I_{h:Re}^{(1)}$ is, nonetheless, not yet accomplished because the unknown variables, i.e. the complex-component voltages $\underline{V}_{a,i:Re}$ and $\underline{V}_{a,i:Im}$, and the magnitude $|\underline{V}_{a,i}|$ still exist in Eq. (4.31). The operation under the steady-state condition is then taken into account. Generally, the voltage magnitude at each bus varies slightly from time to time under the normal steady-state condition. The complex-component

voltages $\underline{V}_{a,i:Re}$ and $\underline{V}_{a,i:Im}$, and the magnitude $|\underline{V}_{a,i}|$ in Eq. (4.31) therefore are approximated to their known values $V^K_{a,i:Re}$, $V^K_{a,i:Im}$, and $|\underline{V}^K_{a,i}|$, respectively. This yields

$$\frac{\partial|\underline{V}_{a,i}|}{\partial I^{(1)}_{1:Re}} = \frac{\tilde{R}^{(1)}_{a,i1}V^K_{a,i:Re}+\tilde{X}^{(1)}_{a,i1}V^K_{a,i:Im}}{|V^K_{a,i}|}. \tag{4.32}$$

Eq. (4.32) demonstrates the equation to determine the sensitivity of the magnitude $|\underline{V}_{a,i}|$ to the real-component sequence current $I^{(1)}_{1:Re}$ at bus 1. In general, the same procedure, which is carried out for Eq. (4.32), can be executed for any phase $p \in \{a, b, c\}$, for any sequence $s \in \{0, 1, 2\}$, and for any bus i, $h \in \{1, 2, \ldots, n\}$. Accordingly, in a general case for any sequence and any bus, the sensitivity

$$S_{VIs:Re,p,ih} = \frac{\partial|\underline{V}_{p,i}|}{\partial I^{(s)}_{h:Re}} = \frac{\tilde{R}^{(s)}_{p,ih}V^K_{p,i:Re}+\tilde{X}^{(s)}_{p,ih}V^K_{p,i:Im}}{\left|V^K_{p,i}\right|} \tag{4.33}$$

of phase voltage magnitude $|\underline{V}_{p,i}|$ in relation to the real-component sequence current $I^{(s)}_{h:Re}$ at bus h is obtained, where $s \in \{0, 1, 2\}$, $p \in \{a, b, c\}$, and i, $h \in \{1, 2, \ldots, n\}$. The unit of the sensitivity $S_{VIs:Re,p,ih}$, from Eq. (4.33) is Volt per Ampere (V/A). The resistance, reactance, and known voltage define the different sensitivity values between phases. To select each element in conjunction with the related buses i and h during the sensitivity analysis, the resistance and reactance must comply with both the target phase $p \in \{a, b, c\}$ and the sequence $s \in \{0, 1, 2\}$, whereas the voltage magnitude must comply solely with the target phase.

Next, the impact of the imaginary-component sequence current $I^{(1)}_{1:Im}$ is investigated. The bus voltage at phase a of bus i and positive-sequence current at bus 1 are still in the example, so the sensitivity of the magnitude $|\underline{V}_{a,i}|$ to the current $I^{(1)}_{1:Im}$ is discussed in this investigation. This sensitivity can be determined in the same manner as the case of the current $I^{(1)}_{1:Re}$. Hence, differentiating $|\underline{V}_{a,i}|$ in Eq. (4.28) with respect to the current $I^{(1)}_{1:Im}$ yields

$$\begin{aligned}\frac{\partial|\underline{V}_{a,i}|}{\partial I^{(1)}_{1:Im}} = {} & \frac{-\tilde{X}^{(1)}_{a,i1}\left(V^K_{a,i:Re}+\sum_{h=1}^{n}\sum_{s=0}^{2}\left[\left(\tilde{R}^{(s)}_{a,ih}I^{(s)}_{h:Re}-\tilde{X}^{(s)}_{a,ih}I^{(s)}_{h:Im}\right)-\left(\tilde{R}^{(s)}_{a,ih}I^{K(s)}_{h:Re}-\tilde{X}^{(s)}_{a,ih}I^{K(s)}_{h:Im}\right)\right]\right)}{\sqrt{\begin{array}{l}\left(V^K_{a,i:Re}+\sum_{h=1}^{n}\sum_{s=0}^{2}\left[\left(\tilde{R}^{(s)}_{a,ih}I^{(s)}_{h:Re}-\tilde{X}^{(s)}_{a,ih}I^{(s)}_{h:Im}\right)-\left(\tilde{R}^{(s)}_{a,ih}I^{K(s)}_{h:Re}-\tilde{X}^{(s)}_{a,ih}I^{K(s)}_{h:Im}\right)\right]\right)^2\\ +\left(V^K_{a,i:Im}+\sum_{h=1}^{n}\sum_{s=0}^{2}\left[\left(\tilde{X}^{(s)}_{a,ih}I^{(s)}_{h:Re}+\tilde{R}^{(s)}_{a,ih}I^{(s)}_{h:Im}\right)-\left(\tilde{X}^{(s)}_{a,ih}I^{K(s)}_{h:Re}+\tilde{R}^{(s)}_{a,ih}I^{K(s)}_{h:Im}\right)\right]\right)^2\end{array}}}\\ & + \frac{\tilde{R}^{(1)}_{a,i1}\left(V^K_{a,i:Im}+\sum_{h=1}^{n}\sum_{s=0}^{2}\left[\left(\tilde{X}^{(s)}_{a,ih}I^{(s)}_{h:Re}+\tilde{R}^{(s)}_{a,ih}I^{(s)}_{h:Im}\right)-\left(\tilde{X}^{(s)}_{a,ih}I^{K(s)}_{h:Re}+\tilde{R}^{(s)}_{a,ih}I^{K(s)}_{h:Im}\right)\right]\right)}{\sqrt{\begin{array}{l}\left(V^K_{a,i:Re}+\sum_{h=1}^{n}\sum_{s=0}^{2}\left[\left(\tilde{R}^{(s)}_{a,ih}I^{(s)}_{h:Re}-\tilde{X}^{(s)}_{a,ih}I^{(s)}_{h:Im}\right)-\left(\tilde{R}^{(s)}_{a,ih}I^{K(s)}_{h:Re}-\tilde{X}^{(s)}_{a,ih}I^{K(s)}_{h:Im}\right)\right]\right)^2\\ +\left(V^K_{a,i:Im}+\sum_{h=1}^{n}\sum_{s=0}^{2}\left[\left(\tilde{X}^{(s)}_{a,ih}I^{(s)}_{h:Re}+\tilde{R}^{(s)}_{a,ih}I^{(s)}_{h:Im}\right)-\left(\tilde{X}^{(s)}_{a,ih}I^{K(s)}_{h:Re}+\tilde{R}^{(s)}_{a,ih}I^{K(s)}_{h:Im}\right)\right]\right)^2\end{array}}}.\end{aligned} \tag{4.34}$$

In Eq. (4.34), the multiplier term of the positive-sequence reactance $\tilde{X}^{(1)}_{a,i1}$ is the real-component voltage $\underline{V}_{a,i:Re}$, while the multiplier term of the positive-sequence resistance $\tilde{R}^{(1)}_{a,i1}$

is the imaginary-component voltage $\underline{V}_{a,i:Im}$. The denominator term is the magnitude $|\underline{V}_{a,i}|$. When all these conditions are adopted, Eq. (4.34) thus can be rewritten as

$$\frac{\partial|\underline{V}_{a,i}|}{\partial I^{(1)}_{1:Im}} = \frac{-\tilde{X}^{(1)}_{a,i1}V_{a,i:Re}+\tilde{R}^{(1)}_{a,i1}V_{a,i:Im}}{|\underline{V}_{a,i}|}. \tag{4.35}$$

Again, by considering the assumption that the analysis is performed under the normal steady-state condition, the complex component voltages $\underline{V}_{a,i:Re}$ and $\underline{V}_{a,i:Im}$, and the magnitude $|\underline{V}_{a,i}|$ in Eq. (4.35) are approximated to their known values $V^K_{a,i:Re}$, $V^K_{a,i:Im}$, and $|\underline{V}^K_{a,i}|$, respectively. This yields

$$\frac{\partial|\underline{V}_{a,i}|}{\partial I^{(1)}_{1:Im}} = \frac{-\tilde{X}^{(1)}_{a,i1}V^K_{a,i:Re}+\tilde{R}^{(1)}_{a,i1}V^K_{a,i:Im}}{|V^K_{a,i}|}. \tag{4.36}$$

Eq. (4.36) portrays the equation to determine the sensitivity of the magnitude $|\underline{V}_{a,i}|$ in relation to the imaginary-component sequence current $I^{(1)}_{1:Im}$ at bus 1. Likewise, not only phase *a* and positive sequence can be considered, but the same procedure carried out for Eq. (4.36) can also be executed for any phase $p \in \{a, b, c\}$, for any sequence $s \in \{0, 1, 2\}$, and for any bus i, $h \in \{1, 2, \ldots, n\}$. For this reason, in the general case for any sequence and any bus, the sensitivity

$$S_{VIs:Im,p,ih} = \frac{\partial|\underline{V}_{p,i}|}{\partial I^{(s)}_{h:Im}} = \frac{-\tilde{X}^{(s)}_{p,ih}V^K_{p,i:Re}+\tilde{R}^{(s)}_{p,ih}V^K_{p,i:Im}}{\left|V^K_{p,i}\right|} \tag{4.37}$$

of phase voltage magnitude $|\underline{V}_{p,i}|$ in relation to the imaginary-component sequence current $I^{(s)}_{h:Im}$ at bus h is acquired, where $s \in \{0, 1, 2\}$, $p \in \{a, b, c\}$, and $i, h \in \{1, 2, \ldots, n\}$. The unit of the sensitivity $S_{VIs:Im,p,ih}$ from Eq. (4.37) is Volt per Ampere (V/A). The phase index of equation elements must comply with the corresponding phase of concern, together with the related buses i and h during the sensitivity analysis. The sequence of the resistance and reactance indicates that the target sequence current and the voltage magnitude must comply with the target phase.

In this section, the derivations of the equations for analysing voltage magnitude sensitivity are demonstrated. The equations are derived on the basis of voltage magnitude description in Eq. (4.28), in which the magnitude is recognised as a function of real and imaginary components of sequence currents. Eventually, Eqs. (4.33) and (4.37) present the general equations to analyse the sensitivities $S_{VIs:Re,p,ih}$ and $S_{VIs:Im,p,ih}$ of the phase voltage magnitude $|\underline{V}_{p,i}|$ at bus i in relation to the sequence current at bus h, where $s \in \{0, 1, 2\}$, $p \in \{a, b, c\}$, and $i, h \in \{1, 2, \ldots, n\}$. The unit of the resulted sensitivity values is V/A. As a result, it can be concluded that these equations show that only the measurement data are required for the sensitivity analysis as defined.

Apart from analysing the sensitivity of bus voltage magnitudes, the sensitivity of the bus voltage angle can also be examined. In the next section, a method for studying the impact of real and imaginary parts of sequence currents on the angle of phase voltages is discussed.

4.3.2 Voltage Angle Sensitivity in Relation to Sequence Currents

The voltage angle is a crucial state variable, which is monitored during the grid operation. The angle difference across a power grid is considered in operational security [229]. It indicates the stress level of that grid, and it is related to the synchronisation of generation units and synchronous machines. In this section, the proposed method for analysing the sensitivity of the bus voltage angle in relation to real and imaginary components of sequence currents is presented. This sensitivity indicates to what extent the angle will change, as a result of the adjusting sequence currents. As is the case of voltage magnitude, the proposed method for analysing the voltage angle is based on the real- and imaginary-component voltages from Eqs. (4.24) and (4.25). Also, the bus voltage at phase *a* of bus *i* is presented as an example of the analysis, whereas the analysis of other phases can be performed in the same way.

Initially, the description of the voltage angle defined for its analysis is given. Adapted from the definition of the bus voltage stated in Eq. (4.7), at phase *a* of bus *i* in an *n*-bus grid, the voltage $\underline{V}_{a,i}$ consists of the known voltage $\underline{V}_{a,i}^{K}$ and the change of bus voltage $\Delta\underline{V}_{a,ih}$ caused by the change of current at bus *h* where $i, h \in \{1, 2, \ldots, n\}$. If this description is expanded to the context of the voltage angle $\delta_{a,i}$, the voltage $\Delta\underline{V}_{a,ih}$ is assumed to provoke the change of voltage angle $\Delta\delta_{a,i}$. The phasor diagram of $\underline{V}_{a,i}$, $\underline{V}_{a,i}^{K}$, and $\Delta\underline{V}_{a,ih}$ is portrayed in Figure 4.4.

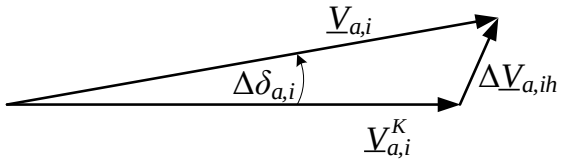

Figure 4.4: Phasor diagram portraying a change voltage angle at phase *a*

To examine the angle $\Delta\delta_{a,i}$, the angle of the voltage $\underline{V}_{a,i}$ is denoted by $\delta_{a,i}$, and the angle of the voltage $\underline{V}_{a,i}^{K}$ is denoted by $\delta_{a,i}^{K}$. Matching with the definition of the bus voltage, the angle

$$\delta_{a,i} = \delta_{a,i}^{K} + \Delta\delta_{a,i} \tag{4.38}$$

is described as the combination of its known angle $\delta_{a,i}^{K}$ and the angle $\Delta\delta_{a,i}$. According to Eq. (4.38), the role of the known angle $\delta_{a,i}^{K}$ can be implied to act as the initial state of the angle $\delta_{a,i}$ before any angle change $\Delta\delta_{a,i}$ happens. The angle $\delta_{a,i}^{K}$ therefore can be regarded as the reference point during the sensitivity analysis. For the sake of simplicity, it is presumed to be zero in this investigation.

$$\delta_{a,i}^{K} = 0 \tag{4.39}$$

Since the angle $\delta_{a,i}^{K}$ is presumably equal to zero, this means, based on Eq. (4.38), the angle change

$$\Delta\delta_{a,i} = \delta_{a,i} - \delta_{a,i}^{K} = \delta_{a,i} \tag{4.40}$$

is equal to the angle $\delta_{a,i}$. Considering the voltage $\underline{V}_{a,i} = V_{a,i:Re} + jV_{a,i:Im}$ according to Eq. (4.26), the trigonometry tangent rule can be used to describe the angle $\delta_{a,i}$ in terms of complex-component voltages $V_{a,i:Re}$ and $V_{a,i:Im}$. The angle $\delta_{a,i}$, therefore, is

$$\delta_{a,i} = arctan\left(\frac{V_{i,Im}}{V_{i,Re}}\right). \tag{4.41}$$

The models of voltage components are used again in this step. Substituting the models of the voltages $V_{a,i:Re}$ and $\underline{V}_{a,i:Im}$ from Eqs. (4.24) and (4.25) to Eq. (4.41) yields

$$\delta_{a,i} = arctan\frac{V_{a,i:Im}^{K} + \Sigma_{h=1}^{n}\Sigma_{s=0}^{2}\left[\left(\tilde{X}_{a,ih}^{(s)} I_{h:Re}^{(s)} + \tilde{R}_{a,ih}^{(s)} I_{h:Im}^{(s)}\right) - \left(\tilde{X}_{a,ih}^{(s)} I_{h:Re}^{K(s)} + \tilde{R}_{a,ih}^{(s)} I_{h:Im}^{K(s)}\right)\right]}{V_{a,i:Re}^{K} + \Sigma_{h=1}^{n}\Sigma_{s=0}^{2}\left[\left(\tilde{R}_{a,ih}^{(s)} I_{h:Re}^{(s)} - \tilde{X}_{a,ih}^{(s)} I_{h:Im}^{(s)}\right) - \left(\tilde{R}_{a,ih}^{(s)} I_{h:Re}^{K(s)} - \tilde{X}_{a,ih}^{(s)} I_{h:Im}^{K(s)}\right)\right]}. \tag{4.42}$$

Eq. (4.42) demonstrates the angle $\delta_{a,i}$, when the impact of all sequence currents in an n-bus grid is included. It is crucial to emphasise again that the terms of the resistance $\tilde{R}_{a,ih}^{(s)}$ and the reactance $\tilde{X}_{a,ih}^{(s)}$ are predetermined, while the known values indexed by subscript K are obtained from measurement data. These terms are regarded as constant accordingly. The angle $\delta_{a,i}$ in Eq. (4.42) can be considered as a function

$$\delta_{a,i} = f\left(I_{1:Re}^{(0)}, I_{1:Re}^{(1)}, I_{1:Re}^{(2)}, \dots, I_{n:Re}^{(0)}, I_{n:Re}^{(1)}; I_{n:Re}^{(2)}, I_{1:Im}^{(0)}, I_{1:Im}^{(1)}, I_{1:Im}^{(2)} \dots, I_{n:Im}^{(0)}, I_{n:Im}^{(1)}, I_{n:Im}^{(2)}\right) \tag{4.43}$$

which is composed of real and imaginary parts of sequence currents. The sensitivity of the angle $\delta_{a,i}$ to sequence currents can be derived. Taking the derivative of Eq. (4.42) with respect to positive-sequence current at bus 1 is shown as an example. Thus, the real- and imaginary-component sequence current $I_{1:Re}^{(1)}$ and $I_{1:Im}^{(1)}$ are counted. First, by applying derivative of arctan [188], differentiating the angle $\delta_{a,i}$ in Eq. (4.42) with respect to the current $I_{1:Re}^{(1)}$ yields

$$\frac{\partial\delta_{a,i}}{\partial I_{1:Re}^{(1)}} = \frac{1}{1+\left(V_{a,i:Im}/V_{a,i:Re}\right)^{2}} \cdot \frac{\tilde{X}_{a,i1}^{(1)} V_{a,i:Re} - \tilde{R}_{a,i}^{(1)} V_{a,i:Im}}{V_{a,i:Re}^{2}}. \tag{4.44}$$

To shorten the visualisation, the complex-component voltages $V_{a,i:Re}$ and $V_{a,i:Im}$ are directly presented in Eq. (4.44) to replace their full description. Eq. (4.44) subsequently can be further arranged into

$$\frac{\partial\delta_{a,i}}{\partial I_{1:Re}^{(1)}} = \frac{\tilde{X}_{a,i1}^{(1)} V_{a,i:Re} - \tilde{R}_{a1,i1}^{(1)} V_{a,i:Im}}{V_{a,i:Re}^{2} + V_{a,i:Im}^{2}}. \tag{4.45}$$

The denominator in Eq. (4.45) is the square of voltage magnitude $|\underline{V}_{a,i}|$. Thus, Eq. (4.45) can be equally written as

$$\frac{\partial \delta_{a,i}}{\partial I_{1:Re}^{(1)}} = \frac{\tilde{X}_{a,i1}^{(1)} V_{a,i:Re} - \tilde{R}_{a1,i1}^{(1)} V_{a,i:Im}}{\left|\underline{V}_{a,i}\right|^2}. \tag{4.46}$$

By considering the assumption that the analysis is performed under a normal steady-state condition, the complex-component voltages $V_{a,i:Re}$ and $V_{a,i:Im}$ as well as the magnitude $|\underline{V}_{a,i}|$ in Eq. (4.46) are approximated to their known values $V_{i,Re}^K$, $V_{i,Im}^K$, and $|\underline{V}_i^K|$, respectively. This yields

$$\frac{\partial \delta_{a,i}}{\partial I_{1:Re}^{(1)}} = \frac{\tilde{X}_{a,i1}^{(1)} V_{a,i:Re}^K - \tilde{R}_{a,i1}^{(1)} V_{a,i:Im}^K}{\left|\underline{V}_{a,i}^K\right|^2}. \tag{4.47}$$

Eq. (4.47) illustrates the sensitivity of the angle $\delta_{a,i}$ to the real-component sequence current $I_{1:Re}^{(1)}$ at bus 1. Then the general equation for this sensitivity analysis can be determined. The same procedure carried out for Eq. (4.47) can be applied to any phase $p \in \{a, b, c\}$, to any sequence $s \in \{0, 1, 2\}$, and to any bus i, $h \in \{1, 2, \ldots, n\}$. Hence, in a general case for any sequence and any bus, the sensitivity

$$S_{\delta Is:Re,p,ih} = \frac{\partial \delta_{p,i}}{\partial I_{h:Re}^{(s)}} = \frac{\tilde{X}_{p,ih}^{(s)} V_{p,i:Re}^K - \tilde{R}_{p,ih}^{(s)} V_{p,i:Im}^K}{\left|\underline{V}_{p,i}^K\right|^2} \tag{4.48}$$

of phase angle $\delta_{p,i}$ in relation to the real-component sequence current $I_{h:Re}^{(s)}$ at bus h is obtained, where $s \in \{0, 1, 2\}$, $p \in \{a, b, c\}$, and $i, h \in \{1, 2, \ldots, n\}$. The unit of the sensitivity $S_{\delta Is:Re,p,ih}$ from Eq. (4.48) is Radian per Ampere (rad/A). To use this equation for the sensitivity analysis, selecting each element for the related buses i and h is essential. The resistance and reactance must comply with both the target phase p and the sequence s, whereas the voltage magnitude must comply only with the target phase.

After the case of the real-component sequence current, the sensitivity of voltage angle in relation to imaginary-component sequence current is investigated. The impact of the current in the positive sequence at bus 1 is still used as the example. By performing the same derivation process, the sensitivity of the angle $\delta_{a,i}$ to the imaginary-component sequence current $I_{h:Im}^{(1)}$ is conducted. Thereby, differentiating $\delta_{a,i}$ in Eq. (4.42) with respect to $I_{h:Im}^{(1)}$ results in

$$\frac{\partial \delta_{a,i}}{\partial I_{1:Im}^{(1)}} = \frac{1}{1+\left(V_{a,i:Im}/V_{a,i:Re}\right)^2} \cdot \frac{\tilde{R}_{a,i1}^{(1)} V_{a,i:Re} + \tilde{X}_{a,i1}^{(1)} V_{a,i:Im}}{V_{a,i:Re}^2}. \tag{4.49}$$

The denominator of Eq. (4.49) can be subsequently organised into

$$\frac{\partial \delta_{a,i}}{\partial I_{1:Im}^{(1)}} = \frac{\tilde{R}_{a,i1}^{(1)} V_{a,i:Re} + \tilde{X}_{a,i1}^{(1)} V_{a,i:Im}}{V_{a,i:Re}^2 + V_{a,i:Im}^2}. \tag{4.50}$$

Converting the denominator of Eq. (4.50) to the square of magnitude $|\underline{V}_{a,i}|$ of the voltage $\underline{V}_{a,i}$ yields

$$\frac{\partial \delta_{a,i}}{\partial I_{1:Im}^{(1)}} = \frac{\tilde{R}_{a,i1}^{(1)} V_{a,i:Re} + \tilde{X}_{a1,i1}^{(1)} V_{a,i:Im}}{\left|\underline{V}_{a,i}\right|^2}. \tag{4.51}$$

Afterwards, the complex-component voltages $V_{a,i:Re}$ and $V_{a,i:Im}$, along with the magnitude $|\underline{V}_{a,i}|$ in Eq. (4.51) can be approximated as their known values $V_{a,i:Re}^K$, $V_{a,i:Im}^K$, and $|\underline{V}_{a,i}^K|$ under the assumption of a steady-state condition. Eq. (4.51) therefore becomes

$$\frac{\partial \delta_{a,i}}{\partial I_{1:Im}^{(1)}} = \frac{\tilde{R}_{a,i1}^{(1)} V_{a,i:Re}^K + \tilde{X}_{a,i1}^{(1)} V_{a,i:Im}^K}{\left|\underline{V}_{a,i}^K\right|^2}. \tag{4.52}$$

Eq. (4.52) expresses the sensitivity of the angle $\delta_{a,i}$ to the current $I_{1:Im}^{(s)}$. Based on the same procedure carried out for Eq. (4.47), the general equation for this sensitivity analysis for any phase $p \in \{a, b, c\}$, any sequence $s \in \{0, 1, 2\}$, and any bus i, $h \in \{1, 2, \ldots, n\}$ can be defined. Hence, in the general case for any sequence and any bus, the sensitivity

$$S_{\delta Is:Im,p,ih} = \frac{\partial \delta_{p,i}}{\partial I_{h:Im}^{(s)}} = \frac{\tilde{R}_{p,ih}^{(s)} V_{p,i:Re}^K + \tilde{X}_{p,ih}^{(s)} V_{p,i:Im}^K}{\left|\underline{V}_{p,i}^K\right|^2} \tag{4.53}$$

phase angle $\delta_{p,i}$ in relation to the imaginary-component sequence current $I_{h:Re}^{(s)}$ at bus h is acquired, where $s \in \{0, 1, 2\}$, $p \in \{a, b, c\}$, and i, $h \in \{1, 2, \ldots, n\}$. The unit of the sensitivity $S_{\delta Is:Im,p,ih}$, from Eq. (4.53) is also Radian per Ampere (rad/A). Similarly, the phase index of the equation elements must comply with the corresponding phase of concern during the sensitivity analysis between the related buses i and h. The sequence of the resistance and reactance indicates the target sequence current.

At this point, the derivations of the equations for the analysis of voltage angle sensitivity have been entirely presented. Eq. (4.42) is the key equation to investigate the sensitivity of the voltage angle. For each individual phase, the voltage angle is perceived as a function of real and imaginary components of sequence currents. Eventually, Eqs. (4.48) and (4.53) provide general equations to analyse the sensitivities $S_{\delta Is:Re,p,ih}$ and $S_{\delta Is:Im,p,ih}$ of voltage angles $\delta_{p,i}$ to the sequence currents, where $s \in \{0, 1, 2\}$, $p \in \{a, b, c\}$, and i, $h \in \{1, 2, \ldots, n\}$. The unit of the resulting sensitivity values is rad/A. These equations show that only the measurement data are required for the sensitivity analysis.

In the next section, an alternative method of voltage sensitivity analysis under the balanced grid condition is provided. Rather than observing the impact of sequence currents, the impact of active and reactive powers on voltage magnitude and angle is investigated. The equations for the sensitivity analysis in this section are further used to establish the relationship between bus voltage and the active or reactive powers.

4.4 Methods for Voltage Sensitivity Analysis under a Balanced Grid Condition

Balanced and unbalanced grid conditions have different influences on the power grid. In the balanced condition, voltage phasors of a bus are equal in magnitude, and the angle displacement between adjacent phasors are also identical. Accordingly, studying only one phase – usually phase *a* – is therefore sufficient to characterise the bus voltage magnitude and angle. By considering the positive sequence, the methods for voltage sensitivity analysis in the unbalanced grid condition from the previous section can be used in the case of the balanced condition. The impact of the positive-sequence current, which is equivalent to the phase current in this case, on the phase voltage can be analysed. Nevertheless, studying the impact of active and reactive powers is commonly preferable, as it is more straightforward to describe bus powers than currents. In this section, a method for analysing the sensitivity of the voltage magnitude and angle in relation to active and reactive powers is proposed. Before this method is presented, first of all, the relation between the complex components of bus current and active and reactive powers is pointed out. This step is to relate the impact of sequence currents on the sensitivity analysis methods from Sections 4.3.1 and 4.3.2 to the impact of active and reactive powers.

4.4.1 The Relationship between the Bus Current and the Three-Phase Powers

The apparent power is ordinarily supplied from electric utilities to the power systems. It is the magnitude of a complex power that is composed of active and reactive powers. In this thesis, the characteristics of three-phase powers also is investigated for the proposed voltage sensitivity analysis under the balanced grid condition. Since the relationship between the bus voltage and the bus current is covered in the previous section, the relationship between bus voltage and the active and reactive powers can be done by investigating the bus current. The relationship between the bus current and the three-phase powers is therefore stated as follows.

Power flow in the power grid is generally in the form of complex power. In this section, the complex power flowing through the buses is taken into account. To begin with, Figure 4.5 portrays an expression of complex power at bus *h*.

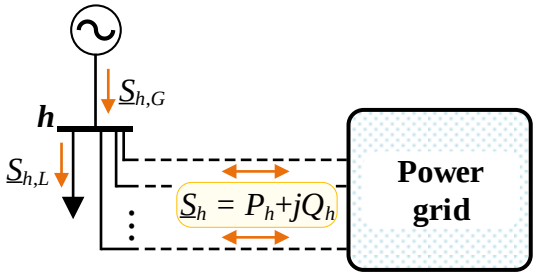

Figure 4.5: Expression of complex power at bus h

Complex power, basically, can be fed into or extracted from the power grid. In Figure 4.5, the generator represents the generation of a fed-in power $\underline{S}_{h,G}$, and the load represents the consumption of the extracted power $\underline{S}_{h,L}$. In the n-bus power grid, the complex power

$$\underline{S}_h = P_h + jQ_h \tag{4.54}$$

at bus h is therefore composed of active power P_h and reactive power Q_h, where $h \in \{1, 2, \ldots, n\}$. If the fed-in power $\underline{S}_{h,G}$ is higher than the extracted power $\underline{S}_{h,L}$, the power $\underline{S}_h$ flows into the grid. On the other hand, if the extracted power $\underline{S}_{h,L}$ is higher than the fed-in power $\underline{S}_{h,G}$, the power $\underline{S}_h$ flows out of the grid. Next, to explore the relationship between bus current and the three-phase powers, the complex power of each phase is considered. For the three-phase system, the complex power

$$\underline{S}_h = \underline{S}_{a,h} + \underline{S}_{b,h} + \underline{S}_{c,h} \tag{4.55}$$

is the sum of the complex power from all phases [182]. The phase complex powers $\underline{S}_{a,h}$, $\underline{S}_{b,h}$, and $\underline{S}_{c,h}$ in Eq. (4.55) belong to phase a, b, and c, respectively. In relation to voltage and current quantities, the complex power

$$\underline{S}_h = \underline{V}_{a,h}\underline{I}^*_{a,h} + \underline{V}_{b,h}\underline{I}^*_{b,h} + \underline{V}_{c,h}\underline{I}^*_{c,h} \tag{4.56}$$

is the product of bus voltage and the conjugate of its corresponding bus current [230]. Phase voltages $\underline{V}_{a,h}$, $\underline{V}_{b,h}$, and $\underline{V}_{c,h}$, and phase currents $\underline{I}_{a,h}$, $\underline{I}_{b,h}$, and $\underline{I}_{c,h}$. are complex quantities of their corresponding phase at bus h in Eq. (4.56). Taking into account the balanced condition, the complex power from each phase is equal. The complex power

$$\underline{S}_h = 3\underline{V}_{p,h}\underline{I}^*_{p,h} \tag{4.57}$$

is therefore a triple complex phase power, where $p \in \{a, b, c\}$. In conjunction with Eq. (4.54), Eq. (4.57) can be expanded to the complex form, as shown in

$$P_h + jQ_h = 3\left(V_{p,h:Re} + jV_{p,h:Im}\right) \cdot \left(I_{p,h:Re} + jI_{p,h:Im}\right)^*. \tag{4.58}$$

Eq. (4.58) establishes the relationship between bus currents and the three-phase active and reactive powers P_h and Q_h. To describe the bus currents in the term of the powers P_h and Q_h, Eq. (4.58) can be rearranged to

$$I_{p,h:Re} + jI_{p,h:Im} = \frac{(P_h + jQ_h)^*}{3(V_{p,h:Re} + jV_{p,h:Im})^*}. \tag{4.59}$$

In turn, Eq. (4.59) equals to

$$I_{p,h:Re} + jI_{p,h:Im} = \frac{P_h - jQ_h}{3(V_{p,h:Re} - jV_{p,h:Im})}. \tag{4.60}$$

After that, multiplying and dividing the conjugate of the denominator $\underline{V}_{p,h:Re} - j\underline{V}_{p,h:Im}$ to Eq. (4.60) results in

$$I_{p,h:Re} + jI_{p,h:Im} = \frac{(P_h V_{p,h:Re} + Q_h V_{p,h:Im}) + j(-Q_h V_{p,h:Re} + P_h V_{p,h:Im})}{3|\underline{V}_{p,h}|^2}. \tag{4.61}$$

Under the steady-state condition, the voltage in Eq. (4.61) can be approximated to its known value $\underline{V}^K_{p,h}$ from the measurement data, since the change of bus voltages is mainly small. Eq. (4.61) therefore can be presented as

$$I_{p,h:Re} + jI_{p,h:Im} \approx \frac{\left(P_h V^K_{p,h:Re} + Q_h V^K_{p,h:Im}\right) + j\left(-Q_h V^K_{p,h:Re} + P_h V^K_{p,h:Im}\right)}{3\left|\underline{V}^K_{p,h}\right|^2}. \tag{4.62}$$

Eq. (4.62) shows that the relationship between complex-component currents $I_{p,h:Re}$ and $I_{p,h:Im}$ and powers P_h and Q_h depends on the complex-component voltages $V^K_{p,h:Re}$ and $V^K_{p,h:Im}$ and square of the known magnitude $|\underline{V}^K_{p,h}|$. As these voltages are known constants, both the real-component current $I_{p,h:Re}$ and the imaginary-component current $I_{p,h:Im}$ are a function of the powers P_h and Q_h. By investigating the real and imaginary components of Eq. (4.62) separately, first of all, the current $I_{p,h:Re}$ can be expressed as

$$I_{p,h:Re} = f(P_h, Q_h) = \frac{P_h V^K_{p,h:Re} + Q_h V^K_{p,h:Im}}{3|\underline{V}^K_{a,h}|^2}. \tag{4.63}$$

From Eq. (4.63), the change of the real-component current $I_{p,h:Re}$ caused by the active power P_h depends on real-component voltage $V^K_{p,h:Re}$ and the square of the magnitude $|\underline{V}^K_{p,h}|$. By differentiating the current $I_{p,h:Re}$ with respect to the active power P_h, this relationship can be mathematically derived as the sensitivity

$$S_{I:ReP,hh} = \frac{\partial I_{p,h:Re}}{\partial P_h} = \frac{V^K_{p,h:Re}}{3\left|\underline{V}^K_{p,h}\right|^2} \tag{4.64}$$

of the real-component phase current $I_{p,h:Re}$ in relation to active power P_h, where $h \in \{1, 2, \ldots, n\}$ and $p \in \{a, b, c\}$.

Meanwhile, the change of the real-component current $I_{p,h:Re}$ caused by the reactive power Q_h depends on the imaginary-component voltage $V_{p,h:Im}^K$ and the square of the magnitude $|\underline{V}_{p,h}^K|$. Likewise, by differentiating the current $I_{p,h:Re}$ with respect to the reactive power Q_h, this relation can be derived as the sensitivity

$$S_{I:ReQ,hh} = \frac{\partial I_{p,h:Re}}{\partial Q_h} = \frac{V_{p,h:Im}^K}{3\left|\underline{V}_{p,h}^K\right|^2} \tag{4.65}$$

of the real-component phase current $I_{p,h:Re}$ in relation to the reactive power Q_h, where $h \in \{1, 2, \ldots, n\}$ and $p \in \{a, b, c\}$. In the following, besides the real component, the investigation of the imaginary component of Eq. (4.62) can also be carried out in the same way. Hence, based on Eq. (4.62), the imaginary-component current $I_{p,h:Im}$ equals to

$$I_{p,h:Im} = f(P_h, Q_h) = \frac{-Q_h V_{p,h:Re}^K + P_h V_{p,h:Im}^K}{3\left|\underline{V}_{p,h}^K\right|^2}. \tag{4.66}$$

The relationship of the active power P_h and the reactive power Q_h to the current $I_{p,h:Im}$ shown in Eq. (4.66) contradicts their relation to the current $I_{p,h:Re}$ presented in Eq. (4.63). Without stating the common impact from the square of the magnitude $|\underline{V}_{p,h}^K|$, the change of the current $I_{p,h:Im}$ caused by the active power P_h depends on the imaginary-component voltage $V_{p,h:Im}^K$. By differentiating the current $I_{p,h:Im}$ in Eq. (4.66) with respect to the active power P_h, this relation can be mathematically derived as the sensitivity

$$S_{I:ImP,hh} = \frac{\partial I_{p,h:Im}}{\partial P_h} = \frac{V_{p,h:Im}^K}{3\left|\underline{V}_{p,h}^K\right|^2} \tag{4.67}$$

of the imaginary-component phase current $I_{p,h:Im}$ in relation to the active power P_h, where $h \in \{1, 2, \ldots, n\}$ and $p \in \{a, b, c\}$. Concurrently, the change of the current $I_{p,h:Im}$ resulted from the reactive power Q_h depends on real-component voltage $V_{p,h:Re}^K$ and the square of the magnitude $|\underline{V}_{p,h}^K|$. By differentiating the current $I_{p,h:Im}$ with respect to the reactive power Q_h, this relationship can be derived as the sensitivity

$$S_{I:ImQ,hh} = \frac{\partial I_{p,h:Im}}{\partial Q_h} = -\frac{V_{p,h:Re}^K}{3\left|\underline{V}_{p,h}^K\right|^2} \tag{4.68}$$

of the imaginary-component phase current $I_{p,h:Im}$ in relation to the reactive power Q_h, where $h \in \{1, 2, \ldots, n\}$ and $p \in \{a, b, c\}$. Together with the sensitivities $S_{I:ReP,hh}$ and $S_{I:ReQ,hh}$ from Eqs. (4.64) and (4.65), the impact of the powers P_h and Q_h on the complex-component currents $I_{p,h:Re}$ and $I_{p,h:Im}$ are thoroughly investigated in an n-bus power grid. The equations for sensitivity analysis derived in this section refer only to phase a. In fact, it must be noted that this derivation procedure can be performed in the same way for other phases as well.

The derived equations in this section, moreover, can be related to the analyses of voltage magnitude and angle sensitivities. As the magnitude and angle of bus voltage are found to be functions of real and imaginary components of sequence currents, the magnitude $|\underline{V}_{p,i}|$ and angle $\delta_{p,i}$ at bus i can be related to the impact of the active and reactive powers P_h and Q_h bus h. How to relate the equations for sensitivity analysis is delineated, starting from the active power in the following section.

4.4.2 Voltage Magnitude Sensitivity in Relation to Three-Phase Powers

An option to examine the sensitivity of bus voltage magnitude to the three-phase active and reactive powers is derived under the balanced condition of the power grid in this section. Accordingly, the sensitivity analyses of phase magnitude in relation to the real and imaginary components of positive-sequence currents are discussed in the derivation process. An n-bus power grid is assumed for deriving the relationship between the voltage magnitude at bus i and the powers at bus h, where $i, h \in \{1, 2, \ldots, n\}$. From this point, the sensitivities of voltage magnitude to active power and reactive power are consecutively presented.

To this end, relevant equations for sensitivity analysis discussed previously in this chapter are applied here. The sensitivity of bus voltage magnitude in relation to sequence currents is discussed in Section 4.3.1. According to Eq. (4.29), voltage magnitude $|\underline{V}_{a,i}|$ at phase a is a function of real- and imaginary-component sequence currents from all n buses. Nonetheless, since the balanced condition is considered in this section, voltage magnitude $|\underline{V}_{a,i}|$ is described in general form as $|\underline{V}_{p,i}|$, where $p \in \{a, b, c\}$, and only the currents of positive sequence take part. When the relationship between voltage magnitude $|\underline{V}_{p,i}|$ at bus i and sequence currents at bus h under the balanced condition is considered, the magnitude $|\underline{V}_{p,i}|$ is understood as

$$|\underline{V}_{p,i}| = f\left(I_{h:Re}^{(1)}, I_{h:Im}^{(1)}\right). \tag{4.69}$$

The positive sequence currents $I_{h:Re}^{(1)}$, and $I_{h:Im}^{(1)}$ are, in turn, equivalent to phase currents $I_{p,h:Re}$ and $I_{p,h:Im}$ in this context, if they are transformed with respect to their corresponding phase of concern $p \in \{a, b, c\}$. Eq. (4.69) therefore equals to

$$|\underline{V}_{p,i}| = f\left(I_{p,h:Re}, I_{p,h:Im}\right). \tag{4.70}$$

Subsequently, the relationship between the magnitude $|\underline{V}_{p,i}|$ and active power P_h and reactive power Q_h can be determined. From Section 4.4.1, the currents $I_{p,h:Re}$ and $I_{p,h:Im}$ are functions of P_h and Q_h, as provided in Eq. (4.63) and Eq. (4.66) respectively. Substituted by Eq. (4.63) and Eq. (4.66), the magnitude $|\underline{V}_{p,i}|$ in Eq. (4.70) therefore can be regarded as a composite function

$$|\underline{V}_{p,i}| = f\left(I_{p,h:Re}(P_h, Q_h), I_{p,h:Im}(P_h, Q_h)\right). \tag{4.71}$$

Based on Eq. (4.71), the sensitivity $S_{VP,ih}$ of the magnitude $|\underline{V}_{p,i}|$ in relation to the power P_h as well as the sensitivity $S_{VQ,ih}$ of the magnitude $|\underline{V}_{p,i}|$ in relation to the power Q_h can be determined. Since Eq. (4.71) is a composite function, the "Chain Rule" from the theory of differentiation can be employed to determine the sensitivities $S_{VP,ih}$ and $S_{VQ,ih}$. In the following, the derivation of the sensitivity $S_{VP,ih}$ is first presented. Applying the Chain Rule in taking the derivative of Eq. (4.71) with respect to P_h yields

$$\frac{\partial|\underline{V}_{p,i}|}{\partial P_h} = \frac{\partial|\underline{V}_{p,i}|}{\partial I_{p,h:Re}} \cdot \frac{\partial I_{p,h:Re}}{\partial P_h} + \frac{\partial|\underline{V}_{p,i}|}{\partial I_{p,h:Im}} \cdot \frac{\partial I_{p,h:Im}}{\partial P_h}. \tag{4.72}$$

The derivatives $\partial|\underline{V}_{p,i}|/\partial I_{p,h:Re}$ and $\partial|\underline{V}_{p,i}|/\partial I_{p,h:Im}$ can be obtained from Eqs. (4.33) and (4.37), while the derivatives $\partial I_{p,h:Re}/\partial P_h$ and $\partial I_{p,h:Im}/\partial P_h$ can be acquired from Eqs. (4.64) and (4.67). Then, substituting all derivatives in Eq. (4.72) by their equations yields

$$\frac{\partial|\underline{V}_{p,i}|}{\partial P_h} = \frac{\tilde{R}^{(1)}_{p,ih}V^K_{p,i:Re}+\tilde{X}^{(1)}_{p,ih}V^K_{p,i:Im}}{\left|\underline{V}^K_{p,i}\right|} \cdot \frac{V^K_{p,h:Re}}{3\left|\underline{V}^K_{p,h}\right|^2} + \frac{-\tilde{X}^{(1)}_{p,ih}V^K_{p,i:Re}+\tilde{R}^{(1)}_{p,ih}V^K_{p,i:Im}}{\left|\underline{V}^K_{p,i}\right|} \cdot \frac{V^K_{p,h:Im}}{3\left|\underline{V}^K_{p,h}\right|^2}. \tag{4.73}$$

Eq. (4.73) provides an equation to calculate the sensitivity of voltage magnitude to active power. However, this equation can be extensively simplified under the assumption that bus voltages are close to their nominal voltage $\underline{V}_N$ in the normal circumstances of a balanced power grid. Based on this assumption, the known voltages $\underline{V}^K_i$ and $\underline{V}^K_h$ can be approximated to the voltage $\underline{V}_N$. The real-component voltages $V^K_{p,i:Re}$ and $V^K_{p,h,Re}$ of bus i and h as well as the imaginary-component voltages $V^K_{p,i:Im}$ and $V^K_{p,h:Im}$ are therefore replaced by $V_{N:Re}$ and $V_{N:Im}$. That is, the magnitudes $|\underline{V}^K_{p,i}|$ and $|\underline{V}^K_{p,h}|$ are replaced by $|\underline{V}_N|$ as well. For this reason, Eq. (4.73) becomes

$$\frac{\partial|\underline{V}_{p,i}|}{\partial P_h} = \frac{\tilde{R}^{(1)}_{p,ih}V_{N:Re}+\tilde{X}^{(1)}_{p,ih}V_{N:Im}}{|\underline{V}_N|} \cdot \frac{V_{N:Re}}{3|\underline{V}_N|^2} + \frac{-\tilde{X}^{(1)}_{p,ih}V_{N:Re}+\tilde{R}^{(1)}_{p,ih}V_{N:Im}}{|\underline{V}_N|} \cdot \frac{V_{N:Im}}{3|\underline{V}_N|^2}. \tag{4.74}$$

Subsequently, Eq. (4.74) can be rearranged to

$$\frac{\partial|\underline{V}_{p,i}|}{\partial P_h} = \frac{\tilde{R}^{(1)}_{p,ih}(V_{N:Re})^2+\tilde{X}^{(1)}_{p,ih}V_{N:Re}V_{N:Im}-\tilde{X}^{(1)}_{p,ih}V_{N:Re}V_{N:Im}+\tilde{R}^{(1)}_{p,ih}(V_{N:Im})^2}{3|\underline{V}_N|^3}. \tag{4.75}$$

The term relevant to reactance $\tilde{X}^{(1)}_{p,ih}$ in Eq. (4.75) can be then eliminated. This yields

$$\frac{\partial|\underline{V}_{p,i}|}{\partial P_h} = \frac{\tilde{R}^{(1)}_{p,ih}((V_{N:Re})^2+(V_{N:Im})^2)}{3|\underline{V}_N|^3}. \tag{4.76}$$

The term $(V_{N:Re})^2 + (V_{N:Im})^2$ in Eq. (4.76) is mathematically equivalent to the square of the magnitude $|\underline{V}_N|$, i.e. $|\underline{V}_N|^2$. After replacing $|\underline{V}_N|^2$ in Eq. (4.76), the sensitivity

$$S_{VP,ih} = \frac{\partial|\underline{V}_{p,i}|}{\partial P_h} = \frac{\tilde{R}^{(1)}_{p,ih}}{3|\underline{V}_N|} \tag{4.77}$$

of the magnitude $|\underline{V}_{p,i}|$ in relation to the power P_h is obtained. Eq. (4.77) shows that this sensitivity depends proportionally on the resistance $\tilde{R}_{a,ih}^{(1)}$ of the bus impedance parameters in $[\underline{\tilde{Z}}_{par,ih}]$, where $p \in \{a, b, c\}$ and $i, h \in \{1, 2, \ldots, n\}$. The unit of this sensitivity is Volt per Watt (V/W).

Next, the derivation of the sensitivity $S_{VQ,ih}$ is presented. Eq. (4.71) is still taken into account here. In this step, the derivative is taken to Eq. (4.71) with respect to Q_h with the application of Chain Rule. This yields

$$\frac{\partial|\underline{V}_{p,i}|}{\partial Q_h} = \frac{\partial|\underline{V}_{p,i}|}{\partial I_{p,h:Re}} \cdot \frac{\partial I_{p,h:Re}}{\partial Q_h} + \frac{\partial|\underline{V}_{p,i}|}{\partial I_{p,h:Im}} \cdot \frac{\partial I_{p,h:Im}}{\partial Q_h}. \tag{4.78}$$

As mentioned before, the derivatives $\partial|\underline{V}_{p,i}|/\partial I_{p,h:Re}$ and $\partial|\underline{V}_{p,i}|/\partial I_{p,h:Im}$ can be obtained from Eqs. (4.33) and (4.37). The derivatives $\partial I_{p,h:Re}/\partial Q_h$ and $\partial I_{p,h:Im}/\partial Q_h$ can be taken, however, from Eqs. (4.65) and (4.68). As a result, Eq. (4.78) becomes

$$\frac{\partial|\underline{V}_{p,i}|}{\partial Q_h} = \frac{\tilde{R}_{p,ih}^{(1)} V_{p,i:Re}^{K} + \tilde{X}_{p,ih}^{(1)} V_{p,i:Im}^{K}}{\left|\underline{V}_{p,i}^{K}\right|} \cdot \frac{V_{p,h:Im}^{K}}{3\left|\underline{V}_{p,h}^{K}\right|^2} + \frac{-\tilde{X}_{p,ih}^{(1)} V_{p,i:Re}^{K} + \tilde{R}_{p,ih}^{(1)} V_{p,i:Im}^{K}}{\left|\underline{V}_{p,i}^{K}\right|} \cdot \frac{-V_{p,h:Re}^{K}}{3\left|\underline{V}_{p,h}^{K}\right|^2}. \tag{4.79}$$

For the same reason as in the case of active power, the nominal voltage $\underline{V}_N$ can substitute the known phase voltage $\underline{V}_{p,i}^{K}$. Thus, replacing the nominal voltage $\underline{V}_N$ including its complex components $\underline{V}_{N:Re}$ and $\underline{V}_{N:Im}$ to the terms of voltages $\underline{V}_{p,i}^{K}$ and its complex components $V_{p,i:Im}^{K}$ and $V_{p,h:Im}^{k}$ in Eq. (4.79) results in

$$\frac{\partial|\underline{V}_{p,i}|}{\partial Q_h} = \frac{\tilde{R}_{p,ih}^{(1)} V_{N:Re} + \tilde{X}_{p,ih}^{(1)} V_{N:Im}}{|\underline{V}_N|} \cdot \frac{V_{N:Im}}{3|\underline{V}_N|^2} + \frac{-\tilde{X}_{p,ih}^{(1)} V_{N:Re} + \tilde{R}_{p,ih}^{(1)} V_{N:Im}}{|\underline{V}_N|} \cdot \frac{-V_{N:Re}}{3|\underline{V}_N|^2}. \tag{4.80}$$

Eq. (4.80) can be then rearranged to

$$\frac{\partial|\underline{V}_{p,i}|}{\partial Q_h} = \frac{\tilde{X}_{p,ih}^{(1)}(V_{N:Im})^2 + \tilde{R}_{p,ih}^{(1)} V_{N:Re} V_{N:Im} - \tilde{R}_{p,ih}^{(1)} V_{N:Re} V_{N:Im} + \tilde{X}_{p,ih}^{(1)}(V_{N:Re})^2}{3|\underline{V}_N|^3}. \tag{4.81}$$

The term relevant to resistance $\tilde{R}_{p,ih}^{(1)}$ in Eq. (4.81) then can be removed. This yields

$$\frac{\partial|\underline{V}_{p,i}|}{\partial Q_h} = \frac{\tilde{X}_{p,ih}^{(1)}((V_{N:Re})^2 + (V_{N:Im})^2)}{3|\underline{V}_N|^3}. \tag{4.82}$$

The term $(\underline{V}_{N:Re})^2 + (\underline{V}_{N:Im})^2$ in Eq. (4.82) is mathematically equivalent to the square of the magnitude $|\underline{V}_N|$, i.e. $|\underline{V}_N|^2$. Once $|\underline{V}_N|^2$ is replaced in Eq. (4.82), the sensitivity

$$S_{VQ,ih} = \frac{\partial|\underline{V}_{p,i}|}{\partial Q_h} = \frac{\tilde{X}_{p,ih}^{(1)}}{3|\underline{V}_N|} \tag{4.83}$$

of the magnitude $|\underline{V}_{p,i}|$ in relation to the power Q_h is characterised. Eq. (4.83) shows that this sensitivity is proportional to the reactance $\tilde{X}_{p,ih}^{(1)}$ of the bus impedance parameters in $[\underline{\tilde{Z}}_{par,ih}]$, where $p \in \{a, b, c\}$ and $i, h \in \{1, 2, \ldots, n\}$. The unit of this sensitivity is Volt per var (V/var).

The method for analysing the sensitivity of voltage magnitude is deduced in this section. As a result, Eqs. (4.77) and (4.83) provide the methods to calculate magnitude sensitivity values, requiring solely a resistance $\tilde{R}_{p,ih}^{(1)}$ or a reactance $\tilde{X}_{p,ih}^{(1)}$ from the matrix $[\underline{\tilde{Z}}_{par,ih}]$ together with the predefined nominal voltage $\underline{V}_N$ of the power grid. Finally, this method is noticeably in line with the impact of R/X ratio in droop control [231]. At the low-voltage level where R/X ratio is high, voltage magnitude is mainly impacted by the active power. On the other hand, at higher voltage levels where R/X ratio is low, voltage the magnitude is primarily impacted by the reactive power.

In addition to the voltage magnitude sensitivity to the powers, the deduction of the voltage angle sensitivity can also be executed. The following section explains how to deduce the voltage angle sensitivity in relation to three-phase powers.

4.4.3 Voltage Angle Sensitivity in Relation to Three-Phase Powers

Under the balanced condition of the power grid, an option to examine the sensitivity of the voltage angle to the three-phase active and reactive powers is given in this section. The sensitivity analysis of the phase angle in relation to the real and imaginary components of the positive-sequence currents is discussed. Again, an *n*-bus power grid is assumed for deriving the relationship between the voltage angle at bus *i* and the powers at bus *h*, where $i, h \in \{1, 2, \ldots, n\}$. Next, the sensitivities of the voltage angle in relation to the active power and the reactive power are consecutively introduced.

The sensitivity of the bus voltage angle in relation to the sequence currents is discussed in Section 4.3.2. Voltage angle $\delta_{a,}$ at phase *a* given in Eq. (4.43) is a function of the real- and imaginary-component sequence currents from all *n* buses to cope with the unbalanced grid condition. However, the balanced condition is considered in this section. The voltage angle $\delta_{a,i}$ is described here as $\delta_{p,i}$, where $p \in \{a, b, c\}$, and only the positive-sequence currents are involved. To begin with, if the relationship between the voltage angle $\delta_{p,i,}$ at bus *i* and the sequence currents at bus *h* is considered, the angle $\delta_{p,i}$ is understood therefore as

$$\delta_{p,i} = f\left(I_{h:Re}^{(1)}, I_{h:Im}^{(1)}\right). \tag{4.84}$$

The positive sequence currents $I_{h:Re}^{(1)}$, and $I_{h:Im}^{(1)}$ are equivalent to the phase currents $I_{p,h:Re}$ and $I_{p,h:Im}$ in this context, if they are transformed with respect to their corresponding phase of concern $p \in \{a, b, c\}$. In other words, Eq. (4.84) equals to

$$\delta_{p,i} = f\left(I_{p,h:Re}, I_{p,h:Im}\right). \tag{4.85}$$

Based on Eq. (4.85), the angle $\delta_{p,i}$ can be related to active power P_h and reactive power Q_h. The currents $I_{p,h:Re}$ and $I_{p,h:Im}$ are functions of P_h and Q_h, as provided in Eq. (4.63) and Eq. (4.66), regarding to Section 4.4.1. By substituting Eq. (4.63) and Eq. (4.66) to Eq. (4.85), the angle $\delta_{p,i}$ can be regarded as a composite function

$$\delta_{p,i} = f\left(I_{p,h:Re}\left(P_h, Q_h\right), I_{p,h:Im}\left(P_h, Q_h\right)\right). \tag{4.86}$$

In the following, Eq. (4.86) is used as the basis for deriving the sensitivity $S_{PhiP,ih}$ of the angle $\delta_{p,i}$ in relation to the power P_h as well as the sensitivity $S_{PhiQ,ih}$ of the angle $\delta_{p,i}$ in relation to the power Q_h. First, the derivation of the sensitivity $S_{PhiP,ih}$ is demonstrated. It takes the derivative, based on the Chain Rule, to Eq. (4.86) with respect to P_h. This results in

$$\frac{\partial \delta_{p,i}}{\partial P_h} = \frac{\partial \delta_{p,i}}{\partial I_{p,h:Re}} \cdot \frac{\partial I_{p,h:Re}}{\partial P_h} + \frac{\partial \delta_{p,i}}{\partial I_{p,h:Im}} \cdot \frac{\partial I_{p,h:Im}}{\partial P_h}. \tag{4.87}$$

The derivatives $\partial\delta_{p,i}/\partial I_{p,h:Re}$ and $\partial\delta_{p,i}/\partial I_{p,h:Im}$ are defined Eqs. (4.48) and (4.53), and the derivatives $\partial I_{p,h:Re}/\partial P_h$ and $\partial I_{p,h:Im}/\partial P_h$ can be acquired from Eqs. (4.65) and (4.68). Next, all derivatives in Eq. (4.87) can be substituted by their equations. This yields

$$\frac{\partial \delta_{p,i}}{\partial P_h} = \frac{\tilde{X}^{(1)}_{p,ih} V^K_{p,i:Re} - \tilde{R}^{(1)}_{p,ih} V^K_{p,i:Im}}{\left|\underline{V}^K_{p,i}\right|^2} \cdot \frac{V^K_{p,h:Re}}{3\left|\underline{V}^K_{p,h}\right|^2} + \frac{\tilde{R}^{(1)}_{p,ih} V^K_{p,i:Re} + \tilde{X}^{(1)}_{p,ih} V^K_{p,i:Im}}{\left|\underline{V}^K_{p,i}\right|^2} \cdot \frac{V^K_{p,h:Im}}{3\left|\underline{V}^K_{p,h}\right|^2}. \tag{4.88}$$

Under the balanced grid condition, the sensitivity of the voltage angle is presumably identical for all phases because the spatial distance between phases is equal and all phase angles shift equally in response to the load situation. Additionally, for the same reason as mentioned in Section 4.4.2 regarding determining the sensitivities $S_{VP,ih}$ and $S_{VQ,ih}$, the nominal voltage $\underline{V}_N$ can substitute the known bus voltages $\underline{V}^K_{p,i}$ and $\underline{V}^K_{p,h}$. The terms of known voltages $\underline{V}^K_{p,i}$ and $\underline{V}^K_{p,h}$ and their complex components $V^K_{p,i:Re}$, $V^K_{p,i:Im}$, $V^K_{p,h:Re}$, and $V^K_{p,h:Im}$ in Eq. (4.88) are, thus, replaced by the nominal voltage $\underline{V}_N$ including its complex components $\underline{V}_{N:Re}$ and $\underline{V}_{N:Im}$. This leads to

$$\frac{\partial \delta_{p,i}}{\partial P_h} = \frac{\tilde{X}^{(1)}_{p,ih} V_{N:Re} - \tilde{R}^{(1)}_{p,ih} V_{N:Im}}{\left|\underline{V}_N\right|^2} \cdot \frac{V_{N:Re}}{3\left|\underline{V}_N\right|^2} + \frac{\tilde{R}^{(1)}_{p,ih} V_{N:Re} + \tilde{X}^{(1)}_{p,ih} V_{N:Im}}{\left|\underline{V}_N\right|^2} \cdot \frac{V_{N:Im}}{3\left|\underline{V}_N\right|^2}. \tag{4.89}$$

Afterwards, Eq. (4.89) can be rearranged to

$$\frac{\partial \delta_{p,i}}{\partial P_h} = \frac{\tilde{X}^{(1)}_{p,ih} (V_{N:Re})^2 - \tilde{R}^{(1)}_{p,ih} V_{N:Re} V_{N:Im} + \tilde{R}^{(1)}_{p,ih} V_{N:Re} V_{N:Im} + \tilde{X}^{(1)}_{p,ih} (V_{N:Im})^2}{3\left|\underline{V}_N\right|^4}. \tag{4.90}$$

The terms related to the resistance $\tilde{R}^{(1)}_{a,ih}$ in Eq. (4.90) can be consequently eliminated, resulting in

$$\frac{\partial \delta_{p,i}}{\partial P_h} = \frac{\tilde{X}^{(1)}_{p,ih} ((V_{N:Re})^2 + (V_{N:Im})^2)}{3\left|\underline{V}_N\right|^4}. \tag{4.91}$$

In Eq. (4.91), the term $(V_{N:Re})^2 + (V_{N:Im})^2$ equals to $|\underline{V}_N|^2$, which is the square of voltage magnitude. By replacing $|\underline{V}_N|^2$ in Eq. (4.91), the sensitivity

$$S_{PhiP,ih} = \frac{\partial \delta_{p,i}}{\partial P_h} = \frac{\tilde{X}^{(1)}_{p,ih}}{3|\underline{V}_N|^2} \tag{4.92}$$

of the angle $\delta_{p,i}$ to the active power P_h is acquired. Eq. (4.92) shows that this sensitivity is proportional to the reactance $\tilde{X}^{(1)}_{p,ih}$ of the bus impedance parameters in $[\underline{\tilde{Z}}_{par,ih}]$, where $p \in \{a, b, c\}$ and $i, h \in \{1, 2, \ldots, n\}$. The unit of this sensitivity is Radian per Watt (rad/W).

From this point, the derivation of the sensitivity $S_{PhiQ,ih}$ is shown. It is still based on Eq. (4.86). This means that the similar derivation process is executed. Hence, taking derivative to Eq. (4.86) with respect to Q_h yields

$$\frac{\partial \delta_{p,i}}{\partial Q_h} = \frac{\partial \delta_{p,i}}{\partial I_{p,h:Re}} \cdot \frac{\partial I_{p,h:Re}}{\partial Q_h} + \frac{\partial \delta_{p,i}}{\partial I_{p,h:Im}} \cdot \frac{\partial I_{p,h:Im}}{\partial Q_h}. \tag{4.93}$$

Identical to the case of $S_{PhiP,ih}$, the derivatives $\partial\delta_{p,i}/\partial I_{p,h:Re}$ and $\partial\delta_{p,i}/\partial I_{p,h:Im}$ can be obtained from Eqs. (4.48) and (4.53). To relate the currents $I_{p,h:Re}$ and $I_{p,h:Im}$ to reactive power Q_h, the derivatives $\partial I_{p,h:Re}/\partial Q_h$ and $\partial I_{p,h:Im}/\partial Q_h$ can be taken from Eqs. (4.64) and (4.68). Accordingly, Eq. (4.93) becomes

$$\frac{\partial \delta_{p,i}}{\partial Q_h} = \frac{\tilde{X}^{(1)}_{p,ih} V^K_{p,i:Re} - \tilde{R}^{(1)}_{p,ih} V^K_{p,i:Im}}{\left|\underline{V}^K_{p,i}\right|^2} \cdot \frac{V^K_{p,h:Im}}{3\left|\underline{V}^K_{p,h}\right|^2} + \frac{\tilde{R}^{(1)}_{p,ih} V^K_{p,i:Re} + \tilde{X}^{(1)}_{p,ih} V^K_{p,i:Im}}{\left|\underline{V}^K_{p,i}\right|^2} \cdot \frac{-V^K_{p,h:Re}}{3\left|\underline{V}^K_{p,h}\right|^2}. \tag{4.94}$$

Again, the nominal voltage $\underline{V}_N$ can substitute the bus voltages in Eq. (4.94) under the normal grid operation. Replacing the voltage $\underline{V}_N$ to the terms of bus voltages in Eq. (4.94) results in

$$\frac{\partial \delta_{p,i}}{\partial Q_h} = \frac{\tilde{X}^{(1)}_{p,ih} V_{N:Re} - \tilde{R}^{(1)}_{p,ih} V_{N:Im}}{|\underline{V}_N|^2} \cdot \frac{V_{N:Im}}{3|\underline{V}_N|^2} + \frac{\tilde{R}^{(1)}_{p,ih} V_{N:Re} + \tilde{X}^{(1)}_{p,ih} V_{N:Im}}{|\underline{V}_N|^2} \cdot \frac{-V_{N:Re}}{3|\underline{V}_N|^2}. \tag{4.95}$$

Eq. (4.95) can be subsequently rearranged to

$$\frac{\partial \delta_{p,i}}{\partial Q_h} = \frac{-\tilde{R}^{(1)}_{p,ih} (V_{N:Im})^2 + \tilde{X}^{(1)}_{p,ih} V_{N:Re} V_{N:Im} - \tilde{X}^{(1)}_{p,ih} V_{N:Re} V_{N:Im} - \tilde{R}^{(1)}_{p,ih} (V_{N:Re})^2}{3|\underline{V}_N|^4}. \tag{4.96}$$

The terms of reactance $\tilde{X}^{(1)}_{a,ih}$ in Eq. (4.96) can be eliminated. This yields

$$\frac{\partial \delta_{p,i}}{\partial Q_h} = \frac{-\tilde{R}^{(1)}_{p,ih} ((V_{N:Re})^2 + (V_{N:Im})^2)}{3|\underline{V}_N|^4}. \tag{4.97}$$

In Eq. (4.97), the term $(\underline{V}_{N:Re})^2 + (\underline{V}_{N:Im})^2$ equals to $|\underline{V}_N|^2$, which is the square of voltage magnitude. By replacing $|\underline{V}_N|^2$ in Eq. (4.97), the sensitivity

$$S_{PhiQ,ih} = \frac{\partial \delta_{p,i}}{\partial Q_h} = \frac{-\tilde{R}^{(1)}_{p,ih}}{3|\underline{V}_N|^2}. \tag{4.98}$$

of the angle δ_i to the reactive power Q_h is obtained. Eq. (4.98) illustrates that this sensitivity is proportional to the reactance $-\tilde{R}_{p,ih}^{(1)}$ of bus impedance parameters in $[\underline{\tilde{Z}}_{par,ih}]$, where $p \in \{a, b, c\}$ and $i, h \in \{1, 2, \ldots, n\}$. The unit of this sensitivity is Radian per Watt (rad/var).

The methods for analysing the sensitivity of voltage angle are derived in this section. Eqs. (4.92) and (4.98), as a result, provide the methods to compute angle sensitivity. The derived methods solely require a phase resistance, e.g. $\tilde{R}_{p,ih}^{(1)}$, or a reactance, e.g. $\tilde{X}_{p,ih}^{(1)}$, from the matrix $[\underline{\tilde{Z}}_{par,ih}]$ together with the predefined nominal voltage $\underline{V}_N$ of the grid. Providing the same outcomes as the case of magnitude sensitivity, this method evidently conforms to the impact of R/X ratio in droop control. In the low-voltage level where the R/X ratio is high, the voltage angle is greatly impacted by the reactive power. In contrast, at the higher voltage levels where the R/X ratio is low, the voltage angle is more impacted by the active power.

In the next section, applications of voltage sensitivity analysis are discussed. They focus on using calculated sensitivity values, resulting from the proposed analysis methods, for regulating voltage profile.

4.5 Applications of Voltage Sensitivity Analysis

Sensitivity values resulting from voltage sensitivity analysis allow the regulation of voltage magnitude and an angle caused by a change of sequence currents, active power, or reactive power. The primary target of the voltage sensitivity analysis in this thesis is to use the resulted sensitivity values to regulate the voltage profile to stay within the desired permissible range. The calculated setpoints, or reference values, can be implemented in a controlling device, such as an inverter, to define the amount of the output that affects the target voltage magnitude in such a way that can bring the voltage magnitude from its initial value to the expected value. In the following subsections, the calculation of the setpoints from the sensitivity values is demonstrated for both voltage magnitude and angle cases.

4.5.1 Use of Sensitivity Values for Regulating the Voltage Magnitude

The use of voltage magnitude sensitivity values for regulating voltage magnitude in both balanced and unbalanced grid conditions is presented in this section. For the unbalanced grid condition, the target is to compute a setpoint of a desired sequence current. For the balanced grid condition, in the meantime, the target is to compute the setpoint of active or reactive powers. The computed setpoint value can be further implemented to achieve the target phase voltage at the expected magnitude.

To showcase the use of voltage magnitude sensitivity values in the unbalanced grid condition, calculating the setpoint for regulating the magnitude of phase voltage is exemplified as follows. Based on Eqs. (4.33) and (4.37), the sensitivities $S_{VIs:Re,p,ih}$ and $S_{VIs:Im,p,ih}$ of phase

voltage magnitude $|\underline{V}_{p,i}|$ at bus *i* to real- and imaginary-component of sequence currents $I_{h:Re}^{(s)}$ and $I_{h:Im}^{(s)}$ at bus *h* from are taken into account, where $s \in \{0, 1, 2\}$, $p \in \{a, b, c\}$, and $i, h \in \{1, 2, \ldots, n\}$. This example shows the calculation of the setpoint currents $I_{set,h:Re}^{(s)}$ and $I_{set,h:Im}^{(s)}$ in a general case for all sequence systems. First, the setpoint $I_{set,h:Re}^{(s)}$ of the real-component sequence current $I_{h:Re}^{(s)}$ is focused on. The sensitivity $S_{VIs:Re,p,ih}$ is approximated to the ratio of the phase voltage change $\Delta|\underline{V}_{p,i}|$ of the phase magnitude $|\underline{V}_{p,i}|$ to the change $\Delta I_{h:Re}^{(s)}$ of sequence current $I_{h:Re}^{(s)}$, given by

$$S_{VIs:Re,p,ih} \approx \frac{\Delta|\underline{V}_{p,i}|}{\Delta I_{h:Re}^{(s)}}. \tag{4.99}$$

To calculate the setpoint $I_{set,h:Re}^{(s)}$, Eq. (4.99) can be rearranged to begin with

$$\Delta I_{h:Re}^{(s)} = \frac{\Delta|\underline{V}_{p,i}|}{S_{VIs:Re,a,ih}}. \tag{4.100}$$

The change $\Delta I_{h:Re}^{(s)}$ of sequence current $I_{h:Re}^{(s)}$ at bus *h* is defined as the difference between the setpoint $I_{set,h:Re}^{(s)}$ and its initial value $I_{ini,h:Re}^{(s)}$. Similarly, the magnitude change $\Delta|\underline{V}_{p,i}|$ is defined as the difference between the magnitude $|\underline{V}_{p,exp,i}|$ of expected phase voltage at bus *i* and the initial phase magnitude $|\underline{V}_{p,ini,i}|$ of its initial voltage. The terms $\Delta I_{h:Re}^{(s)}$ and $\Delta|\underline{V}_{p,i}|$ in Eq. (4.100) therefore can be expanded to

$$\Delta I_{h:Re}^{(s)} = I_{set,h:Re}^{(s)} - I_{ini,h:Re}^{(s)} \tag{4.101}$$

and

$$\Delta|\underline{V}_{p,i}| = |\underline{V}_{p,exp,i}| - |\underline{V}_{p,ini,i}|. \tag{4.102}$$

Next, substituting Eqs. (4.101) and (4.102) for $\Delta I_{h:Re}^{(s)}$ and $\Delta|\underline{V}_{p,i}|$ in Eq. (4.100) yields

$$I_{set,h:Re}^{(s)} - I_{ini,h:Re}^{(s)} = \frac{|\underline{V}_{p,exp,i}| - |\underline{V}_{p,ini,i}|}{S_{VIs:Re,p,ih}}. \tag{4.103}$$

The setpoint current $I_{set,h:Re}^{(s)}$ can be obtained now. By moving the initial current $I_{ini,h:Re}^{(s)}$ in Eq. (4.103) to the right side, the setpoint current

$$I_{set,h:Re}^{(s)} = \frac{|\underline{V}_{p,exp,i}| - |\underline{V}_{p,ini,i}|}{S_{VIs:Re,p,ih}} + I_{ini,h:Re}^{(s)} \tag{4.104}$$

is obtained from this process to achieve the expected phase magnitude $|\underline{V}_{p,exp,i}|$ at bus *i*. Eq. (4.104) illustrates the calculation of the setpoint current $I_{set,h:Re}^{(s)}$ of real-component sequence current $I_{h:Re}^{(s)}$ at bus *h* to achieve the expected phase magnitude $|\underline{V}_{p,exp,i}|$ at bus *i* where $s \in \{0, 1, 2\}$, $p \in \{a, b, c\}$, and $i, h \in \{1, 2, \ldots, n\}$.

Additionally, the setpoint current $I_{set,h:Im}^{(s)}$ of the imaginary-component sequence current $I_{h:Im}^{(s)}$ can be calculated by the identical procedure to case of $I_{set,h:Re}^{(s)}$. The sensitivity $S_{VIs:Im,p,ih}$, from Eq. (4.37) for the imaginary-component sequence current $I_{h:Im}^{(s)}$ is used accordingly. For the considered initial current $I_{ini,h:Im}^{(s)}$, the setpoint current

$$I_{set,h:Im}^{(s)} = \frac{|\underline{V}_{p,exp,i}|-|\underline{V}_{p,ini,i}|}{S_{VIs:Im,p,ih}} + I_{ini,h:Im}^{(s)} \tag{4.105}$$

can be calculated to achieve the expected phase magnitude $|\underline{V}_{p,exp,i}|$ at bus i. Eq. (4.105) portrays the calculation of the setpoint $I_{set,h:Im}^{(s)}$ of imaginary-component sequence current $I_{h:Im}^{(s)}$ at bus h to achieve the expected phase magnitude $|\underline{V}_{p,exp,i}|$ at bus i where $s \in \{0, 1, 2\}$, $p \in \{a, b, c\}$, and $i, h \in \{1, 2, \ldots, n\}$. At this point, all equations for calculating the setpoint currents $I_{set,h:Re}^{(s)}$ and $I_{set,h:Im}^{(s)}$ of any sequence system have been presented. The use of voltage magnitude sensitivity values in the balanced grid condition is demonstrated next.

As the magnitude is identical for all phases in the balanced grid condition, the target phase voltage of any phase can be considered. The sensitivities $S_{VP,ih}$ and $S_{VQ,ih}$ from Eqs. (4.77) and (4.83) are employed. Active and reactive powers are therefore three-phase quantities. Beginning with the regulating voltage magnitude by adjusting active power, in accordance with the sensitivity $S_{VP,ih}$, the change of active power causes the change of voltage magnitude. The sensitivity $S_{VP,ih}$ is approximated to the ratio of the change $\Delta|\underline{V}_{p,i}|$ of the phase magnitude $|\underline{V}_{p,i}|$ at bus i to the change ΔP_h of active power at bus h, which is

$$S_{VP,ih} \approx \frac{\Delta|\underline{V}_{p,i}|}{\Delta P_h} = \frac{|\underline{V}_{p,exp,i}|-|\underline{V}_{p,ini,i}|}{P_{set,h}-P_{ini,h}}. \tag{4.106}$$

In Eq. (4.106), the voltage change $\Delta|\underline{V}_i|$ is the difference between the expected magnitude $|\underline{V}_{p,exp,i}|$ and the initial magnitude $|\underline{V}_{p,ini,i}|$. Meanwhile, the power ΔP_h is the difference between active power setpoint $P_{set,h}$ and initial active power value $P_{ini,h}$. To leverage the sensitivity $S_{VP,ih}$, Eq. (4.106) is subsequently rearranged to

$$P_{set,h} - P_{ini,h} = \frac{|\underline{V}_{p,exp,i}|-|\underline{V}_{p,ini,i}|}{S_{VP,ih}}. \tag{4.107}$$

After moving the initial active power $P_{ini,h}$ to the right side of Eq. (4.107), the active power setpoint

$$P_{set,h} = \frac{|\underline{V}_{p,exp,i}|-|\underline{V}_{p,ini,i}|}{S_{VP,ih}} + P_{ini,h} \tag{4.108}$$

at bus h for the expected magnitude $|\underline{V}_{p,exp,i}|$ at bus i can be calculated. Based on the same procedure carried out for Eq. (4.108), the sensitivity $S_{VQ,ih}$ can also be used to accomplish the expected phase magnitude $|\underline{V}_{p,exp,i}|$. With consideration of the initial reactive power $Q_{ini,h}$, the reactive power setpoint

$$Q_{set,h} = \frac{|\underline{V}_{p,exp,i}| - |\underline{V}_{p,ini,i}|}{S_{VQ,ih}} + Q_{ini,h} \tag{4.109}$$

at bus h therefore can be calculated to achieve the expected phase magnitude $|\underline{V}_{p,exp,i}|$ at bus i. Eqs. (4.108) and (4.109) display the calculation of the active and reactive power setpoints $P_{set,h}$ and $Q_{set,h}$ at bus at bus h for the expected phase magnitude $|\underline{V}_{p,exp,i}|$ where $p \in \{a, b, c\}$ and $i, h \in \{1, 2, \ldots, n\}$.

Thus far, the available sensitivity values resulting from Sections 4.3.1 and 4.4.2 are continuously used: How to compute the setpoint parameters based on the available sensitivity values in the unbalanced or balanced grid conditions have been demonstrated. The resulting setpoints respond to the defined expected voltage magnitude of the target voltage in order to keep bus voltage in the permissible range. Later on, they can be implemented in a controlling device of controllable units.

4.5.2 Use of Sensitivity Values for Regulating the Voltage Angle

In this section, the use of voltage angle sensitivity values for regulating the voltage angle in both balanced and unbalanced grid conditions is examined. A setpoint of a desired sequence current is computed in the unbalanced grid condition, whereas a setpoint of the active power or the reactive power is computed in the balanced grid condition. The computed setpoint value is expected to be implemented later on to meet the target voltage angle at the expected angle.

For the unbalanced grid condition, the setpoint of a sequence current is calculated for regulating the angle of the target phase voltage. The expected angle of the target voltage is thus defined. To demonstrate the use of voltage angle sensitivity values, calculation of the setpoint for regulating the phase voltage angle is presented as an example. Accordingly, the sensitivities $S_{\delta Is:Re,p,ih}$ and $S_{\delta Is:Im,p,ih}$ of the phase voltage angle $\delta_{p,i}$ at bus i to real- and imaginary-component of sequence currents $I_{h:Re}^{(s)}$ and $I_{h:Im}^{(s)}$ at bus h from Eqs. (4.48) and (4.53) are considered, where $s \in \{0, 1, 2\}$, $p \in \{a, b, c\}$, and $i, h \in \{1, 2, \ldots, n\}$. This example shows the calculation of the setpoint currents $I_{set,h:Re}^{(s)}$ and $I_{set,h:Im}^{(s)}$ in a general case for all sequence systems. As the first case, the setpoint $I_{set,h:Re}^{(s)}$ of the real-component sequence current $I_{h:Re}^{(s)}$ is focused on. The sensitivity $S_{\delta Is:Re,p,ih}$ is approximated to the ratio of the angle change $\Delta\delta_{p,i}$ of the phase angle $\delta_{p,i}$ to the change $\Delta I_{h:Re}^{(s)}$ of sequence current $I_{h:Re}^{(s)}$, which is

$$S_{\delta Is:Re,p,ih} \approx \frac{\Delta\delta_{p,i}}{\Delta I_{h:Re}^{(s)}}. \tag{4.110}$$

To calculate the setpoint $I_{set,h:Re}^{(s)}$, Eq. (4.110) can be initially rearranged to

$$\Delta I_{h:Re}^{(s)} = \frac{\Delta\delta_{p,i}}{S_{\delta Is:Re,p,ih}}. \tag{4.111}$$

While the change $\Delta I_{h:Re}^{(s)}$ of sequence current $I_{h:Re}^{(s)}$ at bus h is the difference between the setpoint $I_{set,h:Re}^{(s)}$ and its initial value $I_{ini,h:Re}^{(s)}$ as displayed in Eq. (4.101), the phase angle change $\Delta\delta_{p,i}$ is defined as the difference between the expected phase angle $\delta_{p,exp,,i}$ of at bus i and the initial phase voltage angle $\delta_{p,ini,,i}$. Thus, the term $\Delta\delta_{p,i}$ in Eq. (4.111) can be expanded to

$$\Delta\delta_{p,i} = \delta_{p,exp,i} - \delta_{p,ini,i}. \tag{4.112}$$

Sequentially, Eqs. (4.101) and (4.112) can be substituted for $\Delta I_{h:Re}^{(s)}$ and $\Delta\delta_{p,i}$ in Eq. (4.111). This yields

$$I_{set,h:Re}^{(s)} - I_{ini,h:Re}^{(s)} = \frac{\delta_{p,exp,i} - \delta_{p,ini,i}}{S_{\delta Is:Re,p,ih}}. \tag{4.113}$$

The setpoint current $I_{set,h:Re}^{(s)}$ can be obtained at this point. By moving the initial current $I_{ini,h:Re}^{(s)}$ in Eq. (4.113) to the right side, the setpoint current

$$I_{set,h:Re}^{(s)} = \frac{\delta_{p,exp,i} - \delta_{p,ini,i}}{S_{\delta Is:Re,p,ih}} + I_{ini,h:Re}^{(s)}. \tag{4.114}$$

for the expected phase angle $\delta_{p,exp,,i}$ of bus i is determined. Eq. (4.114) illustrates the calculation of the setpoint current $I_{set,h:Re}^{(s)}$ of real-component sequence current $I_{h:Re}^{(s)}$ at bus h to achieve the expected phase angle $\delta_{p,exp,,i}$ at bus i where $s \in \{0, 1, 2\}$ $p \in \{a, b, c\}$, and $i, h \in \{1, 2, \ldots, n\}$.

Based on the identical procedure to case of $I_{set,h:Re}^{(s)}$, the setpoint current $I_{set,h:Im}^{(s)}$ of the imaginary-component sequence current $I_{h:Im}^{(s)}$ can be computed. Therefore, the sensitivity $S_{\delta Is:Im,p,ih}$ from Eq. (4.53) for the imaginary-component sequence current $I_{h:Im}^{(s)}$ is used. For the considered initial current $I_{ini,h:Im}^{(s)}$, the setpoint current

$$I_{set,h:Im}^{(s)} = \frac{\delta_{p,exp,i} - \delta_{p,ini,i}}{S_{\delta Is:Im,p,ih}} + I_{ini,h:Im}^{(s)} \tag{4.115}$$

can be calculated to achieve the expected angle $\delta_{p,exp,,i}$ at bus i. Eq. (4.115) shows the calculation of the setpoint $I_{set,h:Im}^{(s)}$ of imaginary-component sequence current $I_{h:Im}^{(s)}$ at bus h to achieve the expected phase angle $\delta_{p,exp,,i}$ at bus i where $s \in \{0, 1, 2\}$, $p \in \{a, b, c\}$, and $i, h \in \{1, 2, \ldots, n\}$. At this point, all equations for calculating the setpoint currents $I_{set,h:Re}^{(s)}$ and $I_{set,h:Im}^{(s)}$ of any sequence system have been shown. Subsequently, the use of voltage magnitude angle values in the balanced grid condition is expressed.

For the balanced grid condition, the sensitivity of the voltage angle is equal for all phases. In this case, the setpoint of active or reactive powers is calculated for regulating the target voltage angle at the expected phase angle $\delta_{p,exp,i}$. The sensitivities $S_{PhiP,ih}$ and $S_{PhiQ,ih}$ from

Eqs. (4.92) and (4.98) are used. The sensitivity $S_{PhiP,ih}$, is first considered; the change of active power leads to the change in the voltage angle. The sensitivity $S_{PhiP,ih}$ is approximated to the ratio of a change $\Delta\delta_i$ of the phase anlge $\delta_{p,i}$ at bus i to the change ΔP_h of active power at bus h, which is

$$S_{PhiP,ih} \approx \frac{\Delta\delta_i}{\Delta P_h} = \frac{\delta_{p,exp,i} - \delta_{p,ini,i}}{P_{set,h} - P_{ini,h}}. \tag{4.116}$$

In Eq. (4.116), the angle change $\Delta\delta_{p,i}$ is the difference between the expected phase angle $\delta_{p,exp,i}$ and the initial phase angle $\delta_{p,ini,i}$. Concurrently, the power ΔP_h is the difference between active power setpoint $P_{set,h}$ and initial active power value $P_{ini,h}$. To leverage the sensitivity $S_{PhiP,ih}$, Eq. (4.116) is rearranged to

$$P_{set,h} - P_{ini,h} = \frac{\delta_{p,exp,i} - \delta_{p,ini,i}}{S_{PhiP,ih}}. \tag{4.117}$$

From this point, the initial active power $P_{ini,h}$ can be moved to the right side of Eq. (4.117). The setpoint active power

$$P_{set,h} = \frac{\delta_{p,exp,i} - \delta_{p,ini,i}}{S_{PhiP,ih}} + P_{ini,h} \tag{4.118}$$

at bus h for the expected phase angle $\delta_{p,exp,i}$ at bus i can be then calculated. Following the procedure executed for Eq. (4.118), the sensitivity $S_{PhiQ,ih}$ can be used to achieve the expected phase angle $\delta_{p,exp,i}$. With consideration of the initial reactive power $Q_{ini,h}$, the setpoint reactive power

$$Q_{set,h} = \frac{\delta_{p,exp,i} - \delta_{p,ini,i}}{S_{PhiQ,ih}} + Q_{ini,h}. \tag{4.119}$$

at bus h can be computed for the expected phase angle $\delta_{p,exp,i}$ at bus i. Eqs. (4.118) and (4.119) illustrate the calculation of the active and reactive power setpoints $P_{set,h}$ and $Q_{set,h}$ at bus h for the expected phase angle $\delta_{p,exp,i}$ where $p \in \{a, b, c\}$ and $i, h \in \{1, 2, \ldots, n\}$.

The available angle sensitivity values resulting from Sections 4.3.2 and 4.4.3 are demonstrated so far. The calculations of the setpoint parameters based on the available sensitivity values in the unbalanced or balanced grid conditions have been explained in detail. The defined expected voltage angle of the target voltage can be achieved on the basis of the resulting setpoints.

4.6 Summary

The derivation of the proposed methods for decoupled voltage sensitivity analysis is presented in this chapter. These proposed methods require only measurement data, without involving with substantial information of grid topology. The predetermined $[\underline{Z}_{par}]$ is transformed to the converting bus impedance parameters $[\underline{\tilde{Z}}_{par,ih}]$ to relate the impedance network model to the sensitivity analysis. The voltage models are then formulated from $[\underline{\tilde{Z}}_{par,ih}]$ for the derivation

of the proposed analysis method. Thereby, the sensitivities of the voltage magnitude and angle are analysed for either balanced or unbalanced grid conditions. The sensitivities are analysed with respect to real and imaginary components of sequence currents in the case of an unbalanced condition and with respect to active and reactive powers in the case of a balanced condition. According to the derivation, the elements of the matrix $[\underline{\tilde{Z}}_{par,ih}]$ are used in conjunction with the measured bus voltages to compute the sensitivity values. Where $s \in \{0, 1, 2\}$, $p \in \{a, b, c\}$, and $i, h \in \{1, 2, \ldots, n\}$, the outcomes from the proposed analysis method are listed as follows:

For the unbalanced grid condition

- $S_{VIs:Re,p,ih}$: Sensitivity of the voltage magnitude at phase *a*, *b*, and *c* in relation to the real-component of the bus current in zero, positive, and negative sequence systems (Eq. (4.33))
- $S_{VIs:Im,p,ih}$: Sensitivity of the voltage magnitude at phase *a*, *b*, and *c* in relation to the imaginary-component of the bus current in zero, positive, and negative sequence systems (Eq. (4.37))
- $S_{\delta Is:Re,p,ih}$: Sensitivity of the voltage angle at phase *a*, *b*, and *c* in relation to the real-component of the bus current in zero, positive, and negative sequence systems (Eq. (4.48))
- $S_{\delta Is:Im,p,ih}$: Sensitivity of the voltage angle at phase *a*, *b*, and *c* in relation to the imaginary-component of the bus current in zero, positive, and negative sequence systems (Eq. (4.53))

For the balanced grid condition

- $S_{VP,ih}$: Sensitivity of the voltage magnitude in relation to the active power (Eq. (4.77))
- $S_{VQ,ih}$: Sensitivity of the voltage magnitude in relation to the reactive power (Eq. (4.83))
- $S_{PhiP,ih}$: Sensitivity of the phase angle in relation to the active power (Eq. (4.92))
- $S_{PhiQ,ih}$: Sensitivity of the phase angle in relation to the reactive power (Eq. (4.98))

Next, the applications of the results from the voltage sensitivity analysis are shown. How the sensitivity values are used to calculate power or current setpoint is delineated. Where $s \in \{0, 1, 2\}$, $p \in \{a, b, c\}$, and $i, h \in \{1, 2, \ldots, n\}$, the expected voltage magnitude $|\underline{V}_{p,exp,i}|$ at bus *i* can be achieved by using real- and imaginary-component current setpoints $I^{(s)}_{set,h:Re}$ and $I^{(s)}_{set,h:Im}$ at bus *h* provided in Eqs. (4.104) and (4.105) for the unbalanced grid condition or using active and reactive power setpoints $P_{set,h}$ and $Q_{set,h}$ provided in Eqs. (4.108) and (4.109) for the balanced grid condition. Likewise, the expected phase angle $\delta_{p,exp,i}$ at bus *i* can be achieved by using real- and imaginary-component current setpoints $I^{(s)}_{set,h:Re}$ and $I^{(s)}_{set,h:Im}$ at bus *h* provided

in Eqs. (4.114) and (4.115) for the unbalanced grid condition or using active and reactive power setpoints $P_{set,h}$ and $Q_{set,h}$ provided in Eqs. (4.118) and (4.119) for the balanced grid condition.

Finally, since the results from the voltage sensitivity analysis give the voltage-current or voltage-power impact between buses of interest, they can be further used in many situations, such as using as a parameter in the optimization calculation; setting reference parameters for the controlling algorithm; and used to examine the grid strength. Before the proposed analysis method is employed, it should be verified. In the next chapter, therefore, the method of voltage sensitivity analysis, together with the proposed impedance model, are verified by simulations in different case studies. Both the accuracy and an application of the voltage sensitivity analysis are discussed.

5. Verification of the Proposed Network Model and Voltage Sensitivity Analysis Method

In this thesis, the proposed network model and the proposed voltage sensitivity analysis method for grid monitoring and operations based on the CPSA are verified by simulations through three case studies. The purpose of the verification is to prove their accuracy and usability. The verification of the proposed impedance network model and analysis method is performed in a consecutive process. The impedance model, known as a bus impedance parameters matrix [$\underline{Z}_{par}$], gives the voltage-current characteristics of the considered power grid, as stated in Chapter 3. Then, the proposed voltage sensitivity analysis method is conducted by leveraging the bus impedance parameters, as stated in Chapter 4. Before entering into the case studies, an overview of the verification is worth providing. The verification is concentrated mainly on the distribution level, because this level is the primary aim of the CPSA – the foundation of this thesis. As the proposed method is claimed to be flexible, the case studies are designed to cover different voltage levels, topology types, and grid conditions. The case studies are described as follows:

- The first case study, **Case Study 1**, represents a general power grid, in which the proposed analysis method is conducted on the entire grid area. The purpose of this case study is to verify the proposed impedance model and analysis method in general. The medium-voltage (MV) distribution grid is focused on in this case study, and two exemplified power grids are used accordingly. The first grid is a MV radial grid modified from an IEEE 37-bus feeder [232]. The second grid is a MV mesh grid adapted from a 14-bus system – an example from DIgSILENT PowerFactory [233].
- The second case study, **Case Study 2**, represents a power grid, to which the CPSA is applied, thereafter named as the "cluster-based power grid". The purpose of this case study is to show the contribution of the proposed method in decentralised grid operations based on the CPSA. A low-voltage (LV) power grid is focused on in this case study. The power grid for the simulation is an exemplified LV radial grid, which is modified from the distribution grid in Borchen-Etteln from Westfalen Weser Netz. Based on the principle of the CPSA, four cluster areas are defined on this grid.
- The third case study, **Case Study 3**, showcases an application of using the results from the proposed voltage sensitivity analysis. The cluster-based low voltage grid from Case Study 2 is further used in this case study. Regulations of voltage magnitude and angle based on the calculated sensitivity values are simulated.

Before moving on to Section 5.1, every procedure executed during the verification of the proposed impedance model and sensitivity analysis method is clarified first. The preparation

of the input data for simulations is explained; an overview of the verification process is afterwards given; and finally, abbreviations used throughout this chapter are provided.

Preparation for Simulating the Proposed Method

The inputs – measured bus voltages, bus currents, and line currents – for the simulations of the proposed method are generated by Load Flow Calculation function in PowerFactory, as shown in Figure 5.1(a). Also, the references for the verification purpose are obtained from voltage sensitivity analysis, in the Load Flow Sensitivities function, by PowerFactory, as shown in Figure 5.1(b). In Figure 5.1, the bus number is denoted by i of a power grid with n buses of concern, where $i \in \{1, 2, \ldots, n\}$. Active and reactive power inputs are based on the original data from each simulated grid. They are then expanded to multiple sets by using a random function in MATLAB to ensure linear independency of the resulting voltages and currents.

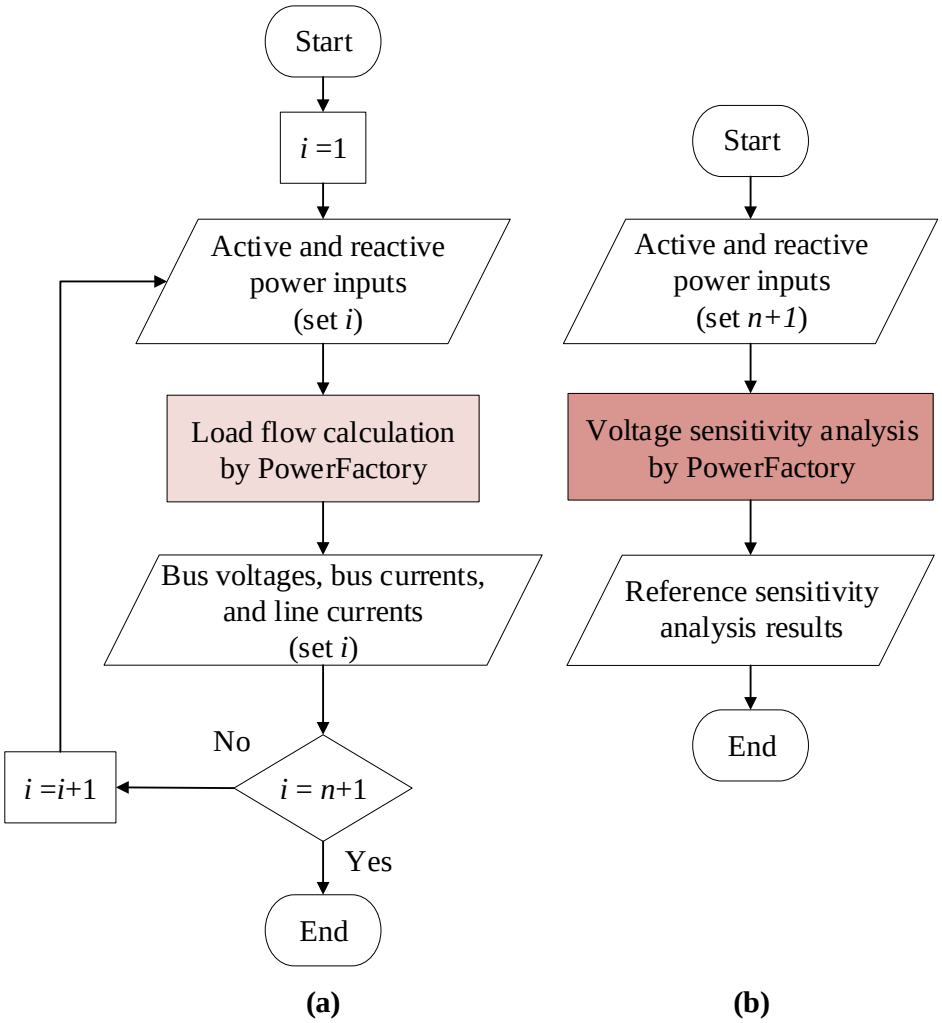

Figure 5.1: Roles of DIgSILENT PowerFactory in the verification process
(a) Generation of bus voltages, bus currents, and line currents
(b) Generation of sensitivity values as the reference for comparison

As a result, n+1 numbers of data sets of voltage and current measurement are gathered as the inputs for the proposed method. The reference sensitivity values are computed from the last data set, which is assumed to be the latest available measurement data.

Simulations of the Proposed Method

The measured voltages and currents are used as the inputs for the proposed method. The proposed voltage sensitivity analysis is conducted in MATLAB. Figure 5.2 portrays the simulation process. In this figure, the generation of the impedance model matrix [$\underline{Z}_{par}$] is included to the process of performing voltage sensitivity analysis. Thereby, both bus impedance parameters and the results from the sensitivity analysis are collected in this step.

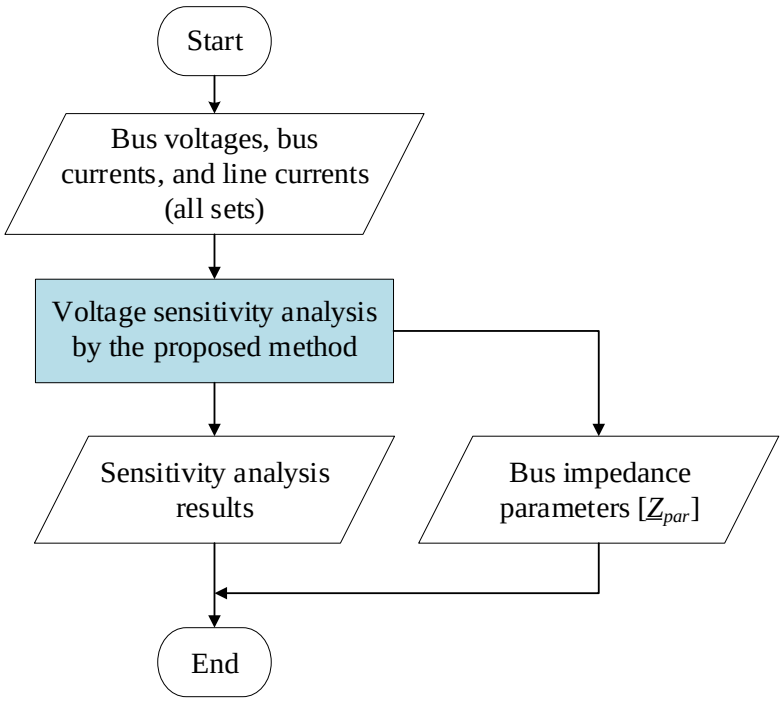

Figure 5.2: Process of results generation from the proposed method

As a result, the matrix [$\underline{Z}_{par}$] is generated for each of the sequence systems, as stated in Chapter 3. The results of the voltage sensitivity analysis are produced for both unbalanced and balanced grid conditions, as stated in Chapter 4.

Accuracy Verification

The accuracy of the proposed impedance model and sensitivity results from the proposed analysis method is verified in the first two case studies by comparing with their reference values. First, the proposed impedance model is compared with the bus impedance matrix, which is the conventional impedance model. The verification of the impedance model is to prove the correctness of the bus impedance parameters matrix [$\underline{Z}_{par}$], determined from measured bus voltages and currents. Based on the same power grid, the correctness is verified from the difference between the elements of the matrix [$\underline{Z}_{par}$] and their references, which are the corresponding elements of bus impedance matrix [$\underline{Z}_{bus}$]. Second, the results from the

proposed analysis method are compared with the results from the Load Flow Sensitivities function of DIgSILENT PowerFactory, which employs the classical method that performs the voltage sensitivity analysis through the Jacobian matrix obtained from the load flow calculation process.

Generally, the elements of the model matrix and the results from the proposed method are the square of the number of concerned buses. For n number of buses, $n \times n$ elements of the matrix $[\underline{Z}_{par}]$ and $n \times n$ results from each sensitivity analysis type are obtained. For this reason, in order to cope with the enormous amount of data in the verification, the matrix $[\underline{Z}_{par}]$ and the results from the proposed method are verified in two aspects. In the first aspect, the mean of absolute percent differences is evaluated to observe the overall magnitude of mismatch between the calculated results and their reference. In the second aspect, the percent differences are plotted in a histogram to envision the overview of the differences between the calculated results and their reference. The mean of percent differences is also shown together with the plotted histogram. Details of the verification process can be found in Appendix A.

Measurement Error Experiment

Apart from the correctness of the proposed method, a big factor that can cause a deviation in the outcome of the proposed voltage sensitivity analysis is the measurement data. The accuracy of the data gathered from measurement units, which are the PMU in this context, must be therefore taken into account. As the practical synchronisation of PMU measurements is not perfect, the measurement data can be error prone [117]. According to IEC/IEEE 60255-118-1 [108], a measure to evaluate the accuracy of the PMU is total vector error (TVE), discussed in Section 2.1.3. It is the normalised difference between the reference synchrophasor and the measured value at the same point in time from the tested unit.

Since 1.0% TVE is the maximum permissible error defined in IEC/IEEE 60255-118-1, the TVE levels of 0.2%, 0.4%, 0.6%, 0.8%, and 1.0% are added to the original measured data of each case study. The original measured data are defined as containing 0% TVE. Figure 5.3 illustrates the process of adding errors based on the TVE to the original measurement data.

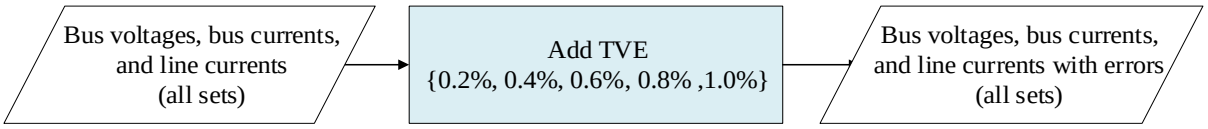

Figure 5.3: Adding errors based on TVE to the original measurement data

Based on the specified TVE levels, magnitude error and phase angle error are randomly added to the original measurement data. The TVE levels are ensured by using Eq. (2.1) to check if the data with errors comply with the defined TVE. The measured data, i.e. input data, added

with the TVE are then added to the process in Figure 5.2 to calculate the sensitivity values. Afterwards, the calculated sensitivity values are compared with their reference again.

Abbreviation Used in This Chapter

The abbreviations of all sensitivity analysis types are listed in Table 5.1 for the analysis in an unbalanced condition, and in Table 5.2 for the analysis in a balanced condition. The tables also include a description of calculated values from the sensitivity analysis and the units; these abbreviations are used throughout this chapter. According to the proposed method from Section 4.3, the sensitivity of voltage under the unbalanced grid condition is analysed with respect to a sequence current. In this verification, the unit of voltage magnitude sensitivity is Per Unit per Ampere (pu/A), while the unit of voltage angle sensitivity is Degree per Ampere (deg/A). The number 0, 1, and 2 are designated for zero-, positive, and negative- sequence, respectively.

Next, the sensitivity of voltage under a balanced grid condition is analysed with respect to active and reactive powers, owing to the proposed method from Section 4.4. Depending on the considered kind of power, the units of voltage magnitude sensitivity are available in Per Unit per Megawatt (pu/MW) and Per Unit per Megavar (pu/Mvar). Mega is used as the prefix for the unit to compensate too-small sensitivity values. Similarly, the units of voltage angle sensitivity are available in Degree per Megawatt (deg/MW) and Degree per Megavar (deg/Mvar).

Table 5.1: Description of voltage sensitivity analysis types for an unbalanced grid condition

Abbreviation	Description	Unit
Svir,0	Sensitivity of voltage magnitude in relation to real part of zero-sequence current	[pu/A]
Svir,1	Sensitivity of voltage magnitude in relation to real part of positive-sequence current	
Svir,2	Sensitivity of voltage magnitude in relation to real part of negative-sequence current	
Svii,0	Sensitivity of voltage magnitude in relation to imaginary part of zero-sequence current	
Svii,1	Sensitivity of voltage magnitude in relation to imaginary part of positive-sequence current	
Svii,2	Sensitivity of voltage magnitude in relation to imaginary part of negative-sequence current	
Sphiir,0	Sensitivity of voltage angle in relation to real part of zero-sequence current	[deg/A]
Sphiir,1	Sensitivity of voltage angle in relation to real part of positive-sequence current	
Sphiir,2	Sensitivity of voltage angle in relation to real part of negative-sequence current	
Sphiii,0	Sensitivity of voltage angle in relation to imaginary part of zero-sequence current	
Sphiii,1	Sensitivity of voltage angle in relation to imaginary part of positive-sequence current	
Sphiii,2	Sensitivity of voltage angle in relation to imaginary part of negative-sequence current	

Table 5.2: Types of voltage sensitivity analysis under a balanced grid condition

Abbreviation	Description	Unit
Svp	Sensitivity of voltage magnitude in relation to active power	pu/MW
Svq	Sensitivity of voltage magnitude in relation to reactive power	pu/Mvar
Sphip	Sensitivity of voltage angle in relation to active power	deg/MW
Sphiq	Sensitivity of voltage angle in relation to reactive power	deg/Mvar

Thus far, the overview of this chapter has been provided. In the following subsections, the three case studies are discussed. Thereby, the results of each case study are examined to verify the bus impedance parameters and the proposed analysis method.

5.1 Case Study 1: Entire Grid

This study case is designed to verify the proposed impedance model and voltage sensitivity analysis method in a general case when the entire power grid is considered. Two important topological connections of the MV power grid are simulated. The first one is a radial grid modified from the IEEE 37-bus feeder [232], and the other one is an exemplified mesh grid adopted from the 14-bus system example in DIgSILENT PowerFactory [233].

To begin with, the modified IEEE 37-bus test feeder is depicted in Figure 5.4. Its nominal voltage is 10 kV. The buses, seen as nodes, in blue colour are buses of concern, thereafter called “active buses”. With regards Figure 5.4, there are 25 active buses in this case study. The active buses are controllable buses from which measurement data can be collected and to which a command can be sent. The modified IEEE 37-bus grid is connected to an external grid at bus 799, whose nominal voltage is 20 kV. The type of the three-phase transformer *Tr1*, connected between bus 799 and bus 701 is 25 MVA 20/10 kV with the vector group Yd5. The load connection is in delta configuration. The complete configuration of the modified IEEE 37-bus test feeder can be found in Appendix B.

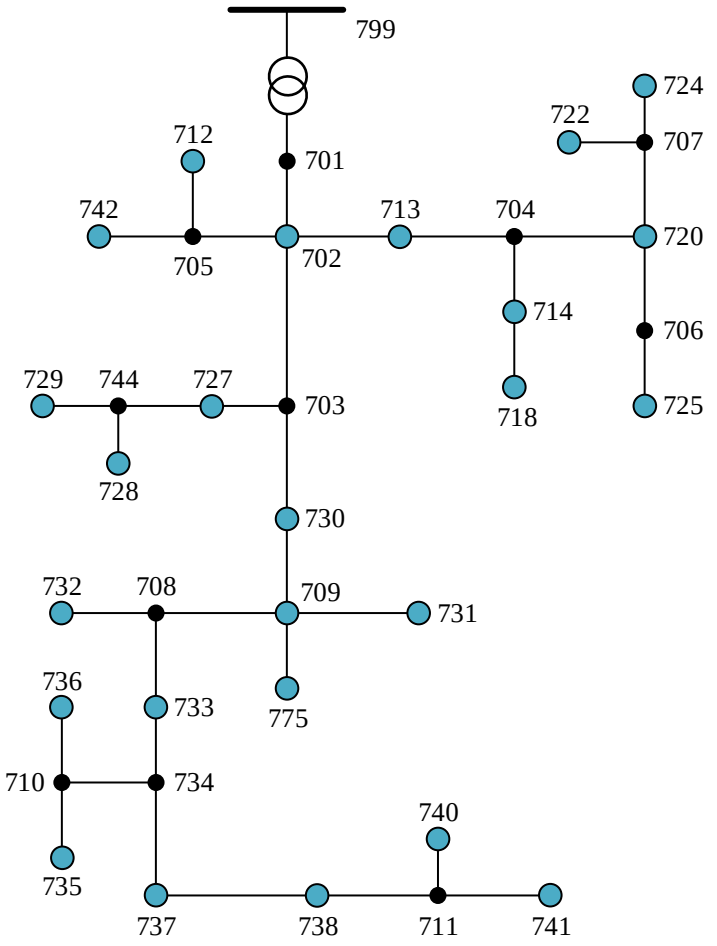

Figure 5.4: Modified IEEE 37-bus test feeder

The other power grid for the simulation is depicted in Figure 5.5. There are 10 active buses out of 12 total buses in this grid. The nominal voltage of this grid is 10 kV, and the nominal voltage of the external grid connected to this grid at bus 100 is 20 kV. The type of the three-phase transformer *Tr#1*, connected between bus 100 to bus 101 is 25 MVA 20/10 kV with Yd0 vector group. The complete configuration of this mesh grid can be found in Appendix C.

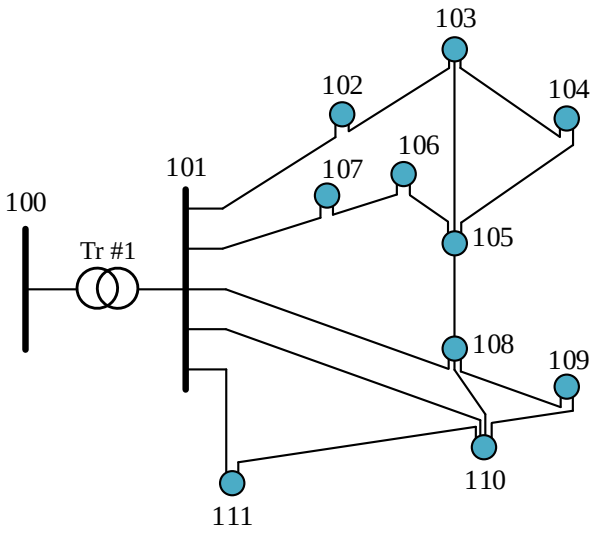

Figure 5.5: Exemplified mesh grid

In the verification of the matrix [$\underline{Z}_{par}$], both matrices [$\underline{Z}_{par}$] and [$\underline{Z}_{bus}$] are determined in sequence systems, i.e. zero, positive, and negative sequence. The matrix [$\underline{Z}_{par}$] is determined from measured voltages and currents collected from simulations of multiple operational scenarios by PowerFactory, while the matrix [$\underline{Z}_{bus}$] is manually computed from the topology data, which describe the same grid for calculating the matrix [$\underline{Z}_{par}$].

To perform the verification, measured bus voltages and currents are obtained from simulating the load flow calculation of each aforementioned grid in PowerFactory. The modified IEEE 37-bus feeder requires 26 data sets of their measured bus voltages and currents with one unique timestamp per data set, since it accommodates 25 active buses. Since an operational scenario for load flow calculation provides a set of bus voltages and currents with a unique timestamp, load flow calculations of 26 different operational scenarios are executed to get the measurement data. In the same manner, the exemplified mesh grid requires 11 data sets, since it contains 10 active buses. Thus, the measurement data are generated from 11 operational scenarios.

Based on the measurement data gathered from load flow calculations, the proposed impedance model and proposed voltage sensitivity analysis method are analysed in the following subsections.

5.1.1 Analysis of the Proposed Impedance Model

The impedance model is normally in the form of a matrix, for example, the matrix [$\underline{Z}_{bus}$], which expresses the voltage-current relationship between buses. The dimension of the impedance model reflects the number of buses of the considered power grid. In this section, the matrix [$\underline{Z}_{par}$] that is proposed as the impedance model for the proposed voltage sensitivity analysis is verified. The accuracy, representing the percent differences between the proposed matrix [$\underline{Z}_{par}$] and the reduced matrix [$\underline{Z}_{bus}$], is discussed. The modified IEEE 37-bus test feeder accommodates 25 active buses, so its matrix [$\underline{Z}_{par}$] contains 625 elements. Also, the exemplified mesh grid accommodates 10 active buses; as a result, its matrix [$\underline{Z}_{par}$] contains 100 elements. Since the matrix [$\underline{Z}_{bus}$], which is the reference in this context, contains the full scale of the power grids, the matrix [$\underline{Z}_{bus}$] is reduced to match with the size of the matrix [$\underline{Z}_{par}$] by using Kron's reduction technique [179], as explained in the Bus Impedance Modification Method in Section 3.2.4. Accordingly, the dimension of the matrix [$\underline{Z}_{bus}$] is reduced from 37×37 to 25×25 for the modified IEEE 37-bus test feeder and reduced from 12×12 to 10×10 for the exemplified mesh grid.

In the following, the matrix [$\underline{Z}_{par}$] is investigated in three aspects. First, the histogram of the percent differences between all 625 corresponding elements of the matrices [$\underline{Z}_{bus}$] and [$\underline{Z}_{par}$] is demonstrated. The results show how close the elements of the matrix [$\underline{Z}_{par}$] are in comparison to that of the matrix [$\underline{Z}_{bus}$], although they are determined by different methods. Then, the mean of absolute percent differences is presented to show the quality of the results from different inputs and cases. The descriptions of the histogram and the result differences are provided in Appendix A. Lastly, the numerical data of some selected elements from the matrices [$\underline{Z}_{par}$] and [$\underline{Z}_{bus}$] are given as an example.

Owing to the configuration of the two power grids, there is no contact to earth in the configuration for either of them. Hence, only bus impedance parameters in positive and negative sequences are taken into account. For the case of the modified IEEE 37-bus test feeder, Figure 5.6 and Figure 5.7 show the histogram of the percent differences between all 625 corresponding elements of the matrices [$\underline{Z}_{bus}$] and [$\underline{Z}_{par}$] in positive and negative sequences. To verify the bus impedance parameters, both matrices [$\underline{Z}_{par}$] and [$\underline{Z}_{bus}$] are divided into resistance and reactance, i.e. real and imaginary parts, in the comparison. According to Figure 5.6, the mean of the percent differences in the case of resistance is 0.062% and 0.101% for positive and negative sequences, respectively. Similarly, according to Figure 5.7, the mean of the percent differences in the case of reactance is 0.027% and 0.031% for positive and negative sequences. The mean values are close to zero, as plotted in a dash line. Hence, high accuracy can be obtained for the determination of the matrix [$\underline{Z}_{par}$] in general.

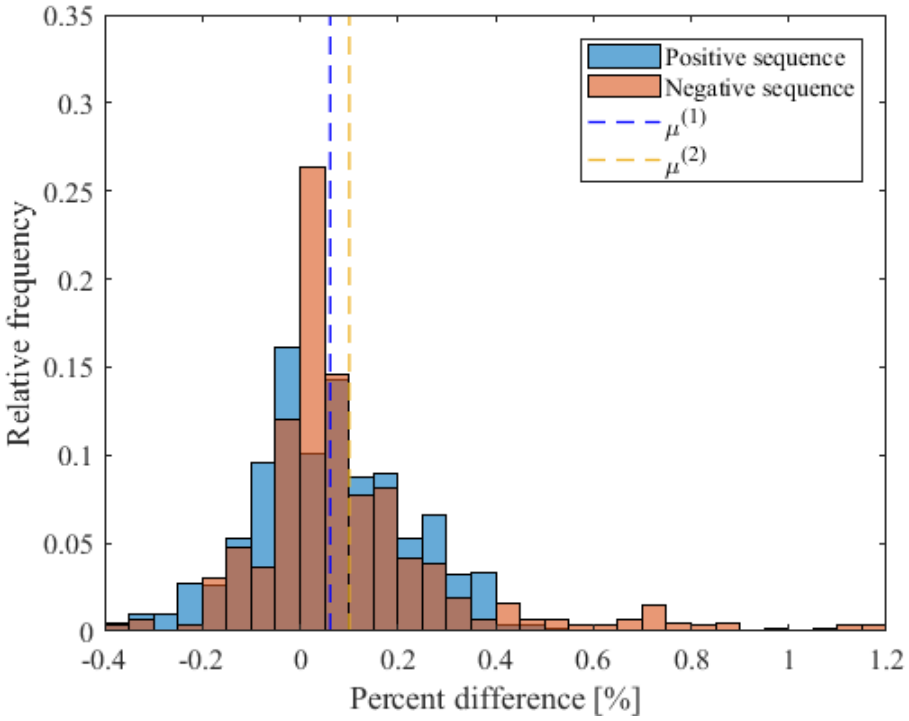

Figure 5.6: Histogram of percent differences of the whole bus resistances for the case of the modified IEEE 37-bus test feeder

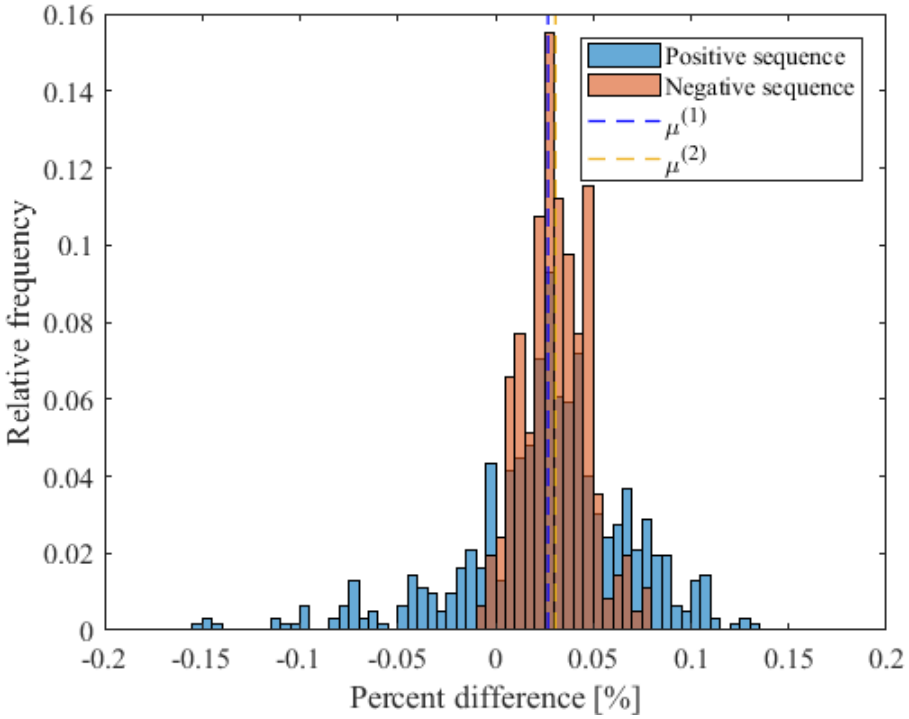

Figure 5.7: Histogram of percent differences of the whole bus reactances for the case of the modified IEEE 37-bus test feeder

Next, the mean of absolute percent differences is discussed. To demonstrate the accuracy in terms of only magnitude of the differences, the comparison of mean absolute percent differences in sequence systems for the case of the modified IEEE 37-bus test feeder is depicted in Figure 5.8. The mean is computed from the differences between 625 corresponding elements of the matrices $[\underline{Z}_{bus}]$ and $[\underline{Z}_{par}]$.

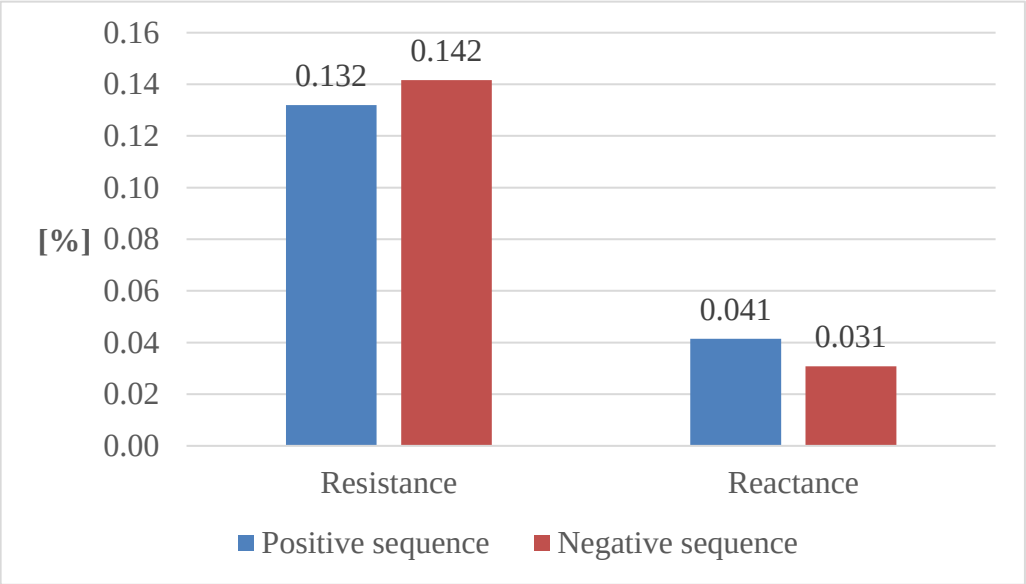

Figure 5.8: Illustration of mean absolute percent differences of bus impedances for the case of the modified IEEE 37-bus test feeder

The comparison shows that the mean values between the corresponding elements of the two matrices are very close for both positive and negative sequences. This means that for the case of the modified IEEE 37-bus test feeder, the absolute percent difference of the resistance of its matrices $[\underline{Z}_{bus}]$ and $[\underline{Z}_{par}]$ is 0.132% in positive sequence and 0.142% in negative sequence. The difference is even lower in the case of the reactance, where the difference is only 0.041% in positive sequence and 0.031% in negative sequence, since the reactance is more dominant in the used cable type. To give more insight into the mean differences, the selected bus resistances $R_{i,j}$ and reactances $X_{i,j}$ in positive and negative sequences are provided in Table 5.3, where subscripts i and j indicate a bus number. The data in this table are taken from the original data, which are used to compute the mean illustrated in Figure 5.8. Evidently, the overall calculated resistance and reactance are close to their reference.

Table 5.3: Comparison of the selected bus impedances in the modified IEEE 37-bus test feeder with their reference

Parameter	Positive sequence		Negative sequence	
[Ohm]	Reference	Calculation	Reference	Calculation
$R_{702,725}$	0.053490	0.053581	0.053490	0.053564
$R_{709,725}$	0.053490	0.053529	0.053490	0.053637
$R_{712,725}$	0.053490	0.053599	0.053490	0.053566
$R_{713,725}$	0.071661	0.071757	0.071661	0.071731
$R_{714,725}$	0.097908	0.098015	0.097908	0.097986
$R_{718,725}$	0.097908	0.098028	0.097908	0.097997
$R_{720,725}$	0.138287	0.138378	0.138287	0.138359
$R_{722,725}$	0.138287	0.138374	0.138287	0.138364
$R_{724,725}$	0.138287	0.138373	0.138287	0.138369
$R_{725,725}$	0.198857	0.198925	0.198857	0.198902
$X_{702,725}$	0.436482	0.436541	0.436482	0.436598
$X_{709,725}$	0.436482	0.436414	0.436482	0.436533
$X_{712,725}$	0.436482	0.436531	0.436482	0.436598
$X_{713,725}$	0.446134	0.446214	0.446134	0.446265
$X_{714,725}$	0.460076	0.460195	0.460076	0.460221
$X_{718,725}$	0.460076	0.460208	0.460076	0.460221
$X_{720,725}$	0.481525	0.481674	0.481525	0.481699
$X_{722,725}$	0.481525	0.481692	0.481525	0.481712
$X_{724,725}$	0.481525	0.481685	0.481525	0.481712
$X_{725,725}$	0.513699	0.513885	0.513699	0.513891

Next, the case of exemplified mesh grid is observed. High accuracy still can be obtained for the determination of the matrix $[\underline{Z}_{par}]$ for this grid. Similar to the case of the modified IEEE 37-bus test feeder, Figure 5.9 and Figure 5.10 illustrate the histogram of the percent differences between all 100 corresponding elements of the matrices $[\underline{Z}_{bus}]$ and $[\underline{Z}_{par}]$ in positive and negative sequences, with the mean value plotted in a dash line The resistance and reactance are separately compared as well. As illustrated in Figure 5.9, the mean of the percent differences in the case of resistance is 0.029% and 0.032% for positive and negative sequence, respectively. Similarly, as illustrated in Figure 5.10, the mean values of the percent differences in the case of reactance are very close to zero at 0.01492% and 0. 01497% for positive and negative sequence, respectively. That is, the calculated resistances and reactances are generally close to their reference.

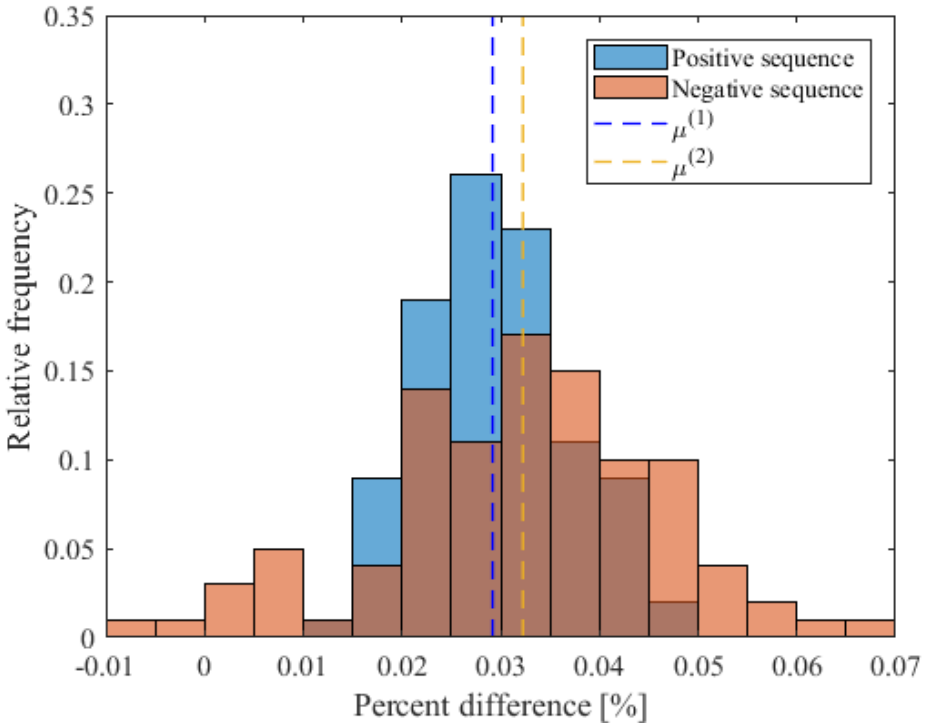

Figure 5.9: Histogram of percent differences of the whole bus resistances for the case of the exemplified mesh grid

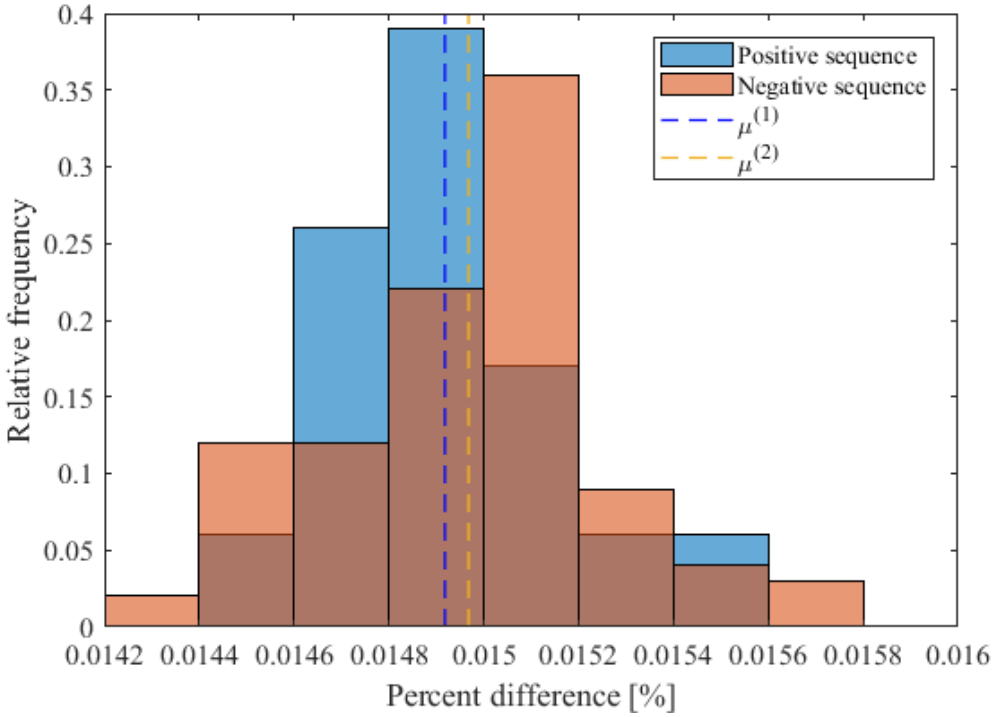

Figure 5.10: Histogram of percent differences of the whole bus reactances for the case of the exemplified mesh grid

The following section examines the accuracy in terms of the size of the differences. Thereby, the mean of the absolute differences between 100 corresponding elements of the matrices [$\underline{Z}_{bus}$] and [$\underline{Z}_{par}$] is compared, as depicted in Figure 5.11. The resistance and reactance are also compared separately.

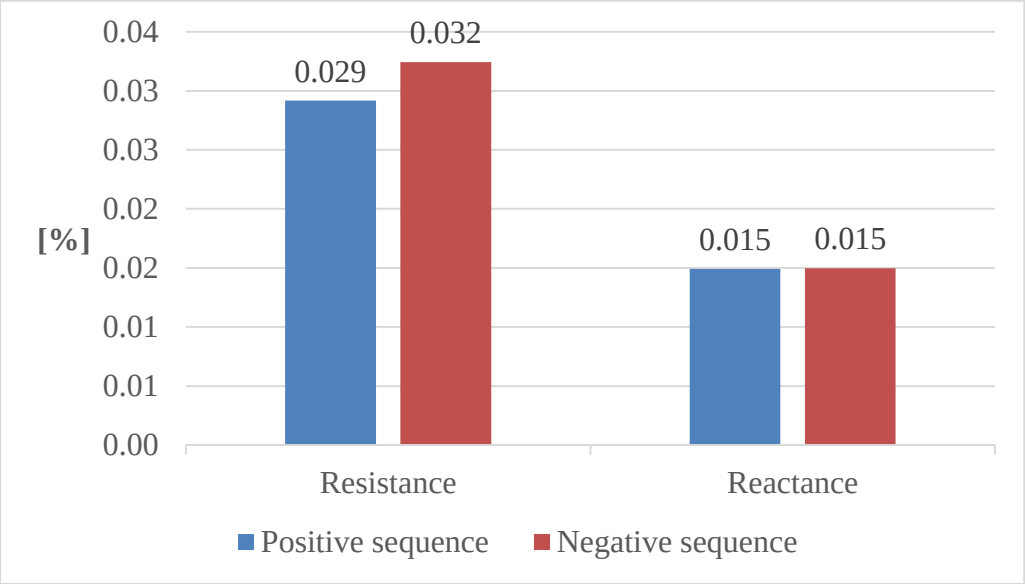

Figure 5.11: Illustration of mean relative percent differences of bus impedances for the case of the exemplified mesh grid

For the case of the exemplified mesh grid, the outcomes are similar to that of the modified IEEE 37-bus test feeder. The absolute percent difference is 0.029% in the positive sequence and 0.032% in the negative sequence for the case of resistance, and 0.015% in both positive and negative sequences for the case of reactance. Hence, according to the comparisons, the proposed matrix [$\underline{Z}_{par}$] is applicable for both radial and mesh topology types. Subsequently, the selected bus resistances $R_{i,j}$ and reactances $X_{i,j}$ in the positive and negative sequences, where subscripts i and j indicate bus number, are provided in Table 5.4 to show how close the calculated resistances and reactances are to their reference.

Table 5.4: Comparison of the selected bus impedances in the exemplified mesh grid with their reference

Parameter	Positive sequence		Negative sequence	
[Ohm]	Reference	Calculated	Reference	Calculated
$R_{102,104}$	0.023985	0.023991	0.023985	0.023995
$R_{103,104}$	0.033836	0.033842	0.033836	0.033845
$R_{104,104}$	0.040438	0.040444	0.040438	0.040448
$R_{105,104}$	0.030481	0.030487	0.030481	0.030490
$R_{106,104}$	0.025401	0.025408	0.025401	0.025411
$R_{107,104}$	0.020322	0.020328	0.020322	0.020332
$R_{108,104}$	0.023925	0.023932	0.023925	0.023934
$R_{109,104}$	0.020567	0.020574	0.020567	0.020576
$R_{110,104}$	0.018888	0.018895	0.018888	0.018897
$R_{111,104}$	0.017365	0.017372	0.017365	0.017373
$X_{102,104}$	0.416613	0.416676	0.416613	0.416676
$X_{103,104}$	0.421730	0.421791	0.421730	0.421793
$X_{104,104}$	0.425208	0.425269	0.425208	0.425271
$X_{105,104}$	0.419889	0.419951	0.419889	0.419952
$X_{106,104}$	0.417110	0.417171	0.417110	0.417173
$X_{107,104}$	0.414330	0.414391	0.414330	0.414393
$X_{108,104}$	0.416431	0.416493	0.416431	0.416493
$X_{109,104}$	0.414414	0.414476	0.414414	0.414477
$X_{110,104}$	0.413406	0.413468	0.413406	0.413468
$X_{111,104}$	0.412408	0.412470	0.412408	0.412471

At this point, the proposed impedance model has been successfully verified. That is, the bus impedance parameters [$\underline{Z}_{par}$] can be determined by using only measured voltages and currents, while low absolute percent differences of the model in comparison to the reduced matrix [$\underline{Z}_{bus}$] is acquired. In the next section, the calculated matrix [$\underline{Z}_{par}$] is further used in the proposed voltage sensitivity analysis method. The verification of the proposed analysis method is then carried out.

5.1.2 Analysis of Results from the Proposed Analysis Method

The proposed voltage sensitivity analysis method is based on the predetermined impedance model [$\underline{Z}_{par}$]. The outcomes of the analysis therefore indicate the impact between buses in terms of voltage change. For this reason, the mean of absolute relative percent differences of all voltage sensitivity values is also used in this verification to present the accuracy of the proposed method in comparison to the reference values from PowerFactory, which utilises the classical method.

In this section, the modified IEEE 37-bus test feeder and the exemplified mesh grid are further utilised for simulations of voltage sensitivity analysis. The proposed method is verified for both unbalanced and balanced grid conditions. The results from the proposed method are investigated in three aspects. First the mean of absolute percent differences of each sensitivity type is delivered to explore the quality of the results from different inputs and sensitivity types. Then the histogram of the percent differences between all corresponding sensitivity values in positive sequence is demonstrated for all sensitivity types, as an example to present an overview of the total results. The descriptions of the histogram and the result differences are provided in Appendix A. Finally, the original sensitivity values of the selected buses are then shown.

5.1.2.1 Results of Sensitivity Analysis in an Unbalanced Grid Condition

In the unbalanced condition, performing the proposed voltage sensitivity analysis yields the sensitivity of bus voltage at phase *a*, *b*, and *c* in relation to the complex sequence current. To facilitate the explanation, the accuracy is determined by the mean differences between the sensitivity values from the proposed method and their reference from the classical method. Starting from the modified IEEE 37-bus test feeder, the mean of absolute percent differences of all sensitivity types – *Svir*,1, *Svir*,2, *Svii*,1, *Svii*,2, *Sphiir*,1, *Sphiir*,2, *Sphiii*,1, *Sphiii*,2 – is displayed in Figure 5.12. The calculations of the sensitivities *Svir*, *Svii*, *Sphiir*, and *Sphiii* are executed respectively by Eq. (4.33), Eq. (4.37), Eq. (4.48), and Eq. (4.52), and the phase and sequence can be selected in these equations accordingly.

These are the sensitivities of voltage magnitude and angle in relation to the complex sequence current, regardless of phase notation. Descriptions of all sensitivity types is given in Table 5.1. The accuracy is inferred by the mean of absolute relative percent differences. Based on Figure 5.12, high accuracy of the results can be achieved by the proposed method. The mean is within the range of 0.509% to 1.213%. It must be noted that the sensitivity of bus voltage to zero-sequence current is excluded from this investigation, since the zero sequence components are unavailable for this grid.

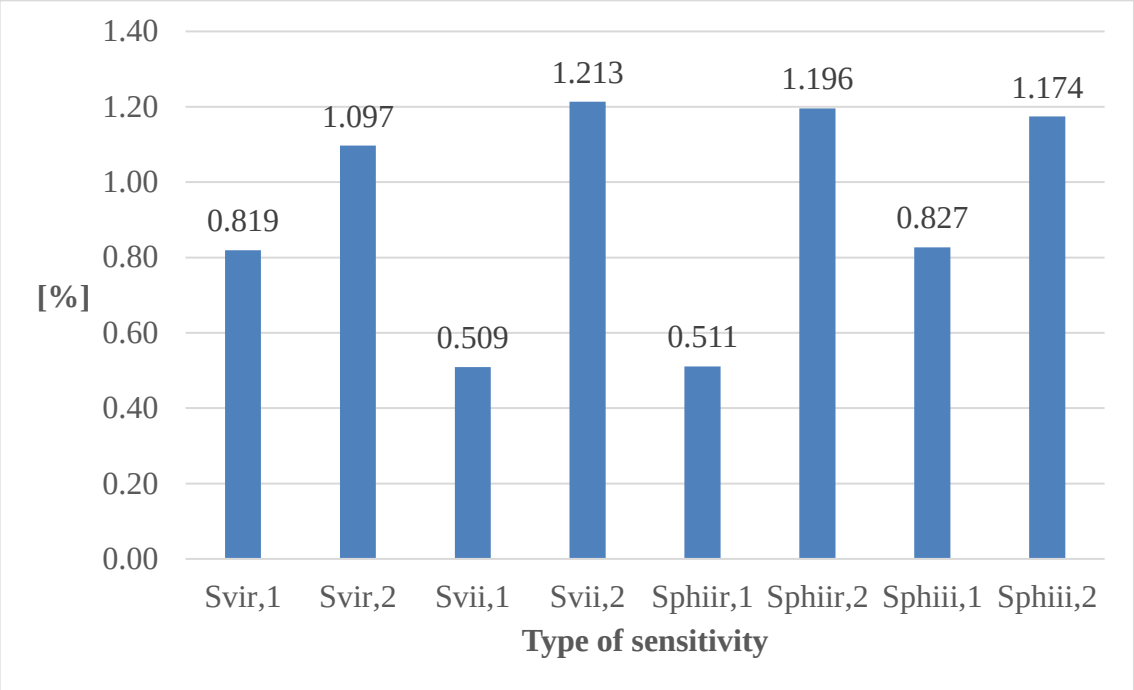

Figure 5.12: Illustration of mean absolute percent differences of sensitivity values in the modified IEEE 37-bus test feeder case

In addition, the percent differences of whole data are also discussed to supplement the accuracy. In this grid case, there are 625 sensitivity values for each sensitivity type, since there are 25 buses of concern. However, as the aim of the following results is to support the accuracy of the proposed method, only the charts showing the results in the positive sequence are presented here. The rest can be found in Appendix B.

Beginning with the sensitivities of voltage magnitude, Figure 5.13 and Figure 5.14 show the histogram charts of percent differences, respectively, in the case of sensitivity *Svir*,1 and *Svii*,1 in phase *a*, *b*, and *c*. As illustrated in Figure 5.13, for phase *a*, *b*, and *c*, the means of the percent differences of the sensitivity *Svir*,1 for each phase are 1.092%, 1.039%, -0.303%. Similarly, as illustrated in Figure 5.14, for phase *a*, *b*, and *c*, the means of the percent differences of the sensitivity *Svii*,1 for each phase are -0.753%, 0.577%, and -0.115%. Hence, the sensitivities *Svir*,1 and *Svii*,1 at any phase are clearly accurate. The mean values are close to zero, as plotted in dash lines.

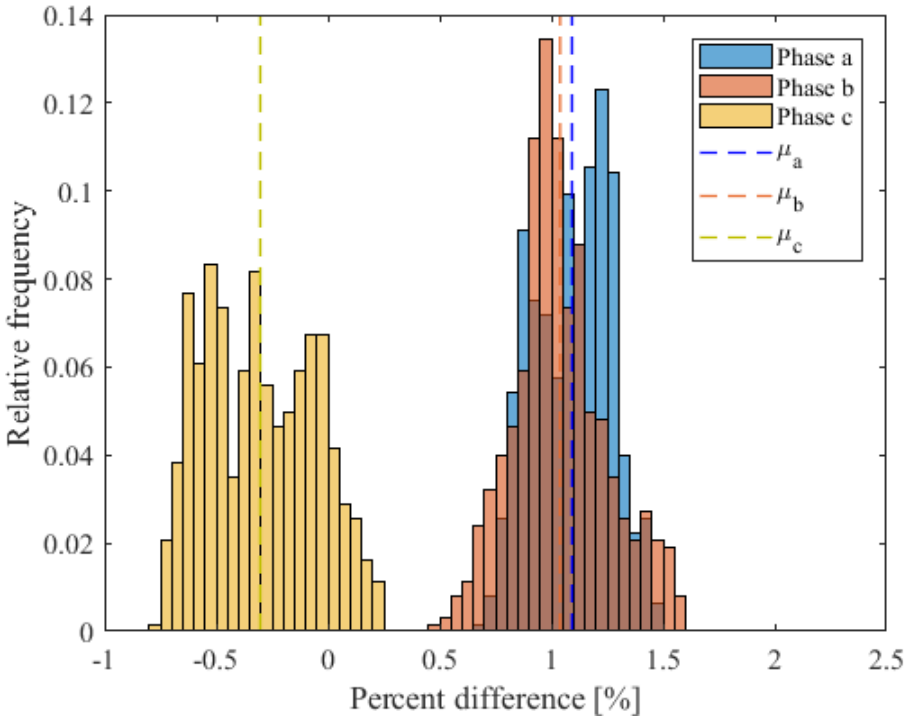

Figure 5.13: Histogram of the whole result differences in *Svir*,1 of the modified IEEE 37-bus test feeder case

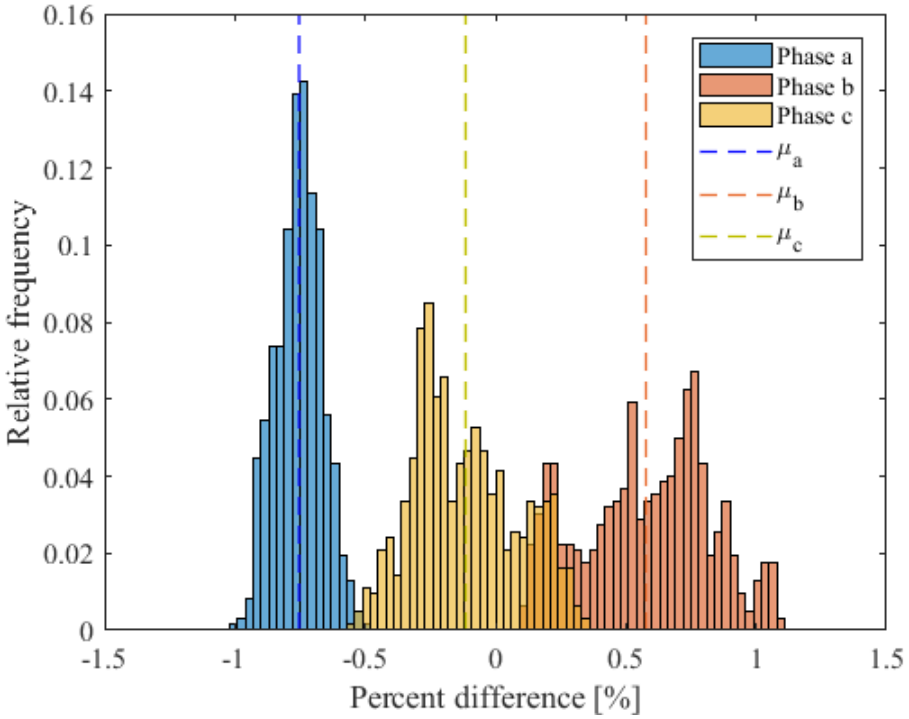

Figure 5.14: Histogram of the whole result differences in *Svii*,1 of the modified IEEE 37-bus test feeder case

Continuing with the sensitivities of the voltage angle, Figure 5.15 and Figure 5.16 display the charts of percent differences respectively, in the case of sensitivity *Sphiir*,1 and *Sphiii*,1 in phase *a*, *b*, and *c*. As portrayed in Figure 5.15, for phase *a*, *b*, and *c*, the means of the percent differences of the sensitivity *Sphiir*,1 for each phase are 0.802%, -0.603%, and 0.121%.

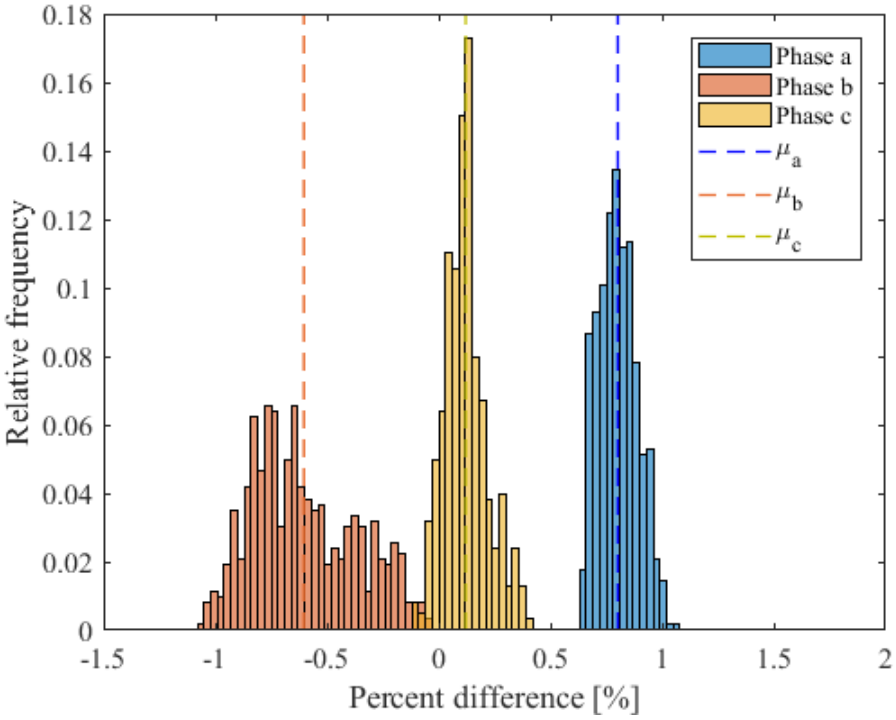

Figure 5.15: Histogram of the whole result differences in *Sphiir*,1 of the modified IEEE 37-bus test feeder case

Likewise, as portrayed in Figure 5.16, for phase *a*, *b*, and *c*, the means of the percent differences of the sensitivity *Sphiii*,1 for each phase are -1.087%, -1.086%, and 0.288%. According to Figure 5.15 and Figure 5.16, the sensitivities *Sphiir*,1 and *Sphiii*,1 at any phase are clearly accurate. The means are close to zero, as plotted in dash lines. Additionally, since the sensitivity analysis is individually executed for each phase, the distribution of the result differences is varied, as shown in Figure 5.13 to Figure 5.16. Further analysis of the variation of the histograms is discussed later in this section.

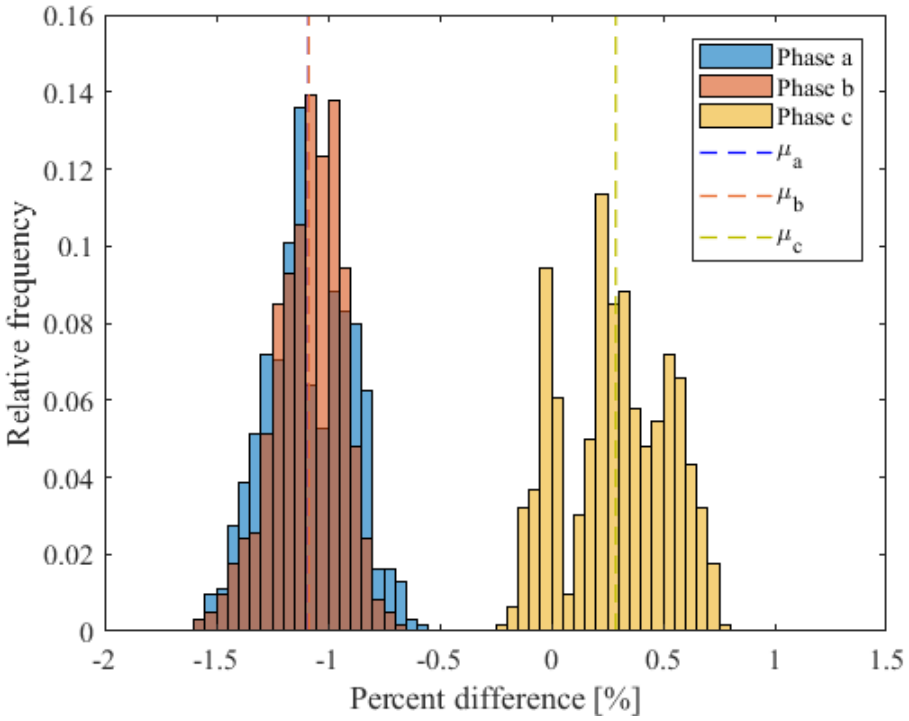

Figure 5.16: Histogram of the whole result differences in *Sphiii*,1 of the modified IEEE 37-bus test feeder case

Apart from the accuracy and the histogram, the comparison of original sensitivity values is also explored. To show the accuracy of the proposed method, the sensitivities of bus voltage magnitude and angle at bus 742 in relation to real and imaginary sequence current at bus 713 are selected as an example. In Figure 5.17 to Figure 5.20, the outcomes from voltage sensitivity analysis of bus 742 are plotted alongside with their reference. All sensitivities are available for all phases *a*, *b*, and *c*.

Voltage magnitude sensitivity is examined at the unit of pu/A. Figure 5.17 illustrates the comparison of the sensitivity values of the sensitivities *Svir*,1 and *Svir*,2. They infer the extent to which the voltage magnitude at each phase of bus 742 is altered in relation to a real component of sequence currents at bus 713. Similarly, Figure 5.18 displays the comparison of the sensitivity values from the proposed method to their reference for the sensitivities *Svii*,1 and *Svii*,2. These sensitivities indicate a change of the voltage magnitude at each phase of bus 742 in relation to an imaginary component of sequence currents at bus 713. The comparisons in both Figure 5.17 and Figure 5.18 show that the sensitivity values from the proposed method are very close to their reference. Accordingly, high accuracy is obtained in both magnitude and direction at the precision of 10^{-5} pu/A. The sensitivity values are placed in the table inside each figure.

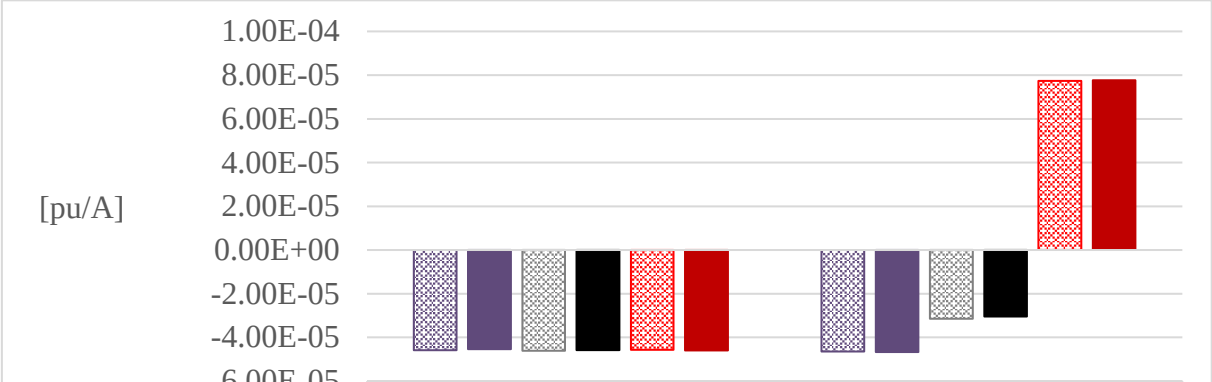

	Svir,1	Svir,2
Reference result (phase a)	-4.58E-05	-4.64E-05
Calculated result (phase a)	-4.53E-05	-4.67E-05
Reference result (phase b)	-4.62E-05	-3.14E-05
Calculated result (phase b)	-4.58E-05	-3.05E-05
Reference result (phase c)	-4.57E-05	7.74E-05
Calculated result (phase c)	-4.59E-05	7.76E-05

Figure 5.17: Calculated sensitivity values of voltage magnitude at bus 742 to the real component of bus current at bus 713 in comparison with the reference

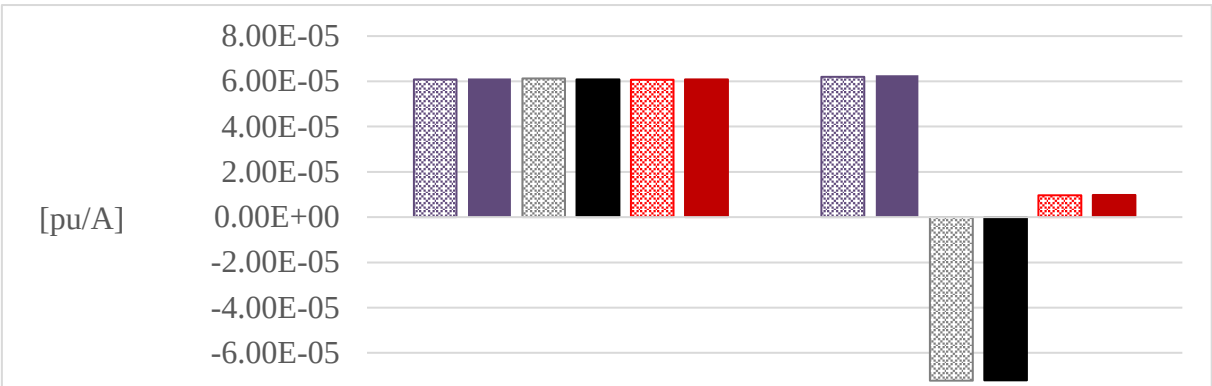

	Svii,1	Svii,2
Reference result (phase a)	6.08E-05	6.20E-05
Calculated result (phase a)	6.12E-05	6.28E-05
Reference result (phase b)	6.13E-05	-7.23E-05
Calculated result (phase b)	6.09E-05	-7.21E-05
Reference result (phase c)	6.07E-05	9.63E-06
Calculated result (phase c)	6.08E-05	9.85E-06

Figure 5.18: Calculated sensitivity values of voltage magnitude at bus 742 to the imaginary component of bus current at bus 713 in comparison with the reference

Subsequently, voltage angle sensitivity is examined at the unit of deg/A. Figure 5.19 depicts the comparison of voltage angle sensitivity values of the sensitivities *Sphiir*,1 and *Sphiir*,2. They indicate how wide the voltage angle alteration is at each phase of bus 742, which is altered in relation to the real component of sequence currents at bus 713. Figure 5.20 depicts the comparison of voltage angle sensitivity values of the sensitivities *Sphiii*,1 and *Sphiii*,2,

which indicate a change of the voltage angle at each phase of bus 742 in relation to the imaginary component of sequence currents at bus 713. The comparisons clearly show high accuracy in both magnitude and direction of the sensitivity values from the proposed method. The original values can be observed from the table inside each figure.

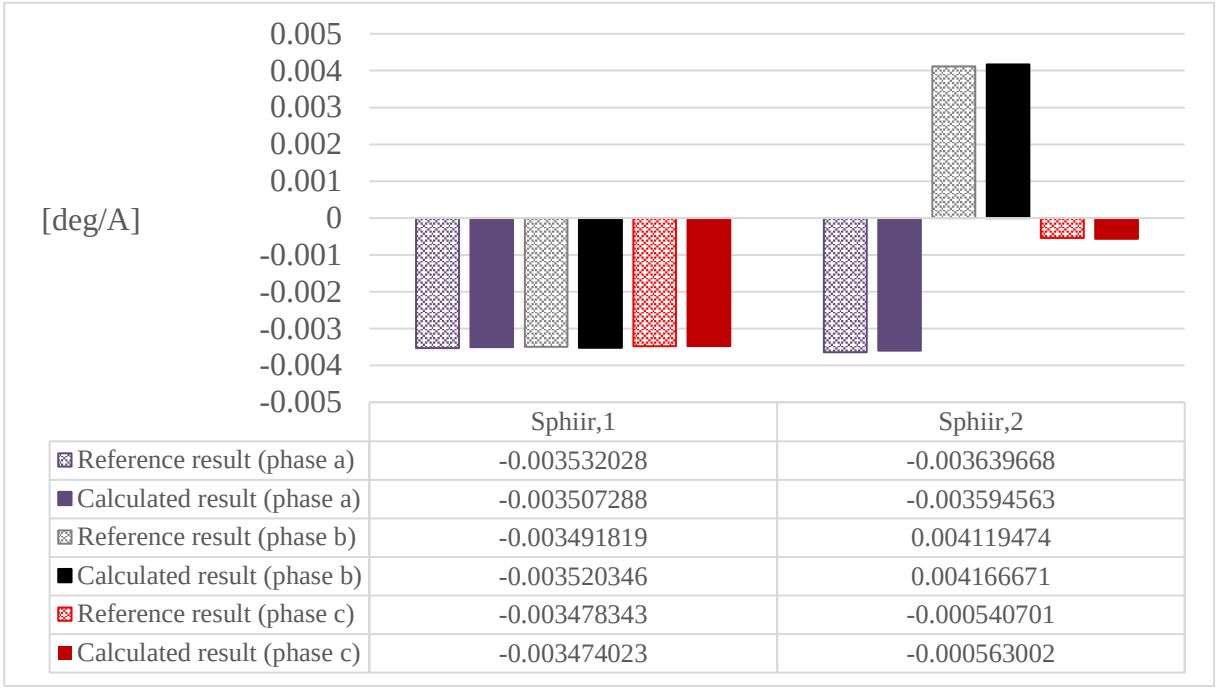

	Sphiir,1	Sphiir,2
Reference result (phase a)	-0.003532028	-0.003639668
Calculated result (phase a)	-0.003507288	-0.003594563
Reference result (phase b)	-0.003491819	0.004119474
Calculated result (phase b)	-0.003520346	0.004166671
Reference result (phase c)	-0.003478343	-0.000540701
Calculated result (phase c)	-0.003474023	-0.000563002

Figure 5.19: Calculated sensitivity values of voltage angle at bus 742 to the real component of bus current at bus 713 in comparison with the reference

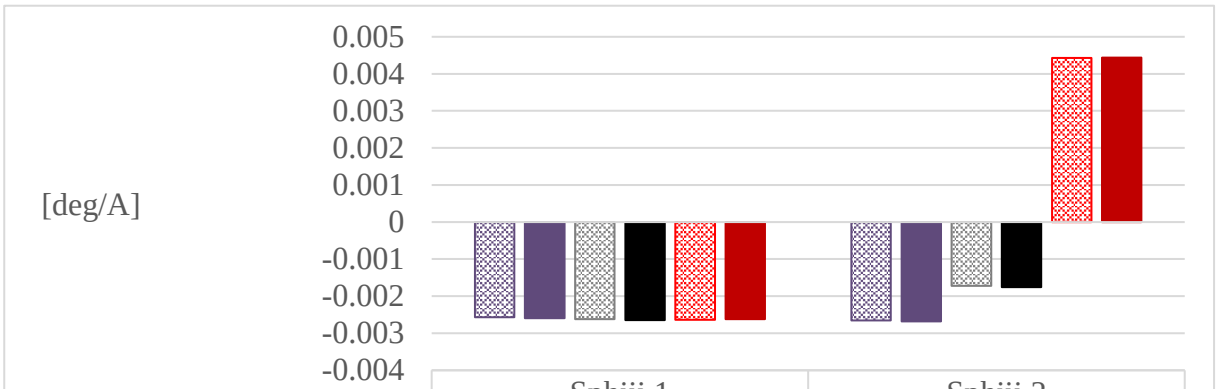

	Sphiii,1	Sphiii,2
Reference result (phase a)	-0.002566193	-0.002658697
Calculated result (phase a)	-0.002596378	-0.002677491
Reference result (phase b)	-0.002618065	-0.001723682
Calculated result (phase b)	-0.002645785	-0.001760329
Reference result (phase c)	-0.002634985	0.004430487
Calculated result (phase c)	-0.002623887	0.004436143

Figure 5.20: Calculated sensitivity values of voltage angle at bus 742 to the imaginary component of bus current at bus 713 in comparison with the reference

The comparisons of voltage magnitude and angle sensitivity in Figure 5.17 to Figure 5.20 prove that the sensitivity values calculated by the proposed method are highly accurate. The original calculated values are just slightly different from their reference.

The verification of the proposed method is subsequently conducted for the exemplified mesh grid. Same as the case of the modified IEEE 37-bus test feeder, the accuracy of all sensitivity types is analysed without zero sequence, because the connection to earth is unavailable in this grid configuration. Figure 5.21 depicts the mean of absolute percent differences of voltage sensitivity for this power grid. The mean of absolute percent differences of each sensitivity type is plotted in each column, which is determined from the difference of all sensitivity values of that sensitivity type from all phases in comparison to their reference from the classical method.

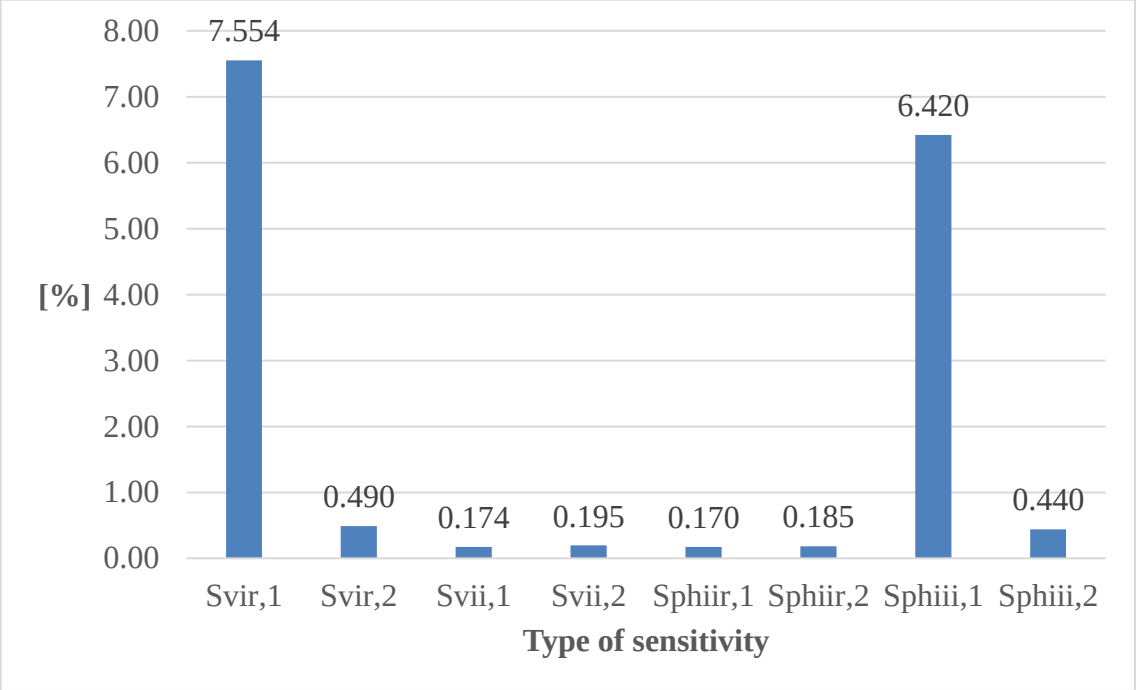

Figure 5.21: Illustration of mean absolute percent differences of sensitivity values in the exemplified mesh grid case

The chart in Figure 5.21 shows high accuracy of the results from the proposed method. The sensitivities *Svir*,1 and *Sphiii*,1 have a clearly higher mean difference than the others at 7.554% and 6.420%, respectively, but their impact is nonetheless low. This can happen because the original values of these sensitivity types are small numbers; and a slight difference of these values can look like a high difference when expressed as a percentage. The original sensitivity values are provided later in this section.

Before seeing the original sensitivity values, the percent differences, without absolute, of whole data are also presented to support the comparison in Figure 5.21. For this grid case, there are 100 sensitivity values for each sensitivity type, since there are 10 buses of concern.

Nonetheless, as the following results are provided as supplementary information, only the charts depicting the differences in the positive sequence are provided. The rest can be found in Appendix C.

Starting from the sensitivities of voltage magnitude, Figure 5.22 and Figure 5.23 demonstrate the charts of percent differences, respectively, in the case of sensitivity *Svir*,1 and *Svii*,1 in phase *a*, *b*, and *c*. As depicted in Figure 5.22, for phase *a*, *b*, and *c*, the mean values of the percent differences of the sensitivity *Svir*,1 for each phase are -11.258%, -4.394%, and -7.010%. Similarly, as depicted in Figure 5.23, for phase *a*, *b*, and *c*, the mean values of the percent differences of the sensitivity *Svii*,1 for each phase are -0.189%, -0.236%, and 0.098%. The mean for each sensitivity type is plotted in a dash line.

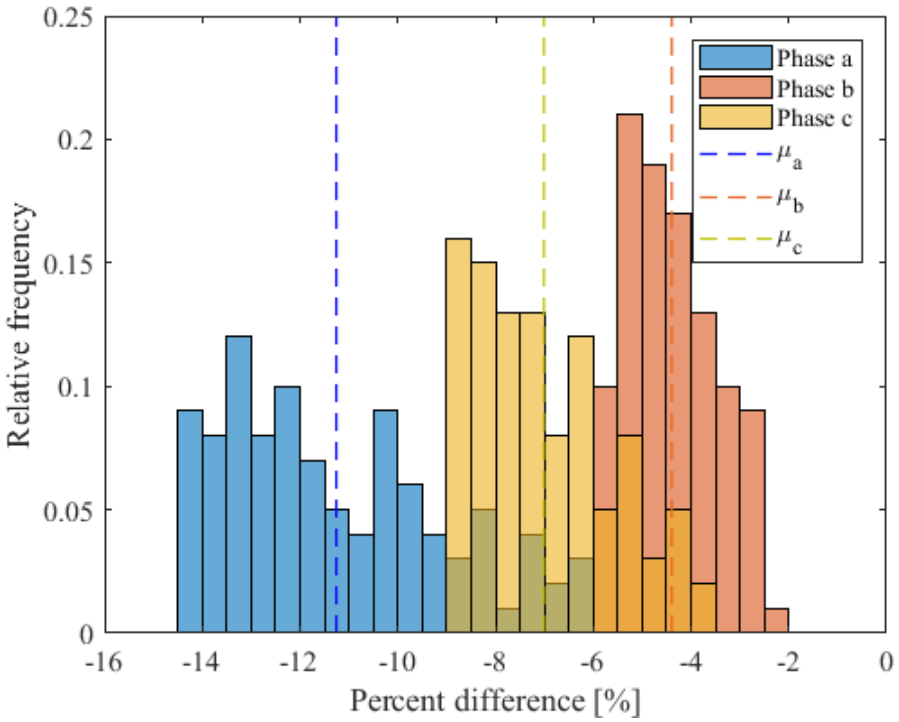

Figure 5.22: Histogram of the whole result differences in *Svir*,1 of the exemplified mesh grid

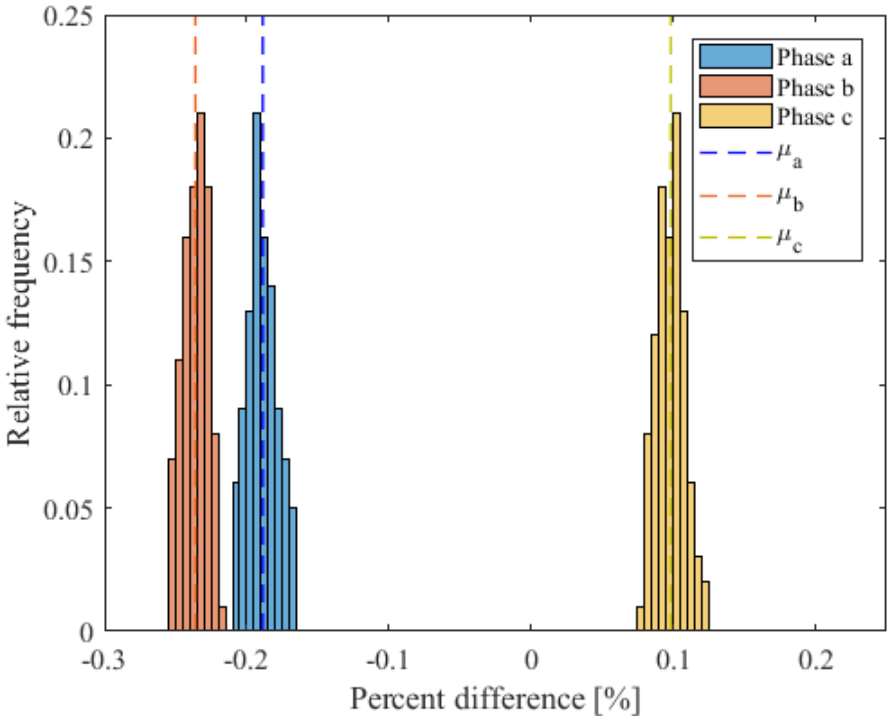

Figure 5.23: Histogram of the whole result differences in *Svii*,1 of the exemplified mesh grid

From Figure 5.22 and Figure 5.23, the sensitivities *Svir*,1 and *Svii*,1 at any phase are accurate. Although the mean in the case of *Svir*,1 at phase *a* reaches -11.258%, the original sensitivity values are relatively small. The impact is thus low.

Continuing with the sensitivities of voltage angle, Figure 5.24 and Figure 5.25 demonstrate the charts of percent differences, respectively, in the case of sensitivity *Sphiir*,1 and *Sphiii*,1 in phases *a*, *b*, and *c*. As demonstrated in Figure 5.24, for phases *a*, *b*, and *c*, the mean values of the percent differences of the sensitivity *Sphiir*,1 for each phase are 0.177%, 0.234%, and -0.099% respectively. Then, as demonstrated in Figure 5.25, for phase *a*, *b*, and *c*, the mean values of the percent differences of the sensitivity *Sphiii*,1 for each phase are 9.124%, 4.037%, and 6.100%.

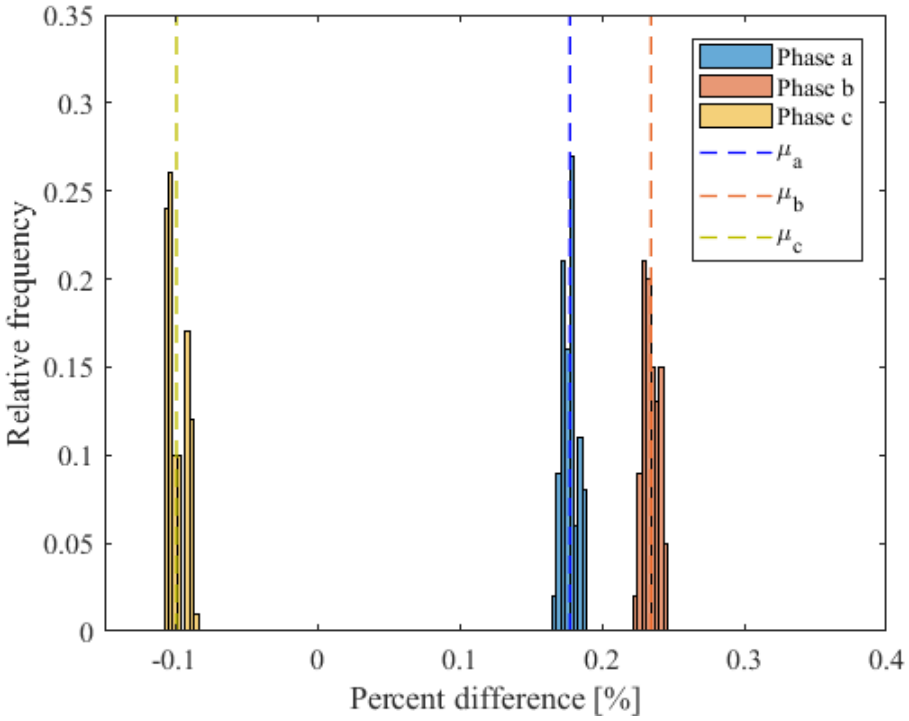

Figure 5.24: Histogram of the whole result differences in *Sphiir*,1 of the exemplified mesh grid

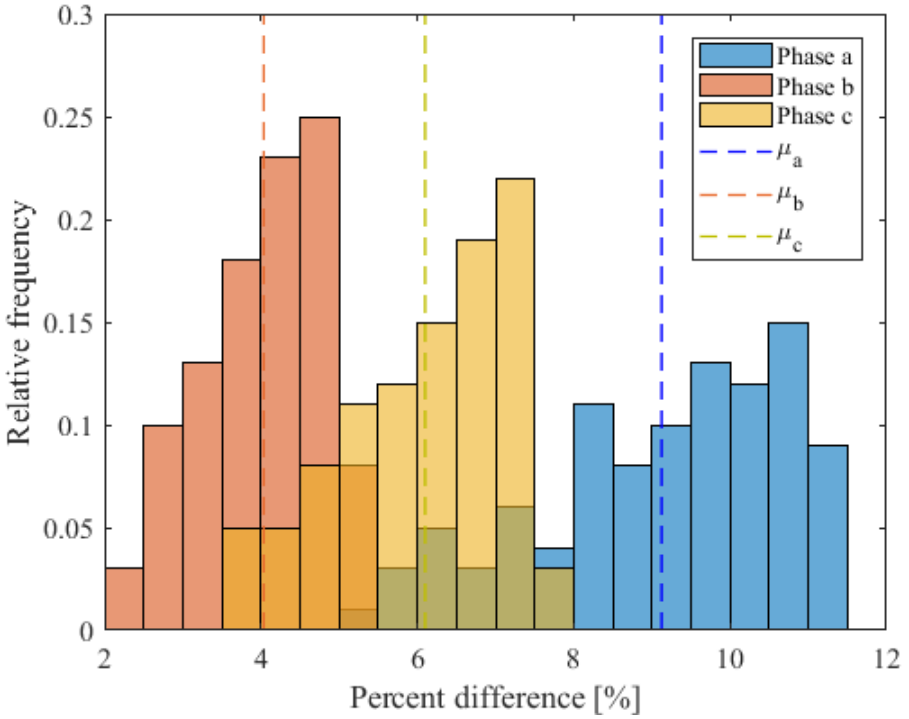

Figure 5.25: Histogram of the whole result differences in *Sphiii*,1 of the exemplified mesh grid

According to Figure 5.24 and Figure 5.25, the sensitivities *Sphiir*,1 and *Sphiii*,1 at any phase are obviously accurate. Only the mean in the case of *Sphiii*,1 at phase *a* is slightly higher than others at 9.124%. The impact of this difference is, however, still comparatively low, since the original sensitivity values are small. Additionally, as can be seen in Figure 5.22 to Figure 5.25, the distribution of the result differences from each phase is varied, as is the case of the modified IEEE 37-bus test feeder, since the sensitivity analysis is individually executed for each phase. Further analysis of the variation of the histograms is discussed later in this section.

At this point, the original sensitivity values are depicted. The self-sensitivity values at bus 104 of the exemplified mesh grid are selected for this discussion. Beginning with voltage magnitude sensitivity, the unit used for Figure 5.26 and Figure 5.27 is pu/A. The sensitivities *Svir*,1 and *Svir*,2 in Figure 5.26 indicate the extent to which the size of the voltage magnitude at each phase of bus 104 is altered in relation to the real component of sequence currents at its own bus. Likewise, the sensitivities *Svii*,1 and *Svii*,2 in Figure 5.27 express the change of the voltage magnitude at each phase of bus 104 in relation to the imaginary component of sequence currents at its own bus. The comparisons of the results show that high accuracy of the sensitivity values can be obtained from the proposed methods, as they are very close to their reference. The precision of the results is approximately 10^{-5} pu/A.

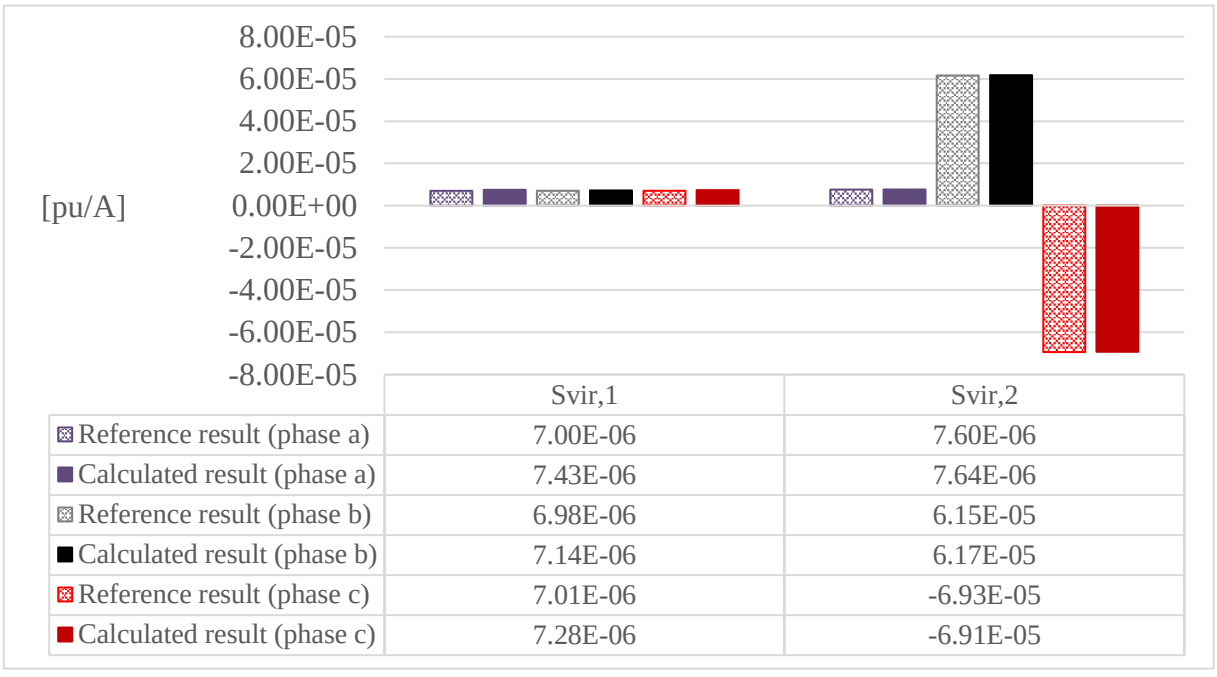

	Svir,1	Svir,2
Reference result (phase a)	7.00E-06	7.60E-06
Calculated result (phase a)	7.43E-06	7.64E-06
Reference result (phase b)	6.98E-06	6.15E-05
Calculated result (phase b)	7.14E-06	6.17E-05
Reference result (phase c)	7.01E-06	-6.93E-05
Calculated result (phase c)	7.28E-06	-6.91E-05

Figure 5.26: Calculated self-sensitivity values of voltage magnitude at bus 104 to the real component of bus current at its bus in comparison to the reference

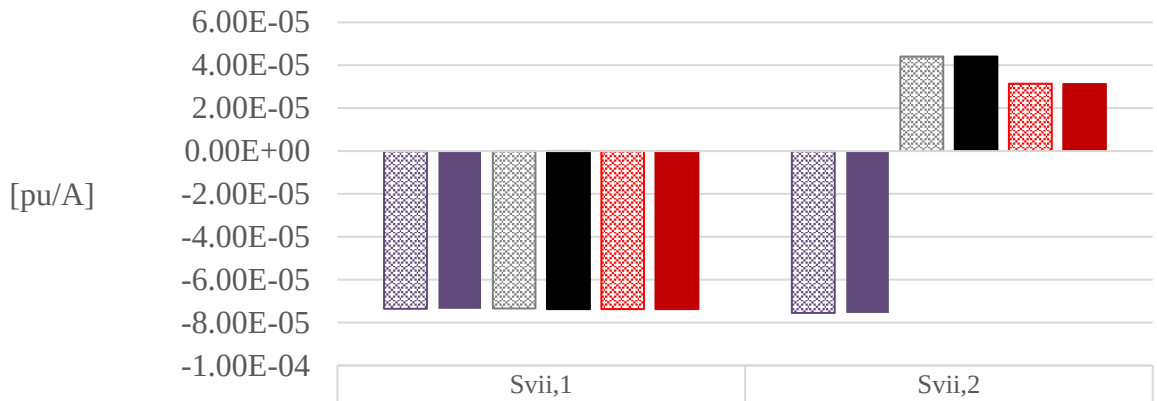

	Svii,1	Svii,2
Reference result (phase a)	-7.35E-05	-7.55E-05
Calculated result (phase a)	-7.36E-05	-7.55E-05
Reference result (phase b)	-7.35E-05	4.41E-05
Calculated result (phase b)	-7.36E-05	4.41E-05
Reference result (phase c)	-7.37E-05	3.15E-05
Calculated result (phase c)	-7.36E-05	3.13E-05

Figure 5.27: Calculated self-sensitivity values of voltage magnitude at bus 104 to the imaginary component of bus current at its bus in comparison to reference

Next, the self-sensitivity values of the voltage angle at bus 104 are investigated in Figure 5.28 and Figure 5.29, where the unit of deg/A is used. The comparison for the sensitivities *Sphiir*,1 and *Sphiir*,2 is illustrated in Figure 5.28, in which the impact of the real-component sequence currents can be observed. In addition, the impact of the imaginary-component sequence currents can be explored from *Sphiii*,1 and *Sphiii*,2 in Figure 5.29. Similar to the case of voltage magnitude, only slight differences of the results in comparison to their reference can be noticed.

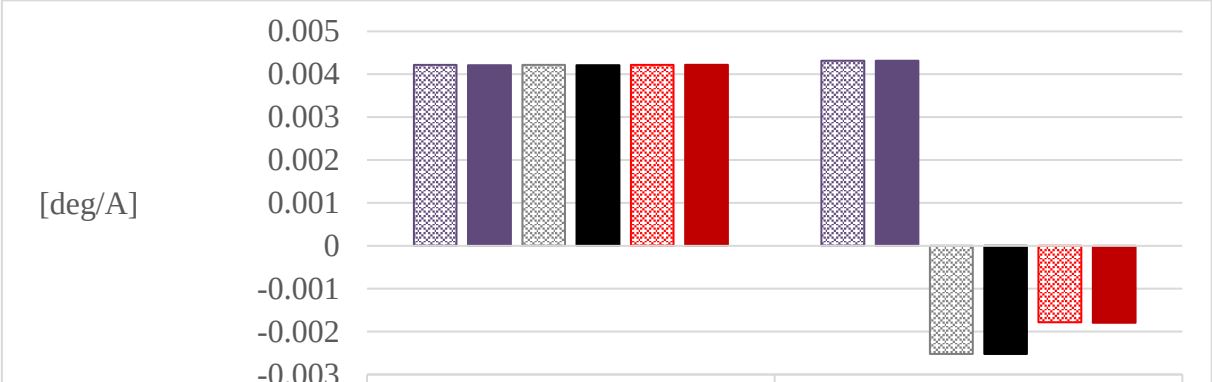

	Sphiir,1	Sphiir,2
Reference result (phase a)	0.004216629	0.004318471
Calculated result (phase a)	0.004209559	0.004317766
Reference result (phase b)	0.004218594	-0.002522656
Calculated result (phase b)	0.00420909	-0.002522334
Reference result (phase c)	0.004216589	-0.00178403
Calculated result (phase c)	0.004221011	-0.001793096

Figure 5.28: Calculated self-sensitivity values of voltage angle at bus 104 to the real component of bus current at its bus in comparison to the reference

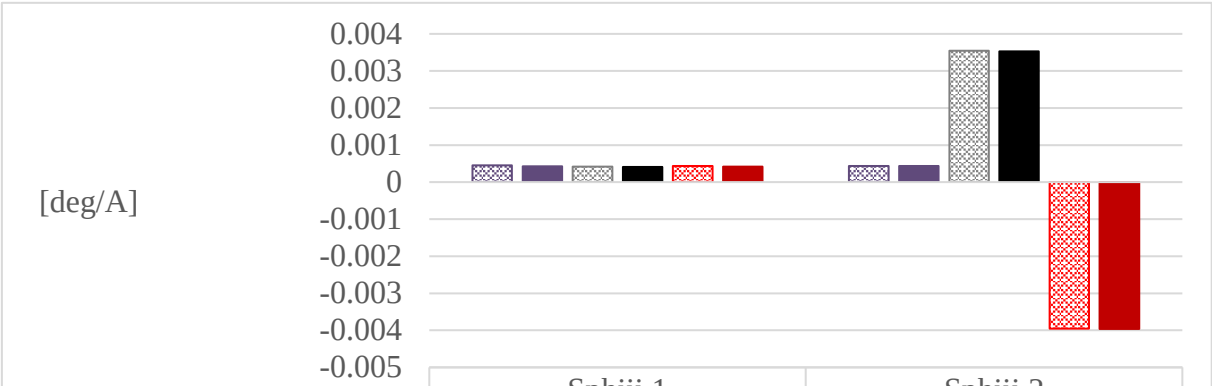

	Sphiii,1	Sphiii,2
Reference result (phase a)	0.000449226	0.000438209
Calculated result (phase a)	0.000424861	0.000436928
Reference result (phase b)	0.00041791	0.003541416
Calculated result (phase b)	0.000408311	0.003528907
Reference result (phase c)	0.000432652	-0.003953837
Calculated result (phase c)	0.000417282	-0.003964049

Figure 5.29: Calculated self-sensitivity values of voltage angle at bus 104 to the imaginary part of bus current at its bus in comparison to the reference

According to Figure 5.26 to Figure 5.29, the original calculated values slightly differ from their reference. That is, the sensitivity values from the proposed method are also accurate for the power grid with mesh topology.

Before moving to the next section, a point on the histograms illustrated in this section is worth discussing. The histograms, presented in Figure 5.13 to Figure 5.16 and Figure 5.22 to Figure 5.25, are not aligned together; and mostly they have shifted from each other. There are two factors to be considered here. The first factor is the results from the analysis themselves, and the second factor is the impact of the angle of phase voltages.

For the first factor, the sensitivity values depend directly on the operational state or scenario. Among phases, the unbalanced loads cause different loading and voltage magnitude, so the sensitivity values are slightly different between phases as well. The sensitivity values in this case study are also relatively small, in the range of $\times 10^{-5}$ to $\times 10^{-3}$. When the percent difference is determined to plot the histogram, the distribution of the sensitivity analysis in different phases can vary accordingly. For the second factor, the complex voltages directly play a role in the voltage sensitivity analysis process, as seen in Eqs. (4.33), (4.37), (4.48), and (4.52). To clarify, the shift among the distributions is further examined on the modified IEEE 37-bus test feeder case by adjusting the reference angle for the simulation. The angle is adjusted by adding ±30º, ±60º, and ±120º to the original reference angle, which is 0º, used in this case study. It must be noted that this further analysis focuses only on the overview of the response from the proposed analysis method, so only the histograms in the case of *Svir*,1 of are presented. Figure 5.30 to Figure 5.32 show the histograms for the case of ±30º, ±60º, and ±120º, respectively. The rest of the histograms can be found in Appendix E.

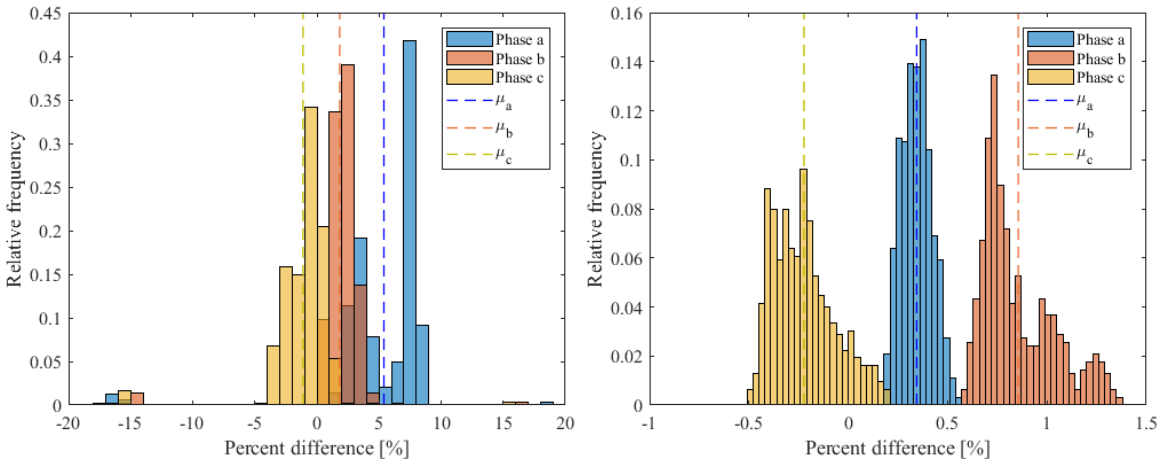

Figure 5.30: Histogram of the whole result differences in *Svir*,1 of the modified IEEE 37-bus test feeder case; (a) Reference angle -30º; (b) Reference angle +30º

To examine the impact of the phase shift, the plots in Figure 5.30 to Figure 5.32 are compared with Figure 5.13, which displays the original histograms for the sensitivity *Svir*,1. Accordingly, the comparison indicates that the phase angle affects the outcome of voltage sensitivity analysis, and the distribution of the histograms varies as the reference angle changes. In Figure 5.30(a) and Figure 5.30(b), for the case of ±30º, the histograms are clearly different from the histograms in Figure 5.13. However, in the case of ±60º and ±120º shown

in Figure 5.31 and Figure 5.32, the histograms of two from three phases and their mean are closely aligned, while that of a phase is separated, since the vectors in ±60º and ±120º cases are relevant to the vectors in the reference case. By considering adding angle ±120º first, the vectors of bus voltages are only shifted to replace the position of the adjacent phase. Meanwhile, the histograms in the case of adding ±60º have an inverse relationship to the case of ±120º. The vectors in the case of -60º are the negative of that of the case +120º, and the vectors in the case of +60º are the negative of that of the case -120º. Hence, the position, i.e. angle, of the vectors clearly affects the outcome of the sensitivity analysis. Lastly, this angle shift effect is also applicable to explain the variation of the histograms in the case of the exemplified mesh grid.

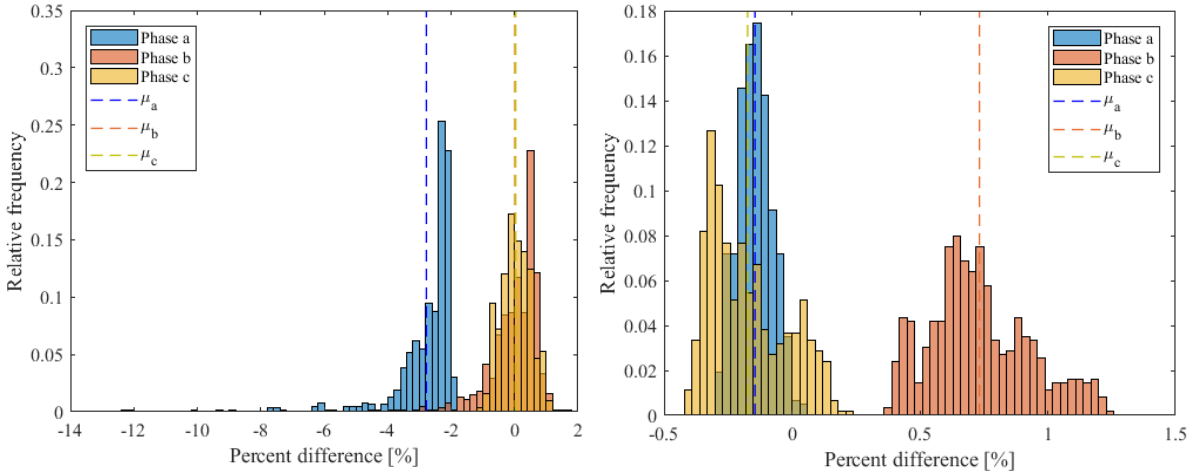

Figure 5.31: Histogram of the whole result differences in *Svir*,1 of the modified IEEE 37-bus test feeder case; (a) Reference angle -60º; (b) Reference angle +60º

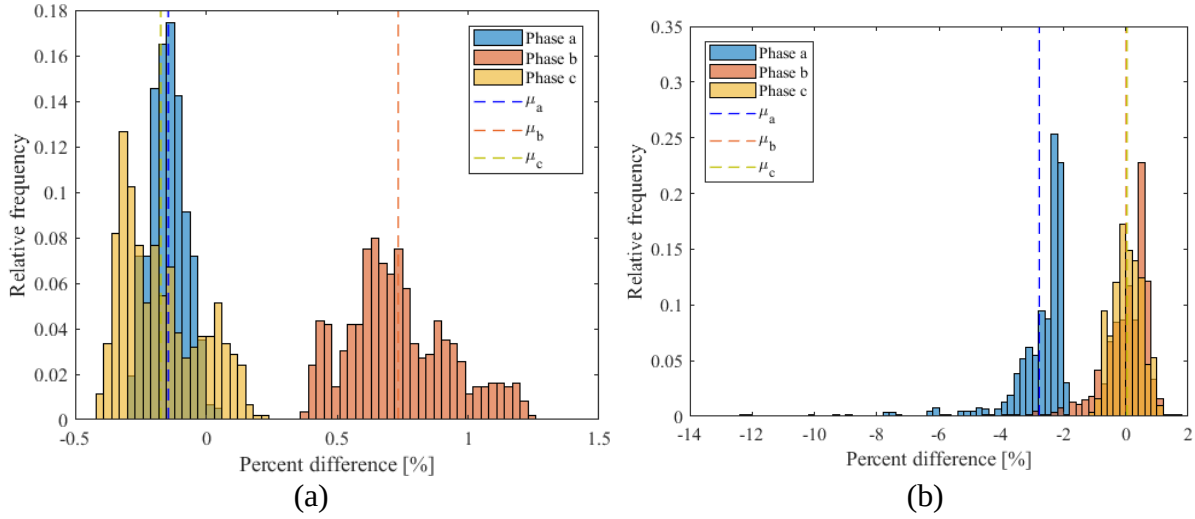

Figure 5.32: Histogram of the whole result differences in *Svir*,1 of the modified IEEE 37-bus test feeder case; (a) Reference angle -120º; (b) Reference angle +120º

The proposed method for voltage sensitivity analysis has been verified in this section for power grids in an unbalanced condition. The results are highly accurate for both radial and mesh grid topologies. In addition to the sensitivity values for the unbalanced condition, the proposed method also offers an alternative of voltage sensitivity analysis for the balanced grid condition. Other results with consideration of the balanced condition are examined in the next section to continue verifying the proposed method.

5.1.2.2 Results of Sensitivity Analysis in a Balanced Grid Condition

The method for voltage sensitivity analysis discussed in this thesis is also possible for a balanced grid condition. Thereby, the sensitivities of voltage magnitude and angle in relation to active and reactive powers – *Svp*, *Svq*, *Sphip*, and *Sphiq* – are analysed. A full description of each sensitivity type is provided in Table 5.2. To verify the proposed method for the balanced grid condition, the same grids used for the simulation under the unbalanced grid condition are employed in this section. Loads and generations in the power grids are set to be equal for all phases accordingly.

First, the modified IEEE 37-bus test feeder depicted in Figure 5.4 is investigated. The mean difference between results from the proposed method and the classical method in each sensitivity type is plotted in Figure 5.33, which shows the accuracy of the proposed method. The mean of the absolute percent differences is small for all sensitivity types in this case.

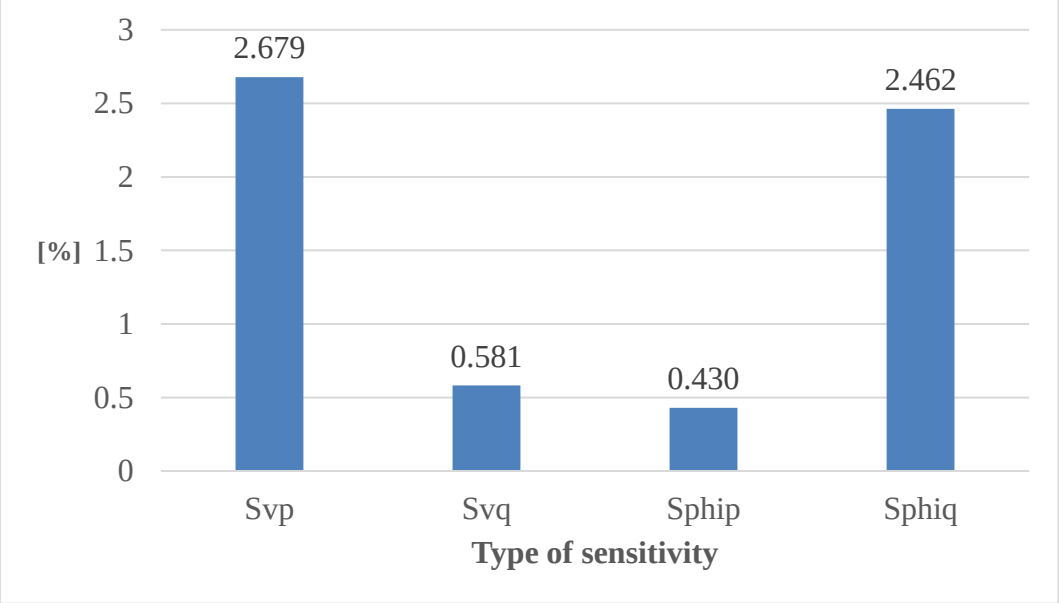

Figure 5.33: Illustration of mean absolute percent differences of sensitivity values in the modified IEEE 37-bus test feeder case in balanced condition

Subsequently, the percent differences, without absolute, of whole data are stated to supplement the accuracy of the proposed method. The result differences are plotted in a histogram, as illustrated in Figure 5.34 and Figure 5.35. The mean values of result differences for all sensitivities *Svp*, *Svq*, *Sphip*, and *Sphiq* are 2.630%, 0.550%, 0.306%, and -2.300% respectively, and are plotted in a dash line. Thus, all sensitivity types give accurate outcomes. The mean values are close to zero. Additionally, the sensitivity analysis results from the proposed method can be observably paired. The characteristics of the results from *Svp* and *Sphiq* displayed in Figure 5.34 are similar because they are based on the resistance of the bus impedance parameters, as shown in Eqs. (4.77) and (4.98). Likewise, the results from *Svq* and *Sphip* displayed in Figure 5.35 have similar characteristics, since both of them are based on the reactance of the bus impedance parameters as provided in Eqs. (4.83) and (4.92). However, the mean values of the sensitivities *Svp* and *Sphiq* are comparatively higher than that of the sensitivities *Svq* and *Sphip*, since the mean of absolute percent differences of the reactances is higher than that of the resistances. Their sensitivity values are also much smaller, consequently affecting the calculation of percent differences.

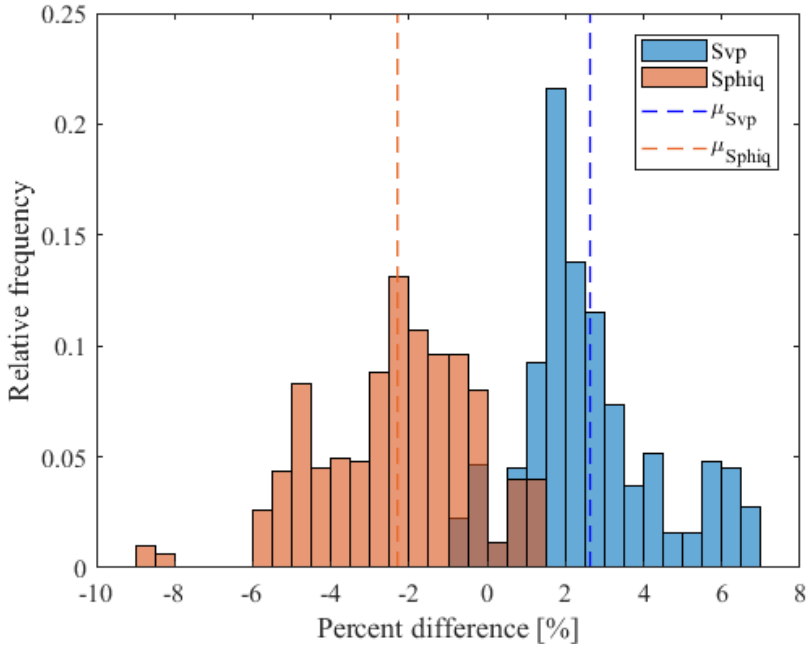

Figure 5.34: Histogram of the whole result differences in *Svp* and *Sphiq* of the modified IEEE 37-bus test feeder case

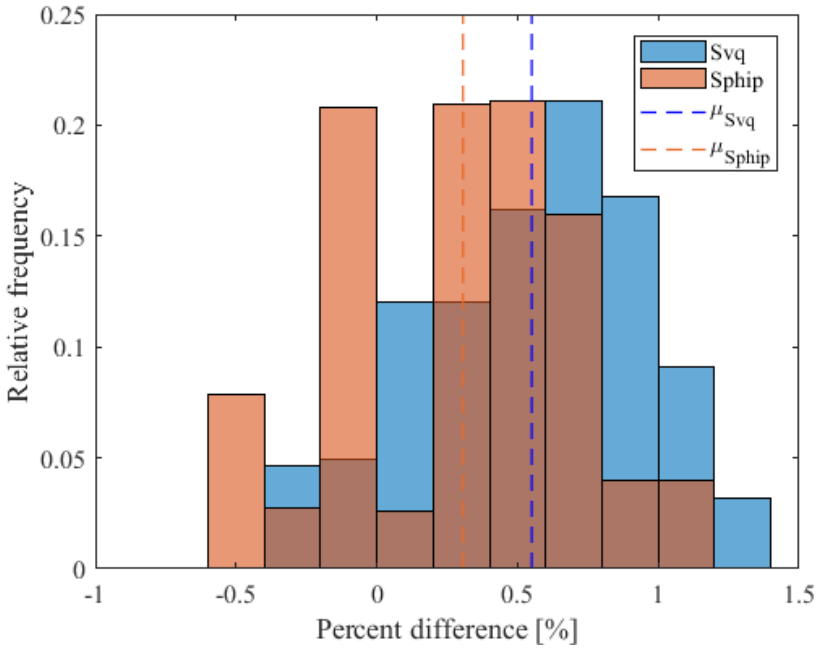

Figure 5.35: Histogram of the whole result differences in *Svq* and *Sphip* of the modified IEEE 37-bus test feeder case

Identical to the verification in the unbalanced grid condition, original sensitivity values are demonstrated in addition to the mean difference. The comparison of voltage magnitude sensitivities *Svp* and *Svq* is portrayed in Figure 5.36. The plotted sensitivity values are self-sensitivity of voltage magnitude at bus 713 in relation to active and reactive powers at its own bus. The units are given together with their name under each respective column. The unit of *Svp* is pu/MW, and the unit of *Svq* is pu/Mvar. Both calculated sensitivity values from the proposed method are noticeably close to their reference. In this grid case, the reactive power has more impact on voltage magnitude than the active power, because the reactance is dominant.

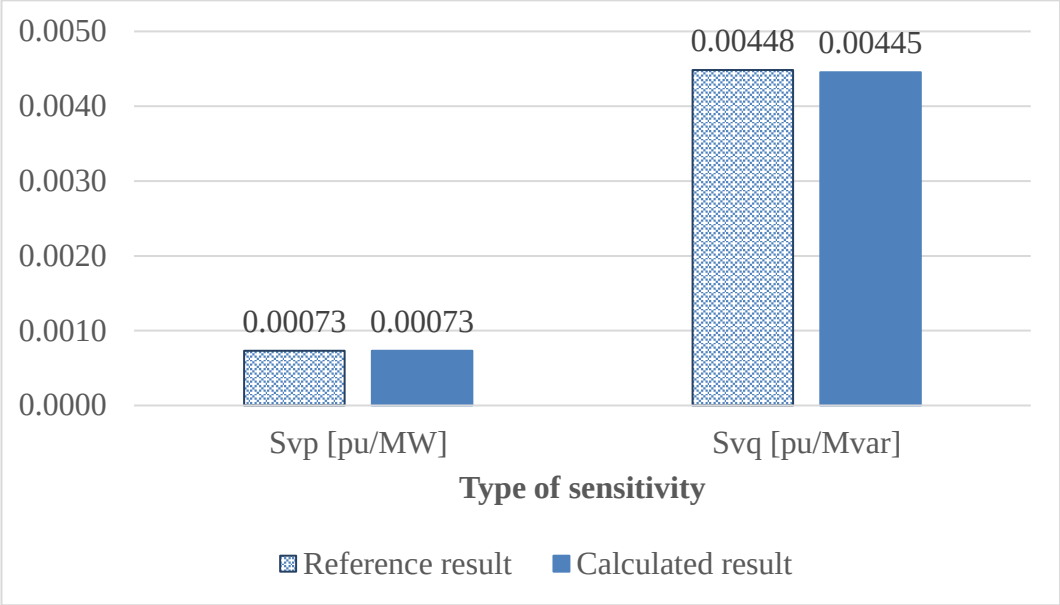

Figure 5.36: Calculated sensitivity values of voltage magnitude at bus 713 in relation to active and reactive powers at its bus in comparison to their reference

The comparison of voltage angle sensitivities *Sphip* and *Sphiq* is then depicted in Figure 5.37. Self-sensitivity is still considered. The calculated sensitivity values of the voltage angle at bus 713 in relation to active and reactive powers at its own bus are plotted together with their reference. The unit of *Sphip* is deg/MW, and the unit of *Sphiq* is deg/Mvar. They are shown with their name under each respective column. Obviously, both calculated angle sensitivity values from the proposed method are precise. Since reactance is dominant in this grid case, the voltage angle is more sensitive to the active power [231].

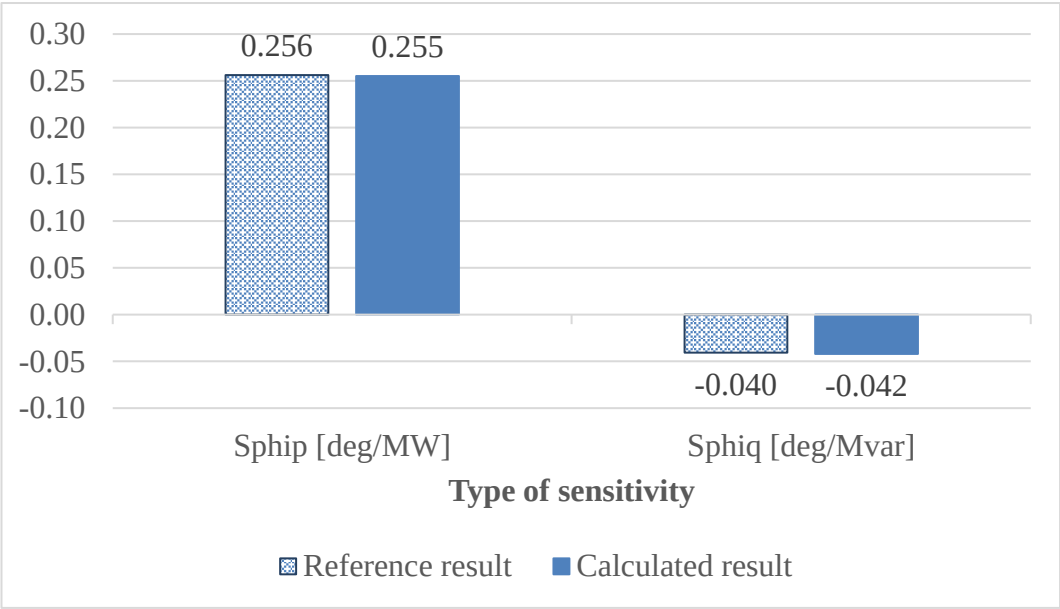

Figure 5.37: Calculated sensitivity values of voltage angle at bus 713 in relation to active and reactive powers at its bus in comparison to their reference

The accuracy and some examples of voltage sensitivity values in radial grid topology have been presented. Next, the proposed method is verified with mesh grid topology. The exemplified mesh grid depicted in Figure 5.5 is investigated accordingly. The mean of absolute percent differences of the calculated sensitivity values from the proposed method is plotted in Figure 5.38.

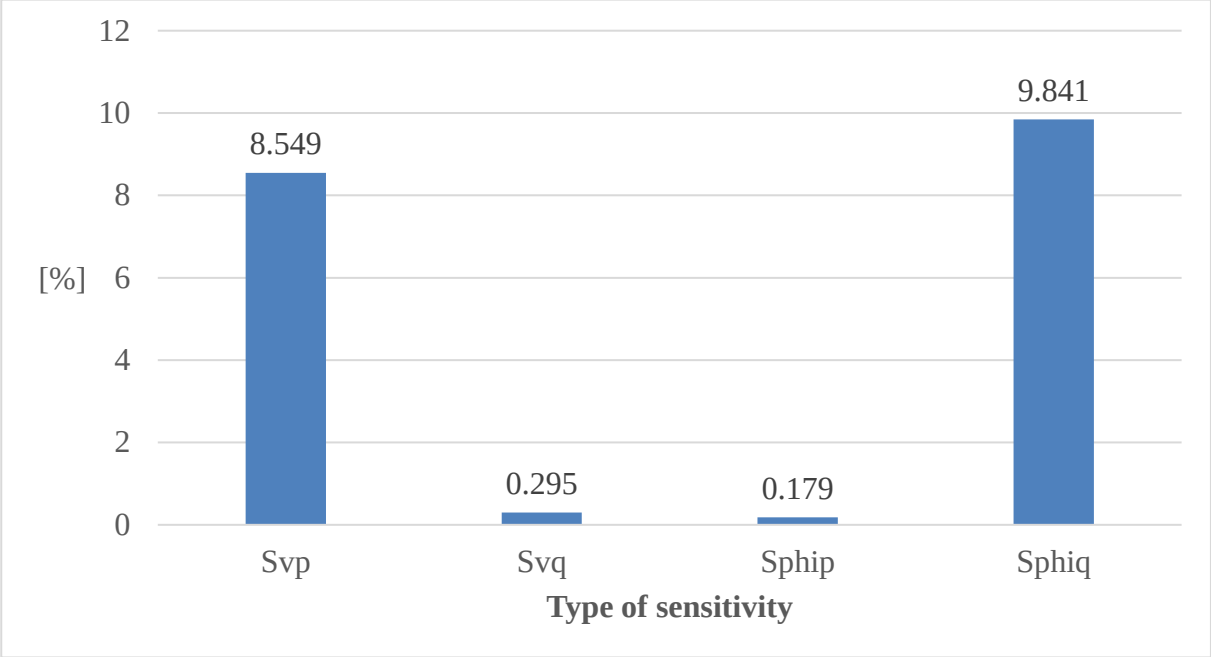

Figure 5.38: Illustration of mean absolute percent differences of sensitivity values in the exemplified mesh grid case in the balanced condition

Svp and *Sphiq* have a relatively higher difference than the other two sensitivities. Stated in Eqs. (4.77) and (4.98), both *Svp* and *Sphiq* are proportional to the same entity, which is the resistive part of the bus impedance parameters. Hence, a similar shape of the result distribution in their sensitivity analysis can be expected. In addition, the sensitivity values in this grid case is very small. A slight deviation of the number can lead to a high number in percentage terms.

Next, to support this verification, the percent differences, without absolute, of whole data are explored. The sensitivities *Svp* and *Sphiq* are portrayed in Figure 5.39, while the sensitivities *Svq* and *Sphip* are portrayed in Figure 5.40. For this grid case, these sensitivity types are plotted separately, because their distribution varied significantly. They cannot be explored when they all are shown together. According to Figure 5.39 and Figure 5.40, the mean of sensitivities *Svp*, and *Sphiq* is 8.549% and -9.841%, respectively. The mean of sensitivities *Svq*, and *Sphip* is 0.295% and 0.179%.

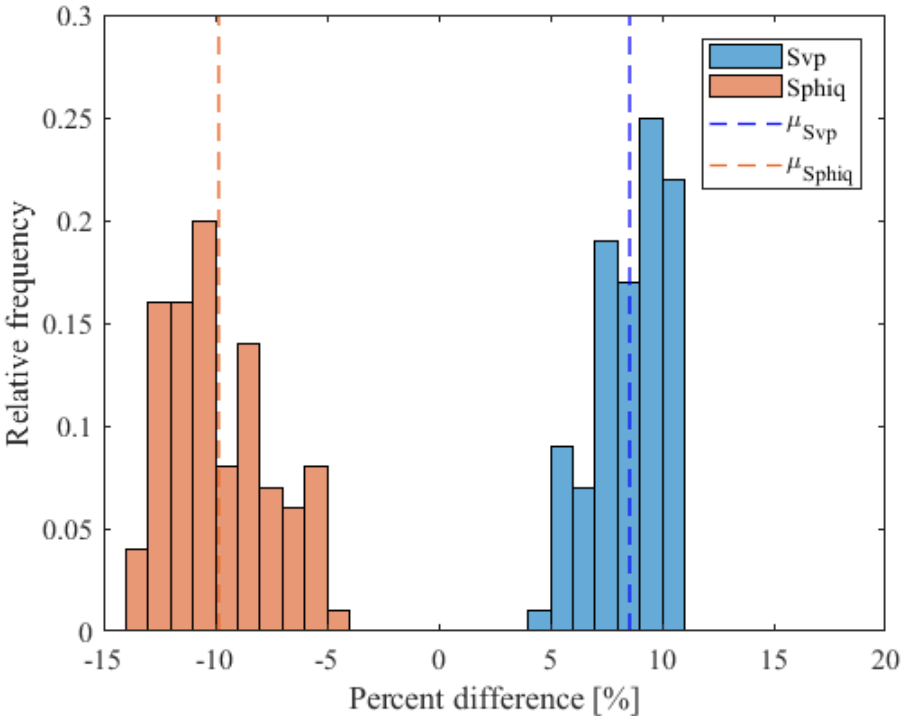

Figure 5.39: Histogram of the whole result differences in *Svp* and *Sphiq* of the exemplified mesh grid case

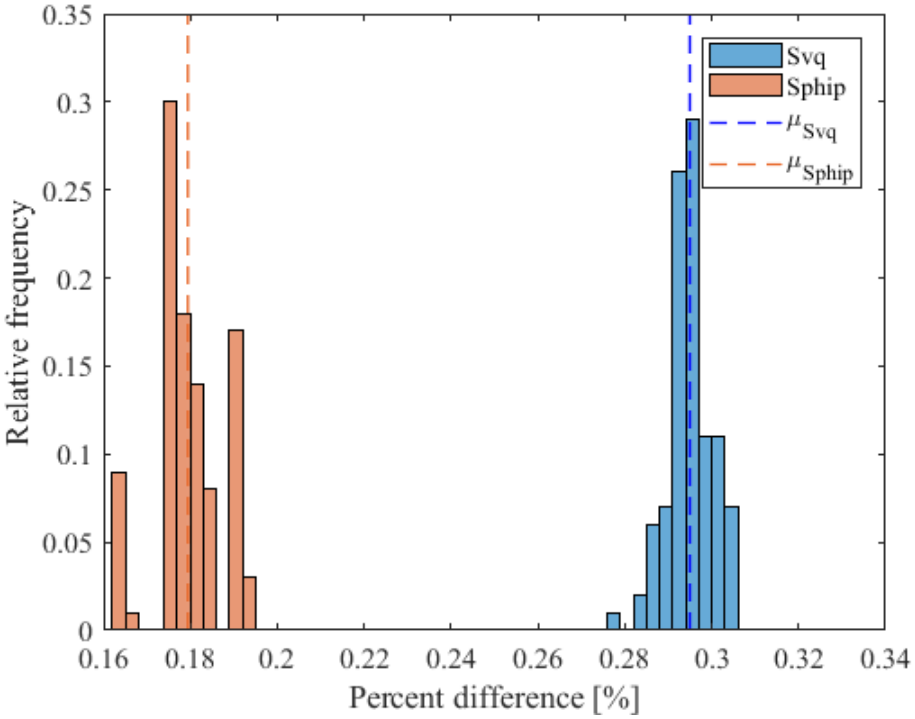

Figure 5.40: Histogram of the whole result differences in *Svq* and *Sphip* of the exemplified mesh grid case

The characteristics of the results from *Svp* and *Sphiq* are similar, because they are based on the resistance of the bus impedance parameters, as shown in Eqs. (4.77) and (4.98). Likewise, the results from *Svq* and *Sphip* have similar characteristics, since both of them are based on the reactance of the bus impedance parameters as provided in Eqs. (4.83) and (4.92). However, the mean values of the sensitivities *Svp* and *Sphiq* are higher than that of the sensitivities *Svq* and *Sphip*. This reflects the higher accuracy of the reactances over the resistances. Additionally, the sensitivity values of *Svp* and *Sphiq* are much smaller, consequently affecting the calculation of relative differences.

As an example, the original sensitivity values are thus presented together with the mean difference to clarify the small number issue. Figure 5.41 illustrates the comparison of voltage magnitude sensitivities *Svp* and *Svq*. The sensitivity values of voltage magnitude at bus 109 in relation to active and reactive powers at bus 104 are plotted. The units are given together with their name under each respective column, at which pu/MW is the unit of *Svp*, and pu/Mvar is the unit of *Svq*. The calculated sensitivity values of *Svp* and *Svq* from the proposed method are visibly close to their reference. As the reactance is more dominant in this grid, the reactive power has more impact on voltage magnitude than the active power.

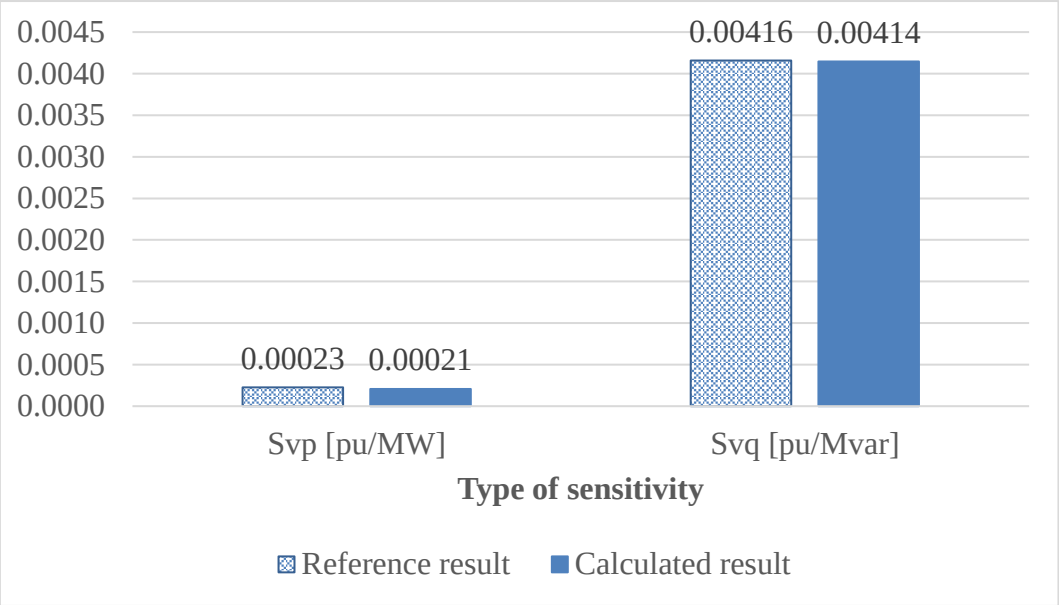

Figure 5.41: Calculated sensitivity values of voltage magnitude at bus 109 in relation to active and reactive powers at bus 104 in comparison to their reference

Regarding to the *Svp* issue in Figure 5.38, the sensitivity *Svp* is 0.00021 pu/MW from the proposed method and 0.00023 pu/MW from the reference in Figure 5.41. That is, though the mean difference is 8.549%, it is within the range of $\times 10^{-4}$ to $\times 10^{-5}$ pu/MW, which is relatively insignificant.

Next, the comparison of voltage angle sensitivities *Sphip* and *Sphiq* is portrayed in Figure 5.42. The calculated sensitivity values of the voltage angle at bus 109 in relation to active and reactive powers at bus 104 are plotted together with their reference. The unit of *Sphip* is deg/MW, and the unit of *Sphiq* is deg/Mvar. Obviously, the calculated angle sensitivity values from the proposed method are precise in this example. According to the chart, the voltage angle is more sensitive to the active power, complying with the characteristics of this reactance-dominant grid.

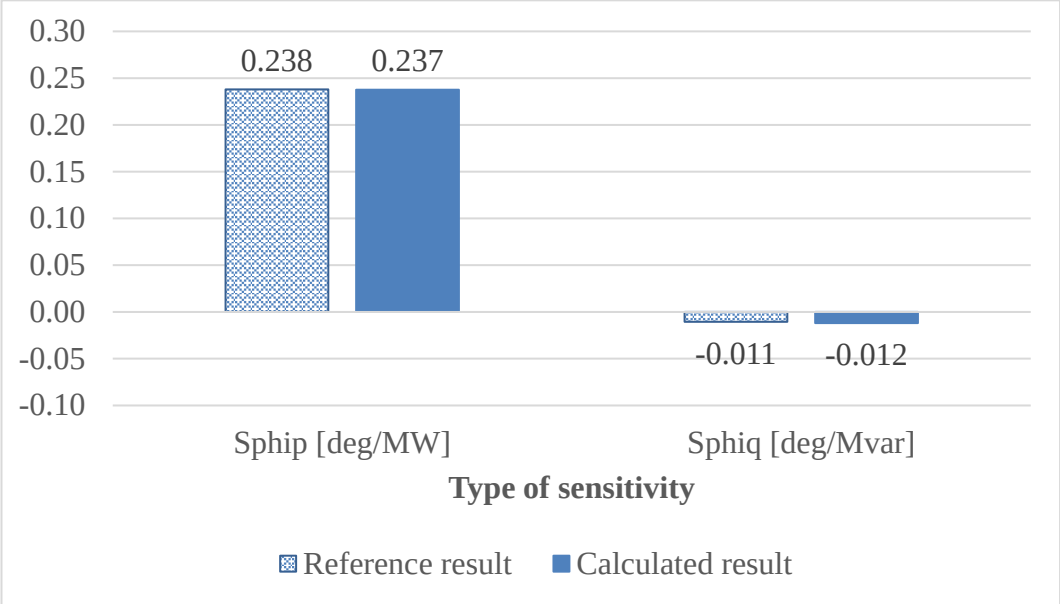

Figure 5.42: Calculated sensitivity values of voltage angle at bus 109 in relation to active and reactive powers at bus 104 in comparison to their reference

Concerning the *Sphiq* issue in Figure 5.38, the sensitivity *Sphiq* is -0.011 deg/Mvar from the reference and -0.012 deg/Mvar from the proposed method in Figure 5.42. This means that although the mean difference is 9.841%, it is within the range of $\times 10^{-2}$ to $\times 10^{-3}$ deg/Mvar, which is also relatively insignificant.

In this section, the proposed method for voltage sensitivity analysis has been verified by simulations of the entire grid case, in which radial and mesh MV grids are investigated. The unbalanced and balanced grid conditions are both taken into account. The verification indicates that the proposed method allows high accuracy in voltage sensitivity analysis by using only measurement data of bus voltages and currents. As the next step, measurement errors are considered to exist in measured bus voltages and currents. The response of the proposed method to measurement errors is examined in the next section.

5.1.3 Impact of Measurement Errors

In this section, the input data for performing voltage sensitivity analysis in Section 5.1.2 are further employed for simulations in both unbalanced and balanced grid conditions. To investigate the impact of measurement errors on the proposed method, five levels of 0.2%, 0.4%, 0.6%, 0.8%, and 1.0% TVE have been added to the initial input data that contain 0% TVE. The results from these five levels of TVE are subsequently analysed. For the unbalanced condition, the mean of absolute percent differences of voltage magnitude and angle sensitivities in relation to sequence currents are compared. Identical to the verification in Section 5.1.2, the mean difference is the comparison between the calculated values from the proposed method and the reference from DIgSILENT PowerFactory. The following results in this experiment are demonstrated for both the modified IEEE 37-bus test feeder and the exemplified mesh grid sequentially. Figure 5.43 and Figure 5.44 portray the investigation in the case of voltage magnitude sensitivities *Svir*,1 and *Svir*,2 of the two grids.

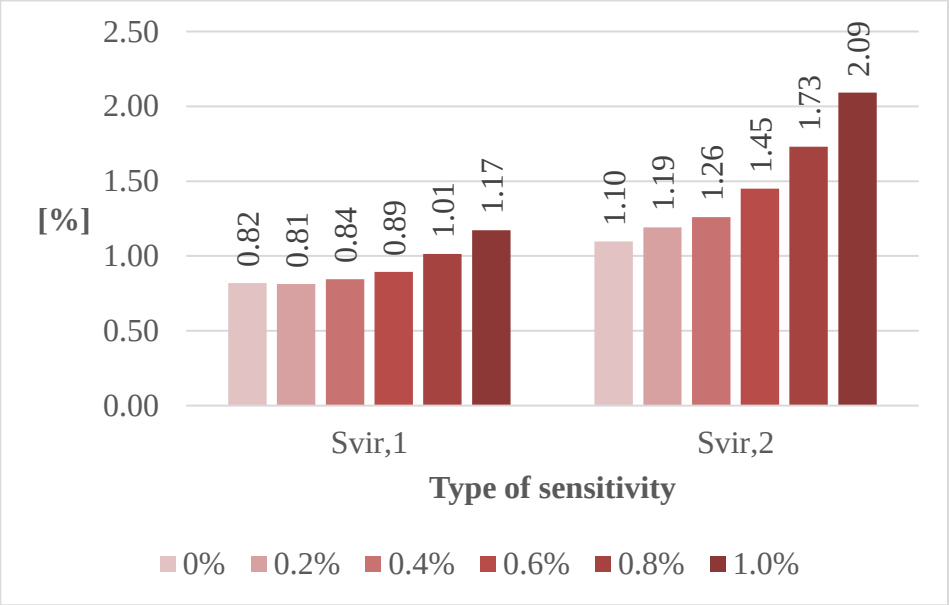

Figure 5.43: Mean values of absolute differences of *Svir* in the modified IEEE 37-bus test feeder with a different TVE

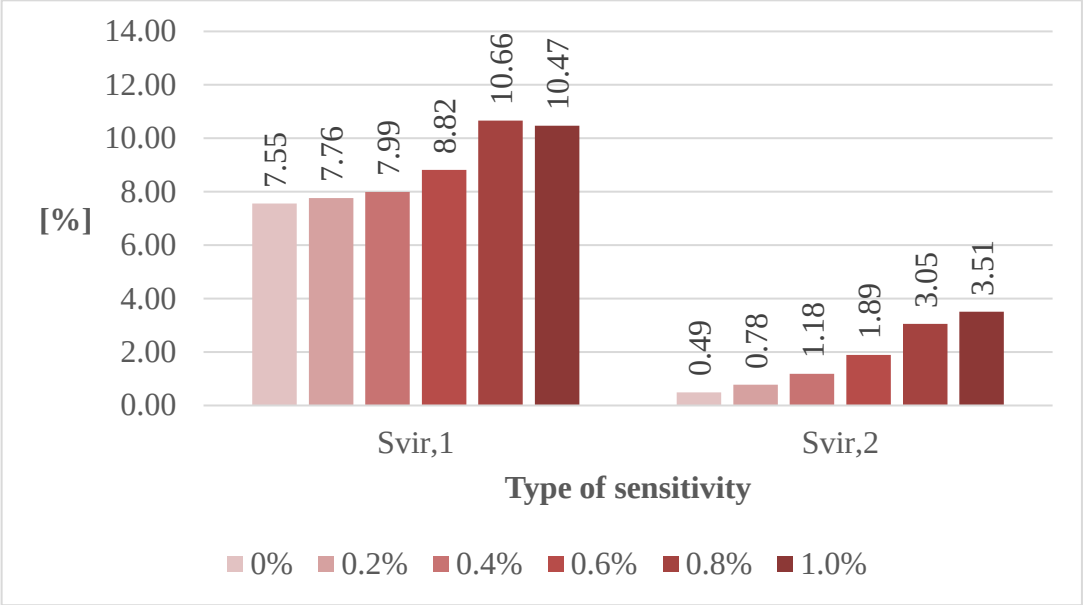

Figure 5.44: Mean values of absolute differences of *Svir*,1 in the exemplified mesh grid with a different TVE

Figure 5.45 and Figure 5.46 portray the investigation in the case of voltage magnitude sensitivities *Svii*,1 and *Svii*,2 in relation to the imaginary component of sequence currents.

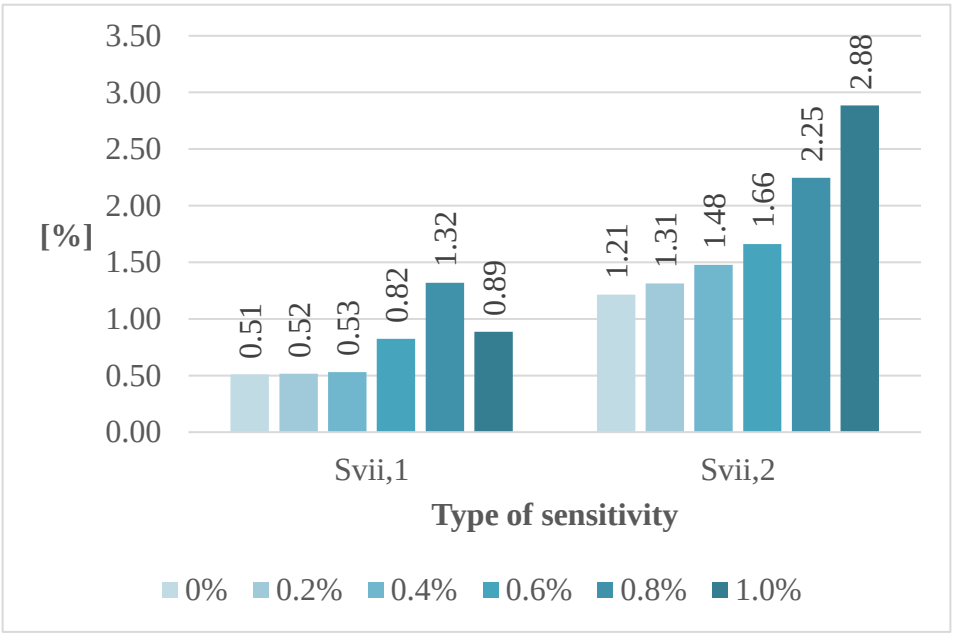

Figure 5.45: Mean values of absolute differences of *Svii*,1 in the modified IEEE 37-bus test feeder with a different TVE

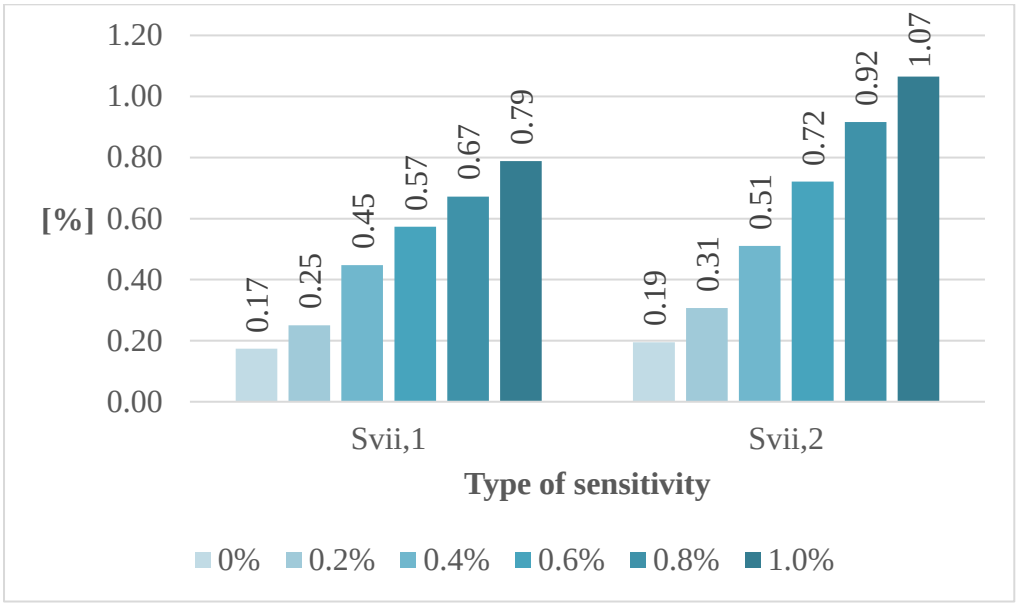

Figure 5.46: Mean values of absolute differences of *Svii*,1 in the exemplified mesh grid with a different TVE

Obviously, the mean of absolute percent differences increases as the TVE increases. Nevertheless, this error is still low when the sensitivity values are used, since the sensitivity values from these two grids are at the range around $\times 10^{-5}$ pu/A.

The same experiment procedure was conducted to investigate voltage angle sensitivities *Sphiir*,1 and *Sphiir*,2 in relation to the real component of the sequence current. These sensitivities are depicted in Figure 5.47 and Figure 5.48.

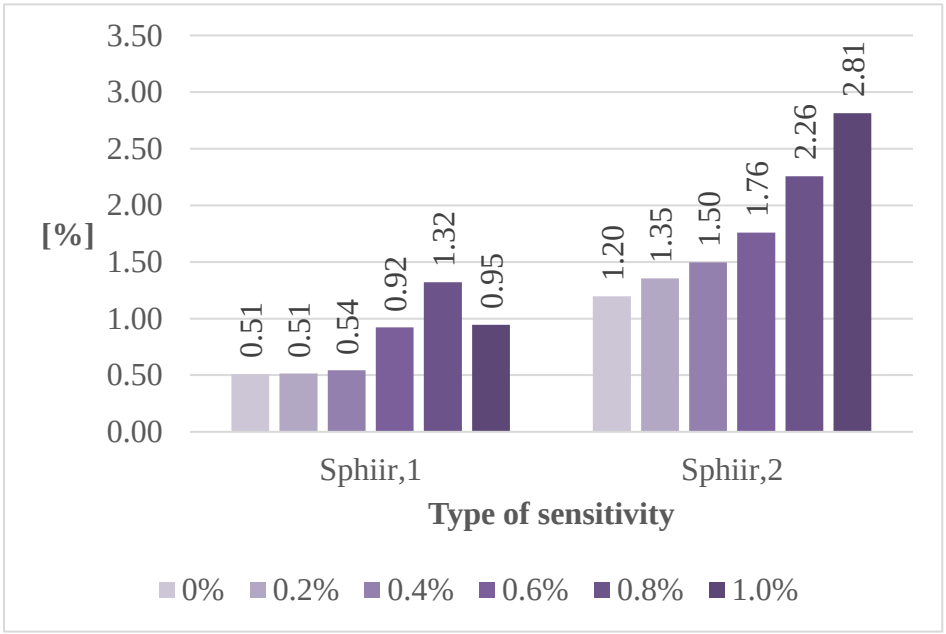

Figure 5.47: Mean values of absolute differences of *Sphiir*,1 in the modified IEEE 37-bus test feeder with a different TVE

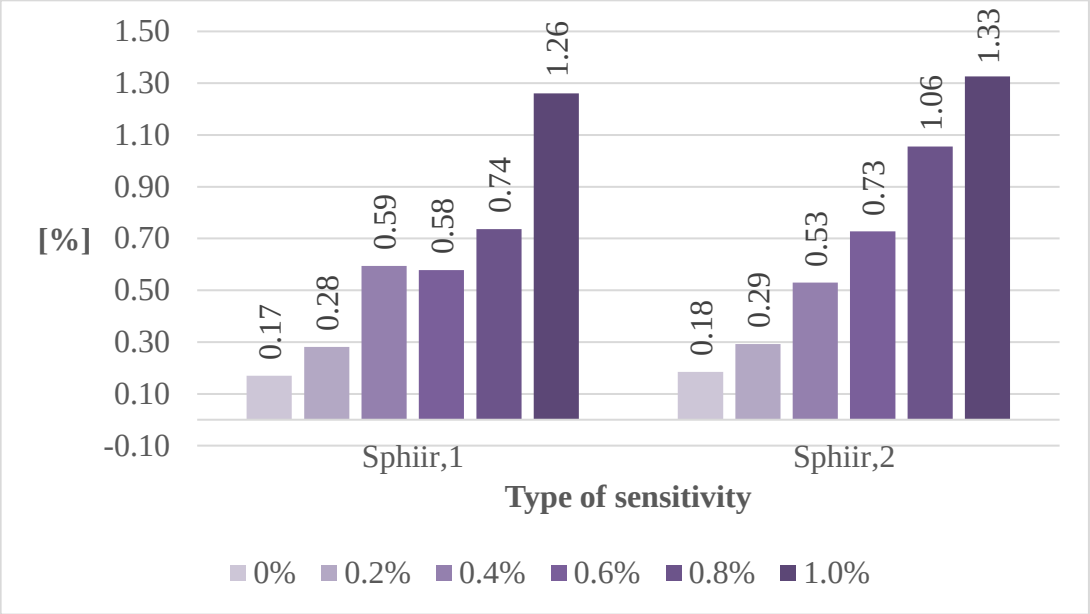

Figure 5.48: Mean values of absolute differences of *Sphiir*,1 in the exemplified mesh grid with a different TVE

Figure 5.49 and Figure 5.50 depict the investigation of voltage angle sensitivities *Sphiii*,1 and *Sphiii*,2 in relation to the imaginary component of sequence current.

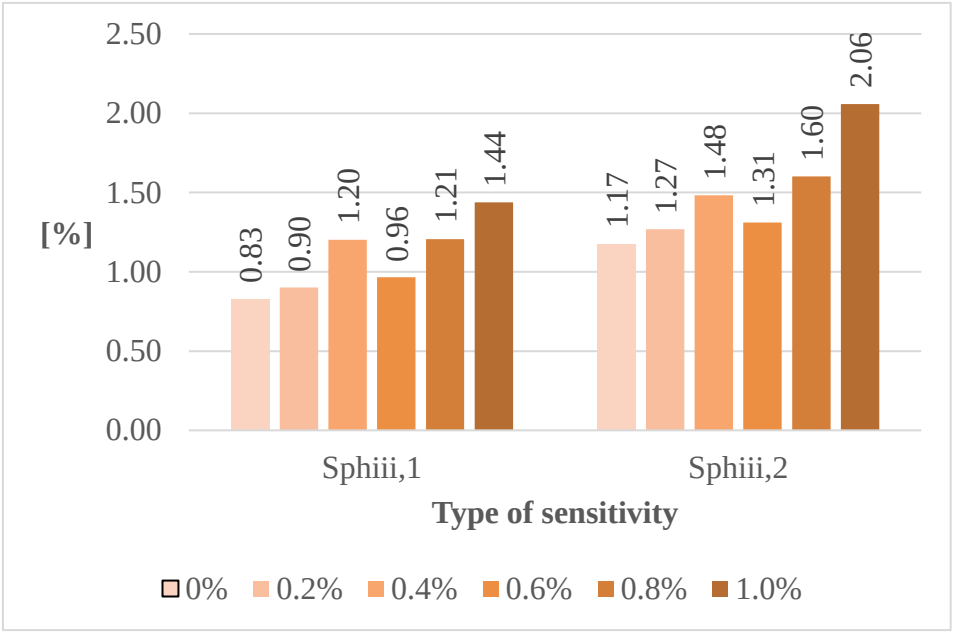

Figure 5.49: Mean values of absolute differences of *Sphiii*,1 in the modified IEEE 37-bus test feeder with a different TVE

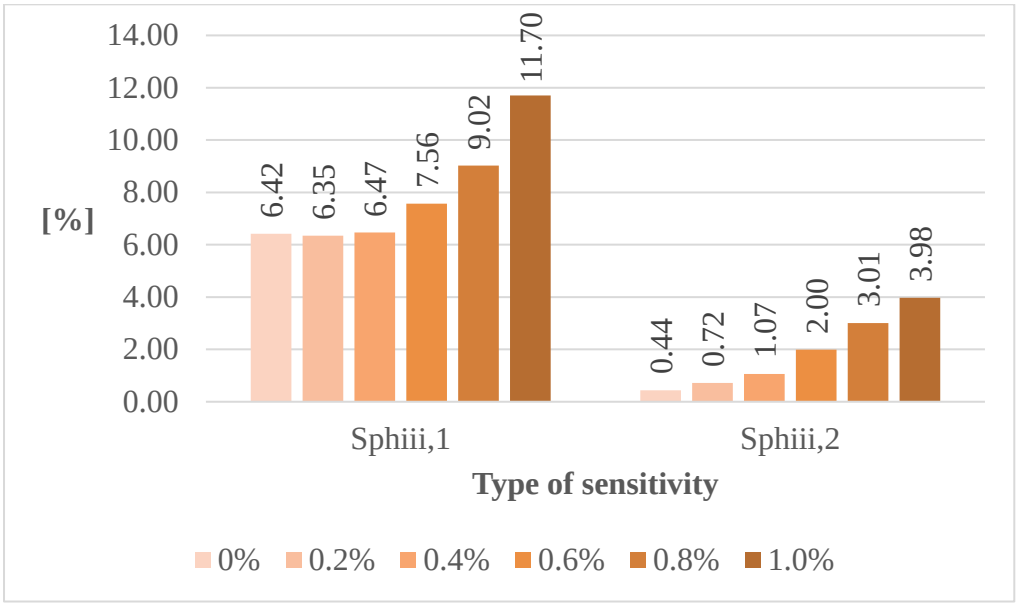

Figure 5.50: Mean values of absolute differences of *Sphiii*,1 in the exemplified mesh grid with a different TVE

As happened in the case of voltage magnitude sensitivities, the mean of absolute percent differences increased in conjunction with the increase of the TVE. The differences in the case of *Svir*,1 and *Svir*,2 have similar characteristics to the case of *Sphii*,1 and *Sphii*,2. Also, the differences in the case of *Svii*,1 and *Svii*,2 have similar characteristics to the case of *Sphir*,1 and *Sphir*,2. This complies with the proposed method for voltage sensitivity analysis, since they share the same relationship between the bus impedance parameters and the complex voltage in their calculation process, which can be explored from the pair of Eqs. (4.33) and (4.53) as well as the pair of Eqs. (4.37) and (4.48) in Chapter 4.

The results from the experiments show that the proposed method can still produce trustful sensitivity analysis when the TVE is in the range defined in the standard of PMU measurement. In case that the TVE exceeds the permissible limit, the mean of absolute percent differences will continue increasing, according to the simulation results.

Next, the impact of measurement error for the balanced grid condition is investigated. For the balanced grid condition, TVE is also added to the initial input, containing 0% TVE, in the same way as that for the unbalanced grid condition. The range of the TVE is still from 0.2%, 0.4%, 0.6%, 0.8%, and 1.0% TVE. The comparison of mean difference of all sensitivity types in modified IEEE 37-bus test feeder and the exemplified mesh grid with different TVE are shown in Figure 5.51 and Figure 5.52, respectively. Since the proposed method for the balanced condition consists of only four sensitivities – *Svp*, *Svq*, *Sphip*, and *Sphiq*, the mean differences of all sensitivities are plotted in the same chart.

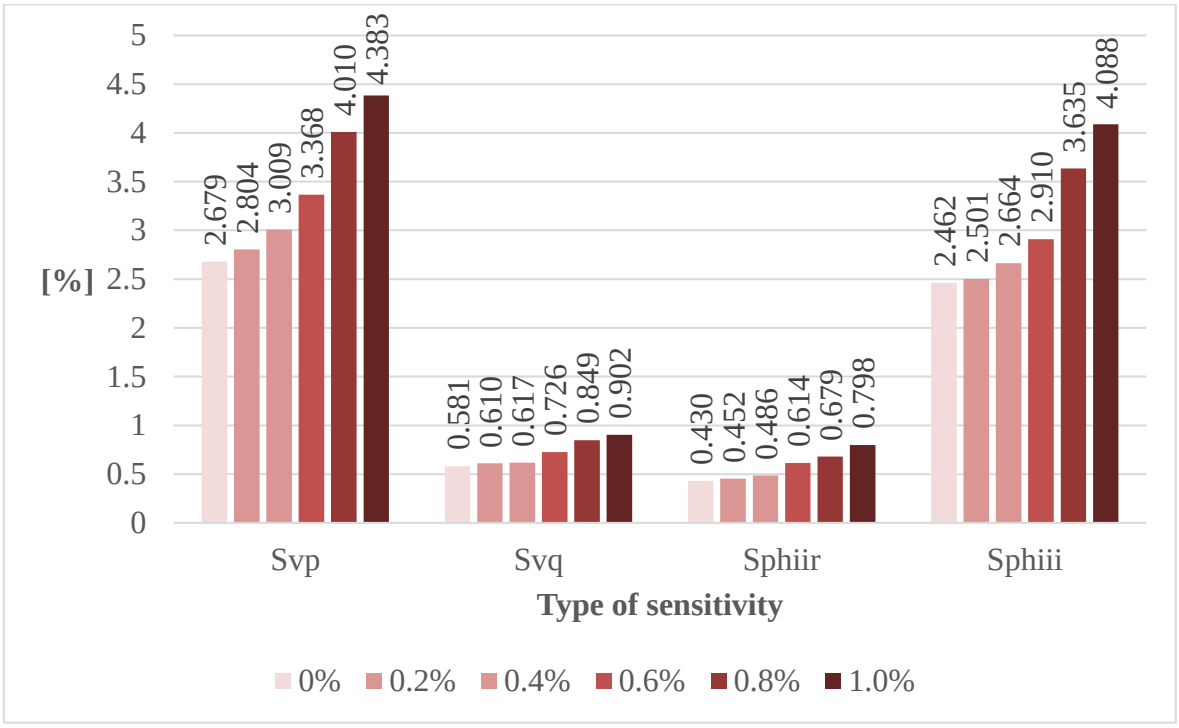

Figure 5.51: Mean values of absolute differences of all sensitivity types for the balanced grid condition in the modified IEEE 37-bus test feeder with a different TVE

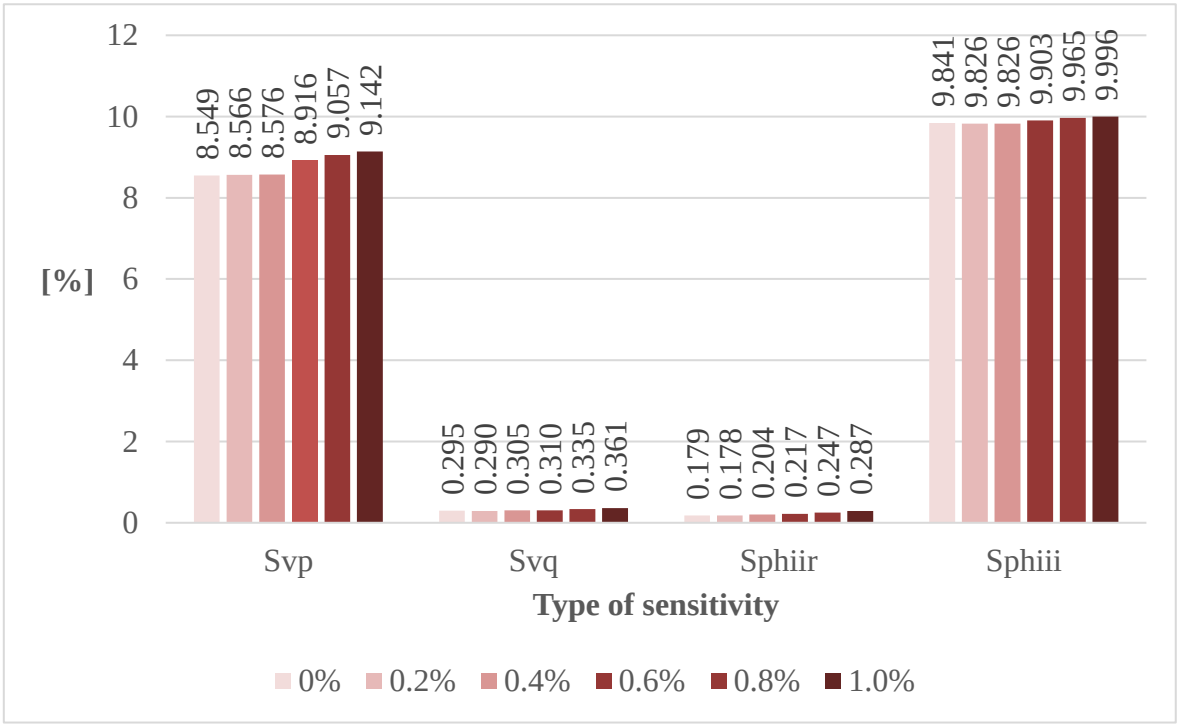

Figure 5.52: Mean values of absolute differences of all sensitivity types for the balanced grid condition in the exemplified mesh grid with a different TVE

The mean differences in Figure 5.51 and Figure 5.52 demonstrate that raising the TVE leads to an increase in the difference between the results from the proposed method and their reference from PowerFactory. However, the increased differences are still acceptable.

Thus far, Case Study 1 has been discussed. The proposed method is successfully verified that it can be efficiently used in the entire grid structure. The modified IEEE 37-bus test feeder and the exemplified mesh grid are employed in the experiments for verification. The unbalanced and balanced grid conditions have been covered. High accuracy of voltage sensitivity analysis is acquired. In addition, the measurement errors based on TVE are explored to study their impact of the errors on the results from the proposed method.

In the next section, Case Study 2 is presented. The proposed method is used in a cluster-based grid located in the low-voltage level, which is an important part of the distribution grid. The cluster-based grid is defined on an exemplified radial low-voltage grid. Thereby, the contribution of the proposed method to the CPSA is explored. This will clearly demonstrate the key benefit of the proposed method over other methods for voltage sensitivity analysis.

5.2 Case Study 2: Cluster-Based Grid

The proposed method for voltage sensitivity analysis is developed with the purpose that it can leverage advantages of decentralised grid operations offered by the CPSA, thus facilitating future smart grids. This case study aims to verify that the proposed method is applicable to allow the decoupled voltage sensitivity analysis, while the accuracy is still ensured at the same time. Since the CPSA is stressed on the low-voltage distribution level, an exemplified cluster-based low-voltage radial grid, thereafter called as "cluster-based grid", is used in the simulations of this case study, which is depicted in Figure 5.53. The topological information of this grid is adapted from an actual distribution grid in Borchen-Etteln from Westfalen Weser Netz. In the simulations, the nominal voltage is 400 V. The type of transformer Tr#1 is 0.4 MVA 20/0.4 kV Dyn5. Bus 100 is set as the reference bus, and bus 1 is a junction. The rest of the buses are connected to a load, which can be considered as a generator when it feeds powers back to the grid. An online simulation under the steady-state condition is executed to generate data of unbalanced bus voltages, bus currents, and line currents. Each data set is gathered at a specified time. The grid from Figure 5.53 is grouped into four cluster areas, denoted by Cluster 1, Cluster 2, Cluster 3, and Cluster 4. The overlapped areas between Cluster 1 and Cluster 2 to Cluster 4 are their border areas. Cluster 1 therefore consists of bus 102, 103, 106, 107, 111, and 112. Cluster 2 is composed of buses 102 to 105. Cluster 3 is composed of buses 106 to 110. Lastly, Cluster 4 is composed of buses 111 to 116. The complete configuration of this cluster-based grid is provided in Appendix D.

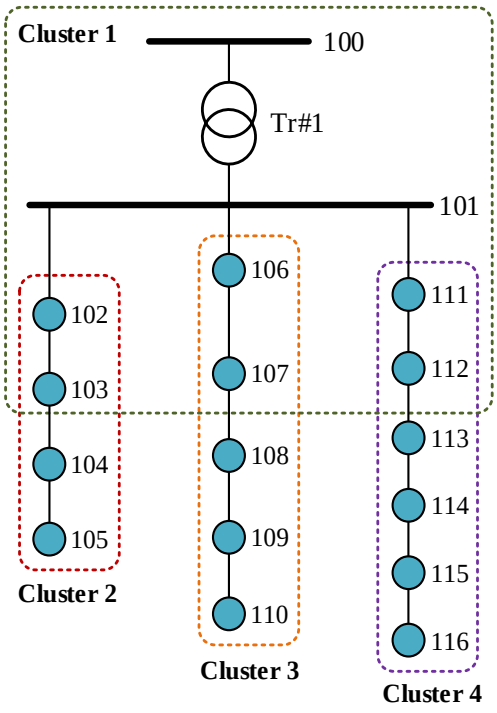

Figure 5.53: Cluster-based low-voltage radial grid

To perform the verifications, measurement data of bus voltages, bus currents, and line currents in the border areas are obtained from the load flow calculation of the cluster-based grid in PowerFactory. The required data sets for each cluster area are varied, depending on their number of active buses. Cluster 1 to Cluster 4 respectively require 7, 5, 6, and 7 data sets. Each data set is resulted from each operational scenario of the input for the load flow calculation and is assigned for one unique timestamp. In the following subsections, first, the impedance model is investigated. Afterwards, the proposed analysis method is analysed under the unbalanced and balanced grid conditions. Finally, the impact of measurement errors on the voltage sensitivity analysis under the CPSA is discussed.

5.2.1 Analysis of the Proposed Impedance Model

The impedance model, or bus impedance parameters [$\underline{Z}_{par}$] in this context, needs to be determined in each cluster area. Thus, the decoupled voltage sensitivity analysis can be performed, once the matrix [$\underline{Z}_{par}$] of each cluster area is available. In this section, the bus impedance parameters, in the matrix [$\underline{Z}_{par}$], with consideration of cluster areas based on the CPSA are verified. The mean of absolute percent differences is demonstrated for all cluster areas to observe the accuracy. The difference is obtained from the comparison between each element in the matrix [$\underline{Z}_{par}$] with their reference, which is the corresponding element from the matrix [$\underline{Z}_{bus}$] calculated manually from the exemplified grid in Figure 5.53. Here, the matrix [$\underline{Z}_{par}$] is investigated in three aspects. First, the histogram of the percent differences between all 225 corresponding elements of the matrices [$\underline{Z}_{bus}$] and [$\underline{Z}_{par}$] is discussed. The results demonstrate how close the elements of the matrix [$\underline{Z}_{par}$] are in comparison to that of the matrix [$\underline{Z}_{bus}$], albeit they are determined by different methods. Afterwards, the mean of the absolute percent differences of all elements in the matrix is presented to show the quality of the results from different inputs and cases. The descriptions of the histogram and the result differences can be found in Appendix A. Lastly, the numerical data of some selected elements from the matrices [$\underline{Z}_{par}$] and [$\underline{Z}_{bus}$] are provided as an example. To verify the bus impedance parameters, both matrices [$\underline{Z}_{par}$] and [$\underline{Z}_{bus}$] are divided into resistance and reactance in the zero, positive, and negative sequences.

This analysis starts by observing the distribution of the results, presented in the histogram of the percent differences between all corresponding elements of the matrices [$\underline{Z}_{bus}$] and [$\underline{Z}_{par}$] in the entire grid of the cluster-based low-voltage radial grid. In turn, the resulted impedances of the entire grid case are compared with that of the cluster-based grid case. Figure 5.54 and Figure 5.55 portray the histogram of the percent differences in the case of resistance and reactance in the sequence systems. In Figure 5.54, the mean of the percent differences of resistance is -0.255%, -0.128%, and -0.081%, as plotted in dash lines for the zero, positive and negative sequences, respectively. Similarly, in Figure 5.55, the mean of the percent

differences of reactance is -0.092%, 0.001%, and 0.01% for the zero, positive and negative sequences. Thus, high accuracy can be obtained from the determination of the matrix [$\underline{Z}_{par}$].

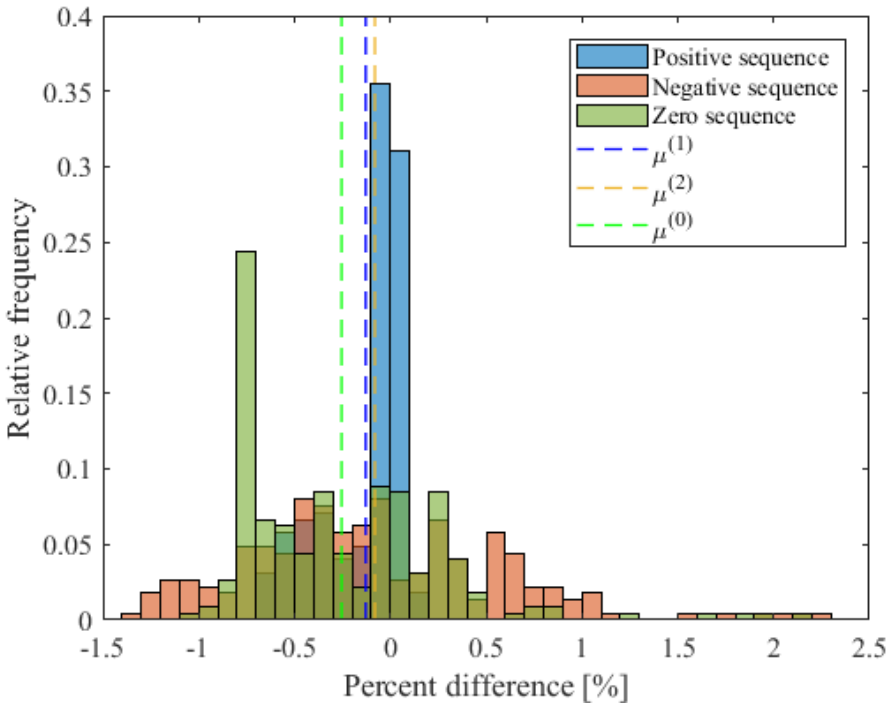

Figure 5.54: Histogram of percent differences of the whole bus resistances for the case of the cluster-based power grid

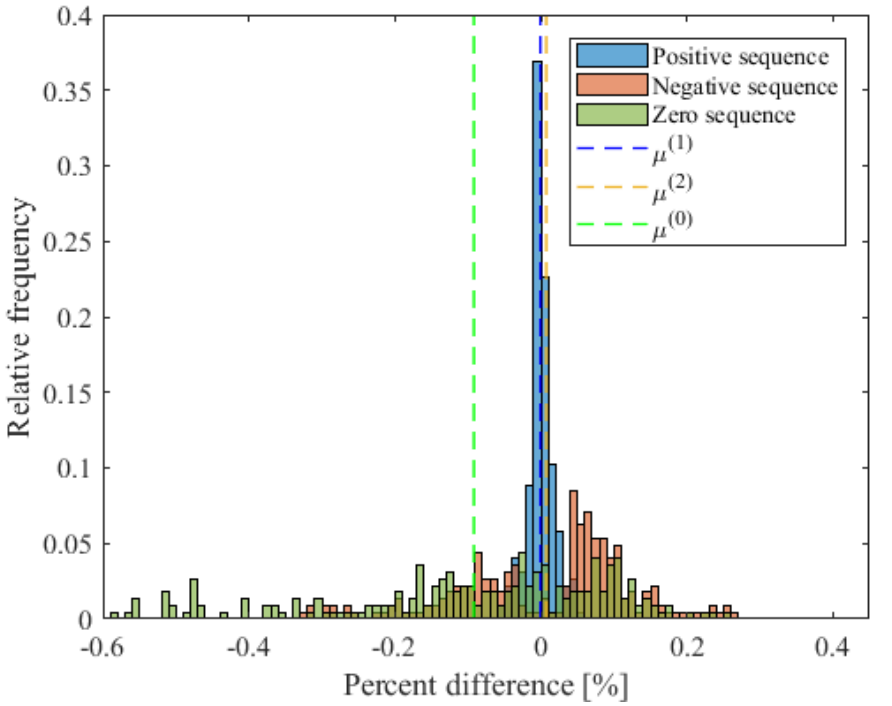

Figure 5.55: Histogram of percent differences of the whole bus reactances for the case of the cluster-based power grid

In the cluster-based grid, integrating the influence of neighbouring cluster areas is required to complete the determination of the matrix $[\underline{Z}_{par}]$ in each cluster area before comparing with the matrix $[\underline{Z}_{bus}]$. When the buses of any cluster area can be considered as internal or external buses, the influence of a neighbouring cluster area is obtained from the self-impedance, which is also a Thévenin impedance in this context, of the external bus looking into that cluster area. Thus, the Thévenin impedance must be exchanged between the neighbouring cluster areas. To simplify the explanation, Table 5.5 presents the buses of each cluster area according to Figure 5.53. An external bus is located at the decoupling point between cluster areas.

Table 5.5: Bus category in each cluster area

Cluster name	Internal bus	External bus
Cluster 1	102; 106; 111	103; 107; 112
Cluster 2	103; 104; 105	102
Cluster 3	107; 108; 109; 110	106
Cluster 4	112; 113; 114; 115; 116	111

Regarding this impedance requesting process, an example of exchanging the Thévenin impedance between cluster areas is envisioned in Figure 5.56. The bus impedance parameters matrices of Cluster 1 to Cluster 4 are denoted by $[\underline{Z}_{par,C1}]$ to $[\underline{Z}_{par,C4}]$. The subscript *C1* to *C4* are designated for Cluster 1 to Cluster 4, respectively. Based on the bus connections depicted in Figure 5.53, Cluster 1 therefore requires the Thévenin impedances $\underline{Z}_{103,C2}$, $\underline{Z}_{107,C3}$, and $\underline{Z}_{112,C4}$ looking into Cluster 2, Cluster 3 and Cluster 4 from bus 103, bus 107, and bus 112, respectively. Likewise, Cluster 2, Cluster 3, and Cluster 4 require the Thévenin impedances $\underline{Z}_{102,C1}$, $\underline{Z}_{106,C1}$, and $\underline{Z}_{111,C1}$ looking into Cluster 1 from bus 102, bus 106, and bus 111.

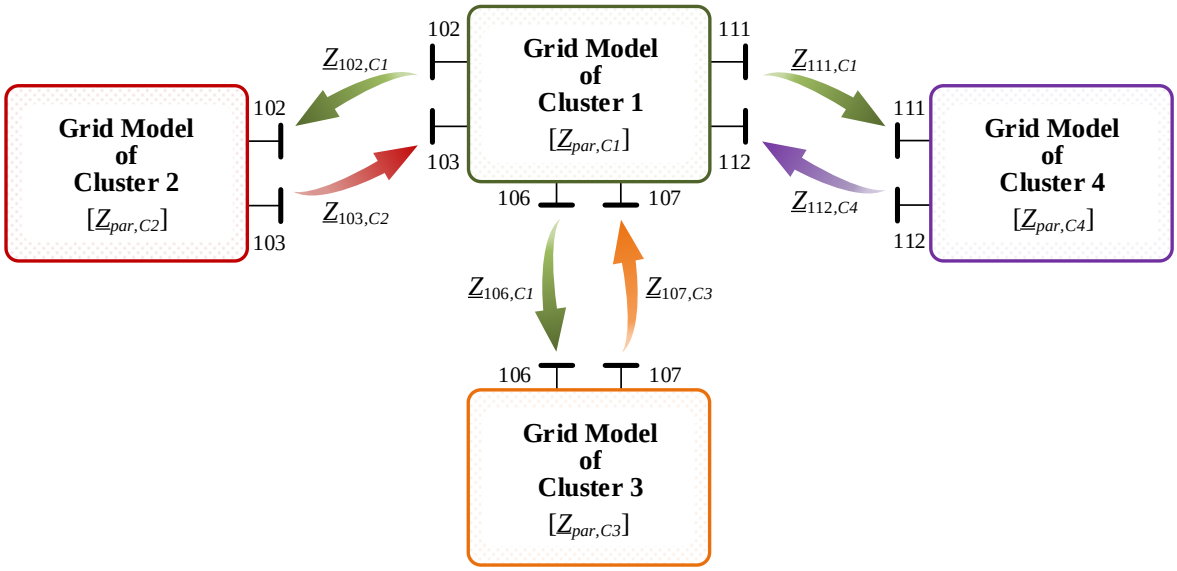

Figure 5.56: Exchange of the Thévenin impedance among cluster areas

After the Thévenin impedance is exchanged and integrated into all relevant cluster areas, the resistance and reactance of the bus impedance parameters are separately explored to observe the accuracy. Figure 5.57 and Figure 5.58 respectively display the mean differences of bus resistance and reactance of the cluster-based power grid in different grid cases. The mean differences between the corresponding elements of the matrices $[\underline{Z}_{bus}]$ and $[\underline{Z}_{par,C1}]$ to $[\underline{Z}_{par,C4}]$ are shown in the zero, positive, and negative sequences.

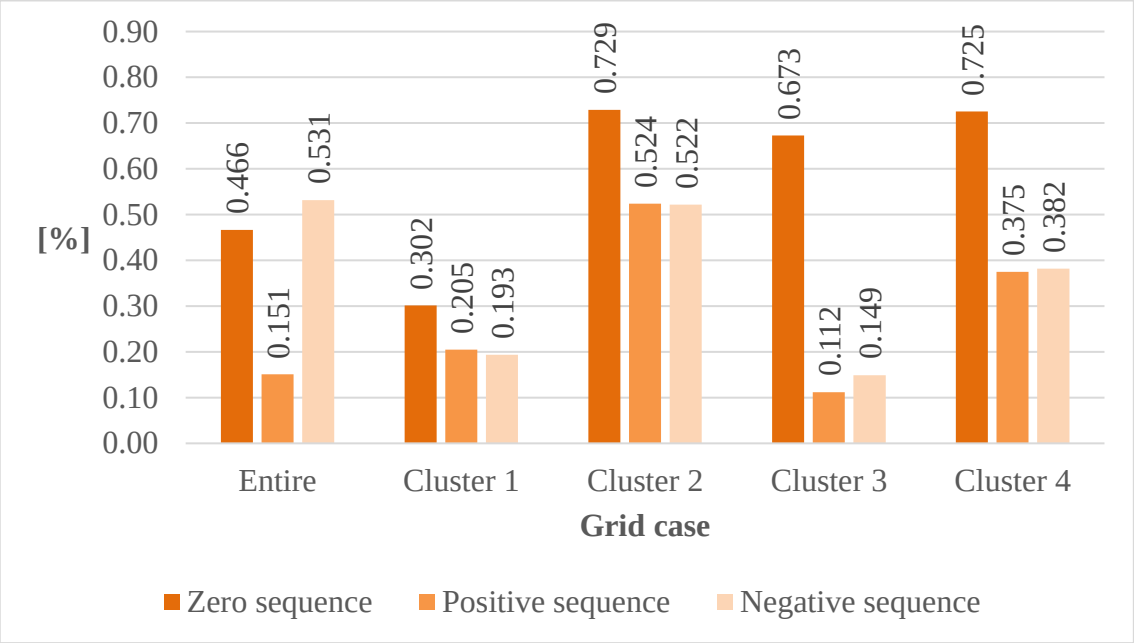

Figure 5.57: Illustration of mean differences of the bus resistances for the cluster-based power grid in different grid cases

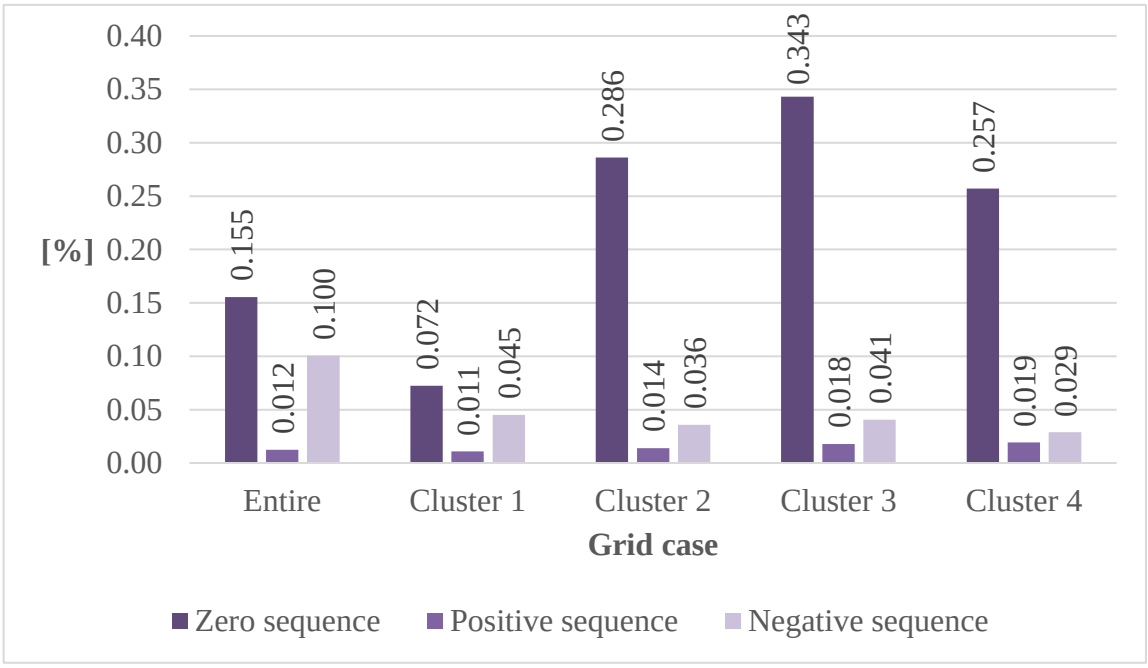

Figure 5.58: Illustration of mean differences of the bus reactances for the cluster-based power grid in different grid cases

The mean difference of both resistances and reactances is mainly increased in the zero sequence. Shown Figure 5.57 and Figure 5.58, though the mean differences are increased, they are still within 1%. That is, high accuracy of the impedance model in each cluster area can be achieved in this simulation. A part of the original resistance R_{ij} and reactance X_{ij} of bus impedance parameters in comparison to their reference is given in Table 5.6 to Table 5.9 for Cluster 1 to Cluster 4, respectively. The resistance R_{ij} and the reactance X_{ij} describe the voltage-current relationship between the bus number indicated in the subscripts *i* and *j*. In this context, the subscript *i* represents number of the target bus at which its voltage magnitude or angle is subject to a change caused by adjusting current at bus *j*.

Table 5.6: Selected bus resistances and reactances in Cluster 1 with their reference

Parameter	Zero sequence		Positive sequence		Negative sequence	
[Ohm]	Reference	Calculation	Reference	Calculation	Reference	Calculation
$R_{102,112}$	0.004800	0.004796	0.004801	0.004800	0.004801	0.004804
$R_{103,112}$	0.004800	0.004795	0.004801	0.004799	0.004801	0.004804
$R_{106,112}$	0.004800	0.004793	0.004801	0.004804	0.004801	0.004804
$R_{107,112}$	0.004800	0.004792	0.004801	0.004807	0.004801	0.004804
$R_{111,112}$	0.051720	0.051362	0.016626	0.016537	0.016626	0.016535
$R_{112,112}$	0.078054	0.077501	0.023210	0.023120	0.023210	0.023118
$X_{102,112}$	0.023515	0.023520	0.023515	0.023513	0.023515	0.023526
$X_{103,112}$	0.023515	0.023520	0.023515	0.023512	0.023515	0.023526
$X_{106,112}$	0.023515	0.023521	0.023515	0.023513	0.023515	0.023526
$X_{107,112}$	0.023515	0.023523	0.023515	0.023510	0.023515	0.023524
$X_{111,112}$	0.053072	0.053007	0.030904	0.030902	0.030904	0.030913
$X_{112,112}$	0.065908	0.065756	0.034113	0.034111	0.034113	0.034120

Table 5.7: Selected bus resistances and reactances in Cluster 2 with their reference

Parameter	Zero sequence		Positive sequence		Negative sequence	
[Ohm]	Reference	Calculation	Reference	Calculation	Reference	Calculation
$R_{102,105}$	0.082882	0.082280	0.024480	0.024336	0.024480	0.024326
$R_{103,105}$	0.112582	0.111754	0.031905	0.031762	0.031905	0.031750
$R_{104,105}$	0.138322	0.137299	0.038340	0.038197	0.038340	0.038184
$R_{105,105}$	0.194752	0.193302	0.052447	0.052306	0.052447	0.052291
$X_{102,105}$	0.072702	0.072540	0.035811	0.035815	0.035811	0.035824
$X_{103,105}$	0.087178	0.086907	0.039430	0.039435	0.039430	0.039444
$X_{104,105}$	0.099724	0.099358	0.042567	0.042572	0.042567	0.042580
$X_{105,105}$	0.127230	0.126656	0.049443	0.049449	0.049443	0.049456

Table 5.8: Selected bus resistances and reactances in Cluster 3 with their reference

Parameter	Zero sequence		Positive sequence		Negative sequence	
[Ohm]	Reference	Calculation	Reference	Calculation	Reference	Calculation
$R_{106,110}$	0.019697	0.019584	0.008555	0.008532	0.008555	0.008529
$R_{107,110}$	0.108467	0.107690	0.030748	0.030729	0.030748	0.030721
$R_{108,110}$	0.132227	0.131273	0.036688	0.036670	0.036688	0.036661
$R_{109,110}$	0.169253	0.168022	0.045944	0.045927	0.045944	0.045917
$R_{110,110}$	0.208853	0.207325	0.055844	0.055828	0.055844	0.055817
$X_{106,110}$	0.032899	0.032873	0.025861	0.025863	0.025861	0.025875
$X_{107,110}$	0.076168	0.075820	0.036678	0.036680	0.036678	0.036691
$X_{108,110}$	0.087749	0.087315	0.039573	0.039575	0.039573	0.039586
$X_{109,110}$	0.105796	0.105227	0.044085	0.044087	0.044085	0.044098
$X_{110,110}$	0.125098	0.124385	0.048910	0.048912	0.048910	0.048923

Table 5.9: Selected bus resistances and reactances in Cluster 4 with their reference

Parameter	Zero sequence		Positive sequence		Negative sequence	
[Ohm]	Reference	Calculation	Reference	Calculation	Reference	Calculation
$R_{111,116}$	0.051720	0.051364	0.016626	0.016540	0.016626	0.016540
$R_{112,116}$	0.078054	0.077499	0.023210	0.023123	0.023210	0.023123
$R_{113,116}$	0.106764	0.105993	0.030387	0.030301	0.030387	0.030301
$R_{114,116}$	0.127158	0.126233	0.035486	0.035399	0.035486	0.035399
$R_{115,116}$	0.147156	0.146081	0.040485	0.040399	0.040485	0.040399
$R_{116,116}$	0.193290	0.191867	0.052019	0.051932	0.052019	0.051932
$X_{111,116}$	0.053072	0.052990	0.030904	0.030904	0.030904	0.030904
$X_{112,116}$	0.065908	0.065734	0.034113	0.034113	0.034113	0.034113
$X_{113,116}$	0.079901	0.079627	0.037611	0.037611	0.037611	0.037611
$X_{114,116}$	0.089842	0.089495	0.040096	0.040096	0.040096	0.040096
$X_{115,116}$	0.099589	0.099172	0.042533	0.042533	0.042533	0.042533
$X_{116,116}$	0.122076	0.121493	0.048155	0.048155	0.048155	0.048155

The proposed impedance model determined individually in each cluster area has been successfully verified. Accordingly, the bus impedance parameters can be calculated by using only measured voltages and currents. The influence between cluster areas is included by integrating the Thévenin impedance representing each cluster area to the predetermined bus impedance parameters. Finally, high accuracy of the model still can be ensured.

In the next section, the matrices $[\underline{Z}_{par,C1}]$ to $[\underline{Z}_{par,C4}]$ are used to perform voltage sensitivity analysis in their individual area. The verification of the decoupled voltage sensitivity analysis method is thus carried out.

5.2.2 Analysis of Results from the Proposed Analysis Method

The proposed voltage sensitivity analysis is executed after the impedance model [$\underline{Z}_{par}$] is determined. In this section, the results from the proposed method are verified in three aspects for both unbalanced and balanced grid conditions. First, the mean of absolute percent differences of each sensitivity type for cluster-based grid is discussed. Same as Section 5.1.2, the mean of absolute percent differences of all voltage sensitivity values is used to show the quality of the results from different inputs and cases. Then, the histogram of the percent differences between all corresponding sensitivity values in the positive sequence is examined for all sensitivity types, as an example to envision the overview of total results. The mean of absolute percent differences and the histogram of the results differences is compared among the entire grid and cluster areas to study the impact of the CPSA applied to the radial grid in Figure 5.53. The descriptions of the histogram and the result differences can be found in Appendix A. Finally, the original sensitivity values of the selected buses are provided.

5.2.2.1 Results of Sensitivity Analysis in an Unbalanced Grid Condition

In this section, all sensitivity types in an unbalanced condition are taken into account. It must be noted, however, that the mean of absolute percent differences in this context is the mean from all phases *a*, *b*, and *c* for both voltage magnitude and angle sensitivities to observe the accuracy. Figure 5.59 and Figure 5.60 illustrate the voltage magnitude sensitivity in relation to real and imaginary components of a sequence current, respectively. The mean calculated from the entire grid case is portrayed together with that of the cluster-based grid case.

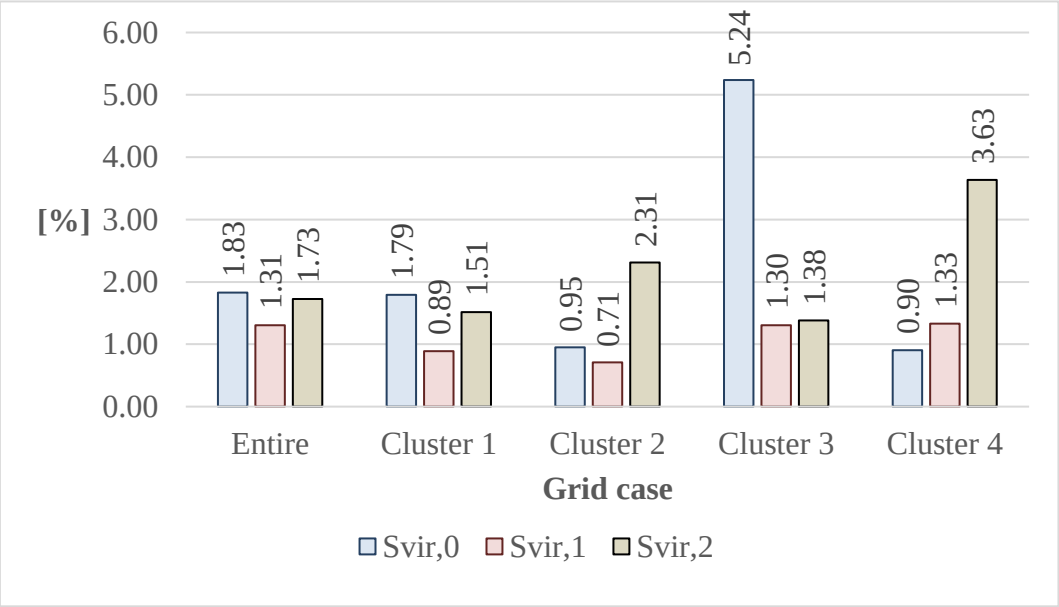

Figure 5.59: Mean values of absolute result differences of voltage magnitude sensitivity in relation to real-component sequence currents in different grid cases

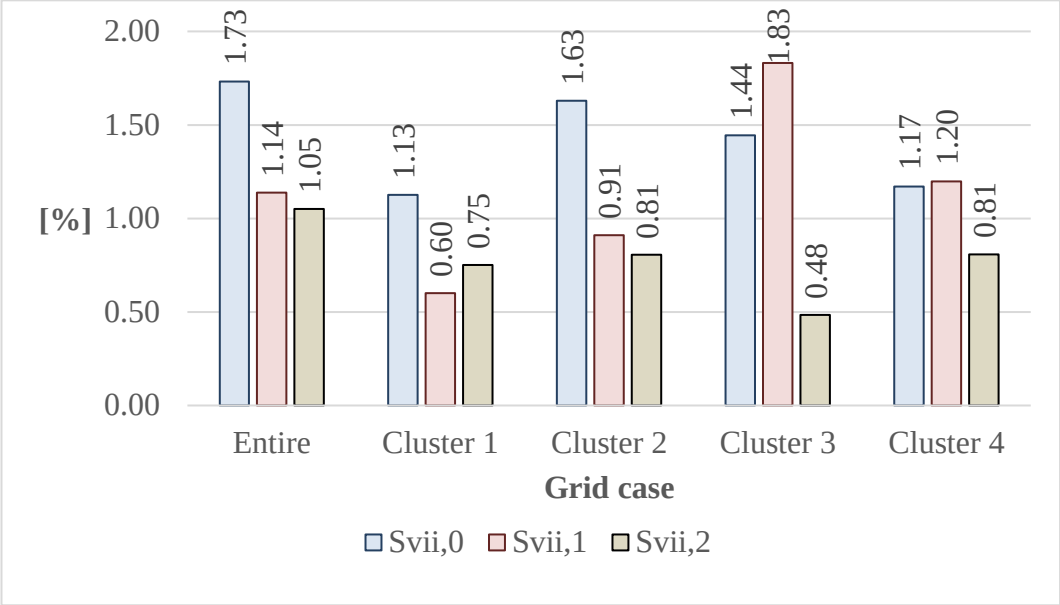

Figure 5.60: Mean values of absolute result differences of voltage magnitude sensitivity in relation to imaginary-component sequence currents in different grid cases

Also, Figure 5.61 and Figure 5.62 display mean difference of the voltage angle sensitivity in relation to real and imaginary components of a sequence current in different grid cases.

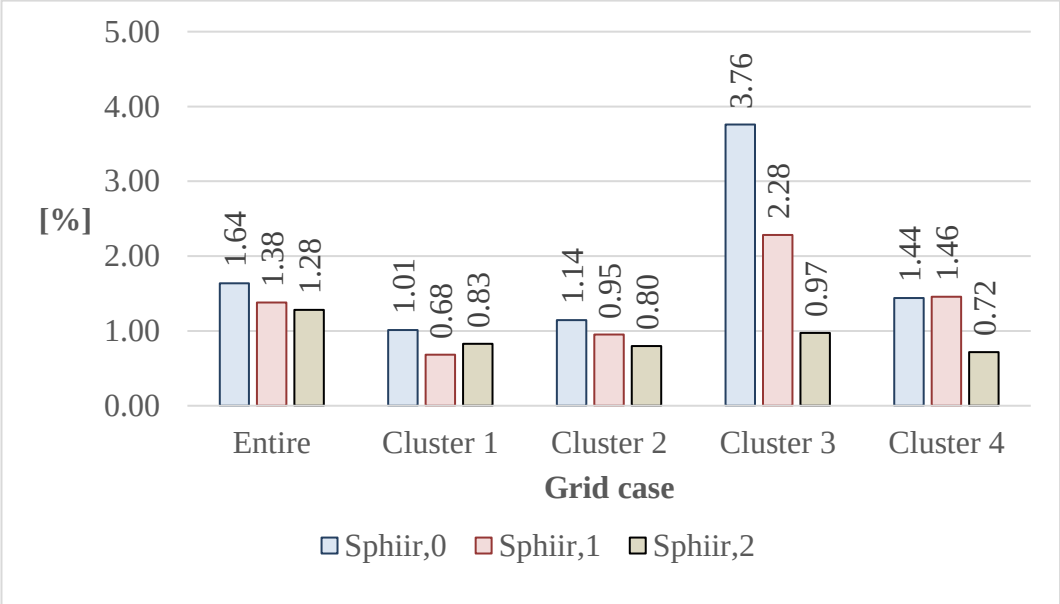

Figure 5.61: Mean values of absolute result differences of voltage angle sensitivity in relation to real-component sequence currents in different grid cases

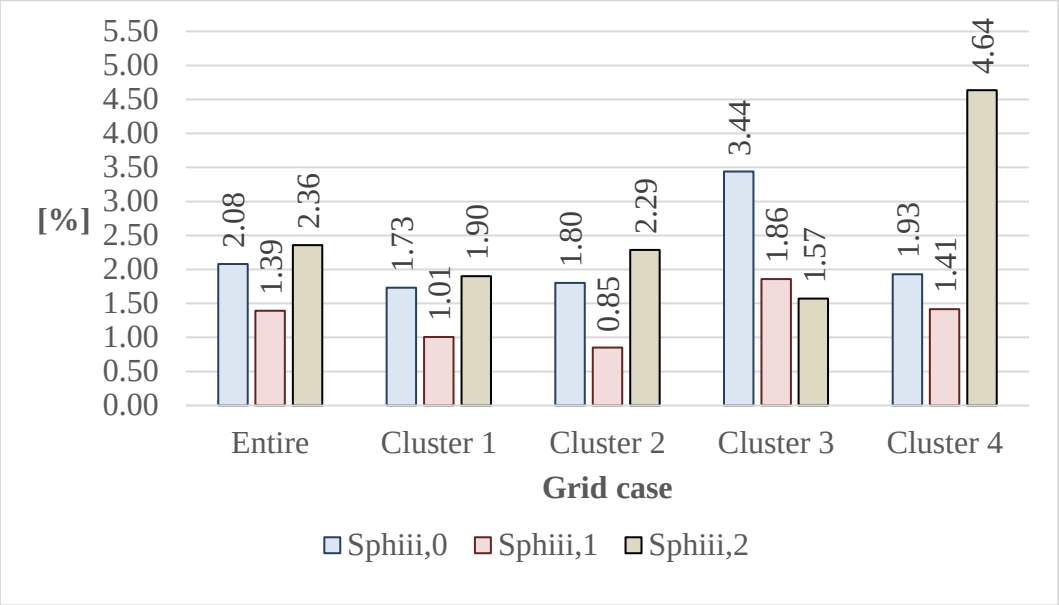

Figure 5.62: Mean values of absolute result differences of voltage angle sensitivity in relation to imaginary-component sequence currents in different grid cases

Regards the charts in Figure 5.59 to Figure 5.62, high accuracy is achieved for all sensitivity analyses as the mean differences are small for either the case of voltage magnitude or angle sensitivities. Generally, the cluster-based cases enable better mean difference in comparison to the entire grid, even though the mean differences in some cluster areas are slightly high. The highest mean difference occurs however at a mere value of 5.24% in *Svir*,0 of Cluster 3 in Figure 5.59. This highest mean is not significant when the original sensitivity values are considered.

In order to provide supplementary information for the accuracy of the proposed method, the percent differences, without absolute, of whole data are moreover discussed. In this case study, 225, 36, 16, 25, and 36 sensitivity values of each sensitivity type are considered for the entire grid, cluster 1, cluster 2, cluster 3, and cluster 4, respectively. Nevertheless, as the aim of the following results is to support the observed accuracy, only the charts showing the results in the positive sequence for phase *a* are presented here. The rest can be found in Appendix D.

Beginning with the sensitivities of voltage magnitude, Figure 5.63 and Figure 5.64 show the histograms of percent differences, respectively, in the case of sensitivity *Svir*,1 and *Svii*,1 at phase *a*. As illustrated in Figure 5.63, the mean values of the percent differences of the sensitivity *Svir*,1 are -0.733%, -0.885%, -1.463%, 1.745%, and -1.899% for the entire grid to cluster 4 cases, respectively. Similarly, from Figure 5.64, for phase *a*, the Mean values of the percent differences of the sensitivity *Svii*,1 are -0.213%, 0.056%, -0.222%, -0.358%, and -0.761%. Thus, the sensitivities *Svir*,1 and *Svii*,1 at phase *a* are accurate in general. For any grid case, the mean values are close to zero, as plotted in dash lines.

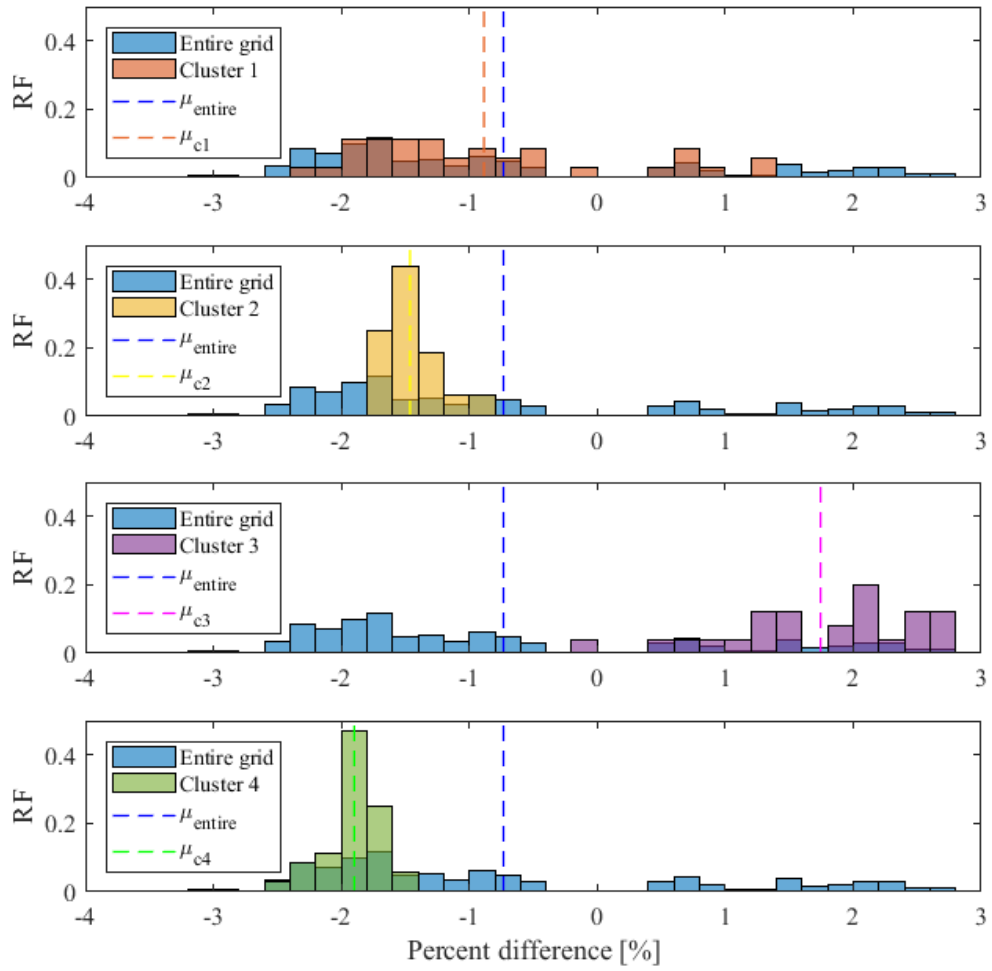

Figure 5.63: Histogram of the whole result differences in *Svir*,1 for phase *a* of the cluster-based grid in different grid cases (RF: Relative frequency)

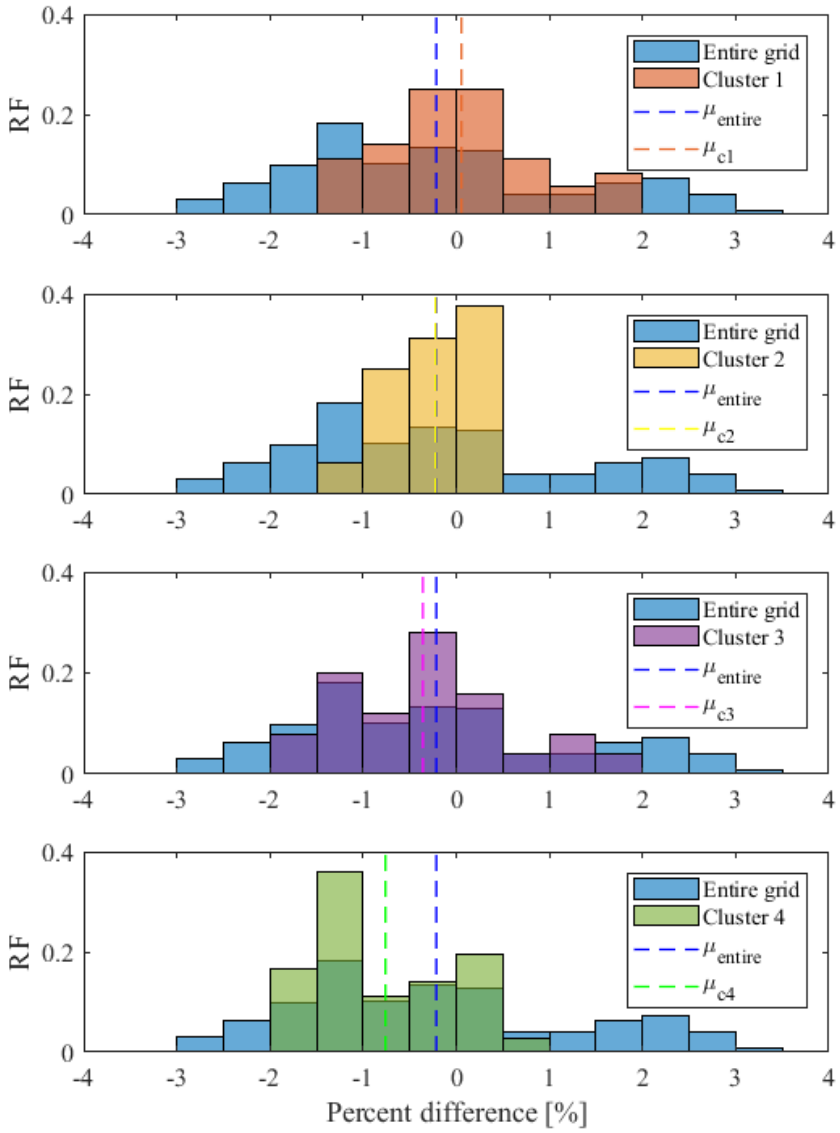

Figure 5.64: Histogram of the whole result differences in *Svii*,1 for phase *a* of the cluster-based grid in different grid cases (RF: Relative frequency)

Continuing with the sensitivities of the voltage angle, Figure 5.65 and Figure 5.66 display the charts of percent differences, respectively, in the case of sensitivity *Sphiir*,1 and *Sphiii*,1 at phase *a*. As displayed in Figure 5.65, the mean values of the percent differences of the sensitivity *Sphiir*,1 are 1.889%, 0.975%, 0.716%, -0.505%, and 1.513% for the entire grid to cluster 4 cases, respectively. Likewise, as displayed in Figure 5.66, the mean values of the percent differences of the sensitivity *Sphiii*,1 are 2.329%, 1.732%, 1.797%, -2.664%, and 2.356%. Accordingly, the sensitivities *Sphiir*,1 and *Sphiii*,1 at phase *a* are accurate. For any grid case, the mean values are around zero.

According to Figure 5.63 and Figure 5.66, accurate and stable sensitivity values are produced by the proposed method. The difference of the calculated sensitivity values and the results from PowerFactory is small. This supports the verification of the proposed method and proves that it can analyse voltage magnitude and angle sensitivities for both entire grid analysis and

decoupled analysis in each cluster area. The slight deviation of the distribution of the result differences in each cluster area from the entire grid case can be caused by a slight numerical error in the matrix modification process in the decoupled analysis after being updated by the Thévenin impedance. Also, the histograms are based on a different amount of data in each grid case. However, the accuracy of the calculated sensitivity values is still clearly ensured. For the rest, the results are provided in Appendix D.

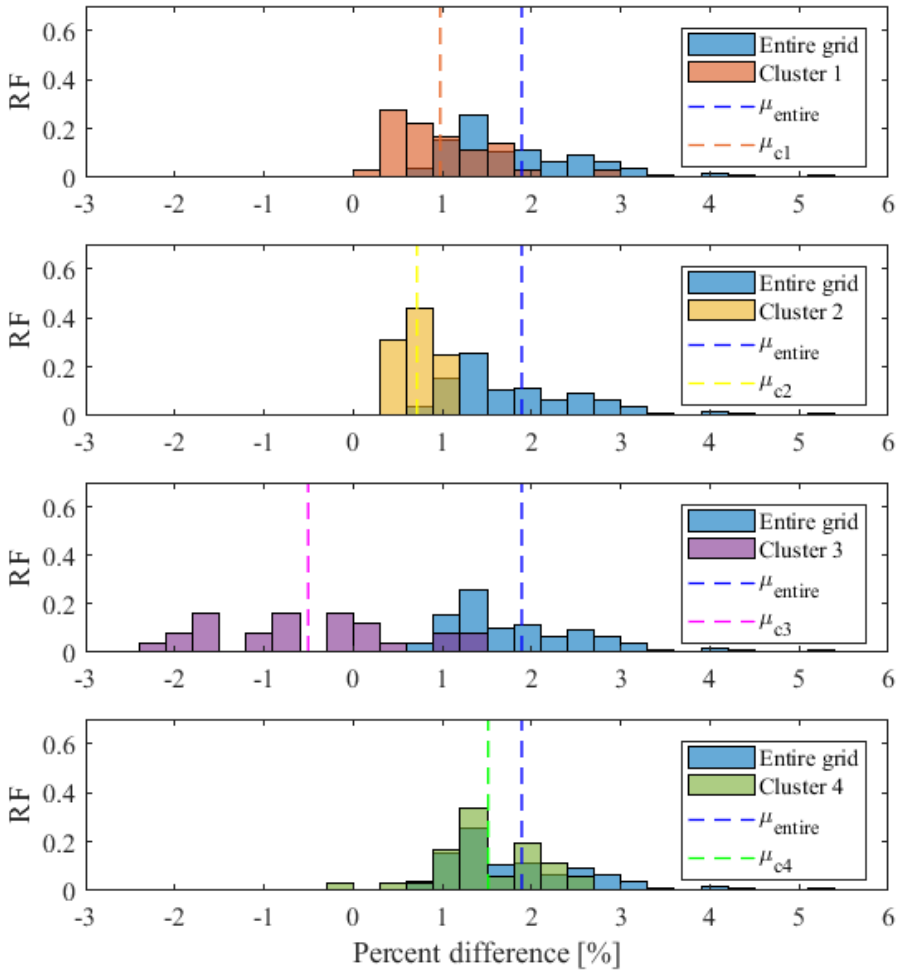

Figure 5.65: Histogram of the whole result differences in *Sphiir*,1 for phase *a* of the cluster-based grid in different grid cases (RF: Relative frequency)

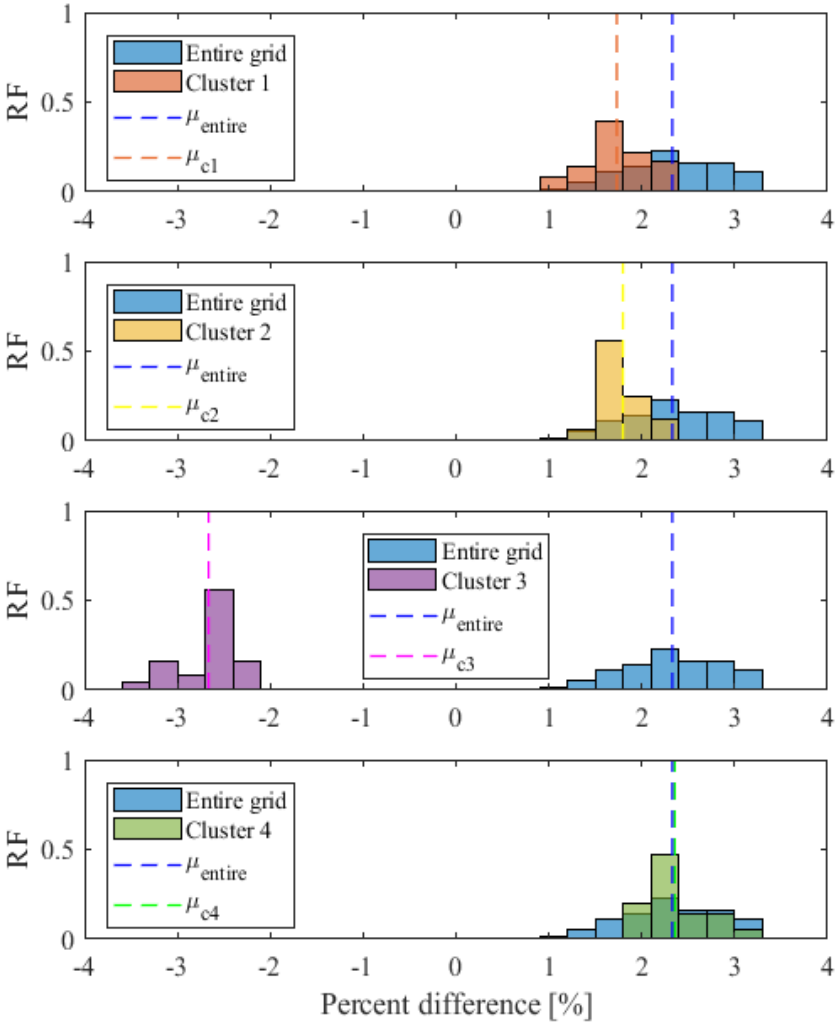

Figure 5.66: Histogram of the whole result differences in *Sphiii*,1 for phase *a* of the cluster-based grid in different grid cases (RF: Relative frequency)

To envision the accuracy of the calculated sensitivity values, the comparison of original sensitivity values is discussed in addition to the mean of absolute percent differences. The values are presented for all phases *a*, *b*, and *c*, since the grid condition is unbalanced. The sensitivity values of bus voltage magnitude and angle at bus 102 in relation to real and imaginary sequence currents at bus 105 are chosen for this discussion. In Figure 5.67 and Figure 5.68, the outcomes from voltage sensitivity analysis of bus 102 are shown together with their reference. Voltage magnitude sensitivity is examined at the unit of pu/A. Figure 5.67 portrays the comparison of the sensitivity values of *Svir*,0, *Svir*,1, and *Svir*,2. These values indicate the extent to which the voltage magnitude at each phase of bus 102 is changed in relation to real component of sequence currents at bus 105. In the same manner, Figure 5.68 illustrates the comparison of the calculated sensitivity values to their reference for *Svii*,0, *Svii*,1, and *Svii*,2. These sensitivities tell a change of the voltage magnitude at each phase of bus 102 in relation to an imaginary component of a sequence current at bus 105. The comparisons in both Figure 5.67 and Figure 5.68 show high precision of the calculated

sensitivity values. High accuracy is achieved in both magnitude and direction at the precision of 10^{-4} pu/A. The original sensitivity values are provided in the table inside each figure.

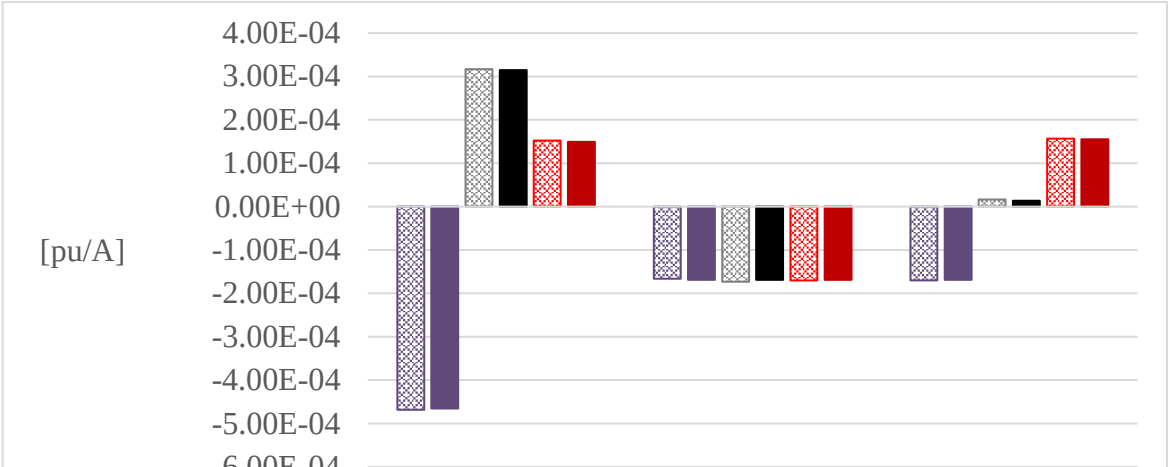

	Svir,0	Svir,1	Svir,2
Reference result (phase a)	-4.69E-04	-1.66E-04	-1.70E-04
Calculated result (phase a)	-4.66E-04	-1.69E-04	-1.69E-04
Reference result (phase b)	0.000317004	-1.73E-04	1.64E-05
Calculated result (phase b)	0.000314553	-1.69E-04	1.34E-05
Reference result (phase c)	1.53E-04	-1.70E-04	1.57E-04
Calculated result (phase c)	1.50E-04	-1.68E-04	1.56E-04

Figure 5.67: Calculated sensitivity values of voltage magnitude at bus 102 to the real component of a bus current at bus 105 in comparison with their reference

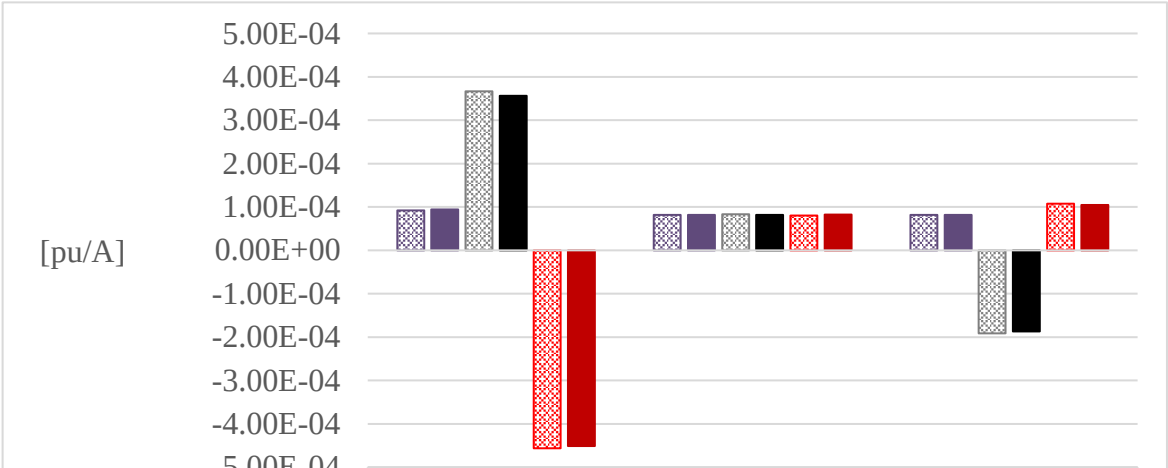

	Svii,0	Svii,1	Svii,2
Reference result (phase a)	9.17E-05	8.17E-05	8.20E-05
Calculated result (phase a)	9.40E-05	8.17E-05	8.17E-05
Reference result (phase b)	3.66E-04	8.30E-05	-1.92E-04
Calculated result (phase b)	3.56E-04	8.18E-05	-1.87E-04
Reference result (phase c)	-4.56E-04	8.02E-05	1.08E-04
Calculated result (phase c)	-4.51E-04	8.24E-05	1.05E-04

Figure 5.68: Calculated sensitivity values of voltage magnitude at bus 102 to the imaginary component of a bus current at bus 105 in comparison with their reference

Now, original values of the voltage angle sensitivities are investigated, as shown in Figure 5.69 and Figure 5.70. The unit of these sensitivities are deg/A. The comparison of *Sphiir*,0 ,*Sphiir*,1, and *Sphiir*,2, in which the impact of real-component sequence currents, is provided in Figure 5.69. Also, the comparison for *Sphiii*,0, *Sphiii*,1, and *Sphiii*,2 is given in Figure 5.70 to explore the impact of imaginary-component sequence currents on the voltage angle. Similar to the case of voltage magnitude, slight differences between the calculated results and their reference can be noticed.

	Sphiir,0	Sphiir,1	Sphiir,2
Reference result (phase a)	-0.005313548	-0.004637718	-0.004631395
Calculated result (phase a)	-0.005380759	-0.0046763	-0.00468005
Reference result (phase b)	-0.020732098	-0.004711742	0.010648481
Calculated result (phase b)	-0.020928313	-0.004810054	0.010995379
Reference result (phase c)	0.026030998	-0.004856627	-0.005858942
Calculated result (phase c)	0.025544474	-0.00466554	-0.005929458

Figure 5.69: Calculated sensitivity values of the voltage angle at bus 102 to the real component of a bus current at bus 105 in comparison with their reference

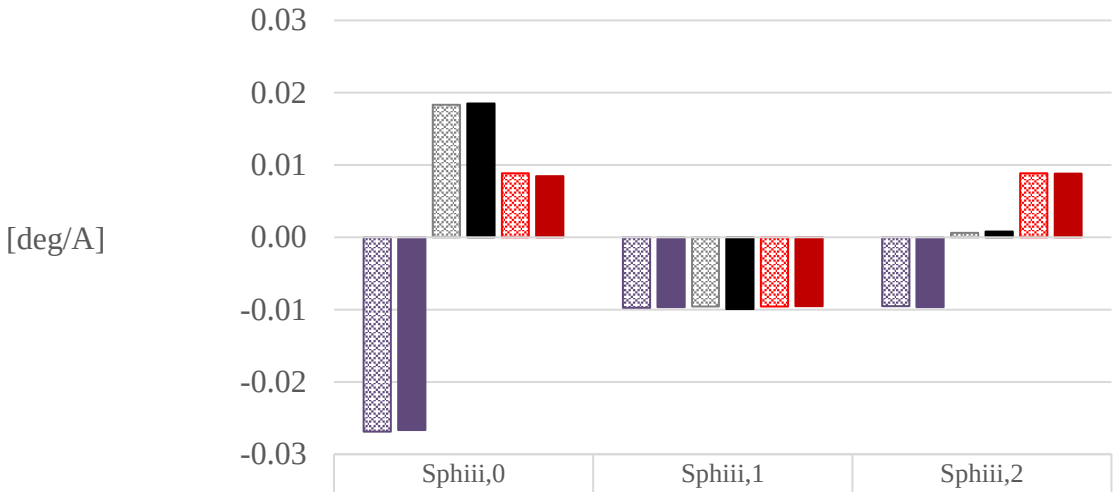

	Sphiii,0	Sphiii,1	Sphiii,2
Reference result (phase a)	-0.026884936	-0.009740567	-0.009508796
Calculated result (phase a)	-0.026668196	-0.009663754	-0.009665309
Reference result (phase b)	0.018334436	-0.009575321	0.000606572
Calculated result (phase b)	0.018491833	-0.009915469	0.000789567
Reference result (phase c)	0.008849577	-0.009563282	0.008867159
Calculated result (phase c)	0.008476032	-0.009541021	0.008814967

Figure 5.70: Calculated sensitivity values of the voltage angle at bus 102 to the imaginary component of a bus current at bus 105 in comparison with their reference

The charts in Figure 5.67 to Figure 5.70 have shown that the original calculated values are slightly different from their reference. Accordingly, the sensitivity values from the proposed method are also applicable and accurate for the cluster-based power grid.

The proposed method for voltage sensitivity analysis has been verified for cluster-based power grids in the unbalanced condition. The results are accurate for decoupled voltage sensitivity analysis in cluster areas. To completely verify the proposed method, in the next section, the proposed method is verified for decoupled voltage sensitivity analysis in the balanced grid condition.

5.2.2.2 Results of Sensitivity Analysis in a Balanced Grid Condition

The method for voltage sensitivity analysis is now explored in the balanced grid condition. Voltage magnitude and angle sensitivities in relation to active and reactive powers – *Svp*, *Svq*, *Sphip*, and *Sphiq* – are analysed accordingly. A full description of each sensitivity type is provided in Table 5.2. The proposed method is further verified in this section by using the same cluster-based grid used for the experiment in the unbalanced grid condition. As well, the accuracy of the sensitivity analysis is inferred from the mean difference between results from the proposed method and the classical method. The mean difference of each sensitivity type is plotted, as illustrated in Figure 5.71. Still, the different grid cases are considered. Unlike the results in the unbalanced condition, the mean differences of all sensitivity types in the balanced condition are clearly improved for cluster areas.

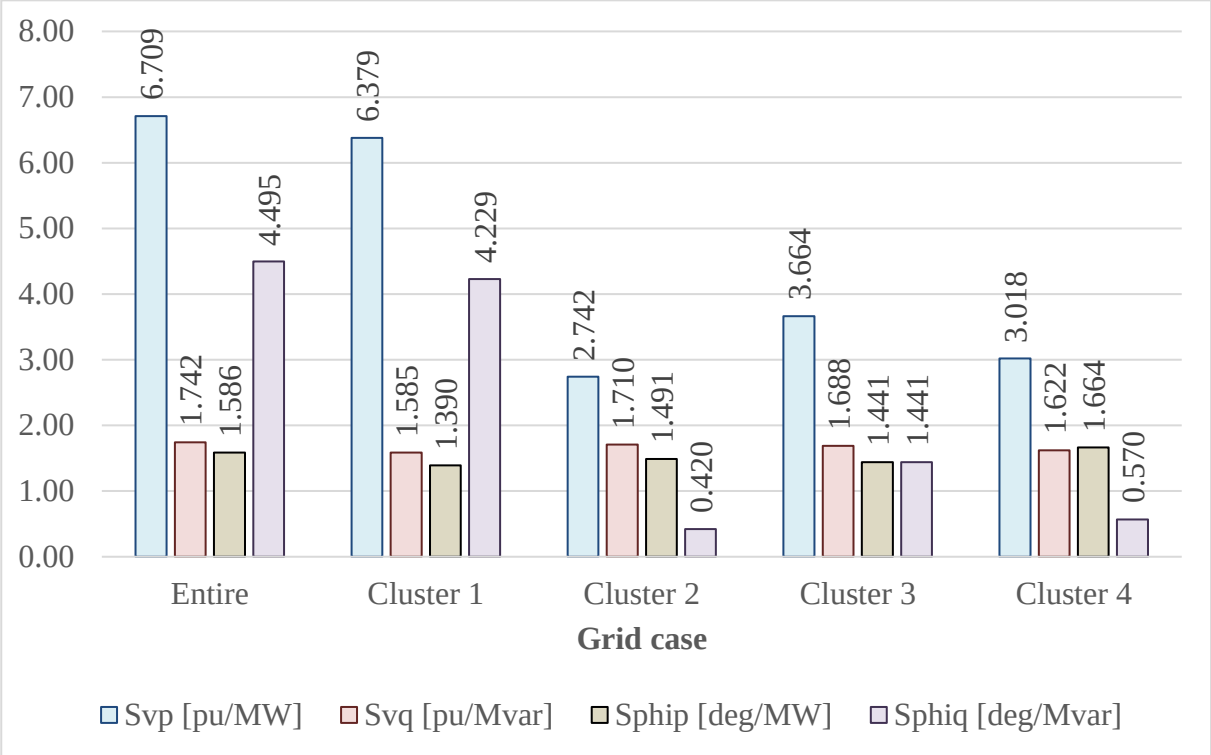

Figure 5.71: Mean values of absolute result differences of sensitivity values among different grid cases in the low-voltage radial grid in a balanced condition

Next, the percent differences, without absolute, of whole data are discussed to support the analysis of result differences. Figure 5.72 to Figure 5.75 depict the histogram of the result differences in the case of *Svp*, *Svq*, *Sphip*, and *Sphiq*, respectively. In each figure, the chart shows the result differences in each grid case together. As Figure 5.72 to Figure 5.75 contain several plots, the mean values of all plots are listed respectively in Table 5.10. They are shown in the figures as dash lines.

Table 5.10: Mean difference of each grid case in Figure 5.72 to Figure 5.75

Sensitivity type	**Mean difference of each grid case [%]**				
	Entire grid	**Cluster 1**	**Cluster 2**	**Cluster 3**	**Cluster 4**
Svp	6.709	6.379	2.742	3.664	3.018
Svq	1.742	1.585	1.710	1.688	1.622
Sphip	1.586	1.390	1.491	1.751	1.664
Sphiq	-4.198	-4.134	0.404	-0.382	0.192

By considering the figures together with the mean values, the proposed method allows accurate sensitivity analysis for all sensitivity types. The mean values are close to zero. Furthermore, similar to the case of the balanced grid condition in Section 5.1.2.2, the sensitivity analysis results from the proposed method can be paired. Bus resistances and reactances play a direct role in the analysis under the balanced grid condition. The characteristics of the results from *Svp* and *Sphiq* are similar, because they are based on the

resistance of the bus impedance parameters, as shown in Eqs. (4.77) and (4.98). Concurrently, the results from *Svq* and *Sphip* have similar characteristics, because they are based on the reactance of the bus impedance parameters, as shown in Eqs. (4.83) and (4.92). Also, the mean values of the sensitivities *Svp* and *Sphiq* are comparatively higher than that of the sensitivities *Svq* and *Sphip*. This is due to higher accuracy of the reactances in comparison with the accuracy of the resistances obtained from the matrix [$\underline{Z}_{par}$] depicted in Figure 5.54 and Figure 5.55. Nonetheless, the sensitivity values of *Svp* and *Sphiq* are much smaller, consequently affecting the calculation of percent differences. Lastly, a slight deviation of the distribution of the result differences in each cluster area from the entire grid case can be caused by slight numerical errors in the matrix modification process of the decoupled analysis. The histograms are also determined from different amounts of data in each grid case. However, the calculated sensitivity values are still clearly accurate.

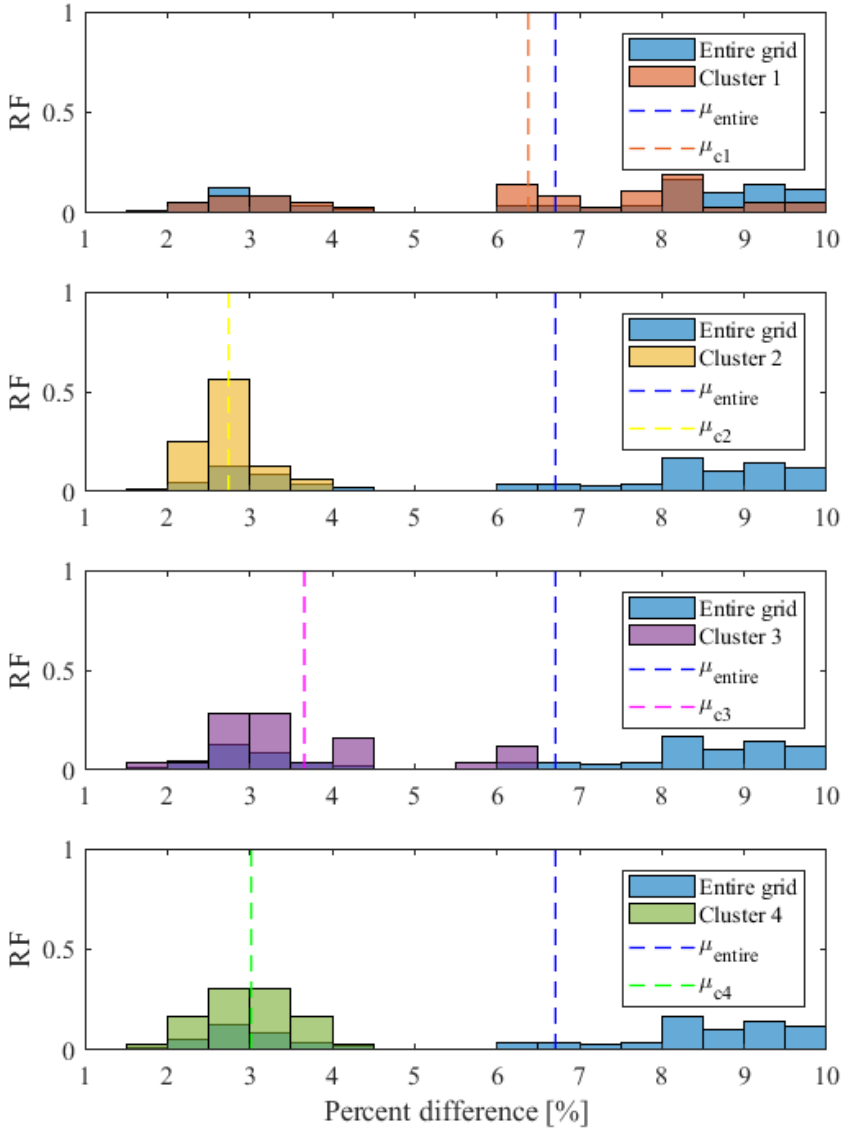

Figure 5.72: Histogram of the whole result differences in *Svp* of the cluster-based grid (RF: Relative frequency)

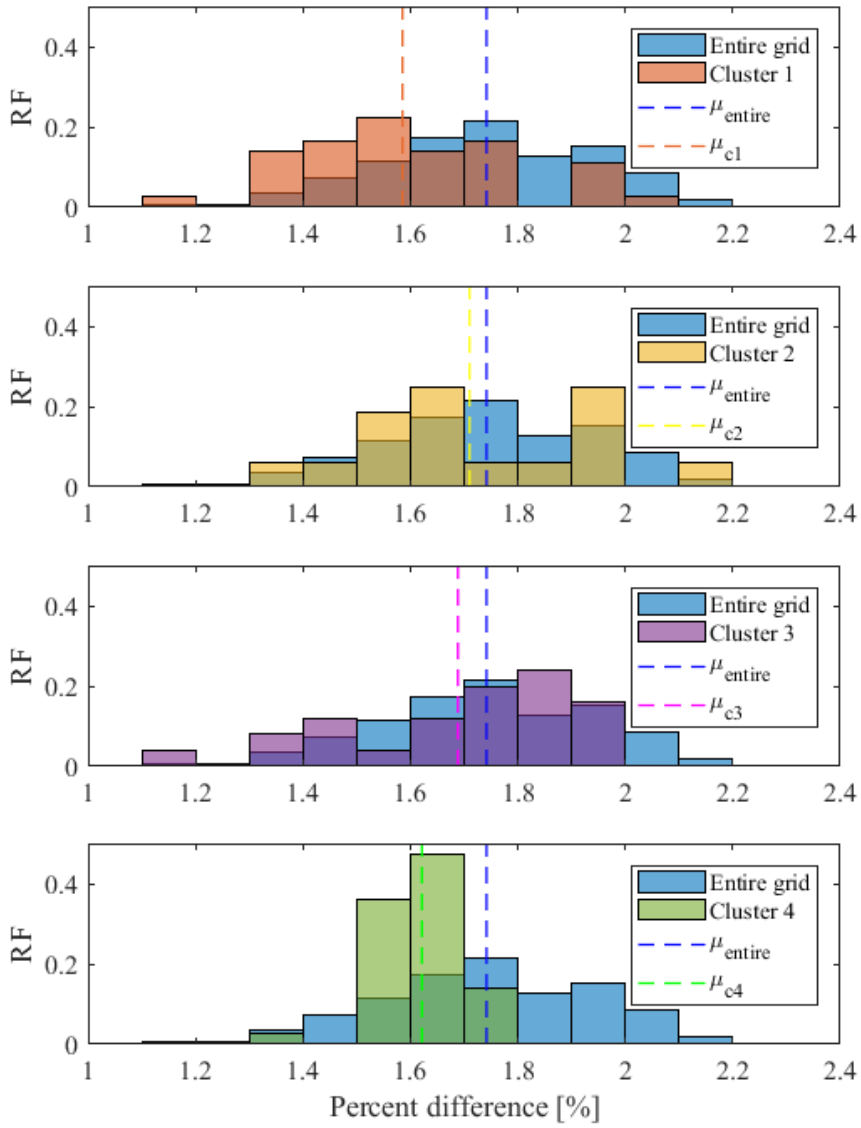

Figure 5.73: Histogram of the whole result differences in *Svq* of the cluster-based grid (RF: Relative frequency)

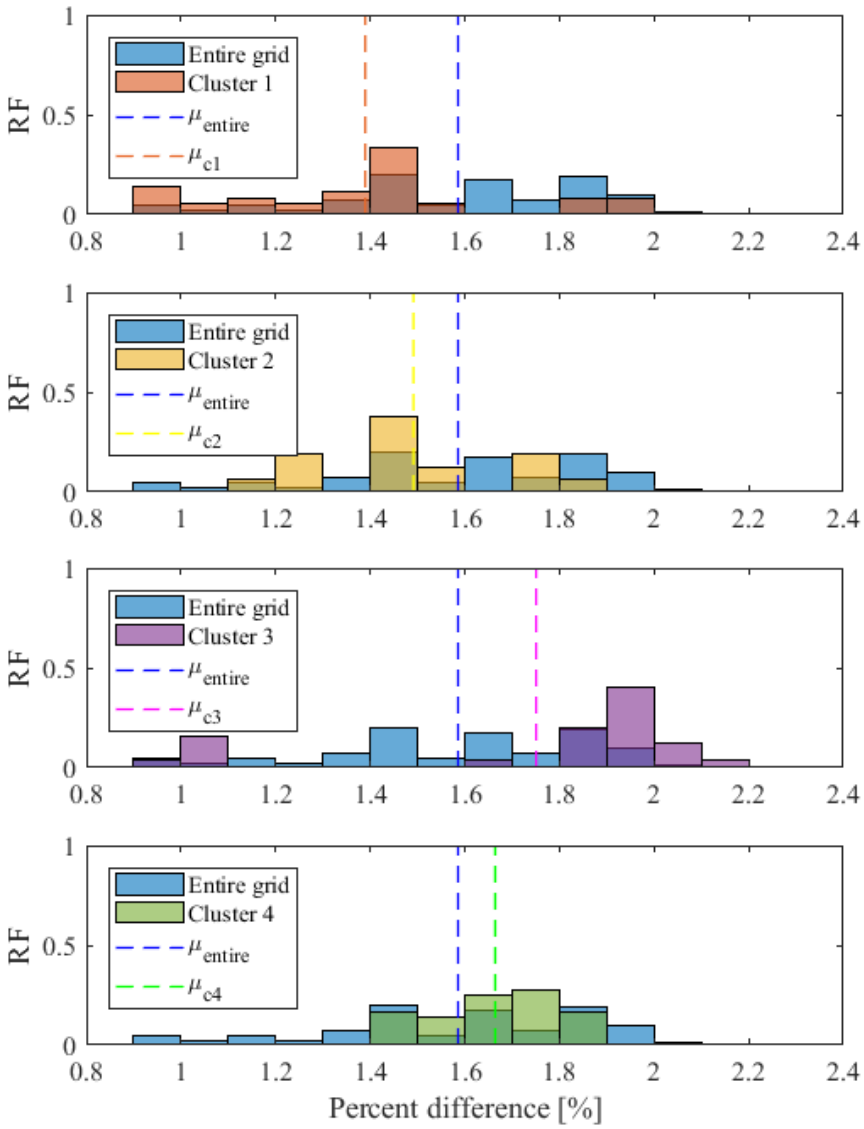

Figure 5.74: Histogram of the whole result differences in *Sphip* of the cluster-based grid (RF: Relative frequency)

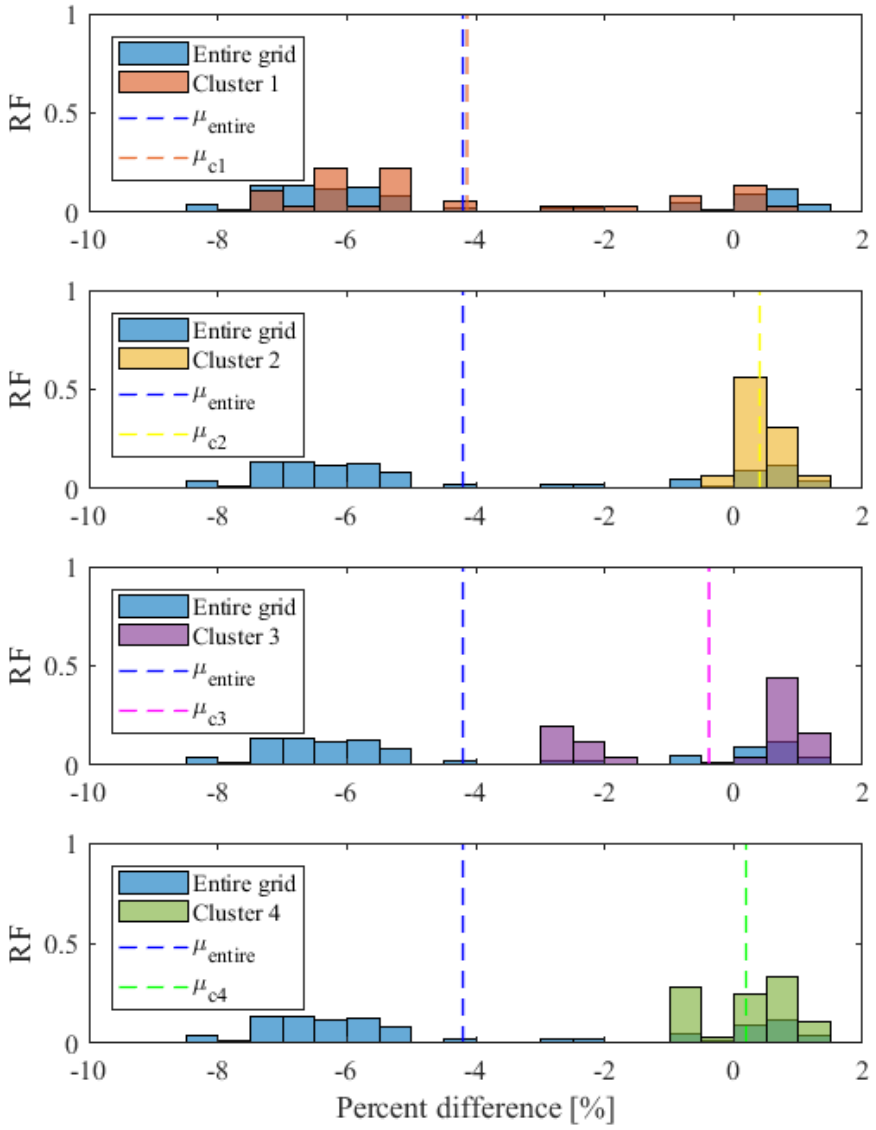

Figure 5.75: Histogram of the whole result differences in *Sphiq* of the cluster-based grid (RF: Relative frequency)

To give more insight into the calculated sensitivity values, the original sensitivity values are demonstrated besides the mean difference. Figure 5.76 depicts the comparison of voltage magnitude sensitivities *Svp* and *Svq*. The sensitivity values in this figure are self-sensitivity of voltage magnitude at bus 105 in relation to active and reactive powers at its own bus. The units of *Svp* is pu/MW, and the unit of *Svq* is pu/Mvar, as provided together with name under its respective columns. Regards Figure 5.76, the calculated values are very close to their reference. The difference is 0.01 pu/MW for *Svp*, whereas the difference is 0.006 pu/Mvar for *Svq*. In this cluster-based grid, the active power has more impact on voltage magnitude than the reactive power since resistance is dominant.

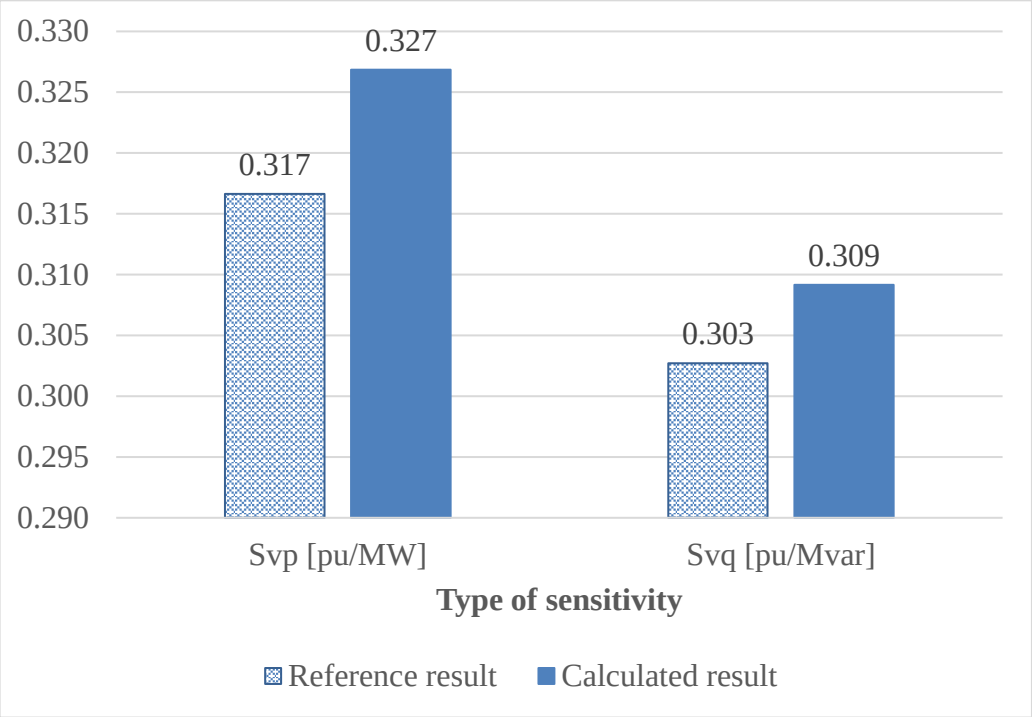

Figure 5.76: Calculated sensitivity values of voltage magnitude at bus 105 to active and reactive powers at its bus in comparison to reference results

Subsequently, the comparison of voltage angle sensitivities *Sphip* and *Sphiq* is shown, as portrayed in Figure 5.77. These sensitivities are self-sensitivity of the voltage angle at bus 105 in relation to active and reactive powers at its own bus. The units are deg/MW and deg/Mvar for *Sphip* and *Sphiq*, which are indicated together with the column name. Obviously, the calculated values of *Sphip* and *Sphiq* are precise. Since reactance is dominant in this grid case, the voltage angle is more sensitive to the active power. The difference is around 0.4 deg/MW for *Sphip* and 0.2 deg/Mvar for *Sphiq*. Moreover, there is a point that corresponds to the case of magnitude sensitivities. As the resistance is more dominant in this cluster-based grid, the voltage angle is more sensitive to the reactive power.

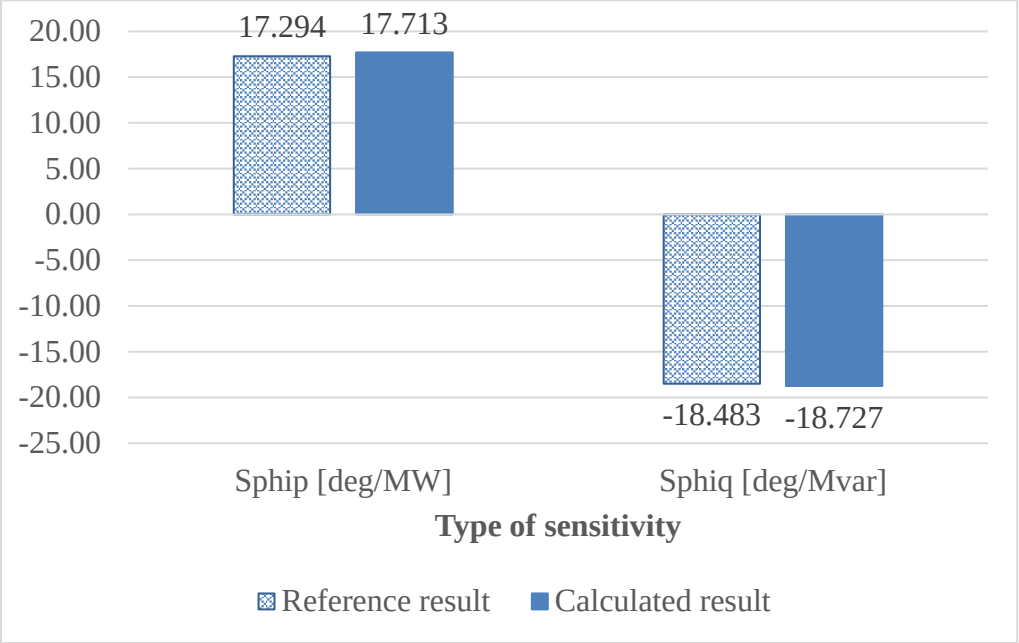

Figure 5.77: Calculated sensitivity values of the voltage angle at bus 105 to active and reactive powers at its bus in comparison to reference results

In this section, the proposed method for voltage sensitivity analysis has been verified by simulations of the entire grid case, in which radial and mesh MV grids are investigated. The unbalanced and balanced grid conditions are both taken into account. The verification indicates that the proposed method allows high accuracy in voltage sensitivity analysis by using only measurement data of bus voltages and currents. As the next step, measurement errors are considered to exist in measured bus voltages and currents. The response of the proposed method to measurement errors is examined in the next section.

5.2.3 Impact of Measurement Errors

As experimented in Case Study 1, the impact of measurement errors is investigated in this case study as well through simulations. The TVE is therefore taken into account. The input data for voltage sensitivity analysis in Section 5.2.2 are still used in this simulation for both unbalanced and balanced grid conditions. Five levels of 0.2%, 0.4%, 0.6%, 0.8% and 1.0% TVE are added to the existing input data, which are regarded as 0% TVE to investigate the impact of measurement errors. The results from these five levels of TVE are explored as follows. The mean differences of each sensitivity type with TVE are compared to observe the outcome from the proposed method. For the unbalanced condition, the accuracy from mean of absolute percent differences of voltage magnitude and angle sensitivities in relation to a sequence current are discussed. To give the overview of the investigation, only the mean differences in the positive sequence are demonstrated in this section. The results of other sequences are provided in Appendix D. The comparisons in the case of voltage magnitude sensitivities $Svir,1$ and $Svii,1$ are, respectively, portrayed in Figure 5.78 and Figure 5.79.

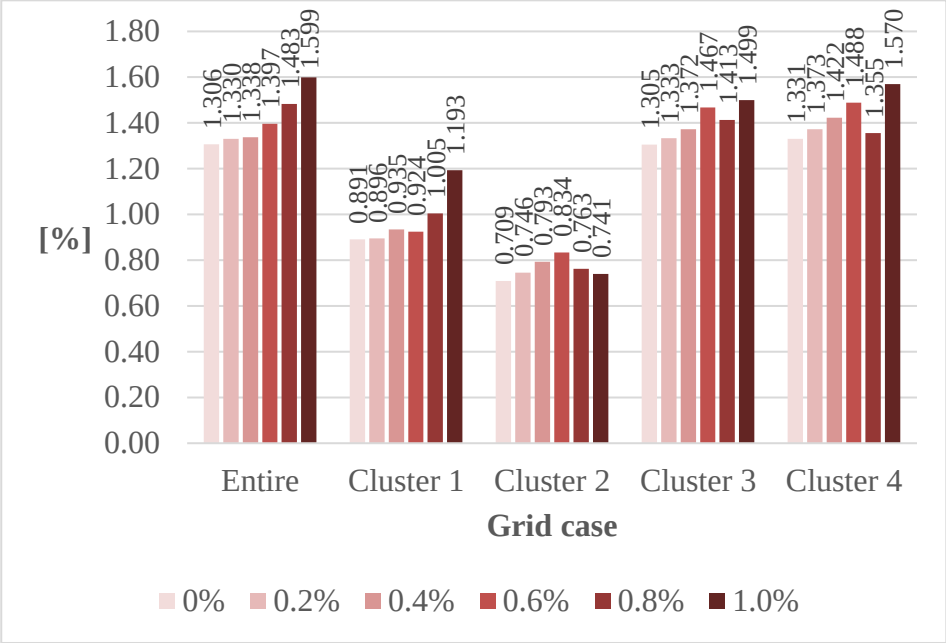

Figure 5.78: Mean values of absolute differences of *Svir*,1 in each grid case at different levels of TVE

Figure 5.79: Mean values of absolute differences of *Svii*,1 in each grid case at different levels of TVE

The mean differences for both sensitivities *Svir*,1 and *Svii*,1 increase as the TVE increases. However, at 1.0% TVE, which is the limit of error defined in IEC/IEEE 60255-118-1 [108], the mean values of the result differences show that the results from the proposed method deviate from their reference only slightly at the maximum of 2.64%. This has low impact as the original values are in the range of $\times 10^{-4}$. Next, the comparisons in the case of voltage angle sensitivities *Sphiir*,1 and *Sphiii*,1 are depicted in Figure 5.80 and Figure 5.81.

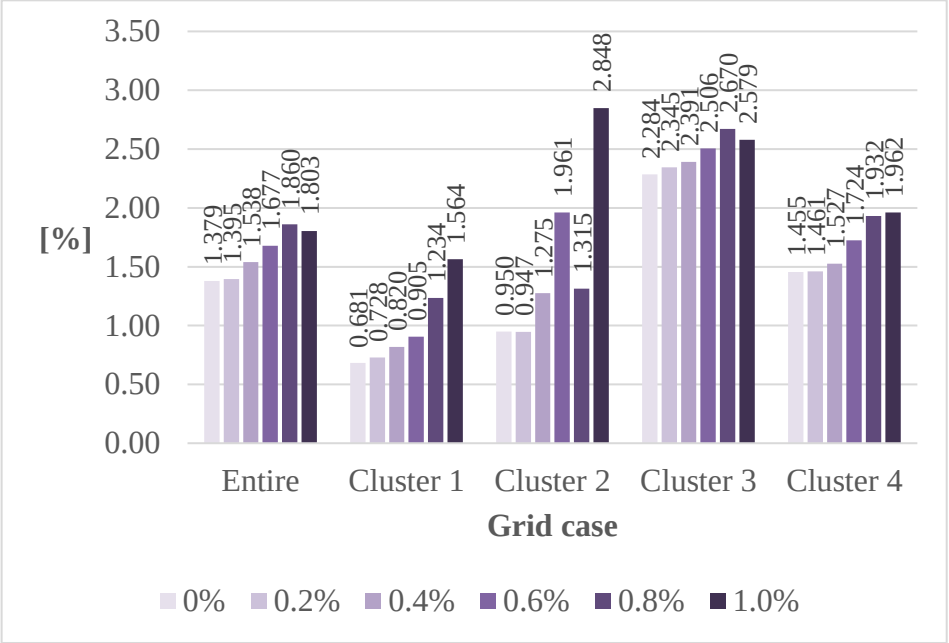

Figure 5.80: Mean values of absolute differences of *Sphiir*,1 in each grid case at different levels of TVE

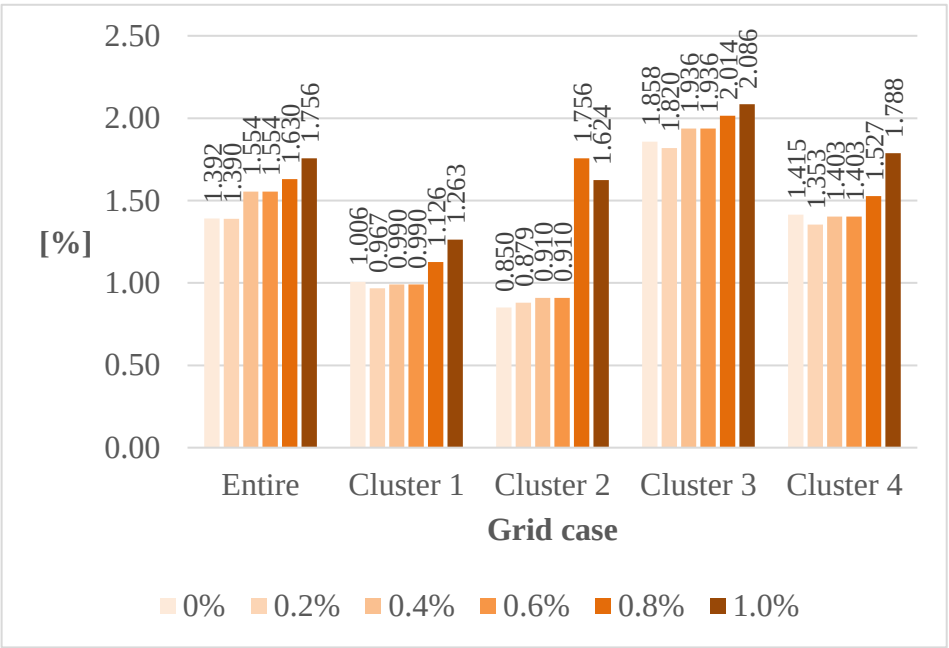

Figure 5.81: Mean values of absolute differences of *Sphiii*,1 in each grid case at different levels of TVE

The proposed method also successfully handles the measurement errors for the sensitivities *Sphiir*,1 and *Sphiii*,1. Mostly, the mean differences of these sensitivities rise following the increase of the TVE. So far, the results from the simulations verify that the proposed method is able to produce precise sensitivity analysis provided that the TVE is in the range 0 to 1.0%.

The impact of the measurement errors for the balanced grid condition is subsequently investigated. The same range of the TVE is applied in this simulation. The mean differences in different grid cases are analysed for each sensitivity type – *Svp*, *Svq*, *Sphip*, and *Sphiq* – individually. The result comparison in the case of voltage magnitude sensitivities *Svp* and *Svq* is portrayed in Figure 5.82 and Figure 5.83. After that, the result comparisons in the case of voltage angle sensitivities *Sphip* and *Sphiq* are displayed in Figure 5.84 and Figure 5.85.

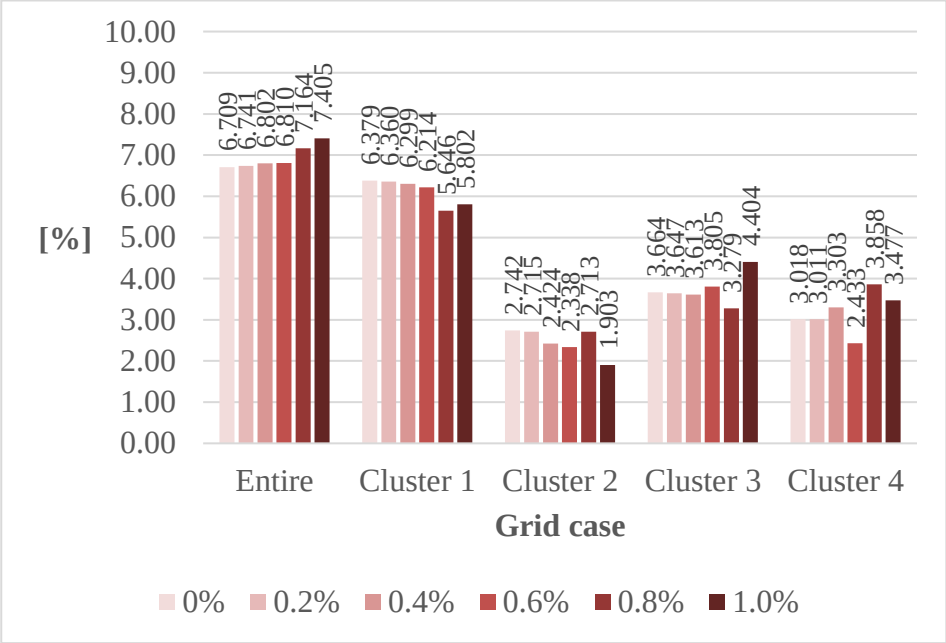

Figure 5.82: Mean values of absolute differences of *Svp* of each grid case at different levels of TVE

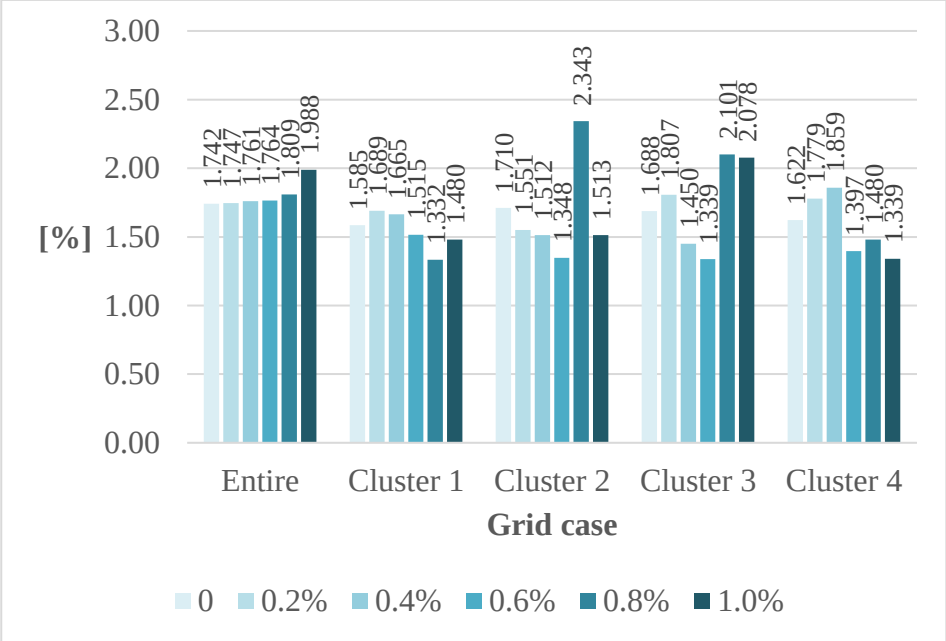

Figure 5.83: Mean values of absolute differences of *Svq* of each grid case at different levels of TVE

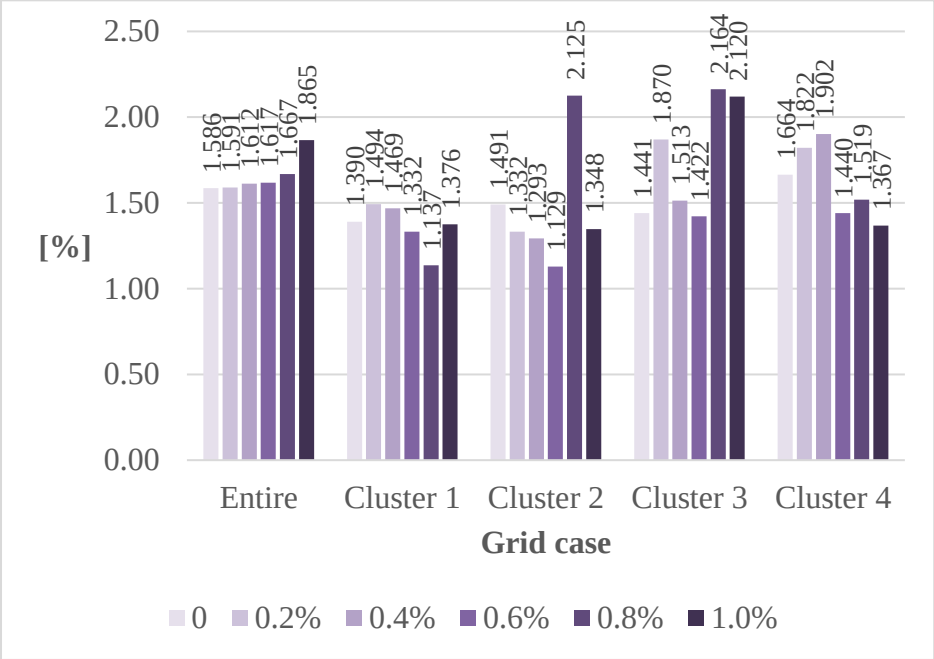

Figure 5.84: Mean values of absolute differences of *Sphip* of each grid case at different levels of TVE

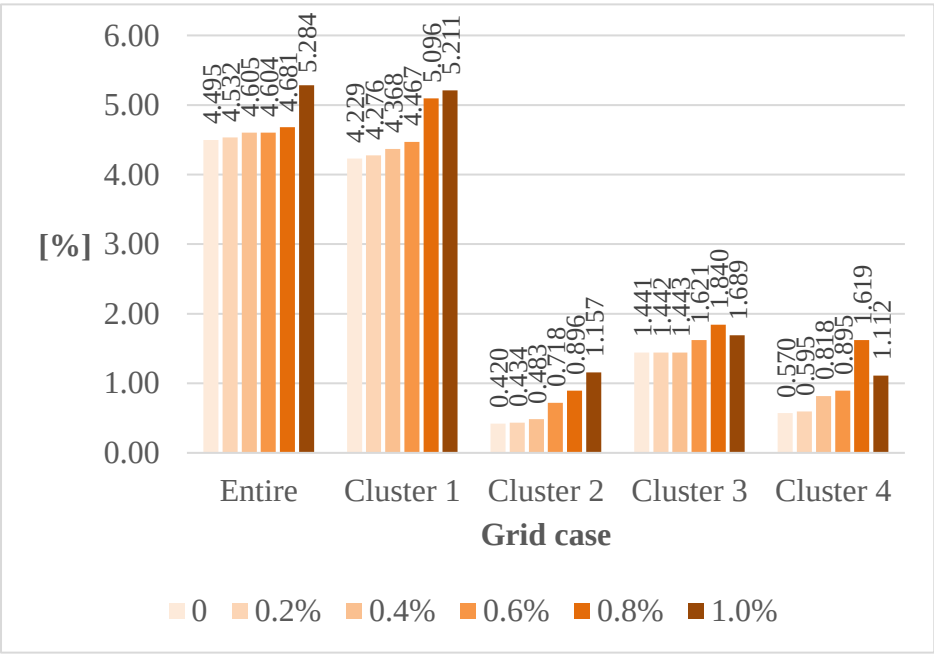

Figure 5.85: Mean values of absolute differences of *Sphiq* of each grid case at different levels of TVE

According to the result comparisons, all sensitivity types respond similarly to the increase of TVE. In some grid cases, the mean difference with 1.0% TVE is lower than the differences in other TVE levels. This can occur, because the sensitivities for the balanced grid condition depend solely on the predetermined bus impedance parameters, as stated in Eq. (4.77), Eq. (4.83), Eq. (4.92), and Eq. (4.98) for *Svp*, *Svq*, *Sphip*, and *Sphiq*. The bus impedance parameters in cluster-based grid is related to the integration process of Thévenin impedance.

Since the impedance parameters are small, the integration process can lead to slight fluctuation in the calculation of relative percent differences, which are then used to determine the mean difference.

Finally, Case Study 2 has been discussed. The verification is performed by the simulation on the exemplified low-voltage radial grid under the unbalanced and balanced grid conditions. By adding a step for the integration of the influence between interconnected cluster areas obtained from Thévenin impedance, individual bus impedance parameters of each cluster area can be determined. After that, using the proposed voltage sensitivity analysis method in cluster-based grid is carried out. Owing to the demonstrated results, high accuracy of voltage sensitivity analysis is achieved. Furthermore, the measurement errors based on TVE are analysed to observe their impact on sensitivity analysis from the proposed method. The results show that the proposed method is able to deal with the measurement errors in the cluster-based grid. In conclusion, the decoupled voltage sensitivity analysis based on the CPSA is successfully verified. The proposed network model and the analysis method reliably perform in the cluster-based grid, as they perform in the entire grid case in Case Study 1.

Case Study 3 is subsequently examined in the next section. Selected applications of the proposed voltage sensitivity analysis are examined. Since decentralised operation based on the CPSA is the focus of this thesis, the cluster-based grid from this case study is continued in Case Study 3. Based on the calculated sensitivity values, regulation of voltage profile can be carried out.

5.3 Case Study 3: Applications of the Proposed Voltage Sensitivity Analysis

The proposed impedance model and method for voltage sensitivity analysis are successfully verified in Case Studies 1 and 2. Their correctness and accuracy have been proved. In this thesis, the proposed voltage sensitivity analysis is designed to adapt to different grid conditions. If the power grid is in the unbalanced condition, the sensitivity of voltage magnitude and angle in relation to complex sequence currents is provided. If the power grid is in the balanced condition, the sensitivity of voltage magnitude and angle in relation to active and reactive powers is delivered. In this section, as the next step, the results, i.e. sensitivity values, from sensitivity analysis are further utilised. Some applications that can leverage the sensitivity values are discussed in Case Study 3.

Two experiments are conducted in this case study to examine voltage magnitude and angle regulations based on the sensitivity values. The CPSA is also taken into account, so the experiments are performed on the cluster-based low-voltage grid depicted in Figure 5.53 from Case Study 2. The cluster-based grid is still composed of four cluster areas. In the experiments, each cluster area performs voltage sensitivity analysis individually in both

unbalanced and balanced grid conditions. To demonstrate applications of the proposed voltage sensitivity analysis, the voltage regulation is simulated in DIgSILENT PowerFactory. Two scenarios – adjusting from a single bus and adjusting from multiple coordinated buses – are defined, as listed in Table 5.11. Bus 105 is chosen as the target for voltage magnitude and angle regulation by the selected controlled bus(es).

Table 5.11: Simulation scenarios

Scenario	Target bus	Controlled bus
Single bus	105	105
Coordinated buses	105	103, 104, 105

In this case study, the controlled buses are assumed to be capable of controlling their output sequence currents in the case of an unbalanced condition and controlling active and reactive powers in the case of a balanced condition. Bus 105 itself is the controlled bus in the single bus scenario, while buses 103, 104, and 105 are the controlled buses in the coordinated buses scenario. In practice, this control can be realised through intelligent devices such as inverters [234–236]. The algorithm for doing so is, however, not discussed, since it is outside of the scope of this thesis.

5.3.1 Experiment on Sensitivity Value in Voltage Magnitude Regulation

Voltage magnitude is a controlled state variable of power grids. In low-voltage grids, the permissible range is nominal voltage ($\underline{V}_N$) ±10%. This simulation is aimed to demonstrate the use of the sensitivity values to regulate the voltage profile. To regulate the voltage magnitude, the sensitivity values are set as the setpoint of current or power output at their corresponding controlled buses.

In this experiment, bus 105 in Cluster 2 is defined as the target for the regulation and set to have high fed-in power. The results from magnitude regulation are first in the balanced grid condition, where the response on voltage regulation on the whole grid is also observed. Then, the results from the unbalanced grid condition are discussed. In this case, the response of the voltage regulation in Cluster 2 is shown. The regulation is performed in two operational scenarios: single bus and coordinated buses.

To perform the experiment of the balanced grid condition, the initial voltage magnitude $|\underline{V}_{ini}|$ at bus 105 is 1.088 pu. A corrective action is assumed to be executed to avoid the magnitude to exceed 1.10 pu or +10% of the nominal voltage. The target is set to reduce the magnitude of bus 105 to the expected magnitude $|\underline{V}_{exp}|$ at 1.075 pu. That is, the magnitude change $\Delta|\underline{V}|$ is required at -0.013 pu. For convenience, voltage magnitude information of the target bus is summarised in Table 5.12.

Table 5.12: Voltage magnitude information of the target bus in a balanced grid simulation

Target bus	Initial magnitude $\lvert\underline{V}_{ini}\rvert$ [pu]	Expected magnitude $\lvert\underline{V}_{exp}\rvert$ [pu]	Required magnitude $\Delta\lvert\underline{V}\rvert$ [pu]
105	1.088	1.075	-0.013

Regards the proposed analysis method, the sensitivities *Svp* and *Svq* are offered for regulation of the voltage magnitude in relation to active and reactive powers. This experiment begins with using the sensitivity *Svp* for adjusting active power *P* to regulate the magnitude of the target bus. The sensitivity values of *Svp* and the required active power ΔP are summarised in Table 5.13. To overcome the required magnitude $\Delta\lvert\underline{V}\rvert$, the required power ΔP is the amount of active power that must be added to the existing power *P* at the controlled bus(es). In the single bus scenario, the power ΔP is determined only for bus 105 to handle the whole magnitude $\Delta\lvert\underline{V}\rvert$ at -0.013 pu. In the coordinated buses scenario, the magnitude $\Delta\lvert\underline{V}\rvert$ is equally covered by bus 103 to bus 105. Accordingly, the magnitude $\Delta\lvert\underline{V}\rvert$ of -0.0043 pu, which is one third of -0.013 pu, is defined for each coordinated bus. In the simulation, the power ΔP is calculated for the controlled bus(es).

Table 5.13: Use of *Svp* for voltage regulation

Scenario	Controlled bus	Required magnitude $\Delta\lvert\underline{V}\rvert$ [pu]	Sensitivity value [pu/MW]	Required ΔP [MW]
Single bus	105	-0.013	0.2770	-0.0469
Coordinated buses	103	-0.0043	0.1685	-0.0255
	104		0.2025	-0.0212
	105		0.2770	-0.0155

Figure 5.86 illustrates the response of all voltage magnitudes in relation to adjusting active power. By adjusting active power, the magnitude $\lvert\underline{V}_{fin}\rvert$ of 1.075 pu and the magnitude $\lvert\underline{V}_{fin}\rvert$ of 1.076 pu are achieved at bus 105 from single and coordinated buses scenarios, respectively. The voltage magnitudes of the rest of the buses in this grid are also reduced, since they are sensitive to the active power *P* of the controlled buses as well. However, the effect is comparatively smaller in this simulation.

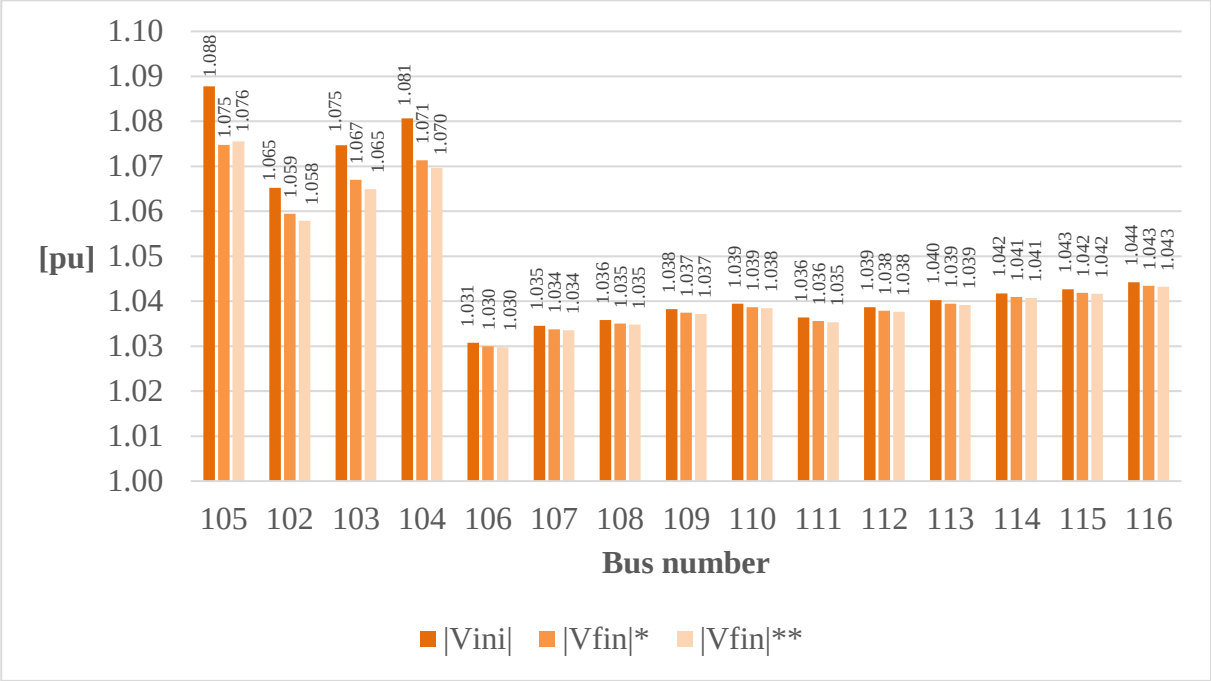

Figure 5.86: Regulating voltage magnitude using *Svp*
* Using only bus 105; ** Coordination of buses 103, 104, and 105

This experiment then proceeds to using the sensitivity *Svq* for adjusting reactive power Q to regulate the target magnitude. The sensitivity values of *Svq* and the required reactive power ΔQ are provided in Table 5.14. To achieve the required magnitude $\Delta|\underline{V}|$, the power ΔQ is the amount of the reactive power required to add to the existing power Q at the controlled bus(es). The allocation of the magnitude $\Delta|\underline{V}|$ is the same as aforementioned in the case of the sensitivity *Svp*.

Table 5.14: Use of *Svq* for voltage regulation

Scenario	Controlled bus	Required magnitude $\Delta\|\underline{V}\|$ [pu]	Sensitivity value [pu/Mvar]	Required ΔQ [Mvar]
Single bus	105	-0.013	0.2612	-0.0498
Coordinated buses	103	-0.0043	0.2083	-0.0206
	104		0.2248	-0.0191
	105		0.2612	-0.0165

Figure 5.87 displays the response of all voltage magnitudes in relation to adjusting reactive power. By adjusting reactive power, the magnitude $|\underline{V}_{fin}|$ of 1.074 pu is acquired from both single and coordinated buses scenarios. The target magnitude $|\underline{V}_{tar}|$ is therefore fulfilled, as the difference between $|\underline{V}_{tar}|$ and $|\underline{V}_{fin}|$ is very small at 0.001 pu. Similar to the case of *Svp*, the

voltage magnitudes of other buses are also affected by adjusting the power *Q*. In this case, nonetheless, the effect is higher, as the amount of *Q* is required more than *P* to fulfil $|\underline{V}_{tar}|$.

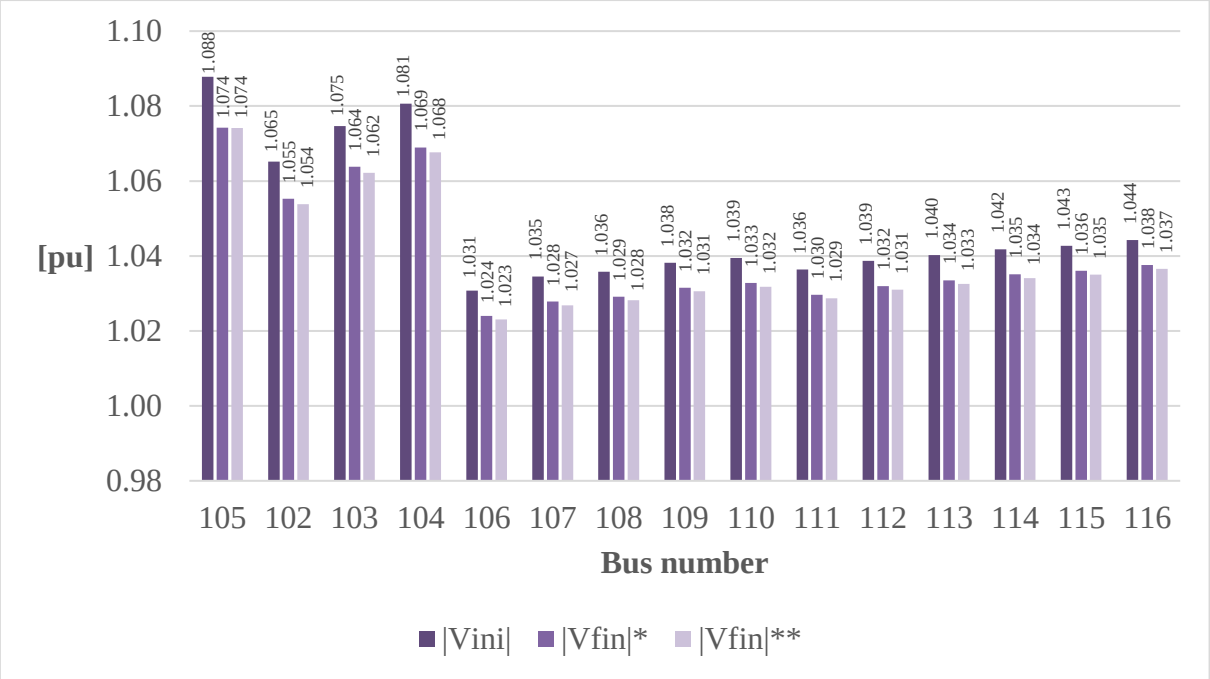

Figure 5.87: Regulating voltage magnitude using *Svq*
* Using only bus 105; ** Coordination of buses 103, 104, and 105

Figure 5.86 and Figure 5.87, hence, showcase voltage magnitude regulation based on the sensitivity values resulting from voltage sensitivity analysis in the balanced grid condition. The magnitude regulation can be executed by either a single bus or multiple buses. The target magnitude $|\underline{V}_{tar}|$ can be achieved in all scenarios. Table 5.15 shows maximum loading of the cables in Cluster 1. The loading decreases as a result of the new active and reactive power setpoints of each corresponding bus.

Table 5.15: Maximum line loading in magnitude regulation using *Svp* and *Svq*
*fbus : From bus, tbus: To bus

Cable (fbus – tbus*)	**Initial loading [%]**	**Final loading [%]**			
		Using *Svp*		**Using *Svq***	
		Single bus	**Coordinated buses**	**Single bus**	**Coordinated buses**
101-102	97.760	83.836	80.303	91.185	90.459
102-103	86.517	70.621	66.703	78.818	78.075
103-104	63.110	47.397	50.514	56.170	57.623
104-105	34.348	20.555	29.142	29.722	31.561

The same procedure is also applied to simulate this grid in the unbalanced condition. In this simulation, the initial situation of the cluster-based grid is nonetheless set to be different from the situation in the balanced condition. The purpose here is to keep voltage magnitude around the nominal voltage. Regulation of the voltage magnitude $|\underline{V}_a|$ at phase *a* of bus 105 is examined as an example. The initial magnitude $|\underline{V}_{a,ini}|$ is set to 1.015 pu, and the expected magnitude $|\underline{V}_{a,exp}|$ is defined at 1.010 pu. Accordingly, -0.005 pu of the magnitude change $\Delta|\underline{V}|$ is required. For convenience, voltage magnitude information of the target bus is summarised in Table 5.16.

Table 5.16: Voltage magnitude information of the target bus in the simulation under an unbalanced grid condition

Target bus	Initial magnitude $\lvert\underline{V}_{a,ini}\rvert$ [pu]	Expected magnitude $\lvert\underline{V}_{a,exp}\rvert$ [pu]	Required magnitude $\Delta\lvert\underline{V}\rvert$ [pu]
105	1.015	1.010	-0.005

The proposed analysis method for the unbalanced grid condition provides the sensitivity of the voltage magnitude in relation to the real and imaginary components of a sequence current. The sensitivities *Svir*,0, *Svir*,1, and *Svir*,2 are used for adjusting the real component I_{Re} of a sequence current, and the sensitivities *Svii*,0, *Svii*,1, and *Svii*,2 are used for adjusting the imaginary component I_{Im} of a sequence current, where 0, 1, and 2 denote zero, positive, and negative sequence respectively.

First, the results from adjusting the real-component current I_{Re} at the control buses is presented. The sensitivity values of *Svir*,0, *Svir*,1, and *Svir*,2 and the required real-component currents ΔI_{Re} are summarised in Table 5.17. The current ΔI_{Re} is the amount of current that must be added to the existing current I_{Re} at the controlled bus(es) to overcome the required magnitude $\Delta|\underline{V}|$. In the single bus scenario, the current ΔI_{Re} is determined only for bus 105 to deal with the whole magnitude $\Delta|\underline{V}|$ at -0.005 pu. In the coordinated buses scenario, the magnitude $\Delta|\underline{V}|$ is assigned equally to bus 103 to bus 105. The magnitude $\Delta|\underline{V}|$ of -0.00167 pu is allocated to the controlled bus. Besides, it must be noted that only the final magnitudes in Cluster 2, in which bus 105 resides, are presented here for brevity, and the response of the entire grid is shown in the balanced grid condition.

Table 5.17: Use of *Svir*,0, *Svir*,1, and *Svir*,2 for voltage magnitude regulation

Scenario	Controlled bus	Target magnitude $\Delta\lvert\underline{V}_a\rvert$ [pu]	Sensitvity type	Sensitivity value [pu/A]	Required current ΔI_{Re} [A]
Single bus	105	-0.005	*Svir*,0	-0.00099	-5.05050
			Svir,1	-0.00030	-16.66667
			Svir,2	-0.00030	-16.66667
Coordinated buses	103	-0.00167	*Svir*,0	-0.00061	-2.73770
			Svir,1	-0.00020	-8.35
			Svir,2	-0.00020	-8.35
	104	-0.00167	*Svir*,0	-0.00073	2.28767
			Svir,1	-0.00024	6.95833
			Svir,2	-0.00024	6.95833
	105	-0.00167	*Svir*,0	-0.00099	1.68687
			Svir,1	-0.00030	5.56667
			Svir,2	-0.00030	5.56667

Figure 5.88 illustrates the results from using sensitivities in Table 5.17. The expected magnitude $|\underline{V}_{a,exp}|$ is succeeded by all scenarios. Using *Svir*,0, *Svir*,1, and *Svir*,2 yields final magnitude $|\underline{V}_{a,fin}|$ at around 1.01 pu. Table 5.18 shows maximum loading among three phases of the cables in Cluster 1 in this voltage magnitude regulation. The loading changes from the initial condition as a result of the new sequence current setpoints of each corresponding bus.

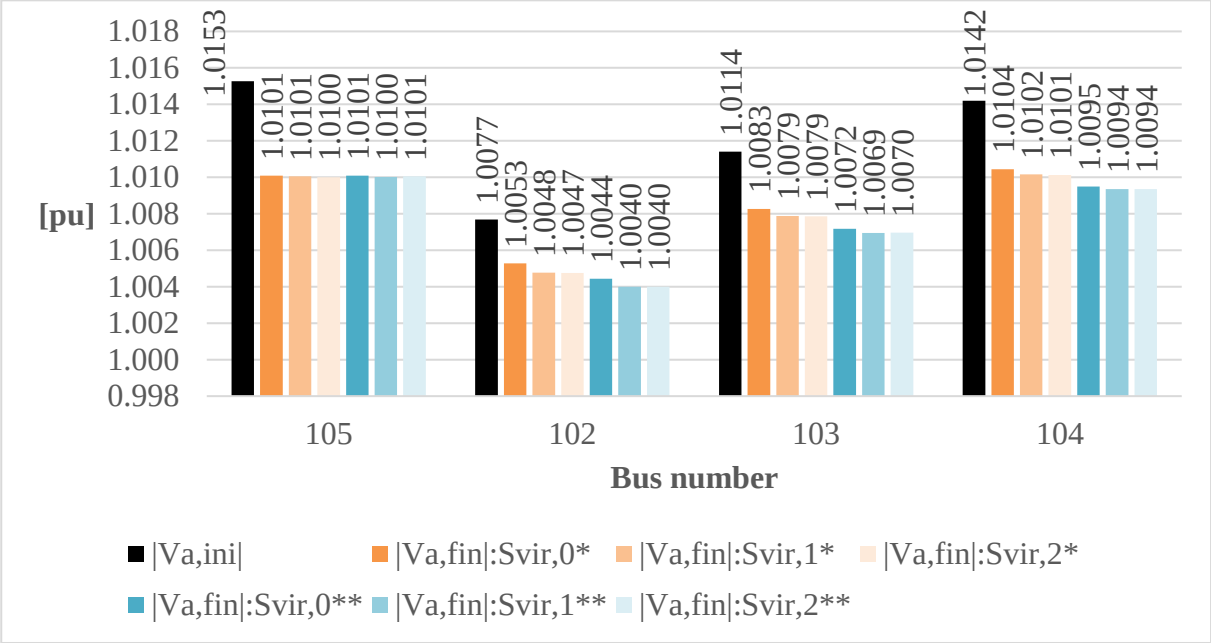

Figure 5.88: Regulating voltage magnitude using *Svir*
* Using only bus 105; ** Coordination of buses 103, 104, and 105

Table 5.18: Maximum line loading in magnitude regulation using *Svir*,0, *Svir*,1, and *Svir*,2
*fbus : From bus, tbus: To bus

Cable (fbus – tbus*)	**Initial loading [%]**	**Final loading [%]**					
		Using *Svir*,0		**Using *Svir*,1**		**Using *Svir*,2**	
		Single bus	**Coordinated buses**	**Single bus**	**Coordinated buses**	**Single bus**	**Coordinated buses**
101-102	8.853	7.426	6.928	8.083	8.062	8.027	8.847
102-103	18.297	15.876	15.308	18.374	18.348	18.294	18.345
103-104	17.616	12.854	13.850	17.688	17.670	17.568	17.647
104-105	7.102	7.891	7.307	2.008	5.260	11.495	8.394

Using the sensitivities *Svii*,0, *Svii*,1, and *Svii*,2 for adjusting the imaginary component I_{Im} of a sequence current is subsequently examined. Table 5.19 shows the sensitivity values of *Svii*,0, *Svii*,1, and *Svii*,2, and the required current ΔI_{Im}. With these sensitivities, the current ΔI_{Im} is the amount of the imaginary-component current required to achieve the required magnitude $\Delta|\underline{V}_a|$. It is then added to the existing current I_{Im} at the controlled bus(es). Lastly, the allocation of the magnitude $\Delta|\underline{V}_a|$ in each scenario is the same as previously provided in Table 5.17.

Table 5.19: Use of *Svii*,0, *Svii*,1, and *Svii*,2 for voltage magnitude regulation

Scenario	Controlled bus	Target magnitude $\Delta\|\underline{V}\|$ [pu]	Sensitvity type	Sensitivity value [pu/A]	Required current ΔI_{Im} [A]
Single bus	105	-0.005	*Svii*,0	0.000054	-92.59259
			Svii,1	0.000071	-70.42254
			Svii,2	0.000072	-69.44444
Coordinated buses	103	-0.00167	*Svii*,0	0.000082	-20.36585
			Svii,1	0.000078	-21.41026
			Svii,2	0.000078	-21.41026
	104	-0.00167	*Svii*,0	0.000073	-22.87671
			Svii,1	0.000076	-21.97368
			Svii,2	0.000076	-21.97368
	105	-0.00167	*Svii*,0	0.000054	-30.92592
			Svii,1	0.000071	-23.52113
			Svii,2	0.000072	-23.19444

Figure 5.89 illustrates the results from using sensitivities *Svii*,0, *Svii*,1, and *Svii*,2. Accurate final magnitude $|\underline{V}_{a,fin}|$ is produced by almost all sensitivities. Except only the use of *Svii*,0 of the sole bus 105, the magnitude $|\underline{V}_{a,fin}|$ is 1.0067 pu that is too low from the expected magnitude $|\underline{V}_{a,exp}|$. However, the magnitude $|\underline{V}_{a,fin}|$ from this sensitivity *Svii*,0 is improved to 1.0092 pu when the coordinated buses take place, where the required current to achieve the target magnitude is shared among buses 103 to 105. This means that higher sensitivity value or low required current is more preferable to lower sensitivity values or higher required currents. Table 5.20 shows maximum loading among three phases of the cables in Cluster 1 in this voltage magnitude regulation. The loading noticeably increases from the initial condition, since the sensitivities *Svii*,0, *Svii*,1, and *Svii*,2 are small, thus having low impact on voltage magnitude. The required current ΔI_{Im} for the new setpoint of each corresponding bus is apparently large, as also provided in Table 5.19.

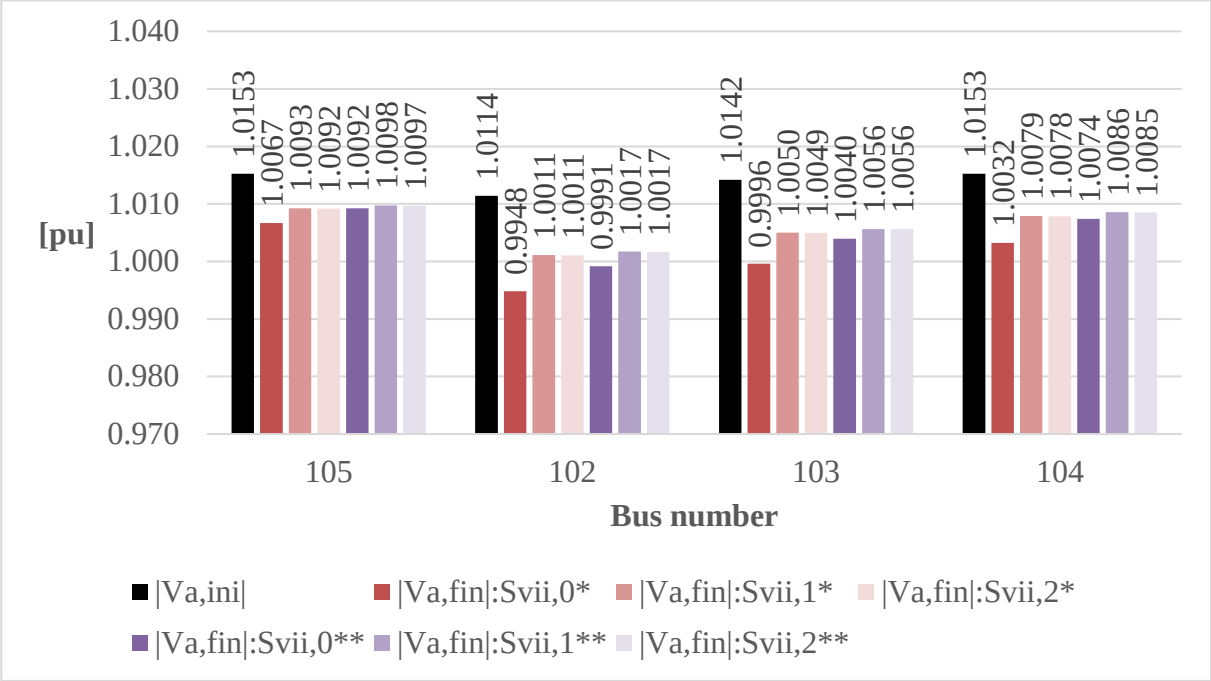

Figure 5.89: Regulating voltage magnitude using *Svii*
* Using only bus 105; ** Coordination of buses 103, 104, and 105

Table 5.20: Maximum line loading in magnitude regulation using *Svii*,0, *Svii*,1, and *Svii*,2

Cable (fbus – tbus)	**Initial loading [%]**	**Final loading [%]**					
		Using *Svii*,0		**Using *Svii*,1**		**Using *Svii*,2**	
		Single bus	**Coordinated buses**	**Single bus**	**Coordinated buses**	**Single bus**	**Coordinated buses**
101-102	8.853	81.600	64.422	23.069	22.142	23.019	22.143
102-103	18.297	108.902	88.885	30.980	30.133	30.927	30.135
103-104	17.616	94.617	54.603	27.745	20.701	29.707	20.787
104-105	7.102	94.191	29.900	26.302	11.519	28.652	13.928

Regulating voltage magnitude based on the sensitivity values in the unbalanced grid condition is successfully demonstrated in Figure 5.88 and Figure 5.89. The magnitude regulation evidently can be accurately executed by either a single bus or coordinated buses. However, in the case that using a single bus requires a high sequence current, using coordinated buses is preferable. Basically, the expected magnitude $|\underline{V}_{a,exp}|$ can be achieved in all scenarios in both balanced and unbalanced grid conditions. In the next section, the experiment of using the sensitivity values in a voltage angle regulation is then discussed. The same scenarios as used in this section are still taken into account. As the voltage magnitude regulation based on the sensitivity values is succeeded, an accurate regulation of the voltage angle is expected.

5.3.2 Experiment on Sensitivity Value in Voltage Angle Regulation

The proposed voltage sensitivity analysis method also produces voltage angle sensitivity values. Hence, this section is devoted to an experiment on a voltage angle regulation based on the outcome from angle sensitivities. This experiment is conducted using simulations. To regulate the angle, the sensitivity values are set as the reference of current or power output at their corresponding active buses.

The cluster-based low voltage grid with four cluster areas from Section 5.3.1 is also used here. In this experiment, bus 105 in Cluster 2 is defined as the target for the regulation. The target angle in this context is the angle of phase *a* for both balanced and unbalanced conditions. First, the results of a voltage angle regulation are delineated in the balanced grid condition, including the response of the entire grid. Afterwards, the results of the angle regulation in the unbalanced condition are discussed. Adopted from Section 5.3.1, the angle regulation is examined in a single bus and coordinated buses scenarios.

For the experimental purpose, the voltage angle δ_a at phase *a* of bus 105 is intentionally set to deviate for +0.3˚ (deg), called deviated angle $\Delta\delta_a$ thereafter. In the simulation, the initial angle $\delta_{a,ini}$. at bus 105 is -147.86˚. The expected angle $\delta_{a,exp}$ therefore is 147.56º. The voltage angle information of the target bus is summarised in Table 5.21.

Table 5.21: Voltage angle information of the target bus in a balanced grid simulation

Target bus	Initial angle $\delta_{a,ini}$ [deg]	Expected angle $\delta_{a,exp}$ [deg]	Deviated angle $\Delta\delta_a$ [deg]
105	-147.86	-147.56	+0.30

According to the proposed analysis method, the sensitivities *Sphip* and *Sphiq* are provided for regulating the voltage angle in relation to active and reactive powers. To begin with, adjusting active power *P* to regulate phase angle δ_a of the target bus is simulated. Thus, the sensitivity *Sphip* is used. Table 5.22 provides the sensitivity values of *Sphip* and the required active power ΔP, which is the amount of active power that must be added to the existing power *P* at the controlled bus(es) to achieve the angle $\Delta\delta_a$. The power ΔP is determined only for bus 105 to handle the angle $\Delta\delta_a$ at +0.3º in the single bus scenario. Then, the power ΔP in the coordinated buses scenario is determined for bus 103 to bus 105, each of which is to equally handle +0.1º of the angle $\Delta\delta_a$ in order to achieve +0.3º in total.

Table 5.22: Use of *Sphip* for a voltage angle regulation

Scenario	Controlled bus	Target angle $\Delta\delta_a$ [deg]	Sensitivity value [deg/MW]	Required power ΔP [MW]
Single bus	105	+0.30	14.9632	0.0200
Coordinated buses	103	+0.10	12.2260	0.0082
	104		13.0527	0.0077
	105		14.9632	0.0067

Figure 5.90 depicts the response of the voltage angle δ_a at phase *a* of bus 105 in relation to adjusting active power *P*. The final angle $\delta_{a,fin,}$ is -147.54º at bus 105 in both single and coordinated buses scenarios. This means that the expected angle $\delta_{a,exp}$ is achieved with only 0.02º error. Similar to the case of voltage magnitude regulation, the rest of the buses are also affected by the required ΔP of the controlled buses, but the effect is comparatively smaller than that of bus 105, which is the target bus.

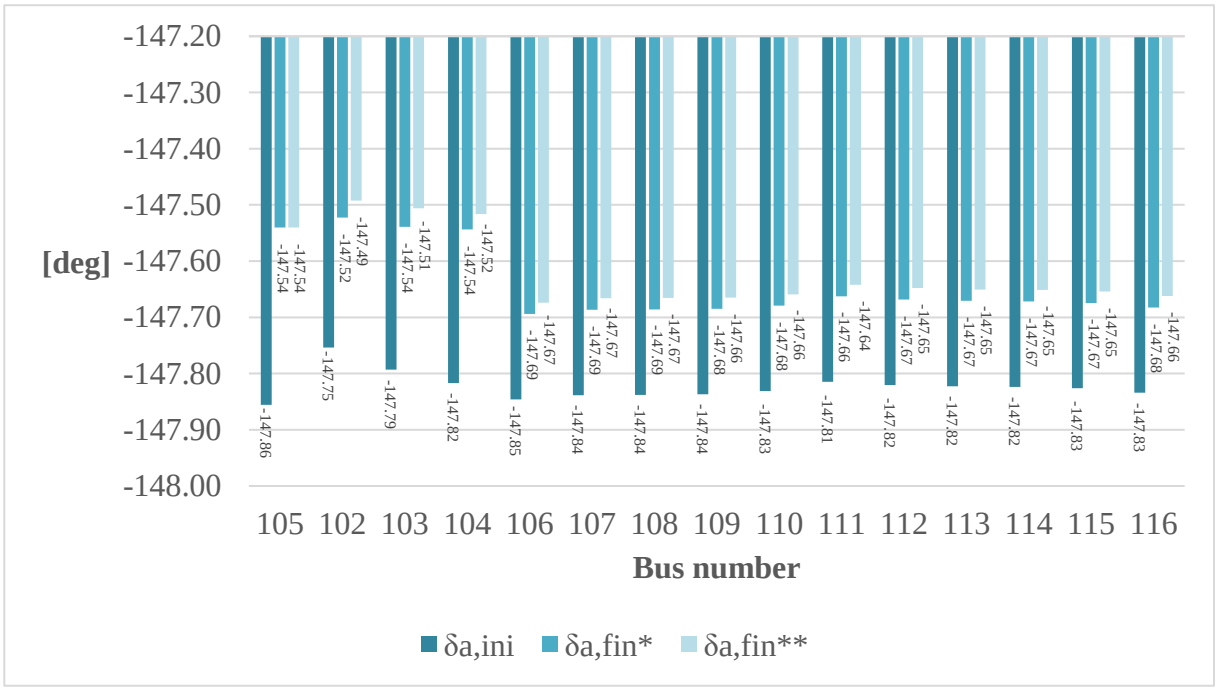

Figure 5.90: Regulating the voltage angle using *Sphip*
* Using only bus 105; ** Coordination of buses 103, 104, and 105

In the next step, adjusting reactive power *Q* based on the sensitivity *Sphiq* to regulate phase angle δ_a of the target bus is simulated. The sensitivity values of *Sphiq* and the required reactive power ΔQ are listed in Table 5.23. The power ΔQ is the amount of reactive power that must be added to the existing power *Q* at the controlled bus(es) to achieve the angle $\Delta\delta_a$.

The allocation of the angle $\Delta\delta_a$ in the single bus and coordinated buses scenarios is carried out in the same manner as the case of the sensitivity *Sphip*.

Table 5.23: Use of *Sphiq* for a voltage angle regulation

Scenario	Controlled bus	Target $\Delta\delta_{a,exp}$ [deg]	Sensitivity value [deg/Mvar]	Required ΔQ [Mvar]
Single bus	105	+0.30	-15.8722	-0.0189
Coordinated buses	103	+0.10	-9.8925	-0.0101
	104		-11.7564	-0.0085
	105		-15.8722	-0.0063

Figure 5.91 depicts the response of the angle δ_a at phase *a* of bus 105 in relation to adjusting the reactive power *Q*. Similar to the simulation in the case of the sensitivity *Sphip*, the expected angle $\delta_{a,exp}$ is achieved with only 0.03º error, as the final angle $\delta_{a,fin,}$ at bus 105 is -147.53º in both single and coordinated buses scenarios. Also, the rest of the buses are slightly affected.

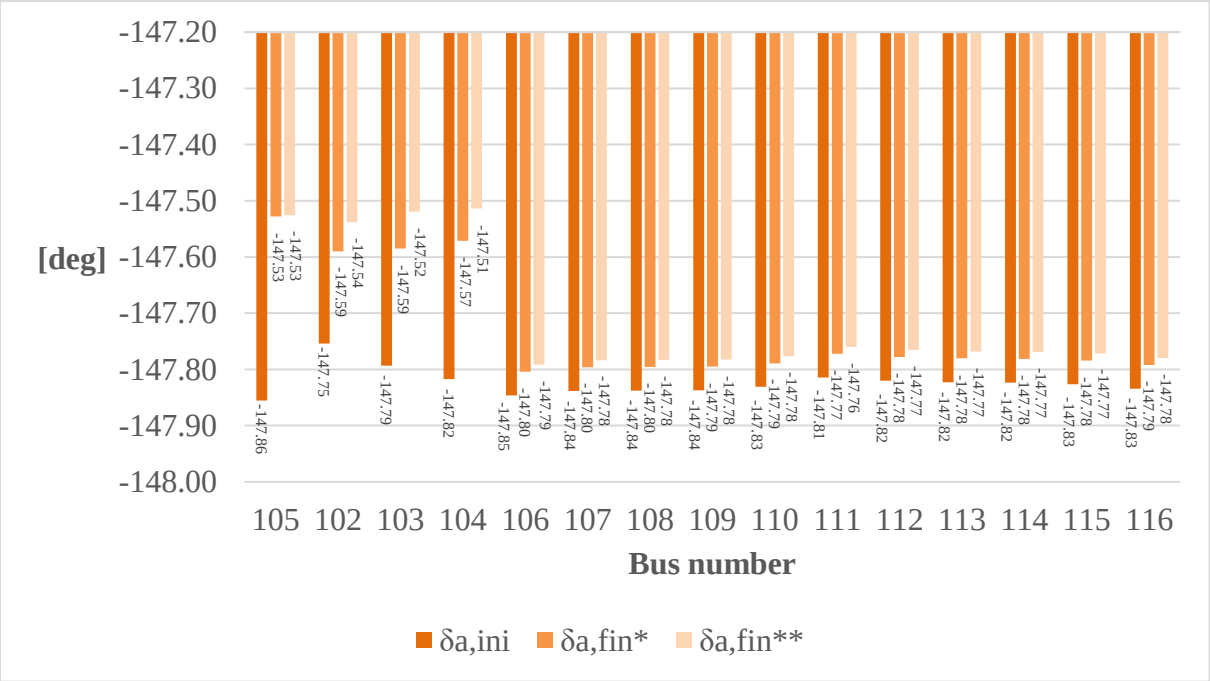

Figure 5.91: Regulating the voltage angle using *Sphiq*

* Using only bus 105; ** Coordination of buses 103, 104, and 105

Regulation of the voltage angle based on the sensitivity values in the balanced grid condition is shown in Figure 5.90 and Figure 5.91 for *Sphip* and *Sphiq*, respectively. The angle regulation can be performed by either a single bus or coordinated buses. As a result, the expected angle $\delta_{a,exp}$ can be achieved in all scenarios. Table 5.24 shows maximum loading of the cables in Cluster 1 in this voltage angle regulation. New loadings in the case of *Sphip* and *Sphiq* change in different direction from the initial condition because the sensitivities *Sphip* and *Sphiq* have an opposite sign or impact on the voltage angle. The required power *P* and *Q* for the new setpoints of each corresponding bus are provided in Table 5.22 and Table 5.23.

Table 5.24: Maximum line loading in angle regulation using *Sphip* and *Sphiq*

Cable (fbus – tbus)	**Initial loading [%]**	**Final loading [%]**			
		Using *Sphip*		**Using *Sphiq***	
		Single bus	**Coordinated buses**	**Single bus**	**Coordinated buses**
101-102	97.760	103.956	104.827	94.905	94.033
102-103	86.517	93.727	94.746	83.036	82.004
103-104	63.110	70.430	68.288	59.676	60.453
104-105	34.348	41.762	36.682	30.979	33.172

The experiment in the unbalanced condition is also executed on the cluster-based grid using the same procedure. The same expected angle $\delta_{a,exp}$ is also applied. Thus, the deviated phase angle $\Delta\delta_a$ is still +0.3˚. For convenience, the voltage angle information of the target bus is summarised in Table 5.25. As an example, regulating the angle δ_a at phase *a* of bus 105 is investigated.

Table 5.25: Voltage angle information of the target bus in an unbalanced grid simulation

Target bus	Initial angle $\delta_{a,ini}$ [deg]	Expected angle $\delta_{a,exp}$ [deg]	Deviated angle $\Delta\delta_a$ [deg]
105	-149.85	-149.55	+0.30

For the unbalanced grid condition, the proposed analysis method produces the sensitivity of the voltage angle in relation to real and imaginary components of a sequence current. Defined that the zero, positive, and negative sequences are respectively denoted by 0, 1, and 2, the sensitivities *Sphiir*,0, *Sphiir*,1, and *Sphiir*,2 are used for adjusting the real component I_{Re} of a sequence current, and the sensitivities *Sphiii*,0, *Sphiii*,1, and *Sphiii*,2 are used for adjusting the imaginary component I_{Im} of a sequence current.

In the following, the results from adjusting the current I_{Re} in the simulation are presented first. The sensitivity values of *Sphiir*,0, *Sphiir*,1, and *Sphiir*,2 and the required real-component currents ΔI_{Re} are summarised in Table 5.26. The current ΔI_{Re} is the amount of current that must be added to the existing current I_{Re} at the controlled bus(es) to acquire the required angle $\Delta\delta_a$. In the single bus scenario, the current ΔI_{Re} is determined only for bus 105 to deal with the whole angle $\Delta\delta_a$ at +0.30º. In the coordinated buses scenario, the expected angle $\delta_{a,exp}$ at bus 105 is still +0.30º, but the angle $\Delta\delta_a$ is equally divided and assigned to each controlled bus. The angle $\Delta\delta_a$ of +0.10º is therefore allocated to bus 103 to bus 105. Besides, it must be noted that only the final angles in Cluster 2 are shown, as the response of the whole grid is shown in the simulation of the balanced grid condition.

Table 5.26: Use of *Sphiir*,0, *Sphiir*,1, and *Sphiir*,2 for a voltage angle regulation

Scenario	Controlled bus	Deviated angle $\Delta\delta_a$ [deg]	Sensitvity type	Sensitivity value [deg/A]	Required current ΔI_{Re} [A]
Single bus	105	+0.30	*Sphiir*,0	-0.00301	-99.66777
			Sphiir,1	-0.00401	-74.81297
			Sphiir,2	-0.00402	-74.62686
Coordinated buses	103	+0.10	*Sphiir*,0	-0.00462	-21.64502
			Sphiir,1	-0.00441	-22.67574
			Sphiir,2	-0.00440	-22.72727
	104	+0.10	*Sphiir*,0	-0.00412	-24.27184
			Sphiir,1	-0.00428	-23.36448
			Sphiir,2	-0.00427	-23.41920
	105	+0.10	*Sphiir*,0	-0.00301	-33.22259
			Sphiir,1	-0.00401	-24.93766
			Sphiir,2	-0.00402	-24.87562

Figure 5.92 portrays the results from using sensitivities *Sphiir*,0, *Sphiir*,1, and *Sphiir*,2. The expected angle $\delta_{a,exp}$ is achieved in almost all scenarios, except only the case of the sensitivity *Sphiir*,0. The final angle $\delta_{a,fin}$ resulting from *Sphiir*,0 is -149.67˚ instead of -149.55˚ in the single bus scenario. Nevertheless, the final angle $\delta_{a,fin}$ from the sensitivity *Sphiir*,0 is improved to -149.60˚ in the coordinated buses scenario, where the required real-component

zero sequence current is shared among buses 103 to 105. This means that, according to the results, higher sensitivity value or low required current is more preferable to lower sensitivity values or higher required current. Table 5.27 shows maximum loading among three phases of the cables in Cluster 1 in this voltage angle regulation. The loading noticeably increases from the initial condition, since the sensitivities *Sphiir*,0, *Sphiir*,1, and *Sphiir*,2 are small, therefore having low impact on the voltage angle. The required current ΔI_{Re} for the new setpoints of each corresponding bus is large, as provided in Table 5.26.

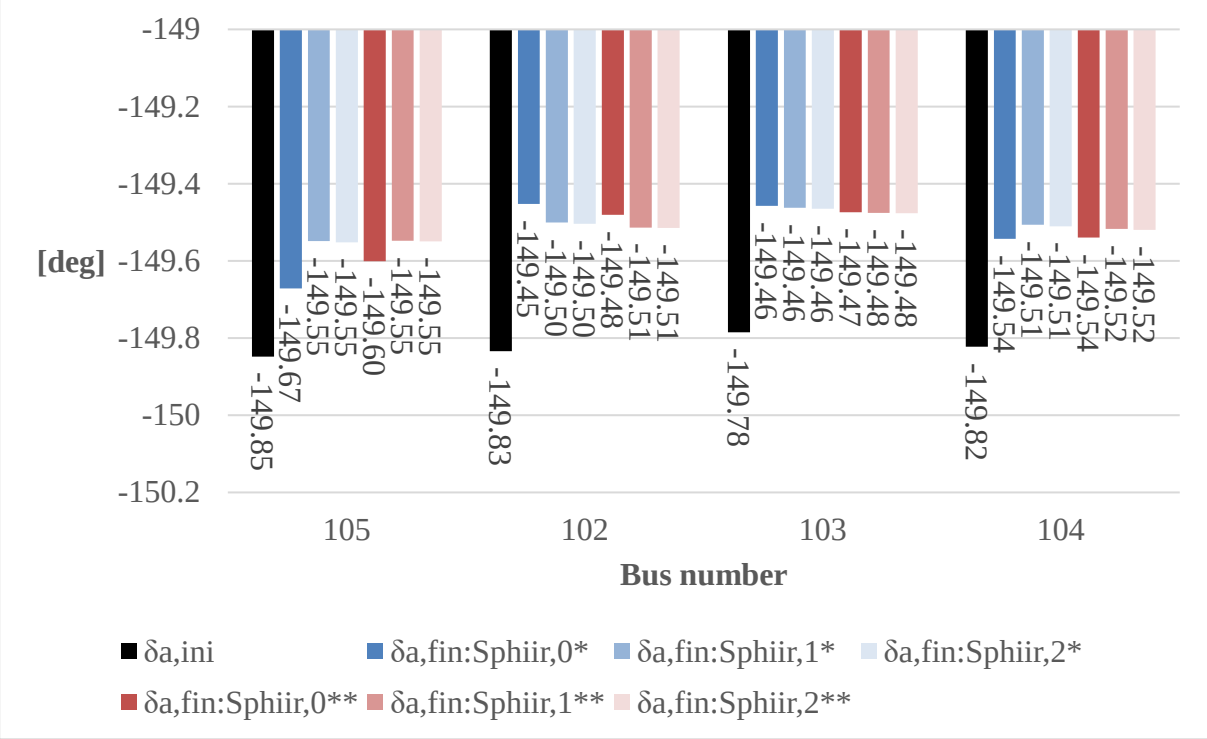

Figure 5.92: Regulating the voltage angle using *Sphiir*
* Using only bus 105; ** Coordination of buses 103, 104, and 105

Table 5.27: Maximum line loading in angle regulation using *Sphiir*,0, *Sphiir*,1, and *Sphiir*,2

Cable (fbus – tbus)	**Initial loading [%]**	**Final loading [%]**					
		Using *Sphiir*,0		**Using *Sphiir*,1**		**Using *Sphiir*,2**	
		Single bus	**Coordinated buses**	**Single bus**	**Coordinated buses**	**Single bus**	**Coordinated buses**
101-102	8.853	90.761	73.199	28.654	28.087	28.619	28.090
102-103	18.297	112.401	92.212	40.421	39.763	40.382	39.766
103-104	17.616	113.255	71.832	36.204	28.309	36.163	28.300
104-105	7.102	98.169	32.783	30.077	14.822	28.599	13.303

Subsequently, using the sensitivities *Sphiii*,0, *Sphiii*,1, and *Sphiii*,2 for adjusting the imaginary component I_{Im} of a sequence current is analysed. The sensitivity values of *Sphiii*,0, *Sphiii*,1, and *Sphiii*,2 and the required current ΔI_{Im} are provided in Table 5.28, in which the allocation of the angle $\Delta\delta_a$ in each scenario is the same as stated in the case of *Sphiir*,0, *Sphiir*,1, and *Sphiir*,2. The current ΔI_{Im} is the amount of the imaginary-component current required to achieve the required angle $\Delta\delta_a$, which is expected to be added to the existing current I_{Im} at the controlled bus(es).

In contrast to the adjusting real-component current ΔI_{Re}, the case of using sensitivities *Sphiii*,0, *Sphiii*,1, *Sphiii*,2 enables a quite stable final angle $\delta_{a,fin}$ at -149.53º and -149.54º, as portrayed in Figure 5.93. Owing to the results presented in this section, regulating the voltage angle based on the sensitivity values in the unbalanced grid condition clearly yields an accurate outcome. The angle regulation can be executed by either a single bus or coordinated buses. Lastly, it must be noted that if using a single bus requires a high sequence current, using multiple buses is preferable. Table 5.29 shows maximum loading among three phases of the cables in Cluster 1 in this voltage angle regulation. The loading changes from the initial condition as a result of the new sequence current setpoints of each corresponding bus.

Table 5.28: Use of *Sphiii*,0, *Sphiii*,1, and *Sphiii*,2 for a voltage angle regulation

Scenario	Controlled bus	Deviated angle $\Delta\delta_a$ [deg]	Sensitvity type	Sensitivity value [deg/A]	Required current ΔI_{Re} [A]
Single bus	105	+0.30	*Sphiii*,0	-0.05606	-5.35140
			Sphiii,1	-0.01702	-17.62632
			Sphiii,2	-0.01701	-17.63668
Coordinated buses	103	+0.10	*Sphiii*,0	-0.03407	-2.93513
			Sphiii,1	-0.01148	-8.71080
			Sphiii,2	-0.01148	-8.71080
	104	+0.10	*Sphiii*,0	-0.04096	-2.44141
			Sphiii,1	-0.01321	-7.57002
			Sphiii,2	-0.01322	-7.56430
	105	+0.10	*Sphiii*,0	-0.05606	-1.78380
			Sphiii,1	-0.01702	-5.87544
			Sphiii,2	-0.01701	-5.87889

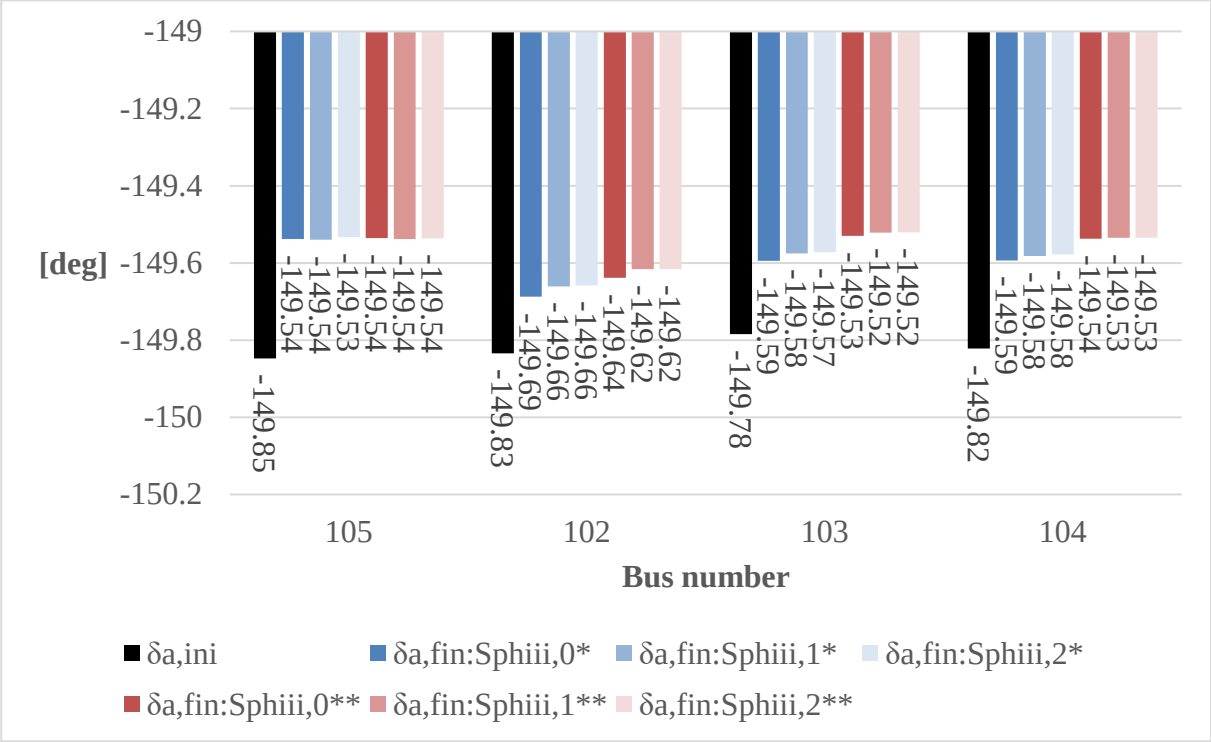

Figure 5.93: Adjusting the voltage angle using *Sphiii*
* Using only bus 105; ** Coordination of buses 103, 104, and 105

Table 5.29: Maximum line loading in angle regulation using *Sphiii*,0, *Sphiii*,1, and *Sphiii*,2

Cable (fbus – tbus)	**Initial loading [%]**	**Final loading [%]**					
		Using *Sphiii*,0		**Using *Sphiii*,1**		**Using *Sphiii*,2**	
		Single bus	**Coordinated buses**	**Single bus**	**Coordinated buses**	**Single bus**	**Coordinated buses**
101-102	8.853	9.056	9.190	10.371	11.111	10.371	11.110
102-103	18.297	21.454	22.755	18.899	19.546	18.899	19.545
103-104	17.616	16.846	16.859	17.654	17.657	17.579	17.596
104-105	7.102	6.829	6.628	9.771	7.629	12.027	8.629

In conclusion, the expected angle $\delta_{a,exp}$ can be achieved in all scenarios in both balanced and unbalanced grid conditions, as shown in Figure 5.90 to Figure 5.93. Clearly, the angle regulation can be precisely performed in either case of a single bus or coordinated buses. Nevertheless, using multiple buses is preferable in the case that using a single bus requires a high sequence current.

5.4 Summary

The proposed network model, or bus impedance parameters, and the method for voltage sensitivity analysis are successfully verified in this chapter through simulations in three case studies: entire grid, cluster-based grid, and applications of voltage sensitivity analysis. To examine the flexibility of the proposed method, three grids with different grid topological types and voltage levels are employed in the simulations. Case Studies 1 and 2 are developed to verify the accuracy and usability of the proposed network model and analysis method, while Case Study 3 is aimed to demonstrate some applications of the proposed voltage sensitivity analysis.

In **Case Study 1**, a modified IEEE 37-bus test feeder and an exemplified mesh grid are used. Both of them are defined to reside in the medium-voltage level. This case study is targeted for the use of the proposed method in the entire grid case. The bus impedance parameters and the proposed analysis method are therefore examined on the entire power grid structure. For each grid in the case studies, the matrix of bus impedance parameters is compared with the bus impedance matrix, i.e. the reference, which is manually calculated from the information of grid topology. Then, the bus impedance parameters are further used in the proposed analysis method. The sensitivity values resulted from the proposed analysis method are compared with the sensitivity values, or reference values, calculated by the classical method in DIgSILENT PowerFactory. The accuracy of the bus impedance parameters and the outcome from proposed analysis method is observed from the percent differences between them and their reference. The percent differences are then portrayed in the form of histograms to examine the overall characteristics. The examination of the results shows that the proposed model and the proposed method are accurate. The mean of the percent differences is close to zero for any type of the analysis. In the case of the proposed analysis method, moreover, the characteristics of the histograms or the distribution of the overall results from the proposed method is based on two factors: the variation of the sensitivity values from each analysis and the phase angle of the voltage vectors. From the experiments, these factors together can impact the height and the alignment of the distribution of the analysis results among different phases when the results are compared with their reference. However, importantly, the accuracy of the sensitivity analysis is still ensured, as the dispersion of the histograms is small, and their mean is close to zero. Finally, the impact of measurement errors based on the TVE is analysed from 0% to 1% TVE. As a result, the proposed method can still provide accurate analysis. The TVE higher than 1% is not examined in this thesis, as 1% TVE is the maximum permissible error for PMU measurement defined in IEC/IEEE 60255-118-1 standard [108].

In **Case Study 2**, a radial low voltage grid adapted from a real power grid is used. It is defined as a cluster-based grid consisting of four cluster areas based on the CPSA. This case study is targeted for the use of the proposed method in the cluster-based grid case, in which the decoupled voltage sensitivity analysis is required to be performed. Percent differences

between the calculated values and their reference are plotted in the form of histograms to examine both the bus impedance parameters and the proposed analysis method. The plots of the histograms show that high accuracy of the results can be obtained, since the dispersion is small and the mean values close to zero. Especially when the mean of absolute percent differences is considered, the accuracy of the proposed method is mostly improved in the cluster-based grid. In addition, the histograms of the outcome from the proposed method in the case of the entire grid is compared to that of each cluster area in the cluster-based grid. As a result, the characteristics of the histograms is similar in both grid cases. The slight deviation between the histograms from each grid case can be caused by the numerical error during the impedance matrix modification to update the impact of the interconnected cluster areas in the decoupled analysis. Finally, the impact of measurement errors is also analysed in the range of 0% to 1% TVE, and the proposed method still provides accurate analysis for the inputs containing errors. This case study not only verifies the proposed network model and the analysis method for decoupled analysis, but also showcases an advantage of using the CPSA on the power grid.

In **Case Study 3**, voltage magnitude and angle regulations based on sensitivity values are presented. The cluster-based grid from Case Study 2 is used for the simulation in this case study. The expected magnitude and angle are defined to represent various circumstances. The sensitivity values are used to calculate new setpoints for the relevant controlled buses. Thereby, required sequence currents are determined for an unbalanced grid condition, and required active or reactive powers are determined for a balanced grid condition. The results show that sensitivity values allow accurate regulation of voltage magnitude and angle. The sensitivity values can be used for the case of single bus and coordinated buses in order to regulate the voltage profile. This case study thus verifies the further utilisation of the outcome from the proposed analysis method in the aspect of voltage magnitude and angle regulations.

To conclude, the proposed network model and analysis method allow decoupled voltage sensitivity analysis, which contributes an option for decentralised grid operations to the CPSA. They are flexible and scalable for different grid structures and grid voltage levels. The proposed analysis method, together with the proposed network model, requires only measurement data of bus voltages and currents to perform voltage sensitivity analysis. Since complete grid topology is not required like in the classical method, light-weight algorithm for future monitoring and control of smart grids is acquired.

6. Conclusion and Recommendations on Future Work

To cope with the challenges of grid modernisation, in which bidirectional energy supply structure is emerged while grid reliability, efficiency, and stability must be met, the concept of smart grids is introduced. A clustering power systems approach (CPSA) is presented as a solution to smart grids by the research group from the Laboratory of Power Systems and Power Economics, South Westphalia University of Applied Sciences, Soest, Germany. Therefore, the CPSA is used as the foundation of this thesis to facilitate decentralisation of grid operations and control. The key idea of the CPSA is to define grid elements on the underlying power grid into several areas, named as cluster areas. The aim of this approach is to enable distributed active-controlled areas in the entire power systems, and to coexist grid operations between the transmission and distribution systems.

In this thesis, an impedance model and a proposed method of decoupled voltage sensitivity analysis are proposed, to enhance online decentralised grid operations and an interaction strategy between distributed areas under the CPSA. The proposed model and method were developed in conjunction with the CPSA to further improve the philosophy of clustering power systems and leverage its benefits. The key points of this thesis are concluded in this chapter. In the following sections, the conclusion of this thesis is drawn and a recommendation on future work is subsequently given.

6.1 Conclusion

The primary aim of this thesis is to propose a method of decoupled steady-state voltage sensitivity analysis by using only measurement data, which are voltage and current phasors obtained from PMU in this context. The method is focused on the distribution level, which is critical for the realisation of the smart grids. Together with the CPSA, the key contribution of this thesis is a flexible, modular, and scalable voltage sensitivity analysis method that enables decoupled analysis in each individual distributed area, i.e. a cluster area. To perform the sensitivity analysis, determining the impedance network model and executing the proposed method are conducted as a sequential process. Initially, the impedance model, known as a bus impedance parameters matrix [$\underline{Z}_{par}$], is determined by using measured data. Then, the sensitivity analysis is performed in conjunction with the bus impedance parameters to generate voltage magnitude and angle sensitivity values. To summarise this thesis, the conclusion is divided into three main aspects: the impedance network model, the proposed voltage sensitivity analysis method, and the application of the sensitivity values. The three aspects are discussed in detail as follows.

First, the bus impedance parameter matrix [$\underline{Z}_{par}$] describes the voltage-current characteristics between buses or terminals. The principle of the matrix [$\underline{Z}_{par}$] is based on the theory of the bus impedance matrix [$\underline{Z}_{bus}$]. The difference between the matrices [$\underline{Z}_{par}$] and [$\underline{Z}_{bus}$] is that the matrix [$\underline{Z}_{par}$] only consists of bus impedances of the buses of concern in the power grid or a cluster area. The matrix [$\underline{Z}_{bus}$], in contrast, contains bus impedances of all buses. For this reason, for the same power grid, the matrix [$\underline{Z}_{par}$] is comparable to the smaller version of the matrix [$\underline{Z}_{bus}$] when the elements of unconcerned buses in the matrix [$\underline{Z}_{bus}$] are eliminated. To cope with both balanced and unbalanced grid conditions, bus impedances of the matrix [$\underline{Z}_{par}$] are described in the sequence systems, which are zero, positive, and negative sequences. In addition, to determine the matrix [$\underline{Z}_{bus}$] of a cluster area, the influence of a cluster area is represented by the Thévenin impedance $\underline{Z}_{Th}$ at the decoupling bus looking into that area. The Thévenin impedance $\underline{Z}_{Th}$ represents the influence of each cluster area.

Second, using only measurement data is still the primary requirement of the sensitivity analysis. The method for voltage sensitivity analysis is derived from a devised mathematical description of bus voltage. The proposed method uses measured voltage phasors, together with the corresponding bus impedance parameters to perform the sensitivity analysis of the concerned buses. As a result, only measurement data are needed throughout the process, from determining the impedance model to performing the sensitivity analysis. The proposed method is available for both balanced and unbalanced grid conditions to analyse voltage magnitude and angle sensitivities. For an unbalanced condition, voltage magnitude and angle sensitivities in relation to the real and imaginary components of a sequence current are obtained. Thus, the impact of the currents in each sequence can be studied and further used. For a balanced grid condition, voltage magnitude and angle sensitivities in relation to active and reactive powers can be obtained. The impact of active and reactive powers flowing through each bus is therefore observed.

The verification of the proposed network model and the proposed voltage sensitivity analysis method is conducted through simulations in 3 case studies. The first case study is to examine the proposed model and analysis method in the entire grid case, which is common for the power system study. The second case study is to examine the proposed model and analysis method in a cluster-based grid, which is based on the CPSA. In this case study, the key features of the proposed model and analysis method are discussed, as they allow decoupled analysis. The third case study showcases the application of the outcome from the sensitivity analysis to facilitate the voltage profile regulation from the DG units.

In the verification, the matrix [$\underline{Z}_{par}$] is first predetermined in each cluster area by using only local measured voltage and current phasors. Afterwards, the predetermined matrix [$\underline{Z}_{par}$] can be updated by including the impedance $\underline{Z}_{Th}$ of the neighbouring cluster areas. Once this integration process is accomplished, the matrix [$\underline{Z}_{par}$] of each cluster area is ready to be further utilised. Subsequently, the correctness of the calculated [$\underline{Z}_{par}$] is verified by comparing

it with the reduced matrix [$\underline{Z}_{bus}$], which is computed from grid topology information. Kron's reduction technique is used to reduce the size of the matrix [$\underline{Z}_{bus}$] to the size of [$\underline{Z}_{par}$] for comparison purposes. For the case of the cluster-based grid, the matrix [$\underline{Z}_{par}$] of each cluster area is a submatrix of the full matrix of the power grid. Next, the verification of the proposed method is the continuous process from the verification of the impedance model. The proposed method can perform steady-state voltage sensitivity analysis in either the entire grid case or the cluster-based grid case, which represents a decentralised operation. The sensitivity values resulted from the proposed analysis method are compared with their references, which are sensitivity values calculated by the classical method in DIgSILENT PowerFactory.

As a result, the first and second case studies demonstrate that only the measured bus voltages and currents are required to determine the proposed network model and to execute the proposed analysis method. As the verification in this thesis seeks to confirm the theory of the proposed method, the measurement data are assumed to be ideal in the simulation, hence containing no noise and possible errors. The proposed model and analysis method are applicable for different grid topologies and grid voltage levels, proving its flexibility, modularity, and scalability characteristics. With these characteristics, the proposed model and analysis method are suitable for smart grid operations, especially in the distribution level where more DG units will reside in the future. The proposed method yields accurate outcome from the steady-state voltage sensitivity analysis in either the entire grid case or cluster-based grid case, which represents decentralised operation. Thus, the accuracy of decoupled voltage sensitivity analysis is verified. Additionally, the proposed analysis method is investigated with the consideration of measurement error based on TVE. The verification demonstrates that the method can cope with a measurement error of 0% to 1% TVE. The maximum of 1% TVE is added to the measurement error, because it is the maximum permissible measurement error of PMU.

After the accuracy is verified, the application of voltage sensitivity analysis is afterwards examined in the third case study. Regulation of the voltage magnitude and angle by using the outcome of the sensitivity analysis is demonstrated. Thereby, the expected magnitude and angle are defined to imitate miscellaneous circumstances. For regulating the voltage magnitude or angle, the resulted sensitivity values are used to compute the required sequence currents in the unbalanced grid condition and required active or reactive powers in the balanced grid condition. Hence, current or power setpoints for the specific controlled buses can be assigned. The results from voltage regulation illustrate that the resulted sensitivity values allow accurate regulation of voltage magnitude and angle. In practice, controllable loads and generators are the potential entities that can utilise the computed setpoints. Hence, the proposed method is considered as a promising way to actively support voltage profile regulation by means of power dispatch management and control of the pervasive distributed generation.

Finally, according to the proposed method, using only measurement data to determine the bus impedance parameters and to the voltage sensitivity analysis allows a light-weight algorithm, since the complete grid topology is not required. For the implementation of the proposed method, up-to-date measurement data are preferable as they reflect the latest grid status. Hence, this enhances simple distributed grid monitoring and control, and makes the proposed network model and voltage sensitivity analysis method more preferable to the classical method for future smart grids.

6.2 Recommendations on Future Work

The proposed method presented in this thesis can be regarded as a theoretical development of decoupled voltage sensitivity analysis, based on the CPSA. For practical implementation in the future, the proposed method still needs further research, which is listed in this section as follows:

- *Consideration of other potential measurement errors*. Apart from the TVE, the measurement data contain other types of errors such as random noise. The errors should be further investigated, since bad data affect accuracy. This includes the use of estimated data from state estimation in the sensitivity analysis.
- *Use of practical real-time measurement data from PMU*. The utilisation of PMU and its measurement quality requires extensive further research to ensure practical use of the measurement data, which may include real-time data collection.
- *Further research of the proposed method with a dynamic measurement*. The proposed method is examined with static measurement data in this thesis. Thus, as a next step, the use of data from the dynamic measurement could also be researched in order to develop the proposed method for various operational situations.
- *Validation of the proposed method on practical power grids*. The proposed method is verified by simulations in this thesis. In the future, it should be validated in the physical environment.
- *Experiments of the sensitivity results in other applications*. The experiments conducted in this thesis demonstrate the utilisation of the sensitivity values to define the current or power output at certain controlled buses for regulating voltage profile. In future research, experiments could also be conducted to examine the utilisation of the sensitivity values with other operational applications. For instance, an optimisation for scheduling can adopt the sensitivity values to support criteria or constraints, or the control algorithm of inverters could consider the sensitivity values in the determination of the reference parameters.

7. List of Abbreviations

Abbreviations	Description
AC	Alternating Current
AMI	Advanced Metering Infrastructure
CPSA	Clustering Power Systems Approach
DC	Direct Current
DERs	Distribution Energy Sources
DG	Distributed Generation
DMS	Distribution Management System
DSOs	Distribution Systems Operators
EMS	Energy Management System
ENTSO-E	Network of Transmission System Operators for Electricity
EVs	Electric Vehicles
FAN	Field Area Network
GPS	Global Positioning System
ICTs	Information and Communication Technologies
IEA	International Energy Agency
IEC	International Electrotechnical Commission
IED	Intelligent Electronic Device
IEEE	Institute of Electrical and Electronics Engineers
LV	Low Voltage
MV	Medium Voltage
NIST	National Institute of Standards and Technology
PMU	Phasor Measurement Unit
μPMU	Micro Phasor Measurement Unit
RESs	Renewable Energy Sources
RMS	Root Mean Square
SCADA	Supervisory Control and Data Acquisition

SGCC	Smart Grid Cluster Controller
TSOs	Transmission Systems Operators
TVE	Total Vector Error
WAMS	Wide Area Monitoring System
WAN	Wide Area Network

8. List of Figures

9. List of Tables

10. References

[1] V. Lagendijk, *Electrifying Europe: The power of Europe in the construction of electricity networks*. Amsterdam: Aksant, 2008.

[2] H. Altomonte, “Japan's Nuclear Disaster: Its Impact on Electric Power Generation Worldwide [In My View],” *IEEE Power and Energy Mag.*, vol. 10, no. 3, 94-96, 2012, doi: 10.1109/MPE.2012.2187578.

[3] BMWI, *Global installierte Leistung der Erneuerbaren Energien im Jahr 2015.* [Online]. Available: http://www.bmwi.de/Redaktion/DE/Infografiken/Europa/global-installierte-leistung-der-erneuerbaren-energien-2015.html (accessed: Sep. 3 2017).

[4] J. R. Aguero, E. Takayesu, D. Novosel, and R. Masiello, “Modernizing the Grid: Challenges and Opportunities for a Sustainable Future,” *IEEE Power and Energy Mag.*, vol. 15, no. 3, pp. 74–83, 2017, doi: 10.1109/MPE.2017.2660819.

[5] IEA, *World Energy Outlook 2021*. [Online]. Available: https://www.iea.org/reports/world-energy-outlook-2021 (accessed: Nov. 21 2021).

[6] European Commission, *2050 Energy strategy.* [Online]. Available: https://ec.europa.eu/energy/en/topics/energy-strategy-and-energy-union/2050-energy-strategy (accessed: Aug. 10 2017).

[7] European Commission, *2030 Energy Strategy.* [Online]. Available: https://ec.europa.eu/energy/en/topics/energy-strategy-and-energy-union/2030-energy-strategy (accessed: Aug. 10 2017).

[8] REN21, *Reference Tables.* [Online]. Available: http://www.ren21.net/gsr-2017/pages/tables/tables/#table-R2 (accessed: Sep. 3 2017).

[9] BDEW, *Erneuerbare Energien und das EEG: Zahlen, Fakten, Grafiken (2017).* [Online]. Available: https://www.bdew.de/ (accessed: Aug. 10 2017).

[10] AGEE-Stat, *Development of Renewable Energy Sources in Germany 2018.* [Online]. Available: https://www.erneuerbare-energien.de/EE/Navigation/DE/Service/Erneuerbare_Energien_in_Zahlen/Entwicklung/entwicklung-der-erneuerbaren-energien-in-deutschland.html (accessed: Jul. 22 2019).

[11] AG Energiebilanzen e.V., *Bruttostromerzeugung in Deutschland ab 1990 nach Energieträgern.* [Online]. Available: https://www.ag-energiebilanzen.de/ (accessed: Jul. 22 2019).

[12] Federal Ministry for Economic Affairs and Energy (BMWi), *Renewable Energy Sources in Figures: National and International Development, 2017.* [Online]. Available: https://

www.bmwi.de/Redaktion/EN/Publikationen/renewable-energy-sources-in-figures-2017.html (accessed: Jul. 29 2019).

[13] Federal Ministry for Economic Affairs and Energy, “Green Paper on Energy Efficienc,”

[14] Bundesnetzagentur, *EEG in Zahlen 2017*. [Online]. Available: https://www.bundesnetzagentur.de/DE/Sachgebiete/ElektrizitaetundGas/Unternehmen_Institutionen/ErneuerbareEnergien/ZahlenDatenInformationen/zahlenunddaten-node.html (accessed: Jul. 29 2019).

[15] IEA, *World Energy Outlook 2016: Executive summary*. [Online]. Available: http://www.iea.org/Textbase/npsum/WEO2016SUM.pdf (accessed: Sep. 3 2017).

[16] C. Liu, K. T. Chau, D. Wu, and S. Gao, “Opportunities and Challenges of Vehicle-to-Home, Vehicle-to-Vehicle, and Vehicle-to-Grid Technologies,” *Proc. IEEE*, vol. 101, no. 11, pp. 2409–2427, 2013, doi: 10.1109/JPROC.2013.2271951.

[17] B. K. Bose, “Power Electronics, Smart Grid, and Renewable Energy Systems,” *Proc. IEEE*, vol. 105, no. 11, pp. 2011–2018, 2017, doi: 10.1109/JPROC.2017.2745621.

[18] D. Tan, “Energy Challenge, Power Electronics & Systems (PEAS) Technology and Grid Modernization,” *CPSS TPEA*, vol. 2, no. 1, pp. 3–11, 2017, doi: 10.24295/CPSSTPEA.2017.00002.

[19] X. Zhao, “Power System Support Functions Provided by Smart Inverters—A Review,” *CPSS TPEA*, vol. 3, no. 1, pp. 25–35, 2018, doi: 10.24295/CPSSTPEA.2018.00003.

[20] “Shunt-Series-Switched Multi-Functional Grid-Connected Inverter for Voltage Regulation in Vehicle-to-Grid Application,” in *2018 IEEE Transportation Electrification Conference and Expo (ITEC)*, Long Beach, CA, USA, 2018, pp. 961–965.

[21] D. B. Wickramasinghe Abeywardana, P. Acuna, B. Hredzak, R. P. Aguilera, and V. G. Agelidis, “Single-Phase Boost Inverter-Based Electric Vehicle Charger With Integrated Vehicle to Grid Reactive Power Compensation,” *IEEE Trans. Power Electron.*, vol. 33, no. 4, pp. 3462–3471, 2018, doi: 10.1109/TPEL.2017.2700944.

[22] Paramet Wirasanti, “Management Strategy for Smart Grid – A Cluster System Analysis Method,” Doctor of Philosophy, The University of Bolton, UK, 2014.

[23] R. E. Brown, C. S. Wilson, and H. van Nispen, “Becoming the Utility of the Future: Risks and Opportunities,” *IEEE Power and Energy Mag.*, vol. 14, no. 5, pp. 57–65, 2016, doi: 10.1109/MPE.2016.2573857.

[24] J. Crispim, J. Braz, R. Castro, and J. Esteves, “Smart Grids in the EU with smart regulation: Experiences from the UK, Italy and Portugal,” *Utilities Policy*, vol. 31, pp. 85–93, 2014, doi: 10.1016/j.jup.2014.09.006.

[25] C. Dufour and J. Belanger, “On the Use of Real-Time Simulation Technology in Smart Grid Research and Development,” *IEEE Trans. on Ind. Applicat.*, vol. 50, no. 6, pp. 3963–3970, 2014, doi: 10.1109/TIA.2014.2315507.

[26] Z. Fan *et al.*, “Smart Grid Communications: Overview of Research Challenges, Solutions, and Standardization Activities,” *IEEE Commun. Surv. Tutorials*, vol. 15, no. 1, pp. 21–38, 2013, doi: 10.1109/SURV.2011.122211.00021.

[27] M. Liserre, T. Sauter, and J. Hung, “Future Energy Systems: Integrating Renewable Energy Sources into the Smart Power Grid Through Industrial Electronics,” *EEE Ind. Electron. Mag.*, vol. 4, no. 1, pp. 18–37, 2010, doi: 10.1109/MIE.2010.935861.

[28] X. Yu, C. Cecati, T. Dillon, and M. Simões, “The New Frontier of Smart Grids,” *EEE Ind. Electron. Mag.*, vol. 5, no. 3, pp. 49–63, 2011, doi: 10.1109/MIE.2011.942176.

[29] X. Yu and Y. Xue, “Smart Grids: A Cyber–Physical Systems Perspective,” *Proc. IEEE*, vol. 104, no. 5, pp. 1058–1070, 2016, doi: 10.1109/JPROC.2015.2503119.

[30] N. Bui, A. Castellani, P. Casari, and M. Zorzi, “The internet of energy: A web-enabled smart grid system,” *IEEE Network*, vol. 26, no. 4, pp. 39–45, 2012, doi: 10.1109/MNET.2012.6246751.

[31] K. V. Katsaros, W. K. Chai, N. Wang, G. Pavlou, H. Bontius and M. Paolone, “Information-centric networking for machine-to-machine data delivery: A case study in smart grid applications,” *IEEE Network*, vol. 28, no. 3, pp. 58–64, 2014, doi: 10.1109/MNET.2014.6843233.

[32] Y. Kabalci, “A survey on smart metering and smart grid communication,” *Renewable and Sustainable Energy Reviews*, vol. 57, pp. 302–318, 2016, doi: 10.1016/j.rser.2015.12.114.

[33] R. Li, C. Gu, F. Li, G. Shaddick, and M. Dale, “Development of Low Voltage Network Templates—Part I: Substation Clustering and Classification,” *IEEE Trans. Power Syst.*, vol. 30, no. 6, pp. 3036–3044, 2015, doi: 10.1109/TPWRS.2014.2371474.

[34] European System Operators for Smart Grids (EDSO), *Coordination of transmission and distribution system operators: a key step for the Energy Union.* [Online]. Available: https://www.edsoforsmartgrids.eu/ (accessed: Aug. 10 2017).

[35] N. K. Roy and H. R. Pota, “Current Status and Issues of Concern for the Integration of Distributed Generation Into Electricity Networks,” *IEEE Systems Journal*, vol. 9, no. 3, pp. 933–944, 2015, doi: 10.1109/JSYST.2014.2305282.

[36] V. Silva, M. Lopez-Botet-Zulueta, and Y. Wang, “Impact of high penetration of variable renewable generation on frequency dynamics in the continental Europe interconnected

system," *IET Renewable Power Generation*, vol. 10, no. 1, pp. 10–16, 2016, doi: 10.1049/iet-rpg.2015.0141.

[37] J. Smith, M. Rylander, L. Rogers, and R. Dugan, "It's All in the Plans: Maximizing the Benefits and Minimizing the Impacts of DERs in an Integrated Grid," *IEEE Power and Energy Mag.*, vol. 13, no. 2, pp. 20–29, 2015, doi: 10.1109/MPE.2014.2379855.

[38] H. Bevrani, A. Ghosh, and G. Ledwich, "Renewable energy sources and frequency regulation: Survey and new perspectives," *IET Renew. Power Gener.*, vol. 4, no. 5, p. 438, 2010, doi: 10.1049/iet-rpg.2009.0049.

[39] J. Byun, I. Hong, B. Kang, and S. Park, "A smart energy distribution and management system for renewable energy distribution and context-aware services based on user patterns and load forecasting," *IEEE Trans. Consumer Electron.*, vol. 57, no. 2, pp. 436–444, 2011, doi: 10.1109/TCE.2011.5955177.

[40] F. F. Wu, K. Moslehi, and A. Bose, "Power System Control Centers: Past, Present, and Future," *Proc. IEEE*, vol. 93, no. 11, pp. 1890–1908, 2005, doi: 10.1109/JPROC.2005.857499.

[41] Green Business Guide, *Distributed generation key to SA's energy*. [Online]. Available: http://www.greenbusinessguide.co.za/distributed-generation-key-sas-energy/ (accessed: Apr. 11 2019).

[42] A. Ilo, "The Energy Supply Chain Net," *EPE*, vol. 05, no. 05, pp. 384–390, 2013, doi: 10.4236/epe.2013.55040.

[43] P. Järventausta, S. Repo, A. Rautiainen, and J. Partanen, "Smart grid power system control in distributed generation environment," *Annual Reviews in Control*, vol. 34, no. 2, pp. 277–286, 2010, doi: 10.1016/j.arcontrol.2010.08.005.

[44] W. Sinsukthavorn, E. Ortjohann, A. Mohd, N. Hamsic, and D. Morton, "Control Strategy for Three-/Four-Wire-Inverter-Based Distributed Generation," *IEEE Trans. Ind. Electron.*, vol. 59, no. 10, pp. 3890–3899, 2012, doi: 10.1109/TIE.2012.2188871.

[45] S. Weckx, C. Gonzalez, and J. Driesen, "Combined Central and Local Active and Reactive Power Control of PV Inverters," *IEEE Trans. Sustain. Energy*, vol. 5, no. 3, pp. 776–784, 2014, doi: 10.1109/TSTE.2014.2300934.

[46] Euroelectric, *Active distribution system management: A key tool for the smooth integration of distributed generation*. Full discussion paper. [Online]. Available: http:// www.eurelectric.org/ (accessed: Aug. 10 2017).

[47] T. Gönen, *Electric Power Distribution Engineering*. Boca Raton: Taylor & Francis, 2014.

[48] C. Shand, A. McMorran, E. Stewart, and Gareth Taylor, “Exploiting Massive PMU Data Analysis for LV Distribution Network Model Validation,” in . [Online]. Available: http://ieeexplore.ieee.org/servlet/opac?punumber=7332335

[49] J. Giri, “Proactive Management of the Future Grid,” *IEEE Power Energy Technol. Syst. J.*, vol. 2, no. 2, pp. 43–52, 2015, doi: 10.1109/JPETS.2015.2408212.

[50] A. Bose, “Smart Transmission Grid Applications and Their Supporting Infrastructure,” *IEEE Trans. Smart Grid*, vol. 1, no. 1, pp. 11–19, 2010, doi: 10.1109/TSG.2010.2044899.

[51] V. Gungor *et al.*, “Smart Grid and Smart Homes: Key Players and Pilot Projects,” *EEE Ind. Electron. Mag.*, vol. 6, no. 4, pp. 18–34, 2012, doi: 10.1109/MIE.2012.2207489.

[52] N. Komninos, E. Philippou, and A. Pitsillides, “Survey in Smart Grid and Smart Home Security: Issues, Challenges and Countermeasures,” *IEEE Commun. Surv. Tutorials*, vol. 16, no. 4, pp. 1933–1954, 2014, doi: 10.1109/COMST.2014.2320093.

[53] R. Ma, H.-H. Chen, Y.-R. Huang, and W. Meng, “Smart Grid Communication: Its Challenges and Opportunities,” *IEEE Trans. Smart Grid*, vol. 4, no. 1, pp. 36–46, 2013, doi: 10.1109/TSG.2012.2225851.

[54] K. D. McBee and M. G. Simoes, “Utilizing a Smart Grid Monitoring System to Improve Voltage Quality of Customers,” *IEEE Trans. Smart Grid*, vol. 3, no. 2, pp. 738–743, 2012, doi: 10.1109/TSG.2012.2185857.

[55] W. Wang, Y. Xu, and M. Khanna, “A survey on the communication architectures in smart grid,” *Computer Networks*, vol. 55, no. 15, pp. 3604–3629, 2011, doi: 10.1016/j.comnet.2011.07.010.

[56] F. Li *et al.*, “Smart Transmission Grid: Vision and Framework,” *IEEE Trans. Smart Grid*, vol. 1, no. 2, pp. 168–177, 2010, doi: 10.1109/TSG.2010.2053726.

[57] European Commission, *Definition, expected services, functionalities, and benefits of smart grids*. [Online]. Available: https://eur-lex.europa.eu/legal-content/EN/TXT/PDF/?uri=CELEX:52011SC0463&from=EN (accessed: Apr. 2 2019).

[58] E. Ortjohann, W. Sinsukthavorn, M. Lingemann, S. Jaloudi, P. Wirasanti, and D. Morton, “Clustered hierarchical control strategy for future power system,” in *2011 IEEE International Symposium on Industrial Electronics*, Gdansk, Poland, 2011, pp. 994–999.

[59] P. Wirasanti, E. Ortjohann, A. Schmelter, and D. Morton, “Clustering power systems strategy the future of distributed generation,” in *International Symposium on Power Electronics Power Electronics, Electrical Drives, Automation and Motion*, Sorrento, Italy, 2012, pp. 679–683.

[60] M. Lingemann, E. Ortjohann, W. Sinsukthavorn, S. Jaloudi, and D. Morton, “Multi-level secondary control for clustered power grids,” in *10th IET International Conference on Developments in Power System Protection (DPSP 2010). Managing the Change*, Manchester, UK, 2010, P16-P16.

[61] M. Lingemann, “Advanced Implementation Strategies for Distributed Energy Converters in Electrical Grids,” Doctor of Philosophy, University of Bolton, 2010.

[62] J. Bank and B. Kroposki, “Development of a real-time, high-speed distribution level data acquisition system,” in *2012 IEEE PES Innovative Smart Grid Technologies (ISGT)*, Washington, DC, USA, 2012, pp. 1–6.

[63] H. Jiang, L. Huang, J. J. Zhang, Y. Zhang, and D. W. Gao, “Spatial-temporal characterization of synchrophasor measurement systems — A big data approach for smart grid system situational awareness,” in *2014 48th Asilomar Conference on Signals, Systems and Computers*, Pacific Grove, CA, USA, 2014, pp. 750–754.

[64] R. Sodhi, S. C. Srivastava, and S. N. Singh, “Optimal PMU placement method for complete topological and numerical observability of power system,” *Electric Power Systems Research*, vol. 80, no. 9, pp. 1154–1159, 2010, doi: 10.1016/j.epsr.2010.03.005.

[65] A. von Meier, D. Culler, A. McEachern, and R. Arghandeh, “Micro-synchrophasors for distribution systems,” in *ISGT 2014*, Washington, DC, USA, 2014, pp. 1–5.

[66] J. de La Ree, V. Centeno, J. S. Thorp, and A. G. Phadke, “Synchronized Phasor Measurement Applications in Power Systems,” *IEEE Trans. Smart Grid*, vol. 1, no. 1, pp. 20–27, 2010, doi: 10.1109/TSG.2010.2044815.

[67] A. G. Phadke *et al.*, “The Wide World of Wide-area Measurement,” *IEEE Power and Energy Mag.*, vol. 6, no. 5, pp. 52–65, 2008, doi: 10.1109/MPE.2008.927476.

[68] S. Prasad and D. M. Vinod Kumar, “Robust meter placement for active distribution state estimation using a new multi-objective optimisation model,” *IET Science, Measurement & Technology*, vol. 12, no. 8, pp. 1047–1057, 2018, doi: 10.1049/iet-smt.2018.5175.

[69] P. M. Joshi and H. K. Verma, “Synchrophasor measurement applications and optimal PMU placement: A review,” *Electric Power Systems Research*, vol. 199, p. 107428, 2021, doi: 10.1016/j.epsr.2021.107428.

[70] M. Hojabri, U. Dersch, A. Papaemmanouil, and P. Bosshart, “A Comprehensive Survey on Phasor Measurement Unit Applications in Distribution Systems,” *Energies*, vol. 12, no. 23, p. 4552, 2019, doi: 10.3390/en12234552.

[71] South Westphalia University of Applied Sciences, *Research Projekt: Digitale Verteilnetze mit strukturierter Betriebsführung (diNET-SB).* [Online]. Available: https://

www.fh-swf.de/de/forschung___transfer_4/forschungsprojekte_1/forschungsprojekt_dinet_sb.php (accessed: Dec. 20 2021).

[72] M. Sanduleac *et al.*, "Next Generation Real-Time Smart Meters for ICT Based Assessment of Grid Data Inconsistencies," *Energies*, vol. 10, no. 7, p. 857, 2017, doi: 10.3390/en10070857.

[73] L. Wen, K. Zhou, S. Yang, and L. Li, "Compression of smart meter big data: A survey," *Renewable and Sustainable Energy Reviews*, vol. 91, pp. 59–69, 2018, doi: 10.1016/j.rser.2018.03.088.

[74] PSCAD, *Conductor Transposition.* [Online]. Available: https://www.pscad.com/webhelp/EMTDC/Transmission_Lines/Conductor_Transposition.htm (accessed: Dec. 15 2021).

[75] V. C. Gungor *et al.*, "Smart Grid Technologies: Communication Technologies and Standards," *IEEE Trans. Ind. Inf.*, vol. 7, no. 4, pp. 529–539, 2011, doi: 10.1109/TII.2011.2166794.

[76] B. Kroposki *et al.*, "Achieving a 100% Renewable Grid: Operating Electric Power Systems with Extremely High Levels of Variable Renewable Energy," *IEEE Power and Energy Mag.*, vol. 15, no. 2, pp. 61–73, 2017, doi: 10.1109/MPE.2016.2637122.

[77] K. S. Reddy, M. Kumar, T. K. Mallick, H. Sharon, and S. Lokeswaran, "A review of Integration, Control, Communication and Metering (ICCM) of renewable energy based smart grid," *Renewable and Sustainable Energy Reviews*, vol. 38, pp. 180–192, 2014, doi: 10.1016/j.rser.2014.05.049.

[78] J. Romero Aguero and A. Khodaei, "Grid Modernization, DER Integration & Utility Business Models - Trends & Challenges," *IEEE Power and Energy Mag.*, vol. 16, no. 2, pp. 112–121, 2018, doi: 10.1109/MPE.2018.2811817.

[79] European Commission, *Vision and Strategy for European Electricity Networks of the Future.* [Online]. Available: http://ec.europa.eu/research/energy/pdf/smartgrids_en.pdf (accessed: Jul. 22 2018).

[80] ETP SmartGrids, *Strategic Research Agenda Update of the SmartGrids SRA 2007 for the needs by the year 2035.* [Online]. Available: https://www.etip-snet.eu/wp-content/uploads/2017/04/sra2035.pdf (accessed: Apr. 10 2019).

[81] S. Borlase, *Smart grids: Infrastructure, technology, and solutions*. Boca Raton, FL: CRC Press, 2013.

[82] X. Fang, S. Misra, G. Xue, and D. Yang, "Smart Grid — The New and Improved Power Grid: A Survey," *IEEE Commun. Surv. Tutorials*, vol. 14, no. 4, pp. 944–980, 2012, doi: 10.1109/SURV.2011.101911.00087.

[83] H. Farhangi, “The path of the smart grid,” *IEEE Power and Energy Mag.*, vol. 8, no. 1, pp. 18–28, 2010, doi: 10.1109/MPE.2009.934876.

[84] United States Department of Energy, *Grid 2030: A national version for electricity's second 100 years.* [Online]. Available: https://www.energy.gov/sites/prod/files/oeprod/DocumentsandMedia/Electric_Vision_Document.pdf (accessed: Mar. 18 2018).

[85] U.S. Department of Energy, *The Smart Grid: An Introduction.* [Online]. Available: https://www.energy.gov/oe/downloads/smart-grid-introduction-0 (accessed: Aug. 9 2019).

[86] European Commission, *Smart Grid projects in Europe: lessons learned and current developments.* [Online]. Available: https://ses.jrc.ec.europa.eu/ (accessed: Jul. 15 2019).

[87] European Commission, *Smart Grids-from innovation to deployment.* [Online]. Available: http://eur-lex.europa.eu/legal-content/EN/TXT/?qid=1409145728890&uri=CELEX:52011SC0463 (accessed: Nov. 12 2017).

[88] F. GANGALE, J. Vasiljevska, C. F. Covrig, A. Mengolini, and G. Fulli, *Smart grid projects outlook 2017*. [Online]. Available: http://ses.jrc.ec.europa.eu/smart-grids-observatory (accessed: Nov. 12 2017).

[89] Vasiljevska, J., Gras, S., Flego, G., “Evaluation of Smart Grid projects for inclusion in the third Unionwide list of Projects of Common Interest,” 2017.

[90] K. C. Budka, J. G. Deshpande, and M. Thottan, *Communication networks for smart grids: Making smart grid real*. London: Springer, 2014. [Online]. Available: http://dx.doi.org/10.1007/978-1-4471-6302-2

[91] S. Khan, R. Khan, and A. H. Al-Bayatti, “Secure Communication Architecture for Dynamic Energy Management in Smart Grid,” *IEEE Power Energy Technol. Syst. J.*, vol. 6, no. 1, pp. 47–58, 2019, doi: 10.1109/JPETS.2019.2891509.

[92] E. Y. Song, G. J. FitzPatrick, and K. B. Lee, “Smart Sensors and Standard-Based Interoperability in Smart Grids,” *IEEE sensors journal*, vol. 17, no. 23, 2017, doi: 10.1109/JSEN.2017.2729893.

[93] C. Greer *et al., NIST Framework and Roadmap for Smart Grid Interoperability Standards, Release 3.0*: National Institute of Standards and Technology, 2014.

[94] Y. Liu *et al.*, “Wide-Area-Measurement System Development at the Distribution Level: An FNET/GridEye Example,” *IEEE Trans. Power Delivery*, vol. 31, no. 2, pp. 721–731, 2016, doi: 10.1109/TPWRD.2015.2478380.

[95] Cisco, *Unified Field Area Network Architecture for Distribution Automation: Internet of Things Field Infrastructure.* [Online]. Available: https://www.cisco.com/c/en/us/

solutions/industries/energy/external-utilities-smart-grid/field-area-network.html (accessed: Jul. 9 2019).

[96] J. Ren, S. S. Venkata, and E. Sortomme, "An Accurate Synchrophasor Based Fault Location Method for Emerging Distribution Systems," *IEEE Trans. Power Delivery*, vol. 29, no. 1, pp. 297–298, 2014, doi: 10.1109/TPWRD.2013.2288006.

[97] R. Morello, S. C. Mukhopadhyay, Z. Liu, D. Slomovitz, and S. R. Samantaray, "Advances on Sensing Technologies for Smart Cities and Power Grids: A Review," *IEEE Sensors J.*, vol. 17, no. 23, pp. 7596–7610, 2017, doi: 10.1109/JSEN.2017.2735539.

[98] Z. Zhong *et al.*, "Power System Frequency Monitoring Network (FNET) Implementation," *IEEE Trans. Power Syst.*, vol. 20, no. 4, pp. 1914–1921, 2005, doi: 10.1109/TPWRS.2005.857386.

[99] Heng-Yi Su and Tzu-Yi Liu, "A PMU-Based Method for Smart Transmission Grid Voltage Security Visualization and Monitoring," *Energies*, vol. 10, no. 8, p. 1103, 2017, doi: 10.3390/en10081103.

[100] O. Samuelsson, M. Hemmingsson, A. H. Nielsen, K. Pedersen, and J. Rasmussen, "Monitoring of Power System Events at Transmission and Distribution Level," *IEEE Trans. Power Syst.*, vol. 21, no. 2, pp. 1007–1008, 2006, doi: 10.1109/TPWRS.2006.873014.

[101] G. T. Heydt, C. C. Liu, A. G. Phadke, and V. Vittal, "Solution for the crisis in electric power supply," *IEEE Comput. Appl. Power*, vol. 14, no. 3, pp. 22–30, 2001, doi: 10.1109/MCAP.2001.952933.

[102] A. Carta, N. Locci, C. Muscas, and S. Sulis, "A Flexible GPS-Based System for Synchronized Phasor Measurement in Electric Distribution Networks," *IEEE Trans. Instrum. Meas.*, vol. 57, no. 11, pp. 2450–2456, 2008, doi: 10.1109/TIM.2008.924930.

[103] ENTSO-E, *Wide Area Monitoring – Current Continental Europe TSOs Applications Overview: System Protection & Dynamics Working Group*. [Online]. Available: https://docstore.entsoe.eu/Documents/SOC%20documents/Regional_Groups_Continental_Europe/CE_WAM_Applications_V5.pdf (accessed: May 17 2019).

[104] N. Save, M. Popov, A. Jongepier, and G. Rietveld, "PMU-based power system analysis of a medium-voltage distribution grid," *CIRED - Open Access Proceedings Journal*, vol. 2017, no. 1, pp. 1927–1930, 2017, doi: 10.1049/oap-cired.2017.1035.

[105] H. Mohsenian-Rad, E. Stewart, and E. Cortez, "Distribution Synchrophasors: Pairing Big Data with Analytics to Create Actionable Information," *IEEE Power and Energy Mag.*, vol. 16, no. 3, pp. 26–34, 2018, doi: 10.1109/MPE.2018.2790818.

[106] M. Farajollahi, A. Shahsavari, E. M. Stewart, and H. Mohsenian-Rad, “Locating the Source of Events in Power Distribution Systems Using Micro-PMU Data,” *IEEE Trans. Power Syst.*, vol. 33, no. 6, pp. 6343–6354, 2018, doi: 10.1109/TPWRS.2018.2832126.

[107] A. von Meier, E. Stewart, A. McEachern, M. Andersen, and L. Mehrmanesh, “Precision Micro-Synchrophasors for Distribution Systems: A Summary of Applications,” *IEEE Trans. Smart Grid*, vol. 8, no. 6, pp. 2926–2936, 2017, doi: 10.1109/TSG.2017.2720543.

[108] IEEE Power and Energy Society/Power System Relaying and Control (PE/PSRCC), “Measuring relays and protection equipment – Part 118-1: Synchrophasor for power systems – Measurements,”

[109] S. R. Samantaray, I. Kamwa, and G. Joos, “Phasor measurement unit based wide-area monitoring and information sharing between micro-grids,” *IET Generation, Transmission & Distribution*, vol. 11, no. 5, pp. 1293–1302, 2017, doi: 10.1049/iet-gtd.2016.1419.

[110] E. O. Schweitzer and D. E. Whitehead, “Real-world synchrophasor solutions,” in *2009 62nd Annual Conference for Protective Relay Engineers*, College Station, TX, USA, 2009, pp. 536–547.

[111] X. Liu, D. M. Laverty, R. J. Best, K. Li, D. J. Morrow, and S. McLoone, “Principal Component Analysis of Wide-Area Phasor Measurements for Islanding Detection—A Geometric View,” *IEEE Trans. Power Delivery*, vol. 30, no. 2, pp. 976–985, 2015, doi: 10.1109/TPWRD.2014.2348557.

[112] M. Dehghani, L. Goel, and W. Li, “PMU based observability reliability evaluation in electric power systems,” *Electric Power Systems Research*, vol. 116, pp. 347–354, 2014, doi: 10.1016/j.epsr.2014.07.008.

[113] M. Esmaili, K. Gharani, and H. A. Shayanfar, “Redundant Observability PMU Placement in the Presence of Flow Measurements Considering Contingencies,” *IEEE Trans. Power Syst.*, vol. 28, no. 4, pp. 3765–3773, 2013, doi: 10.1109/TPWRS.2013.2257883.

[114] R. F. Nuqui and A. G. Phadke, “Phasor Measurement Unit Placement Techniques for Complete and Incomplete Observability,” *IEEE Trans. Power Delivery*, vol. 20, no. 4, pp. 2381–2388, 2005, doi: 10.1109/TPWRD.2005.855457.

[115] Y. Zhang, Y. Liu, L. Chen, J. Guo, and Y. Liu, “Visualization of distribution level voltage magnitude pattern trend in EI system using FNET data,” in *2014 IEEE PES T&D Conference and Exposition*, Chicago, IL, USA, 2014, pp. 1–5.

[116] W. Yuill, A. Edwards, S. Chowdhury, and S. P. Chowdhury, “Optimal PMU placement: A comprehensive literature review,” in *2011 IEEE Power and Energy Society General Meeting*, San Diego, CA, 2011, pp. 1–8.

[117] P. Yang, Z. Tan, A. Wiesel, and A. Nehorai, “Placement of PMUs Considering Measurement Phase-Angle Mismatch,” *IEEE Trans. Power Delivery*, vol. 30, no. 2, pp. 914–922, 2015, doi: 10.1109/TPWRD.2014.2365550.

[118] I. Kamwa, S. R. Samantaray, and G. Joos, “Compliance Analysis of PMU Algorithms and Devices for Wide-Area Stabilizing Control of Large Power Systems,” *IEEE Trans. Power Syst.*, vol. 28, no. 2, pp. 1766–1778, 2013, doi: 10.1109/TPWRS.2012.2221168.

[119] K. Dehghanpour, Z. Wang, J. Wang, Y. Yuan, and F. Bu, “A Survey on State Estimation Techniques and Challenges in Smart Distribution Systems,” *IEEE Trans. Smart Grid*, vol. 10, no. 2, pp. 2312–2322, 2019, doi: 10.1109/TSG.2018.2870600.

[120] S. S. S. R. Depuru, L. Wang, and V. Devabhaktuni, “Smart meters for power grid: Challenges, issues, advantages and status,” *Renewable and Sustainable Energy Reviews*, vol. 15, no. 6, pp. 2736–2742, 2011, doi: 10.1016/j.rser.2011.02.039.

[121] A. Al-Wakeel, J. Wu, and N. Jenkins, “State estimation of medium voltage distribution networks using smart meter measurements,” *Applied Energy*, vol. 184, pp. 207–218, 2016, doi: 10.1016/j.apenergy.2016.10.010.

[122] B. Völker, A. Reinhardt, A. Faustine, and L. Pereira, “Watt’s up at Home? Smart Meter Data Analytics from a Consumer-Centric Perspective,” *Energies*, vol. 14, no. 3, p. 719, 2021, doi: 10.3390/en14030719.

[123] J. Bhatt, V. Shah, and O. Jani, “An instrumentation engineer’s review on smart grid: Critical applications and parameters,” *Renewable and Sustainable Energy Reviews*, vol. 40, pp. 1217–1239, 2014, doi: 10.1016/j.rser.2014.07.187.

[124] Q. Sun *et al.*, “A Comprehensive Review of Smart Energy Meters in Intelligent Energy Networks,” *IEEE Internet Things J.*, vol. 3, no. 4, pp. 464–479, 2016, doi: 10.1109/JIOT.2015.2512325.

[125] Z. A. Khan, D. Jayaweera, and M. S. Alvarez-Alvarado, “A novel approach for load profiling in smart power grids using smart meter data,” *Electric Power Systems Research*, vol. 165, pp. 191–198, 2018, doi: 10.1016/j.epsr.2018.09.013.

[126] Smartgrid.gov, “Advanced metering infrastructure and customer systems: Results from the smart grid investments grant program,” 2016. Accessed: Nov. 1 2021. [Online]. Available: https://www.energy.gov/sites/prod/files/2016/12/f34/AMI Summary Report_09-26-16.pdf

[127] R. Morello, C. de Capua, G. Fulco, and S. C. Mukhopadhyay, “A Smart Power Meter to Monitor Energy Flow in Smart Grids: The Role of Advanced Sensing and IoT in the Electric Grid of the Future,” *IEEE Sensors J.*, vol. 17, no. 23, pp. 7828–7837, 2017, doi: 10.1109/JSEN.2017.2760014.

[128] M. M. Albu, M. Sanduleac, and C. Stanescu, “Syncretic Use of Smart Meters for Power Quality Monitoring in Emerging Networks,” *IEEE Trans. Smart Grid*, vol. 8, no. 1, pp. 485–492, 2017, doi: 10.1109/TSG.2016.2598547.

[129] South Westphalia University of Applied Sciences, *Labor für Energieversorgung EET*. [Online]. Available: https://www4.fh-swf.de/de/home/ueber_uns/standorte/so/fb_eet/doz_eet/profs_eet/ortjohann/fachgebiet_1/index.php (accessed: Aug. 9 2019).

[130] M. S. Mahmoud, F. M. A.L.-Sunni, and M. Saif Ur Rahman, “Review of microgrid architectures – a system of systems perspective,” *IET Renewable Power Generation*, vol. 9, no. 8, pp. 1064–1078, 2015, doi: 10.1049/iet-rpg.2014.0171.

[131] S. Parhizi, H. Lotfi, A. Khodaei, and S. Bahramirad, “State of the Art in Research on Microgrids: A Review,” *IEEE Access*, vol. 3, pp. 890–925, 2015, doi: 10.1109/ACCESS.2015.2443119.

[132] D. E. Olivares *et al.*, “Trends in Microgrid Control,” *IEEE Trans. Smart Grid*, vol. 5, no. 4, pp. 1905–1919, 2014, doi: 10.1109/TSG.2013.2295514.

[133] K. Ravindra, B. Kannan, and N. Ramappa, “Microgrids: A Value-Based Paradigm: The need for the redefinition of microgrids,” *IEEE Electrific. Mag.*, vol. 2, no. 1, pp. 20–29, 2014, doi: 10.1109/MELE.2013.2297738.

[134] A. Jhunjhunwala and P. Kaur, “Solar Energy, dc Distribution, and Microgrids: Ensuring Quality Power in Rural India,” *IEEE Electrific. Mag.*, vol. 6, no. 4, pp. 32–39, 2018, doi: 10.1109/MELE.2018.2871277.

[135] L. Martirano *et al.*, “Aggregation of Users in a Residential/Commercial Building Managed by a Building Energy Management System (BEMS),” *IEEE Trans. on Ind. Applicat.*, vol. 55, no. 1, pp. 26–34, 2019, doi: 10.1109/TIA.2018.2866155.

[136] J. van Roy, N. Leemput, F. Geth, J. Buscher, R. Salenbien, and J. Driesen, “Electric Vehicle Charging in an Office Building Microgrid With Distributed Energy Resources,” *IEEE Trans. Sustain. Energy*, vol. 5, no. 4, pp. 1389–1396, 2014, doi: 10.1109/TSTE.2014.2314754.

[137] X. Wu, Z. Wang, J. Du, and G. Wu, “Optimal Operation of Residential Microgrids in the Harbin Area,” *IEEE Access*, vol. 6, pp. 30726–30736, 2018, doi: 10.1109/ACCESS.2018.2833143.

[138] H. Xie, S. Zheng, and M. Ni, “Microgrid Development in China: A method for renewable energy and energy storage capacity configuration in a megawatt-level isolated microgrid,” *IEEE Electrific. Mag.*, vol. 5, no. 2, pp. 28–35, 2017, doi: 10.1109/MELE.2017.2685818.

[139] Berkeley Lab, *About Microgrids*. [Online]. Available: https://building-microgrid.lbl.gov/about-microgrids (accessed: Aug. 20 2019).

[140] R. Uluski *et al.*, “Microgrid Controller Design, Implementation, and Deployment: A Journey from Conception to Implementation at the Philadelphia Navy Yard,” *IEEE Power and Energy Mag.*, vol. 15, no. 4, pp. 50–62, 2017, doi: 10.1109/MPE.2017.2691239.

[141] Z. Li, M. Shahidehpour, F. Aminifar, A. Alabdulwahab, and Y. Al-Turki, “Networked Microgrids for Enhancing the Power System Resilience,” *Proc. IEEE*, vol. 105, no. 7, pp. 1289–1310, 2017, doi: 10.1109/JPROC.2017.2685558.

[142] S. Chowdhury, S. P. Chowdhury, and P. Crossley, *Microgrids and active distribution networks*. Stevenage: Institution of Engineering and Technology, 2009.

[143] D. Papadaskalopoulos, D. Pudjianto, and G. Strbac, “Decentralized Coordination of Microgrids With Flexible Demand and Energy Storage,” *IEEE Trans. Sustain. Energy*, vol. 5, no. 4, pp. 1406–1414, 2014, doi: 10.1109/TSTE.2014.2311499.

[144] E. Harmon, U. Ozgur, M. H. Cintuglu, R. de Azevedo, K. Akkaya, and O. A. Mohammed, “The Internet of Microgrids: A Cloud-Based Framework for Wide Area Networked Microgrids,” *IEEE Trans. Ind. Inf.*, vol. 14, no. 3, pp. 1262–1274, 2018, doi: 10.1109/TII.2017.2785317.

[145] L. Che, M. Shahidehpour, A. Alabdulwahab, and Y. Al-Turki, “Hierarchical Coordination of a Community Microgrid With AC and DC Microgrids,” *IEEE Trans. Smart Grid*, vol. 6, no. 6, pp. 3042–3051, 2015, doi: 10.1109/TSG.2015.2398853.

[146] J. Li, X.-Y. Ma, C.-C. Liu, and K. P. Schneider, “Distribution System Restoration With Microgrids Using Spanning Tree Search,” *IEEE Trans. Power Syst.*, vol. 29, no. 6, pp. 3021–3029, 2014, doi: 10.1109/TPWRS.2014.2312424.

[147] S. A. Arefifar, Y. A.-R. I. Mohamed, and T. H. M. EL-Fouly, “Comprehensive Operational Planning Framework for Self-Healing Control Actions in Smart Distribution Grids,” *IEEE Trans. Power Syst.*, vol. 28, no. 4, pp. 4192–4200, 2013, doi: 10.1109/TPWRS.2013.2259852.

[148] F. Shahnia, R. P.S. Chandrasena, S. Rajakaruna, and A. Ghosh, *Autonomous Operation of Multiple Interconnected Microgrids with Self–Healing Capability*. Piscataway, NJ: IEEE, 2013.

[149] Z. Wang, B. Chen, J. Wang, and C. Chen, “Networked Microgrids for Self-Healing Power Systems,” *IEEE Trans. Smart Grid*, vol. 7, no. 1, pp. 310–319, 2016, doi: 10.1109/TSG.2015.2427513.

[150] Verband Der Elektrotechnik Elektronik Informationstechnik e.V. (VDE), *Der zellulare ansatz: Grundlage einer erfolgreichen, regionenübergreifenden Energiewende.* [Online]. Available: https://shop.vde.com/de/vde-studie-der-zellulare-ansatz-2 (accessed: Aug. 13 2019).

[151] Verband Der Elektrotechnik Elektronik Informationstechnik e.V. (VDE), *Energieversorgung 4.0: Zellulare Betriebsführungskonzepte im Feldversuch.* [Online]. Available: http://www.tgz-bautzen.de/energieagentur/veranstaltungen/2018/5-bautzener-energieforum.html (accessed: Aug. 22 2019).

[152] Verband Der Elektrotechnik Elektronik Informationstechnik e.V. (VDE), *Der Zellulare Ansatz: Grundlage einer erfolgreichen, Regionen übergreifenden Energiewende.* [Online]. Available: https://www.bund-naturschutz.de/publikationen.html (accessed: Aug. 22 2019).

[153] E. Waffenschmidt, “Cellular Power Grids for a 100 % Renewable Energy Supply,” in *Springer proceedings in energy, Towards 100% Renewable Energy*, T. S. Uyar, Ed., Cham: Springer International Publishing, 2017, pp. 441–447.

[154] E. Waffenschmidt, *Cellular markets for distributed power grids: an exemplary study*.

[155] M. J. Mokarram, M. Nayeripour, T. Niknam, and E. Waffenschmidt, “Multi-Area Economic Dispatch Considering Generation Uncertainty,” in *2018 7th International Energy and Sustainability Conference (IESC): 17-18 May 2018*, Cologne, 2018, pp. 1–6.

[156] Verband Der Elektrotechnik Elektronik Informationstechnik e.V. (VDE), *Zellulares Energiesystem.* [Online]. Available: https://www.vde.com/resource/blob/1884494/98f96973fcdba70777654d0f40c179e5/studie---zellulares-energiesystem-data.pdf (accessed: Aug. 22 2019).

[157] S. Rummeny and E. Waffenschmidt, “Options for an autarkic operation of a communal power grid using a battery and renewable energies,” *Energy Procedia*, vol. 155, pp. 329–335, 2018, doi: 10.1016/j.egypro.2018.11.045.

[158] L. K. Günther, *Zellulare Multisektorale Energienetze: ein neuartiges Organisationsmodell für die k Energieversorgung zur Realisierung der Energiewende* (accessed: Aug. 13 2019).

[159] K. Heuck, K.-D. Dettmann, and D. Schulz, *Elektrische Energieversorgung: Erzeugung, Übertragung und Verteilung elektrischer Energie für Studium und Praxis*, 9th ed. Wiesbaden: Imprint: Springer Vieweg, 2013.

[160] J. Lin *et al.*, "Situation awareness of active distribution network: Roadmap, technologies, and bottlenecks," *CSEE JPES*, vol. 2, no. 3, pp. 35–42, 2016, doi: 10.17775/CSEEJPES.2016.00033.

[161] L. N. Ochoa, F. Pilo, A. Keane, P. Cuffe, and G. Pisano, "Embracing an Adaptable, Flexible Posture: Ensuring That Future European Distribution Networks Are Ready for More Active Roles," *IEEE Power and Energy Mag.*, vol. 14, no. 5, pp. 16–28, 2016, doi: 10.1109/MPE.2016.2579478.

[162] G. Lorenz, D. Trebolle, P. Mandatova, P. Hallberg, and J. Tello Guijarro, "Active distribution system management," in *22nd International Conference and Exhibition on Electricity Distribution (CIRED 2013)*, Stockholm, Sweden, 2013, p. 1378.

[163] ENTSO-E, *Network Code on Load Frequency Control and Reserves (LFCR)*. [Online]. Available: https://www.entsoe.eu/major-projects/network-code-development/load-frequency-control-reserves/Pages/default.aspx (accessed: Aug. 16 2017).

[164] S. Leksawat *et al.*, "Hybrid framework of management systems supporting cluster-oriented smart grid operations," in *2017 IEEE Manchester PowerTech*, Manchester, United Kingdom, 2017, pp. 1–6.

[165] S. Leksawat *et al.*, "Demonstration of cluster-based power system automation for future smart grids," in *2016 IEEE International Energy Conference (ENERGYCON)*, Leuven, Belgium, 2016, pp. 1–6.

[166] E. Ortjohann, P. Wirasanti, M. Lingemann, W. Sinsukthavorn, S. Jaloudi, and D. Morton, "Multi-level hierarchical control strategy for smart grid using clustering concept," in *2011 International Conference on Clean Electrical Power (ICCEP)*, Ischia, Italy, 2011, pp. 648–653.

[167] E. Ortjohann, S. Leksawat, A. Schmelter, P. Wirasanti, D. Holtschulte, and D. Morton, "Integration of clustering power systems approach and data management infrastructure for smart grids," in *2014 International Symposium on Power Electronics, Electrical Drives, Automation and Motion*, Ischia, Italy, 2014, pp. 1278–1283.

[168] E. Ortjohann, J. Kortenbruck, D. Holtschulte, S. Leksawat, A. Schmelter, and D. Morton, "Clustering power system approach with smart distribution network controller," in *2015 International Conference on Clean Electrical Power (ICCEP)*, Taormina, Italy, 2015, pp. 346–352.

[169] D. Holtschulte, A. S. Erlangga, E. Ortjohann, S. Leksawat, J. Kortenbruck, and T. Pregamone, "Genetic optimization for prosumers in clustering power system approach," in *2016 IEEE 16th International Conference on Environment and Electrical Engineering (EEEIC)*, Florence, Italy, 2016, pp. 1–6.

[170] E. Ortjohann, P. Wirasanti, A. Schmelter, H. Saffour, M. Hoppe, and D. Morton, "Cluster fractal model — A flexible network model for future power systems," in *2013 International Conference on Clean Electrical Power (ICCEP)*, Alghero, 2013, pp. 293–297.

[171] E. Ortjohann, A. Schmelter, D. Holtschulte, J. Kortenbruck, *Final Report: Intelligente Verteilnetze mit fraktaler Automatisierungs-Architektur (iNET-FA²)*,. [Online]. Available: https://www.tib.eu/de/suchen/id/TIBKAT%3A1040568033/Abschlussbericht-zum-Verbundforschungsprojekt-Intelligente (accessed: Aug. 26 2019).

[172] S. Leksawat, A. Schmelter, E. Ortjohann, D. Holtschulte, J. Kortenbruck, and D. Morton, "Implementation of communication model and web services for cluster-based power system operation in smart grids," in *2015 IEEE Innovative Smart Grid Technologies - Asia (ISGT ASIA)*, Bangkok, Thailand, 2015, pp. 1–6.

[173] P. Wirasanti, E. Ortjohann, M. Hoppe, H. Saffour, S. Leksawat, and D. Morton, "Automated active distribution network with multi-level cluster control approach," in *IECON 2013 - 39th Annual Conference of the IEEE Industrial Electronics Society*, Vienna, Austria, 2013, pp. 1980–1985.

[174] G. Zhabelova and V. Vyatkin, "Multiagent Smart Grid Automation Architecture Based on IEC 61850/61499 Intelligent Logical Nodes," *IEEE Trans. Ind. Electron.*, vol. 59, no. 5, pp. 2351–2362, 2012, doi: 10.1109/TIE.2011.2167891.

[175] C. S. Saunders, G. Liu, Y. Yu, and W. Zhu, "Data-driven distributed analytics and control platform for smart grid situational awareness," *CSEE JPES*, vol. 2, no. 3, pp. 51–58, 2016, doi: 10.17775/CSEEJPES.2016.00035.

[176] Y. Wang, P. Yemula, and A. Bose, "Decentralized Communication and Control Systems for Power System Operation," *IEEE Trans. Smart Grid*, vol. 6, no. 2, pp. 885–893, 2015, doi: 10.1109/TSG.2014.2363192.

[177] J. Jiang and Y. Qian, "Distributed Communication Architecture for Smart Grid Applications," *IEEE Commun. Mag.*, vol. 54, no. 12, pp. 60–67, 2016, doi: 10.1109/MCOM.2016.1600321CM.

[178] E. Ortjohann, D. Morton, D. Holtschulte, J. Kortenbruck, and S. Leksawat, "Advanced Control Functions for Smart Grid Inverter under Asymmetrical Conditions," in *3rd Renewable Power Generation Conference (RPG 2014)*, Naples, Italy, 2014, 7.2.1-7.2.1.

[179] J. J. Grainger, W. D. Stevenson, and W. D. E. o. p. s. a. Stevenson, *Power system analysis*. New York, London: McGraw-Hill, 1994.

[180] H. Saadat, *Power system analysis*, 2nd ed. Boston, London: McGraw-Hill Primis Custom Publishing, 2002.

[181] N. D. Tleis, *Power systems modelling and fault analysis: Theory and practice / Nasser D. Tleis*. Place of publication not identified: Newnes, 2007.

[182] B. J. Cory, N. Jenkins, J. Ekanayake, G. Strbac, and B. M. Weedy, *Electric power systems*. Hoboken, N.J.: Wiley, 2013.

[183] Ö. Ergül, *Introduction to electrical circuit analysis*. Hoboken, NJ: John Wiley & Sons, 2017.

[184] W. H. Kersting, *Distribution system modeling and analysis*, 2nd ed. Boca Raton, Fla., London: CRC, 2007. [Online]. Available: http://www.loc.gov/catdir/enhancements/fy0701/2006049302-d.html

[185] J. O. Bird, *Electrical circuit theory and technology*, 5th ed. Abingdon, Oxon, New York: Routledge, 2014.

[186] A. Schmelter *et al.*, "Real-time orchestration system for intelligent electricity networks," in *2017 6th International Conference on Clean Electrical Power (ICCEP)*, Santa Margherita Ligure, Italy, 2017, pp. 229–235.

[187] H. Bevrani, M. Watanabe, and Y. Mitani, *Power system monitoring and control*. Hoboken New Jersey: IEEE/Wiley, 2014.

[188] E. Kreyszig, *Advanced engineering mathematics*, 9th ed. New Delhi: Wiley-India, 2013.

[189] M. E. El-Hawary, *Introduction to electrical power systems*. Piscataway, NJ, Hoboken, New Jersey: IEEE Press; Wiley, 2008.

[190] DIgSILENT, *Load Flow Sensitivities.* [Online]. Available: https://www.digsilent.de/en/load-flow-sensitivities.html (accessed: Nov. 2 2019).

[191] T. Neumann and I. Erlich, "Short Circuit Current Contribution of a Photovoltaic Power Plant," *IFAC Proceedings Volumes*, vol. 45, no. 21, pp. 343–348, 2012, doi: 10.3182/20120902-4-FR-2032.00061.

[192] ENTSO-E, *Short circuit contribution of new generating units connected with power electronics and protection behaviour*. [Online]. Available: https://docstore.entsoe.eu/Documents/ (accessed: Nov. 2 2019).

[193] N. Nimpitiwan, G. T. Heydt, R. Ayyanar, and S. Suryanarayanan, "Fault Current Contribution From Synchronous Machine and Inverter Based Distributed Generators," *IEEE Trans. Power Delivery*, vol. 22, no. 1, pp. 634–641, 2007, doi: 10.1109/TPWRD.2006.881440.

[194] DIgSILENT, *PowerFactory 2016: User Manual*. [Online]. Available: http://www.digsilent.de/

[195] V. Kumar, I. Gupta, H. O. Gupta, and C. P. Agarwal, "Voltage and current sensitivities of radial distribution network: A new approach," *IEE Proc., Gener. Transm. Distrib.*, vol. 152, no. 6, p. 813, 2005, doi: 10.1049/ip-gtd:20045068.

[196] M. Brenna, E. D. Berardinis, F. Foiadelli, G. Sapienza, and D. Zaninelli, "Voltage Control in Smart Grids: An Approach Based on Sensitivity Theory," *JEMAA*, vol. 02, no. 08, pp. 467–474, 2010, doi: 10.4236/jemaa.2010.28062.

[197] B. B. Zad, J. Lobry, and F. Vallee, "A centralized approach for voltage control of MV distribution systems using DGs power control and a direct sensitivity analysis method," in *2016 IEEE International Energy Conference (ENERGYCON)*, Leuven, Belgium, pp. 1–6.

[198] B. Bakhshideh Zad, H. Hasanvand, J. Lobry, and F. Vallée, "Optimal reactive power control of DGs for voltage regulation of MV distribution systems using sensitivity analysis method and PSO algorithm," *International Journal of Electrical Power & Energy Systems*, vol. 68, pp. 52–60, 2015, doi: 10.1016/j.ijepes.2014.12.046.

[199] V. Klonari, B. B. Zad, J. Lobry, and F. Vallee, "Application of voltage sensitivity analysis in a probabilistic context for characterizing low voltage network operation," in *2016 International Conference on Probabilistic Methods Applied to Power Systems (PMAPS): October 16-20, 2016, Beijing, China : conference proceedings*, Beijing, 2016, pp. 1–7.

[200] T. Kolacia and J. Drapela, "Voltage sensitivity to power flows related to distributed generation," in *Proceedings, 2016 17th International Scientific Conference on Electric Power Engineering (EPE): EPE 2016*, Prague, Czech Republic, 2016, pp. 1–6.

[201] K. Christakou, J.-Y. LeBoudec, M. Paolone, and D.-C. Tomozei, "Efficient Computation of Sensitivity Coefficients of Node Voltages and Line Currents in Unbalanced Radial Electrical Distribution Networks," *IEEE Trans. Smart Grid*, vol. 4, no. 2, pp. 741–750, 2013, doi: 10.1109/TSG.2012.2221751.

[202] S. Conti, S. Raiti, and G. Vagliasindi, "Voltage sensitivity analysis in radial MV distribution networks using constant current models," in *2010 IEEE International Symposium on Industrial Electronics (ISIE 2010): Bari, Italy, 4-7, July 2010*, Bari, Italy, 2010, pp. 2548–2554.

[203] K. H. Youssef, "A New Method for Online Sensitivity-Based Distributed Voltage Control and Short Circuit Analysis of Unbalanced Distribution Feeders," *IEEE Trans. Smart Grid*, vol. 6, no. 3, pp. 1253–1260, 2015, doi: 10.1109/TSG.2014.2363158.

[204] Y.-J. Kim, “Development and Analysis of a Sensitivity Matrix of a Three-Phase Voltage Unbalance Factor,” *IEEE Trans. Power Syst.*, vol. 33, no. 3, pp. 3192–3195, 2018, doi: 10.1109/TPWRS.2018.2807980.

[205] D. Hazarika, B. K. Talukdar, and R. Das, “Use of local bus measurements for operational planning of a power system,” *IET Generation, Transmission & Distribution*, vol. 7, no. 11, pp. 1296–1309, 2013, doi: 10.1049/iet-gtd.2012.0521.

[206] P. Li, H. Su, C. Wang, Z. Liu, and J. Wu, “PMU-Based Estimation of Voltage-to-Power Sensitivity for Distribution Networks Considering the Sparsity of Jacobian Matrix,” *IEEE Access*, vol. 6, pp. 31307–31316, 2018, doi: 10.1109/ACCESS.2018.2841010.

[207] H. Su, P. Lia, X. Fu, L. Yu, and C. Wang, “Augmented Sensitivity Estimation Based Voltage Control Strategy of Active Distribution Networks with PMU Measurement,” *IEEE Access*, p. 1, 2019, doi: 10.1109/ACCESS.2019.2908183.

[208] H. Retty and J. S. Thorp, “Phasor measurement based voltage sensitivities for contingency analysis,” in *IEEE Power & Energy Society general meeting, 2015: 26-30 July 2015, Denver, CO, USA*, Denver, CO, USA, 2015, pp. 1–4.

[209] S. Weckx, R. D'Hulst, and J. Driesen, “Voltage Sensitivity Analysis of a Laboratory Distribution Grid With Incomplete Data,” *IEEE Trans. Smart Grid*, vol. 6, no. 3, pp. 1271–1280, 2015, doi: 10.1109/TSG.2014.2380642.

[210] M. Shahidehpour and Y. Wang, *Communication and Control in Electric Power Systems*. Hoboken, NJ, USA: John Wiley & Sons, Inc, 2003.

[211] U. Kuhar, M. Pantos, G. Kosec, and A. Svigelj, “The Impact of Model and Measurement Uncertainties on a State Estimation in Three-Phase Distribution Networks,” *IEEE Trans. Smart Grid*, vol. 10, no. 3, pp. 3301–3310, 2019, doi: 10.1109/TSG.2018.2823398.

[212] R. Martínez-Parrales, C. R. Fuerte-Esquivel, and B. A. Alcaide-Moreno, “ANALYSIS OF BAD DATA IN POWER SYSTEM STATE ESTIMATION UNDER NON-GAUSSIAN MEASUREMENT NOISE,” *Electric Power Systems Research*, vol. 186, p. 106424, 2020, doi: 10.1016/j.epsr.2020.106424.

[213] J. Zhao and L. Mili, “A Framework for Robust Hybrid State Estimation With Unknown Measurement Noise Statistics,” *IEEE Trans. Ind. Inf.*, vol. 14, no. 5, pp. 1866–1875, 2018, doi: 10.1109/TII.2017.2764800.

[214] J. Liu, J. Tang, F. Ponci, A. Monti, C. Muscas, and P. A. Pegoraro, “Trade-Offs in PMU Deployment for State Estimation in Active Distribution Grids,” *IEEE Trans. Smart Grid*, vol. 3, no. 2, pp. 915–924, 2012, doi: 10.1109/TSG.2012.2191578.

[215] J. Zhao *et al.*, "Power System Dynamic State Estimation: Motivations, Definitions, Methodologies, and Future Work," *IEEE Trans. Power Syst.*, vol. 34, no. 4, pp. 3188–3198, 2019, doi: 10.1109/TPWRS.2019.2894769.

[216] Z. Jin, Y. Hu, and C. Sun, "Event-triggered state estimation for stochastic hybrid systems with missing measurements," *IET Control Theory & Applications*, vol. 12, no. 18, pp. 2551–2561, 2018, doi: 10.1049/iet-cta.2018.5568.

[217] H. Sun, F. Gao, K. Strunz, and B. Zhang, "Analog-Digital Power System State Estimation Based on Information Theory—Part I: Theory," *IEEE Trans. Smart Grid*, vol. 4, no. 3, pp. 1640–1646, 2013, doi: 10.1109/TSG.2013.2260361.

[218] Y. Zhang and J. Wang, "Towards Highly Efficient State Estimation With Nonlinear Measurements in Distribution Systems," *IEEE Trans. Power Syst.*, vol. 35, no. 3, pp. 2471–2474, 2020, doi: 10.1109/TPWRS.2020.2967173.

[219] R. Deng, G. Xiao, R. Lu, H. Liang, and A. V. Vasilakos, "False Data Injection on State Estimation in Power Systems—Attacks, Impacts, and Defense: A Survey," *IEEE Trans. Ind. Inf.*, vol. 13, no. 2, pp. 411–423, 2017, doi: 10.1109/TII.2016.2614396.

[220] D. Holtschulte and E. Ortjohann, "The Single-Node State Estimation," South Westphalia University of Applied Sciences, May. 2021.

[221] K. Nainar and F. Iov, "Smart Meter Measurement-Based State Estimation for Monitoring of Low-Voltage Distribution Grids," *Energies*, vol. 13, no. 20, p. 5367, 2020, doi: 10.3390/en13205367.

[222] T. Zufferey and G. Hug, "Impact of data availability and pseudo-measurement synthesis on distribution system state estimation," *IET Smart Grid*, vol. 4, no. 1, pp. 29–44, 2021, doi: 10.1049/stg2.12004.

[223] J. M. Cano, P. Arboleya, M. Rashad Ahmed, M. R. R. Mojumdar, and G. A. Orcajo, "Improving distribution system state estimation with synthetic measurements," *International Journal of Electrical Power & Energy Systems*, vol. 129, p. 106751, 2021, doi: 10.1016/j.ijepes.2020.106751.

[224] A. Hassannejad Marzouni, A. Zakariazadeh, and P. Siano, "Measurement devices allocation in distribution system using state estimation: A multi-objective approach," *Int Trans Electr Energ Syst*, vol. 30, no. 8, 2020, doi: 10.1002/2050-7038.12469.

[225] M. Pau, P. A. Pegoraro, A. Monti, C. Muscas, F. Ponci, and S. Sulis, "Impact of Current and Power Measurements on Distribution System State Estimation Uncertainty," *IEEE Trans. Instrum. Meas.*, vol. 68, no. 10, pp. 3992–4002, 2019, doi: 10.1109/TIM.2018.2883844.

[226] Y. Yang and S. Roy, “PMU deployment for optimal state estimation performance,” in *2012 IEEE Globecom Workshops*, Anaheim, CA, USA, 2012, pp. 1464–1468.

[227] E. Kabalcı, Y. Kabalcı, and P. Siano, “Design and implementation of a smart metering infrastructure for low voltage microgrids,” *International Journal of Electrical Power & Energy Systems*, vol. 134, p. 107375, 2022, doi: 10.1016/j.ijepes.2021.107375.

[228] Cigarán Romero Ana, *Network Code on Operational Security*. [Online]. Available: https://www.entsoe.eu/Ffileadmin/Fuser_upload/F_library/Fresources/FOS_NC/F130227-AS-NC_OS_final_.pdf (accessed: Aug. 9 2019).

[229] ENTSO-E, *Operational Security*. [Online]. Available: https://www.entsoe.eu/publications/system-operations-reports/#continental-europe-operation-handbook (accessed: Aug. 9 2019).

[230] S. A. Nasar and F. C. Trutt, *Electric power systems*. Boca Raton Fla.: CRC Press, 1999.

[231] Worpong Sinsukthavorn, “Development of Strategies and Methodologies for Dynamic Control of Distributed Generation in Conventional Grids and Mini-Grids,” Phd Thesis, University of Bolton, UK, 2011.

[232] *Resources | PES Test Feeder*. [Online]. Available: http://sites.ieee.org/pes-testfeeders/resources/ (accessed: Aug. 18 2018).

[233] DIgSILENT, *14 Bus System*. [Online]. Available: www.digsilent.de

[234] J. Kortenbruck *et al.*, “Multilevel and 4-leg topology for smart grid inverter,” in *2016 IEEE International Energy Conference (ENERGYCON)*, Leuven, Belgium, 2016, pp. 1–6.

[235] X. Zhao, “Power System Support Functions Provided by Smart Inverters—A Review,” *CPSS TPEA*, vol. 3, no. 1, pp. 25–35, 2018, doi: 10.24295/CPSSTPEA.2018.00003.

[236] B. K. Bose, “Power Electronics, Smart Grid, and Renewable Energy Systems,” *Proc. IEEE*, vol. 105, no. 11, pp. 2011–2018, 2017, doi: 10.1109/JPROC.2017.2745621.

Appendix A: Histogram and Mean Values

This appendix provides an explanation of the results illustration and the terms of mean used in in Chapter 5 of this thesis. First, the illustration of the results in the form of histogram is explained. How the histogram is used is delineated. Afterwards, the terms of average or mean of result differences and mean of absolute result differences are declared.

A.1 Histogram

Numerical data distribution can be accurately illustrated by a histogram, representing an approximation of the probability distribution for a continuous variable. Further detail about the histogram can be found in literature such as [A1]. In this thesis, the histogram is used in the verification of the proposed model and voltage sensitivity analysis method. It illustrates the number of result differences in comparison between the results from the proposed method and the results from a commercial software. To clarify how the histogram is used, Figure A.1 present an example of a histogram. The total amount of data in this example is 625.

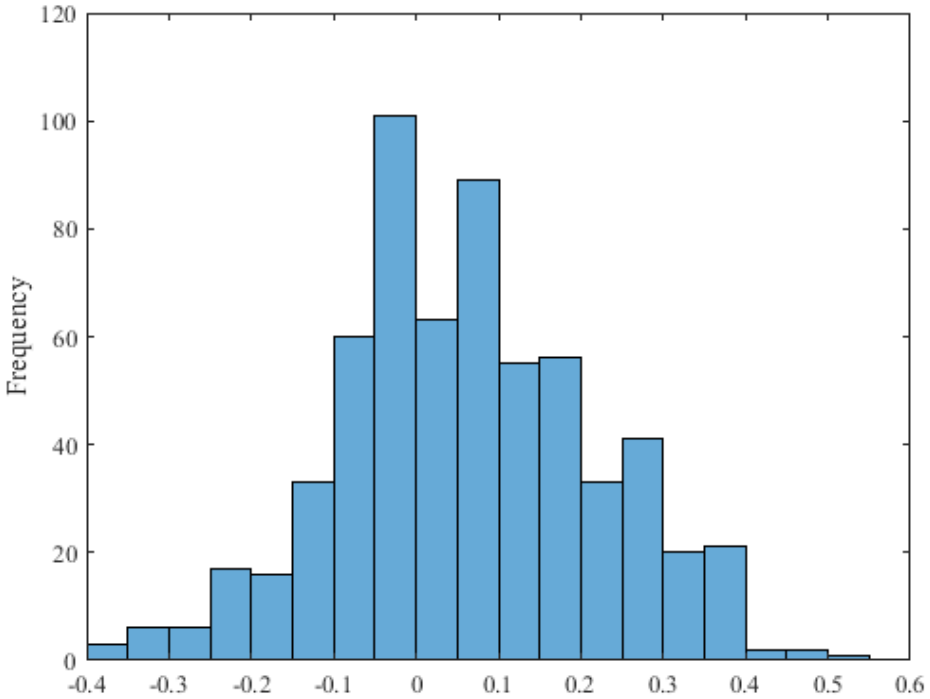

Figure A.1: An example of a histogram

Y axis presents the number of data, also called as frequency, falling in the range shown in X axis. For example, based on Figure A.1, the frequency or the number of data falling in the range between -0.05 to 0 is 100, which is the highest frequency in this chart. In addition, for an analysis purpose, only the frequency itself cannot tell the meaningful proportion of the plotted data. Thus, the histogram can also be shown in the form of relative frequency

$$Relative\ Frequency = \frac{Frequency}{Total\ number\ of\ data} \tag{A.1}$$

which can be interpreted as probabilities as well [A1]. Based on Figure A.1, Figure A.2 displays the histogram whose Y axis is now in relative frequency, determined by Eq. (A.1). The highest frequency, which is 100, represents 16% of total data. That is to say, 16% of total data is in the range of -0.05 to 0.

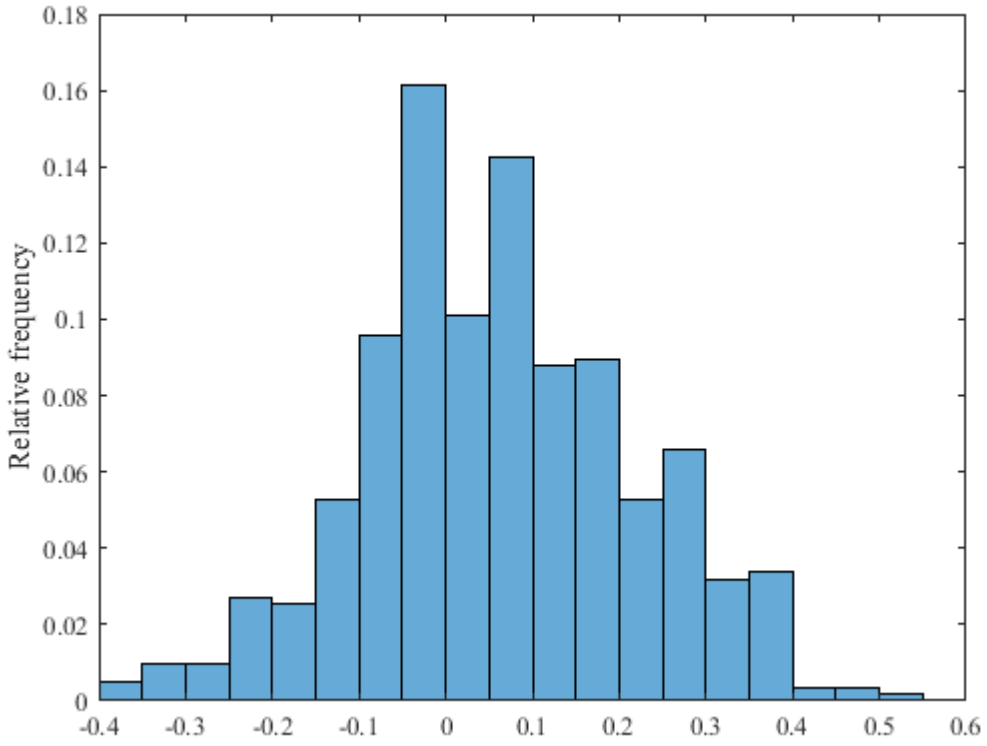

Figure A.2: An example of a histogram in relative frequency

A2. Mean Values

In the results evaluation of this thesis in Chapter 5, two kinds of average or mean are employed: The first one is *mean of differences of results* and the second one is *mean of absolute differences of results* to observe the differences in the term of its magnitude. To make it clear, the term of result differences is clarified to begin with. A result difference

$$\Delta x_{ih} = \frac{x_{ref,ih} - x_{ih}}{x_{ref,ih}} \times 100\% \tag{A.2}$$

is referred to the percent difference between a calculated result xih and its reference $x_{ref,ih}$. The subscripts *i* and *h* of the result difference Δx_{ih} indicate bus *i* and bus *h* in an *n*-bus grid, where $i, h \in \{1, 2, \ldots, n\}$. Then, based on Eq. (A.2), the mean of result differences

$$\mu = \frac{1}{N} \sum_{i=1}^{n} \sum_{h=1}^{n} \Delta x_{ih} \tag{A.3}$$

can be computed, where N is the total number of results ($n \times n$). Figure A.3 displays the mean of result differences (a blue dash line) based on the histogram from Figure A.2.

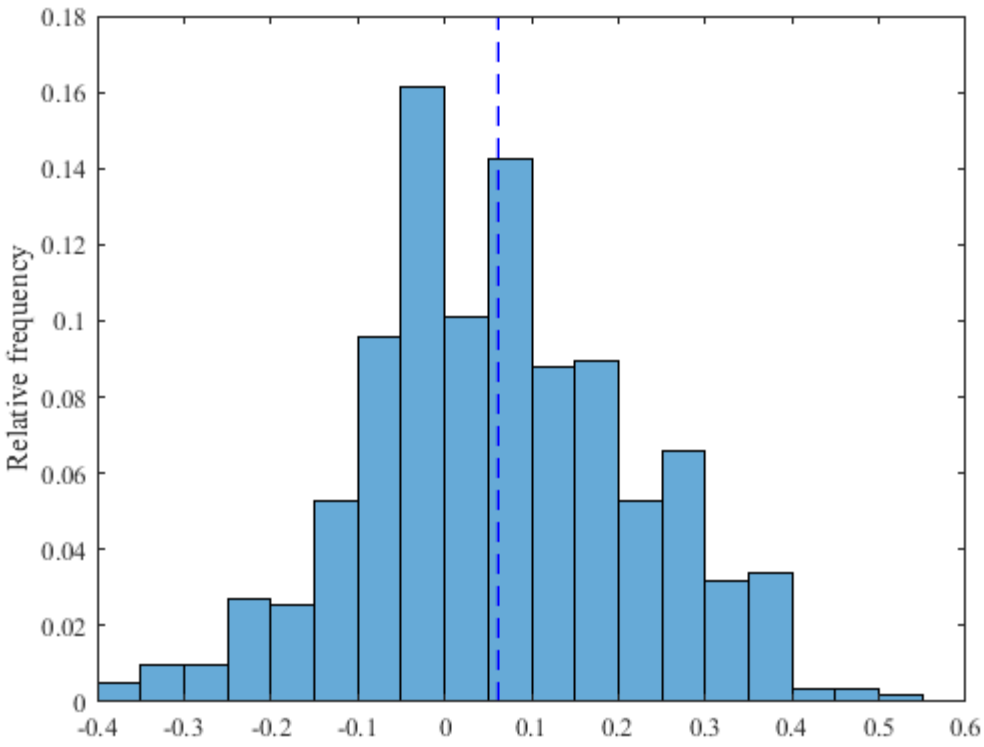

Figure A.3: Illustration of the mean of result differences

Next, the mean of absolute result differences is introduced. The arithmetic mean shown in Figure A.3 is not applicable for some verification scenarios. Comparison of result differences from different sampled results such as different sensitivity types or sequence systems is not suitable, since the positive and negative differences cancelled each other out. The overall size of result differences cannot be observed in positive. The mean of absolute result differences is hence used to compare the means, representing the quality of the proposed method from different samples. Based on the same expression as Eq, (A.2), the term of absolute result differences is clarified. An absolute result difference

$$|\Delta x_{ih}| = \left|\frac{x_{ref,ih} - x_{ih}}{x_{ref,ih}}\right| \times 100\% \tag{A.4}$$

is referred to an absolute difference between a calculated results xih and its reference $x_{ref,ih}$. As well, the subscripts i and h of the absolute percent difference $|\Delta x_{ih}|$ indicate bus i and bus h in an n-bus grid, where $i, h \in \{1, 2, \ldots, n\}$. Accordingly, considering Eq. (A.4), the mean of absolute differences

$$|\mu| = \frac{1}{N}\sum_{i=1}^{n}\sum_{h=1}^{n}|\Delta x_{ih}| \tag{A.5}$$

can be calculated, where N is the total number of results ($n \times n$). If the same data set as Figure A.2 is used, all the values on the negative side will be on the positive side. Figure A.4

illustrates the mean of absolute result differences (a blue dash line) on the same data set as Figure A.2.

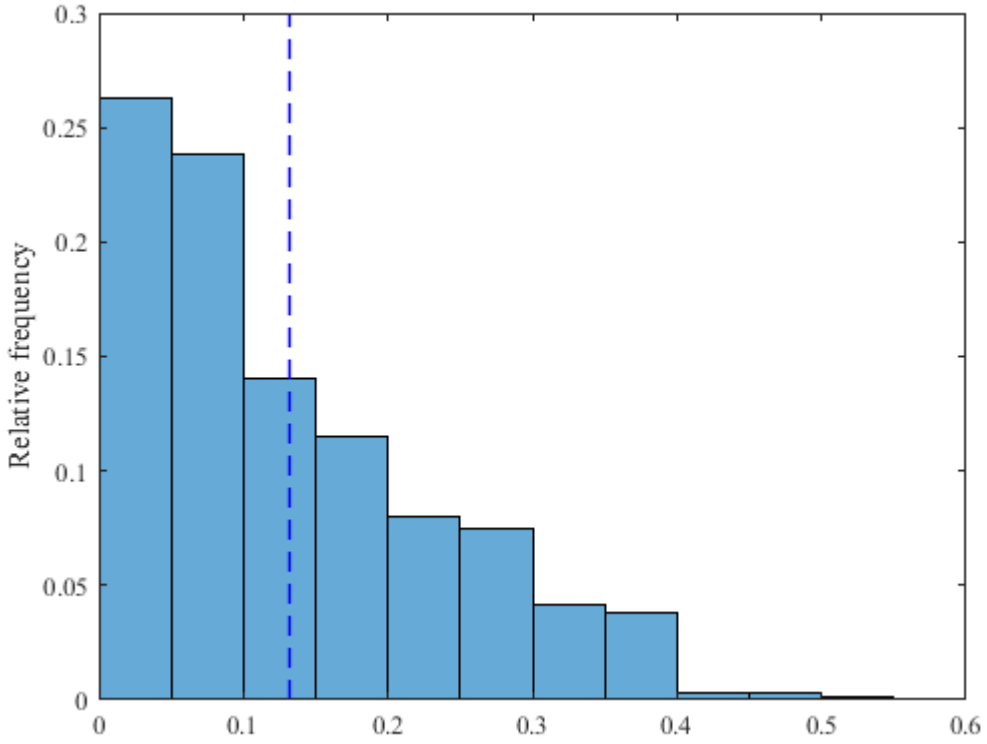

Figure A.4: Illustration of the mean of absolute result differences

To conclude, the difference between the *mean of differences of results* and the *mean of absolute differences of results* has been clarified and also illustrated in Figure A.3 and Figure A.4. The determination of these two mean types is shown in Eqs. (A.3) and (A.5). The next section shows the utilisation of the histogram and the mean values in this thesis.

A.3 Verification Process

This section provides the description of the verification process executed in Case Studies 1 and 2 in Chapter 5. Figure A.5 shows the verification process for the impedance model. The matrix $[\underline{Z}_{bus}]$ is initially computed from the topology data of the power grid. However, it contains bus impedances of all buses. The matrix $[\underline{Z}_{bus}]$ has to be reduced by the modification method, discussed in Section 3.2.4 so that it is equal to the matrix $[\underline{Z}_{par}]$ in size for the verification. The corresponding elements are compared to observe the difference between the matrices $[\underline{Z}_{bus}]$ and $[\underline{Z}_{par}]$ by Eqs. (A.2) and (A.4). To verify the proposed impedance model, $x_{ref,ih}$ is the reference value from the matrix $[\underline{Z}_{bus}]$, and x_{ih} is the calculated value from the matrix $[\underline{Z}_{par}]$ between bus i and bus h. From the analysis process of the corresponding elements of the matrices $[\underline{Z}_{par}]$ and $[\underline{Z}_{bus}]$, the outcomes are shown in two aforementioned aspects: Mean of the absolute percent differences and charts of data distribution in various cases.

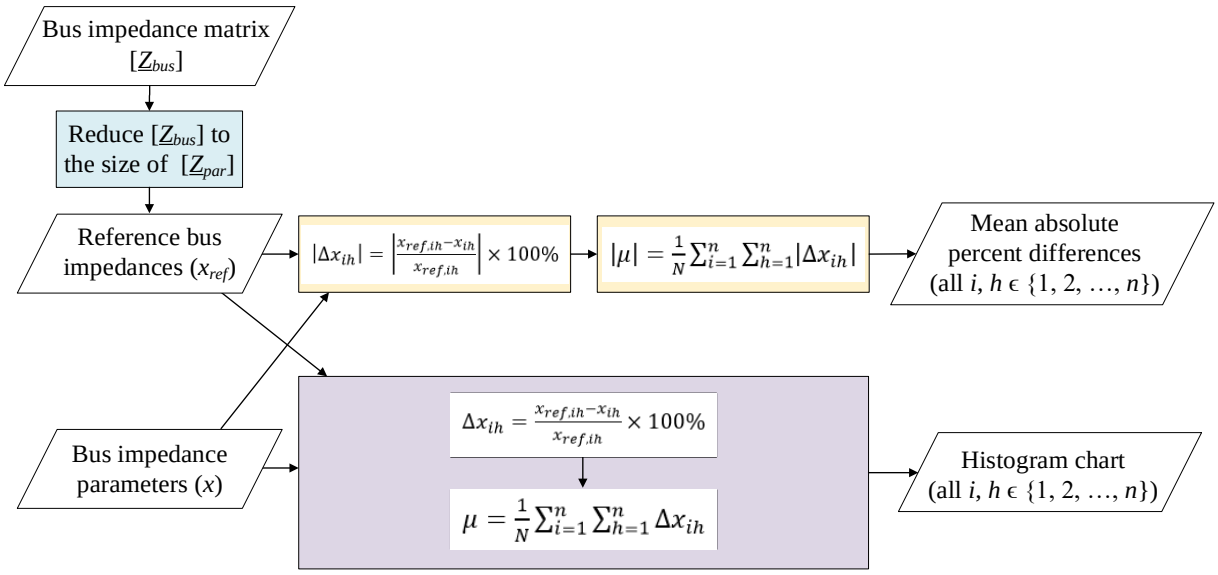

Figure A.5: Analysis process for the proposed impedance model

As a successive step, the results from PowerFactory are then regarded as reference values, since PowerFactory employs the classical method. Figure A.6 shows this verification process of the proposed voltage sensitivity analysis. To verify the proposed voltage sensitivity analysis, the outcomes from the proposed method are compared to observe their difference by using Eqs. (A.2) and (A.4). The comparison is based on the absolute percent difference $|\Delta x_{ih}|$ and the percent difference Δx_{ih} of the sensitivity values between bus i and bus h in an n-bus grid, where $i, h \in \{1, 2, \ldots, n\}$. Thus, $x_{ref,ih}$ is the reference value from PowerFactory, and x_{ih} is the calculated value from the proposed method. Identical to the case of the impedance model, the outcomes are presented in two aforementioned aspects: Mean of the absolute percent differences and charts of data distribution in various cases.

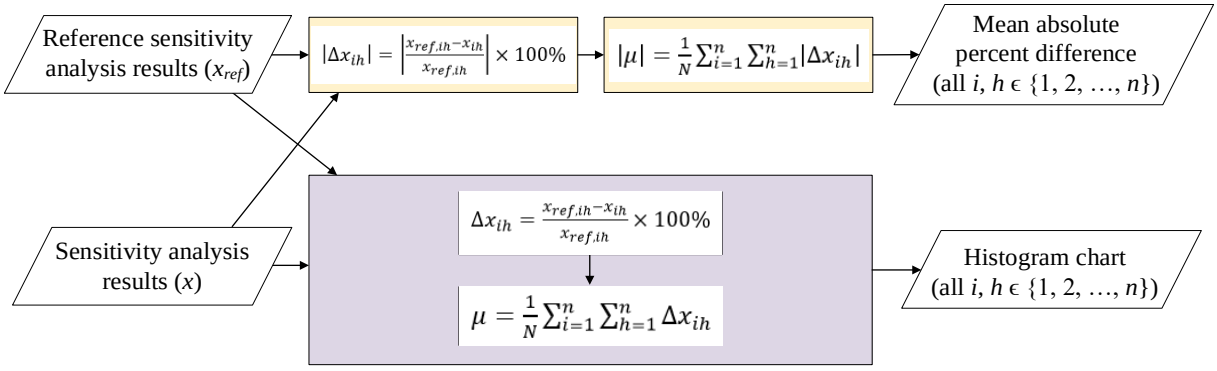

Figure A.6: Analysis process for the results from the proposed method

A.3 References for This Appendix

[A1] E. Kreyszig, *Advanced engineering mathematics*, 9th ed. New Delhi: Wiley-India, 2013.

Appendix B: Additional Information of Modified IEEE 37-Bus Test Feeder

This appendix delivers the additional information, which is not covered in the main content for the modified IEEE 37-bus test feeder in Case Study 1. First, the configurations of this grid are provided. Then, active and reactive powers data used as the inputs in the simulations are shown. Finally, the additional results are demonstrated to complete the presented results of the verification in Chapter 5.

B.1 Grid Configurations

In Case Study 1, IEEE 37-Bus Test Feeder is modified for the simulation of the proposed voltage sensitivity analysis method in medium voltage grid at the nominal voltage of 10 kV and the frequency of 50 Hz. The topological information of this modified grid is provided in Table B.1.

Table B.1: Grid connection information

From bus	To bus	Length [km]	Element Type
799	701	-	25 MVA 20/10 kV
701	702	0.2926	NA2XSY 3x240sm 6/10kV
702	703	0.4023	NA2XSY 3x240sm 6/10kV
702	705	0.1219	NA2XSY 3x185sm 6/10kV
702	713	0.1097	NA2XSY 3x185sm 6/10kV
703	727	0.0732	NA2XSY 3x185sm 6/10kV
703	730	0.1829	NA2XSY 3x240sm 6/10kV
704	714	0.0244	NA2XSY 3x185sm 6/10kV
704	720	0.2438	NA2XSY 3x185sm 6/10kV
705	742	0.0975	NA2XSY 3x185sm 6/10kV
706	725	0.0853	NA2XSY 3x185sm 6/10kV
707	722	0.0366	NA2XSY 3x185sm 6/10kV
707	724	0.2316	NA2XSY 3x185sm 6/10kV
708	709	0.0975	NA2XSY 3x185sm 6/10kV
708	732	0.0975	NA2XSY 3x185sm 6/10kV
708	733	0.0975	NA2XSY 3x185sm 6/10kV
709	730	0.0610	NA2XSY 3x240sm 6/10kV
709	731	0.1829	NA2XSY 3x185sm 6/10kV
709	775	0.1000	NA2XSY 3x240sm 6/10kV
710	735	0.0610	NA2XSY 3x185sm 6/10kV
710	736	0.3901	NA2XSY 3x185sm 6/10kV
713	704	0.1585	NA2XSY 3x185sm 6/10kV
711	740	0.0610	NA2XSY 3x185sm 6/10kV
711	741	0.1219	NA2XSY 3x185sm 6/10kV

712	705	0.0732	NA2XSY 3x185sm 6/10kV
714	718	0.1585	NA2XSY 3x185sm 6/10kV
720	706	0.2804	NA2XSY 3x185sm 6/10kV
720	707	0.1829	NA2XSY 3x185sm 6/10kV
727	744	0.0853	NA2XSY 3x185sm 6/10kV
733	734	0.1707	NA2XSY 3x185sm 6/10kV
734	710	0.1585	NA2XSY 3x185sm 6/10kV
734	737	0.1951	NA2XSY 3x185sm 6/10kV
737	738	0.1219	NA2XSY 3x185sm 6/10kV
738	711	0.1219	NA2XSY 3x185sm 6/10kV
744	728	0.0610	NA2XSY 3x185sm 6/10kV
744	729	0.0853	NA2XSY 3x185sm 6/10kV

The parameters of each element stated in Table B.1 are provided in Table B.2 to Table B.4. These parameters are set in PowerFactory for the simulations. The rest of parameters other than provided here are set by default from the standard library in PowerFactory.

Table B.2: Parameters of 25 MVA 20/10 kV transformer

Parameter	Description	Value	Unit
HV bus	Bus on high voltage side	799	-
LV bus	Bus on low voltage side	701	-
Rated Power	-	25	MVA
Vector group	-	Yd5	-

Table B.3: Parameters of NA2XSY 3x240sm 6/10kV cable

Parameter	Description	Value	Unit
r	1, 2 sequence resistance per length	0.1266	Ohm/km
x	1, 2 sequence reactance per length	0.0848	Ohm/km
r0	Zero sequence resistance per length	0.5063	Ohm/km
x0	Zero sequence reactance per length	0.3393	Ohm/km
B	1, 2 sequence susceptance per length	157.0796	μS/km
B0	Zero sequence susceptance per length	167.4469	μS/km

Table B.4: Parameters of NA2XSY 3x185sm 6/10kV cable

Parameter	Description	Value	Unit
r	1, 2 sequence resistance per length	0.1656	Ohm/km
x	1, 2 sequence reactance per length	0.0880	Ohm/km
r0	Zero sequence resistance per length	0.6625	Ohm/km
x0	Zero sequence reactance per length	0.3519	Ohm/km
B	1, 2 sequence susceptance per length	141.3717	μS/km
B0	Zero sequence susceptance per length	150.1053	μS/km

B.2 Inputs for Simulations

This section delivers the inputs used for the simulations in Case Study 1 for the modified IEEE 37-bus test feeder. There are 25 buses with 26 states, which represent different operational scenarios. First, Table B.5(a) to Table B.5(f) show the inputs for the unbalanced grid condition. Active and reactive powers in phase *a*, *b*, and *c* are represented by *P1* and *Q1*; *P2* and *Q2; and P3* and *Q3*, respectively. The generation process of these inputs is shown in Appendix F.

Table B.5(a): Inputs for the simulation of the modified IEEE 37-bus test feeder in unbalanced grid condition

State	702						709					
	P1 [kW]	Q1 [kvar]	P2 [kW]	Q2 [kvar]	P3 [kW]	Q3 [kvar]	P1 [kW]	Q1 [kvar]	P2 [kW]	Q2 [kvar]	P3 [kW]	Q3 [kvar]
1	114.48	46.25	-217.68	-86.28	238.16	94.94	120.90	60.21	120.05	40.63	-297.71	-133.85
2	109.00	57.28	301.44	115.57	-259.55	-128.27	332.93	136.91	-114.65	-42.34	120.45	43.41
3	-344.16	-184.65	287.04	174.34	-337.58	-202.11	80.66	38.33	142.38	60.46	-190.32	-80.05
4	-108.64	-42.62	284.56	107.34	235.18	142.26	-94.51	-33.40	-278.94	-166.74	-330.79	-194.74
5	-148.34	-70.79	-180.39	-92.26	-138.43	-61.10	349.55	179.57	177.22	88.73	134.05	49.95
6	-141.54	-73.93	-162.34	-75.70	-217.31	-127.86	180.25	104.07	-288.24	-178.59	110.54	66.59
7	-118.25	-52.52	89.68	55.28	236.68	114.73	-98.13	-37.33	120.32	52.03	-235.36	-145.78
8	-118.63	-67.42	305.55	122.16	-287.36	-129.35	-338.59	-195.17	192.40	77.55	162.75	87.55
9	126.53	52.68	100.50	49.08	-198.06	-110.81	89.17	33.70	301.38	108.19	-163.71	-84.04
10	174.14	95.74	157.75	83.77	233.15	79.71	168.37	64.23	277.77	145.81	-124.10	-67.46
11	-206.09	-114.69	-282.52	-134.89	-167.15	-68.66	-305.16	-149.13	-127.85	-60.32	-121.09	-53.43
12	166.01	79.35	113.95	45.17	171.23	88.28	-300.83	-121.35	175.42	77.19	124.81	68.71
13	-232.96	-91.38	-182.19	-79.33	157.37	85.20	124.14	47.27	-121.53	-69.61	220.73	73.64
14	-117.31	-59.35	-280.80	-109.69	-181.19	-65.87	-102.16	-52.35	-112.93	-37.73	106.78	46.35
15	142.59	63.83	273.94	95.78	-233.04	-120.29	-98.78	-46.15	-210.81	-130.49	140.95	61.43
16	-232.83	-133.19	151.51	68.84	-188.29	-116.09	104.09	49.90	100.34	56.98	103.66	41.31
17	214.73	94.20	-263.51	-132.05	-254.39	-148.67	-305.11	-165.32	-341.46	-168.44	-254.51	-153.08
18	-311.14	-168.20	218.12	90.28	-193.54	-86.34	122.24	43.49	-104.87	-49.09	-324.72	-180.25
19	-331.70	-110.28	-116.52	-64.33	-280.67	-131.81	248.54	127.13	-119.98	-66.25	-267.79	-128.94
20	348.90	173.87	-161.06	-82.50	108.75	60.09	-172.23	-61.97	-263.81	-87.18	-180.40	-67.51
21	166.27	87.41	266.67	106.79	146.03	74.94	136.44	66.71	193.91	96.83	204.15	67.29
22	319.02	146.74	299.11	126.10	-115.18	-66.07	-267.29	-136.26	-155.13	-93.88	-100.99	-45.72
23	282.75	104.15	-186.60	-81.36	-86.51	-35.20	256.72	109.43	-120.23	-51.35	-262.61	-161.15
24	327.42	128.13	262.67	136.95	321.38	127.72	244.48	93.51	343.43	191.16	190.41	68.75
25	-289.60	-124.87	-310.25	-177.55	-231.34	-113.46	201.60	114.75	123.80	66.83	151.70	60.56
26	290.36	96.04	130.55	65.33	252.28	150.66	300.09	112.23	-107.61	-59.37	131.28	63.26

State	712						713					
	P1 [kW]	Q1 [kvar]	P2 [kW]	Q2 [kvar]	P3 [kW]	Q3 [kvar]	P1 [kW]	Q1 [kvar]	P2 [kW]	Q2 [kvar]	P3 [kW]	Q3 [kvar]
1	202.77	73.45	312.44	165.69	-306.68	-120.74	331.38	142.99	-231.92	-83.43	-278.84	-110.62
2	116.60	58.44	121.57	69.50	147.77	70.05	-294.36	-145.06	247.74	87.40	313.56	151.64
3	-96.71	-53.70	-129.31	-65.02	-103.93	-40.37	-127.64	-46.42	-168.51	-86.14	107.87	60.32
4	-202.05	-122.91	-104.42	-42.55	-194.10	-106.74	98.10	50.03	93.81	50.91	-151.39	-58.33
5	-226.22	-132.91	181.74	64.97	208.18	88.95	-301.64	-132.24	124.92	50.59	-174.20	-102.74
6	-155.89	-75.62	129.97	62.88	278.43	105.52	172.58	59.23	-347.15	-120.88	82.45	27.12
7	-135.90	-57.86	124.18	64.48	109.02	65.06	-141.82	-76.47	215.22	117.37	256.87	104.86
8	-105.20	-56.12	238.66	96.44	-109.12	-37.17	-282.62	-118.27	-222.56	-115.80	317.40	152.06
9	88.64	54.64	-262.18	-149.30	311.16	132.47	315.14	129.27	-227.61	-124.51	258.99	127.14
10	295.28	130.13	-190.17	-93.34	-299.95	-179.92	-225.59	-128.72	226.88	111.58	106.41	58.23
11	-279.84	-159.35	-125.31	-57.78	-129.18	-45.02	-344.12	-159.94	-188.06	-64.41	92.50	31.60
12	-241.98	-115.80	-288.16	-108.62	-330.12	-112.84	271.14	163.67	248.47	147.32	95.73	51.16
13	-98.53	-34.89	193.62	84.14	-322.40	-166.17	157.18	67.75	348.36	164.69	125.05	62.22
14	-162.71	-80.30	-154.39	-87.77	134.35	62.11	-246.98	-107.53	-112.77	-60.64	-182.71	-86.77
15	309.17	115.48	107.24	37.72	86.11	33.57	-244.00	-142.57	289.79	167.97	93.13	37.29
16	276.65	140.05	285.13	130.00	117.08	70.20	287.51	105.01	98.51	49.85	-151.86	-77.28
17	343.64	126.13	-177.26	-77.96	-181.13	-67.80	-301.41	-173.26	-300.65	-160.29	-184.94	-66.52
18	-233.37	-121.40	194.92	101.18	157.24	89.89	-306.89	-144.78	-98.87	-46.29	-126.25	-74.22
19	241.64	141.30	-94.06	-50.05	126.12	48.46	-335.94	-205.14	-338.66	-193.34	341.79	127.15
20	118.53	59.76	-101.15	-61.83	175.37	67.02	123.51	48.24	290.91	163.71	202.01	88.99
21	-208.86	-107.58	246.62	123.71	119.22	57.45	-154.77	-70.73	-125.02	-58.22	-112.41	-56.60
22	225.27	75.43	94.67	36.78	-110.26	-52.77	94.95	48.49	-342.89	-123.47	257.47	150.23
23	-119.94	-40.29	-94.25	-41.50	186.49	97.25	-108.86	-48.19	80.69	34.38	80.85	49.72
24	-272.19	-146.36	266.47	88.11	340.89	121.04	127.54	66.52	-113.97	-41.91	111.12	57.98
25	122.15	43.03	-271.60	-123.76	100.69	42.88	128.97	42.39	261.47	107.95	195.66	120.37
26	-273.30	-108.06	-275.26	-131.85	217.93	72.34	-144.39	-61.25	80.52	40.25	-186.55	-91.85

Table B.5(b): Inputs for the simulation of the modified IEEE 37-bus test feeder in unbalanced grid condition

State	714						720					
	P1 [kW]	Q1 [kvar]	P2 [kW]	Q2 [kvar]	P3 [kW]	Q3 [kvar]	P1 [kW]	Q1 [kvar]	P2 [kW]	Q2 [kvar]	P3 [kW]	Q3 [kvar]
1	-271.00	-105.09	-219.34	-93.61	266.01	105.25	344.49	119.78	100.19	42.81	-295.84	-105.25
2	256.91	90.45	-98.39	-54.50	301.93	144.13	-190.79	-89.35	167.45	70.79	-339.65	-115.97
3	324.44	144.30	226.81	84.37	101.02	53.99	-152.78	-68.51	-346.40	-193.09	-211.29	-127.84
4	-232.32	-77.47	101.64	40.92	-145.41	-55.71	349.05	156.41	92.88	37.13	-311.51	-168.65
5	192.65	86.12	298.14	173.73	346.51	209.17	147.09	79.70	252.39	99.87	82.46	27.56
6	-316.65	-159.67	201.21	111.17	158.67	89.70	-218.39	-79.19	-315.42	-181.37	-209.73	-113.77
7	88.70	48.43	235.60	110.27	-242.69	-132.03	121.09	74.41	-121.07	-62.64	341.00	204.38
8	-278.73	-107.57	186.21	89.67	-208.49	-86.73	-138.84	-79.86	91.89	47.76	113.38	59.36
9	135.59	47.88	257.23	86.72	191.84	89.05	-323.77	-152.87	246.75	97.70	-92.81	-49.35
10	-252.40	-86.96	119.53	47.99	113.27	50.82	291.66	172.65	305.62	159.91	229.78	102.71
11	-313.00	-180.15	118.11	65.57	-326.22	-179.90	-200.71	-122.32	103.54	48.49	-128.64	-65.42
12	115.10	65.84	-344.19	-205.26	114.29	65.70	-329.30	-175.71	-98.40	-50.19	140.98	65.12
13	-263.37	-91.36	117.89	46.46	335.14	186.39	-267.64	-95.27	87.07	29.59	-306.46	-150.37
14	-129.03	-57.58	262.45	111.55	175.30	104.43	-199.91	-84.87	314.98	134.39	-274.99	-116.89
15	-229.28	-108.01	-108.87	-38.58	329.84	124.59	-121.86	-54.14	-309.41	-126.63	-243.44	-86.51
16	-349.89	-154.63	-147.02	-75.22	289.77	107.14	312.77	186.71	-252.57	-146.96	-170.12	-91.58
17	236.00	78.38	-298.90	-164.96	98.10	42.05	-329.17	-183.86	214.26	82.66	243.54	115.43
18	291.84	114.14	286.93	118.75	178.00	99.14	-123.10	-65.73	182.81	97.95	162.65	70.52
19	-115.61	-41.45	-113.18	-57.81	256.21	115.55	-243.05	-123.89	178.55	84.40	318.20	124.25
20	-130.50	-61.00	286.15	135.39	162.97	87.46	-329.09	-194.70	161.17	97.12	188.82	79.79
21	-131.12	-70.31	96.31	55.64	-252.52	-125.72	275.37	115.96	-132.27	-72.55	-325.70	-131.29
22	-177.28	-88.65	-108.20	-36.72	-265.76	-153.21	332.61	127.87	-329.63	-172.89	317.03	119.30
23	251.06	137.82	-341.52	-159.01	-142.65	-79.80	98.49	41.76	288.85	174.93	316.43	172.87
24	335.53	195.28	-189.30	-110.81	237.64	144.58	-128.37	-52.94	-349.32	-174.73	-295.86	-169.08
25	-221.43	-89.79	229.20	108.98	-347.02	-187.47	297.97	123.63	301.03	140.46	-267.82	-140.95
26	149.61	67.77	-226.78	-126.24	-207.36	-101.99	132.54	81.71	-143.52	-48.67	-130.57	-46.28

State	722						724					
	P1 [kW]	Q1 [kvar]	P2 [kW]	Q2 [kvar]	P3 [kW]	Q3 [kvar]	P1 [kW]	Q1 [kvar]	P2 [kW]	Q2 [kvar]	P3 [kW]	Q3 [kvar]
1	-121.90	-68.08	233.32	140.14	291.29	119.91	-246.81	-151.50	-98.47	-48.92	300.76	174.60
2	86.16	45.78	120.98	54.33	-269.95	-160.96	-82.15	-37.44	148.31	76.11	-280.23	-161.48
3	-101.44	-56.20	264.96	143.82	-227.41	-136.80	132.63	70.21	-232.74	-135.13	111.57	44.12
4	-177.30	-87.55	-97.92	-59.68	282.48	112.23	-146.83	-58.75	-245.82	-141.99	-202.95	-113.58
5	184.65	106.05	219.24	110.20	-153.58	-95.00	348.45	126.95	323.87	198.95	-244.38	-147.15
6	189.39	65.75	346.62	199.63	-231.02	-130.00	280.12	141.50	341.02	168.40	306.51	173.69
7	-98.36	-51.42	108.84	61.35	-188.43	-103.06	317.30	104.50	314.83	149.72	-275.88	-98.55
8	-133.47	-79.70	-106.57	-46.20	104.83	44.54	320.83	123.67	-169.12	-79.65	231.28	124.82
9	254.20	86.44	266.75	116.94	-305.85	-120.29	-336.13	-150.31	305.97	186.23	-146.09	-69.95
10	-252.99	-139.45	191.86	90.74	168.34	73.75	-102.64	-40.96	98.35	38.51	-286.19	-95.82
11	-126.32	-76.65	-130.86	-63.70	133.40	65.76	175.26	58.67	266.16	117.06	-136.26	-65.18
12	120.64	71.69	313.44	192.63	149.99	61.00	279.48	159.93	-186.23	-85.23	268.51	124.86
13	-234.00	-117.18	157.77	58.21	112.05	51.39	-273.42	-137.55	315.55	132.44	-133.87	-75.04
14	-104.75	-47.31	-312.63	-166.92	-127.90	-52.83	-150.33	-76.36	91.95	47.18	309.23	160.93
15	196.77	113.81	301.45	133.02	99.79	45.01	-178.90	-61.06	-91.09	-51.26	201.70	97.36
16	231.45	115.07	-239.40	-93.87	-162.95	-88.61	-212.80	-125.84	-188.41	-84.37	136.36	67.73
17	162.88	76.42	-98.72	-35.12	-237.01	-139.21	113.32	44.38	124.23	48.31	294.75	104.32
18	-139.08	-52.47	-132.41	-52.26	265.62	130.24	-98.11	-48.64	323.24	150.05	-149.42	-63.04
19	100.70	56.02	-91.69	-47.52	-108.84	-52.61	-191.26	-85.71	-117.35	-49.83	-110.37	-47.98
20	-169.45	-88.61	-336.07	-131.89	115.98	64.88	311.31	124.29	273.45	114.56	168.00	96.80
21	336.48	167.64	-249.23	-151.89	163.27	75.35	331.33	117.52	170.85	75.88	-203.51	-118.52
22	-114.41	-41.93	217.13	122.77	222.44	122.41	-220.57	-78.00	-93.63	-44.12	-160.26	-84.70
23	-179.73	-97.94	92.83	40.06	229.70	139.19	-252.84	-83.99	-116.36	-68.19	174.38	107.41
24	155.87	83.27	171.16	76.96	310.45	169.17	-106.35	-37.88	-114.47	-70.44	97.58	46.00
25	-97.25	-40.92	164.78	61.84	170.45	69.18	-197.11	-99.28	-250.01	-115.76	338.03	175.79
26	201.32	93.33	222.44	110.43	184.50	96.22	-190.44	-76.60	-118.95	-60.79	-130.71	-45.38

Table B.5(c): Inputs for the simulation of the modified IEEE 37-bus test feeder in unbalanced grid condition

State	725						727					
	P1 [kW]	Q1 [kvar]	P2 [kW]	Q2 [kvar]	P3 [kW]	Q3 [kvar]	P1 [kW]	Q1 [kvar]	P2 [kW]	Q2 [kvar]	P3 [kW]	Q3 [kvar]
1	195.95	114.11	239.50	110.21	83.56	46.89	85.81	48.89	-237.26	-106.36	-214.14	-99.34
2	-281.29	-169.37	248.80	132.45	287.60	163.36	240.86	106.46	-258.28	-103.47	179.44	90.34
3	-155.28	-87.66	306.44	118.68	-179.23	-96.18	-315.91	-176.24	-183.26	-91.32	118.02	66.28
4	117.48	61.98	207.95	85.89	97.38	42.86	-191.19	-111.50	152.76	88.29	88.59	43.27
5	-91.51	-42.46	177.16	109.45	345.62	179.57	-206.30	-125.04	-285.91	-101.48	152.26	82.91
6	-241.17	-92.74	-342.97	-138.89	310.26	120.13	224.66	90.74	-83.73	-28.93	302.01	147.97
7	-223.58	-77.53	-124.52	-71.93	105.05	51.34	-233.60	-99.02	-312.33	-161.20	-250.63	-107.96
8	-243.00	-114.49	312.90	144.01	190.07	70.92	261.12	117.61	100.52	37.46	-210.23	-119.25
9	343.43	125.46	87.01	29.03	294.57	133.45	349.47	164.88	109.65	45.41	220.54	127.38
10	86.74	34.21	-123.90	-76.46	309.09	117.64	116.70	71.34	251.42	86.06	-187.33	-69.53
11	349.96	203.62	99.02	49.90	-181.69	-110.88	-126.62	-58.74	-105.80	-40.66	181.78	80.29
12	-212.29	-108.21	-303.76	-151.44	191.79	96.34	346.53	118.79	142.89	73.16	99.15	45.82
13	347.08	199.00	-95.87	-57.60	-115.01	-42.00	133.35	51.45	335.02	161.76	286.19	132.50
14	239.23	114.73	201.90	98.41	219.62	118.37	-109.91	-56.55	183.18	80.97	117.83	61.08
15	-248.40	-152.28	113.46	67.71	-337.19	-178.55	196.57	76.98	137.99	55.66	250.43	101.79
16	226.60	90.79	-262.26	-109.40	-299.01	-144.88	-201.25	-72.31	-323.88	-116.07	208.83	126.38
17	-124.20	-55.21	-233.27	-123.85	-204.35	-110.13	237.49	93.07	108.30	46.03	-176.06	-91.06
18	82.43	39.20	317.28	157.53	-181.67	-103.47	-103.86	-55.43	-84.96	-38.12	210.82	97.45
19	-236.49	-138.25	214.10	105.18	-181.80	-80.76	193.36	84.83	-240.65	-81.79	-229.35	-98.20
20	152.63	83.48	217.32	106.66	-153.68	-67.92	109.12	64.46	286.28	171.47	270.27	125.61
21	215.88	73.49	109.27	56.65	169.02	103.41	120.45	46.57	-258.13	-146.62	111.37	56.71
22	-265.85	-127.42	164.61	54.15	-160.75	-73.81	282.89	131.20	-104.47	-42.83	-120.11	-65.21
23	-330.87	-160.42	-99.64	-43.95	288.50	126.46	-219.98	-120.34	320.55	152.46	-143.29	-60.20
24	119.34	64.89	174.96	105.67	116.27	69.89	117.48	69.86	105.71	38.29	-317.95	-126.74
25	166.98	89.18	147.82	84.54	-226.73	-83.62	-218.70	-122.48	-198.62	-97.06	-158.83	-58.76
26	200.54	70.98	-317.65	-164.27	318.45	134.80	208.91	121.86	212.15	71.47	-168.01	-73.15

State	728						729					
	P1 [kW]	Q1 [kvar]	P2 [kW]	Q2 [kvar]	P3 [kW]	Q3 [kvar]	P1 [kW]	Q1 [kvar]	P2 [kW]	Q2 [kvar]	P3 [kW]	Q3 [kvar]
1	-161.09	-76.91	196.56	92.09	-163.64	-56.61	312.55	144.46	119.45	50.53	284.00	171.80
2	-129.11	-51.79	183.44	62.65	92.57	51.08	316.16	152.50	-249.68	-98.81	233.58	87.57
3	-108.90	-66.41	-274.61	-158.37	98.99	34.15	122.91	47.36	139.26	47.23	-118.11	-54.29
4	298.99	174.41	102.82	47.76	134.59	64.90	212.32	112.15	-201.29	-95.67	144.08	66.20
5	162.36	99.40	-219.99	-93.68	111.60	55.98	-175.46	-64.93	89.40	45.78	-144.83	-74.45
6	223.97	87.60	-329.31	-141.13	-335.72	-186.06	-294.01	-157.88	119.80	45.80	-219.45	-107.19
7	149.74	79.80	349.29	130.31	-117.70	-43.97	272.87	117.65	182.99	105.35	259.08	125.71
8	-315.79	-113.57	-123.42	-75.46	-217.48	-112.06	-140.12	-86.66	-151.26	-74.36	-298.32	-117.79
9	-311.26	-110.41	325.88	196.78	165.86	98.82	147.25	77.99	344.35	198.11	291.64	147.07
10	-226.35	-78.96	-95.89	-45.74	138.05	73.33	-134.45	-66.73	-158.87	-89.46	149.99	68.07
11	90.75	45.15	-251.14	-131.16	-98.41	-39.63	-251.00	-136.19	-247.11	-123.49	-244.14	-108.90
12	-296.85	-168.79	-193.03	-91.59	283.26	109.46	117.72	47.67	225.17	109.73	116.89	55.76
13	103.02	60.08	-162.30	-69.08	124.85	75.53	-301.25	-175.95	-318.83	-107.84	346.47	177.11
14	141.07	69.10	-233.25	-123.46	-200.33	-107.81	318.71	120.68	225.14	99.52	-149.93	-64.34
15	-133.72	-80.59	-279.94	-94.32	-116.77	-45.35	125.24	49.96	266.98	91.26	-111.12	-56.15
16	150.01	56.09	317.64	140.09	-109.56	-52.43	-182.26	-78.63	-286.14	-115.58	81.98	45.61
17	-123.42	-71.16	-115.94	-40.29	-83.46	-34.64	-80.28	-41.38	-245.68	-88.77	-317.02	-127.83
18	257.07	131.62	348.18	154.58	-105.16	-53.45	169.58	63.38	-341.10	-209.18	111.29	63.07
19	-340.82	-144.43	-101.16	-61.15	266.78	148.79	226.07	129.25	-178.61	-62.93	-111.65	-59.24
20	200.06	102.13	87.61	44.27	295.29	171.68	86.27	48.60	-345.58	-192.10	-239.00	-125.99
21	241.99	98.96	-258.88	-127.37	155.69	84.94	-298.12	-101.91	207.21	119.57	-280.75	-140.77
22	-282.94	-106.50	-107.72	-37.06	-119.92	-65.33	152.91	76.90	277.96	95.12	-268.69	-102.74
23	326.07	124.88	327.67	152.01	273.02	138.48	-167.25	-76.42	227.25	112.38	319.62	126.51
24	-98.48	-42.65	-335.14	-204.46	-243.25	-148.72	320.79	131.32	-190.61	-114.04	108.75	47.44
25	101.86	48.74	-349.31	-137.67	-286.70	-144.74	104.76	44.87	124.03	46.55	-295.98	-163.49
26	-99.81	-34.47	98.97	52.42	-262.77	-159.15	-265.68	-132.87	-318.39	-195.12	245.91	129.42

Table B.5(d): Inputs for the simulation of the modified IEEE 37-bus test feeder in unbalanced grid condition

State	730						731					
	P1 [kW]	Q1 [kvar]	P2 [kW]	Q2 [kvar]	P3 [kW]	Q3 [kvar]	P1 [kW]	Q1 [kvar]	P2 [kW]	Q2 [kvar]	P3 [kW]	Q3 [kvar]
1	-106.87	-63.99	314.46	189.41	160.64	91.73	112.08	60.07	122.84	43.29	-206.46	-91.02
2	174.03	82.23	-327.00	-125.41	327.17	108.12	131.24	70.36	-125.14	-46.00	332.65	190.67
3	-80.56	-30.73	-245.56	-132.74	178.73	71.10	-103.91	-37.00	-292.56	-123.89	332.63	190.39
4	-140.95	-85.32	-248.08	-90.30	195.21	99.53	167.00	100.94	-123.14	-61.63	234.17	124.78
5	233.88	92.61	216.29	116.36	-180.65	-101.19	-220.82	-94.11	-304.37	-118.99	303.84	135.45
6	-246.13	-151.77	-329.60	-168.26	272.11	140.15	-303.90	-147.07	-234.38	-88.50	159.35	86.72
7	-221.06	-119.59	-85.78	-32.35	-276.38	-139.22	-208.61	-100.14	318.17	181.51	136.40	73.50
8	257.23	144.41	198.18	97.29	-115.16	-69.15	-254.51	-126.79	234.63	123.23	-81.95	-29.98
9	-120.06	-40.31	210.02	101.48	213.51	83.86	180.27	69.29	-275.32	-128.14	345.12	116.01
10	314.02	186.94	-166.13	-71.68	250.52	149.62	349.31	171.84	329.70	188.19	184.44	69.84
11	219.43	92.04	-231.79	-126.44	85.03	30.99	-113.85	-47.51	111.80	55.23	-122.06	-59.25
12	246.85	97.11	80.82	31.41	348.96	129.02	-337.92	-172.86	155.96	89.09	-302.26	-112.15
13	-184.82	-97.52	-332.34	-109.48	148.56	87.78	127.67	75.21	-204.38	-93.63	189.55	80.20
14	-117.11	-40.09	-122.69	-50.33	-292.76	-175.84	-243.76	-125.54	310.90	124.73	88.24	30.44
15	310.16	123.80	99.36	34.98	166.92	83.77	103.30	49.47	99.88	43.88	93.41	51.45
16	-112.44	-55.62	-307.64	-129.93	114.51	41.98	98.15	41.67	-344.74	-208.20	238.61	84.71
17	-192.10	-97.75	159.27	70.51	-126.97	-58.62	-143.96	-87.56	332.28	142.80	250.77	102.58
18	192.26	118.60	273.33	96.83	-338.45	-114.56	179.25	100.24	278.10	121.64	318.11	139.41
19	113.31	58.61	-320.71	-130.68	308.82	143.22	-139.65	-53.88	138.40	83.83	-88.07	-49.33
20	84.63	51.45	-307.73	-177.85	-217.66	-116.56	105.90	52.10	-296.46	-120.56	-241.86	-94.09
21	-142.00	-54.20	-127.80	-48.60	-295.80	-116.30	-98.78	-51.25	135.16	82.53	-242.85	-122.17
22	-347.30	-209.70	-240.66	-80.68	107.98	52.98	-342.17	-172.87	-306.09	-111.32	108.62	55.95
23	-180.38	-103.53	-312.11	-152.32	-120.14	-53.81	-271.32	-126.64	-170.18	-72.12	334.84	164.35
24	257.16	85.54	-154.02	-54.22	97.55	54.98	168.19	82.70	125.17	74.62	306.52	167.97
25	-161.11	-85.11	266.34	126.52	287.31	174.88	-110.25	-62.57	-332.73	-176.52	112.35	51.56
26	314.79	149.42	107.12	45.64	-307.95	-183.41	-217.50	-83.02	-254.82	-148.61	-176.63	-59.93

State	732						733					
	P1 [kW]	Q1 [kvar]	P2 [kW]	Q2 [kvar]	P3 [kW]	Q3 [kvar]	P1 [kW]	Q1 [kvar]	P2 [kW]	Q2 [kvar]	P3 [kW]	Q3 [kvar]
1	278.41	99.30	117.01	48.20	-275.14	-169.20	-263.23	-147.87	289.13	154.19	-319.23	-112.53
2	328.07	109.33	104.40	47.99	267.90	154.68	320.83	174.41	-234.06	-137.00	-177.71	-89.43
3	89.00	44.01	-140.28	-57.36	-189.70	-102.96	-258.26	-140.80	-164.05	-67.88	-254.14	-115.06
4	85.94	32.55	-158.60	-95.66	-152.12	-77.12	-326.05	-193.49	-211.58	-74.77	302.29	129.89
5	113.36	60.12	-340.66	-173.26	-180.71	-97.08	-117.71	-61.06	-342.32	-178.46	-283.37	-112.45
6	259.80	155.31	-100.63	-36.86	176.62	87.73	-176.62	-73.60	-284.84	-167.39	-306.48	-114.61
7	253.64	83.67	307.76	114.12	-335.24	-177.84	-146.06	-74.29	138.42	79.98	136.80	68.37
8	-272.94	-149.45	-149.69	-52.32	-346.75	-201.76	145.22	80.72	-133.95	-50.05	-100.85	-42.37
9	-198.32	-89.58	-168.49	-89.31	-300.73	-164.28	-126.90	-59.45	264.99	129.34	-109.16	-43.98
10	-148.47	-52.77	-267.81	-159.37	-175.15	-83.79	199.83	120.58	-91.42	-51.80	236.18	116.48
11	188.51	103.76	120.61	58.54	265.90	104.74	193.12	114.26	-256.15	-141.51	-313.37	-140.84
12	158.70	83.46	107.40	63.89	-296.52	-98.66	-150.50	-78.12	-156.02	-66.32	-310.01	-133.25
13	-153.73	-62.24	304.44	113.53	296.03	127.96	210.69	72.81	105.56	42.81	320.06	184.30
14	-133.75	-63.97	-223.10	-131.96	-263.35	-149.45	-188.80	-112.63	289.30	141.30	96.34	52.78
15	-152.04	-79.81	249.22	110.64	154.83	90.30	-233.78	-84.46	200.61	71.21	345.34	166.85
16	-100.19	-52.53	-119.63	-63.37	-222.32	-103.09	-326.25	-157.79	182.09	81.80	-236.88	-133.86
17	272.64	110.25	212.86	113.98	-155.56	-92.16	-114.11	-62.99	-269.78	-151.12	320.71	159.62
18	322.18	190.70	-220.13	-83.24	82.57	31.85	195.27	105.50	215.48	83.72	137.34	54.10
19	118.53	70.97	280.17	130.16	-347.65	-135.36	187.43	85.10	107.26	61.66	-98.67	-42.84
20	316.80	108.75	-111.75	-54.74	-322.78	-129.92	-88.66	-51.57	344.14	122.51	-279.40	-153.49
21	249.58	89.89	286.54	127.50	279.72	113.50	-271.51	-159.67	-340.63	-137.21	-186.21	-114.55
22	-187.44	-97.55	-134.43	-74.20	-308.20	-126.18	162.34	95.62	249.92	89.03	-316.99	-142.16
23	-147.53	-87.63	166.63	98.69	106.77	58.99	-191.12	-116.77	-265.16	-148.48	-336.47	-146.06
24	-249.51	-130.05	103.17	53.99	-145.60	-57.00	-130.72	-78.96	317.43	159.34	116.00	59.40
25	329.28	141.22	241.07	115.50	298.44	150.71	330.31	133.19	-144.31	-63.44	311.16	114.38
26	-103.24	-36.92	-251.11	-145.46	148.35	55.34	-347.97	-145.57	112.79	37.14	181.75	88.93

Table B.5(e): Inputs for the simulation of the modified IEEE 37-bus test feeder in unbalanced grid condition

State	735						736					
	P1 [kW]	Q1 [kvar]	P2 [kW]	Q2 [kvar]	P3 [kW]	Q3 [kvar]	P1 [kW]	Q1 [kvar]	P2 [kW]	Q2 [kvar]	P3 [kW]	Q3 [kvar]
1	-91.65	-37.45	257.03	152.23	-257.94	-92.22	195.72	66.13	-191.80	-99.03	-341.45	-167.71
2	295.43	100.13	-113.50	-48.55	282.98	138.33	289.20	107.44	254.78	132.31	-83.96	-50.15
3	-161.54	-69.43	308.51	120.88	327.19	107.71	-289.44	-149.20	205.88	70.78	-106.91	-55.37
4	-182.97	-83.46	-253.94	-86.52	318.29	194.94	-168.29	-101.25	-196.82	-113.52	348.19	166.31
5	266.71	131.19	-344.19	-132.86	-113.04	-41.45	-274.75	-126.08	165.29	81.08	349.97	118.61
6	258.09	151.42	252.23	93.12	218.42	107.58	-80.18	-34.98	-292.57	-99.63	-171.90	-86.22
7	243.47	119.75	-143.91	-66.80	253.31	146.58	206.97	113.46	179.93	63.65	85.21	33.36
8	102.72	44.23	-274.46	-97.85	207.47	91.43	149.94	66.85	136.21	83.94	256.93	93.58
9	340.54	172.68	115.49	68.61	-116.47	-61.24	122.82	49.48	280.83	172.57	96.22	37.11
10	-199.65	-104.99	-222.25	-132.34	-143.03	-84.83	-236.26	-104.46	-129.82	-65.17	88.38	43.05
11	199.78	112.99	142.17	60.47	336.37	176.40	-95.79	-42.34	-251.21	-152.21	-334.21	-135.49
12	-164.94	-93.68	-100.73	-59.03	232.17	101.48	322.82	175.14	-242.37	-91.42	-342.17	-210.86
13	-337.31	-190.44	-99.66	-44.42	-307.74	-178.62	-268.96	-107.27	-116.15	-45.08	154.26	81.22
14	-185.41	-109.09	176.84	59.48	148.99	62.10	115.77	62.78	-148.15	-72.59	262.46	147.74
15	344.87	154.22	301.52	161.34	226.73	110.04	-321.40	-110.09	-155.59	-68.49	264.29	118.13
16	-122.72	-41.92	135.23	62.78	197.02	97.10	-232.68	-117.85	-291.56	-160.87	204.16	108.46
17	345.23	116.63	-151.83	-81.83	80.34	37.27	85.16	42.52	88.78	38.46	-211.23	-119.71
18	-192.92	-71.01	181.57	96.18	206.03	91.37	-95.61	-50.16	-323.06	-177.33	94.24	35.36
19	140.18	57.97	-220.10	-98.31	119.16	65.40	307.47	167.93	88.80	33.41	89.72	37.74
20	180.19	73.52	-159.19	-59.61	214.36	104.10	114.41	39.50	-327.23	-164.30	124.69	66.27
21	180.34	68.94	-251.27	-140.91	125.33	47.08	-121.63	-65.14	-121.47	-44.12	82.85	28.79
22	191.85	105.29	-234.56	-121.43	232.58	99.56	-314.75	-173.46	100.47	35.91	-161.32	-73.97
23	-283.84	-151.41	263.62	148.25	107.32	51.47	105.93	64.31	311.47	113.58	-331.45	-166.83
24	-268.83	-91.76	-245.68	-122.97	-200.48	-81.78	95.82	51.85	-339.83	-162.83	-322.25	-182.20
25	101.37	53.87	-221.64	-107.72	287.08	170.47	287.93	169.79	-162.35	-72.76	-81.70	-46.54
26	88.65	33.79	201.85	82.06	263.05	129.93	191.00	78.75	145.37	85.91	-317.77	-196.03

State	737						738					
	P1 [kW]	Q1 [kvar]	P2 [kW]	Q2 [kvar]	P3 [kW]	Q3 [kvar]	P1 [kW]	Q1 [kvar]	P2 [kW]	Q2 [kvar]	P3 [kW]	Q3 [kvar]
1	258.16	107.67	-90.59	-46.43	83.84	48.28	98.06	41.32	-104.75	-43.63	-131.42	-61.98
2	-181.72	-93.80	-342.34	-183.92	307.57	121.34	263.21	95.53	-99.52	-34.98	-249.64	-97.14
3	-108.89	-49.99	-103.77	-50.68	111.69	69.19	120.39	53.77	-100.48	-42.27	-130.46	-48.55
4	180.11	72.45	-334.28	-110.05	-215.52	-103.68	209.35	114.65	-162.30	-79.68	266.79	103.66
5	260.50	110.08	211.37	72.75	162.28	88.35	-295.20	-168.04	266.82	122.39	-323.22	-129.70
6	-112.79	-39.15	-120.83	-47.14	-181.00	-97.41	-105.62	-35.36	113.67	47.95	327.22	120.58
7	177.98	72.56	326.94	111.26	268.09	118.10	335.57	170.96	111.79	65.99	-339.46	-207.56
8	283.01	162.30	120.26	63.62	-183.26	-90.98	-332.60	-149.48	-301.87	-117.89	-87.28	-29.24
9	128.81	62.36	273.89	100.94	135.26	60.70	-273.21	-96.83	-138.26	-67.65	-120.81	-44.71
10	342.03	184.81	123.81	64.35	91.92	47.39	-330.99	-147.71	-149.69	-64.51	161.94	71.51
11	-245.68	-92.19	-94.12	-53.72	179.46	97.92	-215.12	-124.58	254.54	92.93	114.41	48.51
12	126.85	55.43	105.89	58.49	-86.46	-50.23	-268.10	-149.65	-167.84	-71.92	283.07	98.10
13	160.77	69.13	312.54	144.15	-214.44	-102.83	206.49	72.27	-149.93	-92.54	121.66	61.24
14	-249.48	-146.96	-342.42	-168.83	-102.87	-49.27	-321.72	-156.50	229.27	123.59	174.28	62.61
15	-260.55	-117.95	-181.33	-75.54	-182.85	-85.93	-223.86	-109.34	110.31	51.93	83.89	28.07
16	-264.54	-138.27	-304.59	-118.09	-146.98	-72.49	334.95	158.97	-290.93	-131.00	138.58	69.42
17	-294.41	-150.40	151.56	60.26	165.25	73.29	-188.69	-68.60	197.26	93.57	-233.38	-129.14
18	300.39	170.89	126.82	66.55	185.02	95.66	-118.40	-57.91	-142.31	-87.39	-94.80	-42.38
19	261.98	101.00	-293.98	-170.88	104.33	58.97	-313.66	-188.35	-187.82	-89.02	-290.51	-132.49
20	-135.72	-47.19	151.35	87.64	-310.69	-189.44	-226.46	-91.98	-206.88	-127.20	320.64	197.86
21	-294.76	-106.74	-284.97	-149.03	-207.18	-75.27	256.30	125.36	257.86	100.09	-129.51	-61.38
22	-150.67	-68.62	129.93	63.15	-265.99	-161.28	120.33	69.20	119.38	48.99	264.10	126.46
23	-309.52	-156.50	-246.93	-119.93	232.18	125.82	189.96	102.85	-209.98	-103.42	337.46	120.00
24	-297.17	-183.52	-164.97	-83.20	232.59	140.32	-265.68	-145.23	-186.33	-75.37	-165.70	-94.98
25	183.83	111.54	-146.02	-87.15	152.83	90.90	341.54	185.06	284.64	131.41	252.66	115.34
26	-103.58	-49.58	259.20	105.10	-99.10	-34.02	153.06	53.43	87.56	46.79	-322.31	-199.24

Table B.5(f): Inputs for the simulation of the modified IEEE 37-bus test feeder in unbalanced grid condition

State	740						741					
	P1 [kW]	Q1 [kvar]	P2 [kW]	Q2 [kvar]	P3 [kW]	Q3 [kvar]	P1 [kW]	Q1 [kvar]	P2 [kW]	Q2 [kvar]	P3 [kW]	Q3 [kvar]
1	235.39	92.78	-134.30	-51.16	-136.07	-64.22	-202.09	-96.29	-234.41	-109.57	86.11	37.91
2	101.63	37.04	273.36	147.62	-277.24	-117.62	-141.39	-81.23	286.47	103.34	-347.13	-184.35
3	-180.13	-97.71	244.36	112.53	-195.82	-119.56	268.75	119.64	215.79	130.47	219.72	97.17
4	-211.47	-98.46	-184.52	-62.45	-114.24	-59.60	-290.38	-168.71	-269.47	-116.46	-342.60	-155.02
5	-291.93	-179.40	-95.00	-35.75	335.92	155.72	192.98	68.66	-135.84	-57.54	158.72	62.26
6	99.09	53.35	-309.89	-130.02	-150.55	-79.78	-180.71	-73.83	107.98	37.41	289.02	106.29
7	-267.42	-96.25	-343.22	-149.10	114.37	63.23	-277.85	-98.15	-268.48	-92.26	327.10	136.92
8	210.37	96.24	253.96	100.45	211.93	98.77	250.54	96.06	116.72	45.55	-209.52	-98.18
9	-322.18	-148.51	-291.75	-114.89	110.48	43.44	208.54	128.53	-97.04	-36.37	-120.39	-51.48
10	-342.58	-128.03	82.68	43.50	-177.14	-62.46	209.42	111.71	-123.74	-71.20	96.50	45.38
11	244.89	94.12	251.03	154.14	-90.39	-34.72	-293.12	-158.94	95.23	50.70	239.87	122.34
12	250.81	145.86	141.81	66.41	149.27	53.88	176.45	103.99	262.62	106.00	277.59	159.89
13	-245.31	-148.60	122.06	67.94	320.78	148.48	-102.11	-38.72	257.32	157.13	-252.22	-140.98
14	222.93	82.56	155.47	81.21	294.72	102.33	-293.48	-98.64	223.49	136.25	107.88	63.33
15	-165.60	-83.93	247.54	125.27	259.03	157.73	100.77	47.91	-259.90	-85.77	-331.41	-187.85
16	308.91	179.42	-116.98	-52.10	209.57	87.88	242.50	113.86	119.68	67.18	107.23	64.69
17	278.46	155.90	-317.47	-120.73	-270.22	-120.37	-262.69	-124.49	-244.42	-106.57	283.96	103.93
18	-227.06	-122.10	-217.48	-80.98	146.71	83.21	270.16	143.90	-101.94	-50.65	-91.46	-38.11
19	103.61	42.14	278.99	96.72	107.49	45.56	331.77	155.76	-323.49	-176.99	-192.85	-113.31
20	188.11	100.84	118.85	43.46	-121.13	-44.42	-292.63	-167.46	256.27	138.79	-240.58	-136.74
21	230.35	141.53	-234.32	-137.98	184.72	110.96	-117.24	-55.66	101.09	35.58	270.69	138.94
22	259.98	100.27	-303.13	-127.58	326.44	114.07	211.66	117.94	303.37	113.53	299.78	125.34
23	-97.52	-32.34	-236.11	-104.56	-312.96	-140.31	-173.05	-86.18	189.07	112.29	-220.03	-114.30
24	268.63	90.25	329.22	198.05	-185.64	-99.43	275.53	152.93	-114.00	-66.62	316.77	172.24
25	130.55	59.28	-122.57	-49.36	120.27	56.15	-258.25	-97.50	118.45	51.41	100.61	59.55
26	-217.52	-100.43	188.97	101.31	214.01	127.77	320.32	194.24	115.02	58.45	253.57	100.48

State	742						775					
	P1 [kW]	Q1 [kvar]	P2 [kW]	Q2 [kvar]	P3 [kW]	Q3 [kvar]	P1 [kW]	Q1 [kvar]	P2 [kW]	Q2 [kvar]	P3 [kW]	Q3 [kvar]
1	87.07	28.99	-342.86	-114.09	223.94	79.16	-85.02	-37.22	-210.89	-75.61	121.02	55.94
2	112.12	56.38	-328.27	-154.54	128.98	65.10	273.17	125.73	-128.18	-65.23	-121.33	-48.63
3	-321.38	-164.52	-138.30	-66.70	-89.97	-45.63	156.90	90.83	-342.83	-173.80	110.18	57.79
4	-97.71	-50.20	232.18	125.29	-168.75	-81.68	-82.15	-37.70	-118.22	-68.67	-319.15	-195.04
5	253.49	146.19	-118.64	-55.13	289.58	107.69	267.86	119.74	235.49	114.09	168.58	63.58
6	-113.66	-57.68	-263.49	-141.36	148.26	52.26	-90.86	-49.51	216.74	111.90	215.13	113.79
7	-103.44	-49.84	-162.84	-99.05	180.02	89.37	-320.18	-185.23	-115.79	-62.43	240.66	123.57
8	-181.54	-98.86	-274.09	-134.65	-226.60	-100.00	104.11	49.73	247.35	99.49	282.81	114.27
9	-207.15	-91.21	253.82	107.90	244.73	98.95	-81.15	-44.69	-91.59	-53.75	158.63	55.18
10	280.05	125.82	-112.28	-47.58	161.35	84.91	312.99	187.40	-207.55	-98.24	291.14	170.76
11	-330.83	-140.07	-290.80	-133.79	187.09	83.39	-346.80	-210.77	213.40	80.82	268.18	117.46
12	187.63	103.66	315.40	162.77	197.70	113.72	327.83	196.73	-97.57	-50.77	139.53	83.67
13	-176.88	-86.15	327.57	199.05	99.11	54.24	246.86	120.95	-333.43	-175.20	-108.55	-54.68
14	113.50	60.59	-184.93	-85.27	-325.36	-182.69	202.96	96.07	-131.33	-44.77	100.34	34.99
15	213.36	94.25	256.60	140.01	-101.47	-51.58	201.07	75.46	-120.19	-64.53	-328.82	-149.47
16	319.17	106.95	277.51	149.21	165.24	89.94	-242.02	-131.12	-85.20	-47.74	-276.99	-167.12
17	-196.87	-78.94	125.00	60.02	228.91	113.99	-165.13	-102.16	-178.05	-62.29	120.30	66.21
18	-101.08	-51.96	-103.02	-54.38	-103.26	-42.49	311.98	147.18	-95.65	-41.83	343.90	145.99
19	-334.99	-166.23	165.64	66.05	-300.99	-168.32	-184.64	-83.12	-110.85	-56.61	-134.71	-46.67
20	-98.56	-46.28	-161.50	-65.52	158.57	95.51	264.27	137.39	323.94	165.53	302.37	161.11
21	128.07	55.72	89.58	49.32	242.96	146.11	-85.75	-42.33	103.62	50.49	-99.92	-50.79
22	135.40	54.10	-142.93	-74.62	316.26	175.79	-270.56	-105.40	-85.23	-45.26	-109.04	-47.09
23	81.90	41.77	113.56	62.19	-282.75	-110.78	115.30	68.93	-216.55	-74.16	324.71	200.62
24	-107.37	-45.92	177.91	86.62	309.41	109.05	184.20	110.89	138.34	51.26	126.50	63.60
25	119.69	65.22	-133.52	-66.37	187.98	99.11	98.42	38.42	-145.47	-70.28	262.89	119.30
26	95.83	55.92	-248.47	-88.93	-167.21	-84.45	149.05	82.43	160.94	95.19	-149.37	-54.76

Table B.6(a) and Table B.6(b) show the inputs for the balanced grid condition. Active and reactive powers, *P* and *Q*, are per phase. The generation process of these inputs is shown in Appendix F.

Table B.6(a): Inputs for the simulation of the modified IEEE 37-bus test feeder in balanced grid condition

State	702		709		712		713		714		718	
	P [kW]	Q [kvar]	P [kW]	Q [kvar]	P [kW]	Q [kvar]	P [kW]	Q [kvar]	P [kW]	Q [kvar]	P [kW]	Q [kvar]
1	-109.00	-36.65	143.15	69.48	84.86	37.45	-114.55	-66.69	89.24	44.31	92.34	40.75
2	-86.94	-47.12	-177.94	-96.64	129.60	49.33	103.95	63.59	173.27	84.20	127.30	55.05
3	140.51	64.33	-93.40	-53.36	-89.24	-52.92	84.89	33.32	98.06	49.54	-100.57	-60.77
4	-156.02	-72.38	181.65	62.17	127.00	58.29	109.29	66.38	115.57	42.26	-93.22	-52.23
5	95.94	43.27	-90.55	-37.02	114.75	52.87	-160.03	-69.79	-133.74	-49.67	84.25	48.47
6	173.35	80.94	-110.67	-38.29	179.37	85.76	111.77	55.52	-140.36	-62.59	172.89	61.10
7	102.75	56.02	102.73	44.65	-116.10	-57.72	113.27	44.66	-181.03	-98.09	-93.81	-45.03
8	-178.54	-103.48	155.93	88.95	-107.85	-36.71	173.23	90.73	109.21	59.19	102.98	44.69
9	117.60	48.92	139.19	75.51	-97.11	-55.50	148.92	91.30	83.74	46.43	-91.75	-39.97
10	-128.29	-78.17	91.22	55.13	-183.72	-85.86	-147.26	-82.72	-85.41	-36.27	82.91	49.60
11	115.82	45.71	128.00	77.84	102.05	45.71	177.82	75.16	156.81	63.22	-180.10	-100.86
12	-102.84	-52.50	127.53	69.54	85.66	52.41	-142.09	-66.84	181.72	70.52	142.53	77.54
13	92.05	35.51	-83.25	-47.84	-102.28	-45.33	-137.76	-51.37	132.33	52.04	111.16	39.84
14	-136.69	-46.32	154.10	66.70	-88.85	-34.04	-187.95	-77.85	-130.80	-72.23	-141.92	-79.32
15	167.32	84.68	-83.31	-30.17	-91.07	-46.78	-117.85	-69.83	112.30	44.37	-186.50	-103.26
16	-100.35	-60.77	177.56	93.31	-114.53	-57.49	-124.13	-42.04	132.23	59.10	133.16	57.67
17	-171.08	-68.31	141.47	83.94	-135.84	-81.15	90.75	37.59	90.69	50.63	86.20	38.05
18	-182.58	-81.58	-158.07	-62.82	-162.18	-74.77	-94.83	-58.42	147.39	76.28	107.01	45.47
19	100.46	48.40	-132.94	-65.57	-157.85	-58.76	-145.26	-62.79	172.44	85.79	102.34	39.24
20	174.88	81.32	-159.35	-68.49	177.17	100.08	-95.72	-46.75	103.02	49.88	126.24	52.73
21	-113.22	-60.82	90.19	38.88	-83.82	-49.85	-152.90	-93.36	-185.45	-87.68	162.96	100.16
22	128.84	53.04	-176.39	-89.32	129.57	73.85	149.75	88.28	-145.76	-76.88	109.82	50.55
23	-120.66	-63.92	-89.54	-39.23	-115.38	-50.26	-154.06	-92.37	-183.58	-99.51	-161.04	-57.33
24	-160.16	-59.01	185.85	82.85	-188.15	-78.30	113.09	51.27	174.40	74.11	121.30	72.24
25	85.38	45.30	113.73	54.27	97.75	43.65	130.02	72.52	-85.73	-30.14	-82.67	-38.75
26	-97.00	-38.46	159.02	90.49	-104.18	-51.39	-186.43	-108.54	140.75	64.37	103.84	36.62

State	720		722		724		725		727		728	
	P [kW]	Q [kvar]	P [kW]	Q [kvar]	P [kW]	Q [kvar]	P [kW]	Q [kvar]	P [kW]	Q [kvar]	P [kW]	Q [kvar]
1	-142.13	-66.00	131.81	70.54	-157.08	-83.02	-173.08	-90.67	-145.22	-76.54	96.28	54.68
2	88.08	54.42	-123.99	-67.55	-167.34	-84.74	-175.59	-71.13	-124.98	-51.06	92.72	38.93
3	-159.58	-58.32	178.96	69.59	-115.39	-69.08	108.78	43.53	-174.10	-91.11	155.42	67.62
4	129.69	49.89	-91.34	-48.25	145.03	86.85	-107.43	-65.76	-109.96	-51.48	104.25	62.96
5	-114.48	-46.13	-138.01	-51.36	85.25	51.21	-159.16	-96.44	-178.02	-65.28	-124.81	-64.48
6	-145.08	-57.88	100.99	55.38	157.95	57.31	102.91	54.89	-165.69	-63.37	-164.38	-80.02
7	185.29	96.28	-186.43	-75.12	185.32	62.91	129.16	51.06	-172.75	-95.86	-175.48	-70.77
8	121.08	70.16	-179.61	-81.35	-111.60	-57.44	143.26	64.01	167.08	83.95	99.25	57.63
9	148.16	77.85	-146.74	-90.25	-137.29	-73.59	-125.43	-41.99	-115.17	-44.48	117.78	57.52
10	113.97	50.42	-141.89	-60.38	86.37	40.52	-85.84	-49.61	92.02	53.32	-124.01	-74.51
11	115.46	40.67	122.65	75.50	-105.28	-41.87	-93.57	-42.17	-99.37	-40.58	-88.73	-35.42
12	89.41	53.21	-83.71	-36.07	156.27	61.85	95.95	51.56	178.38	66.12	-102.20	-52.54
13	-144.68	-59.93	152.92	56.62	-127.60	-47.85	134.82	80.53	128.17	62.00	-170.28	-94.85
14	-83.68	-50.64	-96.45	-48.56	152.49	60.37	175.87	65.17	162.90	75.62	-173.26	-103.69
15	84.29	34.44	151.01	67.42	89.87	55.55	-158.45	-72.62	93.74	35.51	-160.99	-96.42
16	148.79	73.59	129.62	59.58	122.66	43.70	-128.63	-69.32	115.51	38.59	112.68	39.87
17	-141.31	-85.90	90.13	50.41	-107.55	-66.15	-99.21	-57.07	-96.13	-38.29	-137.46	-77.73
18	88.66	33.86	-151.46	-60.59	-187.77	-114.92	188.50	99.69	-136.41	-71.74	-133.05	-45.75
19	143.87	82.90	88.92	48.29	-143.81	-60.77	-108.17	-65.12	-158.50	-76.68	-187.93	-99.40
20	-104.77	-61.75	-90.96	-32.27	83.77	39.66	165.89	72.98	-148.61	-82.01	124.51	42.67
21	93.46	51.17	-98.91	-53.43	-184.18	-87.92	-133.00	-73.79	175.26	84.39	84.65	44.69
22	122.19	65.47	-167.62	-79.45	82.01	39.67	-137.20	-56.02	-181.72	-108.86	82.47	49.73
23	-141.40	-64.17	-127.81	-67.81	-123.72	-74.53	187.86	101.45	161.09	97.47	128.14	57.92
24	104.50	45.22	-109.40	-60.90	117.10	65.42	178.27	90.40	87.36	38.91	147.91	69.29
25	-189.98	-63.27	-99.97	-47.13	161.52	95.11	103.17	62.42	143.98	64.89	-95.59	-34.49
26	85.16	28.19	-154.90	-91.60	-184.08	-61.17	82.99	50.76	-82.58	-49.41	-157.37	-89.14

Table B.6(b): Inputs for the simulation of the modified IEEE 37-bus test feeder in balanced grid condition

State	729		730		731		732		733		735	
	P [kW]	Q [kvar]	P [kW]	Q [kvar]	P [kW]	Q [kvar]	P [kW]	Q [kvar]	P [kW]	Q [kvar]	P [kW]	Q [kvar]
1	139.05	66.70	-165.75	-72.90	143.68	84.42	105.87	50.72	-132.02	-77.37	161.51	56.23
2	-106.55	-36.63	-122.53	-63.05	161.39	73.18	-89.05	-46.88	-105.71	-46.90	-86.98	-41.72
3	183.32	100.33	167.80	98.71	-151.61	-67.06	93.15	31.18	-159.58	-77.40	-145.00	-72.46
4	150.65	71.81	-163.34	-54.92	-168.60	-62.61	-106.70	-35.37	127.46	76.84	-117.27	-63.02
5	120.83	43.41	139.56	66.87	-114.85	-41.79	-137.77	-50.18	-83.04	-39.66	-113.02	-55.71
6	-138.42	-77.90	-165.45	-79.77	95.76	58.01	-180.92	-74.78	-185.77	-99.53	-83.92	-33.71
7	-186.29	-72.05	134.31	71.58	-99.10	-40.42	-153.18	-66.87	113.61	42.91	-103.15	-59.32
8	-139.59	-81.41	108.89	61.79	172.13	64.79	-100.39	-41.75	161.40	99.64	100.14	61.47
9	90.75	45.54	135.54	50.85	-176.32	-86.30	160.44	80.59	-156.44	-88.55	175.32	74.22
10	-163.97	-60.85	173.68	95.25	188.56	113.13	-84.12	-43.11	144.60	53.41	-121.14	-55.01
11	154.90	65.79	-147.55	-69.84	110.07	65.58	103.06	57.91	-129.31	-72.66	-131.30	-66.77
12	168.60	81.80	-185.10	-86.93	98.12	55.60	-96.93	-35.77	-184.15	-98.51	171.00	61.22
13	-109.91	-49.77	150.07	51.26	-154.51	-62.12	150.93	52.65	89.37	47.17	172.29	84.56
14	-89.41	-53.57	-88.43	-48.46	-183.04	-93.41	133.92	46.40	174.37	68.91	-115.61	-41.34
15	-189.30	-105.18	-163.92	-90.00	87.39	33.79	-159.86	-94.58	134.64	62.47	-171.65	-83.28
16	-115.38	-70.72	-168.63	-90.56	-182.80	-106.14	-167.76	-101.41	-92.86	-36.31	137.41	48.61
17	-85.55	-32.55	-162.37	-75.98	120.77	50.24	108.48	62.53	122.27	73.00	-158.62	-67.40
18	-127.08	-78.26	-149.69	-77.59	-138.63	-80.42	-99.36	-47.35	-86.48	-49.19	-91.24	-39.02
19	113.95	53.55	183.40	101.68	-128.76	-49.32	-164.13	-98.70	-84.12	-37.60	-84.36	-52.18
20	168.68	99.21	-121.36	-52.57	180.06	84.88	99.71	61.53	176.17	106.22	95.20	45.02
21	86.92	39.91	93.77	51.59	-146.35	-50.09	99.18	59.07	88.91	36.71	-159.52	-81.15
22	-126.33	-56.74	154.53	52.87	141.63	84.96	168.79	76.54	138.07	62.77	93.77	41.95
23	172.83	71.15	-131.25	-63.66	-180.39	-63.43	95.47	57.76	121.55	48.10	-158.29	-74.70
24	-174.58	-93.76	124.52	62.83	-115.80	-60.62	-85.52	-37.50	-155.88	-89.98	-162.32	-91.29
25	100.31	35.86	-93.81	-43.62	182.10	109.65	88.42	40.90	116.30	48.20	-84.14	-39.50
26	177.59	71.17	-115.46	-52.16	-125.92	-42.89	185.70	111.48	-95.52	-39.03	-124.94	-46.87

State	736		737		738		740		741		742		775	
	P [kW]	Q [kvar]	P [kW]	Q [kvar]	P [kW]	Q [kvar]	P [kW]	Q [kvar]	P [kW]	Q [kvar]	P [kW]	Q [kvar]	P [kW]	Q [kvar]
1	-188.81	-95.74	158.14	52.51	182.94	90.91	154.44	64.82	122.55	49.75	-109.34	-64.02	-180.44	-83.02
2	-159.98	-73.18	-182.77	-109.20	86.35	36.90	84.17	30.90	-143.66	-67.91	186.39	87.50	181.89	65.62
3	136.02	74.26	132.63	70.51	-124.25	-73.87	86.88	50.10	-84.40	-48.53	130.40	75.67	163.11	98.65
4	-185.11	-84.72	165.08	90.52	-159.02	-66.13	89.42	50.65	-161.02	-56.82	105.17	57.94	103.31	48.36
5	-155.77	-71.64	98.53	55.42	-152.75	-89.42	156.13	57.60	-156.42	-88.30	161.89	77.08	-187.37	-115.98
6	-113.10	-66.46	122.98	49.87	-125.49	-60.90	-82.88	-41.03	177.33	108.98	84.85	33.18	184.54	106.89
7	167.14	100.12	-90.68	-47.33	-85.87	-47.28	-97.99	-55.87	101.43	46.16	-99.71	-41.92	-97.47	-49.73
8	97.40	59.54	132.13	76.51	-94.98	-43.51	92.89	38.87	-84.72	-38.42	162.10	78.47	-94.08	-52.47
9	-186.18	-107.10	-188.29	-108.47	-87.94	-49.19	-116.79	-43.02	119.86	59.11	-131.02	-47.81	84.47	40.06
10	-115.27	-55.03	-143.56	-52.42	97.45	33.56	-165.73	-65.61	89.12	40.70	-150.64	-52.10	82.39	44.21
11	-143.73	-54.92	-168.05	-58.41	-82.77	-49.92	-100.73	-38.44	106.58	44.65	108.06	53.49	180.13	76.27
12	-123.89	-66.65	-149.70	-71.76	-187.11	-106.88	-136.68	-64.72	136.76	69.76	-128.65	-69.87	155.30	71.34
13	-183.59	-104.48	176.14	108.31	-181.77	-81.53	104.37	58.88	98.32	44.87	-152.18	-53.89	-87.59	-48.72
14	149.35	90.00	153.86	78.00	-94.30	-51.12	136.40	64.88	82.50	41.68	-123.61	-60.00	160.68	96.87
15	133.43	46.36	-157.05	-92.27	185.07	107.99	-86.79	-33.11	-85.51	-50.24	-118.31	-43.82	-96.43	-59.68
16	123.08	68.27	108.57	37.51	92.26	52.56	99.05	55.73	-163.56	-86.05	-188.58	-106.21	-178.20	-101.51
17	147.45	66.09	-180.76	-99.03	168.97	58.10	-123.02	-51.78	169.97	80.06	-135.12	-79.66	-116.22	-56.58
18	133.49	75.41	-154.44	-56.38	-112.20	-60.66	-87.27	-32.74	-86.17	-50.51	110.83	65.05	-113.15	-51.01
19	-161.06	-89.47	-145.66	-53.10	-120.28	-66.96	-114.46	-56.36	-87.52	-52.36	185.60	85.96	-91.29	-53.62
20	-97.76	-40.36	104.89	42.26	160.95	70.48	148.52	73.59	-182.97	-99.28	-128.52	-63.47	-84.85	-49.60
21	-183.30	-106.04	155.57	56.01	136.99	84.75	128.36	44.75	84.50	36.59	98.60	51.22	119.62	64.10
22	-189.69	-73.58	154.81	95.26	-95.34	-57.12	-155.37	-69.50	181.29	90.00	183.24	75.01	-101.85	-60.76
23	-188.32	-112.04	-83.43	-28.61	161.76	86.89	-173.62	-68.27	-123.92	-60.04	-83.88	-41.67	175.95	89.71
24	-149.73	-50.28	137.41	82.43	-87.84	-49.22	89.71	45.92	128.42	77.61	-117.75	-49.95	-125.63	-68.41
25	-153.90	-67.71	-124.08	-67.47	-90.07	-38.50	128.55	68.63	-161.97	-97.24	93.30	32.94	128.89	57.57
26	85.72	46.64	182.17	88.84	-88.02	-37.49	150.58	78.02	134.64	71.28	92.41	35.93	168.18	94.42

B.3 Additional Results

In Section 5.1.2, only the charts of the trend of the whole result differences for this sensitivity analysis in positive sequence are presented. In this appendix, the charts displaying the plots from the sensitivity analysis in negative sequence are provided additionally. The histogram of result differences for voltage magnitude sensitivity analysis are displayed in Figure B.1 and Figure A.2, while the histogram of result differences for voltage angle sensitivity analysis are displayed in Figure B.3 and Figure B.4. The mean values of all phases are provided in Table A.7.

Table A.7: Mean of result differences of each grid sensitivity type (unit: [%])

Sensitivity type	**Mean**		
	Phase *a*	**Phase b**	**Phase c**
Svir,2	0.008	2.753	0.006
Svii,2	-1.397	0.439	-0.021
Sphiir,2	1.341	-0.548	-0.412
Sphiii,2	-0.059	-2.936	-0.084

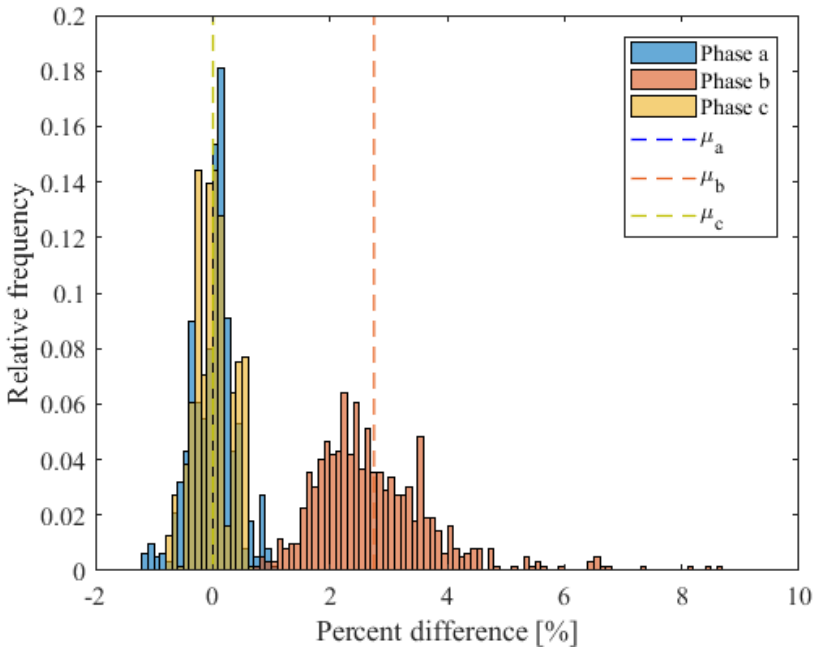

Figure B.1: Histogram of the whole result differences in *Svir*,2 of the modified IEEE 37-bus test feeder case

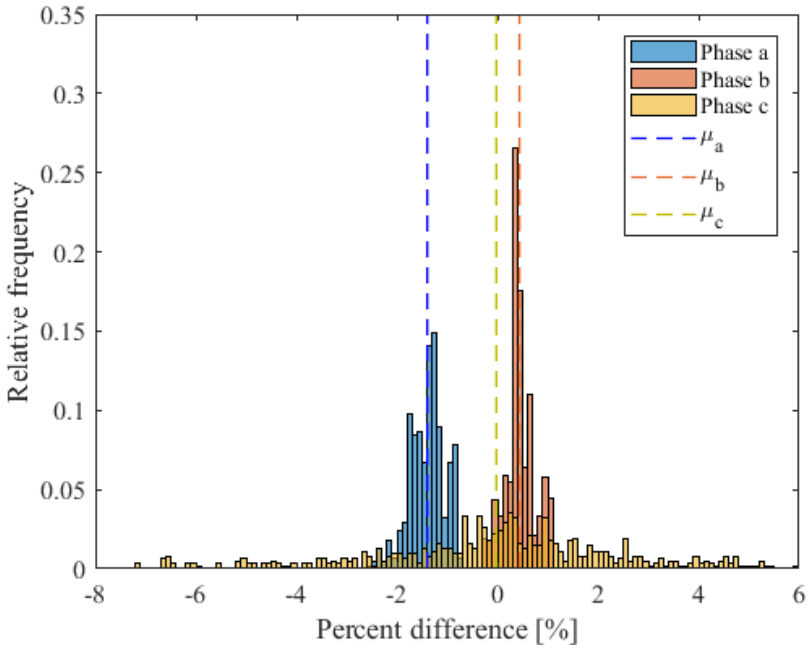

Figure B.2: Histogram of the whole result differences in *Svii*,2 of the modified IEEE 37-bus test feeder case

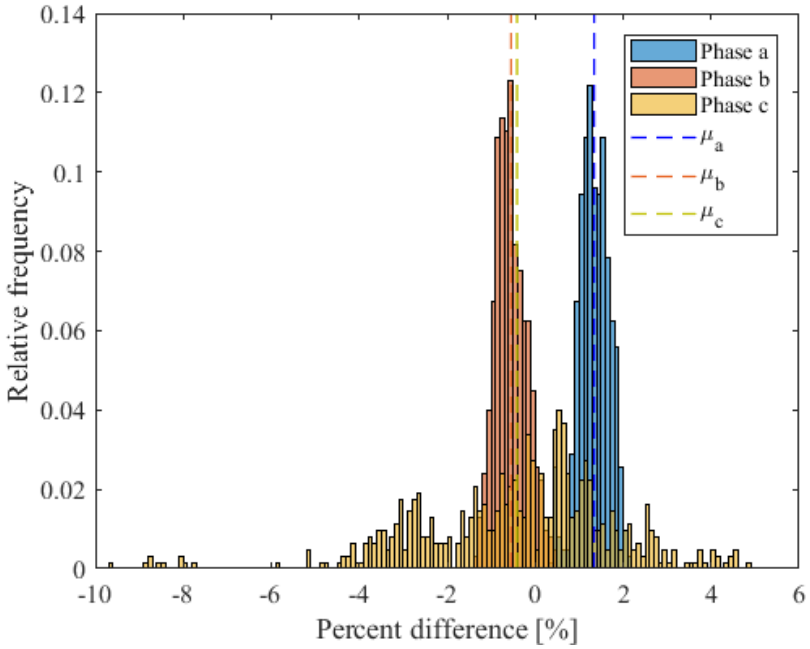

Figure B.3: Histogram of the whole result differences in *Sphiir*,2 of the modified IEEE 37-bus test feeder case

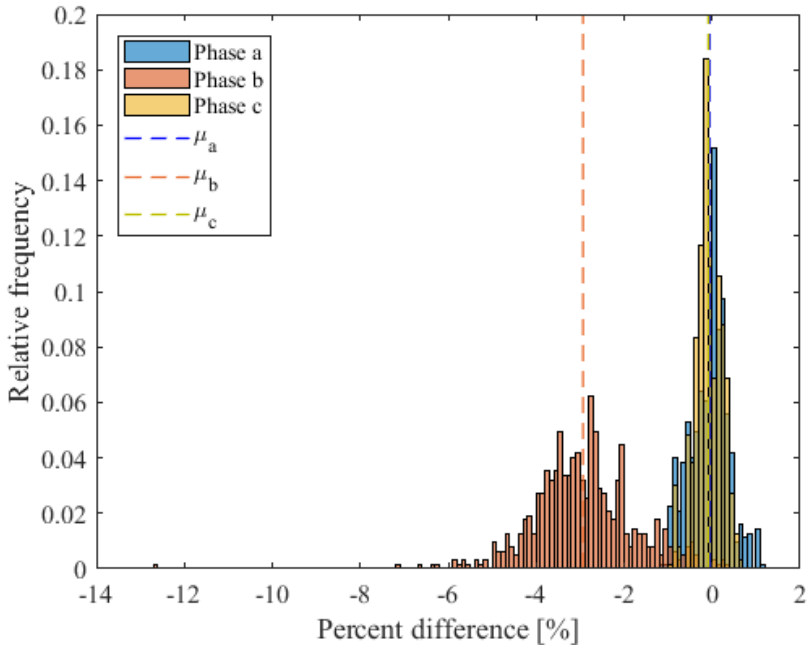

Figure B.4: Histogram of the whole result differences in *Sphiii*,2 of the modified IEEE 37-bus test feeder case

Identical to the case of positive sequence stated in Section 5.1.2, the sensitivities *Svir* can be paired to *Sphiii* and *Svii* can be paired to *Sphir*. Based on the proposed analysis method in Chapter 4, their characteristics are the opposite of each other. Besides, the histograms in Figure B1 to Figure B4 illustrate that high accuracy of the results from the proposed method is still achievable in the case of the sensitivity in relation to complex negative sequence current.

Appendix C: Additional Information of Exemplified Mesh Grid

This appendix provides the additional information, which is not covered in the main content, for the exemplified mesh grid in Case Study 1. First, the configurations of this grid are given. Next, active and reactive powers data used as the inputs in the simulations are shown. Lastly, the additional results are demonstrated to complete the presented results of the verification in Chapter 5.

C.1 Grid Configurations

A mesh grid modified from 14-bus system example in PowerFactory is also simulated in Case Study 1 to investigate the application of the proposed voltage sensitivity analysis method. The simulation is executed at the nominal voltage of 10 kV and the frequency of 50 Hz. The topological information of this modified grid is provided in Table C.1. The transformer parameters are shown in Table C.2. The cable parameters can be found in Table B.3 and Table B.4, since the elements used in this grid are identical to that of Modified IEEE 37-Bus Test Feeder. The rest of parameters other than provided here are set by default from the standard library in PowerFactory.

Table C.1: Cable connection information

From bus	To bus	Length [km]	Element Type
100	101	-	25 MVA 20/10 kV
101	102	0.20	NA2XSY 3x240sm 6/10kV
101	107	0.10	NA2XSY 3x240sm 6/10kV
102	103	0.20	NA2XSY 3x185sm 6/10kV
103	104	0.10	NA2XSY 3x185sm 6/10kV
103	105	0.20	NA2XSY 3x185sm 6/10kV
104	105	0.10	NA2XSY 3x185sm 6/10kV
105	108	0.10	NA2XSY 3x185sm 6/10kV
106	105	0.10	NA2XSY 3x185sm 6/10kV
107	106	0.10	NA2XSY 3x185sm 6/10kV
108	101	0.20	NA2XSY 3x240sm 6/10kV
108	109	0.20	NA2XSY 3x185sm 6/10kV
109	110	0.10	NA2XSY 3x185sm 6/10kV
110	101	0.30	NA2XSY 3x240sm 6/10kV
110	111	0.25	NA2XSY 3x185sm 6/10kV
111	101	0.20	NA2XSY 3x240sm 6/10kV

Table C.2: Parameters of 25 MVA 20/10 kV transformer

Parameter	Description	Value	Unit
HV bus	Bus on high voltage side	100	-
LV bus	Bus on low voltage side	101	-
Rated Power	-	25	MVA
Vector group	-	Yd5	-

C.2 Inputs for Simulation

This section delivers the inputs used for the simulations in Case Study 1 for the exemplified mesh grid. There are 10 buses with 11 states, which represent different operational scenarios. First, Table C.3(a) and Table C.3(b) show the inputs for the unbalanced grid condition. Active and reactive powers in phase *a*, *b*, and *c* are represented by *P1* and *Q1*; *P2* and *Q2; and P3* and *Q3*, respectively. The generation process of these inputs is shown in Appendix F.

Table C.3(a): Inputs for the simulation of the exemplified mesh grid in unbalanced grid condition

State	102						103					
	P1 [kW]	Q1 [kvar]	P2 [kW]	Q2 [kvar]	P3 [kW]	Q3 [kvar]	P1 [kW]	Q1 [kvar]	P2 [kW]	Q2 [kvar]	P3 [kW]	Q3 [kvar]
1	-214.47	-111.73	-188.51	-68.81	164.13	63.58	109.80	49.19	-211.49	-91.77	-164.05	-64.74
2	210.00	95.72	98.41	45.33	197.01	57.11	152.92	69.05	150.90	72.15	110.06	46.03
3	211.70	77.43	174.60	86.76	-181.55	-51.75	179.50	45.42	136.01	65.14	106.05	38.10
4	-185.32	-89.58	197.82	106.74	95.33	46.45	-112.80	-53.12	-159.94	-62.09	-174.55	-47.02
5	-103.13	-36.19	-94.50	-43.50	-106.61	-53.92	-196.30	-88.82	130.37	54.22	-218.42	-74.03
6	123.87	36.21	-142.27	-53.93	-171.40	-48.58	145.48	61.59	110.04	34.53	156.02	60.50
7	-138.75	-54.76	122.71	32.28	101.05	35.39	-127.04	-41.39	178.19	92.74	154.14	70.28
8	151.27	52.31	196.84	103.98	109.74	58.75	175.13	87.60	110.40	30.12	-102.10	-33.41
9	110.27	32.34	96.76	24.05	-159.96	-40.37	-115.92	-30.48	192.50	64.63	-204.09	-88.07
10	-114.22	-54.23	212.77	107.18	99.58	38.87	171.90	88.87	-102.54	-51.49	104.01	38.85
11	-145.19	-52.65	-164.76	-45.86	216.97	82.68	-170.57	-69.45	-119.72	-32.12	-171.24	-43.82

State	104						105					
	P1 [kW]	Q1 [kvar]	P2 [kW]	Q2 [kvar]	P3 [kW]	Q3 [kvar]	P1 [kW]	Q1 [kvar]	P2 [kW]	Q2 [kvar]	P3 [kW]	Q3 [kvar]
1	176.03	62.25	148.93	52.92	208.23	45.23	163.77	45.74	103.08	34.64	-103.26	-44.62
2	191.66	78.71	-102.99	-48.97	-193.27	-102.66	-206.12	-109.30	-102.12	-22.82	-113.56	-45.71
3	202.92	81.87	181.03	69.98	-210.03	-58.32	-140.70	-43.29	-194.22	-58.48	-160.28	-39.33
4	168.32	38.38	-103.38	-33.05	188.15	52.22	122.97	27.61	-213.27	-76.86	-112.78	-60.41
5	-219.62	-113.52	-94.53	-34.08	-150.86	-79.37	-96.90	-42.93	-96.48	-22.08	-211.69	-105.11
6	-219.13	-101.12	-97.52	-35.77	-217.50	-82.79	212.40	74.36	-142.09	-74.37	-101.75	-41.12
7	-195.51	-80.49	-155.75	-64.77	168.18	38.87	149.58	66.26	-124.87	-58.02	-126.66	-48.33
8	-147.00	-53.96	-196.05	-92.48	-180.66	-81.18	113.00	54.20	-139.54	-29.29	213.24	111.61
9	-213.62	-55.59	-201.13	-83.92	186.36	53.89	-136.29	-40.48	-172.15	-52.04	109.52	37.61
10	-101.26	-41.00	188.75	101.35	-193.29	-70.07	-148.29	-47.51	-108.21	-43.60	176.97	45.15
11	-124.50	-51.62	-154.71	-55.70	-121.28	-35.86	188.24	86.92	135.34	45.40	-105.74	-53.89

State	106						107					
	P1 [kW]	Q1 [kvar]	P2 [kW]	Q2 [kvar]	P3 [kW]	Q3 [kvar]	P1 [kW]	Q1 [kvar]	P2 [kW]	Q2 [kvar]	P3 [kW]	Q3 [kvar]
1	-111.42	-43.94	-107.66	-42.30	191.70	86.90	-152.68	-40.59	-125.40	-47.49	-184.28	-79.67
2	-141.54	-71.51	101.55	44.29	-120.98	-40.99	131.77	69.80	141.80	68.14	-172.62	-60.81
3	215.87	108.66	190.39	90.77	-186.35	-64.34	174.99	66.67	-216.18	-79.33	-219.72	-103.71
4	110.45	29.08	157.94	60.68	113.35	43.68	211.64	43.24	-115.26	-57.68	-102.91	-38.32
5	-148.95	-53.92	-200.58	-92.00	185.01	59.81	-159.75	-62.58	198.35	104.23	-97.22	-20.65
6	-182.87	-85.16	-141.94	-73.96	-122.40	-48.19	152.90	40.06	107.01	35.80	-175.24	-47.65
7	106.60	28.32	-113.78	-58.76	-208.26	-83.09	103.55	53.90	-101.31	-36.48	126.71	58.34
8	171.79	89.99	182.11	94.89	-180.14	-71.32	-107.17	-22.45	-94.97	-45.47	-214.98	-71.99
9	174.36	71.21	-102.41	-43.32	-198.55	-46.55	96.81	23.29	-133.49	-56.61	-186.49	-81.78
10	173.34	55.60	-152.83	-77.31	147.35	63.24	-95.22	-35.68	206.23	72.79	206.60	43.34
11	-162.96	-72.38	107.34	44.32	-106.17	-53.89	122.38	50.97	214.96	81.17	213.24	110.19

Table C.3(b): Inputs for the simulation of the exemplified mesh grid in unbalanced grid condition

State	108						109					
	P1 [kW]	Q1 [kvar]	P2 [kW]	Q2 [kvar]	P3 [kW]	Q3 [kvar]	P1 [kW]	Q1 [kvar]	P2 [kW]	Q2 [kvar]	P3 [kW]	Q3 [kvar]
1	-149.91	-70.52	-111.03	-23.83	-131.86	-27.42	141.09	61.44	99.58	30.82	122.62	56.94
2	167.18	75.23	147.20	63.42	143.49	68.41	-104.31	-35.90	-204.93	-104.42	171.56	35.75
3	-196.36	-48.28	168.94	78.92	98.42	41.98	-192.38	-44.91	181.41	66.02	-133.74	-65.39
4	102.75	26.41	108.10	28.14	161.38	53.24	145.68	51.88	-109.98	-45.83	-107.34	-28.65
5	164.17	48.23	-196.20	-56.76	-162.74	-84.96	118.45	54.56	107.44	34.13	187.58	99.58
6	146.87	35.12	198.26	80.76	129.87	40.45	-199.32	-96.24	112.72	52.62	136.16	60.76
7	-180.33	-88.42	-204.99	-105.53	-205.30	-86.19	-186.26	-77.13	130.51	67.05	-152.28	-47.36
8	-111.39	-43.41	101.57	38.06	164.33	47.20	214.85	114.37	-116.01	-47.62	152.75	53.16
9	-121.89	-43.14	-186.72	-91.10	130.00	56.18	-94.90	-24.76	-198.10	-69.23	-138.54	-68.30
10	-100.02	-24.49	-113.56	-43.74	204.88	92.21	-213.72	-76.85	-106.22	-53.47	-142.32	-32.29
11	104.47	35.66	167.59	73.65	-194.36	-40.86	-204.93	-99.04	-206.60	-84.69	-218.29	-83.27

State	110						111					
	P1 [kW]	Q1 [kvar]	P2 [kW]	Q2 [kvar]	P3 [kW]	Q3 [kvar]	P1 [kW]	Q1 [kvar]	P2 [kW]	Q2 [kvar]	P3 [kW]	Q3 [kvar]
1	-149.60	-54.63	109.21	43.79	94.26	34.34	-111.80	-48.46	114.89	32.89	-200.41	-42.05
2	102.00	46.34	98.60	26.72	-127.04	-36.63	-113.20	-50.58	181.90	77.85	206.01	62.45
3	196.33	43.07	-217.90	-62.71	-171.31	-36.15	172.65	76.53	-164.40	-86.33	-175.70	-49.20
4	190.77	48.15	132.90	64.86	115.18	29.57	170.90	48.70	128.29	55.61	-139.80	-45.65
5	-98.90	-48.18	204.89	96.47	101.04	48.54	-107.16	-41.28	192.51	57.99	132.40	48.26
6	-110.03	-59.34	184.59	96.90	150.28	79.69	-113.44	-44.08	-164.24	-81.15	-180.48	-55.86
7	-132.71	-43.06	-188.28	-67.78	-177.01	-72.65	199.24	60.07	-136.48	-33.47	97.38	38.59
8	-204.51	-54.08	-120.72	-36.26	-120.10	-64.37	147.44	74.70	-94.97	-42.74	141.97	37.69
9	151.06	76.62	-152.26	-59.64	-179.69	-72.50	146.54	51.94	189.17	84.54	200.08	104.27
10	-183.05	-96.85	110.89	59.02	178.17	40.50	205.14	90.65	94.40	45.60	144.99	31.75
11	-120.34	-43.75	111.56	23.21	-125.40	-58.98	96.83	43.13	-142.44	-43.33	149.96	76.88

Table C.4 subsequently provides the inputs for the simulation in balanced grid condition. Active and reactive powers *P* and *Q*, shown in the table, are per phase. The generation process of these inputs is shown in Appendix F. In this case, the inputs at the same bus of all states are set to have the same sign.

Table C.4: Inputs for the simulation of the exemplified mesh grid in balanced grid condition

State	102		103		104		105		106	
	P [kW]	Q [kvar]	P [kW]	Q [kvar]	P [kW]	Q [kvar]	P [kW]	Q [kvar]	P [kW]	Q [kvar]
1	-95.92	-38.14	150.94	45.24	-115.36	-29.98	145.46	49.32	-100.84	-38.94
2	-98.52	-38.75	167.62	46.53	-111.58	-29.50	131.82	41.43	-105.32	-31.69
3	-100.10	-41.46	128.88	47.82	-123.50	-43.63	218.83	92.01	-91.23	-35.64
4	-101.77	-27.37	202.09	63.30	-134.55	-52.32	141.00	40.87	-145.42	-60.53
5	-109.05	-33.73	168.29	63.99	-115.46	-34.48	139.63	42.10	-129.22	-38.50
6	-108.99	-36.63	237.94	81.10	-115.76	-34.67	199.92	81.50	-145.96	-46.10
7	-103.05	-38.87	168.26	48.01	-97.49	-29.54	227.33	77.70	-99.81	-30.72
8	-105.06	-42.08	194.48	64.01	-91.47	-27.66	181.99	68.27	-145.27	-46.65
9	-143.58	-46.62	138.52	51.75	-107.41	-44.02	204.32	69.08	-137.68	-49.53
10	-132.19	-33.48	165.76	62.89	-109.05	-34.24	138.43	50.27	-124.64	-45.43
11	-123.34	-49.32	139.34	49.35	-129.22	-45.53	234.41	84.49	-116.40	-33.59

State	107		108		109		110		111	
	P [kW]	Q [kvar]	P [kW]	Q [kvar]	P [kW]	Q [kvar]	P [kW]	Q [kvar]	P [kW]	Q [kvar]
1	158.09	58.55	-112.22	-36.08	209.50	53.14	-122.05	-45.21	201.62	50.70
2	217.74	54.71	-140.49	-55.95	217.57	91.70	-143.12	-51.69	183.34	67.92
3	214.69	84.03	-134.05	-56.19	166.00	56.43	-143.94	-36.56	169.39	43.51
4	222.27	70.97	-124.26	-38.06	194.07	80.11	-127.56	-33.46	192.32	71.50
5	180.68	59.23	-100.61	-37.39	189.06	55.07	-98.27	-30.94	210.06	57.66
6	196.28	71.65	-147.44	-46.86	183.61	46.45	-103.07	-26.09	190.02	67.23
7	234.11	94.64	-105.92	-38.73	153.01	63.63	-100.93	-30.08	186.22	67.17
8	173.28	73.16	-145.47	-47.11	149.84	39.50	-92.51	-34.54	190.03	74.57
9	127.20	45.72	-103.43	-43.72	174.20	73.73	-96.42	-30.61	181.42	73.80
10	224.01	89.09	-112.41	-30.31	147.33	46.20	-126.99	-49.30	129.91	49.09
11	195.74	59.86	-95.25	-27.77	216.53	63.84	-146.38	-55.63	206.35	63.09

C.3 Additional Results

In Section 5.1.2, only the charts of the trend of the whole result differences for this sensitivity analysis in positive sequence are presented. In this appendix, the charts displaying the plots from the sensitivity analysis in negative sequence are provided additionally. The results differences for voltage magnitude sensitivity analysis are illustrated in Figure B.1 and Figure B.3. The mean values of all sensitivity types shown in this section are provided in Table C.5. They are shown in dash line in the figures.

Table C.5: Mean result differences of each grid sensitivity type (unit: [%])

Sensitivity type	**Mean**		
	Phase a	**Phase b**	**Phase c**
Svir,2	-0.873	-0.355	0.242
Svii,2	-0.040	-0.056	0.487
Sphiir,2	0.016	0.030	-0.495
Sphiii,2	0.717	0.343	-0.261

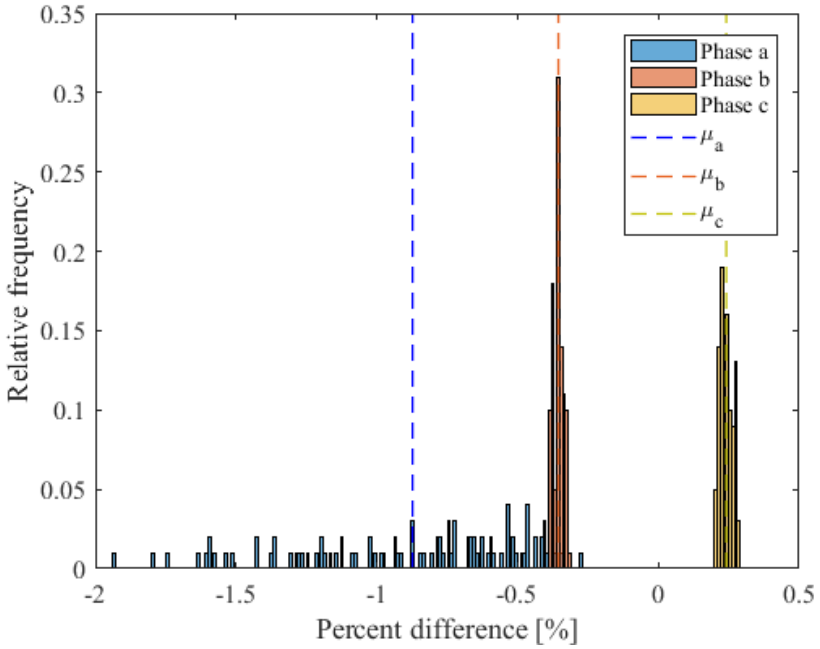

Figure C.1: Histogram of the whole result differences in *Svir*,2 of the exemplified mesh grid

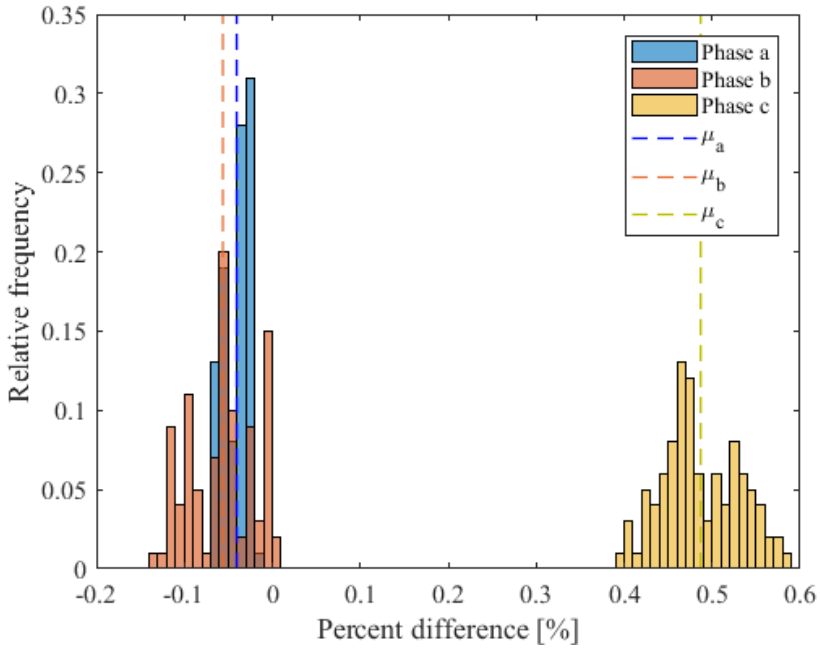

Figure C.2: Histogram of the whole result differences in *Svii*,2 of the exemplified mesh grid

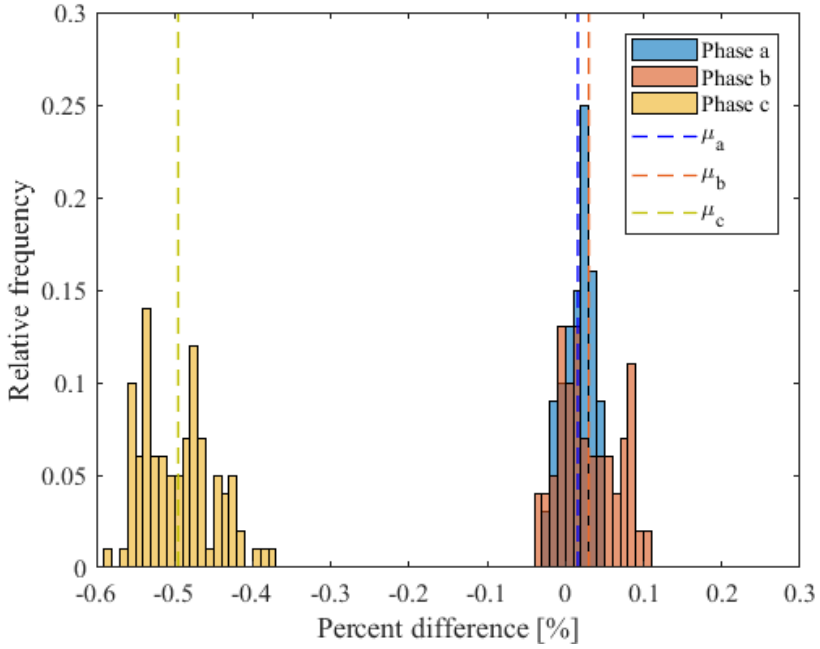

Figure C.3: Histogram of the whole result differences in *Sphiir*,2 of the exemplified mesh grid

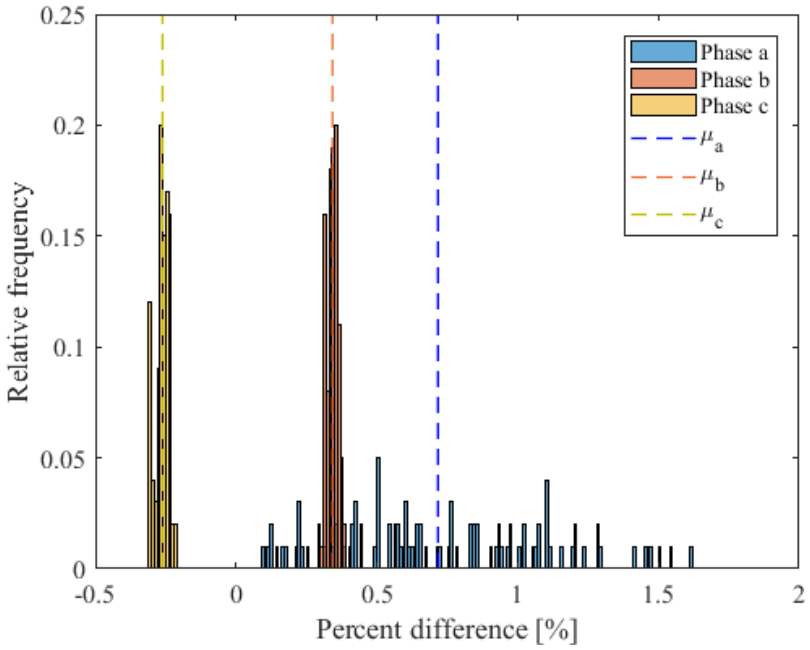

Figure C.4: Histogram of the whole result differences in *Sphiii*,2 of the exemplified mesh grid

The sensitivities *Svir*,2 can be paired to *Sphiii*,2 and *Svii*,2 can be paired to *Sphir*,2 in the case of negative sequence, identical to the case of positive sequence in Chapter 5. Based on the proposed analysis method in Chapter 4, their characteristics are the opposite of each other. Also, the histograms in Figure C1 to Figure C4 demonstrate that the results from the proposed method in this case still achieve high accuracy. The dispersion of the histograms is small, and the mean values are close to zero.

Appendix D: Additional Information of Cluster-Based Grid

This appendix delivers the additional information, which is not covered in the main content for the exemplified mesh grid in Case Study 2 and Case Study 3. First, the configurations of this grid are provided. Then, active and reactive powers data used as the inputs in the simulations are shown. Finally, the additional results are demonstrated to complete the presented results of the verification in Chapter 5.

D.1 Grid Configurations

A radial power grid from an actual distribution grid in Borden-Etteln provided by Westfalen Weser Netz is adapted for the simulations. The clustering power systems approach is applied to this grid to form a cluster-based grid to examine the decoupled voltage sensitivity analysis by the proposed method. The simulation is executed at the nominal voltage of 400 V and the frequency of 50 Hz. The topological information of this modified grid is provided in Table D.1.

Table D.1: Cable connection information

From bus	To bus	Length [km]	Element Type
100	101	-	0.4 MVA 20/0.4 kV
101	111	0.0926	NAYY 4x240SE 0.6/1kV
101	102	0.1541	NAYY 4x240SE 0.6/1kV
101	106	0.0294	NAYY 4x240SE 0.6/1kV
111	112	0.0399	NAYY 4x185SE 0.6/1kV
112	113	0.0435	NAYY 4x185SE 0.6/1kV
113	114	0.0309	NAYY 4x185SE 0.6/1kV
114	115	0.0303	NAYY 4x185SE 0.6/1kV
115	116	0.0699	NAYY 4x185SE 0.6/1kV
102	103	0.0450	NAYY 4x185SE 0.6/1kV
103	104	0.0390	NAYY 4x185SE 0.6/1kV
104	105	0.0855	NAYY 4x185SE 0.6/1kV
106	107	0.1345	NAYY 4x185SE 0.6/1kV
107	108	0.0360	NAYY 4x185SE 0.6/1kV
108	109	0.0561	NAYY 4x185SE 0.6/1kV
109	110	0.0600	NAYY 4x185SE 0.6/1kV

The parameters of each element in Table D.1 can be found in Table D.2 to Table D.4. The rest of parameters other than provided here are set by default from the standard library in PowerFactory.

Table D.2: Parameters of 0.4 MVA 20/0.4 kV transformer

Parameter	Description	Value	Unit
HV bus	Bus on high voltage side	100	-
LV bus	Bus on low voltage side	101	-
Rated Power	-	0.4	MVA
Vector group	-	Dyn5	-

Table D.3: Parameters of NAYY 4x240SE 0.6/1kV cable

Parameter	Description	Value	Unit
r	1, 2 sequence resistance per length	0.1267	Ohm/km
x	1, 2 sequence reactance per length	0.0798	Ohm/km
r0	Zero sequence resistance per length	0.5067	Ohm/km
x0	Zero sequence reactance per length	0.3192	Ohm/km
B	1, 2 sequence susceptance per length	273.3186	µS/km
B0	Zero sequence susceptance per length	132.7951	µS/km

Table D.4: Parameters of NAYY 4x185SE 0.6/1kV cable

Parameter	Description	Value	Unit
r	1, 2 sequence resistance per length	0.1650	Ohm/km
x	1, 2 sequence reactance per length	0.0804	Ohm/km
r0	Zero sequence resistance per length	0.6600	Ohm/km
x0	Zero sequence reactance per length	0.3217	Ohm/km
B	1, 2 sequence susceptance per length	260.7522	µS/km
B0	Zero sequence susceptance per length	121.2341	µS/km

D.2 Inputs for Simulations

This section delivers the inputs used for the simulations in Case Study 2 for the cluster-based grid. There are 15 buses with 16 states, which represent different operational scenarios. First, Table D.5(a) to Table D.5(c) show the inputs for the unbalanced grid condition. Active and reactive powers in phase *a*, *b*, and *c* are represented by *P1* and *Q1*; *P2* and *Q2; and P3* and *Q3*, respectively. The generation process of these inputs is shown in Appendix F.

Table D.5(a): Inputs for the simulation of the cluster-based grid in unbalanced grid condition

State	102						103					
	P1 [kW]	Q1 [kvar]	P2 [kW]	Q2 [kvar]	P3 [kW]	Q3 [kvar]	P1 [kW]	Q1 [kvar]	P2 [kW]	Q2 [kvar]	P3 [kW]	Q3 [kvar]
1	-6.13	-2.37	-5.77	-3.45	3.10	1.24	-3.74	-1.17	-4.72	-2.20	-7.35	-2.72
2	2.63	1.23	-4.50	-1.97	-4.22	-1.24	-3.93	-2.03	7.31	4.50	-4.88	-2.19
3	3.41	0.89	-3.06	-1.20	-6.09	-3.71	6.75	2.20	3.66	1.98	3.07	1.57
4	-5.74	-2.71	-3.84	-1.32	-6.17	-3.42	3.15	1.32	6.47	3.42	-2.84	-1.24
5	-4.11	-2.33	-4.18	-2.26	-6.36	-1.52	4.99	2.09	-3.60	-1.57	-5.62	-2.00
6	4.59	1.95	-3.08	-1.89	4.52	1.07	-6.50	-2.25	-5.17	-2.82	-5.13	-1.58
7	3.24	0.78	-5.17	-2.96	-3.02	-1.39	-3.16	-1.03	-5.75	-2.87	5.36	2.73
8	-6.29	-2.37	-7.67	-2.52	-6.64	-2.05	-7.10	-1.87	3.15	1.07	3.41	1.74
9	-3.44	-1.65	3.90	0.87	4.41	1.09	3.96	2.27	-4.94	-2.34	-6.27	-3.13
10	-3.24	-1.72	-6.09	-2.95	-5.84	-2.17	4.44	1.41	-4.33	-2.60	4.59	1.72
11	2.92	0.85	5.63	1.17	5.64	2.76	7.03	3.90	-7.81	-3.77	-3.18	-0.90
12	-7.77	-1.85	-3.10	-1.57	2.77	1.32	3.92	2.39	3.05	1.37	-3.05	-1.01
13	2.93	1.43	-4.07	-2.33	3.18	1.48	4.28	2.47	7.55	2.28	4.49	1.24
14	7.19	4.29	4.95	2.40	-5.51	-2.03	6.24	3.58	6.20	3.18	-3.19	-0.89
15	-6.72	-3.74	4.96	2.06	5.42	2.46	-2.99	-1.72	-7.90	-2.40	-7.83	-4.38
16	4.79	1.97	-5.91	-2.29	2.92	0.68	-3.10	-0.75	3.61	1.50	-7.10	-2.06

State	104						105					
	P1 [kW]	Q1 [kvar]	P2 [kW]	Q2 [kvar]	P3 [kW]	Q3 [kvar]	P1 [kW]	Q1 [kvar]	P2 [kW]	Q2 [kvar]	P3 [kW]	Q3 [kvar]
1	7.52	2.54	-7.26	-3.30	-6.29	-3.90	2.85	1.26	-3.85	-2.35	-4.45	-2.70
2	5.24	2.34	3.93	2.03	6.35	3.28	-5.29	-1.25	6.18	2.88	-3.61	-1.58
3	6.50	3.15	-7.78	-4.46	-4.69	-2.83	3.41	0.79	-6.08	-2.54	-3.81	-1.02
4	-7.19	-4.31	-4.51	-2.33	2.98	1.38	7.98	2.75	-6.11	-2.35	3.56	1.72
5	3.76	2.05	7.69	4.32	2.87	0.91	-6.42	-3.11	2.70	1.64	3.97	2.06
6	-4.11	-1.74	5.18	2.63	3.41	0.87	7.46	4.52	3.24	1.15	7.91	4.26
7	3.68	1.75	-5.08	-2.95	-4.00	-1.71	-6.51	-2.66	-6.06	-3.40	7.33	4.03
8	6.56	1.72	4.19	1.25	-3.04	-0.95	-5.77	-2.40	3.63	1.47	-3.80	-1.84
9	-3.52	-2.11	-6.35	-1.41	-3.03	-1.26	3.76	1.86	6.13	2.44	-5.68	-2.29
10	5.20	2.40	3.56	1.94	7.81	2.63	-6.46	-1.77	5.39	1.76	7.03	3.70
11	-5.98	-2.55	6.28	2.24	-7.31	-4.51	-7.02	-2.75	-4.83	-2.90	-4.54	-1.78
12	2.84	1.63	6.80	4.12	-3.24	-1.46	3.91	1.53	-4.22	-1.21	3.21	1.00
13	3.53	1.50	-3.82	-1.51	5.50	2.93	-7.67	-3.96	-5.80	-2.81	7.03	4.11
14	4.57	1.31	-2.76	-1.03	3.13	1.60	7.82	4.65	-3.23	-1.55	-6.92	-2.40
15	-4.32	-2.38	4.15	2.52	-4.29	-0.96	3.07	1.59	-4.08	-2.06	-4.91	-1.87
16	-4.84	-2.74	4.45	2.75	6.82	3.73	-3.51	-1.89	-4.64	-1.95	-3.48	-1.57

State	106						107					
	P1 [kW]	Q1 [kvar]	P2 [kW]	Q2 [kvar]	P3 [kW]	Q3 [kvar]	P1 [kW]	Q1 [kvar]	P2 [kW]	Q2 [kvar]	P3 [kW]	Q3 [kvar]
1	7.19	3.06	-3.68	-1.53	7.03	4.15	-5.21	-2.10	3.18	0.74	-3.37	-2.02
2	-6.84	-2.09	-6.50	-3.86	-6.55	-2.79	4.88	2.96	-7.72	-4.41	6.48	3.92
3	3.19	1.14	3.41	1.81	3.10	1.45	6.67	3.99	6.79	2.96	-4.40	-1.35
4	-5.20	-3.14	-3.73	-2.14	-3.68	-1.45	6.32	3.20	-3.16	-0.70	-3.20	-1.52
5	-7.61	-4.33	-3.64	-1.52	4.63	1.94	3.16	1.85	-7.30	-2.79	2.81	1.36
6	2.96	1.59	-7.18	-3.05	2.88	1.56	3.86	2.16	-6.72	-2.66	-7.26	-3.14
7	6.11	3.26	6.41	3.82	-4.87	-2.84	6.98	3.42	7.98	3.61	-5.22	-1.40
8	3.28	1.84	-3.11	-0.65	-2.68	-1.65	-3.40	-2.06	6.40	2.63	-6.58	-3.13
9	6.08	3.27	-7.07	-3.76	6.27	3.76	-4.52	-1.61	3.38	0.87	-6.81	-2.72
10	-5.54	-2.90	6.86	3.49	4.69	2.38	3.58	1.38	-7.68	-3.74	6.68	3.92
11	3.46	0.81	-4.62	-2.38	-5.61	-1.82	-4.45	-2.49	-4.13	-2.23	-7.60	-3.82
12	-5.91	-2.95	3.37	2.04	-6.11	-3.07	3.46	2.07	-3.03	-1.43	6.07	3.46
13	-4.53	-2.34	3.94	1.70	-3.55	-1.40	-7.43	-3.54	-6.81	-3.57	2.69	1.44
14	-7.78	-3.71	-5.60	-2.97	6.35	1.32	7.94	3.61	3.45	1.59	-6.64	-3.23
15	4.42	2.27	7.52	3.58	4.22	1.61	-5.52	-3.03	-4.09	-1.60	-2.71	-1.43
16	7.43	2.48	3.98	0.94	3.61	1.54	3.29	0.92	-3.19	-1.37	3.19	1.74

Table D.5(b): Inputs for the simulation of the cluster-based grid in unbalanced grid condition

State	108						109					
	P1 [kW]	Q1 [kvar]	P2 [kW]	Q2 [kvar]	P3 [kW]	Q3 [kvar]	P1 [kW]	Q1 [kvar]	P2 [kW]	Q2 [kvar]	P3 [kW]	Q3 [kvar]
1	3.60	1.75	4.42	2.09	-3.67	-1.07	-4.21	-1.66	-6.77	-2.29	3.09	1.90
2	5.60	3.41	3.39	1.16	-5.71	-2.43	7.93	3.30	-6.25	-3.18	-6.67	-3.76
3	-5.50	-1.57	3.02	0.81	4.57	1.18	7.81	2.34	4.06	1.77	-5.60	-2.59
4	6.76	2.70	-3.86	-2.36	-5.87	-2.91	7.57	1.74	3.68	1.20	-6.04	-1.99
5	4.95	1.44	4.45	2.55	7.84	1.91	4.00	2.37	-3.53	-1.46	-7.56	-2.78
6	3.04	1.33	-6.07	-2.85	-7.80	-1.93	4.71	1.27	-6.05	-1.41	-4.73	-1.67
7	7.64	4.71	-7.98	-2.64	-7.52	-3.06	-3.99	-1.66	-3.33	-1.86	-5.24	-2.39
8	3.38	0.85	3.34	1.44	5.65	3.31	2.87	1.59	5.60	1.45	-3.70	-0.93
9	-5.39	-2.56	3.16	1.06	6.32	3.10	-4.72	-2.56	-3.20	-1.08	-6.39	-1.34
10	6.29	2.17	3.21	1.80	3.40	1.78	4.62	1.65	5.06	2.63	7.98	1.96
11	6.34	3.60	4.33	1.61	5.05	2.66	5.34	2.15	-4.46	-1.74	2.76	1.26
12	-4.24	-1.30	7.13	2.81	2.83	1.53	-7.03	-2.86	3.68	1.67	-3.35	-0.87
13	-4.08	-1.05	7.33	4.53	3.03	1.88	-5.34	-1.19	6.62	3.81	-5.00	-2.42
14	6.08	1.97	6.84	2.34	-5.71	-1.53	-5.55	-2.27	-5.48	-2.31	-3.62	-1.45
15	-2.69	-0.90	3.25	0.68	2.64	1.21	3.49	2.04	-2.84	-0.63	-3.21	-1.34
16	-7.38	-3.52	7.11	4.10	-7.39	-3.03	4.70	2.64	-6.64	-3.08	7.12	2.08

State	110						111					
	P1 [kW]	Q1 [kvar]	P2 [kW]	Q2 [kvar]	P3 [kW]	Q3 [kvar]	P1 [kW]	Q1 [kvar]	P2 [kW]	Q2 [kvar]	P3 [kW]	Q3 [kvar]
1	-4.58	-2.57	4.22	2.31	3.53	0.96	-3.35	-1.23	7.24	3.54	3.92	1.70
2	3.96	1.46	3.25	1.89	-3.24	-0.84	3.35	1.28	-7.62	-3.87	3.19	1.92
3	3.23	0.89	-7.93	-3.29	5.73	2.53	4.85	2.61	3.12	1.01	-5.28	-1.55
4	3.88	1.30	-4.54	-2.38	-6.26	-2.69	-4.36	-1.96	-7.47	-4.08	4.56	1.84
5	-4.28	-2.31	-3.48	-2.07	7.70	1.99	-7.48	-1.82	-2.90	-0.67	4.69	1.71
6	-4.02	-1.98	-6.24	-3.53	6.01	2.46	6.03	3.23	2.86	0.70	-3.87	-1.48
7	-5.74	-2.83	-7.11	-4.28	-3.92	-1.28	-3.57	-1.95	6.08	2.99	-7.61	-2.98
8	-6.79	-3.58	-3.07	-1.13	3.39	1.28	3.94	2.07	3.50	1.75	6.12	1.42
9	-4.56	-2.29	-3.56	-1.15	-4.35	-1.97	6.75	2.20	-4.94	-1.79	5.24	2.93
10	-3.74	-2.21	5.89	1.83	-6.93	-3.77	-4.71	-2.37	6.86	2.42	2.72	1.22
11	3.03	1.39	3.05	1.61	2.86	1.14	7.97	3.19	5.21	1.64	4.48	1.32
12	7.89	3.62	5.81	1.54	5.90	3.28	6.01	3.34	3.35	1.35	5.49	2.43
13	-7.66	-4.67	-3.08	-1.22	5.17	2.85	5.50	3.24	6.77	3.97	-4.03	-1.34
14	4.51	1.74	-7.83	-4.82	7.37	2.09	3.88	1.99	-3.58	-1.50	6.96	3.88
15	6.86	4.11	-7.94	-3.96	-4.00	-2.30	3.12	1.69	-3.95	-2.39	2.92	1.06
16	6.39	3.59	-6.01	-2.57	-3.32	-1.27	-3.36	-0.87	3.43	1.14	-4.55	-1.16

State	112						113					
	P1 [kW]	Q1 [kvar]	P2 [kW]	Q2 [kvar]	P3 [kW]	Q3 [kvar]	P1 [kW]	Q1 [kvar]	P2 [kW]	Q2 [kvar]	P3 [kW]	Q3 [kvar]
1	-6.05	-2.60	5.83	2.22	7.29	3.05	6.70	2.60	3.91	1.63	-4.89	-1.77
2	-3.46	-1.81	7.12	4.05	-6.89	-2.38	3.03	1.85	-4.09	-2.46	-3.85	-2.26
3	-7.50	-2.25	2.77	1.00	-3.99	-2.39	7.26	1.83	-7.76	-2.16	6.84	3.65
4	-5.29	-1.68	-5.68	-2.22	3.81	1.69	3.42	1.55	3.45	0.98	-7.85	-1.91
5	3.99	2.09	3.23	1.96	2.65	1.43	-4.99	-2.16	-7.56	-3.79	-6.41	-2.88
6	6.46	2.55	-5.62	-1.77	2.97	1.49	-6.77	-2.23	-4.82	-1.06	-3.34	-0.91
7	-3.86	-2.26	-3.08	-0.65	-3.45	-1.45	3.16	1.58	-5.71	-1.33	6.09	1.97
8	-7.67	-2.86	6.24	2.90	5.23	1.78	-3.29	-1.29	-3.21	-0.68	-5.44	-3.34
9	6.86	3.42	-3.45	-1.72	-4.61	-2.19	4.30	2.17	5.22	2.95	7.22	2.37
10	-2.95	-1.10	7.11	4.29	3.79	1.66	5.11	2.61	3.54	2.19	7.64	2.79
11	6.93	3.58	-3.52	-1.91	7.07	4.07	-3.21	-1.23	-4.22	-2.25	-3.50	-0.98
12	-4.06	-1.50	4.38	1.79	-4.03	-2.20	3.41	1.59	-4.50	-2.24	7.82	3.20
13	4.29	2.06	3.06	1.23	5.76	2.98	-5.53	-3.23	-7.06	-3.80	-6.53	-2.55
14	-7.79	-3.75	-6.79	-3.61	5.45	2.51	7.32	3.94	-5.94	-1.99	5.13	2.98
15	2.75	1.51	-3.05	-1.16	-6.51	-3.49	2.75	0.61	4.66	2.52	2.95	1.61
16	-4.02	-1.40	7.10	4.25	-6.11	-3.23	-4.69	-1.69	-6.93	-3.19	3.45	2.10

Table D.5(c): Inputs for the simulation of the cluster-based grid in unbalanced grid condition

State	114						115					
	P1 [kW]	Q1 [kvar]	P2 [kW]	Q2 [kvar]	P3 [kW]	Q3 [kvar]	P1 [kW]	Q1 [kvar]	P2 [kW]	Q2 [kvar]	P3 [kW]	Q3 [kvar]
1	-3.27	-1.34	7.64	3.42	-6.59	-2.00	7.35	1.53	6.82	2.28	4.62	1.79
2	-4.08	-1.59	-6.85	-3.90	-4.86	-3.00	6.25	3.02	-3.25	-1.29	7.94	4.24
3	-4.55	-2.24	6.78	3.45	6.72	3.84	-5.92	-1.78	4.31	0.97	-7.00	-2.06
4	-2.64	-1.02	-7.30	-4.09	7.66	3.43	3.03	0.70	-5.55	-1.81	-2.98	-0.88
5	-5.82	-1.56	-6.52	-2.64	7.93	3.25	-4.46	-1.19	-7.25	-2.99	-6.87	-3.15
6	7.21	3.83	3.57	1.35	-3.84	-1.99	6.83	2.01	3.47	1.60	4.70	2.26
7	7.28	3.79	-3.56	-1.77	-4.49	-2.09	-7.02	-2.58	4.26	2.21	6.94	1.58
8	3.10	1.79	-4.17	-2.50	-5.75	-2.76	5.45	3.05	-4.44	-1.49	-6.96	-4.30
9	-7.99	-3.43	5.55	3.35	4.92	2.82	-5.91	-3.17	3.46	2.03	2.84	1.36
10	6.84	2.08	-4.38	-2.63	4.62	1.08	4.64	2.16	-4.21	-2.45	3.23	1.44
11	4.19	2.16	3.29	1.96	-5.73	-2.83	-5.22	-3.19	5.71	1.97	4.22	1.66
12	-7.11	-2.28	-3.06	-1.88	-3.39	-1.01	-5.51	-2.90	-3.61	-1.79	-4.40	-2.62
13	7.96	3.70	-4.49	-0.99	-7.45	-4.51	-5.41	-1.17	4.39	1.79	3.22	1.84
14	-4.23	-1.78	5.99	2.06	3.87	1.82	7.72	3.94	3.60	1.86	-5.62	-2.13
15	5.71	1.21	3.45	1.16	5.37	3.19	-3.42	-1.41	7.57	2.68	3.88	2.11
16	-3.06	-1.11	-7.15	-4.35	6.35	3.24	3.62	1.44	-5.59	-2.76	4.38	2.54

State	116					
	P1 [kW]	Q1 [kvar]	P2 [kW]	Q2 [kvar]	P3 [kW]	Q3 [kvar]
1	-7.48	-3.81	-5.25	-3.24	-5.17	-1.06
2	-6.01	-3.17	-6.89	-3.37	-4.73	-1.53
3	2.73	1.25	-5.11	-1.63	-7.90	-1.66
4	6.41	2.51	6.83	3.15	7.14	3.18
5	5.20	1.63	-5.39	-3.16	2.84	1.64
6	-6.38	-2.66	-2.85	-0.89	-3.03	-1.38
7	-7.22	-4.41	6.91	2.60	2.88	0.98
8	4.07	1.29	-5.67	-2.61	-3.96	-1.47
9	-2.81	-1.48	-3.22	-1.38	-4.01	-1.11
10	-2.65	-0.80	3.41	1.47	7.86	2.62
11	-4.24	-1.55	3.13	1.22	-2.92	-1.15
12	-4.12	-1.65	3.99	1.53	4.96	2.60
13	6.91	3.34	-4.79	-2.65	4.04	2.03
14	-3.20	-1.91	-2.91	-0.91	5.55	1.65
15	4.98	1.02	5.59	3.09	-4.73	-2.29
16	-5.78	-2.17	7.19	3.41	-4.59	-2.72

Table D.6 then provides the inputs for the simulation in balanced grid condition. Active and reactive powers *P* and *Q*, shown in the table, are per phase. The generation process of these inputs is shown in Appendix F. In this case, the inputs at the same bus of all states are set to have the same sign.

Table D.6: Inputs for the simulation of the cluster-based grid in balanced grid condition

State	102		103		104		105		106	
	P [kW]	Q [kvar]	P [kW]	Q [kvar]	P [kW]	Q [kvar]	P [kW]	Q [kvar]	P [kW]	Q [kvar]
1	-6.57	-2.54	13.92	5.12	-7.42	-2.00	15.75	4.80	-7.66	-2.52
2	-6.78	-2.21	12.49	4.71	-7.22	-1.95	14.12	5.49	-5.99	-2.28
3	-5.87	-1.65	11.29	4.08	-7.42	-2.05	10.79	4.41	-5.45	-1.90
4	-8.19	-3.26	8.48	2.91	-8.17	-3.21	15.34	5.99	-7.41	-2.93
5	-8.48	-2.93	12.00	4.59	-5.08	-2.15	15.58	4.49	-8.88	-3.65
6	-7.90	-2.44	12.13	4.25	-8.95	-3.69	10.66	4.22	-7.98	-3.02
7	-5.52	-2.15	12.14	5.12	-5.35	-1.64	10.02	2.77	-5.45	-2.15
8	-5.38	-1.56	12.05	4.88	-8.60	-3.25	11.59	3.47	-5.70	-1.61
9	-5.37	-1.79	11.38	4.64	-5.95	-2.34	13.92	3.85	-6.29	-1.96
10	-5.78	-1.48	13.24	4.56	-8.24	-3.36	8.78	3.70	-5.35	-1.99
11	-6.77	-1.86	13.77	3.63	-7.46	-2.75	14.26	5.55	-8.06	-2.56
12	-6.27	-1.87	13.33	4.93	-6.12	-2.29	10.17	3.67	-7.06	-2.58
13	-7.58	-2.08	11.95	3.14	-7.60	-2.49	9.03	3.26	-5.67	-1.92
14	-7.97	-2.99	8.77	3.32	-8.55	-3.63	15.59	6.07	-7.32	-2.96
15	-6.33	-1.94	14.48	5.67	-6.52	-2.69	14.55	4.03	-5.85	-1.86
16	-8.27	-2.91	11.16	4.57	-8.47	-2.85	9.01	3.72	-5.62	-1.97

State	107		108		109		110		111	
	P [kW]	Q [kvar]	P [kW]	Q [kvar]	P [kW]	Q [kvar]	P [kW]	Q [kvar]	P [kW]	Q [kvar]
1	11.51	4.12	-7.56	-2.01	13.10	3.74	-6.33	-1.69	15.77	4.36
2	14.23	5.14	-6.60	-1.71	13.81	4.12	-6.95	-1.81	10.92	4.26
3	8.87	3.07	-5.72	-2.23	13.68	4.38	-8.92	-3.72	11.48	4.05
4	13.56	4.56	-8.47	-3.11	13.32	5.61	-8.78	-2.37	14.97	4.05
5	8.48	3.04	-8.56	-2.72	10.76	2.70	-5.61	-1.56	8.72	2.89
6	12.65	3.71	-7.04	-2.66	13.98	4.14	-8.98	-3.81	15.67	6.58
7	10.99	3.96	-5.91	-1.57	14.23	5.33	-7.51	-2.92	12.19	4.67
8	10.87	4.26	-8.71	-3.46	13.42	5.63	-5.33	-1.42	10.62	4.11
9	13.74	4.39	-5.80	-1.79	9.48	3.34	-6.78	-2.39	11.93	4.69
10	13.58	3.60	-7.69	-3.15	10.44	3.48	-6.22	-2.21	13.67	4.31
11	14.36	5.68	-6.88	-2.60	10.51	3.59	-6.79	-2.82	9.53	3.21
12	12.68	3.71	-8.37	-2.46	15.99	6.18	-6.09	-2.10	12.50	4.93
13	11.64	4.24	-5.10	-2.06	14.29	4.14	-5.96	-2.18	12.94	3.28
14	9.51	3.29	-6.81	-2.57	13.60	4.09	-8.83	-3.28	9.22	3.89
15	9.33	2.51	-6.68	-1.99	14.67	4.53	-8.36	-3.55	15.62	4.99
16	15.02	5.44	-5.19	-1.97	10.93	3.14	-8.53	-2.54	9.68	3.98

State	112		113		114		115		116	
	P [kW]	Q [kvar]	P [kW]	Q [kvar]	P [kW]	Q [kvar]	P [kW]	Q [kvar]	P [kW]	Q [kvar]
1	-6.53	-2.15	8.43	2.79	-7.25	-2.22	13.32	3.79	-8.69	-2.81
2	-6.30	-2.18	15.76	5.01	-7.40	-2.41	8.34	2.59	-6.68	-2.29
3	-5.36	-1.58	8.75	2.90	-7.48	-1.91	15.60	5.12	-7.64	-2.25
4	-6.08	-1.75	13.25	5.11	-7.60	-2.94	11.57	3.98	-6.68	-2.31
5	-8.59	-2.34	10.97	3.45	-5.53	-2.11	11.44	4.44	-8.74	-3.50
6	-7.71	-2.57	12.47	3.40	-6.01	-2.03	13.98	4.33	-7.85	-2.71
7	-6.99	-2.94	14.80	5.42	-7.76	-2.02	9.96	3.37	-8.81	-2.53
8	-6.84	-1.78	14.37	5.42	-6.53	-2.53	13.94	3.84	-8.66	-3.10
9	-7.20	-1.96	13.79	5.54	-7.24	-2.46	10.28	4.17	-5.73	-2.30
10	-6.32	-2.55	12.57	3.97	-5.79	-1.92	8.49	2.36	-7.67	-2.42
11	-5.75	-1.82	11.08	3.77	-8.14	-2.84	12.90	3.29	-5.39	-2.06
12	-5.46	-2.28	15.02	4.35	-7.48	-2.61	11.03	4.06	-8.94	-3.28
13	-7.34	-2.04	13.97	4.80	-5.92	-2.25	14.55	5.76	-7.97	-2.90
14	-6.46	-2.16	8.54	3.39	-5.36	-2.13	8.41	2.93	-5.85	-2.38
15	-5.30	-2.00	8.33	2.46	-8.93	-3.48	15.06	5.37	-7.47	-1.93
16	-6.32	-2.59	14.81	4.01	-7.59	-2.64	8.65	3.47	-6.34	-1.64

Aside from the verification of the accuracy from the proposed voltage sensitivity analysis, the use of results from the analysis are demonstrated in Case Study 3. Regulations of voltage magnitude and angle are simulated on both unbalanced and balanced grid conditions. The inputs for the initial condition before the regulations are provided in Table D.7 and Table D.8. The active and reactive powers are then combined with the calculated required powers stated in Case Study 3.

Table D.7: Inputs for the simulations of voltage magnitude and angle regulation in unbalanced grid condition

Bus	P1 [kW]	Q1 [kvar]	P2 [kW]	Q2 [kvar]	P3 [kW]	Q3 [kvar]
102	4.79	1.97	-5.91	-2.29	2.92	0.68
103	-3.10	-0.75	3.61	1.50	-7.10	-2.06
104	-4.84	-2.74	4.45	2.75	6.82	3.73
105	-3.51	-1.89	-4.64	-1.95	-3.48	-1.57
106	7.43	2.48	3.98	0.94	3.61	1.54
107	3.29	0.92	-3.19	-1.37	3.19	1.74
108	-7.38	-3.52	7.11	4.10	-7.39	-3.03
109	4.70	2.64	-6.64	-3.08	7.12	2.08
110	6.39	3.59	-6.01	-2.57	-3.32	-1.27
111	-3.36	-0.87	3.43	1.14	-4.55	-1.16
112	-4.02	-1.40	7.10	4.25	-6.11	-3.23
113	-4.69	-1.69	-6.93	-3.19	3.45	2.10
114	-3.06	-1.11	-7.15	-4.35	6.35	3.24
115	3.62	1.44	-5.59	-2.76	4.38	2.54
116	-5.78	-2.17	7.19	3.41	-4.59	-2.72

Table D.8: Inputs for the simulations of voltage magnitude and angle regulation in balanced grid condition

Bus	P1 [kW]	Q1 [kvar]	P2 [kW]	Q2 [kvar]	P3 [kW]	Q3 [kvar]
102	-18.50	-8.96	-18.50	-8.96	-18.50	-8.96
103	-15.33	-9.10	-15.33	-9.10	-15.33	-9.10
104	-19.40	-10.47	-19.40	-10.47	-19.40	-10.47
105	-22.50	-13.94	-22.50	-13.94	-22.50	-13.94
106	3.00	1.69	3.00	1.69	3.00	1.69
107	2.06	1.23	2.06	1.23	2.06	1.23
108	1.76	0.88	1.76	0.88	1.76	0.88
109	-5.80	-3.31	-5.80	-3.31	-5.80	-3.31
110	-5.78	-2.24	-5.78	-2.24	-5.78	-2.24
111	-6.26	-2.18	-6.26	-2.18	-6.26	-2.18
112	-5.97	-3.46	-5.97	-3.46	-5.97	-3.46
113	4.10	1.85	4.10	1.85	4.10	1.85
114	-5.39	-2.28	-5.39	-2.28	-5.39	-2.28
115	-2.42	-1.00	-2.42	-1.00	-2.42	-1.00
116	-5.73	-3.50	-5.73	-3.50	-5.73	-3.50

D.3 Additional Results for Accuracy Verification

In Section 5.2.2, only the charts comparing the trend of the whole result differences for the sensitivity analysis in positive sequence at phase *a* are presented for all defined grid cases. In this appendix, instead of continuing showing the comparison among different grid cases, the histograms of the whole result differences in all phases of the entire grid case are demonstrated because the results produced by decoupled analysis in cluster areas are clarified in Chapter 5 that they are accurate around the results of the entire grid case. The charts displaying the plots from the sensitivity analysis in zero and negative sequences are further provided here. The mean values of all sensitivity types shown in this section are provided in Table D.9. They are plotted in dash line in the figures.

Table D.9: Mean of result differences of each grid sensitivity type (unit: [%])

Sensitivity type	**Mean**		
	Phase a	**Phase b**	**Phase c**
Svir,0	-0.656	-0.243	0.920
Svir,2	-1.423	0.633	-0.197
Svii,0	0.441	-1.522	0.802
Svii,2	0.157	-1.026	-0.671
Sphiir,0	0.101	1.639	-0.525
Sphiir,2	1.720	0.540	0.081
Sphiii,0	2.986	0.164	0.324
Sphiii,2	3.018	-1.443	-0.111

The result differences for the case of sensitivities *Svir*,0 and *Svir*,1 for all phases are portrayed in Figure D.1 and Figure D.2.

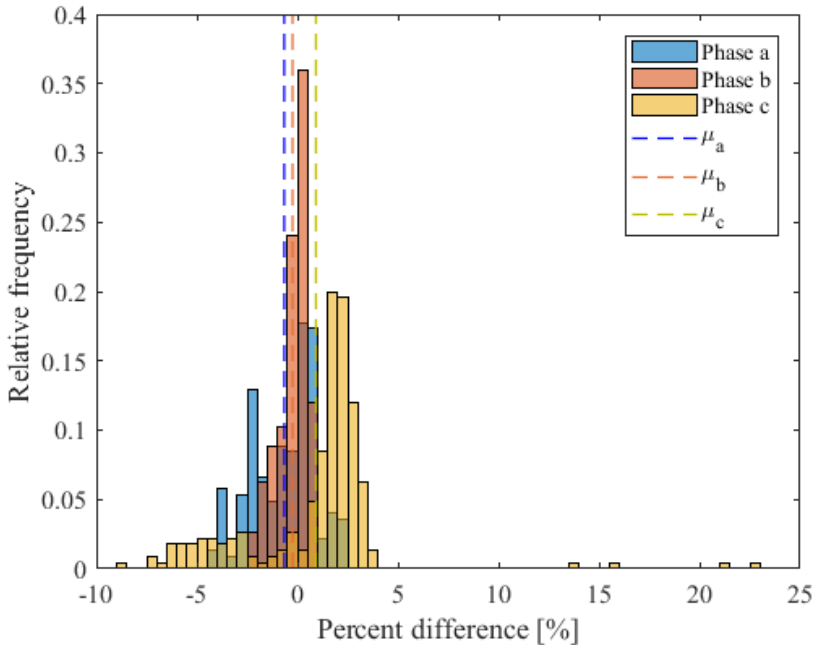

Figure D.1: Histogram of the whole result differences in *Svir*,0 of the cluster-based grid

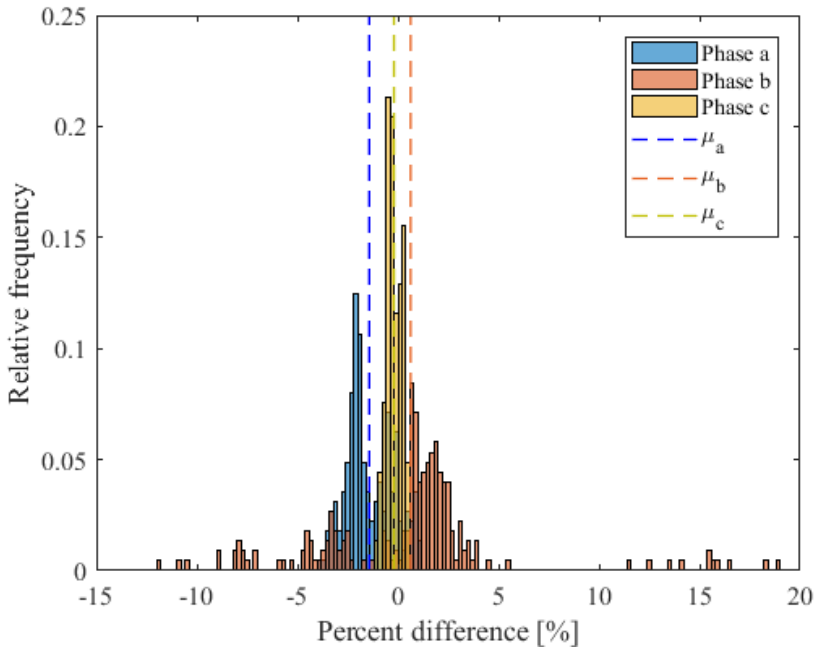

Figure D.2: Histogram of the whole result differences in *Svir*,2 of the cluster-based grid

The result differences for the case of sensitivities *Svii*,0 and *Svii*,2 for all phases are portrayed in Figure D.3 and Figure D.4.

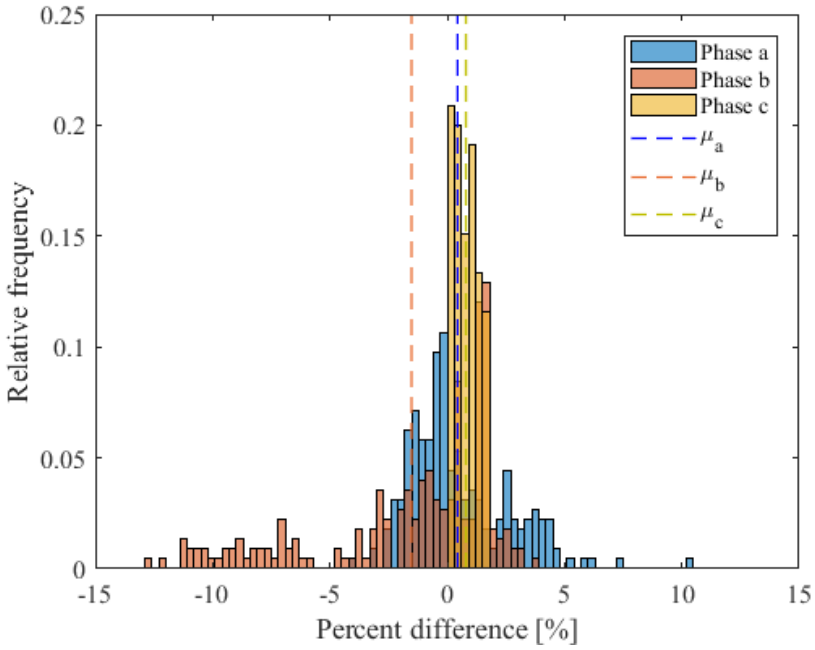

Figure D.3: Histogram of the whole result differences in *Svii*,0 of the cluster-based grid

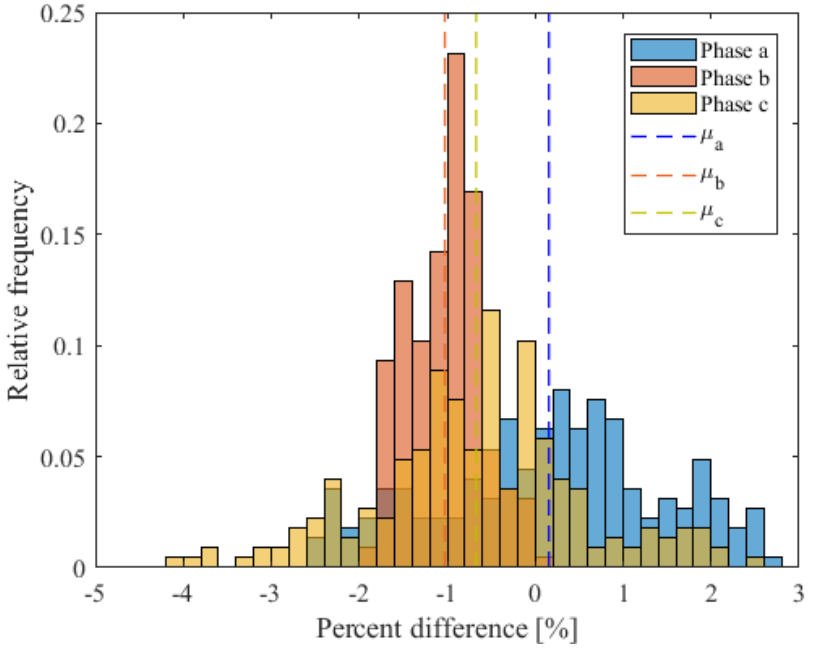

Figure D.4: Histogram of the whole result differences in *Svii*,2 of the cluster-based grid

The result differences for the case of sensitivities *Sphiir*,0 and *Sphiir*,2 for all phases are portrayed in Figure D.5 and Figure D.6.

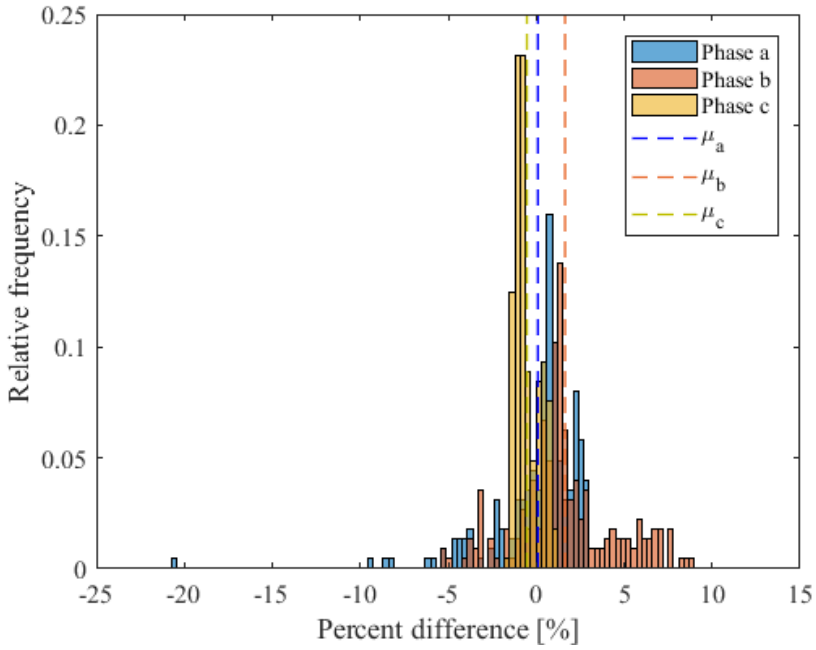

Figure D.5: Histogram of the whole result differences in *Sphiir*,0 of the cluster-based grid

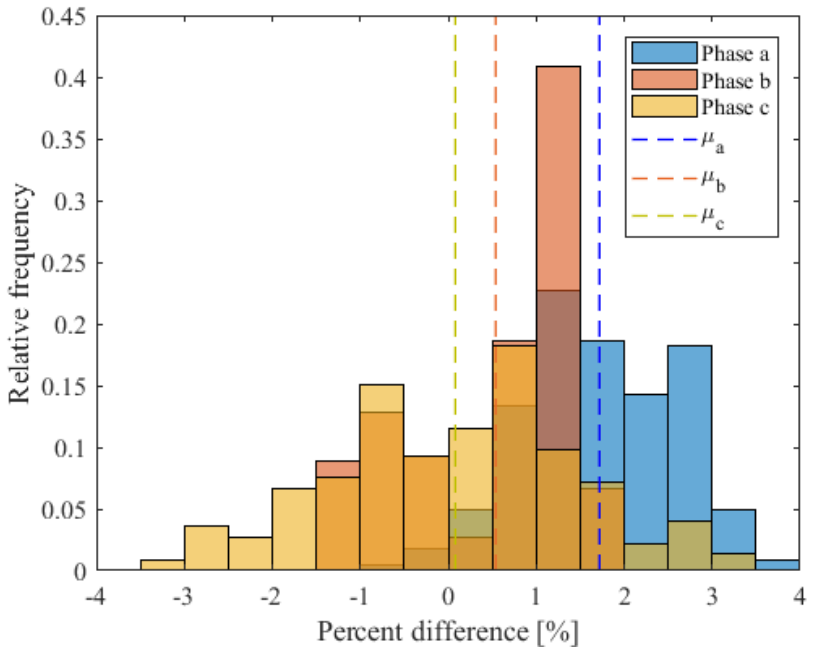

Figure D.6: Histogram of the whole result differences in *Sphiir*,2 of the cluster-based grid

The result differences for the case of sensitivities *Sphiii*,0 and *Sphiii*,2 for all phases are portrayed in Figure D.7 and Figure D.8.

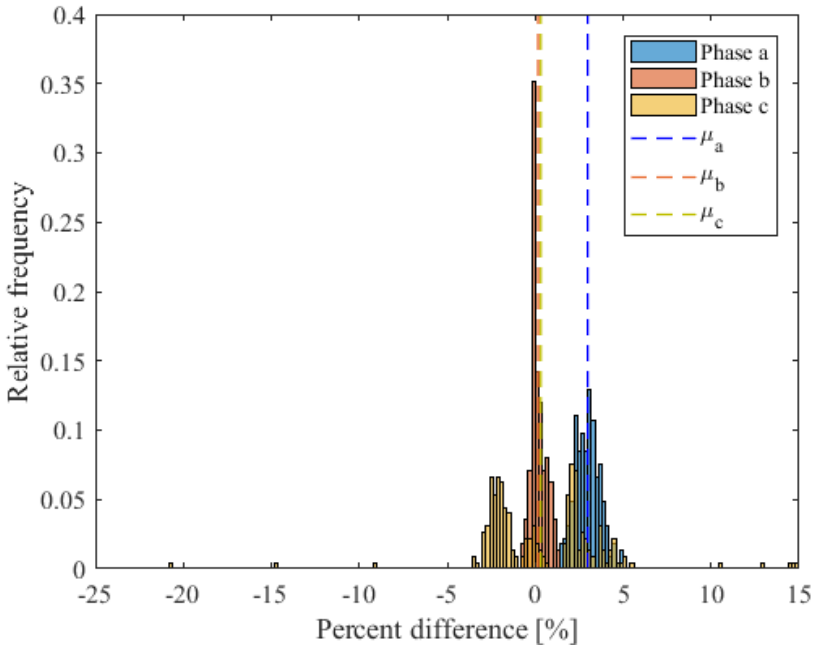

Figure D.7: Histogram of the whole result differences in *Sphiii*,0 of the cluster-based grid

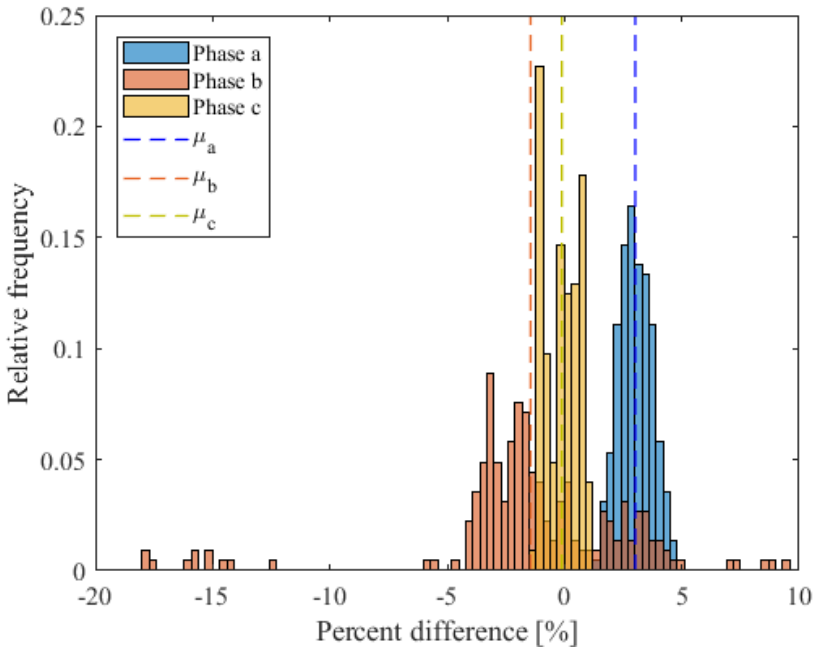

Figure D.8: Histogram of the whole result differences in *Sphiii*,2 of the cluster-based grid

Owing to the proposed method, the sensitivities *Svir* can be paired to *Sphiii* and *Svii* can be paired to *Sphir* in the case of negative and zero sequences, identical to the case of positive sequence shown in the Case Study 2. The histograms in Figure C1 to Figure C8, together with the results from the Case Study 2, show that the results from the proposed method possess high accuracy for any complex sequence current. The dispersion of the histograms is small, and the mean values are close to zero.

D.4 Additional Results for Experiment on Measurement Errors

In Section 5.2.3, only the charts comparing the trend of the whole result differences for the sensitivity analysis in positive sequence are presented. In this appendix, the charts displaying the plots from the sensitivity analysis in zero and negative sequences are shown additionally. For any type of the analysis, the mean of the result differences increases as the TVE level increases, as occurred with the result differences in the positive sequence.

Starting from voltage magnitude sensitivity analysis, the mean of result differences for the sensitivities *Svir*,0 and *Svir*,2 are illustrated in Figure D.9 and Figure D.10.

Figure D.9: Mean of absolute result differences of *Svir*,0 in each grid case at different levels of TVE

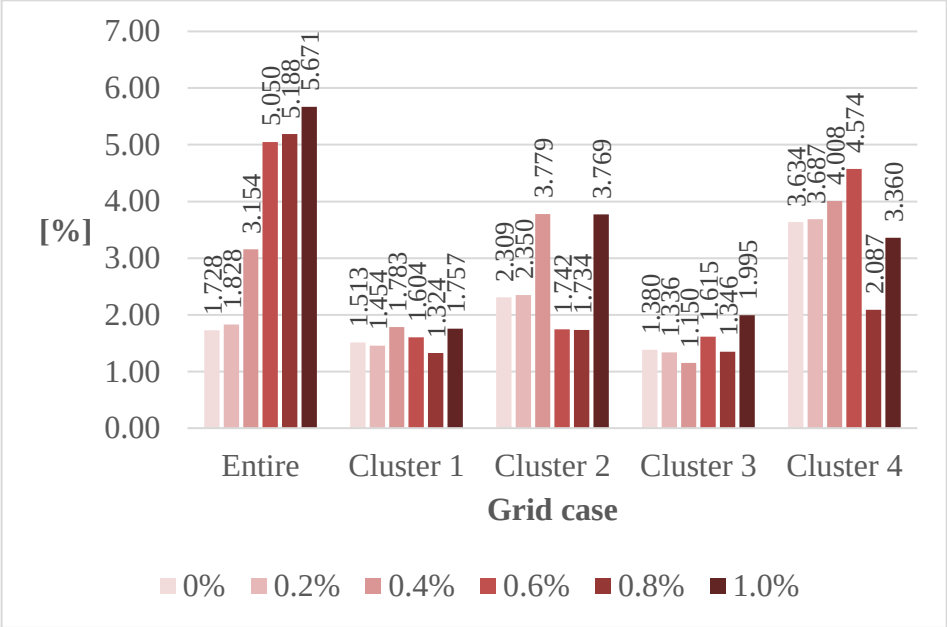

Figure D.10: Mean of absolute result differences of *Svir*,2 in each grid case at different levels of TVE

Next, mean of the result differences for the sensitivities *Svii*,0 and *Svii*,2 are illustrated in Figure D.11 and Figure D.12.

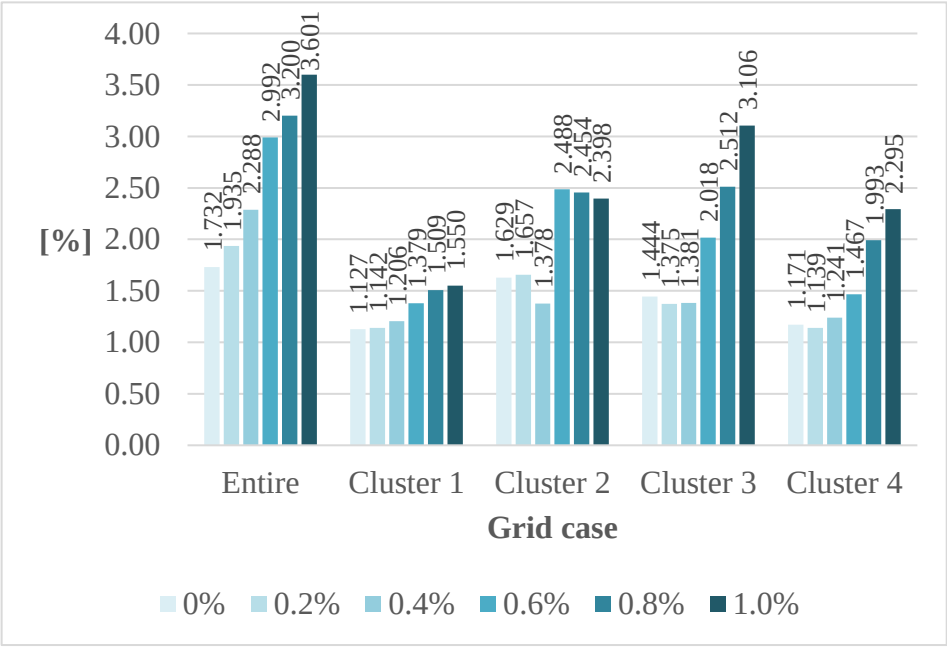

Figure D.11: Mean of absolute differences of *Svii*,0 in each grid case at different levels of TVE

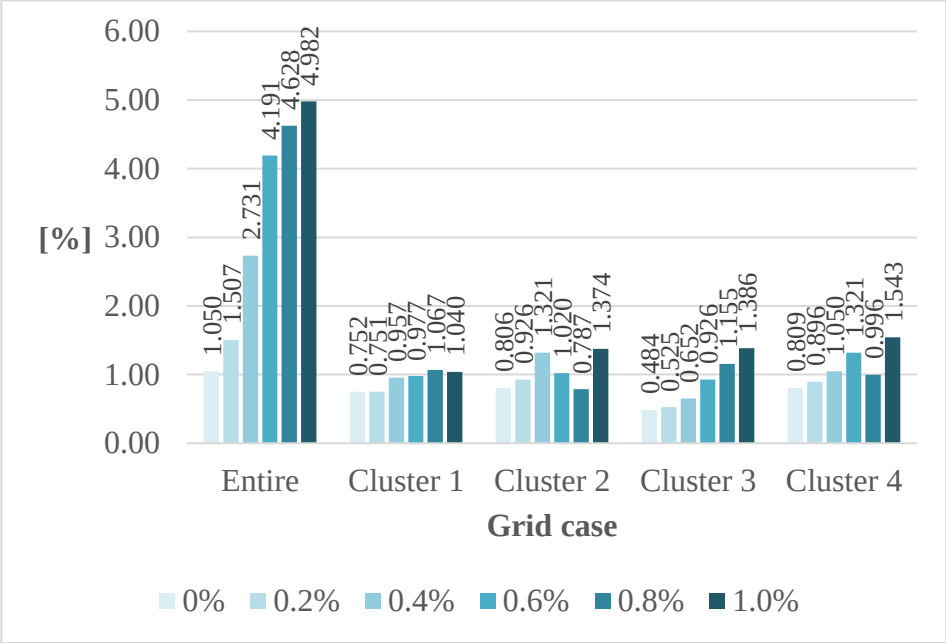

Figure D.12: Mean of absolute differences of *Svii*,2 in each grid case at different levels of TVE

For voltage angle sensitivity analysis, mean of result differences for the sensitivities *Sphiir*,0 and *Sphiir*,2 are illustrated in Figure D.13 and Figure D.14.

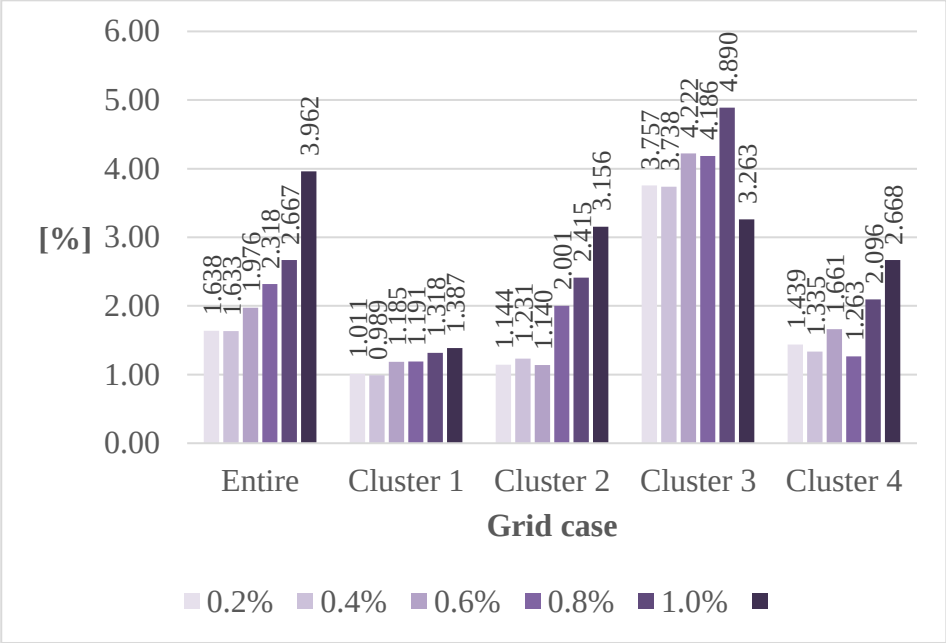

Figure D.13: Mean of absolute differences of *Sphiir*,0 in each grid case at different levels of TVE

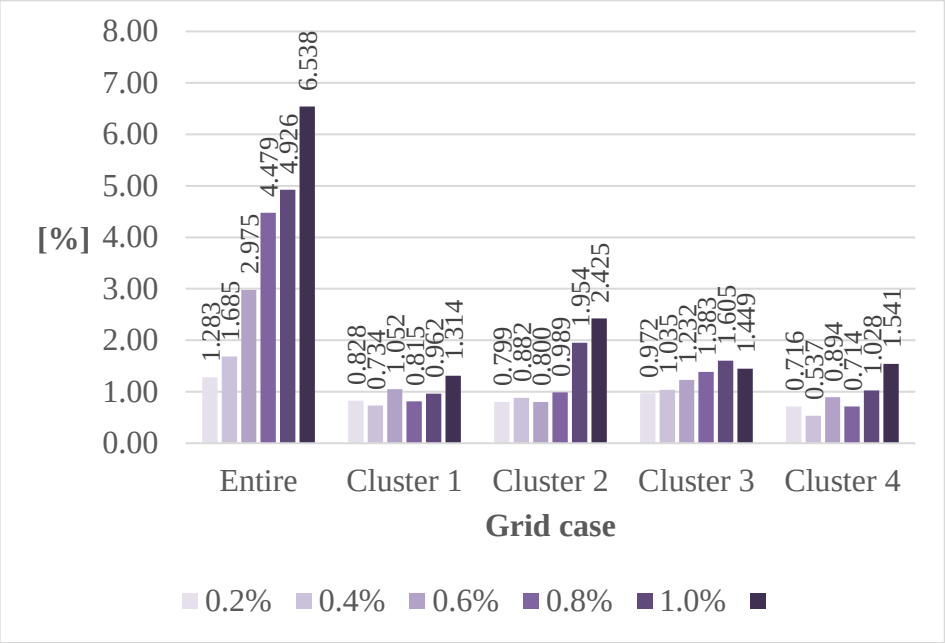

Figure D.14: Mean of absolute differences of *Sphiir*,2 in each grid case at different levels of TVE

For voltage angle sensitivity analysis, mean of result differences for the sensitivities *Sphiir*,0 and *Sphiir*,2 are illustrated in Figure D.15 and Figure D.16.

Figure D.15: Mean of absolute differences of *Sphiii*,0 in each grid case at different levels of TVE

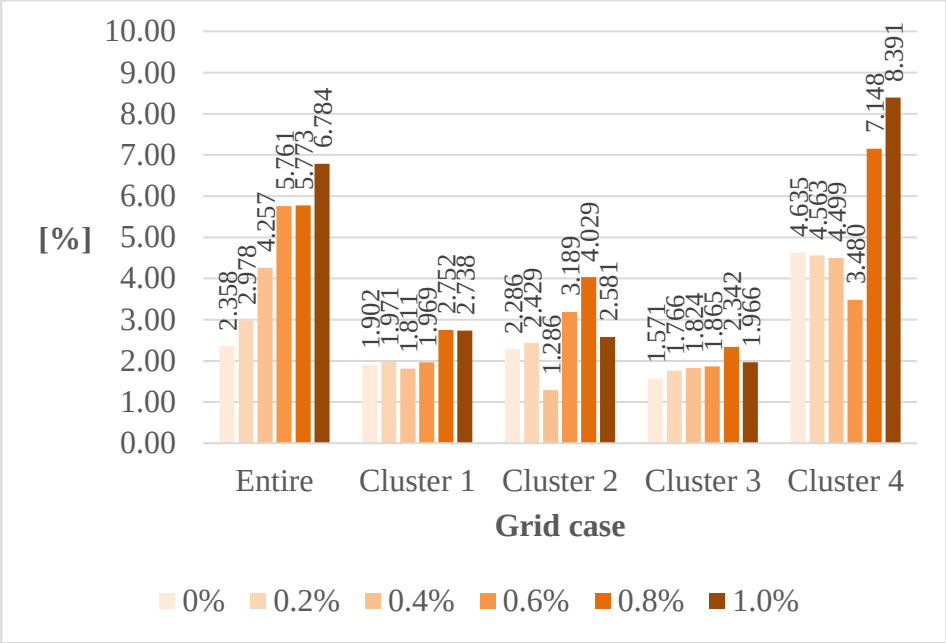

Figure D.16: Mean of absolute differences of *Sphiii*,2 in each grid case at different levels of TVE

Appendix E: Analysis of the Impact Phase Angle on the Proposed Method

This appendix provides the additional results of analysing the impact of phase angle on the outcome of the proposed method. This analysis is conducted to investigate the characteristics of the histograms of the results from the proposed analysis method in Case Study 1, since the histograms among different phases in this case study are shifted from each other in the same sensitivity analysis under the unbalanced grid condition. Based on Eqs. (4.31), (4.35), (4.46), and (4.51), the complex voltages are understood to play a direct role in the voltage sensitivity analysis. For the clarification purpose, the shift among the distributions is further examined on the modified IEEE 37-bus test feeder case by adjusting reference angle for the simulation. The angle is adjusted by adding ±30º, ±60º, and ±120º to the original reference angle, which is 0º, used in this case study.

In Chapter 5, only the results for the sensitivity *Svir*,1 are provided and discussed. Therefore, the rest of the results are shown in this appendix. The histograms resulted from the adjusting the reference angle are depicted in Figure E1 to Figure E6 for the sensitivities *Svii*,1, *Sphiir*,1, *Sphiii*,1, *Svir*,2, *Svii*,2, and *Sphiir*,2, respectively. All figures contain the charts from adding ±30º, ±60º, and ±120º. In the meantime, the histograms for *Sphiii*,2 are divided into Figure E7 and Figure E8, since the charts in the case of ±120˚ require more space.

By observing the histograms in each figure, the characteristics of the histograms are clearly affected by the phase angle. The characteristics can be divided here into two parts for the cases related positive sequence, which are *Svii*,1, *Sphiir*,1, and *Sphiii*,1, and negative sequence current, which are *Svir*,2, *Svii*,2, *Sphiir*,2, and *Sphiii*,2.

For the sensitivity types related to positive sequence, the histograms in the case of adding ±30º are clearly different from the histograms in the case of adding ±60º and ±120º. However, the histograms in the case of ±60º and ±120º are relevant. They have inverse relationship between each other. For instance, in the case of *Svii*,1, the histograms in Figure E1(c) are identical to the histograms in Figure E1(f), whereas the histograms in Figure E2(d) are identical to the histograms in Figure A3(e). This relationship is related to the angle of the vectors of both cases. The vectors in the case of -60º are the negative of that of the case +120º, and the vectors in the case of +60 º are the negative of that of the case -120º. The phase angle thus affects the outcome of the voltage sensitivity analysis. These characteristics can also be observed in Figure E2 and Figure E3 for the sensitivities *Sphiir*,1, and *Sphiii*,1.

For the sensitivity types related to negative sequence, nonetheless, the distribution of all histograms varies. This happens because, in addition to the impact of phase angle shift, the outcome of the sensitivities *Svir*,2, *Svii*,2, *Sphiir*,2, and *Sphiii*,2 are different in for each target voltage and angle at phase *a*, *b*, or *c*. The histograms related to negative sequence can be seen in Figure E4 to Figure E8.

To conclude, the characteristics of the histograms or the distribution of the final results from the proposed method are based on two factors: the variation of the sensitivity values from each analysis and the phase angle of the voltage vectors. From the experiments, these factors together can impact the height and the alignment of the distribution of the analysis results among different phases when the results are compared with their reference. However, the accuracy of the sensitivity analysis obviously still can be ensured, as the dispersion of the histograms are small and their mean is close to zero.

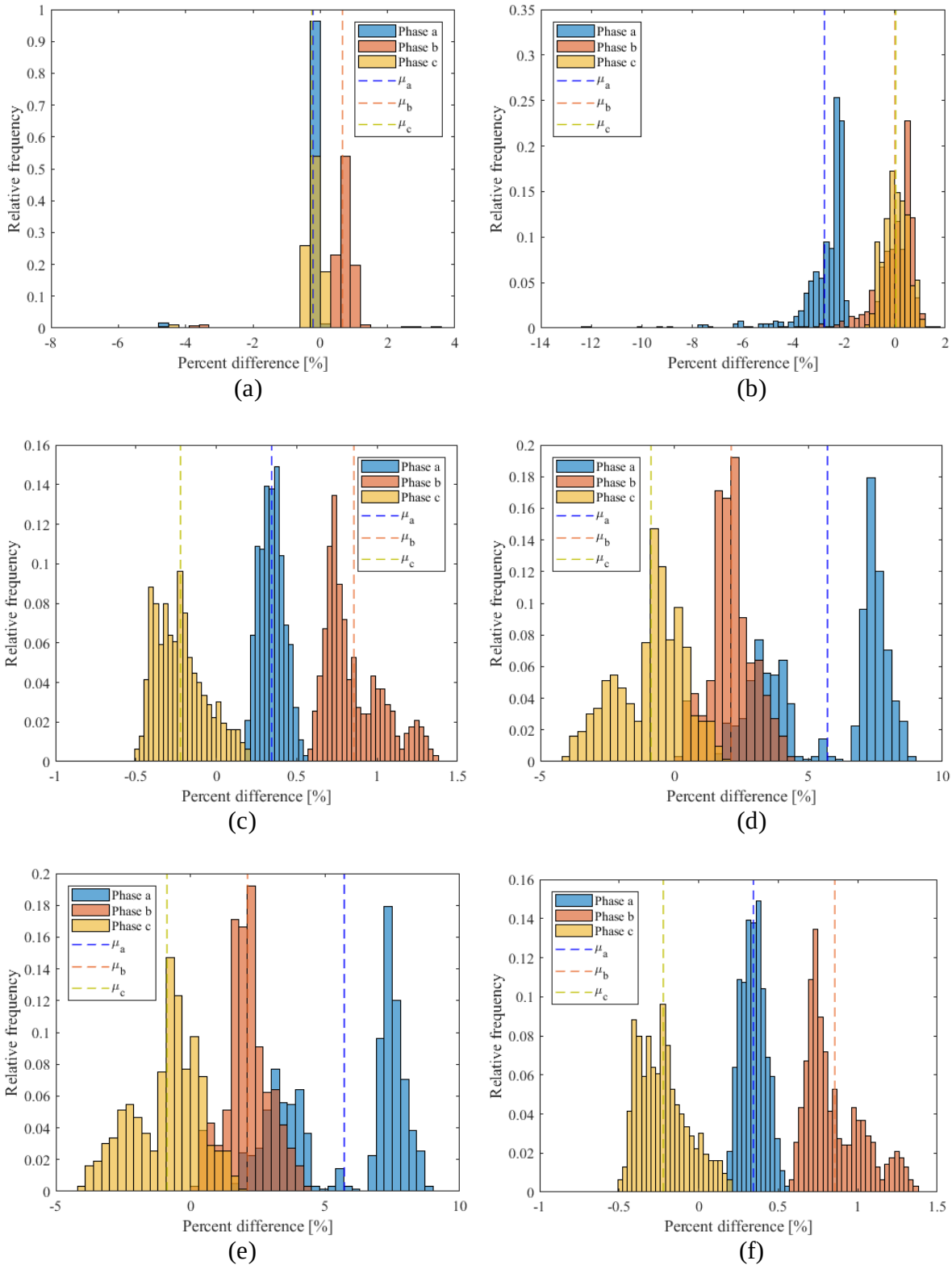

Figure E.1: Histogram of the whole result differences in *Svii*,1 of the modified IEEE 37-bus test feeder case; (a) Reference angle -30º; (b) Reference angle +30º; (c) Reference angle -60º; (d) Reference angle +60º; (e) Reference angle -120º; (f) Reference angle +120º

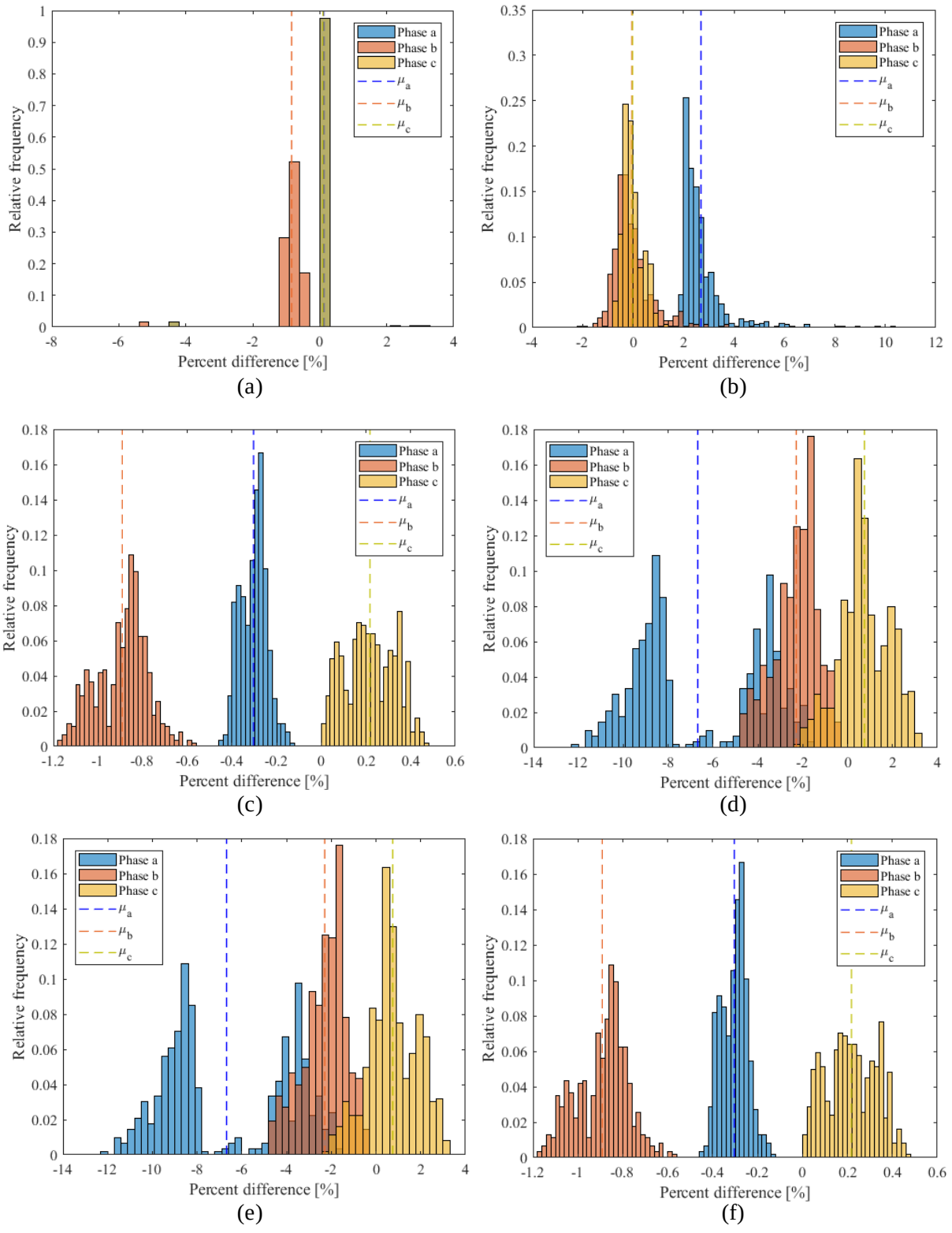

Figure E.2: Histogram of the whole result differences in *Sphiir*,1 of the modified IEEE 37-bus test feeder case; (a) Reference angle -30º; (b) Reference angle +30º; (c) Reference angle -60º; (d) Reference angle +60º; (e) Reference angle -120º; (f) Reference angle +120º

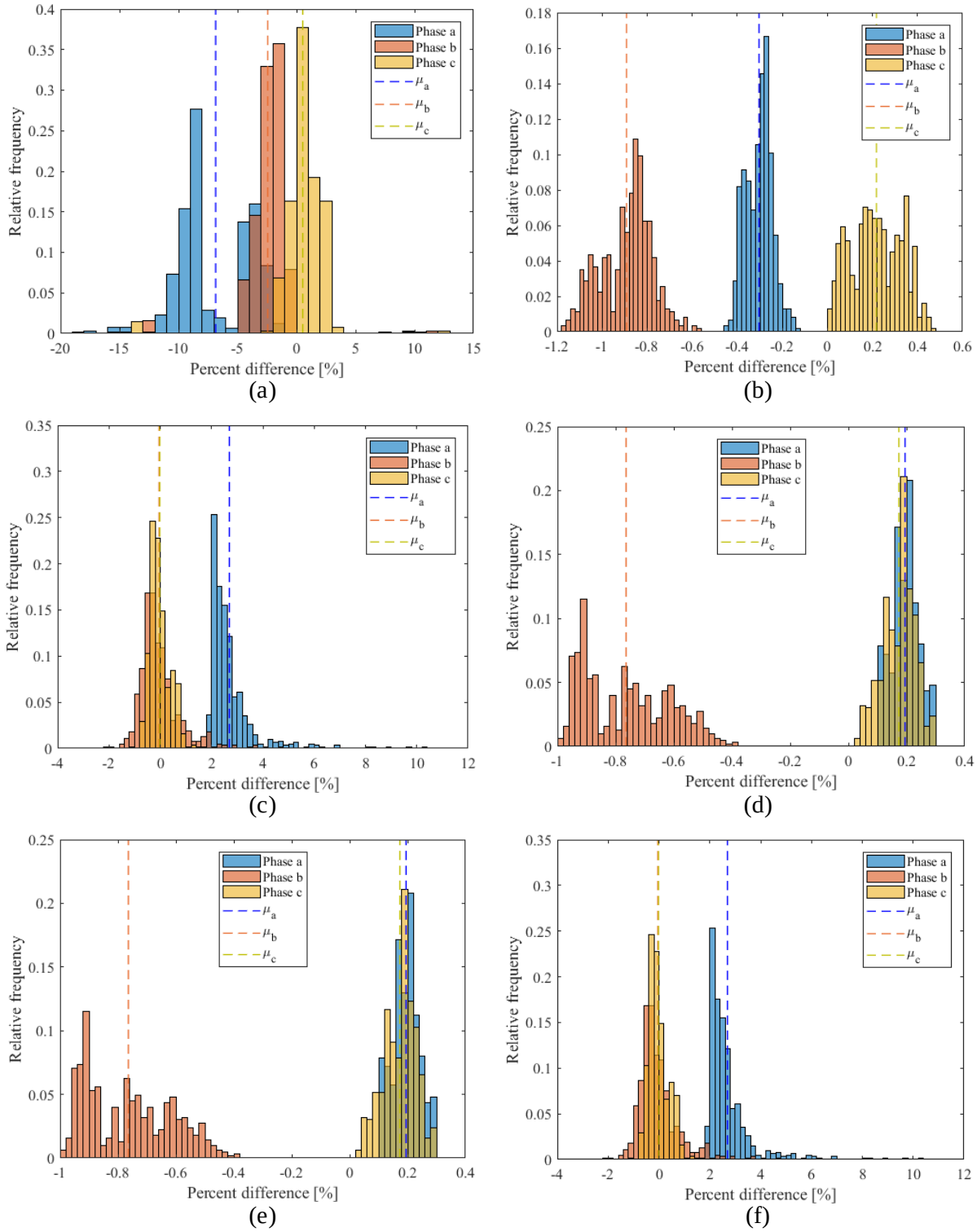

Figure E.3: Histogram of the whole result differences in *Sphiii*,1 of the modified IEEE 37-bus test feeder case; (a) Reference angle -30º; (b) Reference angle +30º; (c) Reference angle -60º; (d) Reference angle +60º; (e) Reference angle -120º; (f) Reference angle +120º

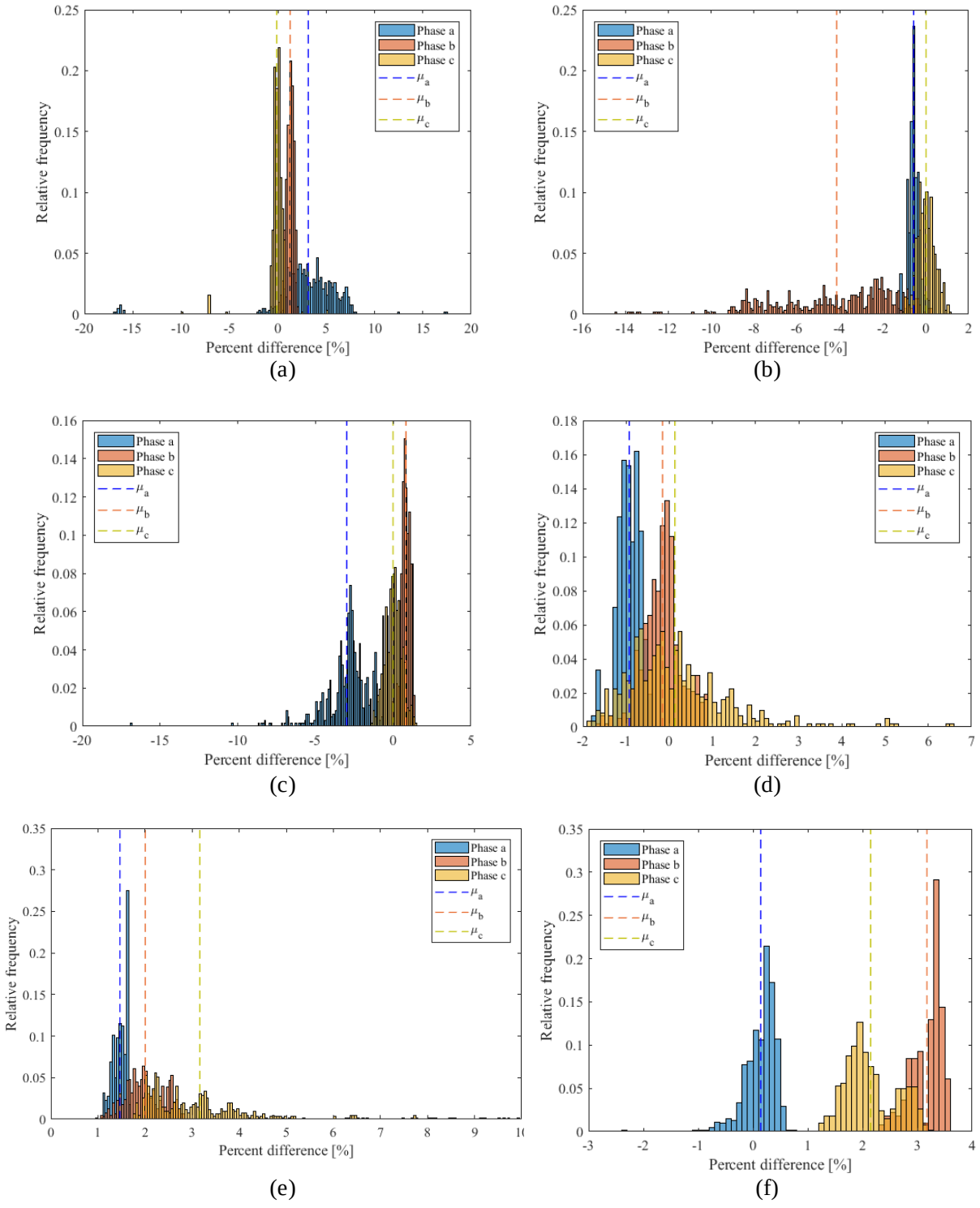

Figure E.4: Histogram of the whole result differences in *Svir*,2 of the modified IEEE 37-bus test feeder case; (a) Reference angle -30º; (b) Reference angle +30º; (c) Reference angle -60º; (d) Reference angle +60º; (e) Reference angle -120º; (f) Reference angle +120º

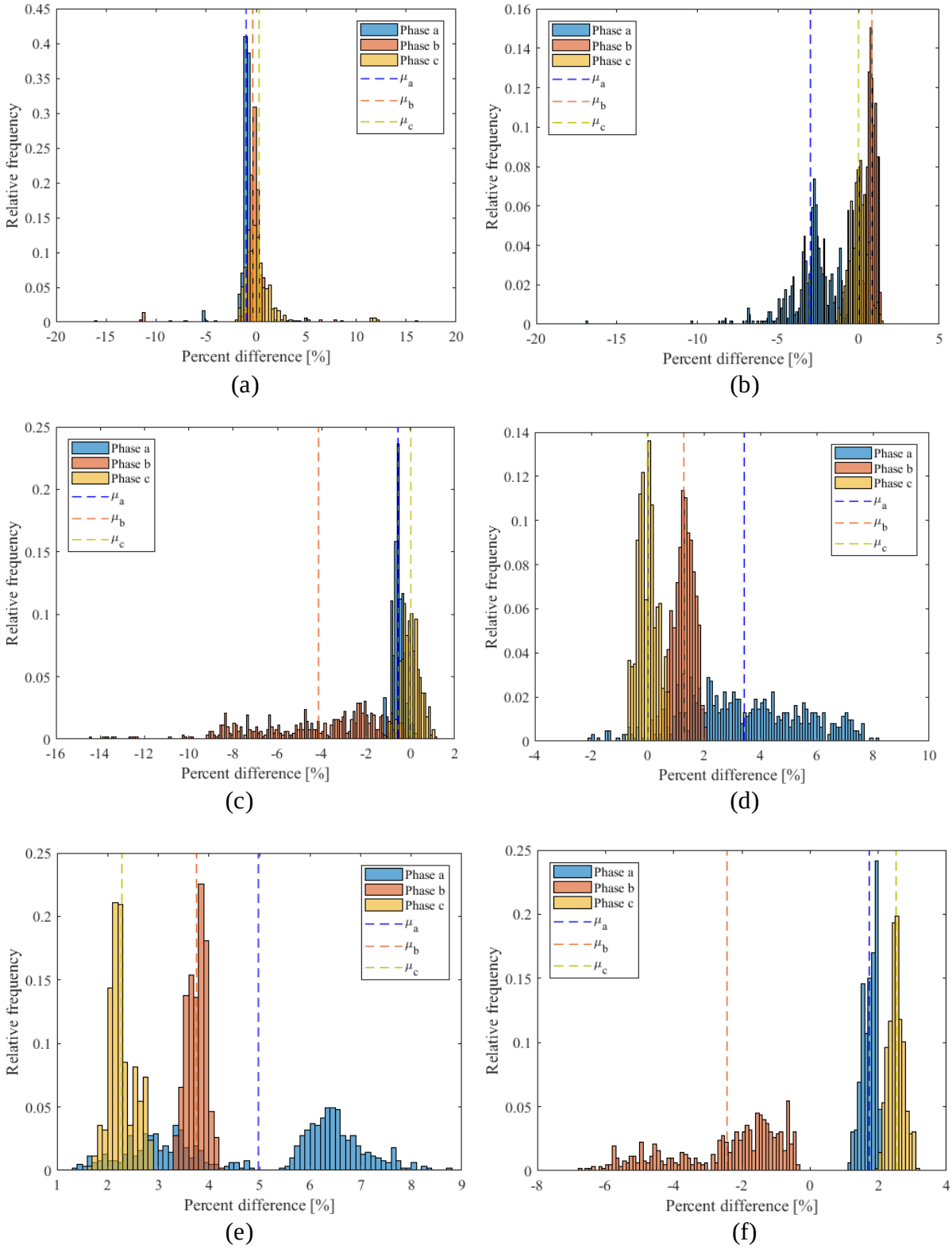

Figure E.5: Histogram of the whole result differences in *Svii*,2 of the modified IEEE 37-bus test feeder case; (a) Reference angle -30º; (b) Reference angle +30º; (c) Reference angle -60º; (d) Reference angle +60º; (e) Reference angle -120º; (f) Reference angle +120º

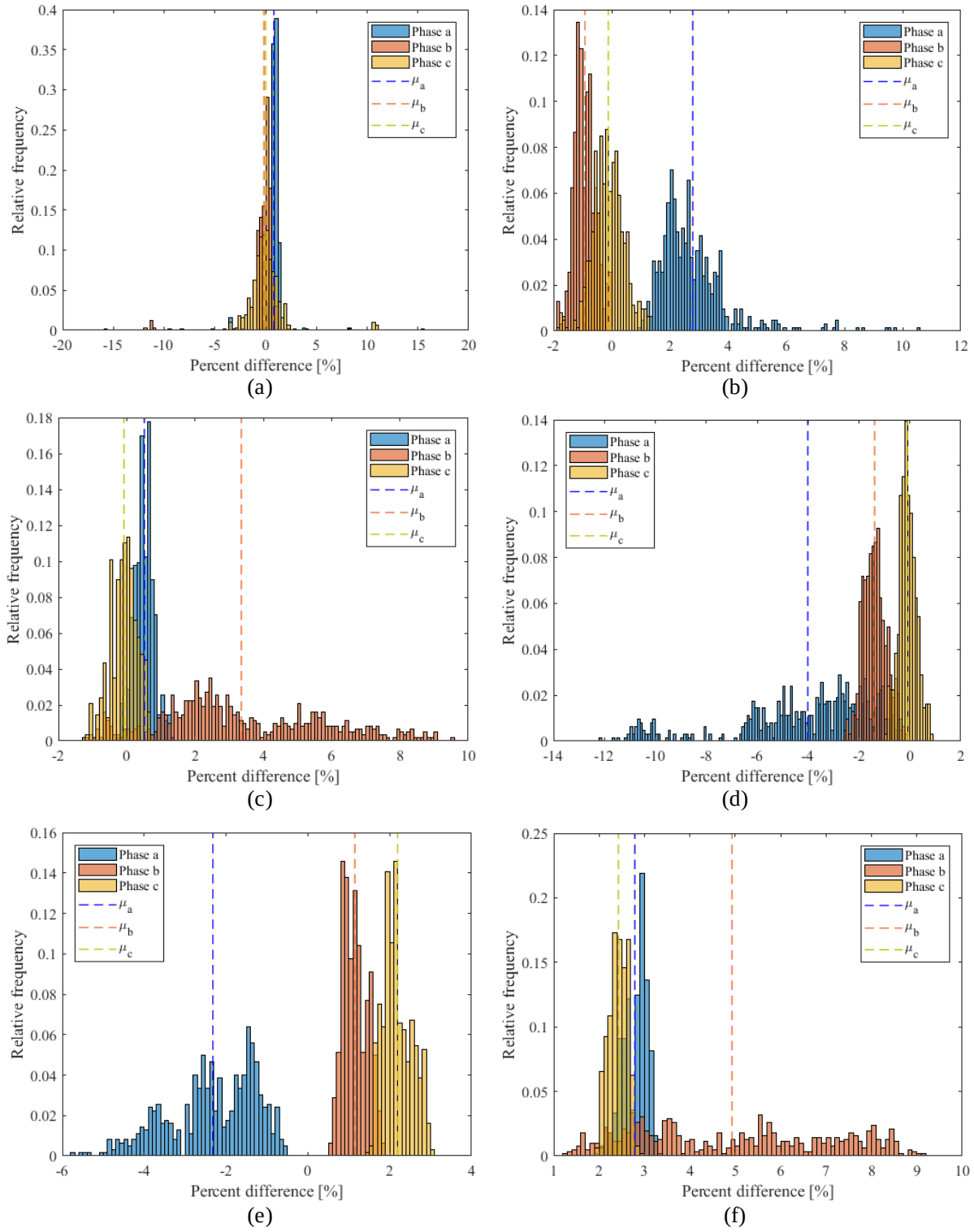

Figure E.6: Histogram of the whole result differences in *Sphiir*,2 of the modified IEEE 37-bus test feeder case; (a) Reference angle -30º; (b) Reference angle +30º; (c) Reference angle -60º; (d) Reference angle +60º; (e) Reference angle -120º; (f) Reference angle +120º

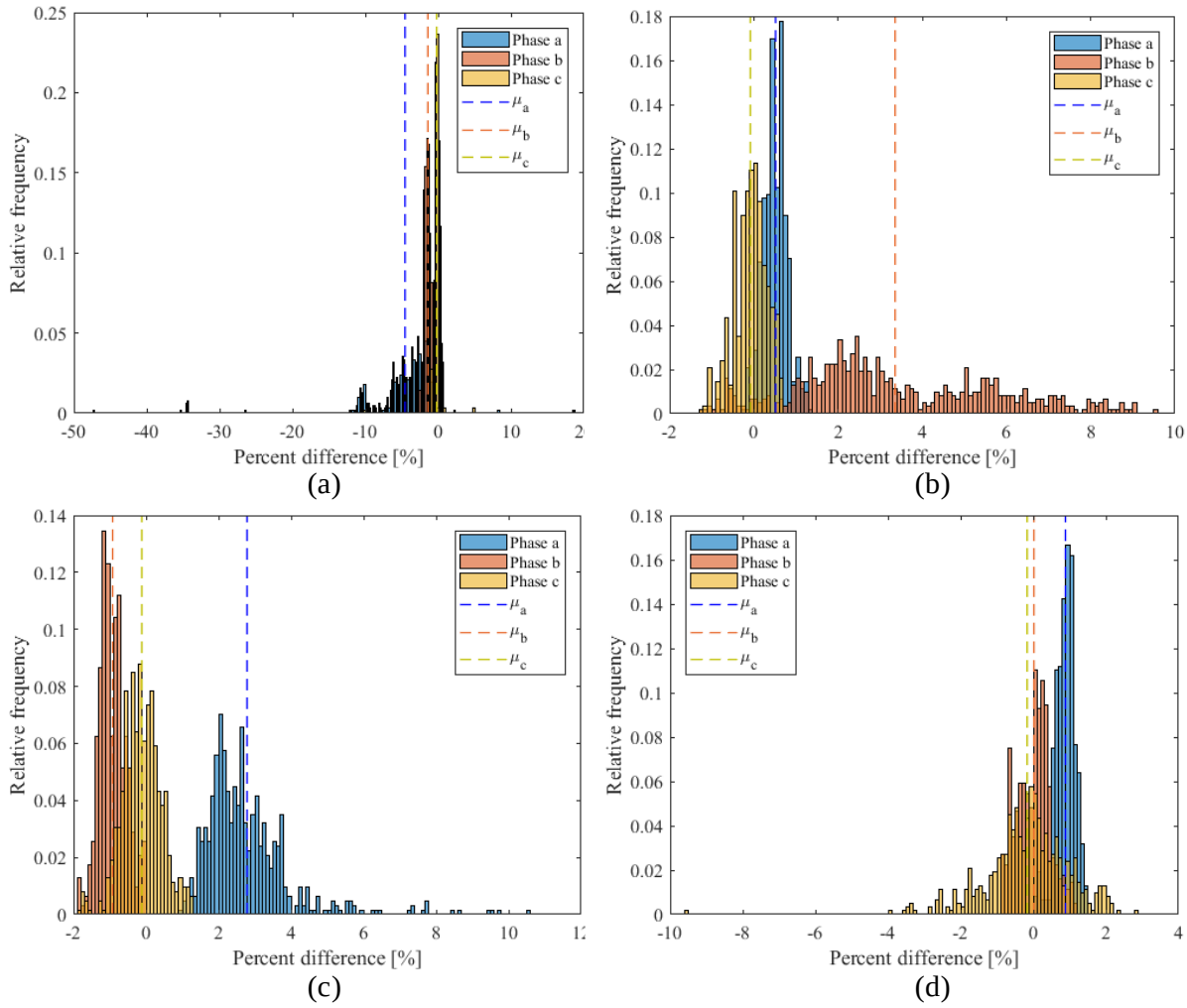

Figure E.7: Histogram of the whole result differences in *Sphiii*,2 of the modified IEEE 37-bus test feeder case; (a) Reference angle -30º; (b) Reference angle +30º; (c) Reference angle -60º; (d) Reference angle +60º

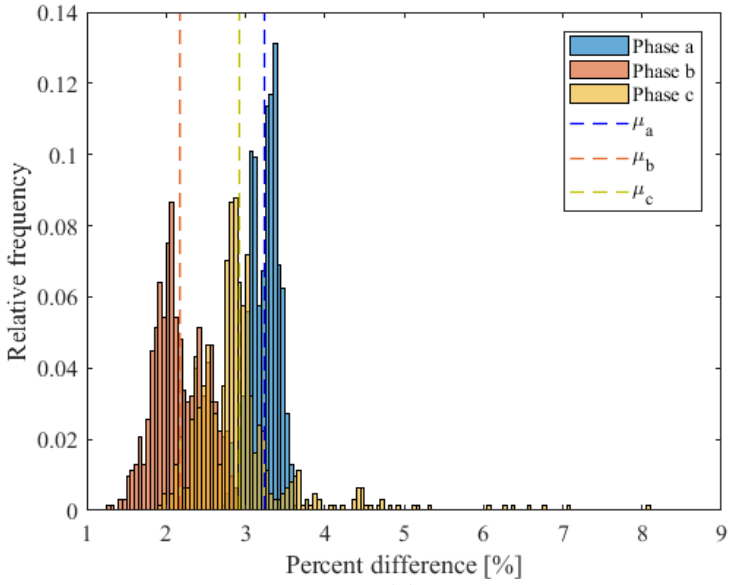

(a)

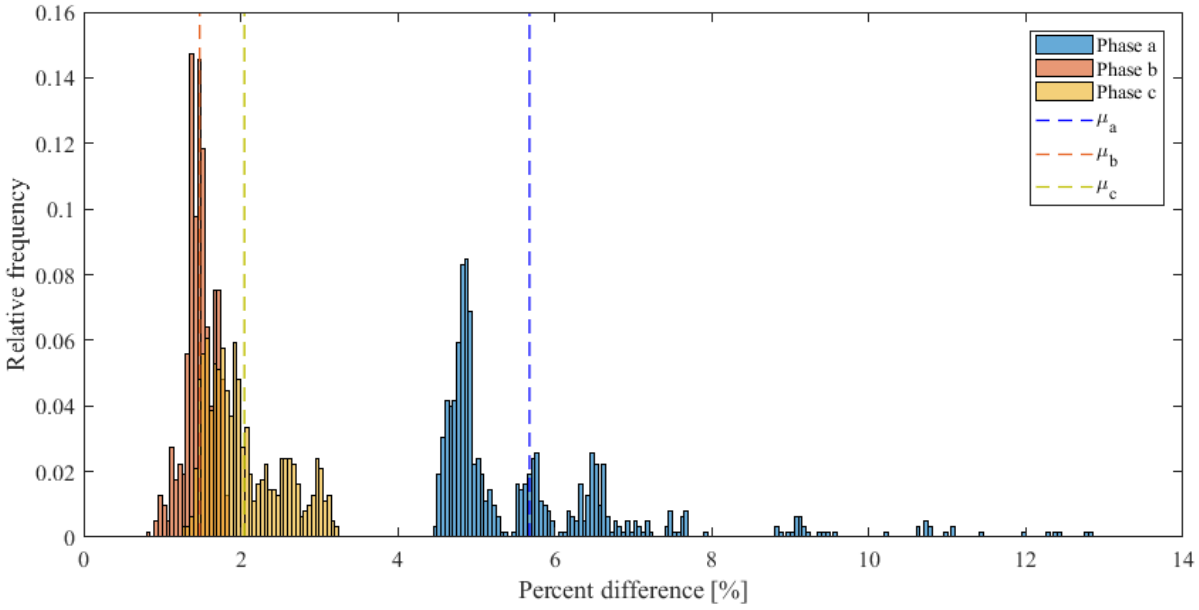

(b)

Figure E.8: Histogram of the whole result differences in *Sphiii*,2 of the modified IEEE 37-bus test feeder case; (e) Reference angle -120º; (f) Reference angle +120º

Appendix F: Generation Process of Inputs for Load Flow Calculation

This appendix provides the process of the generation of active and reactive powers inputs for the load flow calculation in DIgSILENT PowerFactory. Bus voltages and currents resulted from the calculation are referred as the measurement data in this thesis. This process is used for the case studies in Chapter 5. For the load flow calculation, the buses of concern in the case studies are set as the buses with known active and reactive powers, which are randomly generated to represent the amount of load or generation at different time instants. Figure F.1 illustrates the generation process of the inputs.

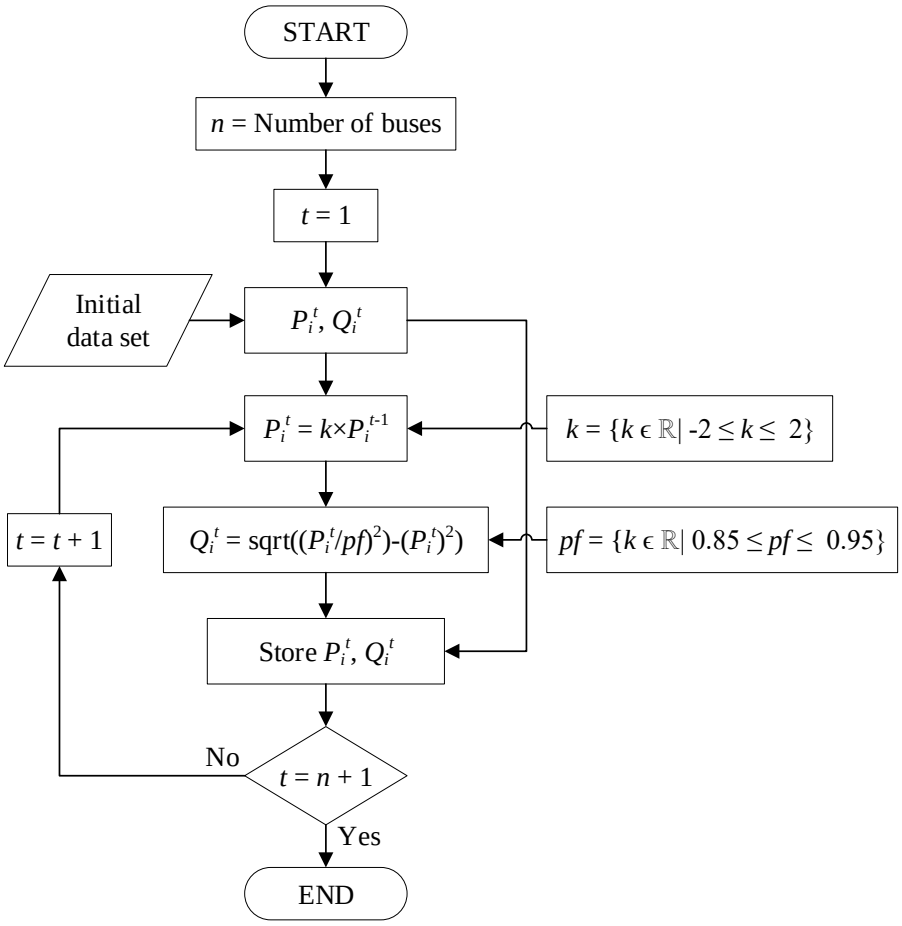

Figure F.1: Generation process of inputs for load flow calculation

Owing to the requirement for determining the bus impedance parameters stated in Chapter 3, the number of inputs required to be generated is n+1 data sets for n+1 time instants, where n is the number of buses in the power grid. In Figure F.1, the initial data set is first acquired from the existing active and reactive power data. The initial data set is first stored in the input

as the first data set. After that, the random generation process starts. In this process, active power P_i^t is randomly generated to begin with. The reactive power Q_i^t is then calculated from the active power P_i^t and the random power factor *pf*. The active power P_i^t in the new data set is related to the active power from the previous set P_i^{t-1}, based on the multiplier *k*. Both the multiplier *k* and the power factor *pf* are a real number in the range of -2 to 2 ($-2 \leq k \leq 2$) and ($0.85 \leq pf \leq 0.95$), respectively. They are generated by the function *rand* for producing random values in MATLAB [F1]. Once n+1 numbers of the input data sets are achieved, the process is finished.

Reference

[F1] MATLAB, *Uniformly distributed random numbers.* [Online] Available: https://de.mathworks.com/help/matlab/ref/rand.html. Accessed on: 30 Oct. 2019.